Lessons from the Ebola epidemic *p. 815*

Safer hydrocyanation via swapping *pp. 817 & 832*

Microbiota and skeletal growth *pp. 830 & 854*

Science

$15
19 FEBRUARY 2016
sciencemag.org

AAAS



Eye on the cosmos

The James Webb Space Telescope takes shape *p. 804*

CONTENTS



815
Lessons from the Ebola epidemic

19 FEBRUARY 2016 • VOLUME 351 • ISSUE 6275



NEWS

IN BRIEF

792 News at a glance

IN DEPTH

796 **GRAVITATIONAL WAVES SERVE UP A BLACK HOLE MYSTERY**
Astrophysicists puzzle over the strange black holes that produced LIGO's signal *By A. Cho*

797 **The scientist who spotted the fateful signal—and let the cat out of the bag**
By A. Cho

799 **PITCHING SCIENCE: A HISTORY OF OBAMA'S RESEARCH BUDGETS**
Economy, politics shape outcome of an uneven record *By J. Mervis*

800 **BARCODING THE BRAIN**
IARPA funds effort to map synaptic connections *By E. Underwood*

801 **POCKET DNA SEQUENCERS MAKE REAL-TIME DIAGNOSTICS A REALITY**
Advances in accuracy of nanopore sequencing help pave the way for on-the-spot DNA tests *By E. Pennisi*

803 **THE RIGHT GUT MICROBES HELP INFANTS GROW**
Studies point the way to using microbial therapy to combat the lasting effects of poor nutrition *By E. Pennisi*
▸ RESEARCH ARTICLE P. 830; REPORT P. 854

FEATURE

804 **THE NEXT BIG EYE**
The pressure is on the builders of the James Webb Space Telescope to ensure that NASA's $8 billion gamble pays off
By D. Clery
▸ VIDEO

INSIGHTS

PERSPECTIVES

810 **HOW DOES THE IMMUNE SYSTEM TOLERATE FOOD?**
Intestinal T cells balance the immune response to microbes and food
By C. Kuhn and H. L. Weiner
▸ REPORT P. 858



811 **CAS9, POISED FOR DNA CLEAVAGE**
Structural rearrangements explain how Cas9 cuts DNA *By H. Chen and S. Bailey*
▸ REPORT P. 867

813 **DIFFERENCES AMONG ASTROCYTES**
Neurons determine the specificity of local astrocytes *By B. Stevens and A. K. Muthukumar*
▸ REPORT P. 849

814 **CONTROLLED INTERACTION OF NANOPARTICLES WITH CELLS**
DNA hybridization can control the exposure of cell-targeting receptors on nanoparticles *By W. J. Parak*
▸ REPORT P. 841

815 **BEYOND EBOLA**
The Ebola epidemic provides lessons for how to respond to future epidemics
By J. Currie et al.

817 **A MOLECULAR SHUTTLE FOR HYDROGEN CYANIDE**
Nickel-catalyzed transfer hydrocyanation enables safe conversion of alkenes into nitriles *By H.-G. Schmalz*
▸ REPORT P. 832

818 **COMPLEXITY THEORY AND FINANCIAL REGULATION**
Economic policy needs interdisciplinary network analysis and behavioral modeling *By S. Battiston*

BOOKS *ET AL.*

821 **INVENTOLOGY**
By P. Kennedy; reviewed by W. Lathe

822 **THE ADAPTORS**
Reviewed by G. R. Goldsmith

LETTERS

824 **PLANT SCIENTISTS: GM TECHNOLOGY IS SAFE**
By N. Fahlgren et al.

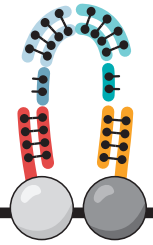
824 **PROTECT THE TASMANIAN WILDERNESS**
By X. Yu

825 **TECHNICAL COMMENT ABSTRACTS**

825 **OUTSIDE THE TOWER: TEACHING TRUST WITH ART**
By P. Sood

Downloaded from on February 18, 2016

Published by AAAS



814 & 841

Nanoparticle modulation by DNA



803, 830, & 854

Microbiota and malnourishment

RESEARCH

IN BRIEF

827 From *Science* and other journals

RESEARCH ARTICLES

830 MICROBIOME
Gut bacteria that prevent growth impairments transmitted by microbiota from malnourished children
L. V. Blanton et al.
RESEARCH ARTICLE SUMMARY; FOR FULL TEXT: dx.doi.org/10.1126/science.aad3311
▸ NEWS STORY P. 803; REPORT P. 854; PODCAST

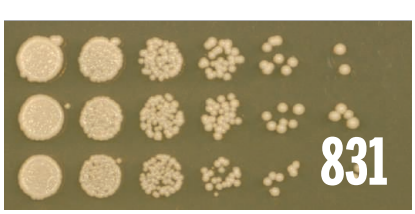
831 PROTEASOME
Rpn1 provides adjacent receptor sites for substrate binding and deubiquitination by the proteasome
Y. Shi et al.
RESEARCH ARTICLE SUMMARY; FOR FULL TEXT: dx.doi.org/10.1126/science.aad9421

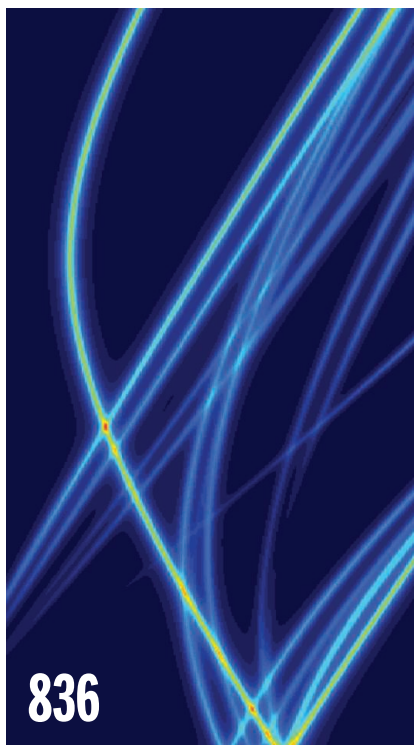
REPORTS

832 ORGANIC CHEMISTRY
Catalytic reversible alkene-nitrile interconversion through controllable transfer hydrocyanation *X. Fang* et al.
▸ PERSPECTIVE P. 817

836 APPLIED PHYSICS
Nuclear magnetic resonance detection and spectroscopy of single proteins using quantum logic *I. Lovchinsky* et al.

841 NANOMATERIALS
DNA-controlled dynamic colloidal nanoparticle systems for mediating cellular interaction *S. Ohta* et al.
▸ PERSPECTIVE P. 814





846 DNA REPAIR
Ubiquitinated Fancd2 recruits Fan1 to stalled replication forks to prevent genome instability *C. Lachaud* et al.

849 NEUROSCIENCE
Neurons diversify astrocytes in the adult brain through sonic hedgehog signaling *W. T. Farmer* et al.
▸ PERSPECTIVE P. 813

854 MICROBIOME
Lactobacillus plantarum strain maintains growth of infant mice during chronic undernutrition
M. Schwarzer et al.
▸ NEWS STORY P. 803; RESEARCH ARTICLE P. 830

858 MUCOSAL IMMUNOLOGY
Dietary antigens limit mucosal immunity by inducing regulatory T cells in the small intestine *K. S. Kim* et al.
▸ PERSPECTIVE P. 810

863 ION CHANNELS
Sequential ionic and conformational signaling by calcium channels drives neuronal gene expression *B. Li* et al.

867 STRUCTURAL BIOLOGY
Structures of a CRISPR-Cas9 R-loop complex primed for DNA cleavage
F. Jiang et al.
▸ PERSPECTIVE P. 811

871 STRUCTURAL BIOLOGY
2.3 Å resolution cryo-EM structure of human p97 and mechanism of allosteric inhibition *S. Banerjee* et al.

876 STRUCTURAL BIOLOGY
Structural basis of lipoprotein signal peptidase II action and inhibition by the antibiotic globomycin *L. Vogeley* et al.

DEPARTMENTS

791 EDITORIAL
Societies can combat harassment
By Marcia McNutt

886 WORKING LIFE
Room for a new generation
By Roc Ordman

ON THE COVER



The $8 billion James Webb Space Telescope, scheduled for launch in October 2018, will be the largest orbiting observatory ever built. This artist's conception shows its segmented mirror—one of several innovative components designed to unfold in space en route to its final orbit 1.5 million kilometers from Earth, or roughly four times as far as the Moon. See page 804.
Photo illustration: James Vaughan

Science Staff 790
New Products 881
Science Careers 882

SCIENCE (ISSN 0036-8075) is published weekly on Friday, except the last week in December, by the American Association for the Advancement of Science, 1200 New York Avenue, NW, Washington, DC 20005. Periodicals mail postage (publication No. 484460) paid at Washington, DC, and additional mailing offices.

Copyright © 2016 by the American Association for the Advancement of Science. The title SCIENCE is a registered trademark of the AAAS.

Domestic individual membership and subscription (51 issues): $165 ($74 allocated to subscription). Domestic institutional subscription (51 issues): $1522; Foreign postage extra: Mexico, Caribbean (surface mail) $55; other countries (air assist delivery) $89. First class, airmail, student, and emeritus rates on request. Canadian rates with GST available upon request, GST #1254 88122. Publications Mail Agreement Number 1069624. **Printed in the U.S.A.**
Change of address: Allow 4 weeks, giving old and new addresses and 8-digit account number. **Postmaster:** Send change of address to AAAS, P.O. Box 96178, Washington, DC 20090–6178. **Single-copy sales:** $15.00 current issue, $20.00 back issue prepaid includes surface postage; bulk rates on request.

Authorization to photocopy material for internal or personal use under circumstances not falling within the fair use provisions of the Copyright Act is granted by AAAS to libraries and other users registered with the Copyright Clearance Center (CCC) Transactional Reporting Service, provided that $35.00 per article is paid directly to CCC, 222 Rosewood Drive, Danvers, MA 01923. The identification code for *Science* is 0036-8075. *Science* is indexed in the *Reader's Guide to Periodical Literature* and in several specialized indexes.

Published by AAAS

Science
AAAS
1200 New York Avenue, NW, Washington, DC 20005
Bateman House, 82-88 Hills Road, Cambridge, UK CB2 1LQ

Editor-in-Chief Marcia McNutt
Executive Editor Monica M. Bradford **News Editor** Tim Appenzeller
Managing Editor, Research Journals Katrina L. Kelner
Deputy Editors Barbara R. Jasny, Andrew M. Sugden(UK), Valda J. Vinson, Jake S. Yeston

Research and Insights

SR. EDITORS Caroline Ash(UK), Gilbert J. Chin, Lisa D. Chong, Julia Fahrenkamp-Uppenbrink(UK), Pamela J. Hines, Stella M. Hurtley(UK), Paula A. Kiberstis, Marc S. Lavine(Canada), Kristen L. Mueller, Ian S. Osborne(UK), Beverly A. Purnell, L. Bryan Ray, Guy Riddihough, H. Jesse Smith, Jelena Stajic, Peter Stern(UK), Phillip D. Szuromi, Sacha Vignieri, Brad Wible, Nicholas S. Wigginton, Laura M. Zahn **ASSOCIATE EDITORS** Brent Grocholski, Keith T. Smith **ASSOCIATE BOOK REVIEW EDITOR** Valerie B. Thompson **ASSOCIATE LETTERS EDITOR** Jennifer Sills **CHIEF CONTENT PRODUCTION EDITOR** Cara Tate **SR. CONTENT PRODUCTION EDITORS** Harry Jach, Lauren Kmec **CONTENT PRODUCTION EDITORS** Jeffrey E. Cook, Chris Filiatreau, Cynthia Howe, Barbara P. Ordway, Catherine Wolner **SR. EDITORIAL COORDINATORS** Carolyn Kyle, Beverly Shields **EDITORIAL COORDINATORS** Joi S. Granger, Lisa Johnson, Anita Wynn **PUBLICATIONS ASSISTANTS** Aneera Dobbins, Jeffrey Hearn, Dona Mathieu, Le-Toya Mayne Flood, Shannon McMahon, Scott Miller, Caitlyn Phillips, Jerry Richardson, Rachel Roberts(UK), Alice Whaley(UK), Brian White **EXECUTIVE ASSISTANT** Anna Bashkirova **ADMINISTRATIVE SUPPORT** Janet Clements(UK), Lizanne Newton(UK), Maryrose Madrid, John Wood(UK)

News

NEWS MANAGING EDITOR John Travis **INTERNATIONAL EDITOR** Richard Stone **DEPUTY NEWS EDITORS** Daniel Clery(UK), Robert Coontz, Elizabeth Culotta, David Grimm, David Malakoff, Leslie Roberts **CONTRIBUING EDITOR** Martin Enserink(Europe) **SR. CORRESPONDENTS** Jeffrey Mervis, Elizabeth Pennisi **NEWS WRITERS** Adrian Cho, Jon Cohen, Jennifer Couzin-Frankel, Carolyn Gramling, Eric Hand, Jocelyn Kaiser, Catherine Matacic, Kelly Servick, Robert F. Service, Erik Stokstad(Cambridge, UK), Emily Underwood **INTERNS** Hanae Armitage, Nala Rogers **CONTRIBUTING CORRESPONDENTS** Michael Balter(Paris), John Bohannon, Ann Gibbons, Mara Hvistendahl, Sam Kean, Eli Kintisch, Kai Kupferschmidt(Berlin), Andrew Lawler, Christina Larson(Beijing), Mitch Leslie, Charles C. Mann, Eliot Marshall, Virginia Morell, Dennis Normile(Shanghai), Heather Pringle, Tania Rabesandratana(London), Gretchen Vogel(Berlin), Lizzie Wade(Mexico City) **CAREERS** Donisha Adams, Rachel Bernstein(Editor) **COPY EDITORS** Julia Cole, Dorie Chevlen, Jennifer Levin (Chief) **ADMINISTRATIVE SUPPORT** Jessica Williams

Executive Publisher Rush D. Holt
Interim Publisher Bill Moran **Chief Digital Media Officer** Rob Covey

BUSINESS OPERATIONS AND PORTFOLIO MANAGEMENT DIRECTOR Sarah Whalen **PRODUCT DEVELOPMENT DIRECTOR** Will Schweitzer **PRODUCT DEVELOPMENT ASSOCIATE** Hal Moore **BUSINESS SYSTEMS AND FINANCIAL ANALYSIS DIRECTOR** Randy Yi **MANAGER OF FULFILLMENT SYSTEMS** Neal Hawkins **SYSTEMS ANALYST** Nicole Mehmedovich **ASSISTANT DIRECTOR, BUSINESS OPERATIONS** Eric Knott **MANAGER, BUSINESS OPERATIONS** Jessica Tierney **BUSINESS ANALYST** Cory Lipman **FINANCIAL ANALYST** Robert Clark **RIGHTS AND PERMISSIONS ASSISTANT DIRECTOR** Emilie David **PERMISSIONS ASSOCIATE** Elizabeth Sandler **RIGHTS, CONTRACTS, AND LICENSING ASSOCIATE** Lili Kiser

MARKETING DIRECTOR Elise Swinehart **ASSOCIATE DIRECTOR OF ACQUISITION AND RETENTION** Julianne Wielga **MARKETING ASSOCIATE** Elizabeth Sattler **SR. MARKETING EXECUTIVE** Jennifer Reeves **ASSOCIATE DIRECTOR, CREATIVE SERVICES** Tzeitel Sorrosa **ART ASSOCIATE** Seil Lee **JR. ART ASSOCIATE** Kim Huynh **ASSISTANT COMMERCIAL EDITOR** Selby Frame **MARKETING PROJECT MANAGER** Angelissa McArthur **PROGRAM DIRECTOR, AAAS MEMBER CENTRAL** Peggy Mihelich **FULFILLMENT SYSTEMS AND OPERATIONS** membership@aaas.org **MANAGER, MEMBER SERVICES** Pat Butler **SPECIALISTS** Terrance Morrison, Latasha Russell **MANAGER, DATA ENTRY** Mickie Napoleoni **DATA ENTRY SPECIALISTS** Brenden Aquilino, Fiona Giblin

INTERIM DIRECTOR, SITE LICENSING Will Schweitzer **PUBLISHER RELATIONS MANAGER** Catherine Holland **PUBLISHER RELATIONS, EASTERN REGION** Keith Layson **PUBLISHER RELATIONS, WESTERN REGION** Ryan Rexroth **SALES RESEARCH COORDINATOR** Aiesha Marshall **MANAGER, SITE LICENSE OPERATIONS** Iquo Edim **SENIOR PRODUCTION SPECIALIST** Robert Koepke **SENIOR OPERATIONS ANALYST** Lana Guz **FULFILLMENT ANALYST** Judy Lillibridge **ASSOCIATE DIRECTOR, MARKETING** Christina Schlecht **MARKETING ASSOCIATES** Thomas Landreth, Isa Sesay-Bah

WEB TECHNOLOGIES SR. DEVELOPER Chris Coleman **DEVELOPERS** Dan Berger, Jimmy Marks, Ryan Jensen **SR. PROJECT MANAGER** Trista Smith **PROJECT MANAGER** Nick Fletcher

DIGITAL MEDIA DIRECTOR OF ANALYTICS Enrique Gonzales **DIGITAL REPORTING ANALYST** Eric Hossinger **SR. WEB PRODUCER** Sarah Crespi **WEB PRODUCER** Alison Crawford **VIDEO PRODUCER** Nguyen Nguyen **SOCIAL MEDIA PRODUCER** Brice Russ

DIRECTOR OF OPERATIONS PRINT AND ONLINE Lizabeth Harman **DIGITAL/PRINT STRATEGY MANAGER** Jason Hillman **QUALITY TECHNICAL MANAGER** Marcus Spiegler **PROJECT ACCOUNT MANAGER** Tara Kelly **DIGITAL PRODUCTION MANAGER** Lisa Stanford **ASSISTANT MANAGER DIGITAL/PRINT** Rebecca Doshi **SENIOR CONTENT SPECIALISTS** Steve Forrester, Antoinette Hodal, Lori Murphy, Anthony Rosen **CONTENT SPECIALISTS** Jacob Hedrick, Kimberley Oster

DESIGN DIRECTOR Beth Rakouskas **DESIGN EDITOR** Marcy Atarod **SENIOR DESIGNER** Garvin Grullón **DESIGNER** Chrystal Smith **GRAPHICS MANAGING EDITOR** Alberto Cuadra **SENIOR SCIENTIFIC ILLUSTRATORS** Chris Bickel, Katharine Sutliff **SCIENTIFIC ILLUSTRATOR** Valerie Altounian **SENIOR ART ASSOCIATES** Holly Bishop, Nathalie Cary, Preston Huey **PHOTOGRAPHY MANAGING EDITOR** William Douthitt **PHOTO EDITORS** Leslie Blizard, Christy Steele

DIRECTOR, GLOBAL COLLABORATION, CUSTOM PUBLICATIONS, ADVERTISING Bill Moran **EDITOR, CUSTOM PUBLISHING** Sean Sanders: 202-326-6430 **ASSISTANT EDITOR, CUSTOM PUBLISHING** Tianna Hicklin: 202-326-6463 **ADVERTISING MARKETING MANAGER** Justin Sawyers: 202-326-7061 science_advertising@aaas.org **ADVERTISING SUPPORT MANAGER** Karen Foote: 202-326-6740 **ADVERTISING PRODUCTION OPERATIONS MANAGER** Deborah Tompkins **SR. PRODUCTION SPECIALIST/GRAPHIC DESIGNER** Amy Hardcastle **SR. TRAFFIC ASSOCIATE** Christine Hall **SALES COORDINATOR** Shirley Young **ASSOCIATE DIRECTOR, COLLABORATION, CUSTOM PUBLICATIONS/CHINA/TAIWAN/KOREA/SINGAPORE** Ruolei Wu: +86-186 0082 9345, rwu@aaas.org **COLLABORATION/CUSTOM PUBLICATIONS/JAPAN** Adarsh Sandhu + 81532-81-5142 asandhu@aaas.org **EAST COAST/E. CANADA** Laurie Faraday: 508-747-9395, FAX 617-507-8189 **WEST COAST/W. CANADA** Lynne Stickrod: 415-931-9782, FAX 415-520-6940 **MIDWEST** Jeffrey Dembski: 847-498-4520 x3005, Steven Loerch: 847-498-4520 x3006 **UK EUROPE/ASIA** Roger Goncalves: TEL/FAX +41 43 243 1358 **JAPAN** Katsuyoshi Fukamizu(Tokyo): +81-3-3219-5777 kfukamizu@aaas.org **CHINA/TAIWAN** Ruolei Wu: +86-186 0082 9345, rwu@aaas.org

WORLDWIDE ASSOCIATE DIRECTOR OF SCIENCE CAREERS Tracy Holmes: +44 (0) 1223 326525, FAX +44 (0) 1223 326532 tholmes@science-int.co.uk **CLASSIFIED** advertise@sciencecareers.org **U.S. SALES** Tina Burks: 202-326-6577, Nancy Toema: 202-326-6578 **EUROPE/ROW SALES** Sarah Lelarge **SALES ASSISTANT** Kelly Grace **JAPAN** Hiroyuki Mashiki(Kyoto): +81-75-823-1109 hmashiki@aaas.org **CHINA/TAIWAN** Ruolei Wu: +86-186 0082 9345 rwu@aaas.org **MARKETING MANAGER** Allison Pritchard **MARKETING ASSOCIATE** Aimee Aponte

AAAS BOARD OF DIRECTORS RETIRING PRESIDENT, CHAIR Gerald R. Fink **PRESIDENT** Geraldine (Geri) Richmond **PRESIDENT-ELECT** Barbara A. Schaal **TREASURER** David Evans Shaw **CHIEF EXECUTIVE OFFICER** Rush D. Holt **BOARD** Bonnie L. Bassler, May R. Berenbaum, Carlos J. Bustamante, Stephen P.A. Fodor, Claire M. Fraser, Michael S. Gazzaniga, Laura H. Greene, Elizabeth Loftus, Mercedes Pascual

SUBSCRIPTION SERVICES For change of address, missing issues, new orders and renewals, and payment questions: 866-434-AAAS (2227) or 202-326-6417, FAX 202-842-1065. Mailing addresses: AAAS, P.O. Box 96178, Washington, DC 20090-6178 or AAAS Member Services, 1200 New York Avenue, NW, Washington, DC 20005

INSTITUTIONAL SITE LICENSES 202-326-6730 **REPRINTS:** Author Inquiries 800-635-7181 **COMMERCIAL INQUIRIES** 803-359-4578 **PERMISSIONS** 202-326-6765, permissions@aaas.org **AAAS Member Services** 202-326-6417 or http://membercentral.aaas.org/discounts

Science serves as a forum for discussion of important issues related to the advancement of science by publishing material on which a consensus has been reached as well as including the presentation of minority of conflicting points of view. Accordingly, all articles published in *Science*—including editorials, news and comment, and book reviews—are signed and reflect the individual views of the authors and not official points of view adopted by AAAS or the institutions with which the authors are affiliated.

INFORMATION FOR AUTHORS See pages 624 and 625 of the 5 February 2016 issue or access www.sciencemag.org/authors/science-information-authors

SENIOR EDITORIAL BOARD
Gary King, *Harvard University,* **Susan M. Rosenberg,** *Baylor College of Medicine,*
Ali Shilatifard, *Northwestern University Feinberg School of Medicine*

BOARD OF REVIEWING EDITORS (Statistics board members indicated with **(S)**

Adriano Aguzzi, *U. Hospital Zürich*
Takuzo Aida, *U. of Tokyo*
Leslie Aiello, *Wenner-Gren Foundation*
Judith Allen, *U. of Edinburgh*
Sonia Altizer, *U. of Georgia*
Sebastian Amigorena, *Institut Curie*
Kathryn Anderson, *Memorial Sloan-Kettering Cancer Center*
Meinrat O. Andreae, *Max-Planck Inst. Mainz*
Paola Arlotta, *Harvard U.*
Johan Auwerx, *EPFL*
David Awschalom, *U. of Chicago*
Clare Baker, *University of Cambridge*
Jordi Bascompte, *University of Zurich*
Facundo Batista, *London Research Inst.*
Ray H. Baughman, *U. of Texas, Dallas*
David Baum, *U. of Wisconsin*
Carlo Beenakker, *Leiden U.*
Kamran Behnia, *ESPCI-ParisTech*
Yasmine Belkaid, *NIAID, NIH*
Philip Benfey, *Duke U.*
May Berenbaum, *U. of Illinois*
Gabriele Bergers, *U. of California, San Francisco*
Bradley Bernstein, *Massachusettes General Hospital*
Peer Bork, *EMBL*
Bernard Bourdon, *Ecole Normale Supérieure de Lyon*
Chris Bowler, *École Normale Supérieure*
Ian Boyd, *U. of St. Andrews*
Emily Brodsky, *U. of California, Santa Cruz*
Ron Brookmeyer, *U. of California Los Angeles* **(S)**
Christian Büchel, *U. Hamburg-Eppendorf*
Joseph A. Burns, *Cornell U.*
Carter Tribley Butts, *U. of California, Irvine*
Gyorgy Buzsaki, *New York U. School of Medicine*
Blanche Capel, *Duke U.*
Mats Carlsson, *U. of Oslo*
Ib Chorkendorff, *U. of Denmark*
David Clapham, *Children's Hospital Boston*
Joel Cohen, *Rockefeller U., Columbia U.*
James J. Collins, *MIT*
Robert Cook-Deegan, *Duke U.*
Lisa Coussens, *Oregon Health & Science U.*
Alan Cowman, *Walter & Eliza Hall Inst.*
Robert H. Crabtree, *Yale U.*
Roberta Croce, *Vrije Universiteit*
Janet Currie, *Princeton U.*
Jeff L. Dangl, *U. of North Carolina*
Tom Daniel, *U. of Washington*
Frans de Waal, *Emory U.*
Stanislas Dehaene, *Collège de France*
Robert Desimone, *MIT*
Claude Desplan, *New York U.*
Dennis Discher, *U. of Pennsylvania*
Gerald W. Dorn II, *Washington U. School of Medicine*
Jennifer A. Doudna, *U. of California, Berkeley*
Bruce Dunn, *U. of California, Los Angeles*
William Dunphy, *Caltech*
Christopher Dye, *WHO*
Todd Ehlers, *U. of Tuebingen*
David Ehrhardt, *Carnegie Inst. of Washington*
Tim Elston, *U. of North Carolina at Chapel Hill*
Gerhard Ertl, *Fritz-Haber-Institut, Berlin*
Barry Everitt, *U. of Cambridge*
Ernst Fehr, *U. of Zurich*
Anne C. Ferguson-Smith, *U. of Cambridge*
Michael Feuer, *The George Washington U.*
Toren Finkel, *NHLBI, NIH*
Kate Fitzgerald, *U. of Massachusetts*
Peter Fratzl, *Max-Planck Inst.*
Elaine Fuchs, *Rockefeller U.*
Daniel Geschwind, *UCLA*
Karl-Heinz Glassmeier, *TU Braunschweig*
Ramon Gonzalez, *Rice U.*
Julia R. Greer, *Caltech*
Elizabeth Grove, *U. of Chicago*
Nicolas Gruber, *ETH Zurich*
Kip Guy, *St. Jude's Children's Research Hospital*
Taekjip Ha, *U. of Illinois at Urbana-Champaign*
Christian Haass, *Ludwig Maximilians U.*
Michael Hasselmo, *Boston U.*
Martin Heimann, *Max-Planck Inst. Jena*
Yka Helariutta, *U. of Cambridge*
James A. Hendler, *Rensselaer Polytechnic Inst.*
Janet G. Hering, *Swiss Fed. Inst. of Aquatic Science & Technology*
Kai-Uwe Hinrichs, *U. of Bremen*
David Hodell, *U. of Cambridge*
David Holden, *Imperial College*
Lora Hooper, *UT Southwestern Medical Ctr. at Dallas*
Tamas Horvath, *Yale University*
Raymond Huey, *U. of Washington*
Fred Hughson, *Princeton U.*
Auke Ijspeert, *EPFL Lausanne*
Stephen Jackson, *U. of Arizona, USGS*
Steven Jacobsen, *U. of California, Los Angeles*
Stephen Jackson, *U. of Arizona*
Kai Johnsson, *EPFL Lausanne*
Peter Jonas, *Inst. of Science & Technology (IST) Austria*
Matt Kaeberlein, *U. of Washington*
William Kaelin Jr., *Dana-Farber Cancer Inst.*
Daniel Kahne, *Harvard U.*
Daniel Kammen, *U. of California, Berkeley*
Abby Kavner, *U. of California, Los Angeles*
Masashi Kawasaki, *U. of Tokyo*
V. Narry Kim, *Seoul National U.*
Joel Kingsolver, *U. of North Carolina at Chapel Hill*
Robert Kingston, *Harvard Medical School*
Etienne Koechlin, *Ecole Normale Supérieure*
Alexander Kolodkin, *Johns Hopkins U.*
Thomas Langer, *U. of Cologne*
Mitchell A. Lazar, *U. of Pennsylvania*
David Lazer, *Harvard U.*
Thomas Lecuit, *IBDM*
Virginia Lee, *U. of Pennsylvania*
Stanley Lemon, *U. of North Carolina at Chapel Hill*
Ottoline Leyser, *Cambridge U.*
Wendell Lim, *U.C. San Francisco*
Marcia C. Linn, *U. of California, Berkeley*
Jianguo Liu, *Michigan State U.*
Luis Liz-Marzan, *CIC biomaGUNE*
Jonathan Losos, *Harvard U.*
Ke Lu, *Chinese Acad. of Sciences*
Christian Lüscher, *U. of Geneva*
Laura Machesky, *CRUK Beatson Inst. for Cancer Research*
Anne Magurran, *U. of St. Andrews*
Oscar Marin, *CSIC & U. Miguel Hernández*
Charles Marshall, *U. of California, Berkeley*
C. Robertson McClung, *Dartmouth College*
Graham Medley, *U. of Warwick*
Tom Misteli, *NCI*
Yasushi Miyashita, *U. of Tokyo*
Mary Ann Moran, *U. of Georgia*
Richard Morris, *U. of Edinburgh*
Alison Motsinger-Reif, *NC State U.* **(S)**
Thomas Murray, *The Hastings Center*
Daniel Neumark, *U. of California, Berkeley*
Kitty Nijmeijer, *U. of Twente*
Pär Nordlund, *Karolinska Inst.*
Helga Nowotny, *European Research Advisory Board*
Ben Olken, *MIT*
Joe Orenstein, *U. of California Berkeley & Lawrence Berkeley National Lab*
Harry Orr, *U. of Minnesota*
Pilar Ossorio, *U. of Wisconsin*
Andrew Oswald, *U. of Warwick*
Steve Palumbi, *Stanford U.*
Jane Parker, *Max-Planck Inst. of Plant Breeding Research*
Giovanni Parmigiani, *Dana-Farber Cancer Inst.* **(S)**
John H. J. Petrini, *Memorial Sloan-Kettering Cancer Center*
Samuel Pfaff, *Salk Institute for Biological Studies*
Joshua Plotkin, *U. of Pennsylvania*
Albert Polman, *FOM Institute AMOLF*
Philippe Poulin, *CNRS*
Jonathan Pritchard, *Stanford U.*
David Randall, *Colorado State U.*
Felix Rey, *Institut Pasteur*
Trevor Robbins, *U. of Cambridge*
Jim Roberts, *Fred Hutchinson Cancer Research Ctr.*
Barbara A. Romanowicz, *U. of California,Berkeley*
Amy Rosenzweig, *Northwestern University*
Mike Ryan, *U. of Texas, Austin*
Mitinori Saitou, *Kyoto U.*
Shimon Sakaguchi, *Kyoto U.*
Miquel Salmeron, *Lawrence Berkeley National Lab*
Jürgen Sandkühler, *Medical U. of Vienna*
Alexander Schier, *Harvard U.*
Vladimir Shalaev, *Purdue U.*
Robert Siliciano, *Johns Hopkins School of Medicine*
Denis Simon, *Arizona State U.*
Uri Simonsohn, *U. of Pennsylvania*
Alison Smith, *John Innes Centre*
Richard Smith, *U. of North Carolina* **(S)**
John Speakman, *U. of Aberdeen*
Allan C. Spradling, *Carnegie Institution of Washington*
Jonathan Sprent, *Garvan Inst. of Medical Research*
Eric Steig, *U. of Washington*
Paula Stephan, *Georgia State U. and National Bureau of Economic Research*
Molly Stevens, *Imperial College London*
V. S. Subrahmanian, *U. of Maryland*
Ira Tabas, *Columbia U.*
Sarah Teichmann, *Cambridge U.*
John Thomas, *North Carolina State U.*
Shubha Tole, *Tata Institute of Fundamental Research*
Christopher Tyler-Smith, *The Wellcome Trust Sanger Inst.*
Herbert Virgin, *Washington U.*
Bert Vogelstein, *Johns Hopkins U.*
Cynthia Volkert, *U. of Göttingen*
David Wallach, *Weizmann Inst. of Science*
Ian Walmsley, *U. of Oxford*
Jane-Ling Wang, *U. of California, Davis* **(S)**
David A. Wardle, *Swedish U. of Agric. Sciences*
David Waxman, *Fudan U.*
Jonathan Weissman, *U. of California, San Francisco*
Chris Wikle, *U. of Missouri* **(S)**
Ian A. Wilson, *The Scripps Res. Inst.* **(S)**
Timothy D. Wilson, *U. of Virginia*
Rosemary Wyse, *Johns Hopkins U.*
Jan Zaanen, *Leiden U.*
Kenneth Zaret, *U. of Pennsylvania School of Medicine*
Jonathan Zehr, *U. of California, Santa Cruz*
Len Zon, *Children's Hospital Boston*
Maria Zuber, *MIT*

BOOK REVIEW BOARD
David Bloom, *Harvard U.,* **Samuel Bowring,** *MIT,* **Angela Creager,** *Princeton U.,*
Richard Shweder, *U. of Chicago,* **Ed Wasserman,** *DuPont*

EDITORIAL

Societies can combat harassment



Marcia McNutt
Editor-in Chief
Science *Journals*

Imagine a student presenting a poster at a scientific meeting, thrilled when a senior scientist stops by to view the work. Chances are good, given the continuing underrepresentation of women at senior levels of academia, that the senior scientist is male. If the student is also male, he likely has no doubt that the senior scientist wants to learn more about the research. If the student is female, she may wonder: Does he want to get acquainted with my work, or me? This is the scenario that Meg Urry of Yale University, current president of the American Astronomical Society, posed during a session on "Forward Focused Ethics—What is the Role of Scientific Societies in Responding to Harassment and Other Workplace Climate Issues?" at the Fall Meeting of the American Geophysical Union in December 2015.

Scientific societies have an intrinsic responsibility in this regard. They sponsor meetings, workshops, conferences, field trips, and other offsite events that place scientists in close proximity for long hours in unfamiliar settings. Urry, who spoke out on the responsibility of scientific societies for taking action in the wake of the Geoff Marcy scandal, and other session speakers and panelists had excellent suggestions for promoting an environment free of harassment. Scientific societies need to widely disseminate policies that declare their intolerance for harassment of any sort. These must describe how violations of such policies can be reported, and to whom, and the process for investigating those violations. And societies should clearly prescribe what consequences could be levied against offenders: Immediate expulsion from the meeting? From future meetings? From the society? Ineligibility for honors such as fellowships and medals? Barred from publishing in society journals? Blocking offending scientists' access to meetings, publications, and professional colleagues can be an effective means to limit professional advancement, especially when the relevant institutional employer is slow or somehow prevented from taking concrete actions. (For the policy of AAAS, the publisher of *Science*, see http://meetings.aaas.org/program/code-of-conduct/.)



"...it is always the student who pays the professional price..."

Urry puts the responsibility squarely on senior scientists for the consequences of any personal relationships that develop with students, because it is always the student who pays the professional price if and when such relationships disintegrate. She suggested that unless the senior scientist is willing to change institutions to avoid an uncomfortable situation for the student if the relationship dissolves, don't get involved in the first place. Many universities expressly forbid any relationships between professors and undergraduates.

In the discussion after the presentations, several attendees, noting that the room was largely filled with women, asked what could be done to encourage more men to take leadership on addressing harassment issues. Blair Schneider, president of the Association of Women Geoscientists (AWG), offered that AWG looks for opportunities to bestow its awards on deserving men who are setting outstanding examples in educating and advancing the careers of women geoscientists.

Perhaps the most disturbing comment came from a foreign student studying in the United States who described an incident of unwanted attention from a senior colleague. She availed herself of her institution's formal channels to raise a complaint, only to be told that she must have misinterpreted her senior colleague's behavior on account of her unfamiliarity with the country's language and culture. As her command of English was excellent, she asked if she should record future interactions to prove her claims. The response was that it would be illegal. This experience illustrates the continuing battles that women face in getting their concerns treated seriously.

Scientific societies are governed by scientists for scientists. Therefore, it is the responsibility of the officers, board, and council members of scientific societies to make sure that policies and procedures are in place to combat harassment in all forms during all society-sponsored events.

– Marcia McNutt

10.1126/science.aaf4216

PHOTOS: (INSET) IZABELA HABUR/ISTOCKPHOTO.COM; (TOP) STACEY PENTLAND PHOTOGRAPHY

Downloaded from on February 18, 2016

Published by AAAS

NEWS

“Sleep well, little @Philae2014!”

ESA Science (@esascience), tweeting on 12 February, as scientists from the German Aerospace Center announced they’d given up hope of re-establishing contact with the comet lander, last heard from in July 2015. **http://scim.ag/_Philae**

IN BRIEF

3D printed body parts, large as life



The outer contours of this freshly printed ear may look complex, but they’re simple compared with the structure inside. The 3D manufacturing system that crafted it, called the “integrated tissue-organ printer” (ITOP), laces the artificial body parts with living cells, according to a study published on 15 February in *Nature Biotechnology*. Researchers have printed with live cells before, but until now they only made tiny pieces of gelatinous living material, both because large structures tended to collapse and because the cells inside tended to die from lack of oxygen. Thanks to two innovations, the ITOP can make life-sized body parts in which cells thrive. First, it interweaves a gooey, cell-friendly hydrogel with a stiffer substance that offers structural support. Second, it leaves tiny channels for oxygen to enter so that cells in the middle won’t suffocate. When researchers implanted ITOP-generated bone, muscle, and cartilage into rats and mice, the printed materials developed blood supplies and internal structures resembling those of natural tissue. The researchers are currently working with the Food and Drug Administration to set up human trials, with the ultimate goal of creating replacement body parts for people who need them, says Anthony Atala, a tissue engineer at the Wake Forest Institute for Regenerative Medicine in Winston-Salem, North Carolina, and one of the study’s authors.

PHOTO: WAKE FOREST INSTITUTE FOR REGENERATIVE MEDICINE

AROUND THE WORLD

United against sexual harassment

TEMPE, ARIZONA | An online statement against sexual misconduct in academia, written and circulated by three human evolution experts at Arizona State University, Tempe, has garnered about 900 signatures since it was launched on 9 February. The petition, inspired by recent cases of alleged sexual harassment in astronomy, biology, and anthropology, calls on those who sign it to make an “individual commitment” to “zero tolerance of sexual misconduct” and to publicly support its victims. Paleoanthropologist William Kimbel, anthropologist Katie Hinde, and paleoecologist Kaye Reed say that asking researchers to make an individual, public commitment to ending sexual misconduct will accelerate the cultural change in academia that many scientists believe is essential to enforcing zero tolerance policies. “It is an easy thing to sign the form, but the power of the collective commitment of hundreds of signers is undeniable,” Kimbel says. **http://scim.ag/harasspetition**

Karolinska head resigns

STOCKHOLM | The vice-chancellor of the Karolinska Institute (KI) resigned last week in the wake of a scandal involving surgeon Paolo Macchiarini (*Science*, 5 February, p. 546). Anders Hamsten had dismissed misconduct charges against Macchiarini last year, but new attention to the case from a television documentary aired in January persuaded Hamsten that he had “completely misjudged” the surgeon and that his decision in the case was likely wrong, he wrote in a newspaper commentary in which he also said he would step down (**http://scim.ag/Hamstenresig**). The resignation came 2 days after the Royal Swedish Academy of Sciences issued a statement saying it was worried that the credibility of Swedish science is at stake. “A number of shortcomings and ethically indefensible working methods have been uncovered, leading to a crisis of confidence in Swedish medical research,” the 11 February statement said. The academy demanded a new, fully independent investigation and called for a 2011

Downloaded from on February 18, 2016

Published by AAAS

The Lancet paper by Macchiarini, which detailed the first artificial trachea implant, to be corrected. It says it is establishing a separate committee to propose recommendations for clinicians and scientists working at the intersection between clinical research and medical care. http://scim.ag/KIscandal

Panel recommends bite-mark ban

HUNTSVILLE, TEXAS | The analysis of bite marks as a way to identify an attacker is unscientific and has no place in the courtroom, a Texas commission made up of scientists, attorneys, and forensic practitioners ruled last week. The recommendation is the first of its kind in the United States, and arose from a 6-month review by the Texas Forensic Science Commission, a state agency that investigates allegations of negligence of misconduct in crime labs. Some specialists have claimed that they could reliably identify who left a bite on a victim based on similarities to dental impressions from a suspect, despite a lack of scientific evidence; since 2000, bite-mark analysis has played a role in at least 25 convictions that were later reversed based on DNA evidence, according to the Innocence Project. The commission's call to ban such testimony from trials is not legally binding, but is expected to influence judges and lawyers nationwide.

CRISPR dubbed a WMD

WASHINGTON, D.C. | "Genome editing" joins North Korea's nuclear weapons program and Russian cruise missiles on a list of weapons of mass destruction released by U.S. Director of National Intelligence James Clapper last week. The worldwide threat assessment report from the U.S. intelligence community evokes fears that terrorists might harness increasingly cheap and efficient genome-editing techniques such as CRISPR to create "potentially harmful biological agents or products." The U.S. public, meanwhile, registered its uneasiness about some of CRISPR's potential uses in a poll released on 11 February by *Stat* and Harvard University. Of 1000 people surveyed, 65% thought it should be illegal to alter the genes of unborn babies to reduce the risk of serious diseases, and 83% opposed such editing to improve "intelligence or physical characteristics."

U.K. allows animal-human chimeras

LONDON | The United Kingdom has issued new guidelines for research that involves using human material in animals. The new rules say that it could be permissible for



Mary Somerville was an astronomer, mathematician, and science writer.

Scottish astronomer will be first woman to appear on U.K. money

Astronomer Mary Somerville (shown), who lived from 1780 to 1872, was a pioneer in her field, studying math and science over the objections of her family and first husband, serving as the first female member of the Royal Astronomical Society, and contributing calculations that led to the discovery of the planet Neptune. Now, she's set to be a pioneer in a different arena: Somerville will be the first woman, other than the queen of the United Kingdom, to appear on a Scottish banknote. Following a contentious Facebook vote that pitted her against two other Scottish scientists, physicist James Clerk Maxwell and civil engineer Thomas Telford, Somerville emerged victorious last week. Her likeness will appear on the Royal Bank of Scotland's £10 note in 2017. (Meanwhile, Jane Austen is set to appear on the Bank of England's £10 note next year.)

IMAGE: THOMAS PHILLIPS/WIKIMEDIA COMMONS

Published by AAAS



Battling Zika in Brazil

As part of a campaign to limit Brazil's ongoing Zika outbreak, President Dilma Rousseff took aim at mosquitoes carrying the virus, spraying larvicide on 13 February in a Rio de Janeiro neighborhood. Three days earlier, scientists reported in two separate papers that they had found Zika virus in the brains of several infants with microcephaly, bolstering suspicions that the virus causes the birth defect (**http://scim.ag/Zikamicro**). The babies' mothers had symptoms of Zika early in their pregnancies, but had recovered. The researchers also found the virus in placental and fetal tissues from two women who miscarried after suffering symptoms of Zika infection. The findings strengthen the case for a link between the virus and an observed increase in microcephaly incidence in Brazil. Brazil's ministry of health said on 12 February that it had confirmed 462 cases of microcephaly that might be linked to an infection during pregnancy, out of 5079 suspected cases. Also last week, 30 journals and research funding organizations pledged to encourage wide sharing of Zika-related work, by making all Zika-related papers available for free and requiring grantees to share their data as rapidly and widely as possible.

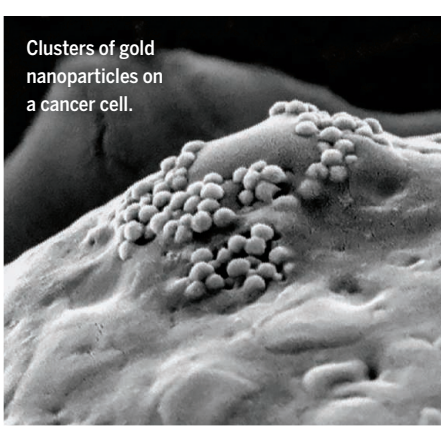
Brazilian President Dilma Rousseff (at far left) launched a national campaign to fight the Zika virus on 13 February.

researchers to insert human cells into animal embryos, if they clear multiple levels of ethical and scientific review by local and national regulators. Several researchers have said they would like to try to grow human organs in animal bodies using such techniques. The U.S. National Institutes of Health said last year that it would not fund such research while it reconsidered the ethical implications of the work (*Science*, 16 October 2015, p. 261).

FINDINGS

Nanobubble pops kill cancer cells

Clusters of gold atoms known as nanoparticles can detect and kill cancer cells left behind after tumor-removal surgery, researchers report online this week in *Nature Nanotechnology*. Scientists have previously shown that when nanoparticles are injected into the bloodstream, they tend to seep out of vessels and congregate around tumors. The tumor cells engulf the nanoparticles—which act as Trojan horses. Researchers hit the gold atoms with infrared laser light, and the particles heat up and kill the cancer cells. But this can also damage healthy tissue. In the new study, scientists showed they could focus the heat damage on the cancer cells by decorating the nanoparticles with immune protein antibodies that latch onto receptors on the surface of human squamous cells implanted in mice. This not only prevented the heat from damaging healthy cells, but also increased temperatures around the clusters, vaporizing nearby water molecules; the bursting bubbles ripped apart the cancer cells. The researchers are now designing a clinical trial that could begin testing the therapy in humans in the next 2 years. **http://scim.ag/explodenanobub**



Clusters of gold nanoparticles on a cancer cell.

NEWSMAKERS

Pachauri in hot water again

The former chair of the International Panel on Climate Change (IPCC), **Rajendra Pachauri**, was already facing charges of sexual harassment made against him in February 2015 by a former co-worker. Last week, a second former co-worker made a fresh set of allegations, on the heels of a media storm surrounding Pachauri's promotion from director-general of The Energy and Resources Institute (TERI) in New Delhi, where he has been since 2001, to its executive vice chairman. Pachauri denied last year's allegations and stepped down from IPCC (*Science*, 27 February 2015, p. 931). Although an internal TERI investigation concluded that his alleged actions constituted harassment, the institute has taken no disciplinary action against him. But last week, a second former TERI employee released a statement alleging that Pachauri repeatedly sexually harassed her from 2003 to 2005. Pachauri is on voluntary leave from TERI, he told *Science* in an email. "I have a large amount of writing to do, which is the reason for this decision, and I would also focus on several other pending matters," he wrote. **http://scim.ag/Pachauripromotion**

McNutt elected to head NAS

Marcia McNutt, editor-in-chief of *Science*, has been elected president of the U.S. National Academy of Sciences (NAS). She begins her 6-year term in July, succeeding Ralph Cicerone, who is stepping down after 12 years as president. A geophysicist, McNutt was director of the U.S. Geological Survey from 2009 to 2013 during the first Obama administration. Before that she had been chief executive of the Monterey Bay Aquarium Research Institute in California. Her election was a foregone conclusion after the NAS governing council put her name forward last July, as she faced no opposition in a vote by the NAS membership (*Science*, 10 July 2015, p. 123). A search is underway for her successor at *Science*.

PHOTOS: (TOP TO BOTTOM) REUTERS/RICARDO MORAES; D. S. WAGNER *ET AL.*, *BIOMATERIALS*, **31** (2010)

Published by AAAS

AAAS

2016 Annual Meeting

The AAAS (which publishes *Science*) Annual Meeting, held in Washington, D.C., from 11 to 15 February, drew thousands of participants, including scientists, journalists, and visitors to Family Science Days activities. Here are some highlights from the meeting; for more AAAS coverage, including reports from sessions and interviews with scientists, visit http://scim.ag/aaas2016.

Toward a better bug light

Choice of light bulb matters when it comes to keeping flying pests away from the veranda on a summer evening, finds a study that compared insect traps outfitted with six major types of commercially available lights, including traditional incandescent bulbs, LED bulbs that emit warm and cold colored light, and yellow tinted "bug lights" marketed as being less attractive to insects. In one summer, researchers collected and catalogued 8887 insects and spiders from a neighborhood in Appomattox, Virginia. Incandescent bulbs brought in the largest insect haul, averaging about eight per hour. The bug lights and warm-colored LEDs were roughly tied for least attractive, at about 4.5. But bug lights had a downside—two insect orders found them more enticing than the warm LED: Hemiptera, which includes so-called "stink bugs," and Dermaptera, better known as "earwigs."

Preserving sites with 3D scans

Historical sites around the world are threatened by weathering, as well as pollution, vandalism, and even terrorism. Last year, a structure protecting a 2.5-millennia-old Olmec altar in Chalcatzingo, Mexico, burned down, exposing the altar to the elements. Repairing the site would have required guesswork—had researchers not scanned and digitized it 3 years earlier using 3D laser scanning technology. Along with a team of Mexican archaeologists working to preserve the Chalcatzingo site, archaeologist Lori Collins of the University of South Florida in Tampa and her team digitally deconstructed the 3D model of the altar into individual rocks. They were able to map out each piece—and this week, on-the-ground archaeologists are working to reconstruct the site exactly as it was before the fire. Thanks to their meticulous digitization work, the team even found details in the rock carvings that had never before been noticed. Such 3D scans will help archaeologists preserve heritage in politically unstable regions, Collins says, while also allowing students and researchers around the world to access a piece of history.

Keen students on one wavelength

Teachers who wonder whether their class is engaged could one day be able to find out—by checking how synchronized their brain waves are with one another. Neuroscientist Ido Davidesco of New York University in New York City and colleagues logged the neural activity of 12 high school students and their teacher with electroencephalography headsets over 11 classes. Not surprisingly, patterns of brain activity were more similar when students were all focused on the same task. But the researchers also found that when a student reported being more engaged, the frequency of their brain waves better matched the group. Activities the students liked more—group discussions and videos versus a lecture or being read to aloud—seemed to put them more in sync.



Biologists worry that a deadly fungus devastating European salamanders may reach the United States, threatening native species such as this red eft.

PHOTO: JASONONDREICKA/ISTOCK PHOTO

The race to keep an amphibian-killing fungus out of the U.S.

Two years ago, scientists first described the deadly fungus *Batrachochytrium salamandrivorans,* or *Bsal*, which wiped out the fire salamander population in the Netherlands. Now, U.S. scientists are fighting to keep the fungus out of the United States, which has the world's largest biodiversity of salamanders—and the best way to do that is by restricting the salamander pet trade, said amphibian biologists speaking at the annual AAAS meeting in Washington, D.C., last week. Last month, the U.S. Fish and Wildlife Commission banned the import of 201 species of salamander into the United States, as well as between state boundaries. *Bsal*, which likely originated in Asia, is a sister species of the *Bd* fungus that has caused declines and extinctions in multiple amphibian species around the globe. Both cause chytridiomycosis, which eats away at the skin of amphibians. Those extinctions ripple through ecosystems, said Karen Lips, an ecologist at the University of Maryland, College Park, at the meeting; among other ecosystem services, amphibians can help control insect populations, including mosquitoes that spread diseases such as Zika and dengue fever. http://scim.ag/Amphfungus

Published by AAAS



LIGO spotted waves from a pair of black holes (simulated here) with unusually high masses.

Downloaded from on February 18,

ASTROPHYSICS

Gravitational waves serve up a mystery

Astrophysicists puzzle over the strange black holes that produced LIGO's signal

By **Adrian Cho**

For decades, physicists had claimed that the detection of gravitational waves—ripples in spacetime set off by ultraviolent astrophysical events—would usher in a new type of astronomy and reveal new wonders. That was the rationale for spending more than $1 billion on the Laser Interferometer Gravitational-Wave Observatory (LIGO)—a duo of detectors in Hanford, Washington, and Livingston, Louisiana. Last week LIGO fulfilled on that promise, say astrophysicists, delivering both the first detection of a signal and a stellar surprise.

The gravitational waves spotted by the recently upgraded machines (*Science*, 12 February, p. 645) were predicted by Albert Einstein, whose general theory of relativity says that spacetime is a bendy thing and that gravity comes about when massive objects warp it. Computer models showed that LIGO's signal came from two black holes, 29 and 36 times as massive as the sun, spiraling together 1.3 billion light-years away. No one had ever seen a pair of orbiting black holes or detected "stellar mass" black holes so heavy, astrophysicists say—and they are hard to fit into current theory.

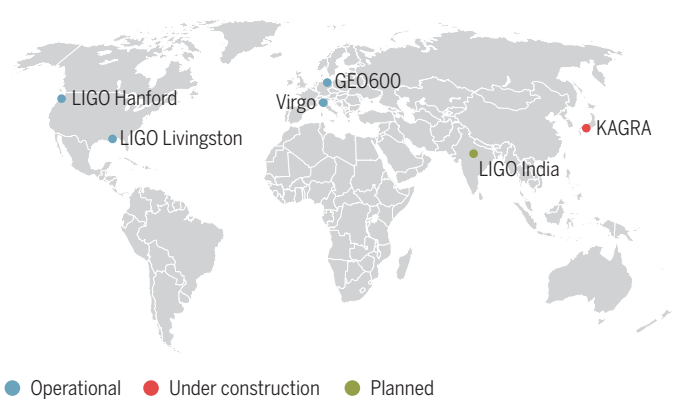
"I'm sure that in the next few months there will be 100 papers about the evolution pathways" of such a pair, predicts Ira Wasserman, a theorist at Cornell University. Jeffrey McClintock, an astrophysicist at the Harvard-Smithsonian Center for Astrophysics in Cambridge, Massachusetts, says that spotting merging black holes was LIGO's ultimate goal, and seeing them immediately "exceeds all expectations for new, new, new. ... What more do you want, mermaids?"

A black hole can form when a huge star burns out and collapses to a point, leaving behind a gravitational field so strong near the point that not even light can escape. That field is the black hole, and thanks to Einstein's equivalence of energy and mass, $E=mc^2$, it has a mass. Astrophysicists have spotted stellar-mass black holes mostly in our galaxy by searching for systems in which a black hole consumes a companion star. From the motion of the star and the gas streaming into the black hole, researchers have deduced that the heaviest of them weighs about 15 times as much as the sun, McClintock says. (Much heavier black holes, with masses of millions of suns, lurk at the heart of our galaxy and many others.)

A star big enough to produce a 30-stellar-mass black hole would have to be very unusual. That's because any huge star peppered with elements heavier than helium will lose weight as it burns out. Ions of oxygen, calcium, and iron will absorb the star's light, which will blow the ions and most of the star's mass

A gravitational wave detector network

As new detectors come online, physicists should be able to measure the polarization of gravitational waves and pinpoint sources in the sky.



CREDITS: (IMAGE) LIGO; (DATA) LIGO

Published by AAAS

into space. "If you start with a 40-solar-mass star, by the time of collapse it's down to 10 solar masses," McClintock says.

One possibility is that the stars formed very early, when the universe was a couple billion years old and contained only hydrogen and helium. (Heavier elements were forged later, in supernova explosions.) But giant stars burn out in a few million years, Wasserman says, and it's hard to imagine how the black holes they spawned would have hung around for billions of years before spiraling together. McClintock leans toward a second explanation: The stars were born more recently, in dwarf galaxies like the Large Magellanic Cloud that are lower in heavy elements than the Milky Way is.

LIGO should be able to determine which scenario is correct, says Vicky Kalogera, an astrophysicist and LIGO team member at Northwestern University in Evanston, Illinois. In the next 2 or 3 years, LIGO could spot dozens of black hole mergers, she says. How far away and, hence, how old they are should reveal which formation scenario happened more often. "It's not one or the other," Kalogera predicts. LIGO should also be able to measure merging black holes' spins. If the spins are aligned, Kalogera says, the black holes probably formed from stars that already orbited each other; otherwise, they formed separately and hooked up later.

Even sooner, LIGO could test Einstein's theory of gravity, general relativity, in new ways. For example, says Clifford Will, a theorist at the University of Florida in Gainesville, just as light waves can be polarized horizontally or vertically, gravitational waves can wriggle in various more complex polarization patterns or modes. General relativity predicts that gravitational waves will have just two distinct polarization modes. But some alternative theories of gravity predict as many as six. Because of the way they're aligned, LIGO's detectors can't determine the waves' polarization, Will says. But they should be able to do it with the help of the upgraded Virgo detector near Pisa, Italy, scheduled to restart later this year. "If any other modes were detected, that would be bad news for general relativity," Will says.

Farther down the road, LIGO researchers hope to greatly improve their ability to pinpoint sources in the sky by adding a fourth detector to the LIGO-Virgo network, in India (*Science*, 14 February 2014, p. 717). Scientists also hope to launch a space-based detector array, which could sense much lower frequency waves from objects such as stars circling the massive black hole in the heart of our galaxy (*Science*, 20 November 2015, p. 894). But well before then, gravitational wave astronomy may pay early dividends. ■

The scientist who spotted the fateful signal—and let the cat out of the bag

By **Adrian Cho**

Of the more than 1000 physicists working with the Laser Interferometer Gravitational-Wave Observatory (LIGO), the first to see the long-awaited sign of gravitational waves was a soft-spoken postdoc who plays classical piano and has published two fantasy novels. Marco Drago, a 33-year-old native of Padua, Italy, was at his office at the Max Planck Institute for Gravitational Physics in Hanover, Germany, where 30 members of the LIGO team work on data analysis. Drago oversees one of four data "pipelines" that automatically comb the raw data from LIGO's detectors in Hanford, Washington, and Livingston, Louisiana, for promising signals.

On 14 September 2015, while Drago was on the phone with a colleague, his pipeline sent him an email alert telling him that both LIGO detectors had registered an "event" (a nonroutine reading) 3 minutes earlier, at 11:50:45 a.m. local time. It was a big one, with a signal-to-noise ratio more than twice as high as usual, Drago says. At first, he didn't believe the signal was real—and with good reason. To test the detectors, LIGO physicists have developed a system to "inject" artificial signals, and the signal seemed too good to be true. "No one was expecting something so huge," Drago says, "so I was assuming that it was an injection."

If all had gone as planned, Drago would have carried on thinking just that. However, the story veered off-script. LIGO researchers perform injections in two ways: openly when they tune up the machines and secretly when they are taking data. Those "blind" injections are supposed to prevent team members from knowing whether a signal is real or not. Only four LIGO leaders know when they're made, and they reveal that information only after a signal has been written up for publication. That's how things unfolded in 2010, when LIGO physicists learned at the last minute that a tantalizing signal was in fact a blind injection (*Science*, 15 March 2013, p. 1260).

This time, however, LIGO physicists were still reviving their machines after a 5-year upgrade, and Drago knew that the injection system was supposed to be off. He wondered whether he had misunderstood and someone had performed an open injection and perhaps failed to record it. Drago asked his fellow postdoc in Hanover, Andrew Lundgren, to check. Lundgren found no evidence of an injection. Next, Drago and Lundgren called the control rooms in Livingston and Hanford, where it was the small hours of the morning, to see whether anybody had monkeyed with the detectors or noticed anything unusual. Drago reached only one of them—"Livingston, I think," he says—but was told all was normal.

Finally, about an hour after receiving the alert, Drago broadcast an email to the entire LIGO collaboration. "I asked if anybody was aware of anything that could be an injection," Drago says. Nobody said yes. But now everybody in the collaboration knew that the instruments had seen a whopping big signal that on the face of it could not be a blind injection—exactly what they were not supposed to know. A few days later, LIGO leaders sent around a notice saying that the signal probably was not an injection.

On 18 September 2015, LIGO switched to data-taking mode. A press release said the hunt for gravitational waves had resumed, but researchers were collecting data primarily to validate the signal they already had, says Gabriela González, a physicist at Louisiana State University, Baton Rouge, and spokesperson for the LIGO scientific collaboration. By 5 October 2015, they had enough data to estimate the signal's statistical significance. The team even spent weeks investigating whether the signal could have been a prank before writing up the results.

Meanwhile, word of the discovery leaked out on social media and theorists' blogs. González says it was stressful addressing—or ignoring—inquiries, especially from the press. "It's been a lot of pressure, answering to people, not answering to people," she says. "But we never lied." ■

Published by AAAS



President Barack Obama with science adviser John Holdren in October 2009 during the first-ever White House Astronomy Night.

U.S. FUNDING

Pitching science: A history of Obama's research budgets

Economy, politics shape outcome of an uneven record

By **Jeffrey Mervis**

Seven years ago, in his first budget request to Congress, President Barack Obama sought to double spending on cancer research and to create a cluster of energy innovation hubs. Last week, in his final budget, Obama proposed a "moonshot" to fight cancer and urged legislators to fund a massive investment in clean energy and transportation research.

Déjà vu? Not really. Support for biomedical and energy research have been two consistent themes for Obama throughout his presidency. But the president doesn't get to call all the shots. The fate of science funding during his presidency has been shaped by difficult economic conditions and the rise of a powerful conservative faction in Congress bent on slowing the growth of government spending. Still, it seems fair to ask: What do those annual spending blueprints say about Obama's strategy and tactics as scientific salesman-in-chief?

Presidential science adviser John Holdren is fond of saying that, when it comes to science, "this president gets it." And although many research advocates generally agree, they have often been disappointed that Obama's requests for major science funding agencies, including the National Institutes of Health (NIH) and the National Science Foundation (NSF), haven't contained the steady and predictable growth that academic leaders say is essential to preserve U.S. leadership in science. Instead, the numbers have fluctuated from feast to famine.

Obama took office in January 2009 with the political winds at his back. The election had handed Democrats the White House and majorities in both houses of Congress. And facing the worst economic crisis since the Great Depression, legislators moved quickly to approve the American Recovery and Reinvestment Act, a massive economic stimulus package that arguably was the budgetary high point for science in the Obama presidency. It contained more than $20 billion in short-term research grants and shovel-ready scientific facilities for NIH, NSF, and half a dozen other research agencies.

Fresh from that victory, Obama told members of the U.S. National Academy of Sciences in April 2009 that he would boost the nation's investment in research above 3% as a fraction of its gross domestic product—a record level. He pledged to do it "through policies that invest in basic and applied research, create new incentives for private innovation, promote breakthroughs in energy and medicine, and improve education in math and science."

But a few weeks later, in his first budget request, Obama offered researchers a mixed message. The good news included an 8.5% boost in 2010 for the $6 billion NSF. His pledge to double cancer research over 8 years, however, was shoehorned into just a 1.5% increase for the $30 billion NIH. Still, Congress largely followed the White House's lead and even sweetened the pot, giving NIH $1 billion more than Obama's request.

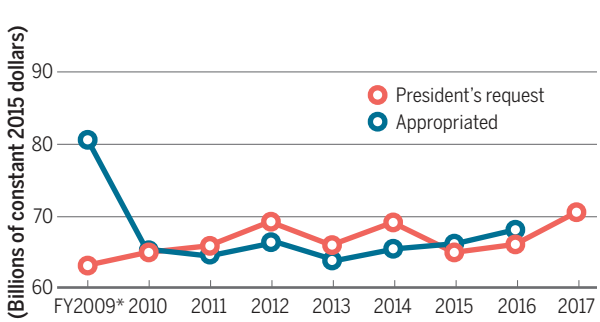
But that fast pace slowed dramatically. The administration was facing rising political pressure to curb a federal deficit that had soared past $1 trillion. Obama's response was a promise to freeze domestic spending for at least 3 years. Still, his 2011 request, submitted in February 2010, sought increases in a number of areas, including for several research agencies.

The freeze meant that Democratic legislators would have to cut something else to bolster research, however. The resulting deadlock stretched into the 2010 elections—which delivered a game-changing setback to the White House, as Republicans won control of the House of Representatives.

The new majority quickly proposed massive cuts in all federal spending, including research. Republicans eventually relented, but by the summer the White House and Congress had agreed to do something po-

President proposes, Congress disposes

Obama's requested levels for basic and applied research have waxed and waned even before Congress took final action.



*George W. Bush request; appropriation includes stimulus package

CREDITS: (PHOTO) AP PHOTO/PABLO MARTINEZ MONSIVAIS; (DATA) OMB, CONGRESS

Downloaded from on February 18, 2016

Published by AAAS

tentially even more damaging to science budgets: Reduce the federal deficit by $1.2 trillion over 10 years. A failure to agree on how to make the necessary spending reductions would trigger deep, automatic cuts known as sequestration.

Despite repeated predictions from all sides that sequestration would never happen, the cuts went into effect in March 2013. Continued wrangling over the budget led to a 16-day government shutdown in October 2013 before lawmakers agreed to temporarily ease the spending caps.

Even before sequestration took effect, however, Obama revived a strategy first adopted by the George W. Bush administration to make the case for higher research spending. His 2014 budget request sought double-digit increases for three agencies that fund the physical sciences—NSF, the Department of Energy, and the National Institute of Standards and Technology—in an effort to catch up with the pace of NIH's increases from 1998 to 2003, when its budget was doubled. But final appropriations fell far below the request.

Obama switched strategies again in his 2015 request, proposing minuscule increases for the major research agencies as a demonstration of fiscal restraint. The request also included a gimmick—a so-called "opportunity budget" designed to show what the United States could achieve in research and other areas if the spending caps were lifted. Lawmakers essentially ignored the aspirational budget but did approve modest increases for research.

The 2016 request contained healthier increases. But the budget process largely ground to a halt until the two sides negotiated a 2-year budget deal last December that paved the way for research spending increases even greater than Obama had proposed. Most notably, legislators doubled his $1 billion requested increase for NIH.

Last week, Obama threw in a new twist: spending an additional $4 billion on research through, for example, proceeds from the sale of government assets or from specific taxes or license fees. Such "mandatory spending" isn't usually on the table in the annual appropriations process, and the Republican majority in Congress immediately labeled the maneuver another gimmick. The fate of the president's 2017 budget request won't be known until lawmakers finish their work on spending bills, possibly not until after the November election.

As Obama prepares to walk off the political playing field for the last time, his scientific legacy remains up for grabs. The community cheered his intentions. But it's still weighing the effectiveness of his approach. ■

NEUROSCIENCE

Barcoding the brain

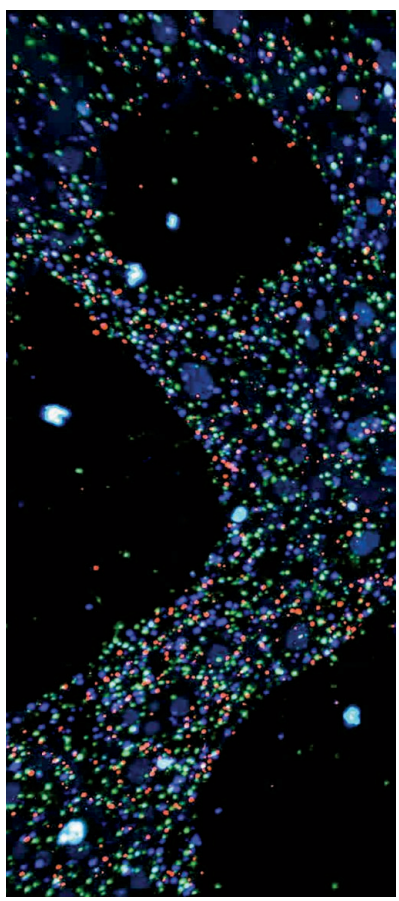
IARPA funds effort to map synaptic connections

By **Emily Underwood**

About 5 years ago, neuroscientist Tony Zador saw a slide at a scientific meeting that changed the course of his career. It showed a slice of mouse brain tissue containing a bright rainbow of neurons. Under most microscopes, neurons normally look gray and so densely packed as to be indistinguishable. But here each cell had been genetically engineered to produce a random, colorful fluorescent molecule.

Zador was struck by an idea: If he could replace the half-dozen distinct colors with a label consisting of, say, 30 random nucleotides—the building blocks of RNA and DNA—he could give unique barcodes to an almost infinite number of neurons. Then, if he also found a way to chemically link barcodes together across synapses, Zador could use high-throughput gene sequencing to build a synapse-by-synapse map of brain connections—a goal dear to neuroscientists who want to understand how the brain's intricate wiring underlies its functions. Unlike existing brain-mapping methods, the process could be thorough, accurate, and fast.

Now, after a decade-long "slog" and a marriage with another technology for tracking the barcodes in intact brain tissue, the researcher at Cold Spring Harbor Laboratory in New York believes the technique is ready for prime time. "A lot of individual steps and problems needed to be solved," says Ed Callaway, a neuroscientist at the Salk Institute for Biological Studies in San Diego, California. But the refined version "could, in one shot, get all [the connections of] a single [mouse] brain."



Inserting unique nucleotide barcodes (fluorescent dots, above) in neurons allows scientists to map cell networks in intact brain tissue.

IMAGE: WYSS INSTITUTE/HARVARD UNIVERSITY

The U.S. government is placing a large bet on Zador's method. As part of a project led by molecular engineer George Church of Harvard University, the technique was selected last month to receive a $21 million, 5-year brain mapping grant, one of six new projects under the Machine Intelligence from Cortical Networks, or MICrONS, program, sponsored by the Intelligence Advanced Research Projects Activity (IARPA). Part of the U.S. Brain Research through Advancing Neurotechnologies initiative, launched at President Barack Obama's request in 2013, MICrONS aims to map every neuron and synaptic connection within a 1-cubic-millimeter chunk of tissue from the mouse visual cortex. Ultimately, IARPA hopes those detailed brain connection maps will help scientists design computer architectures able to perform tasks that are easy for a brain but out of reach for artificial intelligence: recognizing a person or object from many different angles after seeing it only once, for example.

In an earlier version of his method, Zador and his team mapped neural connections in mice by injecting viruses encoding nucleotide barcodes into their brains. They would then use a custom-designed chemical to join and extract the paired barcodes on either side of a synapse from the post-mortem brain. Although the technique could reveal which neurons were connected to other neurons, fine spatial information about where cells were located was lost be-

Published by AAAS

cause they had to mash up the brain tissue to extract the barcodes, Zador says. "It was a brain-in-a-blender approach," R. Jacob Vogelstein, the IARPA program manager who runs the project in McLean, Virginia, says.

The companion technique, developed by Church, solves that issue by allowing Zador to read the barcodes without the need to extract them from the brain. The technique, called FISSEQ, applies washes of different fluorescent molecules to the tissue. Each molecule links to specific nucleotides, so successive washes cause each "letter" in a barcode to light up one at a time, like a series of brightly colored Christmas lights. An optical microscope captures the sequence: If a barcode in a given cell is ATGGCG, for example, the sequence of colors might be red-yellow-green-green-cyan-green, Zador says. When barcodes from two different cells show up within a synapse's distance of each other, a computer program infers that those two neurons are connected, Zador says.

Zador and Church predict their joint technique can extract the connectivity of a cubic millimeter of mouse brain tissue in days or weeks—not the months or years typical of electron microscopy. But hurdles remain, Zador says. Injecting the viruses does not guarantee that 100% of neurons receive only one unique barcode apiece. To address that problem, Church is now working on a way to genetically engineer mice to express random RNA sequences, barcodes, in their neurons during development.

Though he supports the general direction of the project, Karel Svoboda, a neuroscientist at Janelia Research Campus in Ashburn, Virginia, is skeptical that the barcoding strategy or its main competitor, improved electron microscopy, can fulfill IARPA's lofty ambitions. He suspects the mapping will contain too many errors. And Svoboda questions the premise of MICrONS. Given that most important brain functions are distributed across several brain regions, devising useful or fundamental neural computations based on the connection maps of a cubic millimeter of cortex is "a pipe dream, in my opinion," he says.

Vogelstein is more optimistic. If the brain has stereotypical rules that govern cortical circuitry, a cubic millimeter is "a sufficiently large chunk" of brain tissue that it should give a good picture of how neurons are wired to perform complex computations. "We believe and hope that there is this modularity," he says—indeed, "all of neuroscience is banking on it." If not? MICrONS may be the first to produce "solid evidence" of that disappointing fact, Vogelstein says. ■

GENOMICS

Pocket DNA sequencers make real-time diagnostics a reality

Advances in accuracy of nanopore sequencing help pave the way for on-the-spot DNA tests

By **Elizabeth Pennisi**

Not so long ago, sophisticated DNA sequencing required massive equipment and lots of time and money. Now, relatively cheap, pocket-sized devices are on the verge of giving real-time sequencing abilities to the masses. These so-called nanopore sequencers, produced so far by a single company, have suffered from poor accuracy. But this month, researchers reported that the instruments passed an important field test, conducting on-the-spot sequencing of viruses isolated from patients during last year's Ebola epidemic in West Africa. In the lab, meanwhile, other researchers are tweaking sample preparation and data analysis to boost the devices' accuracy and speed. Real-time analyses of pathogens and the rest of life are within reach, they say.

Ecologists, public health officials, epidemiologists, food safety officials, and many others may reap the benefits. Nanopore sequencing "is a point of departure in the way DNA is sequenced on this planet," says Mark Akeson, a molecular biologist at the University of California, Santa Cruz, who developed some of the technology that makes this approach possible and who consults with and holds stock in Oxford Nanopore Technologies, the U.K. company that is commercializing the technology. "It's democratizing sequencing."

> *"There's going to be one of these things in everyone's lab."*
>
> **Justin O'Grady**, University of East Anglia

To date, most sequencing works by building a DNA strand complementary to the one being sequenced. The building blocks, or bases, must be chemically tagged so that they can be identified as they are added one-by-one to the new strand, and the technique yields many short stretches of sequence that have to be pieced together. The nanopore approach instead reads the bases more directly, as a single strand of DNA is pulled through a microscopic pore. Each base interrupts an ionic current in the pore in a distinctive way that reveals its identity. The technique allows DNA strands thousands of bases long to be decoded in a single pass, without the delay and effort needed to piece together many short reads.

The idea is more than 25 years old, and it has been 4 years since Oxford Nanopore announced that it had used its prototype nanopore sequencer, called MinION, to decipher the DNA of a virus (*Science*, 4 May 2012, p. 534). Yet academic researchers have complained that the sequencer did a poor job of naming the bases. "The first thing everyone knows about nanopore [sequencing] is that it's not very accurate at the per-read level," says Rory Bowden, a genomicist at the Oxford Genomics Centre in the United Kingdom. To make the correct "call" for each base, the nanopore data had to be combined with conventional sequencing data pulled from databases (*Science*, 21 February 2014, p. 829).

Over about the past 2 years, hundreds of labs have been trying out the MinION through an early access program run by the company and have made steady improvements. Last month, for example, a team led by Niranjan Nagarajan, a computational biologist at the Genome Institute of Singapore, reported a way to improve accuracy without modifying the sequencing process. His group uses the MinION to identify bacteria in a sample of, say, skin or stool. To distinguish bacterial species, researchers sequence all copies of a ribosomal gene called *16S* in each sample, as each species has a unique version. But conventional sequencing methods yield just parts of the gene, sometimes not enough for a positive identification. The MinION can capture more, or all, of the gene, which should make species identification more precise—if the sequences are accurate enough.

To increase accuracy, Nagarajan's strategy is to treat the DNA with a chemical that makes each *16S* gene form a circle. Then he adds a special DNA-replicating enzyme that copies the circular DNA, creating strings of the same DNA repeated over and over. When

Downloaded from on February 18, 2016

Published by AAAS



This pocket sequencer, used here during the Ebola outbreak in West Africa, read viral genomes from human samples.

each string goes through the MinION's pore, that *16S* gene is sequenced multiple times. About six repetitions are enough to guarantee each base is accurately identified, Nagarajan and his colleagues reported on 27 January in a paper posted on bioRxiv, a preprint repository.

The recent Ebola fieldwork depended on a different strategy for improving the MinION's accuracy. Nicholas Loman, a microbial genomicist at the University of Birmingham in the United Kingdom, and his colleagues realized that they could extract further clues to a base's identity from the change in ionic current as the base moves through the pore. "There is yet more data encoded in the electrical signature," notes Winston Timp, a biomedical engineer at Johns Hopkins University in Baltimore, Maryland; for example, each base's signature is influenced by the bases on either side of it. With a new computer program for analyzing these "squiggles," developed by Jared Simpson from the Ontario Institute for Cancer Research in Toronto, Canada, and Loman's graduate student Joshua Quick, the team managed to sequence a bacterium in the lab with nanopore data alone.

They then took their sequencer to West Africa, where they successfully sequenced 148 Ebola virus genomes from patients, the group reported in the 3 February issue of *Nature*. Even under field conditions, they could complete a genome in 24 hours. "It means we can start taking public health measures based on genomic data," says microbiologist Andy Kilianski, a National Research Council fellow at the U.S. Army Edgewood Chemical Biological Center in Gunpowder, Maryland.

Matthew Loose, a developmental and computational biologist at the University of Nottingham in the United Kingdom, is tweaking the data analysis as well, but his goal is to reduce the time wasted sequencing unnecessary DNA. In 2014, Oxford Nanopore suggested that the MinION could kick a piece of DNA out of a pore before it was fully sequenced by reversing the pore current. Loose and his colleagues have now worked out a way to predict from the first 250 bases moving through a pore whether that piece likely has already been sequenced, as they reported 3 February in a paper posted on bioRxiv. Sequencing "will be faster in the end because every single read that you get, you want," says Justin O'Grady, a microbiologist at the University of East Anglia in Norwich, U.K. Loose, who described his group's latest work last week at the annual Advances in Genome Biology and Technology meeting in Orlando, Florida, hopes to get the number of bases needed to reject a strand down to 64 or even 32.

Several groups are working on other ways to increase efficiency of nanopore sequencing for diagnostics by speeding up DNA sample preparation and sequence analysis. That's important because "with Ebola, we knew what we were looking for," says Oxford Nanopore microbiologist Daniel Turner. "With [a typical] infection, you have no idea." Kilianski's team has in the works a MinION-based test that could go into the field and diagnose in a matter of hours RNA virus infections, including corona, dengue, Ebola, chikungunya, and Zika.

And O'Grady and his team can now pinpoint the cause of urinary tract infections in 4 hours, which will enable physicians to prescribe pathogen-specific antibiotics instead of broad-spectrum ones. "For me, nanopore is the only sequencing technology that gets us into the timeframe for actionable clinical diagnostics," he says.

Ideally, such tests should take less than an hour, O'Grady says. The latest MinION in the works could help; it passes 350 bases through the pore a second, up from 70. An even newer machine, the PromethION, integrates 48 MinIONs for high speed. That may help address another drawback of nanopore sequencing: low throughput—the base-by-base output is fast, and the reads long enough to quickly assemble small microbial genomes, but the overall amount of DNA that can be read by each MinION is fairly limited, which puts sequencing whole human genomes out of reach. It may also help for samples such as human blood, which have so much human DNA that the rarer pathogen's genetic material stands a good chance of being missed unless the sequencer can quickly and comprehensively process a sample.

The improvements all point in one direction, says O'Grady, who has been given free access to Oxford Nanopore's machine but has no financial stake in the company: "There's going to be one of these things in everyone's lab." And one day, perhaps in everyone's pocket, adds Camilla Ip of the Oxford Genomics Centre, who helped coordinate a multicenter evaluation of the MinION. "It will be like the mobile phone," she predicts. ■

PHOTO: EUROPEAN MOBILE LAB/TOMMY TRENCHARD

Published by AAAS

MICROBIOME

The right gut microbes help infants grow

Studies point the way to using microbial therapy to combat the lasting effects of poor nutrition

By **Elizabeth Pennisi**

Almost 180 million children across the globe are stunted, a severe, disabling consequence of malnutrition and repeated childhood infections that puts them at risk for cognitive impairment and disease. New studies now point to another player in stunting: the gut microbiome. The right combination of microbes, it seems, can tip the balance between stunting and healthy growth, even when calories are scarce—a tantalizing, if preliminary, clue to possible interventions.

The three studies, reported in this week's issues of *Science* and *Cell*, "are a watershed moment in global health generally, and in nutrition specifically," says William Petri, Jr., an infectious disease expert at the University of Virginia in Charlottesville. Petri was not involved in the current work, but he has spent years tracking the health of infants in Bangladesh. He and others have been long been frustrated by the inability of dietary supplements to reverse the negative effects of poor nutrition.



In Malawi, studies of infant growth—and undergrowth—are revealing a key role for microbes.

PHOTO: LUCY BOLLINGER/WASHINGTON UNIVERSITY IN ST. LOUIS

When Petri heard that gut bacteria might influence obesity, he reasoned that they might also influence a person's response to hunger. So he and Tahmeed Ahmed from the International Centre for Diarrheal Disease Research in Bangladesh teamed up with Jeffrey Gordon, a microbiologist at Washington University in St. Louis in Missouri, to collect monthly fecal samples from healthy and malnourished Bangladeshi children under 2. Petri and Gordon found that as children matured, their community of gut bacteria normally shifted as well. But as they reported in 2014, stunted children didn't have the appropriate bacterial community for their age, but an "immature" one more typical of a younger child.

On p. 830, Gordon's team reports finding the same pattern in infants in Malawi, and they present evidence that these microbial communities influence growth. Working with mice bred to have no gut microbes of their own, Gordon's graduate student Laura Blanton fed them a mash of the same food typically eaten by Malawian children. Germ-free mice given the "immature" microbiomes of children with symptoms of malnourishment grew poorly, whereas mice on the same diet given "mature" microbiomes of healthy children put on more muscle and developed seemingly denser bones.

François Leulier, a biologist from the École Normale Supérieure de Lyon in France and colleagues report a similar finding on p. 854. His postdoc Martin Schwarzer showed that young, germ-free mice don't put on as much muscle or grow bones as big as mice that have the normal complement of bacteria, even when they eat the same amount of food. The team also glimpsed a mechanism: They found that the microbes affect the animals' own hormones.

In healthy animals, growth hormone stimulates an increase in a second hormone, insulinlike growth factor 1 (IGF-1), which in turn promotes tissue growth. Germ-free mice still have the same amount of growth hormone as other mice, but the activity of IGF-1 in their blood, liver, and muscles is lower, Leulier's team found. It's not clear how the microbes influence the hormones. But injecting germ-free mice with IGF-1 brought their growth on par with the other mice, as did giving them one particular strain of lactobacillus.

A breakdown in this microbiome-hormone connection may help explain stunting in undernourished children. But why do only some of them end up with an immature microbiome? In the *Cell* study, Gordon, graduate student Mark R. Charbonneau, and their colleagues show that breast-feeding may help the right microbes get established and set the baby's growth on the right trajectory. Healthy mothers typically produce modified sugar molecules called sialylated human milk oligosaccharides. Babies don't make use of these nutrients, but their gut microbes thrive on them, recent research has shown (*Science*, 15 August 2014, p. 747). The new work shows that mothers of children who show signs of severe malnutrition make less of this microbiome "food."

When the researchers added oligosaccharides purified from whey to the Malawian diets of mice with microbes from a severely malnourished infant, the mice grew more muscle, bigger bones, and had quite "dramatic changes" in brain and liver metabolism, Gordon says. He speculates that by processing these sugars, the bacteria may in turn produce molecular building blocks to help the host's body grow well. The group has also seen this beneficial effect in germ-free piglets, whose physiology is more humanlike than mice, they report.

To David Relman, a microbiologist at Stanford University in Palo Alto, California, the implications are "profound. … The nutritional status of children might be modifiable through manipulation of the gut microbiota." Gordon and Leulier plan to test that possibility in people, particularly malnourished children, this year with dietary interventions.

A safe and effective probiotic "would be tremendous," Petri says. Success in laboratory animals may not translate to humans, of course. And researchers need to be sure that any added microbes don't cause unwanted effects, such as inflammatory disease or obesity, adds Eric Pamer, an infectious disease expert at the Memorial Sloan Kettering Cancer Center in New York City. But one thing is certain, he says: "The health-promoting impact of [these] microbiota is astonishing." ■

Downloaded from on February 18, 2016

Published by AAAS



Downloaded from on February 18, 2016



One of Webb's gold-coated beryllium mirror segments is inspected before assembly.

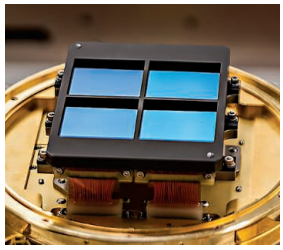
PHOTOS: (LEFT TO RIGHT) NASA/CHRIS GUNN; K. W. DON, UNIVERSITY OF ARIZONA

THE NEXT BIG EYE

The pressure is on the builders of the James Webb Space Telescope to ensure that NASA's $8 billion gamble pays off

By **Daniel Clery**, *in Greenbelt, Maryland*

For months, inside the towering Building 29 here at Goddard Space Flight Center, the four scientific instruments at the heart of the James Webb Space Telescope (JWST, or Webb) have been sealed in what looks like a house-sized pressure cooker. A rhythmic chirp-chirp-chirp sounds as vacuum pumps keep the interior at a spacelike ten-billionth of an atmosphere while helium cools it to −250°C. Inside, the instruments, bolted to the framework that will hold them in space, are bathed in infrared light—focused and diffuse, in laserlike needles and uniform beams—to test their response.



Sensors proved too fragile in testing, forcing a redesign.

The pressure cooker is an apt metaphor for the whole project. Webb is the biggest, most complex, and most expensive science mission that NASA has ever attempted, and expectations among astronomers and the public are huge. Webb will have 100 times the sensitivity of the Hubble Space Telescope. It will be able to look into the universe's infancy, when the very first galaxies were forming; study the birth of stars and their planetary systems; and analyze the atmospheres of exoplanets, perhaps even detecting signs of life. "If you put something this powerful into space, who knows what we can find? It's going to be revolutionary because it's so powerful," says Matt Mountain, director of the Association of Universities for Research in Astronomy in Washington, D.C., and former JWST telescope scientist. Like that of Hubble, however, Webb's construction has been plagued by redesigns, schedule slips, and cost overruns that have strained relationships with contractors, partners in Canada and Europe, and—most crucially—supporters in the U.S. Congress. Other missions had to be slowed or put on ice as Webb consumed available resources. A crisis in 2010 and 2011 almost saw it canceled, although lately the project has largely kept within its schedule and budget, now about $8 billion (*Science*, 24 April 2015, p. 388).

But plenty could go wrong between now and the moment in late 2018 when the telescope begins sending back data from its vantage point 1.5 million kilometers from Earth. It faces the stresses of launch, the intricate unfurling of its mirror and sunshield after it emerges from its chrysalis-like launch fairing, and the possibility of failure in its many cutting-edge technologies. Unlike Hubble, saved by a space shuttle mission that repaired its faulty optics, it is too far from Earth to fix. And not just the future of space-based astronomy, but also NASA's ability to build complex science missions, depends on its success.

That's why those instruments sat in Goddard's pressure cooker for what is known as cryo-vacuum test 3 (CV3). And it is why Webb's other components—including the mirror and telescope structure, the "bus"

Published by AAAS

BUILDING THE BIGGEST EYE IN SPACE

Constructing a successor to the Hubble Space Telescope has been an epic undertaking involving more than 1000 people in 17 countries over 2 decades. As that effort reaches its climax, the telescope components face a complex series of tests to ensure that the telescope deploys—and works—perfectly.

July
Structure to hold Webb's instrument module arrives at Goddard Space Flight Center.

December
Main mirror segments finish testing at Marshall Space Flight Center.

April
Center section of main mirror's backplane support structure finished.

May
First instrument arrives at Goddard from Europe.

July–Sept.
Remaining three instruments delivered to Goddard.

February
Main mirror backplane wing structures complete.

August–Nov.
First cryo-vacuum test of instrument module.

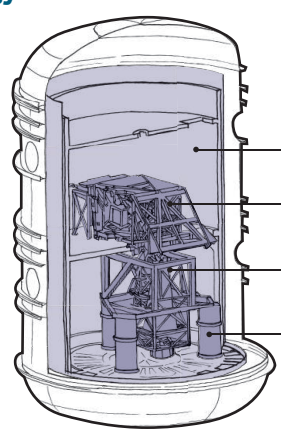
December
Main mirror segments delivered to Goddard.

2011 2012 2013 2014

Testing and technology

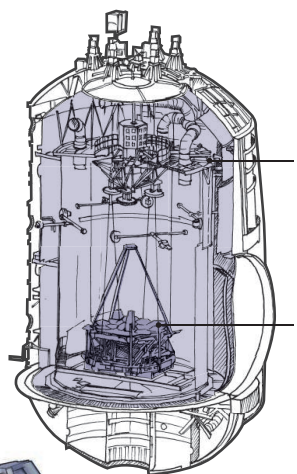
Instrument module test

Webb's instruments were tested three times inside a pressure vessel at Goddard to simulate the cold and vacuum of space. While inside, various forms of light were shone through the instruments to test their operating modes.



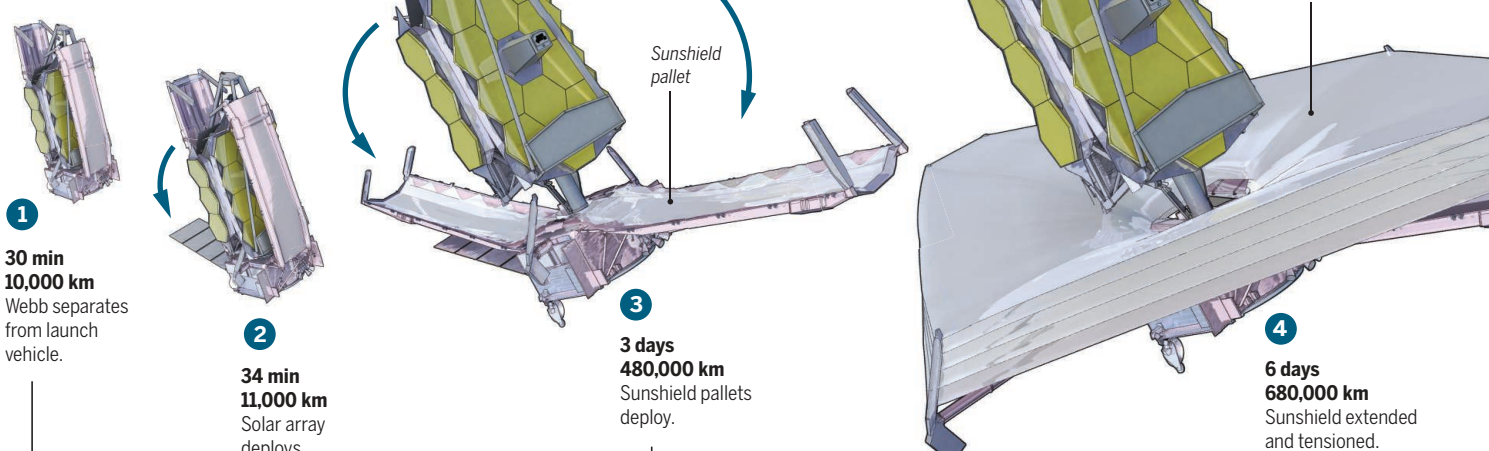
Telescope test

The combined telescope and instruments will be tested in 2017 inside the giant Chamber A at Johnson Space Center. Suspended from the ceiling to reduce vibration, the telescope will look up at an artificial universe.



Deployment in space

Like a butterfly emerging from its cocoon, Webb will unfurl its components step by step on its way to its final orbit.



1
30 min
10,000 km
Webb separates from launch vehicle.

2
34 min
11,000 km
Solar array deploys.

3
3 days
480,000 km
Sunshield pallets deploy.

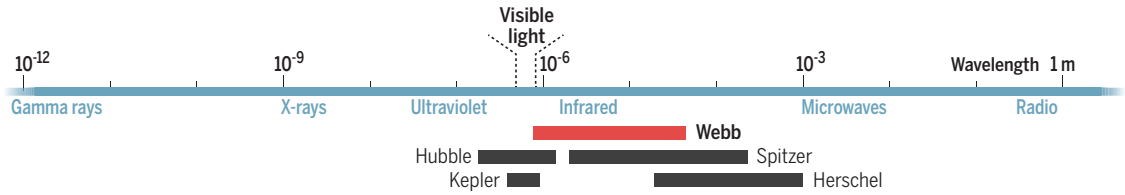
4
6 days
680,000 km
Sunshield extended and tensioned.

Earth — Moon 384,800 km

Published by AAAS

Webb's range of vision

Webb is designed to study the infrared sky, for the first time at such high resolution.



May–Sept. Second cryo-vacuum test of instrument module.

April Telescope deployment tower completed.

June–July Vibration and acoustic testing of instrument module.

October–January Third cryo-vacuum test of instrument module and mirror segments fitted to backplane.

April Telescope and instrument module joined.

Feb.–May Telescope/instruments in cryo-vacuum test in Johnson's Chamber A.

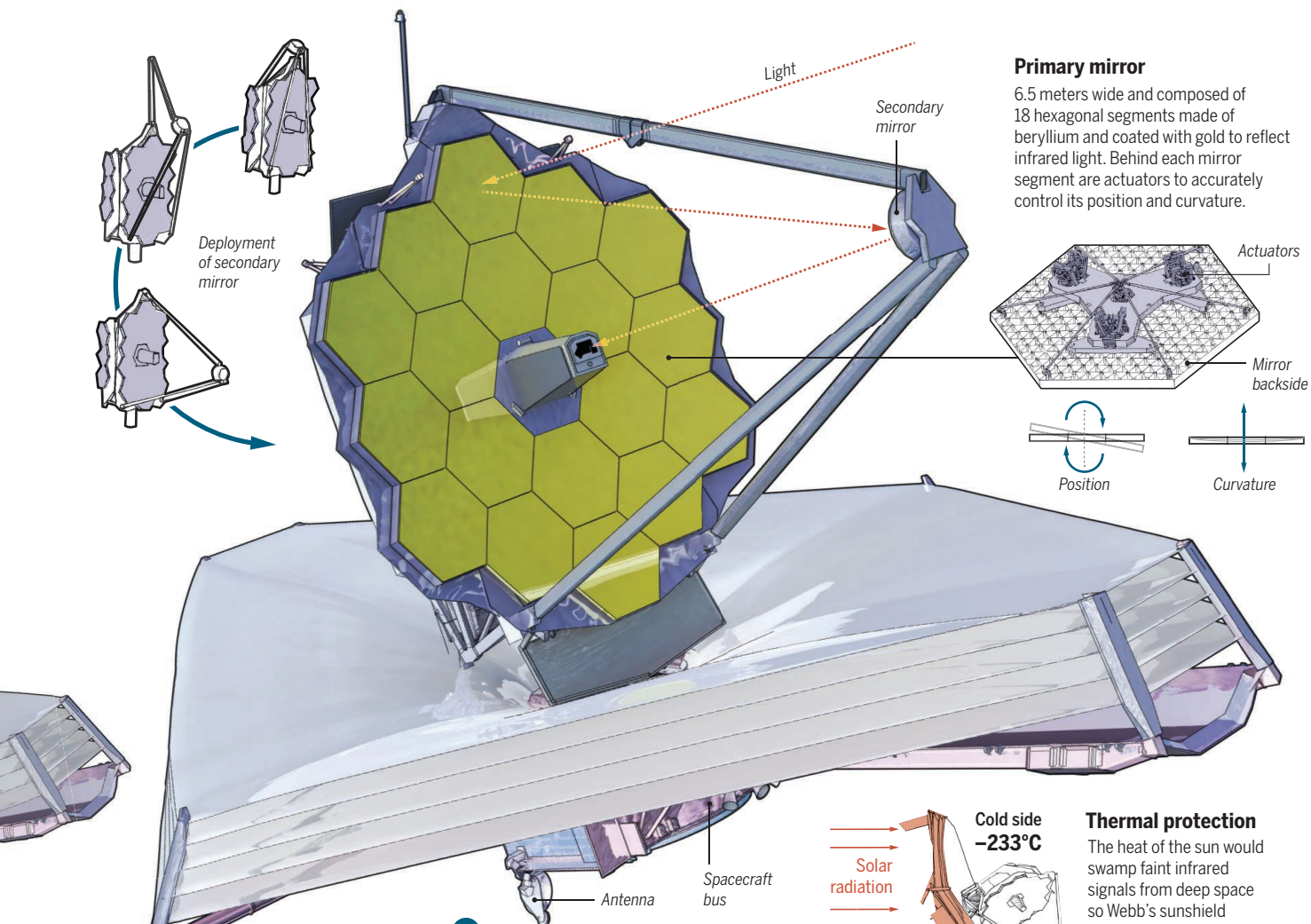
May Telescope/instruments shipped to California.

Oct.–May Telescope/instruments combined with bus/sunshield and tested.

August Webb transferred by ship to French Guiana.

October Launch on Ariane 5 from ESA spaceport.

2016 2017 2018

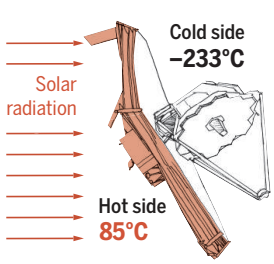


Primary mirror

6.5 meters wide and composed of 18 hexagonal segments made of beryllium and coated with gold to reflect infrared light. Behind each mirror segment are actuators to accurately control its position and curvature.

5

11–14 days
1,000,000 km
After the secondary mirror swings into place on its supports, the wings of the main mirror rotate into position and mirror phasing begins.



Thermal protection

The heat of the sun would swamp faint infrared signals from deep space so Webb's sunshield reduces solar heat to less than one-millionth its normal value.

Day 29
Final orbit of telescope.

1,500,000 km

CREDITS: (DATA) NASA; (ILLUSTRATIONS) SOHAIL AL JAMEA; A. CUADRA/*SCIENCE*

Published by AAAS

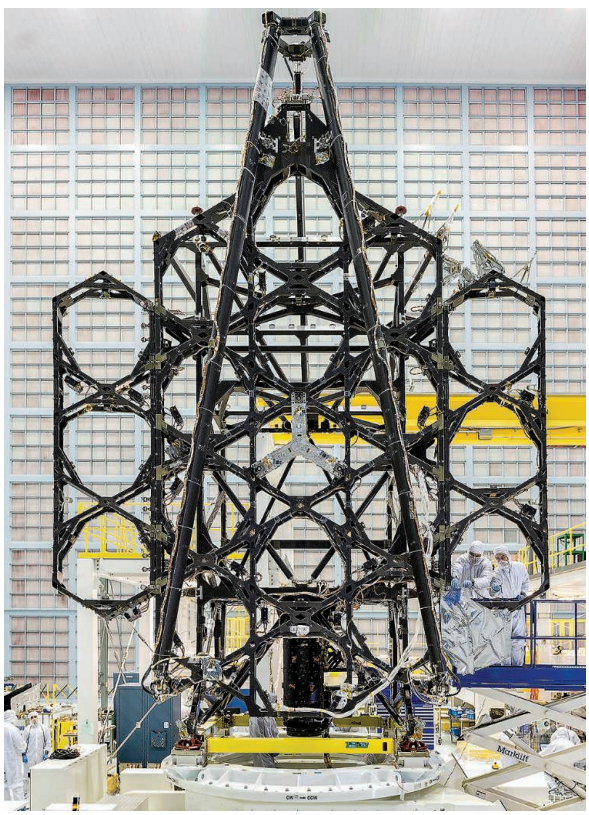
that will supply power and control the telescope, and the tennis court–sized, multilayer parasol that will help keep it cool—must undergo a gauntlet of testing, alone and in combinations, until the whole spacecraft is ready. For those on the inside, the strain will only increase as assembly continues, the tests get bigger and more comprehensive, and the spacecraft is launched into space. Only when Webb opens its eye and successfully focuses on its first star will the strain be released.

IN THE MID-1990s, after Hubble had had its optics corrected and was busy revolutionizing astronomy, researchers began planning its successor. The catch phrase in NASA at the time, championed by agency chief Daniel Goldin, was "faster, better, cheaper." Goldin challenged NASA engineers and the astronomical community to come up with a follow-on that was cheaper than Hubble but bigger, with a mirror 8 meters across. He received a standing ovation when he described the plans to the American Astronomical Society in 1996. Whereas Hubble covered the whole range of visible light, plus a smidgen of ultraviolet and infrared, the Next Generation Space Telescope (as it was then known) would be a dedicated infrared observatory.

For astronomers, the infrared spectrum was a beckoning frontier. Visible light from the most distant objects in the universe, the very first stars and galaxies that formed after the big bang, gets stretched so much by the expansion of the universe that it ends up in the infrared range by the time it reaches us. Many chemical signatures in exoplanet atmospheres also show themselves in the infrared region. Yet Earth's atmosphere blocks most infrared. Webb will give us "the first high-definition view of the midinfrared universe," says Matt Greenhouse, JWST project scientist for the instrument payload at Goddard.

To capture that light, however, NASA engineers had to overcome huge challenges. The first was heat: To keep the infrared glow of the telescope itself from swamping faint astronomical signals, Webb would need to operate at about –233°C, 40° above absolute zero (40 K). That would require entirely new instrument designs. Size and weight constraints posed additional hurdles: An 8-meter mirror would never fit inside a rocket fairing, so it would have to fold up for launch. The sunshield, too, would have to be collapsible and made of a superthin, lightweight membrane. And the telescope structure would have to be absolutely rigid but lightweight enough to limit the weight of the whole orbiting observatory to no more than 6 tonnes, just a few percent of the weight of a similar-size ground-based telescope. "We knew we would have to invent 10 new technologies" to make the telescope work, says NASA's JWST Program Director Eric Smith, in Washington, D.C.

Take the mirror. Hubble's was made from a single slab of glass, but Webb's folding mirror would need to be segmented, made up of separate hexagonal pieces—a design used in many top ground-based instruments, including the Keck telescopes in Hawaii. The segments would have to be minutely controlled to meld them into a single optical surface, with their reflected light completely in step—a process known as phasing. In Webb, each hexagonal segment will sit on six actuators that control its orientation, plus one in the center to adjust its curvature.



Webb's mirror backplane is made from a graphite composite that is lightweight and rigid, retaining its shape down to cryogenic temperatures.

Choosing the mirror material itself was a challenge, because it would have to stand up to a grueling ordeal. Because any material will change shape as it cools, each segment would have to be ground to a shape that is optically wrong at room temperature but warps into one that is correct—to within nanometers—at 40 K. To do that, the mirrormakers planned to combine sophisticated computer modeling with a laborious, iterative process of grinding, cooling, measuring, warming, regrinding, cooling again, and so on. After testing both glass and the metal beryllium, Webb planners chose beryllium because it is strong and light, and it behaves more predictably during repeated cooling and warming cycles.

The final design for Webb fell short of NASA's original ambitions. Beginning in 2001, concerns about the swelling cost of the telescope forced NASA to shrink the mirror from 8 meters to 6.5 meters, reducing the number of mirror segments from 36 to 18 and its light-collecting area from 50 square meters to 25. But review panels decided that Webb could still achieve its scientific goals. To cut costs further, NASA decided to use less precise mirrors that could be manufactured with many fewer cooling-warming-grinding steps. The change would make Webb less sharp at near-infrared wavelengths between 1 and 2 micrometers—no great loss, as ground-based telescopes already cover that part of the spectrum.

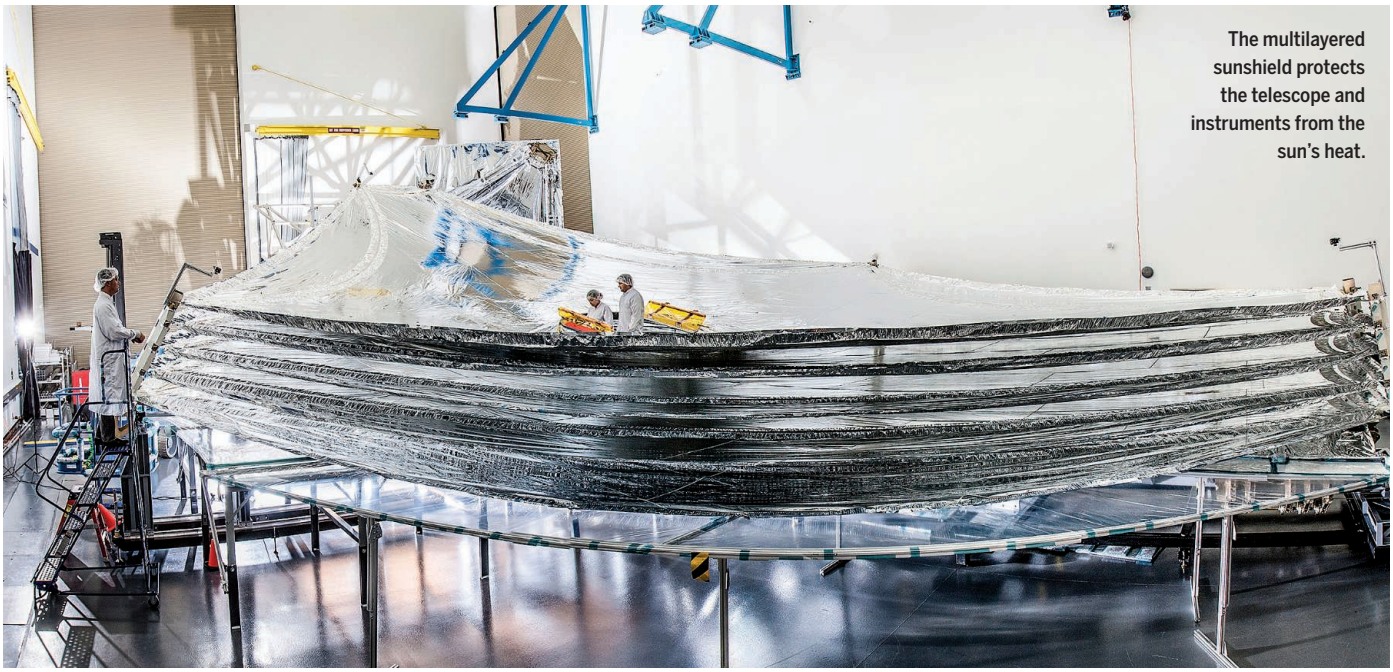
By 2006, all of Webb's key technologies had been tested and proven viable. The final design was drawn up, and construction of components got underway. Meanwhile, NASA engineers began dreaming up the byzantine series of tests each separate component would have to pass—and the additional tests to be done as components were combined to form larger elements of the spacecraft. "As soon as we put two or three parts together, we test them," says Scott Willoughby, who is in charge of the Webb effort at Northrop Grumman in Redondo Beach, California.

To put Webb's enormous mirror through its paces, engineers at the Johnson Space Center in Houston, Texas, completely refitted Chamber A, a huge cryo-vacuum chamber built to test the crew-carrying spacecraft of the Apollo program. For the instruments, they devised the peculiar tortures at Goddard.

THE FLIGHT MODELS of the instruments began arriving in 2012: four infrared imagers and spectrographs built by collaborators including the European Space Agency, a NASA/European consortium, the University of Arizona, and the Canadian Space Agency. Once the instruments were secured on their rigid framework, they were vigorously shaken to simulate the stresses of launch, as well as blasted with 150 decibels by loudspeaker horns as tall as a person.

PHOTO: NASA/CHRIS GUNN

Published by AAAS



The multilayered sunshield protects the telescope and instruments from the sun's heat.

Next came the first cryo-vacuum test to simulate space conditions.

Problems emerged almost immediately. The heating and cooling caused the delicate multilayer semiconductor sandwiches that make up the infrared detectors to swell and crack. Another critical technology, the microshutter array in the near-infrared spectrograph, also succumbed. This is a device the size of four postage stamps with a grid of 250,000 tiny flaps that can be opened selectively so that the instrument can take separate spectra from, say, 100 galaxies in a single field of view—the first such multiobject spectrograph to fly in space. But the deafening noise of the acoustic chamber caused many of the flaps to jam.

Instrument teams and manufacturers scrambled to identify the problems and produce new parts. Meanwhile, testing went on. All the replacements came together in time for the recent CV3 test, and as the test ended in late January the signs were encouraging that the fixes had worked. "We're quite pleased with the performance," says astronomer Marcia Rieke of the University of Arizona's Steward Observatory in Tucson, principal investigator for the near-infrared camera. "We're very close to ready for launch."

While the instruments underwent their ordeal, white-clad engineers in a nearby clean room were painstakingly fitting the mirror segments onto their support, known as the backplane. Hollowed out on the back to reduce weight, each 1.3-meter-wide segment can be carried by a single person, and each has a particular destination on the backplane, depending on its precise optical qualities.

Now that the instruments have been tested and the mirror assembled, these two elements will be mated in March. Then the combined telescope and instrument package, collectively known as OTIS, will endure the shaker tables and acoustic chamber before being inserted into a specially built shipping container. In the dead of night, a truck will carry the container at just 8 kilometers per hour from Goddard to Joint Base Andrews, where it will be placed into a huge C-5 Galaxy transport plane, with just centimeters of clearance, for its flight to Houston.

The few months OTIS spends in Chamber A early next year will be the most critical it will face. Light sources on the ceiling will create an artificial universe, allowing NASA engineers to run light all the way through the system from main mirror to detectors for the first and only time in spacelike conditions. They will practice phasing up the mirror and will check out all observing modes of the four instruments. "Hubble didn't do an end-to-end optical test. We're not skipping that on this program," Greenhouse says.

Then it's back into the shipping container and another C-5 flight to Redondo Beach, where Northrop Grumman has been building the bus and sunshield. There the full observatory will take shape as the telescope and instruments are mated to these last two elements.

Now too large to fit inside a plane, Webb will make its final prelaunch journey by ship, down the California coast and through the Panama Canal to French Guiana—home of Europe's spaceport, and a waiting Ariane 5 launcher, part of Europe's contribution to the project. In October 2018, the Ariane will fling Webb toward L2, a gravitational balance point 1.5 million kilometers from Earth, directly away from the sun. The journey will take 29 days.

Webb will begin unfolding and deploying components almost as soon as it hits space. Deployment will be "3 weeks of terror," Mountain says. "No one has done this before, ever." First to deploy will be solar arrays and antennas to provide power and communications with Earth; then the sunshield will unfurl to begin cooling the telescope and instruments; finally, the secondary mirror will swing into position and the main mirror wings will snap into place. Once the mechanical gymnastics routine is finished, there will come the heart-stopping moment when the mirror first looks at the sky. Then the mirror has to be phased up, and the instruments cooled and all their modes tested. Commissioning is expected to take a full 6 months after launch.

"A whole chain of things have to be done to get that really good-looking star," says Lee Feinberg, JWST telescope manager at Goddard. "But then we can really rest."

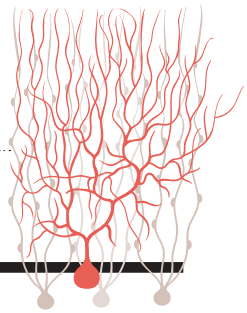
Until then, the pressure will be unrelenting. But the builders of Webb say they do find time to reflect on what they are doing. Pierre Ferruit, JWST project scientist at the European Space Agency in Noordwijk, the Netherlands, recalls watching from the control room at Goddard during CV3 as technicians carried mirror segments into the clean room and fitted them to the backplane. "Even for someone working on the mission, it's quite incredible," he says. Rieke had the same sensation: "It's just enchanting to be witnessing history." ■

PHOTO: NORTHROP GRUMMAN/ALEX EVERS

Published by AAAS

Understanding astrocyte diversity p. 813 ▸

Testing tools to protect the global financial system p. 818



PERSPECTIVES

IMMUNOLOGY

How does the immune system tolerate food?

Intestinal T cells balance the immune response to microbes and food

By **Chantal Kuhn** *and* **Howard L. Weiner**

The gastrointestinal immune system (gut-associated lymphoid tissue) has the unique capacity to discriminate between harmless and potentially dangerous material. It can raise a protective response against pathogenic microbes and toxins while tolerating food antigens and commensal microbes. This is a challenge given the vast number of foreign antigens, mainly derived from food (>100 g of protein per day), and commensal microbes colonizing the gut (an estimated 100 trillion, 10 times the number of cells in the human body). Dysfunction of this delicate balance between immunity and tolerance can lead to pathologies such as food allergy, autoimmune diseases, and infections. On page 858 of this issue, Kim *et al.* (*1*) show that dietary antigens trigger the generation of a regulatory T (T_{reg}) cell type in the small intestine that suppresses immune responses to food. These T_{reg} cells are phenotypically and functionally distinct from those in the colon that suppress immune responses to commensal microbes (*2, 3*).

The phenomenon of continuous oral administration of low-dose foreign antigen

Ann Romney Center for Neurologic Diseases, Brigham and Women's Hospital, Harvard Medical School, Boston, MA 02115, USA. E-mail: hweiner@rics.bwh.harvard.edu



Tolerance. Understanding the mechanisms that induce and maintain immune tolerance to food antigens will provide insights into human diseases such as food allergy.

Downloaded from on February 18, 2016

Published by AAAS

inducing local and systemic hyporesponsiveness to a subsequent challenge with the fed antigen has been called "oral tolerance" (*4*, *5*). T_{reg} cells are key to this tolerance. They control pathogenic immune responses and are characterized by the expression of the transcription factor forkhead box p3 (Foxp3) (*6*). Thymus-derived (tT_{reg}) cells are essential for maintaining immune tolerance to self and immune homeostasis. However, Foxp3 can also be expressed in conventional T cells in response to foreign antigen (*6*). These peripheral T_{reg} (pT_{reg}) cells control immunity at sites of inflammation, especially at mucosal surfaces, and differ from tT_{reg} cells by a decreased expression of the surface marker neuropilin-1 (*7*, *8*). Although feeding of experimental antigens induces the generation of pT_{reg} cells (*4*), the influence of a normal diet on these cells has remained unknown.

To separate the influence of food antigens from the impact of microbiota, Kim *et al.* used germ-free mice (devoid of microbiota) raised and bred on an elemental "amino acid" diet lacking food antigens (antigen-free mice) and compared them to germ-free mice and mice that harbored microbiota but no pathogenic microbes. Depletion of dietary antigen (antigen-free mice) led to a decrease of antigen-experienced T ($CD4^+$) cells in the tissue of the small intestine relative to the effect of such a diet on mice lacking all gut microbes or mice harboring only "good" gut microbes. Consistent with previous data (*2*, *3*), pT_{reg} cells were abundant in the lamina propria of the small intestine and the colon of mice with good microbes, but decreased in the colon of germ-free mice. In the latter mice, absence of food antigens led to additional depletion of pT_{reg} cells in the small intestine, which suggests that food antigens trigger the production of pT_{reg} cells in the small intestine, whereas microbiota elicit pT_{reg} cell generation in the colon.

Kim *et al.* found that pT_{reg} cells that arise in response to food antigens or microbiota can be distinguished by the presence of a transcription factor called retinoid-related orphan receptor gamma t (RORγt). Depletion of microbiota-induced pT_{reg} cells by using germ-free mice or administering antibiotics to normal mice decreased $ROR\gamma t^+$ pT_{reg} cells, whereas the weaning of mice harboring only good gut microbes on a diet free of food antigens decreased $ROR\gamma t^-$ pT_{reg} cells. Because a decrease in pT_{reg} cell numbers might be triggered by preferential depletion of tolerogenic antigen-presenting cells (such as dendritic cells) that spur pT_{reg} generation, Kim *et al.* analyzed dendritic cell subsets in the small intestine of food antigen–free mice. Dendritic cells ($CD103^+CD11b^+$) that stimulate the production of pT_{reg} cells (*9*, *10*) decreased by 40%, indicating a role in the production of pT_{reg} cells in response to food antigens. However, other factors that regulate pT_{reg} cell production remain to be elucidated, as indicated by the small decrease in the number of these dendritic cells.

Because food antigen–free mice showed no intestinal pathology after a normal chow diet, Kim *et al.* used two different experimental models to assess how food antigen–induced pT_{reg} cells modulate the immune response against fed antigens. Transgenic $CD4^+$ T cells that respond to ovalbumin were transferred into food antigen-free or germ-free mice, or into mice harboring only good gut microbes, before the animals were fed ovalbumin. Ovalbumin increased the proliferation of ovalbumin-specific $CD4^+$ T cells while inhibiting generation of ovalbumin-specific pT_{reg} cells in the small intestine of food antigen–free mice as compared to mice with good gut microbes or germ-free mice. This effect was also observed in the mesenteric lymph nodes that drain the gut, but not in the spleen, indicating a local but not systemic loss of tolerance. Feeding ovalbumin to a mouse strain that was more susceptible to allergy, and that was also free of food antigen in its diet, triggered severe diarrhea and boosted immunoglobulin E production against ovalbumin, suggesting that food antigen–induced pT_{reg} cells contribute to controlling allergy.

Together, these data show that components in food induce $ROR\gamma t^-$ pT_{reg} cell production in the small intestine. These cells seem to contribute to controlling local T cell responses (T helper cells) depending on the experimental context, and are phenotypically and functionally distinct from microbiota-induced $ROR\gamma t^+$ pT_{reg} cells (*3*, *9*). However, it is unclear whether these food antigen–induced pT_{reg} cells are also responsible for the systemic effects of oral tolerance. It has been suggested that circulating food antigen that is taken up and presented by liver-resident cells contributes to establishing systemic tolerance (*5*). It would also be interesting to analyze the transcriptional profile of food antigen–induced pT_{reg} cells. Do they express other T cell lineages (*6*) or tissue-specific transcription factors (*11*) that offer insight into their generation, maintenance, and function? ■

REFERENCES

1. K. S. Kim *et al.*, *Science* **351**, 858 (2016).
2. C. Ohnmacht *et al.*, *Science* **349**, 989 (2015).
3. E. Sefik *et al.*, *Science* **349**, 993 (2015).
4. H. L. Weiner *et al.*, *Immunol. Rev.* **241**, 241 (2011).
5. O. Pabst, A. M. Mowat, *Mucosal Immunol.* **5**, 232 (2012).
6. S. Z. Josefowicz *et al.*, *Annu. Rev. Immunol.* **30**, 531 (2012).
7. M. Yadav *et al.*, *J. Exp. Med.* **209**, 1713 (2012).
8. J. M. Weiss *et al.*, *J. Exp. Med.* **209**, 1723 (2012).
9. J. L. Coombes *et al.*, *J. Exp. Med.* **204**, 1757 (2007).
10. C.-M. Sun *et al.*, *J. Exp. Med.* **204**, 1775 (2007).
11. J. Lu *et al.*, *Cell. Immunol.* **297**, 53 (2015).

10.1126/science.aaf2167

PHOTO (OPPOSITE PAGE): © WEESTOCK IMAGES/ALAMY STOCK PHOTO

STRUCTURAL BIOLOGY

Cas9, poised for DNA cleavage

Structural rearrangements explain how Cas9 cuts DNA

By **Hongfan Chen** *and* **Scott Bailey**

Over the past 3 years, the technique known as CRISPR—clustered regularly interspaced short palindromic repeats—has revolutionized the field of genome editing (*1*). A single enzyme called CRISPR-associated protein 9 (Cas9) can be programmed with CRISPR-derived RNAs (crRNAs) to introduce double-stranded DNA (dsDNA) breaks at specific sites in the genome. On page 867 of this issue, Jiang *et al.* (*2*) describe structures of *Streptococcus pyogenes*

"Understanding how binding...activates...Cas9 ...provides a framework for ...improved genome editing."

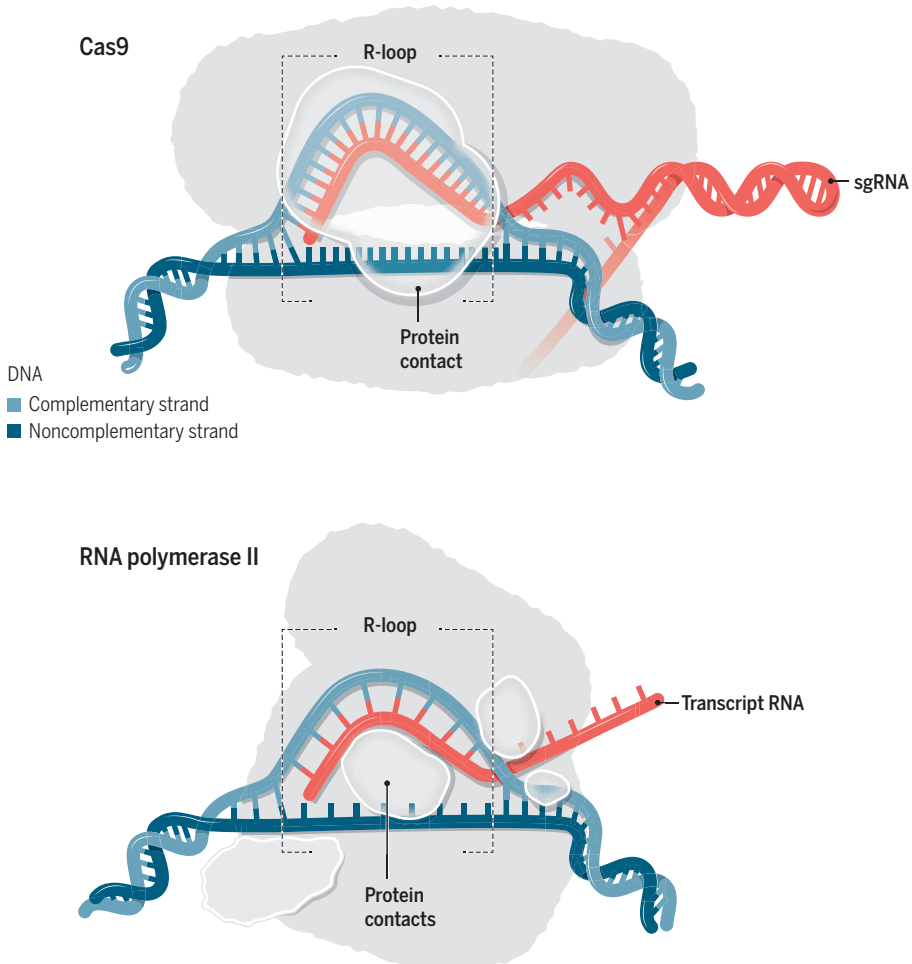
Cas9 captured in a state poised for DNA cleavage. This new snapshot, together with those from previous structures, explains how binding to a dsDNA target allosterically activates DNA cleavage by the Cas9 endonuclease.

To generate dsDNA breaks, Cas9 must cleave each strand of the duplex target. As such, Cas9 contains two nuclease domains, the HNH domain and the RuvC domain. Cas9 identifies DNA as a target if it contains a protospacer sequence, which is a sequence that is complementary to the guide region of the crRNA, and a short protospacer adjacent motif (PAM). DNA targeting by Cas9 requires not only a crRNA but also a trans-acting crRNA (tracrRNA) (*3*, *4*) that can be artificially fused with the crRNA as one single-guide RNA (sgRNA) (*3*), a strategy often used in genome editing experiments. Target binding triggers

Department of Biochemistry and Molecular Biology, Bloomberg School of Public Health, Johns Hopkins University, Baltimore, MD 21205, USA. E-mail: scott.bailey@jhu.edu

Downloaded from on February 18, 2016

Published by AAAS



Strands apart. Interactions between Cas9 and the two separated strands of the DNA target activate the nuclease activity of Cas9. The subsequent dsDNA breaks form the basis of CRISPR-mediated genome editing. Cas9 stabilizes the R-loop structure, similar to how an RNA polymerase II stabilizes an R-loop.

formation of an R-loop in which the guide region of the crRNA invades the dsDNA target to form a base pair with the complementary strand, displacing the opposing noncomplementary strand. Similar R-loop structures are formed at sites of transcription by RNA polymerase II (see the figure). Formation of an R-loop signals the HNH domain of Cas9 to cleave the complementary DNA strand and the RuvC domain to cleave the noncomplementary strand (*3*, *4*). Concerted cleavage by the two nuclease domains ensures that either both or neither of the two strands are cleaved (*5*).

Structures of Cas9 alone (*6*), bound to sgRNA (*7*) or to partially double-stranded targets containing a PAM (*8*–*10*), revealed that Cas9 can adopt distinct conformational states but failed to explain how the Cas9 nuclease domains generate dsDNA breaks. In each of the earlier structures, the HNH domain active site is positioned at least 30 Å away from its intended cleavage site on the complementary strand. Moreover, DNA bound at the active site of the RuvC domain also was not observed in previous structures, owing to a lack of an intact noncomplementary DNA strand. The crystal structure reported by Jiang *et al.* captures a dsDNA target in an unwound, precleaved state with the HNH and RuvC domains positioned near their respective cleavage sites. The complex adopts a conformation, more compact than observed in previous DNA-containing structures, that drives the structural rearrangements necessary for efficient and coordinated cleavage of the dsDNA target.

The most prominent structural rearrangement upon dsDNA binding occurs with the HNH domain, which during its repositioning toward the complementary strand rotates nearly 180° from its location in the partially dsDNA-bound complex (*9*). The two hinge regions connecting the HNH and RuvC domains also undergo local structural rearrangements that appear to help stabilize the R-loop structure through contacts with the separated DNA strands, and to help direct the noncomplementary strand into the RuvC active site. Together the repositioning of the HNH domain and the structural rearrangements of the linker regions provide clear structural evidence for observed allostery between the HNH and RuvC domains through these hinge regions (*5*).

To gain more insight into how Cas9 binds dsDNA targets, Jiang *et al.* used cryo–electron microscopy (cryo-EM) to determine the 6.0 Å structure of the Cas9-sgRNA complex bound to a longer dsDNA target, as well as the 4.6 Å structure of the Cas9-sgRNA complex. They reveal that interactions between Cas9 and both ends of the open dsDNA target confer a 30° helical bend angle in the DNA that provides the structural distortion required for R-loop stabilization. These studies not only elucidate the mechanism of DNA binding by Cas9 but also further highlight recent advances in cryo-EM (*11*). Although higher-resolution cryo-EM structures have been reported in other systems, the resolution of a cryo-EM structure is ultimately limited by the nature of the specimen. Given the relatively small size of the Cas9 complexes (~220 kDa) and the conformational plasticity of Cas9, the resolution of the cryo-EM structures reported should not be underappreciated.

Understanding how binding to a bona fide dsDNA target activates the DNA endonuclease activity of Cas9 not only provides greater insight into the specificity of Cas9 cleavage but also provides a framework for further manipulation of this system for improved genome editing. Variants of Cas9 have already been developed that show improved specificity (*12*, *13*). The studies by Jiang *et al.* facilitate the rational design of further variants to minimize off-target cleavage, a major concern for gene editing at the bench and in potential therapeutic strategies. This new structural information also provides a blueprint for fluorescence-based experiments that could exploit these conformational changes to report on DNA binding by Cas9 in cells. ■

REFERENCES

1. J. Travis, *Science* **350**, 1456 (2015).
2. F. Jiang *et al.*, *Science* **351**, 867 (2016).
3. M. Jinek *et al.*, *Science* **337**, 816 (2012).
4. G. Gasiunas, R. Barrangou, P. Horvath, V. Siksnys, *Proc. Natl. Acad. Sci. U.S.A.* **109**, E2579 (2012).
5. S. H. Sternberg, B. LaFrance, M. Kaplan, J. A. Doudna, *Nature* **527**, 110 (2015).
6. M. Jinek *et al.*, *Science* **343**, 1247997 (2014).
7. F. Jiang, K. Zhou, L. Ma, S. Gressel, J. A. Doudna, *Science* **348**, 1477 (2015).
8. H. Nishimasu *et al.*, *Cell* **156**, 935 (2014).
9. C. Anders, O. Niewoehner, A. Duerst, M. Jinek, *Nature* **513**, 569 (2014).
10. H. Nishimasu *et al.*, *Cell* **162**, 1113 (2015).
11. E. Callaway, *Nature* **525**, 172 (2015).
12. I. M. Slaymaker *et al.*, *Science* **351**, 84 (2016).
13. B. P. Kleinstiver *et al.*, *Nature* **529**, 490 (2016).

10.1126/science.aaf2089

ILLUSTRATION: V. ALTOUNIAN/*SCIENCE*

Published by AAAS

CELLULAR NEUROSCIENCE

Differences among astrocytes

Neurons determine the specificity of local astrocytes

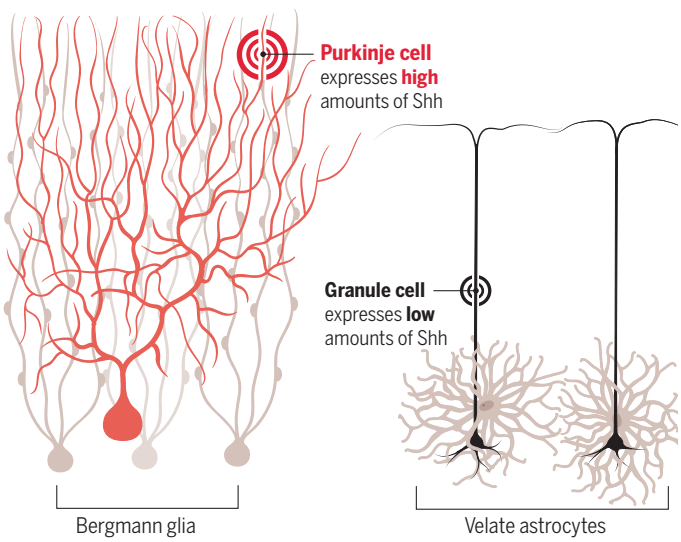
By **Beth Stevens** *and* **Allie K. Muthukumar**

Astrocytes are diverse in morphology and molecular makeup (*1*, *2*), potentially enabling them to provide for the varying needs of their diverse neuronal counterparts (*3*). What accounts for and maintains astrocyte heterogeneity are only beginning to be explored. One possibility is that the signals specifying astrocyte subpopulations might operate only during the critical phases of development, after which the cell is hardwired. Alternatively, these signals might be operational at all times. On page 849 of this issue, Farmer *et al.* (*4*) reveal that neuronal signals drive the molecular programs of astrocytes even during adult stages of life. This challenges the idea that astrocyte function is hardwired during development and provides a new mechanism for cellular plasticity in the adult brain.

Unlike morphological variety, the molecular and functional heterogeneity among astrocytes (*5*–*9*) has only recently gained appreciation. For example, comparison of actively translating messenger RNA in astrocytes from different regions of the mammalian brain revealed stark differences in gene expression profiles (*5*). Such findings support the idea that subpopulations of astrocytes have specialized regulatory functions on local neuronal circuits.

Spatially defined progenitor cells can give rise to distinct astrocyte populations in the mammalian brain that remain within restricted spatial domains as the nervous system matures (*10*). This raises the question of whether there might be region-specific neuron-astrocyte interactions that determine astrocyte identity. Interestingly, in germinal regions of the adult mammalian brain, morphogen gradients such as sonic hedgehog (Shh) can specify the fate of newly generated astrocytes (*11*), but it is not known whether these mechanisms affect terminally differentiated astrocytes.

Farmer *et al.* show that Shh signaling in the adult mouse brain drives the molecular profiles of mature astrocytes. The authors focused on the cerebellar cortex, which has two astrocyte populations: Bergmann glia (BG) and velate astrocytes (VAs). These two populations are morphologically and molecularly distinct and associate with different neurons. Farmer *et al.* observed that neurons in contact with BG express higher amounts of Shh than neurons in contact with VAs (see the figure). By manipulating the level of Shh signaling between neurons and astrocytes and studying its effects on the molecular features that define BG and VAs, the authors reveal that Shh signaling drives distinct astrocyte profiles in the mature brain.



Local control. Bergmann glia associate with neurons (Purkinje cells) that express high amounts of Shh, whereas velate astrocytes associate with neurons (granule cells) that express low amounts of Shh. Neuron-derived Shh regulates the molecular and functional features of nearby astrocytes in the adult mammalian brain.

To determine the role of Shh signaling in maintaining BG molecular features, Farmer *et al.* deleted the expression of Smo, a protein needed for Shh signal transduction, in astrocytes. This disrupted the expression of proteins that confer BG-specialized properties. Proteins that show characteristically high expression [such as the glutamate A1 (GluA1) and GluA4 subunits of the α-amino-3-hydroxy-5-methyl-4-isoxazolepropionic acid (AMPA) receptor] decreased, whereas proteins that have low expression [aquaporin (AQP4)] increased. When Shh was deleted from neurons, changes in gene expression in neighboring BG mimicked those seen after astrocyte-specific Smo deletion. Changes that resulted from disrupting Shh signaling were sufficient to alter BG physiology. Decreased expression of the AMPA glutamate receptor, which functions in synaptic transmission, corresponded with reduced current conductance by the glial cells. The study indicates that stable Shh signaling between BG and local neurons sustain the specialized properties of BG.

In contrast to BG, VAs receive a low amount of Shh input. Farmer *et al.* found that activating Shh signaling in astrocytes (by expressing mutant Smo that is constitutively active) disrupted the molecular features that characterize VAs. RNA sequencing demonstrated that VAs with increased Shh signaling had a transcriptional profile that more closely resembled that of BG than that of VAs. Thus, maintaining a low level of Shh signaling in VAs is necessary to sustain their defining molecular features.

Is Shh regulation of astrocytes widespread? Farmer *et al.* examined regions outside the cerebellar cortex and confirmed that Shh signaling regulates astrocyte features throughout the mammalian brain. Intriguingly, they discovered that Shh induces disparate changes in astrocytes in different brain regions. It is likely that several factors, including Shh, act cooperatively to determine astrocyte specificity. What these molecular signals are and how they interact with Shh signaling in the mature brain should be investigated in the future. The study by Farmer *et al.* firmly supports the idea that cellular function is not solely defined during development but continues to be defined and regulated throughout adulthood, bringing to light a previously unappreciated form of cellular plasticity in the brain. ■

Department of Neurology, F. M. Kirby Neurobiology Center, Boston Children's Hospital, Boston, MA 02115, USA. E-mail: beth.stevens@childrens.harvard.edu

ILLUSTRATION: K. SUTLIFF/*SCIENCE*

REFERENCES

1. O. A. Bayraktar *et al.*, *Cold Spring Harb. Perspect. Biol.* **7**, a020362 (2015).
2. Y. Zhang, B. A. Barres, *Curr. Opin. Neurobiol.* **20**, 588 (2010).
3. N. J. Allen, *Annu. Rev. Cell Dev. Biol.* **30**, 439 (2014).
4. W. T. Farmer *et al.*, *Science* **351**, 849 (2016).
5. J. P. Doyle *et al.*, *Cell* **135**, 749 (2008).
6. R. M. Bachoo *et al.*, *Proc. Natl. Acad. Sci. U.S.A.* **101**, 8384 (2004).
7. C. Perego *et al.*, *J. Neurochem.* **75**, 1076 (2000).
8. G. M. McKhann, R. D'Ambrosio, D. Janigro, *J. Neurosci.* **17**, 6850 (1997).
9. S. Poopalasundaram *et al.*, *Glia* **30**, 362 (2000).
10. H.-H. Tsai *et al.*, *Science* **337**, 358 (2012).
11. R. A. Ihrie *et al.*, *Neuron* **71**, 250 (2011).

10.1126/science.aaf2849

Downloaded from on February 18, 2016

Published by AAAS

NANOMATERIALS

Controlled interaction of nanoparticles with cells

DNA hybridization can control the exposure of cell-targeting receptors on nanoparticles

By **Wolfgang J. Parak**[1,2]

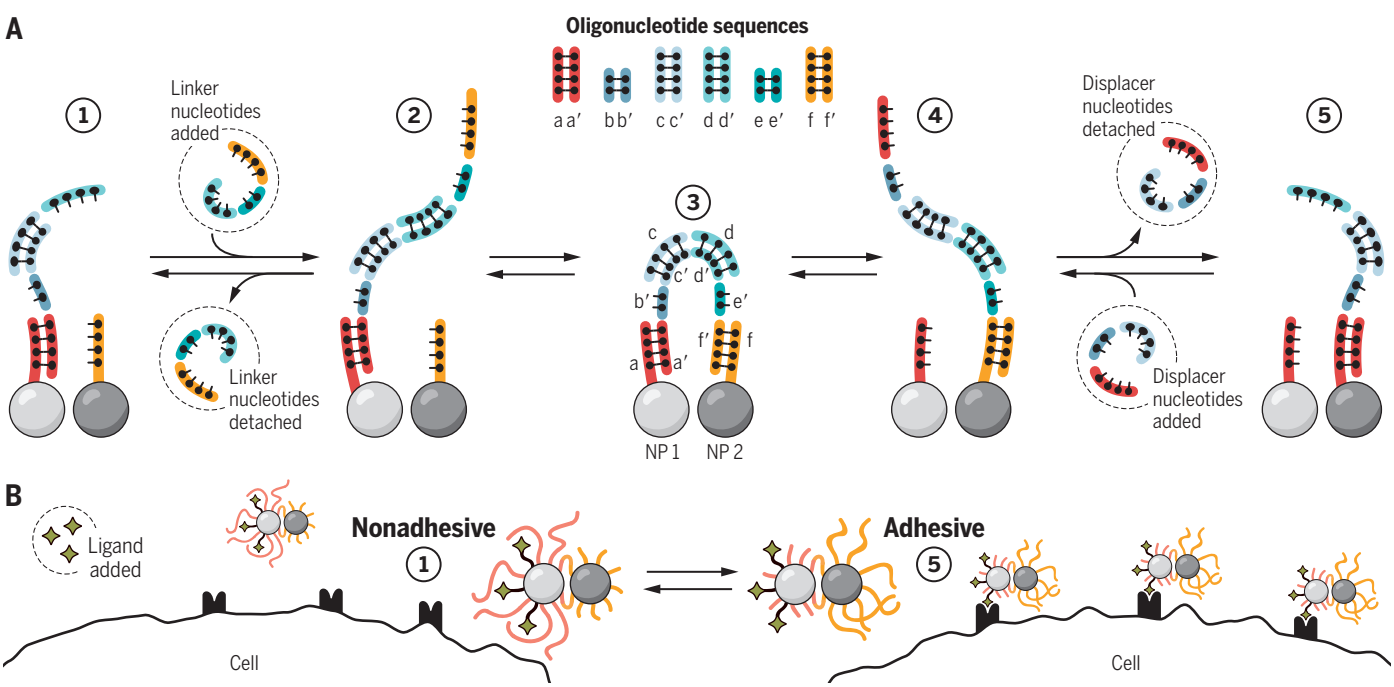
For many medical applications, controlled interaction of cells with surfaces is desirable. For example, in the already clinically applied cell-sheet technology, cells detach from a polymer surface upon cooling, which causes the polymer to swell and become nonadhesive (*1*). On page 841 of this issue, Ohta *et al*. applied the same idea to the surface of colloidal nanoparticles (NPs) (*2*). In the adhesive state, in which ligands on the NP surface are accessible, the NPs specifically adhere to the surface of cells bearing a corresponding receptor and are internalized. In the nonadhesive state, the targeting ligands are inaccessible; the NPs do not show specific adhesion to cells and are internalized to a much lower extent. This switching is initiated by the presence of short oligonucleotide sequences, so NPs (and any cargo, such as drugs) could be targeted to cells on the basis of characteristic overexpressed oligonucleotides on cell surfaces.

The trick for switching between the two modes (shown schematically in panel A of the figure) exploits the capability to hybridize one longer oligonucleotide to either of two NPs, NP1 or NP2. First, long DNA molecules (sequences a′b′c′cd′, where a prime indicates the complement strand) are bound to a short complementary oligonucleotide sequence, a, on NP1, whereas NP2 only bears short oligonucleotides, f (state 1). If linker nucleotides d′e′f′ are added, they will hybridize and bind to NP1. The ends of the DNA molecules attached to NP1 (f′) are now complementary to the oligonucleotides (f) attached to NP2 (state 2). After hybridization of the complementary oligonucleotides (duplex formation ff′), NP1 and NP2 are linked by DNA a′b′c′cdd′e′f′ (state 3). DNA a′b′c′cdd′e′f′ may now detach from NP1 and transfer to NP2 (state 4).

Note that hybridization from state 3 is fully reversible and can go in both directions. The direction to reach equilibrium is governed by the concentrations of the linker (d′e′f′;a′b′c′) and detachment (abc; def) oligonucleotides, such as those used to create state 5. If the displacer nucleotide abc is added, the oligonucleotide a′b′c′ is displaced from NP2, under formation of the DNA duplex aa′bb′cc′. Displacement is possible, as hybridization of aa′bb′cc′ prevails over hybridization of cc′ only. This results in NP1 with only the oligonucleotides a attached, and NP2 modified with long DNA molecules cdd′e′f′f. In this way, either NP1 (state 5) or NP2 (state 1) has long DNA strands attached.

The second trick now involves addition of targeting ligands such as folic acid to the surface of NP1, which is linked by DNA to NP2 (see the figure, panel B). If NP1 bears the long DNA strands, they cover the targeting ligands and the entire NP is in a nonadhesive state. In the presence of the appropriate linker and detachment oligonucleotides, long DNA is moved to NP2. Now the targeting ligands on the surface of NP1 are accessible. The entire NP is in the adhesive state and can specifically bind to cells expressing the receptor for the targeting ligand, and is then incorporated into cells via receptor-mediated endocytosis.

[1]Fachbereich Physik, Philipps Universität Marburg, 35037 Marburg, Germany. [2]CIC Biomagune, San Sebastian, Spain. E-mail: wolfgang.parak@physik-uni-marburg.de



Exposed versus covered up. (**A**) Sketch of DNA exchange between two nanoparticles. The sequences of the oligonucleotides in the scheme are arbitrary (they do not correspond to the ones used by Ohta *et al.*) and represent multiple ligands covering the surface. Numerals in circles are state numbers as described in text. (**B**) Switching of nanoparticles between adhesive and nonadhesive states, exposing ligands (arrows) that target receptors on cells.

ILLUSTRATION: K. SUTLIFF/*SCIENCE*

Downloaded from on February 18, 2016

Published by AAAS

Functional NPs of all types can be tailored with high precision (*3*). DNA has been used for forming NP assemblies (*4*, *5*) and also as a general structural element (*6*–*8*), which in turn allows for more complex assembly of NPs (*9*). DNA assemblies based on the displacement and rehybridization of oligonucleotides have also been used as dynamic structural elements (*10*). Ohta *et al.* made use of several of these conceptual elements, but their work is far from incremental in that they have achieved an excellent degree of control and uniformity.

Although there are many studies of NPs decorated with molecules that can change their structure to introduce functionality, the mechanisms of such change have been proven only indirectly, with an element of intuition sometimes involved. In contrast, Ohta *et al.* demonstrate structural transition from the nonadhesive to the adhesive state by labeling with additional small NPs that can be directly visualized by transmission electron microscopy (TEM). The TEM images reveal not only the nonadhesive (DNA-covered) state 1 and the adhesive (exposed) state 5, but also the transition state 3. In addition, TEM images of many NP assemblies at lower magnification show that they are uniform, which is of particular importance for future pharmaceutical formulation.

Although the work of Ohta *et al.* is a technical breakthrough, our knowledge about the interaction of NPs is incomplete. These assemblies contain genetic material, and the potential long-term side effects of their use as pharmaceutical formulations are still under discussion (*11*). Inside the human body, assemblies may also degrade and thus lose their functionality before they reach their target (*12*). The use of colloidal NPs as pharmaceutical formulations has just begun, as building blocks with sufficient purity and uniformity have only recently become available. In this way, materials nanoscience is progressing into medical nanotechnology. ■

REFERENCES AND NOTES

1. M. Yamato, T. Okano, *Mater. Today* **7**, 42 (May 2004).
2. S. Ohta, D. Glancy, W. C. W. Chan, *Science* **351**, 841 (2016).
3. W. J. Parak, *Science* **334**, 1359 (2011).
4. A. P. Alivisatos *et al.*, *Nature* **382**, 609 (1996).
5. C. A. Mirkin, R. L. Letsinger, R. C. Mucic, J. J. Storhoff, *Nature* **382**, 607 (1996).
6. J. H. Chen, N. C. Seeman, *Nature* **350**, 631 (1991).
7. P. W. K. Rothemund, *Nature* **440**, 297 (2006).
8. S. M. Douglas *et al.*, *Nature* **459**, 414 (2009).
9. G. P. Acuna *et al.*, *Science* **338**, 506 (2012).
10. B. Yurke, A. J. Turberfield, A. P. Mills, F. C. Simmel, J. L. Neumann, *Nature* **406**, 605 (2000).
11. Z. K. Ballas *et al.*, *J. Immunol.* **167**, 4878 (2001).
12. W. G. Kreyling *et al.*, *Nat. Nanotechnol.* **10**, 619 (2015).

ACKNOWLEDGMENTS

Supported by the European Commission (project FutureNanoNeeds).

10.1126/science.aaf0751

INFECTIOUS DISEASES

Beyond Ebola

The Ebola epidemic provides lessons for how to respond to future epidemics

By **Janet Currie,[1] Bryan Grenfell,[1] Jeremy Farrar[2]**

On 14 January 2016, Liberia was declared Ebola-free. A new case was identified shortly after the announcement, but it is nevertheless clear that the West African epidemic has moved on to a more hopeful phase. What lessons can be drawn from the Ebola crisis to help the international community to prepare for and respond to the next global epidemic? This question is particularly pertinent given the recent declaration of the Zika virus as a public health emergency.

RESPECTFUL LOCAL HEALTH CARE. Over US$7 billion were raised for the Ebola response, and international efforts were made to supply personnel. But it was ultimately underequipped local workers on the ground who bore the brunt of the epidemic: More than 800 health care workers were infected, and more than 500 died. These facts underscore the importance of rebuilding and strengthening local health care and health surveillance networks, as well as building trust in both the health care system and political structures.

In public remarks on the epidemic, Margaret Chan, the Director-General of the World Health Organization (WHO), stated that "when communities saw for themselves that hiding patients in homes could lead to the death of entire households, they found their own way to separate the healthy from the infected… These changes in community behaviours helped bring some of the earliest hotspots under control" (*1*). In fact, treating the rights of the infected and their families as secondary to the urgent need for infection control proved counterproductive: It undermined containment of the epidemic and led to the loss of more lives. Former Irish President Mary Robinson has argued that safeguarding the human rights of victims is essential to effective control of an epidemic (*2*).

INTERNATIONAL RESPONSE. At the same time, a more efficacious, timely international response is essential. The first Ebola cases were confirmed in March 2014; just 2 months later, Médecins San Frontières declared the epidemic to be out of control. Yet, the WHO did not convene an international meeting on the outbreak and declare it a Public Health Emergency of International Concern (PHEIC) until August 2014. As the international body charged with responding to infectious disease outbreaks, the WHO must have the mandate, authority, and capacity to respond faster and with much greater impact.

The need for reforms at the WHO has been stressed from several expert panels (*3*–*6*). All these panels have recommended the setting up of a dedicated Center for Health Emergency Preparedness and Response within the WHO, with an independent advisory group, transparent decision-making, and a protected budget that cannot be cannibalized for other issues. The WHO must also implement its existing mandate to require and assist countries to define and develop minimum core capacities for detecting and reporting outbreaks. The United Nations should oversee the progress of these initiatives and offer assistance, especially in fragile and failed states. Finally, research must be sustained and coordinated both between and during epidemics. The National Academy of Medicine frames these issues as matters of global security and estimates implementation costs of $4.5 billion per year (*5*).

MULTIPLE PERSPECTIVES. Although the expert panels discussed above emphasize the need for coordinated research, their focus is mainly on biomedical disciplines. A more successful approach to future outbreaks needs to coordinate knowledge from many disciplines in two main ways. First, scientists must quantify and ideally predict the course of an epidemic from its zoonotic origins in reservoir species, through the course of the epidemic, to its wider effects on health systems and society. Second, every aspect of this research program needs to move beyond customary disciplinary silos, integrating insights from the natural sciences, public health, and clinical medicine with those from engineering, social science, and ethics.

Three examples underline the multidisciplinary nature of the research challenge (see the table). First, the risk of zoonotic emergence must be mapped using innovative surveillance methods, data that track human movement, and computational methods (*7*). However, the risk of human contact and the emergence of disease also depend on economic and social factors such as travel, migration, and urbanization (*8*).

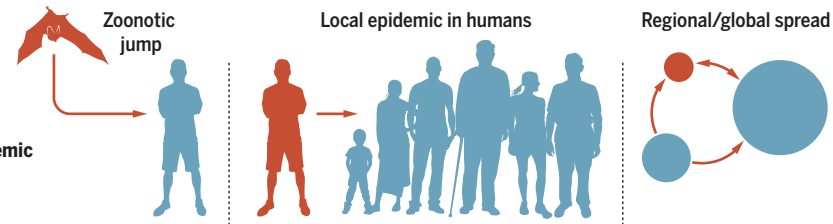
Second, integrating data from genetic analysis of pathogens and medical surveillance into epidemiological models is a key

[1]*Princeton University, Woodrow Wilson School, Princeton, NJ 08540, USA.* [2]*Wellcome Trust, 215 Euston Road, London NW1 2BE, UK. E-mail: jcurrie@princeton.edu*

Downloaded from on February 18, 2016

Published by AAAS

Research needs for different stages of emerging zoonotic infections



Research priorities	Reservoir and pathogen transmission rates and dynamics; pathogen surveillance and novel host serology; pathways for contact with humans.	Public health, syndromic and pathogen genetic surveillance; development of rapid diagnostics and informatics; estimation of transmission rates and construction of epidemiological models; quantifying pathogen evolution; vaccine and drug treatment development; testing, logistics, and sensitive deployment of control strategies; behavior change.	Mapping spread through quantifying human mobility; broader deployment of control measures; mobilizing political and economic will to prevent spread and aid victims.
Fields of research needed	Veterinary science, ecology, evolutionary biology, microbiology, immunology, anthropology, sociology, geography, and economics.	Biomedicine, pharmacology, epidemiology, pathogen evolutionary biology, biostatistics, engineering and supply chain logistics, economics, sociology, anthropology, ethics, politics, and communications.	Geography and informatics, epidemiology, politics, economics, ethics and law.

step in understanding epidemic spread and the effects of control efforts. Understanding implications from molecular virology and immunology for the dynamics of population herd immunity is a crucial area for research. However, the Ebola epidemic has shown that social structures, living environments, and human behavior all shape the course of an epidemic (*9*). Understanding behavior change (and especially culturally appropriate ways to influence it) requires expertise from fields such as anthropology and psychology; without such insights, control measures can founder.

Third, safe, efficient, and deployable vaccines and treatments, along with close-to-patient diagnostics, could mitigate future outbreaks and protect frontline health workers. The recent successful and remarkably rapid trial of a safe and effective Ebola vaccine in Guinea is a triumph (*10*), but there is no technical reason why it (and alternative Ebola vaccines) could not have been available for deployment several years ago. The main impediment has been the lack of a reliable market for a vaccine. The 20 January agreement by the Global Alliance for Vaccines and Immunizations (GAVI) to purchase the Merck vaccine when it becomes available illustrates what can be done.

Developing an international cooperative mechanism to support the development and licensing of vaccines is an urgent priority (*11*). We hope that the Ebola crisis will provide the impetus to finally get this effort off the ground, particularly because new threats, such as the Zika virus, continue to emerge. The Zika virus epidemic also underlines the importance of research and development in the control of vector-borne diseases.

ACTING SYNERGISTICALLY. Past epidemics show that international aid can be highly successful (*12*). HIV-AIDS has become a chronic rather than fatal condition, even in many low-income countries, because of access to life-saving drugs; childhood deaths due to malaria have been massively reduced in the past 15 years (*13*); and access to vaccines has been much improved, all as a result of coordinated national and international efforts. This history shows that the best results are achieved when international mechanisms act synergistically with strong local governance and health systems and with a shared agenda.

The difficulty in extinguishing Ebola in Liberia and Sierra Leone highlights the very real challenge of eradicating human infection from a country after it has become well established. Because of the possibility of long-term human carriage of Ebola, low-level sexual transmission, and relapse, the road to zero cases still requires massive effort and commitment. Death and disease stemming from an outbreak are likely to linger long after the last country is declared Ebola-free. In the aftermath of the Ebola epidemic, strains on already fragile health systems can exacerbate other infectious disease outbreaks (*14*).

Trauma, stigmatization, hunger, and poverty stemming from the outbreak are also likely to have long-term consequences on survivors, their families, and communities. The effects may be particularly severe for the youngest children affected. Documented effects of exposure to other infectious diseases in utero and early childhood include stunting, cognitive deficits, severe mental health problems, disability, and greater susceptibility to other diseases (*15*). Long-term health care needs in the Ebola-affected countries will therefore likely be even greater than before.

FROM CHALLENGE TO OPPORTUNITY. The need for rebuilding health systems also presents an opportunity. The delivery of basic health services at a community level is key to establishing trust, improving surveillance, and creating the capacity to mount a rapid response. Community health workers who are well trained and supported have local trust, as well as the information and the capability to work with national and international partners to confront the next epidemic. They must be seen as part of the solution and integrated with national public health care systems and international partners.

These advances will only be possible with a strong, reformed, and adequately funded WHO (*3*–*6*). It must again become the respected global health body with a clear mandate to provide the global health leadership that is sorely needed in a fragmented but increasingly interconnected world. This transformation will require binding commitments from the international community alongside an ability and willingness of the WHO to lead. Only then can all the disciplinary tools of 21st-century public health be harnessed in an equitable, effective, and integrated way. ■

REFERENCES AND NOTES

1. Keynote address at the conference on *Modern Plagues: Lessons Learned From the Ebola Crisis*, 2 to 3 November 2015, Dublin, Ireland. See www.who.int/dg/speeches/2015/princeton-ebola-lessons/en.
2. Remarks to the conference on *Modern Plagues: Lessons Learned From the Ebola Crisis*, 2 to 3 November 2015, Dublin, Ireland.
3. WHO, *Report of the Ebola Interim Assessment Panel* (WHO, Geneva, July 2015).
4. Institute of Medicine, *An Operational Framework for Identifying and Effectively Responding to Global Infectious Disease and Public Health Emergencies in the 21st Century* (Institute of Medicine, Washington, DC, 2015).
5. National Academy of Medicine Secretariat, *The Neglected Dimension of Global Security: A Framework to Counter Infectious Disease Crises* (National Academies Press, Washington, DC, 2016).
6. S. Moon *et al.*, *Lancet* **386**, 2204 (2015).
7. D. M. Pigott *et al.*, *eLife* **3**, e04395 (2014).
8. D. T. Cronin *et al.*, *PLOS ONE* **10**, e0134464 (2015).
9. A. Kucharski *et al.*, *Proc. Natl. Acad. Sci. U.S.A.* **112**, 14366 (2015).
10. A. Henao-Restrepo *et al.*, *Lancet* **386**, 857 (2015).
11. S. A. Plotkin, A. A. Mahmoud, J. Farrar, *N. Engl. J. Med.* **373**, 297 (2015)
12. E. Bendavid, J. Bhattacharya, *JAMA Internal Medicine* **174**, 881 (2014).
13. WHO/UNICEF, *Achieving the Malaria MDG Target: Reversing the Incidence of Malaria 2000–2015* (WHO/UNICEF, September 2015).
14. S. Takahashi *et al.*, *Science* **347**, 1240 (2015).
15. J. Currie, T. Vogl, *Annu. Rev. Econ.* **5**, 1 (2013).

ACKNOWLEDGMENTS

This Perspective is based on the conference on *Modern Plagues: Lessons Learned from the Ebola Crisis*, 2–3 Nov. 2015, Dublin, Ireland, which was supported by Princeton University's Fung Forum and Princeton's Center for Health and Wellbeing in the Woodrow Wilson School.

10.1126/science.aad8521

ILLUSTRATION: P. HUEY/*SCIENCE*

Published by AAAS

A molecular shuttle for hydrogen cyanide

Nickel-catalyzed transfer hydrocyanation enables safe conversion of alkenes into nitriles

By **Hans-Günther Schmalz**

In recent decades, transition-metal catalysis has become an indispensable tool in organic synthesis. Nevertheless, there remains a need for practical, safe, and efficient protocols for some transformations. A challenging example is nickel-catalyzed hydrocyanation (*1*), in which nonactivated olefins (alkenes) are converted to branched or linear nitriles through addition of hydrogen cyanide (HCN) (see the figure, panel A). This transformation is used industrially on a very large scale to produce adiponitrile, a key intermediate for Nylon-66 (see the figure, panel B). However, it is rarely used in laboratory or fine chemical syntheses because of safety concerns regarding HCN, an extremely toxic, volatile, and flammable agent. On page 832 of this issue, Fang *et al.* (*2*) report a method that avoids the use of HCN in the conversion of alkenes to nitriles and vice versa.

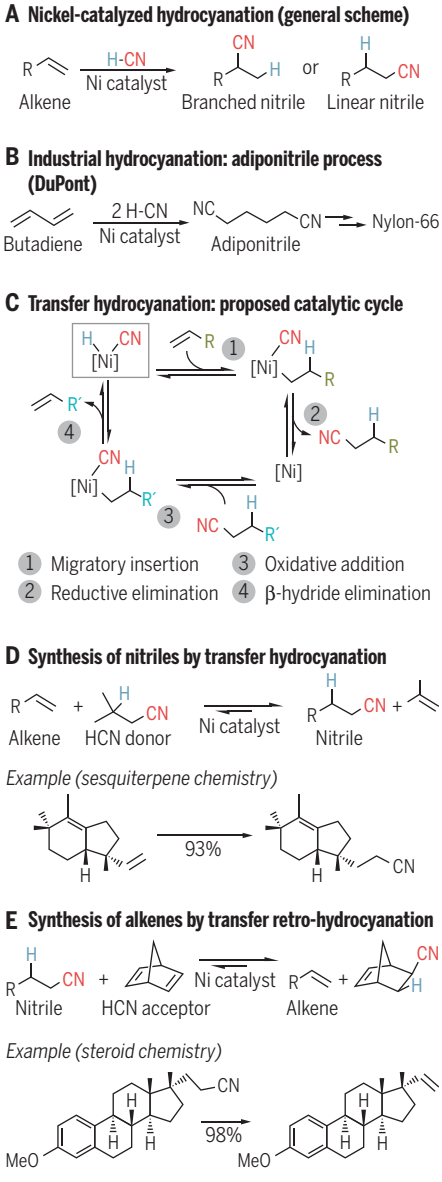
Less dangerous and easier-to-handle reagents, such as trimethylsilyl cyanide, have been used for the in situ generation of HCN (*3*). However, these reagents still represent a potential hazard. Fang *et al.*'s approach is radically different: In their transfer-hydrocyanation process, no free HCN is generated at all.

The authors use a nickel catalyst, which can abstract HCN from a nitrile (leaving behind an alkene) and transfer it to another alkene. In the proposed catalytic cycle (see the figure, panel C), a Ni(II)HCN intermediate serves as a HCN shuttle. This shuttle readily reacts with an alkene through migratory insertion and reductive elimination to yield a nitrile and a Ni(O) species.

All steps in this reaction are reversible, meaning that the overall process is thermodynamically controlled. The equilibrium can be influenced easily: With isovaleronitrile as a preferred HCN donor, a broad variety of mainly terminal alkenes are hydrocyanated, resulting in the selective formation of the linear products in good to excellent yield (see the figure, panel D). For the retro-hydrocyanation, the authors use norbornadiene, which accepts HCN under reduction of ring strain. The latter protocol allows the elimination of HCN from various terminal alkyl nitriles to efficiently yield the corresponding alkenes (see the figure, panel E). Selected examples from natural products chemistry convincingly demonstrate the power of the method.

A common reaction in organic synthesis involves the transition metal–catalyzed transfer of hydrogen (H_2) from one molecule to the other, a process called transfer hydrogenation (*4*). However, only a few processes are known in which transition metals mediate the transfer of a carbon-containing unit. One example for such a group transfer process is the joint transfer of hydrogen and carbon monoxide (transfer hydroformylation), recently reported by Murphy *et al.* (*5*), in a rhodium-catalyzed protocol that allows the interconversion of aldehydes and alkenes. Both this transfer hydroformylation (*5*) and the transfer hydrocyanation reported by Fang *et al.* are based on the general reversibility of well-known catalytic cycles. The important contribution of the two studies is the implementation of clever strategies to influence the equilibria in a synthetically useful manner by exploiting thermodynamic principles.

Nitriles are highly versatile intermediates in organic synthesis. Fang *et al.*'s practical and safe protocols for the HCN-free transfer hydrocyanation of alkenes are likely to fertilize nitrile chemistry by stimulating the application of nickel-catalyzed hydrocyanation in both academic and industrial laboratories. It remains to be seen, however, whether transfer hydrogenation will be considered by industry for large-scale applications. Classical hydrocyanation is fully atom economic (*6*)—that is, all atoms of the reactants (HCN + alkene) end up in the nitrile product. In contrast, Fang *et al.*'s process involves the formation of stoichiometric amounts of by-products, which must be separated together with excess reagents. Chemical companies with experience in the safe handling of neat HCN will therefore not have much reason to consider this method in the design of future hydrocyanation processes. On the other hand, the new protocol has the potential to find application in the production of high-value fine chemicals, such as intermediates for pharmaceuticals or fragrances. ■



Safer chemistry. In contrast to the classical hydrocyanation reaction, a new transfer-hydrocyanation protocol developed by Fang *et al.* allows the interconversion of alkenes and nitriles in a safe manner without using toxic hydrogen cyanide (HCN).

Department of Chemistry, University of Cologne, 50939 Köln, Germany. E-mail: schmalz@uni-koeln.de

REFERENCES

1. L. Bini, C. Müller, D. Vogt, *ChemCatChem* **2**, 590 (2010).
2. X. Fang, P. Yu, B. Morandi, *Science* **351**, 832 (2016).
3. A. Falk, A.-L. Göderz, H.-G. Schmalz, *Angew. Chem. Int. Ed.* **52**, 1576 (2013).
4. D. Wang, D. Astruc, *Chem. Rev.* **115**, 6621 (2015).
5. S. K. Murphy, J.-W. Park, F. A. Cruz, V. M. Dong, *Science* **347**, 56 (2015).
6. B. M. Trost, *Science* **254**, 1471 (1991).

10.1126/science.aaf2215

ILLUSTRATION: P. HUEY/*SCIENCE*

Downloaded from on February 18, 2016

Published by AAAS

COMPLEX SYSTEMS

Complexity theory and financial regulation

Economic policy needs interdisciplinary network analysis and behavioral modeling

By Stefano Battiston,[1]* J. Doyne Farmer,[2,3] Andreas Flache,[4] Diego Garlaschelli,[5] Andrew G. Haldane,[6] Hans Heesterbeek,[7] Cars Hommes,[8,9]† Carlo Jaeger,[10,11,12] Robert May,[13] Marten Scheffer[14]

Traditional economic theory could not explain, much less predict, the near collapse of the financial system and its long-lasting effects on the global economy. Since the 2008 crisis, there has been increasing interest in using ideas from complexity theory to make sense of economic and financial markets. Concepts, such as tipping points, networks, contagion, feedback, and resilience have entered the financial and regulatory lexicon, but actual use of complexity models and results remains at an early stage. Recent insights and techniques offer potential for better monitoring and management of highly interconnected economic and financial systems and, thus, may help anticipate and manage future crises.

POLICY

TIPPING POINTS, WARNING SIGNALS. Financial markets have historically exhibited sudden and largely unforeseen collapses, at a systemic scale. Such "phase transitions" may in some cases have been triggered by unpredictable stochastic events. More often, however, there have been endogenous underlying processes at work. Analyses of complex systems ranging from the climate to ecosystems reveal that, before a major transition, there is often a gradual and unnoticed loss of resilience. This makes the system brittle: A small disruption can trigger a domino effect that propagates through the system and propels it into a crisis state.

[1]*Department of Banking and Finance, University of Zurich, 8032 Zürich, Switzerland.* [2]*Institute for New Economic Thinking, Oxford Martin School, and Mathematical Institute, University of Oxford, Oxford OX1 2JD, UK.* [3]*Santa Fe Institute, Santa Fe, NM 87501, USA.* [4]*Department of Sociology, University of Groningen, 9712 TG Groningen, Netherlands.* [5]*Lorentz Institute for Theoretical Physics, University of Leiden, 2333 CA Leiden, Netherlands.* [6]*Bank of England, London, EC2R 8AH, UK.* [7]*Faculty of Veterinary Medicine, University of Utrecht, 3512 JE Utrecht, Netherlands.* [8]*Amsterdam School of Economics, University of Amsterdam, 1018 WB Amsterdam, Netherlands.* [9]*Tinbergen Institute, 1082 MS Amsterdam, Netherlands.* [10]*Beijing Normal University, 100875 Beijing, China.* [11]*Potsdam University, 14469 Potsdam, Germany.* [12]*Global Climate Forum 10178 Berlin, Germany.* [13]*Department of Zoology, University of Oxford, Oxford OX1 2JD, UK.* [14]*Environmental Sciences, Wageningen University 6708 PB Wageningen, Netherlands.* *Authors are in alphabetical order. †Corresponding author. E-mail: C.H.Hommes@uva.nl

Recent research has revealed generic empirical quantitative indicators of resilience that may be used across complex systems to detect tipping points. Markers include rising correlation between nodes in a network and rising temporal correlation, variance, and skewedness of fluctuation patterns. These indicators were first predicted mathematically and subsequently demonstrated experimentally in real complex systems, including living systems (*1*). A recent study of the Dutch interbank network (*2*) showed that standard analysis using a homogeneous network model could only lead to late detection of the 2008 crisis, although a more realistic and heterogeneous network model could identify an early warning signal 3 years before the crisis (see the chart).

Ecologists have developed tools to quantify the stability, robustness, and resilience of food webs and have shown how these depend on the topology of the network and the strengths of interactions (*3*). Epidemiologists have tools to gauge the potential for events to propagate in systems of interacting entities, to identify superspreaders and core groups relevant to infection persistence, and to design strategies to prevent or limit the spread of contagion (*4*).

Extrapolating results from the natural sciences to economics and finance presents challenges. For instance, publication of an early warning signal will change behavior and affect future dynamics [the Lucas critique (*5*)]. But this does not affect the case where indicators are known only to regulators or when the goal is to build better network barriers to slow contagion.

TOO CENTRAL TO FAIL. Network effects matter to financial-economic stability because shock amplification may occur via strong cascading effects. For example, the Bank of International Settlements recently developed a framework drawing on data on the interconnectedness between banks to gauge the systemic risk posed to the financial network by Global Systemically Important Banks. Recent research on contagion in financial networks has shown that network topology and positions of banks matter; the global financial network may collapse even when individual banks appear safe (*6*). Capturing these effects is essential for quantifying stress on individual banks and for looking at systemic risk for the network as a whole. Despite on-going efforts, these effects are unlikely to be routinely considered anytime soon.

Information asymmetry within a network—e.g. where a bank does not know about troubled assets of other banks—can be problematic. The banking network typically displays a core-periphery structure,

> ***"...policies and financial regulation [that] weaken positive feedback... stabiliz[e] experimental macroeconomic systems..."***

with a core consisting of a relatively small number of large, densely interconnected banks that are not very diverse in terms of business and risk models. This implies that core banks' defaults tend to be highly correlated. That, in turn, can generate a collective moral hazard problem (i.e., players take on more risk, because others will bear the costs in case of default), as banks recognize that they are likely to be supported by the authorities in situations of distress, the likelihood amplifies their incentives to herd in the first place.

Estimating systemic risk relies on granular data on the financial network. Unfortunately, business interactions between banks are often hidden because of confidentiality issues. Tools being developed to reconstruct networks from partial information and to estimate systemic risk (*7*) suggest that publicly available bank information does not allow reliable estimation of systemic risk. The estimate would improve greatly if banks publicly reported the number of connections with other banks, even without disclosing their identity.

In addition to data, understanding the effects of interconnections also relies on integrative quantitative metrics and concepts that reveal important network aspects, such as systemic repercussions of the failure of individual nodes. For example, DebtRank, which measures the systemic importance of individual institutions in a financial network (*8*), shows that the issue of too-central-to-fail may be even more important than too-big-to-fail.

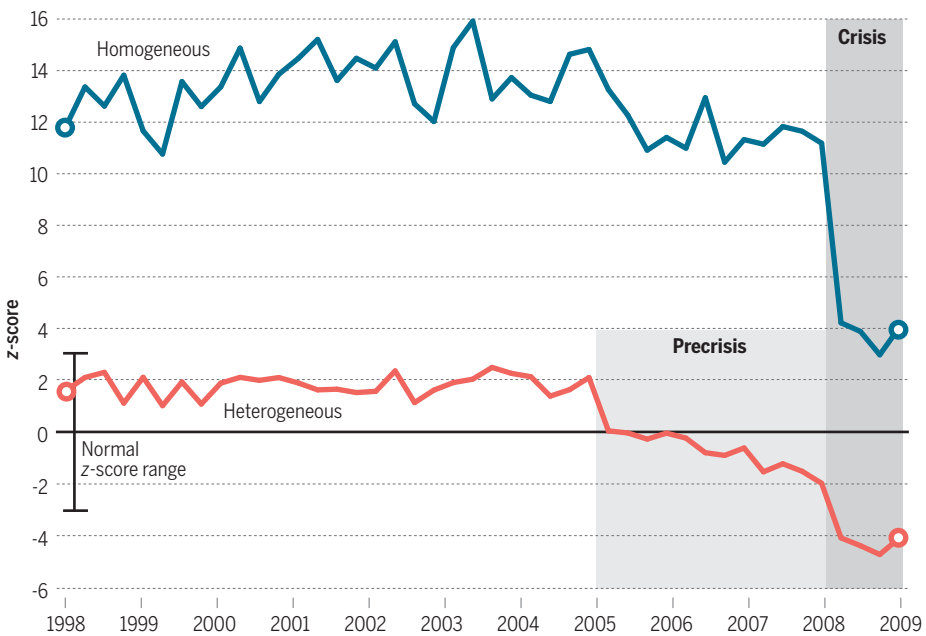
Downloaded from on February 18, 2016

Published by AAAS

AGENTS AND BEHAVIOR. Agent-based models (ABMs) are computer models in which the behavior of agents and their interactions are explicitly represented as decision rules mapping agents' observations onto actions. Although ABMs are less well established in analyzing financial-economic systems than in, e.g., traffic control, epidemiology, or battlefield conflict analyses, they have produced promising results. Axtell (*9*) developed a simple ABM that explains more than three dozen empirical properties of firm formation without recourse to external shocks. ABMs provide a good explanation for why the volatility of prices is clustered and time-varying (*10*) and have been used to test systemic risk implications of reforms developed by the Basel Committee on Banking Supervision, which show how dynamically changing risk limits can lead to booms and busts in prices (*11*, *12*). ABMs of market dynamics can be linked with ABM work on opinion dynamics in the social sciences (*13*) to understand how propagation of opinions through social networks affects emergent macro behavior, which is crucial to managing the stability and resilience of socioeconomic systems.

Laboratory experiments with human subjects can provide empirical validation of individual decision rules of agents, their interactions, and emergent macro behavior. Recent experiments studying behavior of a group of individuals in the laboratory show that economic systems may deviate significantly from rational efficient equilibrium at both individual and aggregate levels (*14*). This generic feature of positive feedback systems leads to persistent deviations of prices from equilibrium and emergence of speculation-driven bubbles and crashes, strongly amplified by coordination on trend-following and herding behavior (*15*). There is strong empirical evidence of these behaviors in financial markets in practice, and these controlled laboratory experiments provide more detailed understanding of mechanisms, causality, and conditions for emergence of macro phenomena.

A simple behavioral model, with agents gradually switching to better performing heuristics, explains individual, as well as emergent, macro behavior in these laboratory economies. The experiments also provide a general mechanism for managing social contagion in such systems. For example, monetary and fiscal policies and financial regulation designed to weaken positive feedback are successful in stabilizing experimental macroeconomic systems when properly calibrated (*16*). Complexity theory provides mathematical understanding of these effects.



Early-warning signals of the 2008 crisis in the Dutch interbank network. The figure portrays a temporal analysis of two loops, pairs of banks that are at the same time debtor and creditor to each other. Although the raw number of two loops is not very informative about possible ongoing structural changes, its comparison with a random network model benchmark is. A *z*-score represents the number of standard deviations by which the number of two loops in the real network deviates from its expected value in the model. Small magnitude *z*-scores (<3) indicate approximate consistency with the model, whereas larger magnitudes indicate statistically significant deviations. Two different random network models were used: a homogeneous network with the same total number of links as in the real network (top) and a heterogeneous network where every bank has the same number of connections as in the real network (bottom). The homogeneous model, often used in standard analyses, highlights only a late and abrupt structural change (2008). The more realistic heterogeneous model also identifies a gradual, early-warning "precrisis" phase (2005–2007). [Modified from (*2*)]

POLICY DASHBOARD. It is an opportune time for academic economists, complexity scientists, social scientists, ecologists, epidemiologists, and researchers at financial institutions to join forces to develop tools from complexity theory, as a complement to existing economic modeling approaches (*17*). One ambitious option would be an online, financial-economic dashboard that integrates data, methods, and indicators. This might monitor and stress-test the global socioeconomic and financial system in something close to real time, in a way similar to what is done with other complex systems, such as weather systems or social networks. The funding required for essential policy-relevant and fundamental interdisciplinary progress in these areas would be trivial compared with the costs of systemic financial failures or the collapse of the global financial-economic system. ■

REFERENCES AND NOTES

1. M. Scheffer *et al.*, *Science* **338**, 344 (2012).
2. T. Squartini *et al.*, *Sci. Rep.* **3**, 3357 (2013).
3. R. M. May *et al.*, *Nature* **451**, 893 (2008).
4. H. Heesterbeek *et al.*, *Science* **347**, aaa4339 (2015).
5. R. E. Lucas Jr., *Carnegie-Rochester Conf. Ser. Public Policy* **1**, 19 (1976).
6. S. Battiston *et al.*, J. *Econ. Dynam. Control* **36**, 1121 (2012).
7. G. Cimini *et al.*, *Sci. Rep.* **5**, 15758 (2015).
8. S. Battiston *et al.*, *Sci. Rep.* **2**, 541 (2012).
9. R. Axtell, "Endogenous dynamics of multi-agent firms" (Working paper version 1.5, Univ. of Oxford, Oxford 2014); www.css.gmu.edu/~axtell/Rob/Research/Pages/Firms.html.
10. B. LeBaron, in *Handbook of Computational Economics*, vol.2, *Agent-Based Computational Economics*, L. Tesfatsion, and K. L. Judd, Eds. (North-Holland, Amsterdam, 2006), pp. 1187–1233.
11. S. Thurner *et al.*, *Quant. Finan.* **12**, 695 (2012).
12. C. Aymanns, J. D. Farmer, *J. Econ. Dyn. Control* **50**, 155 (2015).
13. A. Flache, M. W. Macy, *J. Conflict Resolut.* **55**, 970 (2011).
14. T. Bao, C. Hommes, T. Makarewicz, "Bubble formation and (in)efficient markets in learning-to-forecast and –optimize experiments" (TI 2015-107/II Working paper, Tinbergen Institute, Amsterdam, 2015); http://papers.tinbergen.nl/15107.pdf
15. C. H. Hommes, *Behavioral Rationality and Heterogeneous Expectations in Complex Economic Systems* (Cambridge Univ. Press, Cambridge, 2013).
16. T. Bao, C. H. Hommes, "When speculators meet constructors: Positive and negative feedback in experimental housing markets" (CeNDEF Working paper 15-10, University of Amsterdam, Netherlands, 2015); http://bit.ly/WP15-10.
17. A. G. Haldane, "On microscopes and telescopes," Workshop on Socio-Economic Complexity, Lorentz Center, Leiden, 23 to 27 March 2015 (Bank of England, London, 2015); http://bit.ly/1VIJlvX.

ACKNOWLEDGMENTS

We acknowledge financial support from The Netherlands Institute of Advanced Studies in the Humanities and Social Sciences, The Netherlands Organisation for Scientific Research, the Lorentz Center, and the Tinbergen Institute.

10.1126/science.aad0299

ILLUSTRATION: C. SMITH/*SCIENCE*

Published by AAAS

SCIENTIFIC METHODS

Innovation inspiration

Engaging anecdotes abound, but a new treatise on the process of invention falls short on actionable advice

By **Warren Lathe**

INVENTology
How We Dream Up Things That Change the World
Pagan Kennedy
Houghton Mifflin Harcourt, 2016. 304 pp.



The inventor of the Post-it note, Art Fry, defined "inventing" as the act of translating a thought into an object. The process, he maintained, will likely require dreaming, prototyping, observation, and tinkering, ending with a working prototype. In her new book, *INVENTology*, Pagan Kennedy profiles a variety of historical and contemporary inventors in an effort to unpack the process of invention.

If we take Fry's definition of invention at face value, we might argue that humans, by our very nature, are inventors. One particularly striking example is the case of animation. Early in human history, some 30,000 years ago, Paleolithic artists invented systems of breaking down movement and visual narratives, depicting animals on a spinning disc, for example (1). From phenakistoscopes and zoetropes to complex three-dimensional computer renderings and computer-generated imagery sequences, we have since created ever more sophisticated ways to bring our stories to life. Inventing, it seems, is something we have been doing for millennia.

Solutions to large global challenges, such as climate change, drug-resistant infectious diseases, and widespread illiteracy, are likely to be found only if we continue to nurture our innate ability to invent. As Kennedy rightly points out in several places throughout the book, modern society is defined by an amazing set of tools and capabilities that should cultivate such innovation: instantaneous mass communication through the Internet, the ability to crowdsource funding and ideas, the plummeting cost of technology, and even the proliferation of community-oriented workspaces known as "makerspaces." Her goal—to delineate and illuminate "how we dream up things that change the world"—is therefore a worthy one.

Kennedy breaks the book into sections that are intended to reflect different aspects of the invention process—problem finding, discovery, prophecy, connecting, and empowerment—and uses a series of anecdotes about inventors to illustrate these elements. At times, these tales are inspiring and can be quite illustrative. For example, in the "Prophecy" section, Kennedy tells the story of Martin Cooper and his ability to envision a future in which our innate desire to be mobile ultimately led to the creation of the cell phone. The notion that "one day everyone would be issued a phone number at birth that would be retired at death" was something Cooper liked to joke about in the 1960s, when such a thing was unfathomable. Such anecdotes invite us to consider a future unburdened by the constraints of current expectations and technology.



Crowdfunding sites allow modern inventors to "fail rapidly and cheaply" when a promising product misses the mark with potential customers.

Several other anecdotes throughout the book were just as fascinating and well crafted, but I frequently found myself wondering how they related to the author's stated goal of extracting lessons from such stories ("What can the rest of us learn from the data on successful invention?"). Near the end of *INVENTology*, for example, Kennedy tells the story of Genrich Altshuller, the Soviet inventor and science fiction writer who was imprisoned and charged with a long list of political crimes for composing an open letter to Stalin criticizing the Communist regime's stifling effects on creativity. Although she describes Altschuller's story with great care—detailing, for example, how he crafted a set of "paper eyes" that fooled the guards charged with depriving him of sleep during his imprisonment—it is not clear how one might gain a sense of "empowerment" (the title of the section) from the story.

The penultimate chapter illustrates the greatest weakness of *INVENTology*. In "Tinkering with Education," Kennedy spends most of the chapter telling the story of Saul Griffith, an MIT Media Lab graduate who is working to develop a curriculum that teaches inventive thinking. However, she neglects to clearly tie this story to any broader ideas about how we do and might teach that mindset. Even a short telling of some of the many initiatives under way in the United States and around the world would have been helpful.

There is a rich history of invention and creation in human history, and there is much to be learned about how we do it. *INVENTology* touches on some of what we have learned and at times can be quite inspiring. However, on finishing the book, readers may still find themselves wondering how exactly we as a society can nurture and encourage invention.

The reviewer is at the Maker Education Initiative, Oakland, CA 94608, USA. E-mail: trey@makered.org

REFERENCES

1. M. Azéma, F. Rivère, *Antiquity* **332**, 316 (2012).

10.1126/science.aad8552

PHOTO: © AS400 DB/CORBIS

Downloaded from on February 18, 2016

Published by AAAS





From energy-efficient "Earthships" to sex-swapping lizards, unusual adaptations to climate change take center stage in *The Adaptors*.

PODCAST

If a tree falls in a forest...

Will a podcast about climate change reach the audiences that need to hear it most?

By **Gregory R. Goldsmith**

In desperate times, just how desperate are the measures we are willing to pursue? The stark implications of climate change are leading to no shortage of proposals. Should we drink water recycled from flushed toilets? Or try to generate electricity from massive artificial tornadoes? What if we could engineer humans to have cat eyes that are capable of seeing in lower light so as to reduce nighttime energy use? That last idea prompts Flora Lichtman to break stride and voice aloud what many of us are likely thinking: "Are you for real?"

Lichtman is the host of the podcast series *The Adaptors*, which explores innovative ideas for mitigating climate change. New episodes have been released about twice a month and have often been accompanied by a short video on the program's website. The episodes vary in length but average between 10 and 15 minutes. There's even an interactive component called "Climate Confessions," in which listeners are invited to call in and reveal their personal struggles to be better stewards of the environment. The series, produced by Katherine Wells, just completed its first year with major funding from the Alfred P. Sloan Foundation and now awaits additional funding for further episodes.

The Adaptors
Season 1
www.theadaptors.org

Lichtman is a veteran of the public radio program *Science Friday* and the coproducer of the brilliant *Animated Life* video series (*1*). Her style invokes a comfortable conversation with a friend: always informative but not overly reverent or scripted. While describing the sludge used to produce methane in the New York City wastewater treatment plant, Lichtman confides that "it smells…yeah... like you would expect, and although it looks probably like you would expect, too, I felt compelled to take a ton of photos."

Episodes of *The Adaptors* are intrinsically stories about people. From conservation biologist Joel Berger, who carries photos of yaks in his wallet, to astronaut Cady Coleman's frank discussion of wastewater recycling on the International Space Station, the series has done a fantastic job of finding compelling subjects to feature on the program.

The series frequently weighs in on complex and difficult issues, including the ecological and evolutionary implications of climate change, but it is at its best when the topics border on the implausible, such as when ethicist Matthew Liao proposes giving humans fur to help us cope with extreme weather.

And yet, despite the engaging nature of *The Adaptors*, it's hard not to wonder who exactly is tuning in to hear about climate change on a regular basis. Both in episodes of *The Adaptors* and in interviews elsewhere, Lichtman has been quick to note the difficulties associated with winning and sustaining interest in climate change. True, those who are likely to read this review will no doubt enjoy the podcast, but talking climate change to scientists is like preaching to the choir. Yes, they'll learn something new, but they already believe deeply in the tenets.

Given that research suggests that those with partisan views on a highly politicized topic such as climate change are more likely to seek out information consistent with their viewpoint (*2*, *3*), it follows that efforts like that of *The Adaptors* face an uphill battle in educating a broad audience. What would motivate someone to tune in when there are so many other options competing for their attention?

Time is running short on climate change, and resources for science engagement are limited. We must think carefully about whether such efforts are the best way to engage everyone. But given that we still need all the intelligent and thought-provoking information we can get on this topic, *The Adaptors* represents a clever, edgy contribution to the climate conversation.

The reviewer is in the Ecosystem Fluxes Group, Laboratory for Atmospheric Chemistry, Paul Scherrer Institute, 5232 Villigen, Switzerland. E-mail: gregory.goldsmith@psi.ch

REFERENCES

1. *New York Times*, Op-Docs, *Animated Life*; www.nytimes.com/video/opdocs-animated-life.
2. W. L. Bennett, S. Iyengar, *J. Communication* **58**, 707 (2008).
3. S. Knobloch-Westerwick, B. K. Johnson, A. Westerwick, *J. Computer-Mediated Communication* **20**, 171 (2015).

10.1126/science.aae0110

PHOTOS: (LEFT TO RIGHT) BIODIESEL33/WIKIMEDIA COMMONS; © 167/BROOKE WHATNALL/OCEAN/CORBIS

Published by AAAS

LETTERS

Edited by **Jennifer Sills**

Plant scientists: GM technology is safe

THE AMERICAN SOCIETY of Plant Biologists (ASPB) "supports the continued responsible use of genetic engineering… as an effective tool for advancing food security and reducing the negative environmental impacts of agriculture" (*1*). A recent petition advocating the ASPB position collected more than 1400 signatories from the plant science community (*2*). The ASPB, the petition signatories, and other scientists in governmental and scientific organizations throughout the world (*3*, *4*) demonstrate a clear consensus: Current use of genetic modification technology for crops is safe and effective, and future use should be guided by scientific evidence.

Despite such broad support for the technology, anti–genetically modified organism (GMO) advocates have had an extensive and troubling impact on policy—at the governmental level and through biasing public opinion—regarding the use of GMO-based ingredients in consumer products and food. More worrisome is that these arguments are often founded on science previously demonstrated to be unsound (*5*), such as the retracted Séralini *et al.* paper (*6*), which claimed that rats fed genetically modified corn and the herbicide RoundUp have higher rates of tumor formation.

The European Network of Scientists for Social and Environmental Responsibility (ENSSER) organized a petition signed by 313 individuals in 2013 claiming that "no consensus" exists regarding the safety of GMOs for human health and the environment (*7*). Commercial entities have seized upon ENSSER's statements. The Non-GMO Project, for example, cites the ENSSER petition (*8*) in its efforts to verify the absence of GMOs in over 4500 branded products. The fast-food restaurant chain Chipotle cites the ENSSER petition to justify a campaign against GMO ingredients (*9*).

Questions abound about how to best implement GM technologies, but as we move forward, we must make decisions informed by science. To meet our current and future food supply demands, without destroying our planet, we need every efficacious tool available (*10*). We hope that the consensus on GM technology among plant scientists is heard by policy-makers, the business community, and the general public. We invite advocates of the responsible use of such tools to make your voices heard to encourage a scientific approach in agricultural research and GMO policy.

Noah Fahlgren,[1] Rebecca Bart,[1] Luis Herrera-Estrella,[2] Rubén Rellán-Álvarez,[2] Daniel H. Chitwood,[1]* José R. Dinneny[3]*

[1]Donald Danforth Plant Science Center, St. Louis, MO 63132, USA. [2]Nacional de Genómica para la Biodiversidad, Irapuato, 36821, Mexico. [3]Carnegie Institution for Science, Stanford, CA 94305, USA.

*Corresponding author. E-mail: jdinneny@carnegiescience.edu; dchitwood@danforthcenter.org

REFERENCES

1. American Society of Plant Biologists, "Revised position statement on plant genetic engineering" (2014); https://c.ymcdn.com/sites/aspb.site-ym.com/resource/group/6d461cb9-5b79-4571-a164-924fa40395a5/Statements/ASPB_GE_revision.APPROVED_ed.pdf.
2. Cornell Alliance for Science, "Scientists in support of GMO technology for crop improvement" (http://cas.nonprofit-soapbox.com/aspbsupportstatement).
3. Institute of Medicine and National Research Council of the National Academies, *Safety of Genetically Engineered Foods* (National Academies Press, Washington, DC, 2004); www.nap.edu/read/10977/chapter/1.
4. World Health Organization, "Food, genetically modified" (www.who.int/topics/food_genetically_modified/en/).
5. ENSSER, "Democratising Science & Decision Making" (2012); www.ensser.org/democratising-science-decision-making/.
6. G.E. Séralini *et al.*, *Food Chem. Toxicol.* **50**, 4221 (2012) [RETRACTED].
7. ENSSER, "No scientific consensus on GMO safety" (2015); www.ensser.org/fileadmin/user_upload/150120_signatories_no_consensus_lv.pdf.
8. J. Fagan, M. Antoniou, C. Robinson, *GMO Myths and Truths* (Earth Open Source, London, ed. 2, 2014); www.nongmoproject.org/wp-content/uploads/2015/03/GMO-Myths-and-Truths-edition2.pdf.
9. Chipotle, Food with integrity: G-M-OVER IT (https://chipotle.com/gmo).
10. P. A. Sharp, A. Leshner, "We need a new Green Revolution," *New York Times* (4 January 2016); www.nytimes.com/2016/01/04/opinion/we-need-a-new-green-revolution.html.



China has approved the development of genetically modified corn.

PHOTO: XIN KUN/IMAGINECHINA

Protect the Tasmanian wilderness

AUSTRALIA'S TASMANIAN Wilderness World Heritage Area (TWWHA) is one of the three largest remaining temperate wilderness regions in the Southern Hemisphere (*1*). It covers about 1.6 million hectares, almost a quarter of Australia's State of Tasmania (*1*). Pristine wilderness is the most important core value of the region.

In January 2014, to encourage local economic growth, the Australian federal government sought to remove 74,039 hectares of land from the TWWHA (*2*). Although the request was rejected by the World Heritage Committee in June 2014 (*3*), the Tasmanian state government still supports housing, airport, road, mining, and logging projects within the TWWHA. The World Heritage Committee urged the federal government to stop any such development within the property (*4*). It is unclear how the federal government will address the Committee's demand, which leaves the values and integrity of the TWWHA at risk.

Australia is only the third country in the world, after Oman and Tanzania, to seek the delisting of its World Heritage areas (*5*). Australian governments, especially the federal one, should show leadership in implementing the World Heritage Convention. Local and national communities should also raise their voices to politicians and governments to make clear that the values and integrity of the

Published by AAAS



Mount Pelion East in the Tasmanian Wilderness World Heritage Area.

TWWHA cannot be sacrificed by any socioeconomic development.

Xiaojiang Yu

School of Geosciences, University of Sydney, Sydney, NSW 2006, Australia.
E-mail: xiaojiang.yu@sydney.edu.au

REFERENCES

1. Department of Primary Industries, Parks, Water and Environment, Tasmania, *The 2014 Draft Tasmanian Wilderness World Heritage Area Management Plan* (Hobart, 2014).
2. A. Darby, "Abbott government to cut 74,000 ha of forest from World Heritage Zone," *Sydney Morning Herald* (31 January 2014).
3. The World Heritage Committee, *Decisions Adopted by the World Heritage Committee at Its 38th Session* (Doha, 2014).
4. The World Heritage Committee, *Decisions Adopted by the World Heritage Committee at Its 39th Session* (Bonn, 2015).
5. B. Williams, "Bob Brown says UNESCO decision on Tasmanian World Heritage Forests is a bittersweet victory," *Courier-Mail* (24 June 2014).

TECHNICAL COMMENT ABSTRACTS

Comment on "Cortical folding scales universally with surface area and thickness, not number of neurons"

Marc H. E. de Lussanet

The cerebrum of large mammals is convoluted, whereas that of small mammals is smooth. Mota and Herculano-Houzel (Reports, 3 July 2015, p. 74) inspired a model on an old theory that proposed a fractal geometry. I show that their model reduces to the product of gray-matter proportion times the folding index. This proportional relation describes the available data even better than the fractal model.

Full text at http://dx.doi.org/10.1126/science.aad0127

Comment on "Cortical folding scales universally with surface area and thickness, not number of neurons"

Eric Lewitus, Iva Kelava, Alex T. Kalinka, Pavel Tomancak, Wieland B. Huttner

Mota and Herculano-Houzel (Reports, 3 July 2015, p. 74) assign power functions to neuroanatomical data and present a model to account for evolutionary patterns of

OUTSIDE THE TOWER

Teaching trust with art

As a young medical intern, I spent 3 months in the northern Indian village of Qutabgarh, Kanjhawala, working in a single-room dispensary. Early on, I realized that many patients did not trust doctors. Most patients were poor, with elementary or no education, and medical jargon made them suspicious. Pen and paper became my best friends. Simple drawings that conveyed medical information as stories helped reassure anxious patients.

For a mother whose child wouldn't suckle, I drew a picture of what was ailing her child's gut. Once she understood the problem, I was able to convince her to visit the city doctor I recommended. A skeptical old man with trichiasis kept insisting that he just needed more eye drops, until I convinced him with drawings that he needed to get the offending eyelashes removed too. My illustrations also helped persuade parents to get their children vaccinated in time. Children everywhere fear doctors, but they love stories. The dispensary's porch and the garden thus became an excellent stage. Short stories and bits of dramatics about the grumpy, growling bacteria and the slimy worm feasting in their gut mesmerized them and motivated them to take their medicine and listen to their mothers.



As communication and trust grew, we began to handle more sensitive cases, such as taking into confidence the parents and spouse of a young man with hepatitis B to get vaccinations for them and proper treatment for him. Within a couple of months, the number of patients grew from 40 to nearly 200 every day. The village chiefs noticed, giving us an opportunity to educate them about drinking water, sanitation, and quacks.

Now I practice both medicine and science, and I have access to computers, cartoons, animations, and movies to help explain medical concepts. But my time at this village taught me that one-to-one communication builds the strongest bridges. I practice it to this day with people from all walks of life, from rickshaw pullers and street children to senior doctors and scientists. When faces I have long forgotten come and tell me how we transformed their lives, it reinforces my faith in good communication and my responsibility to advocate science. I have always held on to the first lesson from my textbook of internal medicine, that the word "doctor" (Latin: docere) literally means "to teach."

Prashant Sood

Institute of Medical Sciences, University of Aberdeen, Aberdeen City, AB25 2ZD, UK.
E-mail: drprashantsood@gmail.com

PHOTOS: (TOP TO BOTTOM) ©CHRISTIAN KOBER/ROBERTHARDING/CORBIS; PRASHANT SOOD

Published by AAAS

cortical folding in the mammalian brain. We detail how the model assumptions are in conflict with experimental and observational work and show that the model itself does not accurately fit the data.
Full text at http://dx.doi.org/10.1126/science.aad2029

Response to Comment on "Cortical folding scales universally with surface area and thickness, not number of neurons"

Bruno Mota and Suzana Herculano-Houzel

De Lussanet claims that our model that accounts for the degree of folding of the cerebral cortex based on the product of cortical surface area and the square root of cortical thickness is better reduced to the product of gray-matter proportion and folding index. Lewitus *et al.*, in turn, claim that the assumptions of our model are in conflict with experimental data; that the model does not accurately fit the data; and that the ancestral mammalian brain was gyrencephalic. Here, we show that both claims are inappropriate.
Full text at http://dx.doi.org/10.1126/science.aad2346

Comment on "Global assessment of arbuscular mycorrhizal fungus diversity reveals very low endemism"

Thomas D. Bruns and John W. Taylor

Davison *et al.* (Reports, 28 August 2015, p. 970) claim that virtual taxa of Glomeromycota show little endemism and that endemism that exists is similar to the levels seen in plant families. We show that this is likely due to the conservative species definition rather than to any ecological pattern.
Full text at http://dx.doi.org/10.1126/science.aad4228

Response to Comment on "Global assessment of arbuscular mycorrhizal fungus diversity reveals very low endemism"

Maarja Öpik, John Davison, Mari Moora, Meelis Pärtel, Martin Zobel

Bruns and Taylor argue that our finding of widespread distribution among Glomeromycota "virtual taxa" is undermined by the species definition applied. Although identifying appropriate species concepts and accessing taxonomically informative traits are challenges for microorganism biogeography, the virtual taxa represent a pragmatic classification that corresponds approximately to the species rank of classical Glomeromycota taxonomy, yet is applicable to environmental DNA.
Full text at http://dx.doi.org/10.1126/science.aad5495

Published by AAAS

TECHNICAL COMMENT

BRAIN STRUCTURE

Comment on "Cortical folding scales universally with surface area and thickness, not number of neurons"

Marc H. E. de Lussanet

The cerebrum of large mammals is convoluted, whereas that of small mammals is smooth. Mota and Herculano-Houzel (Reports, 3 July 2015, p. 74) inspired a model on an old theory that proposed a fractal geometry. I show that their model reduces to the product of gray-matter proportion times the folding index. This proportional relation describes the available data even better than the fractal model.

A question that has inspired generations of neuroanatomists is why our cerebrum is walnut-shaped—and why that of small mammals is lissencephalic (smooth), whereas that of the largest ones is even more strongly convoluted than our own. Mota and Herculano-Houzel claim to have solved this mystery (*1*).

At least two earlier models exist that make quantitative predictions for the scaling of the mammalian cerebrum. Braitenberg (*2*) used a small data set and found that his model fits relatively small cerebra but not the human data. A larger data set (*3*) has confirmed that Braitenberg's model fails dramatically for all large brains. Zhang and Sejnowski (*4*) did validate their model using a large data set, with very good results. Unfortunately, a closer look shows that they assumed that the cortical thickness scales with cerebral size by a power law, which is not the case (*5*). It can be shown that correcting for this is fatal for Zhang and Sejnowski's model (*6*).

Thus, it is great news if a scaling relation is found that does have a theoretical and quantitative biological underpinning. Mota and Herculano-Houzel developed a 25-year-old hypothesis that the folding pattern of the mammalian cerebrum follows a fractal geometry and scaling (*7*). Fractal geometry is the self-similarity over a large range of scales. Classical examples from nature are coastal lines (*8*) and clouds (*9*). Mota and Herculano-Houzel derived a scaling relation using a model that was based on the tension hypothesis by D. C. Van Essen (*10*).

The authors did not acknowledge that the fractal hypothesis was first formulated by Hofman (*7*) [although they did use his data set (*11*)]; moreover, the tension model was only referred to in the supplement, and none of the existing quantitative models for cerebral scaling relations were cited.

Institute of Sports Science, University of Münster, Horstmarer Landweg 62b, D-48149 Münster, Germany.
E-mail: lussanet@uni-muenster.de

The scaling relation derived by Mota and Herculano-Houzel is

$$k A_E^{5/4} = A_T \sqrt{T} \quad (1)$$

with the exposed cortical surface area, the total cortical surface area, and cortical thickness T. Let us call the dimensionless constant k the "fractal constant." Mota and Herculano-Houzel defined cortical thickness as "equivalent thickness," which is the ratio of gray-matter volume to the cortical surface area $T = V_G/A_T$. (*12*)

Given the huge size range of mammalian cerebra, relations are typically plotted on a double logarithmic scale, which has the disadvantage that deviations appear to be very small and provide values that are very close to 1. A standard method to display the goodness of fit is to plot the residuals (Fig. 1A).

Given that $T = V_G/A_T$, the fractal model can be written as

$$A_E^{5/4} = k\sqrt{A_T V_G} \quad (2)$$

Taking the square and solving to k gives

$$k^2 = \frac{(A_T V_G)}{(A_E^{(5/2)})} \quad (3)$$

For better comparability, k^2, rather than k, will be used in the following. Obviously, the fractal constant is not nearly constant but increases with the exposed surface area (Fig. 1B), consistent with the trend in the fitting residual (Fig. 1A). In the original manuscript (*1*), this fact was hidden: Rather than showing the model fit, the authors chose to fit not only k but also the power of A_E, and concluded that the power (1.29) was "close to" 5/4. However, this seemingly small difference between fitted and predicted power is statistically highly significant: $t(56) = 8.2$, $P < 0.0001$.

An implicit assumption of Mota and Herculano-Houzel is that the overall shape of the cerebrum scales in an isometric manner (i.e., that the overall, "exposed" shape is independent of the size of the cerebrum). This assumption can be made explicit, as follows. For a perfect sphere, the relation between the exposed surface A_{sphere} and the total volume V_{sphere}, is $V_{sphere} = \sigma A_{sphere}^{3/2}$, with $\sigma = \frac{1}{6\pi}\sqrt{\pi}$. Because a cerebral hemisphere is not a perfect sphere, its volume is smaller than that of a perfect sphere that has the same surface area. We can therefore write for the relation between the exposed surface and the cerebral volume, $V_T = \sigma s A_E^{3/2}$, with $s < 1$ being a constant that expresses the sphericity of the cerebrum. Thus, substituting Eq. 3 with $A_E^{5/2} = A_E \times A_E^{3/2} = A_E V_T/\sigma s$ gives

$$\frac{V_G}{V_T}\frac{A_T}{A_E} = \kappa \quad (4)$$

with the "folding constant" kappa, $\kappa = \sigma s k^2$, a new dimensionless cerebral parameter (Fig. 1C). Thus, what looked like a fractal dimension of the outer surface in Eq. 1 is simply the product of the proportion of gray-matter volume V_G/V_T times the folding index $I = A_T/A_E$.

We conclude, first, that what looked like a complex fractal relation between exposed surface, total cortical surface, and cortical thickness is really a simple proportional relation of gray-matter volume and the folding index. Consequently, there is a proportionate relation $V_T \propto A_E^{3/2}$, provided that the exposed shape of the cerebrum is approximately invariant. Here lies the critical difference between Eqs. 1 and 4: Whereas Eq. 1 involves $\sqrt{A_E^{5/2}}$, Eq. 4 uses the product of A_E/V_T.

Second, k^2 and κ are not simply equivalent because they differ by a factor σs where the sphericity s of the cerebral hemispheres differs between species (*3*). Whereas k is a just a fitting constant without biological meaning (Eq. 1), κ has direct biological relevance, being the product of the folding index and the proportion of gray matter. Here, the data clearly speak in favor of the proportional relation (Eq. 4), because κ has a much smaller coefficient of variance (COV) than k^2. This is even clearer when comparing cerebra of similar exposed surface area (see Fig. 1, B and C). The difference between the variances is statistically reliable [$F(41,41) = 0.4$, $P = 0.009$, after removal of a linear trend].

This brings us to a third conclusion. Because κ shows extraordinary little variance for cerebra of similar size, the figure reveals that κ increases with cerebral size in a complex manner. Since $\kappa \approx 1$ for $A_E < 10^3$ mm^2 but gradually increases for larger cerebra, the relation between κ and cerebral size cannot be explained by a simple power relation (*13*).

Mota and Herculano-Houzel motivated their supposed fractal relation with a developmental growth model that was inspired by the tension model (*10*). The present analysis suggests that their model fails to explain a trend in the data that cannot be mended in a simple manner, such as slightly changing the power relation as Mota and Herculano-Houzel did. The data also strongly suggest that the model addresses the wrong parameters ($A_E^{5/4}$ instead of $A_E V_T$). Nevertheless, we cannot conclude that the cerebral surface does not have a fractal shape, because there is no evidence against that. However, at present there is

Downloaded from on February 18, 2016

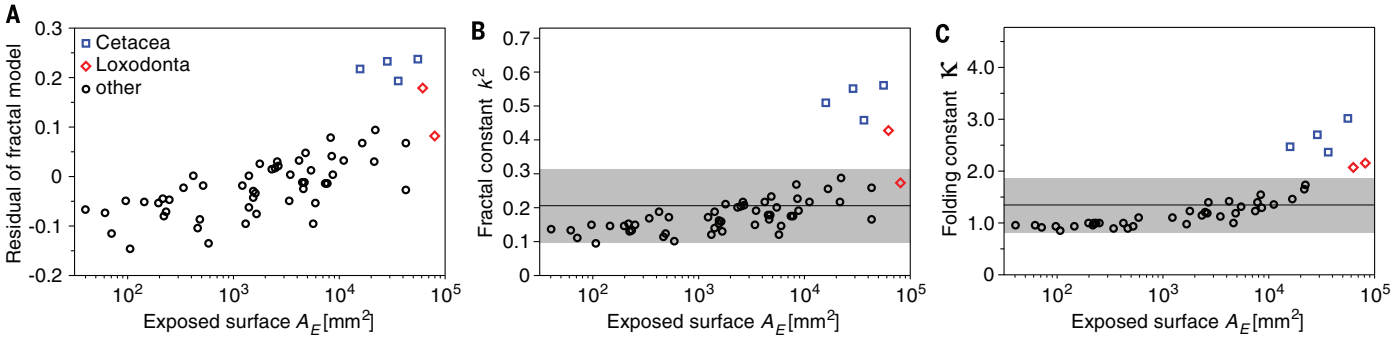


Fig. 1. The residual of the fractal model shows a marked trend, whereas the folding constant κ describes the data better than the fractal constant. (**A**) The residuals of the fractal model (Eq. 1) show a clear trend as a function of the exposed surface (in log units; note that 0.3 log scale corresponds to approximately a factor of 2). (**B**) The dimensionless fitting constant of the fractal model, here expressed as k^2, shows the same trend (COV = 0.53). Mean and SD are indicated by the gray band. (**C**) The dimensionless folding constant κ has a considerably smaller COV (0.39) than k^2. Data are shown for the 40 species (N = 42) from (*1*) for which the A_E, V_T, and V_G are reported in the original studies.

no evidence, empirical nor theoretical, in favor of a clear fractal relation. A more promising strategy would probably be to return to the definition of fractal shapes and analyze the self-similarity of the cortical surface of a few, particularly strongly convoluted, cerebra across a range of scales, as well as to search for a folding rule, rather than plotting the whole variety of mammalian species.

Small mammalian cerebra consist almost entirely of gray matter (*4*) and are lissencephalic so that $\kappa \approx 1$. Larger, convoluted, cerebra have an increasingly large proportion of white matter so that the ratio V_G/V_T is less than one. Because, for these cerebra, the folding index increases disproportionately to the reduction in the fraction of gray-matter volume, κ is larger than one. Also, even though the cetaceans seem to be less extreme in terms of κ than in terms of k^2, they might still be systematically off the general trend for mammalian cerebra. Explanations range from the exclusively aquatic life mode, which seems to increase cortical thickness (i.e., V_G) as a result of lack of REM sleep (*14*), to increased glia for heating the brain (*15*).

However, the fractal model does not describe the data satisfactorily. The κ model describes the relation to the exposed surface area better, but, paradoxically, the systematic increase of κ with cerebral size shows even more convincingly that both models fail to explain the scaling relation of the cerebrum. Obvious "repairs" by fitting the power as in Mota and Herculano-Houzel (*1*), or as given in note (*13*), lack theoretical biological underpinning. Thus, the remarkably regular scaling relations of the mammalian cerebrum remain a highly intriguing but yet unsolved mystery.

REFERENCES AND NOTES

1. B. Mota, S. Herculano-Houzel, *Science* **349**, 74–77 (2015).
2. V. Braitenberg, *J. Comput. Neurosci.* **10**, 71–77 (2001).
3. M. H. E. de Lussanet, How the flow and processing of information shapes the cerebrum. *PeerJ PrePrints* **3**, e1518 (2015). https://doi.org/10.7287/peerj.preprints.239v2.
4. K. Zhang, T. J. Sejnowski, *Proc. Natl. Acad. Sci. U.S.A.* **97**, 5621–5626 (2000).
5. M. A. Hofman, *Prog. Neurobiol.* **32**, 137–158 (1989).
6. Using the logarithmic relation of Hofman (*5*) or the fit of the cortical thickness by de Lussanet [figure S1 in (*3*)] leads to large errors, especially for small cerebra.
7. M. A. Hofman, *J. Hirnforsch.* **32**, 103–111 (1991).
8. B. B. Mandelbrot, *Proc. Natl. Acad. Sci. U.S.A.* **72**, 3825–3828 (1975).
9. F. S. Rys, A. Waldvogel, *Phys. Rev. Lett.* **56**, 784–787 (1986).
10. D. C. Van Essen, *Nature* **385**, 313–318 (1997).
11. M. A. Hofman, *Brain Behav. Evol.* **27**, 28–40 (1985).
12. The equivalent thickness does not truly measure the cortical thickness because the cortical surface is not flat (hence, "equivalent" thickness).
13. One could get rid of the trend in κ if one would allow to scale the folding index (Eq. 4) by a power of 2/5 (i.e., $\hat{\kappa} = I^{2/5} V_G/V_T$). The resulting relation has a COV of just 0.08 and no systematic dependency of the exposed surface area.
14. J. M. Siegel, *Nature* **437**, 1264–1271 (2005).
15. P. R. Manger, *Biol. Rev. Camb. Philos. Soc.* **81**, 293–338 (2006).

ACKNOWLEDGMENTS

I thank K. Boström and H. Wagner for their inspiring discussions.

14 August 2015; accepted 29 December 2015
10.1126/science.aad0127

TECHNICAL COMMENT

BRAIN STRUCTURE

Comment on "Cortical folding scales universally with surface area and thickness, not number of neurons"

Eric Lewitus,[1]* Iva Kelava,[2] Alex T. Kalinka,[3] Pavel Tomancak,[4] Wieland B. Huttner[4]*

Mota and Herculano-Houzel (Reports, 3 July 2015, p. 74) assign power functions to neuroanatomical data and present a model to account for evolutionary patterns of cortical folding in the mammalian brain. We detail how the model assumptions are in conflict with experimental and observational work and show that the model itself does not accurately fit the data.

How brains evolve to store more information has always been of interest to neurobiologists. There is clear evidence that changes in neuron production during development affect cortical morphology in adulthood (e.g., primary microcephaly) and that both neuron production and cortical morphology vary considerably across mammalian species. However, there remains considerable controversy over what developmental mechanisms and evolutionary selective pressures drive the cortex to fold as it does. Mota and Herculano-Houzel (*1*) recently presented a model that aims to explain both the developmental and evolutionary drivers of cortical folding through a single, universal power law. They arrive at their model using regression analyses on interspecific data and mathematical evaluations of the fractal folding patterns of paper. We think, however, that the authors have overlooked some key findings that may call into question some of their analytical assumptions and that giving a second thought to some of the decisions the authors made in their analyses can only help to strengthen what we know about development and evolution of the mammalian brain.

The authors conclude that the cortical folding index regresses against brain mass with a "fairly low r^2." There are several issues here. First, it is never explained how surface area and cortical thickness are calculated across all species and studies. No single method is indicated or explicated. Considering data were collected from studies that used different source material (histological slides and MRIs), different preservation techniques (formalin immersion and paraformaldehyde fixation), different methods (stereology and pachymetry), and that span 40 years of data collection, we think some deliberation on the effect of measurement variability on the authors' results is warranted. Second, an $r^2 = 0.75$ ($P < 0.0001$) is considerably robust and should really only be considered "fairly low" if compared with other models. Third, figure 1E in (*1*) shows that "the folding index does not vary as a significant power function of cortical thickness across gyrencephalic species," something that was previously shown (*2*). Fourth, the regression analysis is conducted on only a selection of species (i.e., those below a certain folding index). As folding index is a continuous trait, the authors need to present some statistical justification for removing those data from their analysis. Previous work has found that the relationship between folding index and brain mass (and cortical neuron number) is best fit by two linear functions, leading to two mammalian groups (*3*), a result that is further supported by clustering analyses and phylogenetic modeling on gyrencephaly and life-history traits. Therefore, we think the authors' claim that there are not "two clusters of gyrencephaly" is not justified. If they are confident that their model fits the data better than previous models, then it is incumbent on them to demonstrate it.

Further to this point, we reanalyzed the Mota and Herculano-Houzel data from table S1 in (*1*), which contains cortical surface area (A_G) and thickness (T) estimates for 57 species. We show that A_G and T predict two clusters of species, one with a gyrencephaly index (GI) below 1.5 and one with a GI above 1.5 (Fig. 1). This recovers the original result reported in (*3*), in which high- and low-GI groups were identified with a boundary GI value of 1.5. Figure 1 helps to clarify that species transitioning from the low- to the high-GI group must do so by increasing their cortical surface area with relatively little change in their cortical thickness.

If, as the authors assert, "the degree of gyrification is much larger in artiodactyls than in primates," "a better fit is found for total surface area" as a function of folding index, and "the precise relationship between T and A_G across gyrencephalic species differs across orders," then some statistical support needs to be implemented. This last statement, in particular, requires further analysis, because previous work has shown that the relationship between T and A_G disappears when phylogenetic relatedness, a hallmark of species comparisons (*4*), is taken into account (*2*). The authors cite (*2*, *3*) as corroborating evidence that "gyrification actually scales differently across mammalian orders," even though the cited work shows quite the opposite.

The most recent common mammalian ancestor was gyrencephalic (*3*, *5*). There have been many transitions in mammalian evolution from gyrencephaly to lissencephaly (*3*, *6*). Experimental work in the marmoset has shown that, despite being a lissencephalic species, it retains the neurogenic program of a gyrencephalic species (*6*). Together, these studies suggest that species may evolve a lissencephalic phenotype from a gyrencephalic one, exemplifying secondary lissencephaly. The authors do not address this evidence in their claim that "there is no such thing as 'secondary lissencephaly'", nor in their interjection that "Remarkably, there is no a priori reason for lissencephaly." They furthermore suggest that the earliest mammalian brain was "smooth," citing as evidence work that makes no claim whatsoever to the smoothness of the earliest mammalian brain [reference 31 in (*1*)].

Finally, there is formidable corroboration for a positive role of the developmental neurogenic program in determining the folding pattern of the adult cortex. Experimental work in mammals has demonstrated a predictive relationship between the distribution of neuron progenitors along the ventricle during development and the programmed pattern of gyri and sulci in the adult (*7*). These patterns are preceded by distinct gene expression profiles particular to prospective gyri and sulci in the developing neocortex (*8*). This explains, in part, why we see conserved patterns of cortical folding across closely related species, even when those species have considerably different folding indices [see (*2*)]. The authors' "crumpled paper" model—which claims that gyrencephaly is not achieved "through the generation of larger numbers of neurons" but is instead the mechanistic by-product of surface area expanding faster than cortical thickness over evolutionary time—does not account for these phenomena observed across species at the morphological, cellular, and genomic level.

The analytical and conceptual approach that Mota and Herculano-Houzel bring to the study of cortical development is crucially important and presents great potential in moving the field forward. However, we think the claims they make are not sufficiently supported and therefore should not yet be taken as rote formulae for explaining mammalian brain evolution.

[1]Institut de Biologie, École Normale Supérieure, Paris, France. [2]MRC Laboratory of Molecular Biology, Francis Crick Avenue, Cambridge Biomedical Campus, Cambridge CB2 0QH, UK. [3]Institute of Population Genetics, Vetmeduni, Vienna, Austria. [4]Max Planck Institute of Molecular Cell Biology and Genetics, Dresden, Germany.
*Corresponding author. E-mail: lewitus@biologie.ens.fr (E.L.); huttner@mpi-cbg.de (W.H.)

REFERENCES AND NOTES

1. B. Mota, S. Herculano-Houzel, *Science* **349**, 74–77 (2015).
2. E. Lewitus, I. Kelava, W. B. Huttner, *Front. Hum. Neurosci.* **7**, 424 (2013).
3. E. Lewitus, I. Kelava, A. T. Kalinka, P. Tomancak, W. B. Huttner, *PLOS Biol.* **12**, e1002000 (2014).

Downloaded from on February 18, 2016

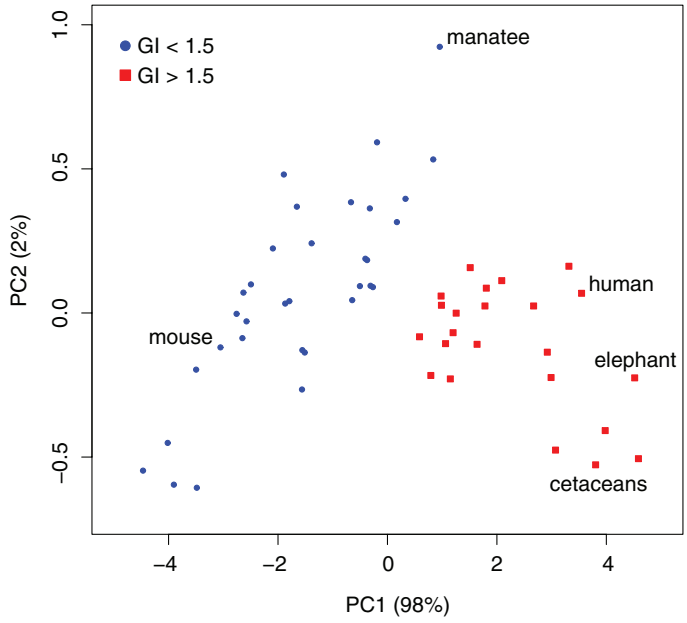


Fig. 1. Two clusters of mammalian species with GI values either below or above 1.5. Total A_G and T data [table S1 in (*1*)] were log-transformed, and a mixed clustering algorithm that uses factorial analysis and a combination of hierarchical (Ward's method) and *K*-means clustering was used to sort the species into distinct groups [implemented in the *R* package FactoClass (*9*)]. The clusters are shown using the two principal components of the data (GI < 1.5, blue circles; GI > 1.5, red squares). Relevant species, or groups of species, are highlighted. The cat (*Felis catus*) is not shown [see (*3*)].

4. J. Felsenstein, *Am. Nat.* **125**, 1–15 (1985).
5. M. A. O'Leary *et al.*, *Science* **339**, 662–667 (2013).
6. I. Kelava *et al.*, *Cereb. Cortex* **22**, 469–481 (2012).
7. I. Reillo, C. de Juan Romero, M. A. García-Cabezas, V. Borrell, *Cereb. Cortex* **21**, 1674–1694 (2011).
8. C. de Juan Romero, C. Bruder, U. Tomasello, J. M. Sanz-Anquela, V. Borrell, *EMBO J.* **34**, 1859–1874 (2015).
9. C. E. Pardo, P. C. DelCampo, *Revista Colombiana de Estadistica* **30**, 231–245 (2007).

ACKNOWLEDGMENTS

W.B.H. was supported by grants from the Deutsche Forschungsgemeinschaft (DFG) (SFB 655, A2) and the European Research Council (250197), by the DFG-funded Center for Regenerative Therapies Dresden, and by the Fonds der Chemischen Industrie. E.L. was supported by the Max Planck Gesellschaft and the Centre National de la Recherche Scientifique. E.L. thanks Evan Charles for helpful discussion.

7 August 2015; accepted 28 December 2015
10.1126/science.aad2029

TECHNICAL RESPONSE

BRAIN STRUCTURE

Response to Comments on "Cortical folding scales universally with surface area and thickness, not number of neurons"

Bruno Mota[1] and Suzana Herculano-Houzel[2]*

De Lussanet claims that our model that accounts for the degree of folding of the cerebral cortex based on the product of cortical surface area and the square root of cortical thickness is better reduced to the product of gray-matter proportion and folding index. Lewitus *et al*., in turn, claim that the assumptions of our model are in conflict with experimental data; that the model does not accurately fit the data; and that the ancestral mammalian brain was gyrencephalic. Here, we show that both claims are inappropriate.

In our original Report (*1*), we showed for the first time that the relationship between total surface area (A_T) and exposed surface area (A_E) of the mammalian cerebral cortex can be universally described, across lissencephalic and gyrencephalic species alike, by the power function $A_T T^{1/2} = kA_E^{1.305 \pm 0.010}$, where T is the average thickness of the cortical gray matter (Fig. 1A). Our model predicts the degree of folding of the mammalian cerebral cortex (that is, the relationship between A_T and A_E) with an r^2 of 0.998; that is, 99.8% of the variance in $A_T T^{1/2}$ across species is explained by the variation in $kA_E^{1.305}$. The empirical function is very close to our theoretical function $A_T T^{1/2} = kA_E^{1.25}$ that expresses the relationship between A_T and A_E, given T, that minimizes the effective free energy of a growing cortical volume—that is, the function that describes the most stable conformation of a growing, elastic, deformable cerebral cortex given its surface area and thickness. We thus propose that folding occurs as the expanding cortex, during development, settles at each moment in time into the most energetically favorable conformation, one that depends simply on its current combination of A_T and T, not number of neurons.

Based on the calculation from our data of values of k for the theoretical exponent of 1.25, de Lussanet notes that the residuals of the function $A_T T^{1/2} = kA_E^{1.25}$, that is, k, vary systematically with increasing A_E across species (*2*). This indicates a (presumably hidden) significant discrepancy between the exponent for A_E predicted by our effective free energy–minimization theory and the empirical exponent 1.305 (excluding cetaceans) that is found in the data. Our original Report makes it clear that, with a value of 1.305 ± 0.010, the exponent for A_E that best fits the data is close to, but statistically distinguishable (given the standard error) from, the theoretical exponent of 1.250, which is not surprising for a mean-field model based on a number of simplifying assumptions.

The origin of the discrepancy of 0.055 in the scaling exponent is an important question. In purely theoretical terms, the use of A_E as an order parameter was a necessary simplification, based on the expected relationship $V_T \sim A_E^{3/2}$ [made explicitly in the supplementary information in (*1*), and a good empirical approximation, given that we obtain $V_T \sim A_E^{1.52}$]. Whether modifications to correct for Gaussian curvature of the surface and the presence of deep nuclei would suffice to close the gap of 0.055 between theoretical and empirical exponents is an open question.

That our theory-based empirical relationship of exponent 1.305 nevertheless successfully predicts a single relationship that applies universally to both lissencephalic and gyrencephalic cortices can be shown using de Lussanet's own recourse of calculating k and examining for systematic variation. As shown in Fig. 1B, we find that $k = (A_T T^{1/2})/A_E^{1.305}$, calculated for each data point, does not vary significantly with A_E across noncetacean species [cetaceans are examined in the supplementary information in (*1*)].

Next, de Lussanet assumes, as we did, that the total cortical volume V_T and exposed area A_E are related as $V_T \sim A_E^{3/2}$ and rearranges the terms in our scaling law to give $\kappa = (A_T/A_E)(V_G/V_T)$. This equation, however, is tautological: It carries exactly the same information as the original relationship in our model, because it is simply a rewriting based on no distinct biological foundation. Moreover, the rewriting is explicitly dependent on an exponent of precisely 1.25. Given that de Lussanet himself shows (and we agree) that the empirical exponent is significantly different from 1.25, it follows that his rearrangement is not mathematically valid. That his proposed "model" with no theoretical basis other than our own fails to fully account for the data by his own standards is shown in Fig. 1C: The constant κ predicted by his formula is not invariant but rather varies systematically with A_E, in contrast to the constant k calculated using our empirical relationship (Fig. 1B). We thus believe that our empirical scaling relationship with an exponent of 1.305 ± 0.010, which is a very good approximation of the theoretical equation that describes the combination of parameters that minimize the effective free energy of the cortical volume, offers for the first time a useful and robust predictive account of the degree of cortical folding across mammalian species. This is in contrast to the work of Hofman (*3*), who identified not one universal function between A_T and A_E, but three, which applied separately to lissencephalic species, terrestrial gyrencephalic species, and marine gyrencephalic species.

We used exclusively data on surface area and cortical thickness that had already been published. Contrary to the claim of Lewitus *et al.* (*4*), all original reports were cited in the text, and those reports explained extensively how A_T, A_E, and T were obtained according to the standards in the neuroanatomy literature: respectively, as the total extent of the pial surface area of the gray matter; the total exposed gyral surface area not included in sulci; and the ratio between total gray-matter volume and total pial surface area. Most important is the fact that, whether traced from images of brain slices or from magnetic resonance imaging data, from tissue fixed by immersion or by perfusion, and regardless of the exact method of measurement, all values converge on the same, single relationship for which 99.8% of the variance in $A_T T^{1/2}$ is explained by the variation in $kA_E^{1.305}$. This goes to show (i) that data collected in these various ways are robust and method-insensitive enough to be comparable across laboratories, and thus really useful, and (ii) that our model indeed applies universally across species and data sets.

Importantly, these are precisely the same data that yield an r^2 of only 0.751 for the relationship between folding index of gyrencephalic species and brain mass, given in our original figure 1A. An r^2 of 0.751 is much smaller than an r^2 of 0.998, and we thus consider the former to be "fairly low," indeed. Only gyrencephalic species are considered in the analysis of scaling of folding index with brain mass because the folding index, expressed as the ratio A_T/A_E, is not a smooth function of brain mass but a two-tiered trait, because it has a hard lower bound of 1.0 and, by definition, no variation across all lissencephalic species. Including lissencephalic species would only worsen the already poor fit of a power function to the data. Remarkably, our analysis of the relationship between $A_T T^{1/2}$ and A_E carried out for all species, lissencephalic and gyrencephalic alike, yields an r^2 of 0.998 that is even higher than the r^2 of 0.996 obtained for gyrencephalic species alone (*1*). We thus concluded that the relationship between $A_T T^{1/2}$ and A_E is much stronger than the relationship

[1]Instituto de Física, Universidade Federal do Rio de Janeiro, Brasil. [2]Instituto de Ciências Biomédicas, Universidade Federal do Rio de Janeiro, Brasil.
*Corresponding author. E-mail: suzanahh@gmail.com

Downloaded from on February 18, 2016

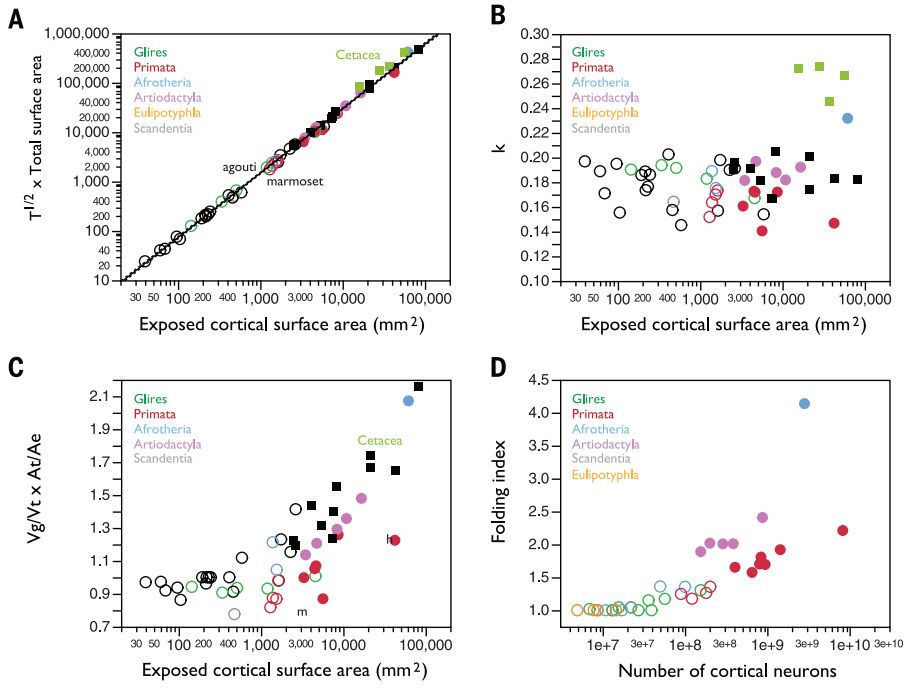


Fig. 1. Universal scaling relationship of exponent 1.305 describes cortical folding across mammalian species. All figures were plotted from data in (*1*), showing species with folding index <1.5 as open circles and species with folding index >1.5 as solid symbols. (**A**) $A_T T^{1/2}$ varies with $A_E^{1.305 \pm 0.010}$ ($r^2 = 0.998$, $P < 0.0001$) across lissencephalic and gyrencephalic species (cetaceans were excluded here; inclusion changes the exponent slightly to 1.325 ± 0.009). Marmoset and agouti, which are gyrencephalic species, are indicated. (**B**) $k = (A_T T^{1/2})/A_E^{1.305}$ calculated for each data point does not vary significantly with A_E across species (Spearman correlation, $P = 0.8883$) nor across species with folding below or above 1.5 (Wilcoxon, $P = 0.5477$). (**C**) $\kappa = (V_G/V_T) \times (A_T/A_E)$, which de Lussanet predicts to be constant, varies significantly with increasing A_E (Spearman correlation, $\rho = 0.771$, $P < 0.0001$). (**D**) Folding index is not a single function of the number of cortical neurons (shown for a single hemisphere) and also not simply as two clusters for species with folding index above (solid circles) or below (open circles) 1.5. Rather, species with folding indices above 1.5 show different scaling of folding, with the number of cortical neurons depending on whether they are artiodactyls (pink) or primates (red).

between folding index (A_T/A_E) and any other variable examined.

That "the degree of gyrification is much larger in artiodactyls than in primates for similar numbers of cortical neurons" is shown very obviously in our original figure 1B, reproduced here as Fig. 1D. There is no overlap between primates and artiodactyls. For instance, the cerebral cortex in the pig (an artiodactyl) and baboon (a primate) have the same folding index of 1.9, whereas one cortical hemisphere has only 146 million neurons in the former but 1.6 billion neurons in the latter, a difference of more than one order of magnitude. Statistical analyses are hardly necessary to prove that the two groups do not overlap.

Our assertions that "a better fit is found for [folding index against] total surface area" than against total brain mass and that "the precise relationship between T and A_G across gyrencephalic species differs across orders" ["with a much smaller exponent for primates than for artiodactyls (Fig. 3B, red and pink lines)," our original text continues] are founded on the r^2 values, exponents, standard errors, and 95% confidence intervals provided in the respective figure legends. The criticisms by Lewitus *et al.* thus require no further comment.

Regarding the so-called "clusters of gyrencephaly," there are indeed different groups in the relationship between folding index and number of cortical neurons, as we show in our original figure 1B, reproduced here (Fig. 1D), in line with the different, clade-specific relationships between A_T and T, as shown in our original figure 3B (although we don't call these "clusters"). The two candidate groups to form different "clusters of gyrencephaly," primates and artiodactyls, are however not the "two mammalian groups" to which Lewitus *et al.* refer in (*5*). Figure 1D shows that, for similar numbers of cortical neurons, artiodactyls have much larger folding indices than primates. In contrast, Lewitus *et al.* (*5*), who did not analyze our data on artiodactyls, arbitrarily defined two groups as those with folding index above 1.5 (the larger primates in their sample, including humans) and below 1.5 (rodents and the smallest primates, which includes lissencephalic species). This is a finding that essentially replicated our previous demonstration that the relationship between folding index and number of neurons differs across primates and rodents (*6*), without giving credit to it. Lewitus *et al.* (*5*) went on to propose that this arbitrary threshold of 1.5 corresponds to ~10^9 neurons. Figure 1D redraws our data identifying species with folding indices above and below 1.5 and illustrates how the "adaptive threshold" of gyrencephaly and the clustering around a threshold of folding index 1.5 proposed by Lewitus *et al.* (*5*) fail to hold in the face of data. Four of the five artiodactyls in our data set have fewer than 10^9 cortical neurons in both cortical hemispheres but folding indices of 1.9 and higher; cortices with similar numbers of neurons, all well below 10^9, have much higher folding indices in artiodactyls than in primates; and primates exhibit a continuous relationship between folding index and numbers of cortical neurons well below and well above 10^9, as we had already shown in (*6*) and reported again in our original figure 1B. Most importantly, there is no difference in our empirical k between species with folding indices above or below 1.5 (Fig. 1B). Thus, there are no "two clusters of gyrencephaly": All species, regardless of numbers of cortical neurons, of being lissencephalic or gyrencephalic, and of how gyrencephalic they are, share the same relationship $A_T T^{1/2} = kA_E^{1.305}$ (Fig. 1A).

The statement by Lewitus *et al.* that "there is formidable corroboration for a positive role of the developmental neurogenic program in determining the folding pattern of the adult cortex" is also incorrect, in the face of the data that we presented, here shown in Fig. 1D. More neurons do not necessarily translate into a more folded cortex, nor are they a mandatory requirement. These are fundamental realizations for the study of cortical development and evolutionary scaling (*1*). Developmental models of cortical expansion and evolution, including that of Lewitus *et al.* (*7*), can no longer consider that cortical surface area (and folding) grows proportionately across species as a single function of increasing numbers of neurons.

Still, in regard to development, it is in light of the clade-specific relationships between A_T and T that we state that "there is no a priori reason for lissencephaly." There is no known developmental mechanism that necessarily ties A_T to kT^2, the necessary condition for lissencephaly, because A_T and T are most likely controlled by different developmental mechanisms. That the relationship between A_T and T that maintains lissencephaly is not obligatory is shown by the very fact that not all species are lissencephalic.

The claim by Lewitus *et al.* that "the most recent common mammalian ancestor was gyrencephalic" (*5*) is based on unfortunate phylogenetic inferences instead of actual fossils and indeed flies in the face of the ample fossil evidence of lissencephalic ancestral mammals (*8*–*11*). We did, however, cite the wrong paper in regard to there being "no secondary lissencephaly"; we should have cited (*5*) instead of (*12*). Incidentally, we note that the marmoset, a species cited by Kelava *et al.* (*12*) as an example of secondary lissencephaly, is actually gyrencephalic, with a folding index of 1.175, similar to the agouti, and both fit perfectly on the universal scaling relationship that we identified (Fig. 1A).

The reason that the inference by Lewitus *et al.* (*5*) of a common gyrencephalic ancestor to all mammals is unfounded is that it was based on the finding that clades of extant mammalian species have average folding indices larger than 1.36. This is akin to calculating the average body mass of extant mammalian clades, finding that in all clades this average is larger than 1 kg, and thus concluding that the ancestral mammal also had a body mass larger than 1 kg. Actually, it is worse; given that folding indices are by definition never smaller than 1.0, their mathematical analysis could never obtain an average folding index of 1.0 for any clade, given that all of them contain gyrencephalic species. O'Leary *et al.* (*13*), cited by Lewitus *et al.* (*5*), used a similarly flawed inference to conclude that the ancestral placental mammal was gyrencephalic.

In the context of the ample fossil evidence of lissencephalic ancestral mammals (*8*–*11*) and of our finding that extant lissencephalic and gyrencephalic species alike obey the same relationship (*1*), $A_T T^{1/2} = k A_E^{1.305}$, and given the small size of those ancestral brains, it would be extraordinary indeed if any of the small ancestral cortices were found to be folded as Lewitus *et al.* suggest. They would stand out as the sole, major outliers to the universal scaling relationship that we identified.

REFERENCES AND NOTES

1. B. Mota, S. Herculano-Houzel, *Science* **349**, 74–77 (2015).
2. M. H. E. de Lussanet, *Science* **351**, 825 (2016).
3. M. A. Hofman, *Brain Behav. Evol.* **27**, 28–40 (1985).
4. E. Lewitus, I. Kelava, A. T. Kalinka, P. Tomancak, W. B. Huttner, *Science* **351**, 825 (2016).
5. E. Lewitus, I. Kelava, A. T. Kalinka, P. Tomancak, W. B. Huttner, *PLOS Biol.* **12**, e1002000 (2014).
6. L. Ventura-Antunes, B. Mota, S. Herculano-Houzel, *Front. Neuroanat.* **7**, 3 (2013).
7. E. Lewitus, I. Kelava, W. B. Huttner, *Front. Hum. Neurosci.* **7**, 424 (2013).
8. T. Macrini, C. de Muizon, R. L. Cifelli, T. Rowe, *J. Vertebr. Paleontol.* **27**, 99–107 (2007).
9. T. E. Macrini, G. W. Rougier, T. Rowe, *Anat. Rec.* **290**, 875–892 (2007).
10. E. C. Kirk, P. Daghighi, T. E. Macrini, B.-A. Bhullar, T. B. Rowe, *J. Hum. Evol.* **74**, 82–95 (2014).
11. T. B. Rowe, T. E. Macrini, Z. X. Luo, *Science* **332**, 955–957 (2011).
12. I. Kelava, E. Lewitus, W. B. Huttner, *Front. Neuroanat.* **7**, 16 (2013).
13. M. A. O'Leary *et al.*, *Science* **339**, 662–667 (2013).

ACKNOWLEDGMENTS

Financial support was provided by Fundação de Amparo à Pesquisa do Estado do Rio de Janeiro, Conselho Nacional de Desenvolvimento Científico e Tecnológico, and the James S. McDonnell Foundation.

28 August 2015; accepted 28 December 2015
10.1126/science.aad2346

TECHNICAL COMMENT

FUNGAL SYMBIONTS

Comment on "Global assessment of arbuscular mycorrhizal fungus diversity reveals very low endemism"

Thomas D. Bruns* and John W. Taylor

Davison *et al*. (Reports, 28 August 2015, p. 970) claim that virtual taxa of Glomeromycota show little endemism and that endemism that exists is similar to the levels seen in plant families. We show that this is likely due to the conservative species definition rather than to any ecological pattern.

The Glomeromycota is a globally important group of fungi that form mutualistic interactions with the roots of the majority of land plants. They cannot be grown in axenic culture, and their taxonomy is currently based on differences in spore morphology and sequences of conserved genes (*1*). Davison *et al.* (*2*) use partial small subunit (SSU, or 18*S*) ribosomal RNA gene sequences to argue that their "virtual taxa," which are "approximately species-level taxonomic units" of Glomeromycota fungi, have very limited endemism compared with larger organisms and that their pattern is more similar to that seen at the plant family level. However, there is a logical error in their methods, because they compare fungal taxa defined by partial SSU sequence to species in plants defined by multiple criteria and assume that they are comparing equivalent units.

We ask the question of what SSU-defined virtual taxa would look like if this approach were applied to animals or plants. To do this, we retrieved the human sequence for the same 520–base pair region, starting immediately after the NS31 primer, of the SSU gene used by Davison *et al.*, and then used Basic Local Alignment Search Tool (BLAST) on this sequence to see the taxonomic depth that would be captured by a 97% identity threshold, the criteria they used. We found that the human gene fragment was a 99% match to house mouse (*Mus musculus*), pig (*Sus scrofa*), white-tailed deer (*Odocoileus virginianus*), western European hedgehog (*Erinaceus europaeus*), and horse (*Equus caballus*), and a 97% match to the common wombat (*Vombatus ursinus*) and several other marsupials. Thus, SSU-defined virtual taxa, if applied to mammals, would also show little or no endemism because most or all would be a single unit. Furthermore, if all species of mammals were defined by morphological differences in their egg cells, which are within the same scale as spore of the Glomeromycota, we would expect to see few, widely dispersed species that might well be correlated with the slight differences in the SSU gene.

We repeated this process by retrieving the homologous region from wheat (*Triticum*) and applying BLAST to it. We found that all available genera in family Poaceae (*Oryza*, *Zea*, *Lolium*, *Fescue*, *Alloteropsis*, *Sorghum*, *Lecomtella*, and *Anarthria*) had SSU regions 98 to 99% identical to *Triticum*. Furthermore, at 96% identity, members of several Eudicot family were retrieved, including *Caryocar glabrum* (Caryocaraceae), *Ackama rosifolia*, *Caldcluvia paniculosa*, *Opocunonia papuana* (Cunoniaceae), and *Hevea brasiliensis* (Euphorbiaceae). With these results in mind, Davison *et al.*'s finding that Glomeromycota virtual taxa had similar levels of endemism to plant families makes sense, but only because similar levels of molecular divergence are then being compared in both groups; there is no evidence that one group has less endemism than another. It is conceivable that fungal species have less conservation SSU genes, but when we used the SSU region from *Nectria*, from the well-sampled order Hypocreales, we found 99% identity with all sampled genera in the order. Thus, the entire order would be equivalent to one SSU-defined virtual taxon.

Morphologically defined species in the Glomeromycota have always been delimited by the characters available in their spores, and these "species" do correlate fairly well with SSU-defined units, but that does not mean that they are comparable to species in other groups. Knowing that these SSU-defined taxa are actually equivalent to family- or order-level taxonomic units in plants, animals, and other fungi should give us pause to consider the alternative: that all of these "species" in the Glomeromycota are actually collections of fairly distantly related taxa.

The main problem with respect to the Glomeromycota and all other small organisms is that there are very few observable phenotypic characters that allow us to distinguish and classify them. As a result, taxonomic concepts from species to phyla end up being much broader than those applied to larger, better-studied organisms. Broad species concepts led to hypotheses that, for small organisms, such as bacteria and protists, there is no endemism because "everything is everywhere" (*3*, *4*). When more variable DNA sequences are used for comparison in small organisms, it has been shown that almost nothing is everywhere, whether fungi (*5*), protists (*6*), bacteria (*7*), or archaea (*8*). Now, population genomics is showing that natural barriers to fungal gene flow occur over geographic distances well below the size of continents (*9*–*11*), with dispersal limitation playing a key role in the assembly of fungal communities (*12*). When similar variable markers and population genomics can be applied to arbuscular mycorrhizal fungi, we predict that narrowly endemic species and populations will be discovered to be the rule, and what we now call species will be revealed to be collections of distantly related taxa.

Certainly, SSU-defined taxa are very useful in the Glomeromycota, and they currently provide one of the only ways to begin to catalog their global patterns. Furthermore, the correlation of these SSU taxa with other ecological parameters, and the modest level of endemism they reveal, is impressive and provides good evidence that they capture some of the evolutionary signal. However, claims of differences in endemism between them and macroscopic plants or animals only demonstrate how different the taxonomic concepts are; they say nothing about the comparative ecology of these organisms.

Department of Plant and Microbial Biology, 111 Koshland Hall, Berkeley, CA 94720-3102, USA.
*Corresponding author. E-mail: pogon@berkeley.edu

REFERENCES AND NOTES

1. D. Redecker *et al.*, *Mycorrhiza* **23**, 515–531 (2013).
2. J. Davison *et al.*, *Science* **349**, 970–973 (2015).
3. L. G. M. Baas-Becking, *Geobiologie of Inleiding Tot de Milieukunde* (W. P. Van Stockum and Zoon, The Hague, Netherlands, 1934).
4. T. Fenchel, B. J. Finlay, *Bioscience* **54**, 777–784 (2004).
5. J. W. Taylor, E. Turner, J. P. Townsend, J. R. Dettman, D. Jacobson, *Philos. Trans. R. Soc. London B Biol. Sci.* **361**, 1947–1963 (2006).
6. M. S. Robeson *et al.*, *Proc. Natl. Acad. Sci. U.S.A.* **108**, 4406–4410 (2011).
7. C. A. Hanson, J. A. Fuhrman, M. C. Horner-Devine, J. B. H. Martiny, *Nat. Rev. Microbiol.* **10**, 497–506 (2012).
8. R. J. Whitaker, D. W. Grogan, J. W. Taylor, *Science* **301**, 976–978 (2003).
9. S. Branco *et al.*, *Mol. Ecol.* **24**, 2747–2758 (2015).
10. C. E. Ellison *et al.*, *Proc. Natl. Acad. Sci. U.S.A.* **108**, 2831–2836 (2011).
11. P. Gladieux *et al.*, *Mol. Ecol.* **24**, 5657–5675 (2015).
12. K. G. Peay, M. Garbelotto, T. D. Bruns, *Ecology* **91**, 3631–3640 (2010).

ACKNOWLEDGMENTS

Funding was provided by NSF grant 1046115 to T.D.B. and J.W.T.

11 September 2015; accepted 13 January 2016
10.1126/science.aad4228

Downloaded from on February 18, 2016

TECHNICAL RESPONSE

FUNGAL SYMBIONTS

Response to Comment on "Global assessment of arbuscular mycorrhizal fungus diversity reveals very low endemism"

Maarja Öpik,* John Davison, Mari Moora, Meelis Pärtel, Martin Zobel

Bruns and Taylor argue that our finding of widespread distribution among Glomeromycota "virtual taxa" is undermined by the species definition applied. Although identifying appropriate species concepts and accessing taxonomically informative traits are challenges for microorganism biogeography, the virtual taxa represent a pragmatic classification that corresponds approximately to the species rank of classical Glomeromycota taxonomy, yet is applicable to environmental DNA.

Bruns and Taylor (*1*) refute our claim in Davison *et al.* (*2*) that approximately species-level taxa in the arbuscular mycorrhizal (AM) fungi (Glomeromycota) exhibit relatively low endemism. We used nuclear ribosomal small subunit RNA (SSU, or 18*S* rRNA) gene–based virtual taxa (VT) as the basic taxonomic units to classify AM fungi in a global set of environmental samples. We found that, although dispersal limitation contributes to the assembly of AM fungal communities, very few VT are endemic, producing a global distribution pattern similar to that observed in families of plants. Bruns and Taylor argue that the VT of AM fungi are not comparable to the taxonomic ranks of macro-organisms and that, consequently, our comparison uses nonequivalent units. We agree that the availability and accuracy of taxonomic information are key issues in microorganism biogeography. However, we consider specific criticism of the VT approach to be wide of the mark.

Species are usually taken as the basic unit of biodiversity, and described species lists for some macroorganisms—e.g., plants—are probably close to complete for some regions on Earth. The completeness of microorganism species lists is considerably lower, although less so for fungi than for bacteria (*3*). However, for many microorganisms, AM fungi included, the number of known DNA-based, approximately species-level taxa is far higher than that of species possessing Latin binomials, and DNA-based "species" records are generally better linked with ecological metadata. In these respects, DNA-based "species" offer the more complete classification for describing microorganism biodiversity patterns.

The gold standard for delimiting fungal species is the genealogical concordance method, which uses multiple genomic loci to assess limits on recombination (*4*). In practice, morphological and phylogenetic species concepts are applied in specimen-based classification of the apparently asexual Glomeromycota. About 300 species of Glomeromycota have been described on the basis of morphology (mostly, but not exclusively, of spores) and DNA sequences [internal transcribed spacer (ITS) region or large subunit (LSU, also called 28*S*) rRNA gene, both widely used markers in the taxonomy of Fungi]. Although this number is low in the context of some microorganism groups, it is consistent with species number estimates in other early-diverging fungal clades (*5*). Furthermore, evidence for cryptic species among Glomeromycota is limited; rather, merging of described species has been proposed (*6*). Although we see no compelling evidence to suggest massive underestimation of Glomeromycota species numbers in the current taxonomy, Bruns and Taylor are right to point out that reliance on conserved or limited traits for taxonomic assignment is a potential stumbling block for microorganism taxonomy. It is notable that, irrespective of species boundaries, widespread AM fungal taxa are known to harbor globally distributed genotypes (*7*, *8*). Nonetheless, we trust that progress in officially describing new fungal species on the basis of DNA data, including population genetics approaches, will improve estimates of global fungal species numbers (*9*) and prove to be a catalyst for advancing Glomeromycota taxonomy and understanding species-level distribution patterns.

DNA-based taxonomies incorporating both specimen-derived and environmental records have identified approximately 350 SSU rDNA-based VT (at ≥97% similarity threshold) (*10*) and more than 2000 ITS-based species hypotheses (SH) (at 98.5% similarity threshold) (*11*) among Glomeromycota. Application of other, nonribosomal markers has revealed similar classifications and species number estimates (*12*, *13*). Both VT and SH are pragmatic species classifications, validation of which is ongoing. VT are known to be slightly higher in taxonomic rank than (morpho-)species of Glomeromycota and may be equivalent to groups of closely related species in some genera. However, the species-discriminatory power of the SSU rDNA marker is only slightly lower than that of the markers widely used by taxonomists (*14*), and VT are clearly finer in taxonomic rank than the families or genera of classical Glomeromycota taxonomy (*10*). Thus, given the best available taxonomic information, the VT approach provides an effective means to survey approximately species-level diversity in the group.

We contend that the biogeographies of different organism groups are comparable but that taxonomic assignments must be made using appropriate traits, and these differ from group to group. For example, species-discriminating morphological traits for plants are frequently those of flowers; for animals, those of bones. The quest for DNA-level traits for species discrimination has not yet identified a universally suitable marker region. Plastid markers are used for plants, mitochondrial cytochrome oxidase I for animals, and nuclear ribosomal ITS for fungi. These markers are rarely optimal for all species within organism groups, and the ITS region is known to be too conserved or too variable in some fungal groups (*15*). We argue that the central fragment of the SSU rRNA gene distinguishes approximately species-level taxa among Glomeromycota and is therefore practical for research on the diversity patterns of these fungi. However, we recognize that use of this marker region for species identification of other fungi, let alone of plants or animals, would be as inappropriate and fruitless as an attempt to identify plants using bones, or animals using flowers.

Department of Botany, University of Tartu, 40 Lai Street, 51005 Tartu, Estonia.
*Corresponding author. E-mail: maarja.opik@ut.ee

REFERENCES AND NOTES

1. T. Bruns, J. Taylor, *Science* **351**, 826 (2016).
2. J. Davison *et al.*, *Science* **349**, 970–973 (2015).
3. C. E. Hinchliff *et al.*, *Proc. Natl. Acad. Sci. U.S.A.* **112**, 12764–12769 (2015).
4. J. W. Taylor *et al.*, *Fungal Genet. Biol.* **31**, 21–32 (2000).
5. J. E. Stajich *et al.*, *Curr. Biol.* **19**, R840–R845 (2009).
6. R. J. Bills, J. B. Morton, *Mycorrhiza* **25**, 485–498 (2015).
7. S. Rosendahl, P. McGee, J. B. Morton, *Mol. Ecol.* **18**, 4316–4329 (2009).
8. H. C. den Bakker, N. W. Vankuren, J. B. Morton, T. E. Pawlowska, *Mol. Biol. Evol.* **27**, 2474–2486 (2010).
9. J. R. Herr, M. Öpik, D. S. Hibbett, *New Phytol.* **205**, 27–31 (2015).
10. M. Öpik, J. Davison, M. Moora, M. Zobel, *Botany* **92**, 135–147 (2014).
11. UNITE database, https://unite.ut.ee/.
12. R. Borriello, V. Bianciotto, A. Orgiazzi, E. Lumini, R. Bergero, *Mol. Phylogenet. Evol.* **75**, 1–10 (2014).
13. H. Stockinger, M. Peyret-Guzzon, S. Koegel, M. L. Bouffaud, D. Redecker, *PLOS ONE* **9**, e107783 (2014).
14. M. Krüger, C. Krüger, C. Walker, H. Stockinger, A. Schüssler, *New Phytol.* **193**, 970–984 (2012).
15. C. L. Schoch *et al.*, *Proc. Natl. Acad. Sci. U.S.A.* **109**, 6241–6246 (2012).

ACKNOWLEDGMENTS

Funding was provided by grants from the Estonian Science Foundation (9050 and 9157), the Estonian Research Council (IUT-20-28 and IUT-20-29), and the European Regional Development Fund (Frontiers in Biodiversity Research Centre of Excellence).

16 October 2015; accepted 13 January 2016
10.1126/science.aad5495

Downloaded from on February 18, 2016

RESEARCH ARTICLE SUMMARY

MICROBIOME

Gut bacteria that prevent growth impairments transmitted by microbiota from malnourished children

Laura V. Blanton, Mark R. Charbonneau, Tarek Salih, Michael J. Barratt, Siddarth Venkatesh, Olga Ilkaveya, Sathish Subramanian, Mark J. Manary, Indi Trehan, Josh M. Jorgensen, Yue-mei Fan, Bernard Henrissat, Semen A. Leyn, Dmitry A. Rodionov, Andrei L. Osterman, Kenneth M. Maleta, Christopher B. Newgard, Per Ashorn, Kathryn G. Dewey, Jeffrey I. Gordon*

INTRODUCTION: As we come to appreciate how our microbial communities (microbiota) assemble following birth, there is an opportunity to determine how this facet of our developmental biology relates to the healthy or impaired growth of infants and children. Childhood undernutrition is a devastating global health problem whose long-term sequelae, including stunting, neurodevelopmental abnormalities, and immune dysfunction, remain largely refractory to current therapeutic interventions.

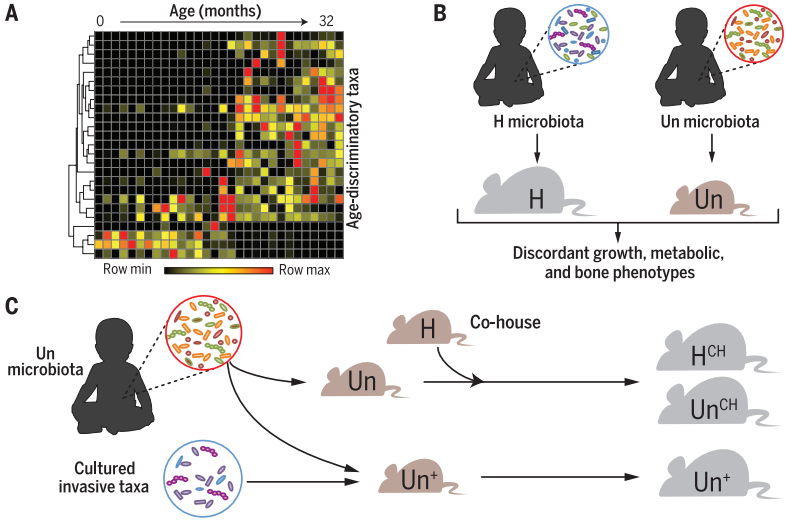
RATIONALE: To test the hypothesis that perturbations in the normal development of the gut microbiota are causally related to undernutrition, we first applied random forests (RF), a machine learning method, to bacterial 16*S* ribosomal RNA data sets generated from fecal samples that were collected serially from healthy Malawian infants and children during their first 3 postnatal years. Age-discriminatory bacterial taxa were identified with distinctive time-dependent changes in their relative abundances; they were used to construct a sparse RF-derived model describing a program of normal postnatal gut microbiota development that is shared across biologically unrelated individuals. A metric based on this model (microbiota-for-age *Z*-score) was used to define the state of development (maturation) of fecal microbiota from infants and children with varying degrees of undernutrition. Fecal samples obtained from 6- and 18-month-old children with healthy growth patterns or with varying degrees of undernutrition were transplanted into young germ-free mice that were fed a representative Malawian diet. The recipient animals' rate of lean body mass gain was characterized by serial quantitative magnetic resonance, their metabolic phenotypes were determined by targeted mass spectrometry, and their femoral bone morphologic features were delineated by microcomputed tomography.

RESULTS: Undernourished children in the Malawian birth cohort that we studied have immature gut microbiota. Unlike microbiota from healthy children, immature microbiota transmit impaired growth, altered bone morphology, and metabolic abnormalities in the muscle, liver, and brain to recipient gnotobiotic mice. The representation of several age-discriminatory taxa in the transplanted microbiota harbored by recipient animals correlated with their growth rates. Microbiota from 6-month-old infants produced greater effects on growth than did microbiota from 18-month-old children, although in each age bin, the growth effects produced by a healthy donor's community were greater than those produced by an undernourished donor's community. Cohousing coprophagic mice shortly after they received microbiota from healthy or severely stunted and underweight 6-month-old infants resulted in the invasion of age- and growth-discriminatory taxa from the former into the latter microbiota in the recipient animals, with associated prevention of growth impairments. Introducing cultured members from this group of invasive species ameliorated growth and metabolic abnormalities in recipients of microbiota from undernourished donors.

ON OUR WEB SITE

Read the full article at http://dx.doi.org/10.1126/science.aad3311

CONCLUSION: These preclinical findings provide evidence that gut microbiota immaturity is causally related to childhood undernutrition. The age- and growth-discriminatory taxa that we identified should help direct studies of the effects of host and environmental factors on gut microbial community development, and they represent therapeutic targets for repairing or preventing gut microbiota immaturity. ■



Preclinical evidence that gut microbiota immaturity is causally related to childhood undernutrition. (**A**) A model of normal gut microbial community development in Malawian infants and children, based on the relative abundances of 25 bacterial taxa that provide a microbial signature defining the "age," or state of maturation, of an individual's (fecal) microbiota. (Hierarchical clusterings of operational taxonomic units are indicated on the left.) (**B**) Fecal samples from healthy (H) or stunted and underweight (Un) infants and children were transplanted into separate groups of young germ-free mice that were fed a Malawian diet. The immature microbiota of Un donors transmitted impaired growth phenotypes to the mice. (**C**) Evidence that a subset of age-discriminatory taxa are also growth-discriminatory. Cohousing mice shortly after they received microbiota from 6-month-old healthy or undernourished donors resulted in the invasion of taxa from the healthy donor's microbiota (H^{CH}) into the undernourished donor's microbiota (Un^{CH}) among recipient animals and prevented growth impairments. Adding cultured invasive growth-discriminatory taxa directly to the Un donor's microbiota (Un^{+}) improved growth.

The list of author affiliations is available in the full article online.
*Corresponding author. E-mail: jgordon@wustl.edu
Cite this article as L. V. Blanton *et al.*, *Science* 351, aad3311 (2016). DOI: 10.1126/science.aad3311

Downloaded from on February 18, 2016

RESEARCH ARTICLE

MICROBIOME

Gut bacteria that prevent growth impairments transmitted by microbiota from malnourished children

Laura V. Blanton,[1] Mark R. Charbonneau,[1] Tarek Salih,[1] Michael J. Barratt,[1] Siddarth Venkatesh,[1] Olga Ilkaveya,[2] Sathish Subramanian,[1] Mark J. Manary,[3,4] Indi Trehan,[3,5] Josh M. Jorgensen,[6] Yue-mei Fan,[7] Bernard Henrissat,[8,9] Semen A. Leyn,[10] Dmitry A. Rodionov,[10,11] Andrei L. Osterman,[11] Kenneth M. Maleta,[4] Christopher B. Newgard,[2,12] Per Ashorn,[7,13] Kathryn G. Dewey,[6] Jeffrey I. Gordon[1]*

Undernourished children exhibit impaired development of their gut microbiota. Transplanting microbiota from 6- and 18-month-old healthy or undernourished Malawian donors into young germ-free mice that were fed a Malawian diet revealed that immature microbiota from undernourished infants and children transmit impaired growth phenotypes. The representation of several age-discriminatory taxa in recipient animals correlated with lean body mass gain; liver, muscle, and brain metabolism; and bone morphology. Mice were cohoused shortly after receiving microbiota from healthy or severely stunted and underweight infants; age- and growth-discriminatory taxa from the microbiota of the former were able to invade that of the latter, which prevented growth impairments in recipient animals. Adding two invasive species, *Ruminococcus gnavus* and *Clostridium symbiosum,* to the microbiota from undernourished donors also ameliorated growth and metabolic abnormalities in recipient animals. These results provide evidence that microbiota immaturity is causally related to undernutrition and reveal potential therapeutic targets and agents.

Undernutrition is a leading cause of infant and childhood mortality worldwide (*1*–*5*). The mechanisms that underlie this disorder's manifestations, ranging from persistent abnormalities in growth and immune function to cognitive deficits, remain obscure. Childhood undernutrition is not due to food insecurity alone; it also results from a combination of factors including diets with low nutrient density or bioavailability, pathogen burden, and gut mucosal barrier dysfunction (*6*–*8*).

The World Health Organization has used a cohort of 8440 healthy children living in six countries to develop anthropometric standards that define nutritional status [weight-for-height *Z*-score (WHZ), weight-for-age *Z*-score (WAZ), and height-for-age *Z*-score (HAZ)] (*9*, *10*). A recent study (*11*) of infants and children with healthy growth phenotypes living in Mirpur, an urban slum in Dhaka, Bangladesh, involved monthly fecal collection from birth through the end of the second year of life. In this study, a 16*S* ribosomal RNA (rRNA) analysis of bacterial membership in the gut microbiota and the application of a machine learning method [random forests (RF) (*12*)] revealed 24 "age-discriminatory" taxa, whose changes in relative abundance over time define a program of normal maturation of the microbiota across biologically unrelated individuals (*11*). This model served as the basis for computing two related metrics, relative microbiota maturity and microbiota-for-age *Z*-score (MAZ), that significantly correlated with the chronological age of children with healthy growth phenotypes. Applying these metrics showed that children living in Mirpur with moderate acute malnutrition (MAM) or severe acute malnutrition (SAM) have gut microbiota that are "immature;" in other words, the representation of the age-discriminatory taxa in their gut communities was more similar to younger than to age-matched healthy individuals from the same locale. Moreover, the degree of this immaturity was greater in SAM than MAM (*11*). Treatment of children with SAM with either one of two ready-to-use therapeutic foods produced only incomplete and transient improvement in this immaturity and no improvement in their HAZ scores (*11*).

These findings raise several questions. To what extent are these age-discriminatory taxa also indicative of the normal development of the gut microbiota of infants and children elsewhere? Are the age-discriminatory taxa biomarkers of gut microbiota development, or are they mediators of healthy growth? If the latter, can their introduction into immature microbiota prevent disease?

A Malawian model of gut microbiota development

To address these questions, we first developed a RF-based model of gut microbial community development from a serially sampled cohort of Malawian twins that were concordant for healthy growth. We investigated correlations between nutritional status and microbiota maturation to ascertain whether an MAZ score could predict future growth performance.

In a previous study, we followed a cohort of 317 twin pairs and three sets of triplets, living in five rural villages in southern Malawi, from birth to 36 months of age, with periodic sampling of their fecal microbiota (*13*). To define healthy microbiota development in this population, we took the polymerase chain reaction amplicons generated from variable region 4 (V4) of bacterial 16*S* rRNA genes and sequenced them. We used 220 fecal samples collected from 27 twin pairs and two sets of triplets whose serial anthropometric measurements were indicative of consistently healthy growth [WHZ = 0.09 ± 0.93; fecal collection over an age range of 0.6 to 33.5 months; 4.0 ± 1.6 samples (mean ± SD) per individual; tables S1A and S2A provide microbiota donor characteristics and a summary of sequencing data sets]. V4 16*S* rRNA reads with ≥97% nucleotide sequence identity were grouped into operational taxonomic units (97% ID OTUs), and taxonomic assignments were made (*14*, *15*).

We modeled microbiota maturation in these healthy Malawian infants and children by using RF to regress OTUs against chronological age in a subset ("training set") of the healthy twin cohort (Fig. 1A). The application of the training set–based model to the subset excluded from model building ("test set") yielded a positive and significant correlation between host chronological age and predicted microbiota age (coefficient of determination R^2 = 0.80, P < 0.0001) (Fig. 1C and fig. S1). The model was further validated using an additional randomized nutritional intervention trial that took place in the Mangochi district of southern Malawi, in which subjects were studied at 6, 12, and 18 months of age [the

[1]Center for Genome Sciences and Systems Biology and Center for Gut Microbiome and Nutrition Research, Washington University School of Medicine, St. Louis, MO 63108, USA. [2]Sarah W. Stedman Nutrition and Metabolism Center and Duke Molecular Physiology Institute, Duke University Medical Center, Durham, NC 27710, USA. [3]Department of Pediatrics, Washington University School of Medicine, St. Louis, MO 63110, USA. [4]School of Public Health and Family Medicine, College of Medicine, University of Malawi, Chichiri, Blantyre 3, Malawi. [5]Department of Paediatrics and Child Health, College of Medicine, University of Malawi, Chichiri, Blantyre 3, Malawi. [6]Department of Nutrition and Program in International and Community Nutrition, University of California–Davis, Davis, CA 95616, USA. [7]Department for International Health, University of Tampere School of Medicine, Tampere 33014, Finland. [8]Architecture et Fonction des Macromolécules Biologiques, Centre National de la Recherche Scientifique and Aix-Marseille Université, 13288 Marseille Cedex 9, France. [9]Department of Biological Sciences, King Abdulaziz University, Jeddah, Saudi Arabia. [10]A. A. Kharkevich Institute for Information Transmission Problems, Russian Academy of Sciences, Moscow 127994, Russia. [11]Infectious and Inflammatory Disease Center, Sanford Burnham Prebys Medical Discovery Institute, La Jolla, CA 92037, USA. [12]Department of Pharmacology and Cancer Biology and Department of Medicine, Duke University Medical Center, Durham, NC 27710, USA. [13]Department of Pediatrics, Tampere University Hospital, Tampere 33521, Finland.
***Corresponding author. E-mail: jgordon@wustl.edu**

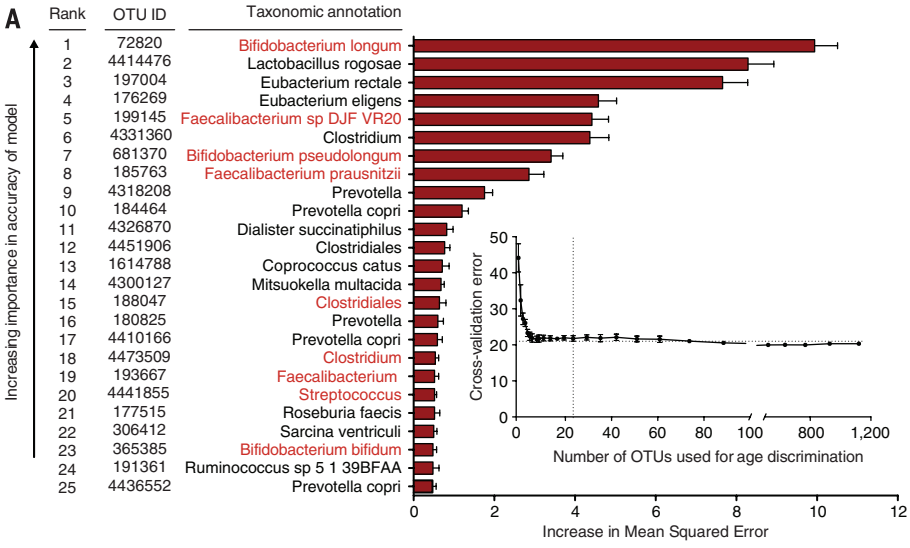
iLiNS-DYAD-M study (*16*)]. We again saw a positive and significant correlation between chronological age and predicted microbiota age (R^2 = 0.71, P < 0.0001). Multiple OTUs from the sparse Malawian model had ≥97% sequence identity to OTUs in the sparse Bangladeshi model (Fig. 1A and table S3B) (*11*).

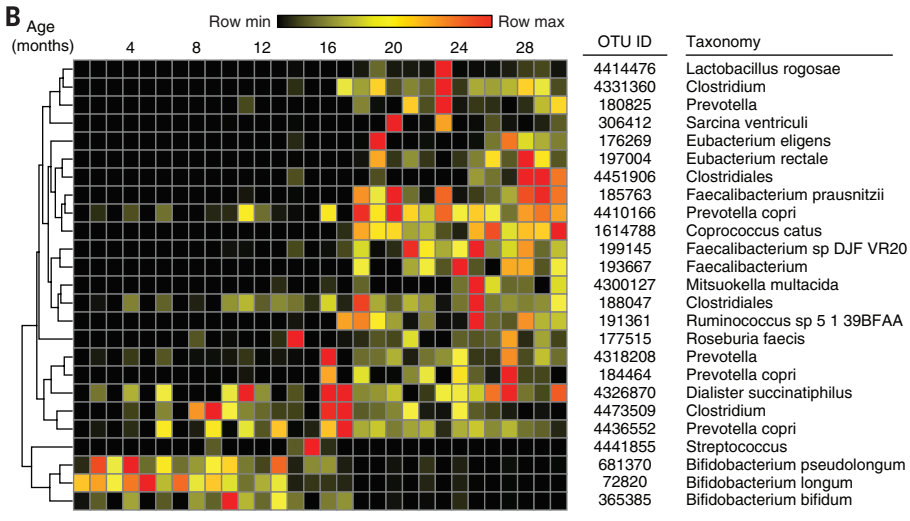
We then used the Malawian RF-derived model to analyze the relationship between microbiota maturity and nutritional status in 259 children enrolled in iLiNS-DYAD-M who had fewer than three reported days of antibiotic consumption from 6 to 18 months of age (table S1B). There was a significant positive correlation between their MAZ scores and their WHZ (Spearman's rank correlation coefficient ρ = 0.1664, P = 0.0073) and WAZ scores (ρ = 0.1715, P = 0.0056) but not their HAZ scores (ρ = 0.1022, P = 0.1) (table S2B). There was a significant correlation between MAZ at 12 months and anthropometry at 18 months [ρ = 0.1406 and P = 0.02 for WHZ; ρ = 0.1373 and P = 0.02 for WAZ (for HAZ, ρ = 0.1184 and P = 0.05)]. These results suggest that MAZ may be useful for predicting future (ponderal) growth. Further studies and analyses are required to discern the effects of several variables, such as the duration of prior antibiotic use, enteropathogen load, number of diarrheal days, geography, and various nutritional interventions, on the relationship of MAZ measurements at various postnatal ages to anthropometry and other metrics of healthy growth (e.g., cognitive testing and immunization responses).

Identification of age-discriminatory taxa that are also growth-discriminatory

To test whether there is a causal relationship between microbiota maturity and growth, we selected fecal samples from 19 Malawian donors representing either healthy or undernourished growth phenotypes for transplantation into 5-week-old, actively growing germ-free C57BL/6J mice. Of the 19 donor samples, nine were from 6-month-old infants, four of which were classified as healthy [WHZ = 1.45 ± 0.57 (mean ± SD), WAZ = 1.75 ± 0.56, and HAZ = 1.27 ± 0.45] and five of which were classified as moderately or severely underweight and stunted (WHZ = −1.27 ± 0.49, WAZ = −3.90 ± 1.82, and HAZ = −4.36 ± 2.07). Ten samples were from 18-month-old children, four with healthy weights (WHZ = 1.44 ± 0.08, WAZ = −0.3 ± 0.57, and HAZ = −2.84 ± 0.99) and six who were moderately or severely underweight and stunted (WHZ = −1.75 ± 0.17, WAZ = −2.88 ± 0.42, and HAZ = −3.28 ± 0.82) (table S4A includes MAZ metrics; all 18-month-old donors were members of twin pairs, in which HAZ scores are typically lower than in singletons, and all 6-month-old donors were singletons). Fecal samples from the 18-month-old children were from the Malawi twin cohort; the 6-month-old microbiota donors were participants in the iLiNS-DYAD-M study who had not yet received a nutritional supplement.

Each microbiota sample was transplanted into a separate group of 5-week-old male germ-free mice (N = 5 animals per sample). Three days





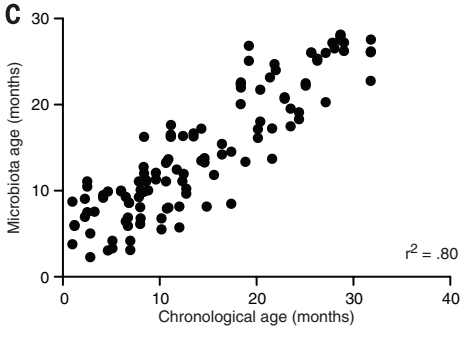


Fig. 1. Sparse RF-derived model of gut microbiota maturation obtained from concordant healthy Malawian twins and triplets. (**A**) A RF regression of fecal bacterial 97% ID OTUs from a training set of healthy Malawian infants and children (N = 31) on chronological age yielded a rank order of age-discriminatory taxa. RF assigns a mean squared error (MSE), or feature importance score, to each OTU; this metric indicates the extent to which each OTU contributes to the accuracy of the model. The 25 most age-discriminatory taxa, ranked by MSE, yielded a sparse model that predicted microbiota age and accounted for ~80% of the observed variance in the healthy cohort (table S3A gives a complete list of OTUs and MSE values). The top 25 most discriminatory OTUs with their taxonomic assignments are shown ranked by feature importance (mean ± SD of the increase in MSE). The inset shows the results of 10-fold cross-validation; as OTUs are added to the model in order of their feature importance rank, the model's error decreases. Taxa highlighted in red indicate OTUs with >97% nucleotide sequence identity with an OTU present in a sparse RF-based model of microbiota maturation in healthy Bangladeshi infants and children (*11*). (**B**) A heat map of changes over time in the relative abundances of the 25 OTUs in fecal microbiota collected from healthy Malawian infants and children constituting the test set (N = 29). OTUs are hierarchically clustered according to pairwise distances determined by Pearson correlation. (**C**) Predictions of chronological age using the sparse 25-OTU model of microbiota age in healthy children constituting the test set. R^2 was calculated by Pearson correlation.

before transplantation, all mice were switched onto a sterile (irradiated) Malawian diet formulated based on the results of a dietary survey of the complementary feeding practices for 9-month-old Malawian children enrolled in the iLiNS-DOSE study (ClinicalTrials.gov identifier: NCT00945698) that took place in the Mangochi district. We selected eight ingredients to produce a cooked diet representative of that consumed by Malawian children (M8; see the supplementary materials); its micro- and macronutrient content does not fulfill the needs of humans or mice (table S5, A and B, gives a list of ingredients and the results of a direct nutritional analysis).

After a single gavage of the donor microbiota, recipient mice were observed for 4 to 5 weeks (Fig. 2A shows the experimental design). Fecal samples were collected for bacterial V4 16*S* rRNA analysis. Growth was monitored by serial measurements of total body weight and body composition [lean mass and fat mass, as defined by quantitative magnetic resonance (qMR)]; after euthanasia, femurs were removed for micro-computed tomographic (micro-CT) characterization of bone morphology.

Mice colonized with microbiota from healthy donors (N = 8 donors) gained significantly more weight and lean body mass than mice colonized with microbiota from undernourished donors (N = 11) [$P < 0.0001$ and $P = 0.0001$, respectively, determined by two-way analysis of variance (ANOVA); table S6, A and B], yet there was no significant difference in food consumption between the groups ($P > 0.05$, determined by Student's t test; table S7). 16*S* rRNA sequencing of fecal samples obtained from recipient mice revealed variable transplantation efficiency. Of the 19 donor samples, eight produced transplantation efficiencies of ≥50%. When we restricted our analysis to the eight donor samples producing ≥50% transplantation efficiency, the discordant growth phenotypes between recipients of healthy versus undernourished microbiota were pronounced (weight gain, $P < 0.0001$; lean mass gain, $P = 0.0005$; two-way ANOVA; Fig. 2, B and C). There was no significant difference in fat mass gain ($P = 0.78$, two-way ANOVA; table S6B) or food consumption between the groups ($P > 0.05$, Student's t test; tables S6, A and B, and S7).

For both the 6-month and 18-month age bins, mice colonized with healthy donor microbiota gained significantly more total body weight and lean mass than those colonized with undernourished donor microbiota (weight, $P = 0.0003$ and $P = 0.0043$ for recipients of the 6- and 18-month-old donor microbiota, respectively; lean mass, $P = 0.03$ and $P = 0.0013$, respectively; two-way ANOVA; table S6, A and B). Recipients of microbiota from healthy or undernourished 6-month-old donors grew more than recipients of microbiota from 18-month-old healthy or undernourished donors ($P < 0.0001$ for healthy and $P < 0.0001$ for undernourished, based on lean mass gain; two-way ANOVA).

Growth over the course of the 5-week experiment in the 19 different groups of recipient mice ranged from 107 to 156% of the starting weight (averaged per group; table S6A). There was no significant relationship between growth phenotypes and bacterial diversity in the fecal microbiota of recipient animals (table S6A). We applied RF to regress the growth phenotypes of recipient gnotobiotic mice against 97% ID OTUs identified in their fecal microbiota. Two models were

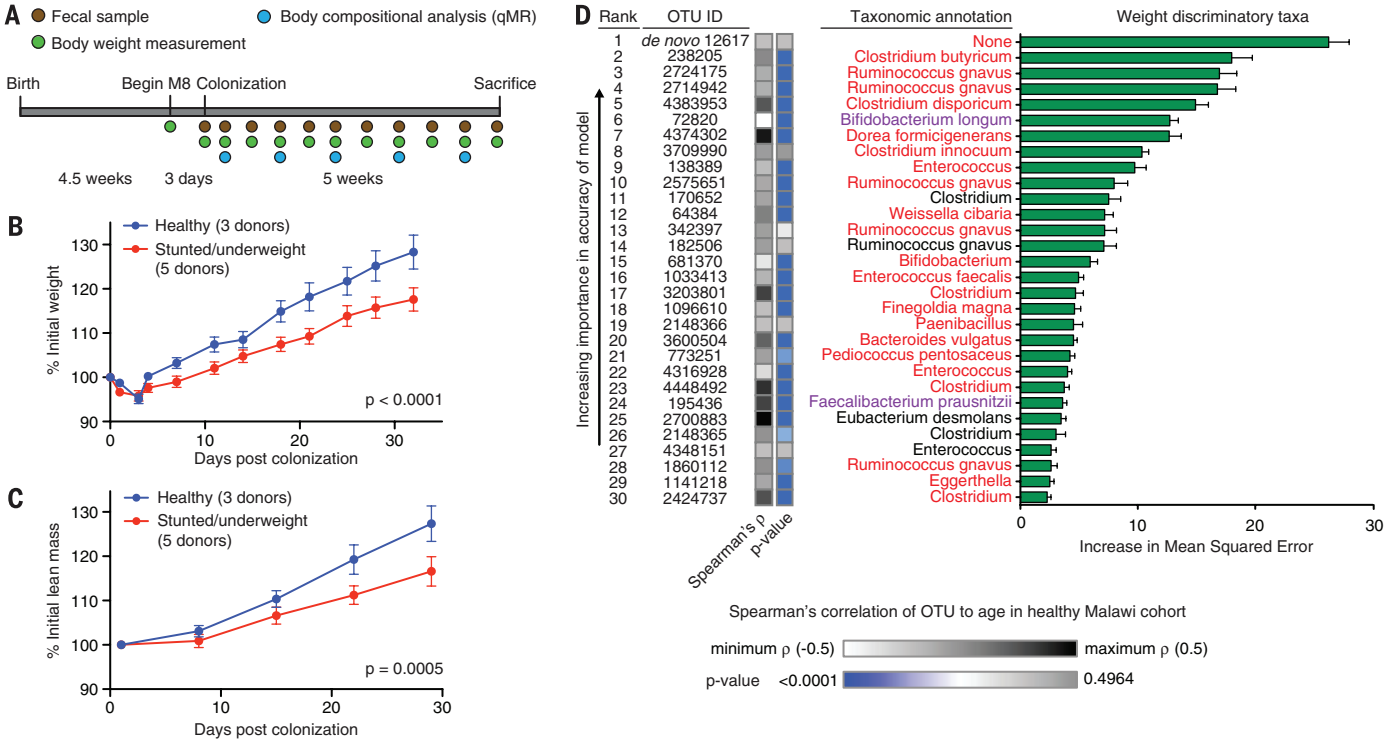


Fig. 2. Transplantation of microbiota from 6- and 18-month-old donors to young germ-free mice provides evidence of a causal relationship between gut microbiota maturity and growth phenotypes. (**A**) Experimental design of the microbiota screen. Mice (4.5 weeks old) were switched to the M8 diet 3 days before gavage with the selected microbiota donor's fecal sample (N = 5 mice per donor). Fecal samples, body weight, and body composition were defined at the indicated time. (**B** and **C**) Gnotobiotic mice colonized with fecal samples from healthy donors gain more total body weight (B) and lean mass (C) than mice colonized with microbiota from undernourished donors (the graphs show means ± SEM; P values shown for the donor status effect are based on two-way ANOVA). All recipient mice harbor microbiota that represent ≥50% of the OTU diversity that is present in the intact uncultured donor's sample. (**D**) The 30 most weight gain–discriminatory OTUs and their taxonomic assignments, ranked by feature importance (the bar graph shows increase in mean MSEs ± SD). The weight gain model explained ~66% of the observed phenotypic variation ($P < 0.0001$, determined by a permutation test with 999 permutations). Taxa in red indicate OTUs that appear within the 30 most discriminatory OTUs for the RF-based models of both weight and lean mass gain. Taxa in purple indicate species that appear in the 25-member sparse RF-derived model of Malawian gut microbiota maturation. Colors to the right of the OTU ID numbers represent Spearman's rank correlation of the same OTU ID with chronological age within the healthy Malawian infant and child cohort (table S9).

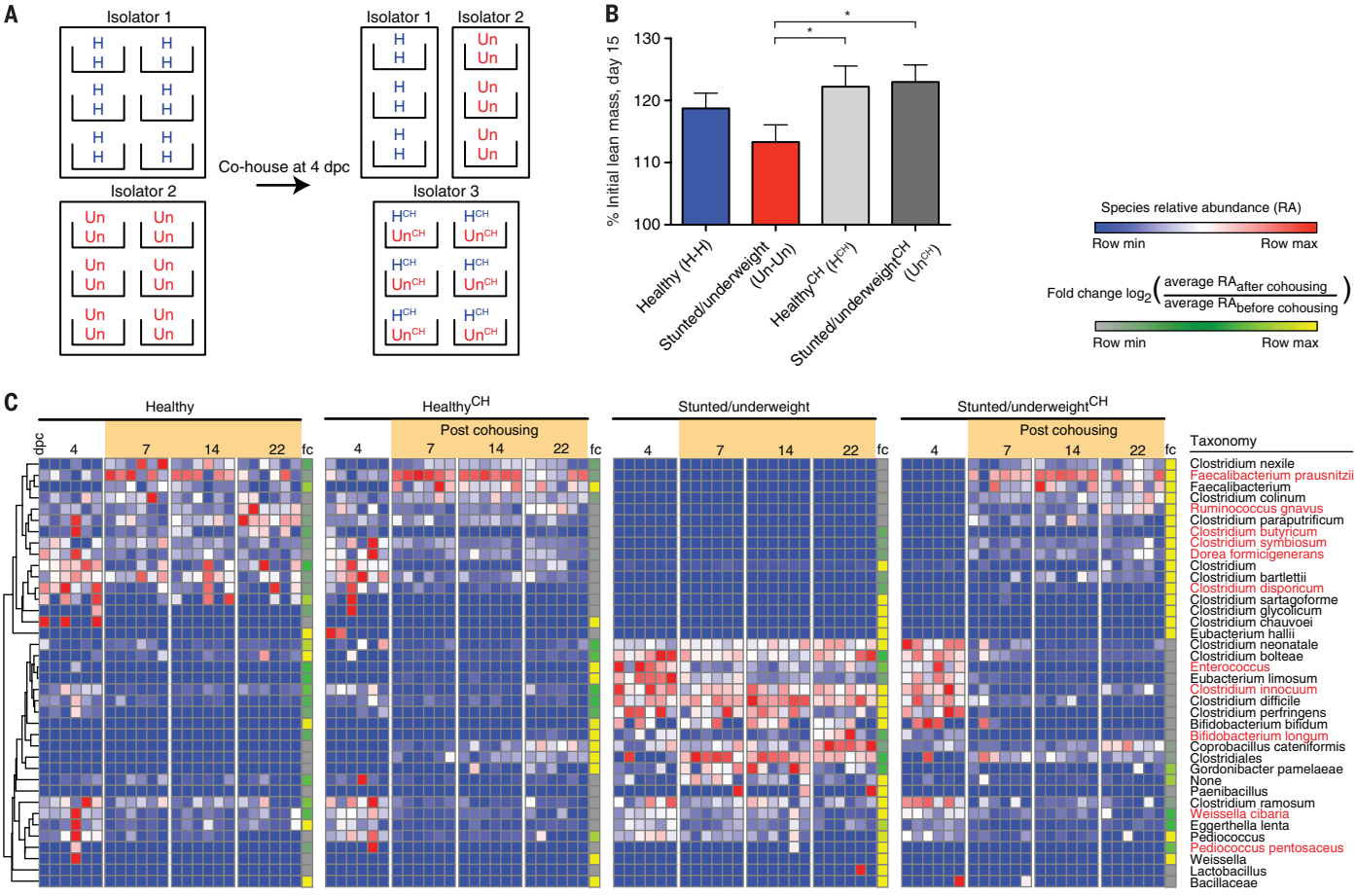


Fig. 3. Cohousing results in the transfer of species from the microbiota of cagemates colonized with the healthy donor's community into the microbiota of cagemates colonized with the severely stunted and underweight donor's community, resulting in the prevention of growth impairments. (**A**) Experimental design for the cohousing experiments. Dually housed 4.5-week-old mice were switched to the M8 diet and colonized 3 days later with intact uncultured microbiota from either the healthy or the stunted and underweight donor. Four days post-colonization (dpc), subsets of the mice were cohoused (H^{CH} and Un^{CH}), while control mice colonized with microbiota from the healthy or stunted and underweight donors remained in their original isolators and were paired with a new cagemate from that isolator (H-H and Un-Un controls). Fecal samples were collected throughout the experiment; growth was assayed by changes in total body weight and body composition (the latter by qMR). Mice were euthanized three weeks after colonization. (**B**) H^{CH} and Un^{CH} mice had significantly higher lean mass gain (indicated by the asterisks) relative to the Un-Un controls 15 days after colonization (Un-Un versus H^{CH}, $P = 0.0447$; Un-Un versus Un^{CH}, $P = 0.0121$; Mann-Whitney test; $N = 6$ cages of cohoused mice and 3 cages of each dually housed control group; two independent experiments). (**C**) Heat map showing the results of the invasion assay. To quantify invasion further, we used the mean and SD of the null distribution of invasion scores (defined as the scores from recipients of the H or Un donor's microbiota that had never been cohoused with each other) to calculate a *z* value (standard score) and a Benjamini-Hochberg adjusted *P* value for the invasion score of each species in H^{CH} and Un^{CH} mice (see the supplementary materials). We defined a taxon as a successful invader if it (i) had a Benjamini-Hochberg adjusted $P \leq 0.05$ and (ii) had a relative abundance of ≤0.05% before cohousing and ≥0.5% in the fecal microbiota at the time of euthanasia. Table S12 provides information about the direction and success of invasion. Each row represents a species-level taxon, and each column represents a mouse at a given day after colonization. The rows of the heat map were hierarchically clustered according to pairwise distances using Pearson correlation. Bars at the right side of each experimental arm represent the fold change (fc) in that species' relative abundance before and after cohousing [fold change is defined as the $\log_2$ of the average relative abundance of the species after cohousing (days 7 through 22), divided by the average relative abundance of the species before cohousing (day 4)]. Species in red represent those identified as one of the top 30 growth-discriminatory taxa by the RF-based models of weight or lean mass gain shown in Fig. 2.

generated, one based on weight gain, the other based on lean mass gain (Fig. 2D and fig. S2, respectively, and table S8, A and B). Two of the growth-discriminatory species represented in the RF-based models of weight and lean mass gain, *Bifidobacterium longum* and *Faecalibacterium prausnitzii*, were highly age-discriminatory, ranking first and eighth, respectively, in the Malawian model shown in Fig. 1A, and fifth and first in the Bangladeshi model (*11*). In the healthy Malawian and Bangladeshi populations used to create these models, *B. longum* is an early colonizer with its highest mean relative abundance at 5 months of age, whereas *F. prausnitzii* becomes more prominent later (highest mean relative abundance achieved at 19 months) (Fig. 1B) (*11*).

The relative abundances of 13 OTUs that were significantly correlated with weight gain and seven OTUs that were significantly correlated with lean mass gain also had significant correlations with chronological age in concordant healthy Malawian twins and triplets, including three OTUs for *F. prausnitzii* ($P < 0.0001$; Fig. 2D and fig. S2; table S9 gives a complete list of OTUs with their Spearman's rank correlation coefficients). Moreover, 15 OTUs that were positively and significantly correlated with weight gain and 11 OTUs that were positively and significantly correlated with lean mass gain were also significantly correlated with chronological age for the 259 infants and

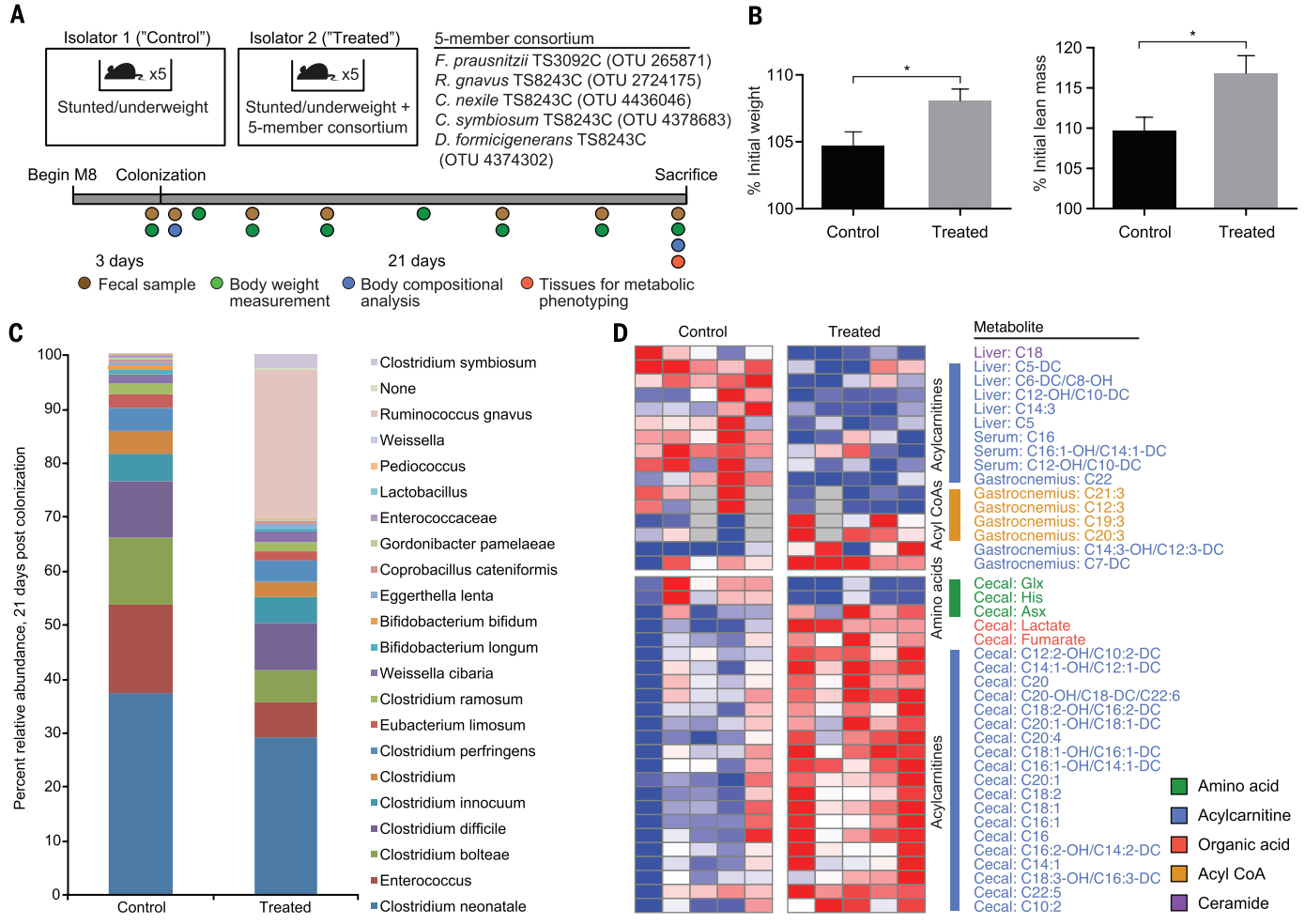


Fig. 4. A consortium of cultured growth-discriminatory OTUs augments the growth of mice colonized with the 6-month-old severely stunted and underweight donor's microbiota. (**A**) Experimental design, including the composition of the five-member consortium of cultured bacterial strains. (**B**) Weight gain and lean mass gain (21 days after gavage) of mice colonized with the donor microbiota, with (treated) or without (control) the cultured consortium. (**C**) Comparison of the fecal microbiota of mice belonging to untreated control and treated experimental groups, showing the establishment of OTUs from the consortium at 21 days after colonization. (**D**) The effects of treatment with the consortium on host metabolism ($P < 0.05$ for all metabolites shown, determined by Student's *t* test). Each row represents a metabolite from a given tissue, and each column represents an individual mouse. Tissues were collected 21 days after colonization.

children from iLiNS-DYAD-M, including the same three OTUs for *F. prausnitzii* that were significantly correlated with age in the cohort of healthy Malawian twins and triplets ($P < 0.0001$ for all correlations; table S9).

The relationship between age- and growth-discriminatory taxa and femoral bone phenotypes

We used micro-CT to assay the morphology of trabecular and cortical regions of femurs obtained from mice harboring microbiota with ≥50% transplantation efficiency. There were strong trends toward higher cortical ratios of bone volume to tissue volume (BV/TV) and volumetric bone mineral density in recipients of gut microbial communities from undernourished donors ($P = 0.05$ and $P = 0.07$, respectively; Mann-Whitney test). Differences between mice harboring microbiota from 6- and 18-month-old donors were evident in trabecular rather than in cortical bone, regardless of donor nutritional status; mice colonized with 6-month-old donor communities had significantly higher bone mineral density, BV/TV, and trabecular connectivity and number, as well as significantly lower trabecular spacing, irrespective of their nutritional status ($P < 0.001$ for all bone metrics; Mann-Whitney test; fig. S3). We extended our RF and Spearman ranked correlation analyses to identify OTUs that discriminate these femoral bone phenotypes (fig. S4 and table S10). Six of the OTUs represented in both of the growth-discriminatory RF-based models, including one assigned to *B. longum*, were also represented among the top 20 most discriminatory features in at least three of the five RF-based models of bone metrics (fig. S4). Although our sample size was small, these results provide additional evidence for microbiota-dependent regulation of bone morphology (*17*), with the effects being influenced by the age and nutritional status of the donor.

Repairing impaired growth phenotypes

We next determined whether age- and growth-discriminatory bacterial species were capable of repairing the growth abnormalities associated with microbiota from stunted and underweight donors. We selected gnotobiotic recipients of microbiota from two 6-month-old donors that transmitted the most discordant growth phenotypes in the initial screen of 19 microbiota (fig. S5A). One was a healthy infant from Mangochi (HAZ = 1.49, WAZ = 1.43, and WHZ = 0.9) with age-appropriate microbiota maturity (microbiota age of 6.7 months); the other was a severely stunted and underweight infant (HAZ = −3.35, WAZ = −3.08, and WHZ = −0.79) from Malindi (located 20 km from Mangochi) with an immature microbiota

(microbiota age of 4.6 months). The configurations of these transplanted microbiota were distinct: Mice colonized with the healthy donor community were dominated by *F. prausnitzii* (33 ± 19% relative abundance), whereas mice colonized with microbiota from the undernourished donor were dominated by *Clostridium neonatale* (37 ± 11% relative abundance) ($N = 5$ mice per donor). Of the 27 species (66 97% ID OTUs) present in recipients of the healthy donor community and the 22 species (33 97% ID OTUs) present in recipients of immature microbiota from the undernourished donor, 13 OTUs representing 13 different species were present in both (see fig. S5B and table S11).

Taking advantage of the coprophagic behavior of mice, we gavaged 5-week-old male germ-free C57BL/6J animals with microbiota from either the healthy or the stunted and underweight donor. Four days later, before phenotypic differences were apparent, we combined (dually housed) mice containing the healthy (H) donor microbiota (H-H controls). We also combined mice that received the undernourished (Un) donor community (Un-Un controls). The experimental group consisted of H and Un mice that were cohoused with one another (H^{CH}-Un^{CH}) (see Fig. 3A). All animals were fed the M8 diet beginning three days before colonization and throughout the course of the 3-week experiment. Animals were weighed twice a week; body composition and fecal samples were assayed once a week.

H^{CH} and Un^{CH} cagemates both gained significantly more lean mass than Un-Un controls did (Un^{CH}, $P = 0.0121$; H^{CH}, $P = 0.0447$; Mann-Whitney test; Fig. 3B) but had no significant difference in lean mass gain relative to H-H controls. We characterized invasion using a previously described approach (*18*) that uses Microbial SourceTracker [(*19*) and supplementary materials]. The fecal microbiota of H-H or Un-Un controls sampled 4 days after gavage (just before cohousing) were treated as source communities. The fecal communities belonging to each H^{CH} and Un^{CH} mouse were then traced to these sources (see the supplementary materials). Results indicated significant invasion by members of the healthy microbiota into the microbiota of Un^{CH} cagemates (Fig. 3C and table S12). Nine OTUs from the H^{CH} cagemates' microbiota were consistent invaders (a total of 12 cohoused mice). Based on the rank order of their invasion scores, the two most successful invaders were *F. prausnitzii*, an age- and growth-discriminatory taxon in the RF models and the most abundant OTU in the fecal microbiota of Un^{CH} mice at the conclusion of the cohousing experiment, and *Ruminococcus gnavus*, a growth-discriminatory taxon. In contrast, only two OTUs from the microbial community of the undernourished donor successfully invaded the gut community of H^{CH} mice; one was assigned as *Enterococcus* and the other as *Eubacterium limosum*, which together represented 2.7 ± 1.7% of the community after cohousing [the *Enterococcus* OTU 4316566 had a significant negative correlation with lean mass gain in the initial screen of 19 donor microbiota ($\rho = -0.14$, $P = 0.0065$)].

Culturing discriminatory taxa and characterizing their effects on growth

Acquisition of H^{CH}-derived bacterial taxa in the microbiota of Un^{CH} cagemates was accompanied by reductions in the relative abundances of 19 OTUs in the latter, six of which were below the limits of detection (<0.01%) by the end of the cohousing experiment. These observations raised two questions. Which invasive OTUs mediated the observed effects on growth phenotypes? Did the reduction in other OTUs improve growth in Un^{CH} cagemates? Therefore, we attempted to culture *F. prausnitzii* and *R. gnavus* from the fecal microbiota of healthy Malawian infants from the iLiNS-DYAD-M cohort. These efforts yielded three additional strains—*Clostridium nexile* (positively correlated with lean mass gain), *Clostridium symbiosum* (lean mass gain–discriminatory), and *Dorea formicigenerans* (weight gain– and lean mass gain–discriminatory)—making for a five-member consortium.

Analogous to the cohousing experiment, male germ-free C57BL/6J mice were placed on the M8 diet at 4.5 weeks of age; 3 days later, five mice were each given a single gavage with the intact microbiota from the Un donor, with or without the five-member consortium (Fig. 4A). The five-member consortium produced a significant increase in body weight and lean mass gain compared with the untreated group ($P = 0.03$ and $P = 0.01$, respectively, at the time of euthanasia 21 days after gavage; Mann-Whitney test) (Fig. 4B). Only two members of the consortium, *R. gnavus* strain TS8243C and *C. symbiosum* strain TS8243C, successfully colonized recipient mice [relative abundances of 27 ± 3% (mean ± SD) and 2.6 ± 0.3%, respectively, in feces obtained at euthanasia] (Fig. 4C; fig. S6 and table S13 show the results of reconstructions of selected metabolic subsystems in *R. gnavus* TS8243C and *C. symbiosum* TS8243C). None of the other members were detected in recipients sampled on days 4, 7, and 14 after gavage. Moreover, the efficiency of incorporation of members of the Un donor's microbiota into recipient mice was indistinguishable between the two treatment arms; i.e., (i) *R. gnavus* and *C. symbiosum* did not result in extirpation of any major constituents of the community [the only species that fell below 0.1% of the community's composition was *Bifidobacterium bifidum*, whose relative abundance was only 0.6 ± 0.1% (mean ± SD) in the control group at the time of euthanasia], and (ii) the proportional representation of OTUs in the Un community was similar between the experimental and control groups (Fig. 4C and table S14). These results provide direct evidence that the cultured strains of *R. gnavus* and *C. symbiosum* ameliorate the impaired growth phenotype transmitted by an undernourished donor's immature microbiota.

The presence of these two organisms also affected metabolic phenotypes (Fig. 4D and table S15). The metabolic features that most discriminated mice with *R. gnavus* and *C. symbiosum* from the untreated group were acylcarnitines (C5 to C22), which were significantly increased in cecal samples and decreased in the liver and serum of fed mice harboring the two taxa ($P < 0.05$, Student's t test). Some of these acylcarnitines also distinguished mice harboring the H versus the Un donor microbiota (fig. S7, A and B). Among metabolites that were decreased in the livers of treated mice were the C5, C5-DC, and C6-DC acylcarnitines, all of which can be derived from branched-chain amino acid catabolism. As proposed for the comparison of mice harboring the H versus the Un donor microbiota (see the supplementary materials), the decrease in these liver metabolites suggests an impact of the presence of two growth-promoting taxa on host metabolic machinery that drives amino acids away from oxidation in favor of protein synthesis and lean mass formation. The mechanisms by which the gut microbiota communicates metabolically with other tissues remain to be defined.

Acknowledging that the generalizability of these effects needs to be directly tested using additional microbiota from other undernourished infants and children, we proceeded to assess whether the growth-discriminatory taxa identified in our preclinical model correlate with growth in Malawian infants and children. To do this, we used the 220 samples from the healthy Malawian twin cohort to generate two RF-based models. One regressed the 30 most weight gain–discriminatory OTUs shown in Fig. 2D against WHZ; the other regressed the 30 most lean mass gain–discriminatory taxa described in fig. S2 against this metric. We then evaluated how well the models were able to predict WHZ scores in the 259 members of the iLiNS-DYAD-M cohort across all time points surveyed (6, 12, and 18 months old for each individual). During this brief 12-month window, there were significant and positive correlations between predicted and observed WHZ using either the weight gain– or lean mass gain–discriminatory taxa (weight gain–discriminatory model, $\rho = 0.12$ and $P < 0.0008$; lean mass gain–discriminatory model, $\rho = 0.11$ and $P < 0.002$; $P < 0.0001$ for both models in a permutation test with 999 permutations). In both models, *B. longum* was the most discriminatory taxon, with *F. prausnitzii* OTUs following as the second or third most discriminatory in the weight gain and lean mass gain models, respectively (fig. S10). The increasing ability to assemble the genomes of bacterial strains from shotgun sequencing of fecal community DNA (*20*) should allow these types of analyses to be further developed in Malawian and other populations that are surveyed longitudinally at frequent intervals over extended periods of time. This approach would also provide direct information about the representation of the strains that we cultured and subsequently characterized in our preclinical model.

Prospectus

The studies reported here indicate that gut microbiota immaturity is not only associated with undernutrition but causally related to it. There

are several interrelated factors that could disrupt normal gut microbiota succession in infants and children. They include, but are not limited to, (i) poor maternal nutritional status, (ii) enteropathogen invasion, (iii) the history of consumption of antibiotics, (iv) disturbances in gut mucosal immune system development (*21*), and/or (v) the history of complementary feeding. Phenotyped birth cohorts provide an opportunity to perform correlation analyses designed to test the significance of the relationship between microbiota maturity (and the representation of specific age- and growth-discriminatory taxa), anthropometry, and the factors listed above, as well as the enigmatic disorder currently described as environmental enteric dysfunction (*22*).

In this study, we showed that microbiota from 6-month-old donors produced greater effects on growth in recently weaned mice than microbiota from 18-month-old donors, although overall, the effects produced by a healthy donor's age-appropriate community were greater than those produced by an undernourished donor's immature microbiota. Though it will be important to extend these analyses to microbiota sampled from additional individuals representing this and other geographic sites and cultural traditions, these findings suggest that in healthy children, microbiota development is optimized to satisfy the different growth needs of the host at different ages. An immature microbiota appears to cause a form of neoteny that is not conducive to healthy growth when nutrients are limiting. How will a host adapt to therapeutic interventions that result in rapid progression to an age-appropriate microbiota? Are there mechanisms (including those involving the mucosal immune system) that feed back to regulate the rate of microbiota development? The answers have implications for designing therapeutic strategies for durable repair and prevention of stunting and neurodevelopmental and/or immunologic abnormalities associated with undernutrition.

So far, ready-to-use complementary foods with and without antibiotics have generally produced only modest effects on growth and the longer-term sequelae of undernutrition (*23*). Certain locally available complementary foods that are provided after the cessation of exclusive breastfeeding may have the ability to promote colonization of growth-discriminatory gut taxa in proportions that are age-appropriate, and these could be tested for their clinical value in systematic trials. In this respect, gnotobiotic mice colonized with microbiota from chronologically age-matched healthy and undernourished donors, and fed diets representative of those consumed by the microbiota donors, should permit highly controlled direct tests of the effects of antibiotics, breast milk components (e.g., bovine mimics of human breast oligosaccharides), and complementary foods on the mechanisms by which growth-promoting bacterial strains influence growth, metabolic, bone, immune, and neurologic phenotypes.

REFERENCES AND NOTES

1. C. G. Victora *et al*., Maternal and child undernutrition: Consequences for adult health and human capital. *Lancet* **371**, 340–357 (2008). doi: 10.1016/S0140-6736(07)61692-4; pmid: 18206223
2. L. Gaayeb *et al*., Effects of malnutrition on children's immunity to bacterial antigens in Northern Senegal. *Am. J. Trop. Med. Hyg.* **90**, 566–573 (2014). doi: 10.4269/ajtmh.12-0657; pmid: 24445198
3. M. Kosek *et al*., Fecal markers of intestinal inflammation and permeability associated with the subsequent acquisition of linear growth deficits in infants. *Am. J. Trop. Med. Hyg.* **88**, 390–396 (2013). doi: 10.4269/ajtmh.2012.12-0549; pmid: 23185075
4. D. P. Waber *et al*., Impaired IQ and academic skills in adults who experienced moderate to severe infantile malnutrition: A 40-year study. *Nutr. Neurosci.* **17**, 58–64 (2014). doi: 10.1179/1476830513Y.0000000061; pmid: 23484464
5. R. E. Black *et al*., Maternal and child undernutrition and overweight in low-income and middle-income countries. *Lancet* **382**, 427–451 (2013). doi: 10.1016/S0140-6736(13)60937-X; pmid: 23746772
6. S. A. Richard, B. J. McCormick, M. A. Miller, L. E. Caulfield, W. Checkley *et al.*, Modeling environmental influences on child growth in the MAL-ED cohort study: Opportunities and challenges. *Clin. Infect. Dis.* **59**, S255–S260 (2014). doi: 10.1093/cid/ciu436; pmid: 25305295
7. G. T. Keusch *et al*., Environmental enteric dysfunction: Pathogenesis, diagnosis, and clinical consequences. *Clin. Infect. Dis.* **59**, S207–S212 (2014). pmid: 25305288
8. K. G. Dewey, The challenge of meeting nutrient needs of infants and young children during the period of complementary feeding: An evolutionary perspective. *J. Nutr.* **143**, 2050–2054 (2013). doi: 10.3945/jn.113.182527; pmid: 24132575
9. M. de Onis *et al*., The WHO Multicentre Growth Reference Study: Planning, study design, and methodology. *Food Nutr. Bull.* **25**, S15–S26 (2004). doi: 10.1177/15648265040251S103; pmid: 15069916
10. M. de Onis, A. W. Onyango, J. Van den Broeck, W. C. Chumlea, R. Martorell, Measurement and standardization protocols for anthropometry used in the construction of a new international growth reference. *Food Nutr. Bull.* **25**, S27–S36 (2004). doi: 10.1177/15648265040251S104; pmid: 15069917
11. S. Subramanian *et al*., Persistent gut microbiota immaturity in malnourished Bangladeshi children. *Nature* **510**, 417–421 (2014). pmid: 24896187
12. L. Breiman, Random forests. *Mach. Learn.* **45**, 5–32 (2001). doi: 10.1023/A:1010933404324
13. M. I. Smith *et al*., Gut microbiomes of Malawian twin pairs discordant for kwashiorkor. *Science* **339**, 548–554 (2013). doi: 10.1126/science.1229000; pmid: 23363771
14. R. C. Edgar, Search and clustering orders of magnitude faster than BLAST. *Bioinformatics* **26**, 2460–2461 (2010). doi: 10.1093/bioinformatics/btq461; pmid: 20709691
15. Q. Wang, G. M. Garrity, J. M. Tiedje, J. R. Cole, Naive Bayesian classifier for rapid assignment of rRNA sequences into the new bacterial taxonomy. *Appl. Environ. Microbiol.* **73**, 5261–5267 (2007). doi: 10.1128/AEM.00062-07; pmid: 17586664
16. P. Ashorn *et al*., The impact of lipid-based nutrient supplement provision to pregnant women on newborn size in rural Malawi: A randomized controlled trial. *Am. J. Clin. Nutr.* **101**, 387–397 (2015). doi: 10.3945/ajcn.114.088617; pmid: 25646337
17. K. Sjögren *et al*., The gut microbiota regulates bone mass in mice. *J. Bone Miner. Res.* **27**, 1357–1367 (2012). doi: 10.1002/jbmr.1588; pmid: 22407806
18. V. K. Ridaura *et al*., Gut microbiota from twins discordant for obesity modulate metabolism in mice. *Science* **341**, 1241214 (2013). doi: 10.1126/science.1241214; pmid: 24009397
19. D. Knights *et al*., Bayesian community-wide culture-independent microbial source tracking. *Nat. Methods* **8**, 761–763 (2011). doi: 10.1038/nmeth.1650; pmid: 21765408
20. B. Cleary *et al*., Detection of low-abundance bacterial strains in metagenomic datasets by eigengenome partitioning. *Nat. Biotechnol.* **33**, 1053–1060 (2015). doi: 10.1038/nbt.3329; pmid: 26368049
21. A. L. Kau *et al*., Functional characterization of IgA-targeted bacterial taxa from undernourished Malawian children that produce diet-dependent enteropathy. *Sci. Transl. Med.* **7**, 276ra24 (2015). doi: 10.1126/scitranslmed.aaa4877; pmid: 25717097
22. R. J. Crane, K. D. J. Jones, J. A. Berkley, Environmental enteric dysfunction: An overview. *Food Nutr. Bull.* **36**, S76–S87 (2015). doi: 10.1177/15648265150361S113; pmid: 25902619
23. K. G. Dewey, S. Adu-Afarwuah, Systematic review of the efficacy and effectiveness of complementary feeding interventions in developing countries. *Matern. Child Nutr.* **4**, 24–85 (2008). doi: 10.1111/j.1740-8709.2007.00124.x; pmid: 18289157

ACKNOWLEDGMENTS

We are indebted to the parents and children from Malawi for their participation in this study. We thank S. Wagoner, D. O'Donnell, M. Karlsson, and J. Serugo for their assistance with gnotobiotic mouse husbandry; D. Leib and M. Silva for their assistance with bone morphology assays; J. Guruge for help with anaerobic microbiology; B. Dankenbring for assistance with maintenance of the biospecimen repository; and M. Meier, S. Deng, and J. Hoisington-Lopez for their contribution to various facets of the DNA sequencing pipeline. This work was supported by the Bill and Melinda Gates Foundation and the NIH (grant DK30292). Additional funding was provided by the Office of Health, Infectious Diseases and Nutrition, Bureau for Global Health, U.S. Agency for International Development under the terms of cooperative agreement no. AID-OAA-A-12-00005, through the Food and Nutrition Technical Assistance III Project managed by FHI 360. Data management and statistical analysis for the iLiNS-DYAD-M clinical study were also funded by the Academy of Finland (grant 252075) and the Medical Research Fund of Tampere University Hospital (grant 9M004). Micro-CT analysis was performed in the Washington University Musculoskeletal Research Center, which is supported by NIH grant P30 AR057235. L.V.B. received stipend support from NIH predoctoral training grants NIH T32 AI007172 and T32 GM007067 and from the Lucille P. Markey Special Emphasis Pathway in Human Pathobiology. D.A.R. and S.A.L. were supported by the Russian Science Foundation (grant 14-14-00289). Collection of the human specimens included in this study was approved by the University of Malawi College of Medicine Research Ethics Committee. Specimens were provided to Washington University in St. Louis under a materials transfer agreement (MTA) between the University of Malawi and Washington University, and their collection and use for this study was approved by the Washington University Human Research Protection Office (Federalwide Assurance no. FWA00002284). 16*S* rRNA sequences, generated from fecal samples in raw format before post-processing and data analysis, and shotgun sequencing data sets, generated from the *R. gnavus* TS8243C and *C. symbiosum* TS8243C genomes, have been deposited in the European Nucleotide Archive under accession number PRJEB9853. J.I.G. is a cofounder of Matatu, a company characterizing the role of diet-by-microbiota interactions in animal health. A.L.O. is an adjunct vice president for research for Buffalo BioLabs. L.V.B., M.R.C., and J.I.G. designed the gnotobiotic mouse studies; L.V.B. and M.R.C. performed the experiments with gnotobiotic animals; I.T. and M.J.M. designed and implemented the clinical monitoring and sampling for the twin study and participated in patient recruitment, sample collection and preservation, and/or clinical evaluations; K.M.M., Y.F., J.M.J., K.G.D., and P.A. designed and oversaw the clinical studies, sample collection and processing, and/or clinical monitoring and evaluations in the iLiNS-DYAD-M study; L.V.B. generated the 16*S* rRNA data; L.V.B., M.R.C., S.V., and O.I. generated the metabolomics data; T.S. and L.V.B. cultured bacterial isolates; B.H., D.A.R., S.A.L., and A.L.O. performed metabolic reconstructions of the *R. gnavus* and *C. symbiosum* genomes; L.V.B., M.R.C., M.J.B., S.S., C.B.N., and J.I.G. analyzed the data; and L.V.B. and J.I.G. wrote the paper.

SUPPLEMENTARY MATERIALS

www.sciencemag.org/content/351/6275/aad3311/suppl/DC1
Materials and Methods
Supplementary Text
Figs. S1 to S10
Tables S1 to S17
References (*24*–*41*)

28 August 2015; accepted 23 December 2015
10.1126/science.aad3311

RESEARCH ARTICLE SUMMARY

PROTEASOME

Rpn1 provides adjacent receptor sites for substrate binding and deubiquitination by the proteasome

Yuan Shi,* Xiang Chen,* Suzanne Elsasser,* Bradley B. Stocks,* Geng Tian, Byung-Hoon Lee, Yanhong Shi, Naixia Zhang, Stefanie A. H. de Poot, Fabian Tuebing, Shuangwu Sun, Jacob Vannoy, Sergey G. Tarasov, John R. Engen,† Daniel Finley,† Kylie J. Walters†

INTRODUCTION: The ubiquitin-proteasome system comprises hundreds of distinct pathways of degradation, which converge at the step of ubiquitin recognition by the proteasome. Five proteasomal ubiquitin receptors have been identified, two that are intrinsic to the proteasome (Rpn10 and Rpn13) and three reversibly associated proteasomal ubiquitin receptors (Rad23, Dsk2, and Ddi1).

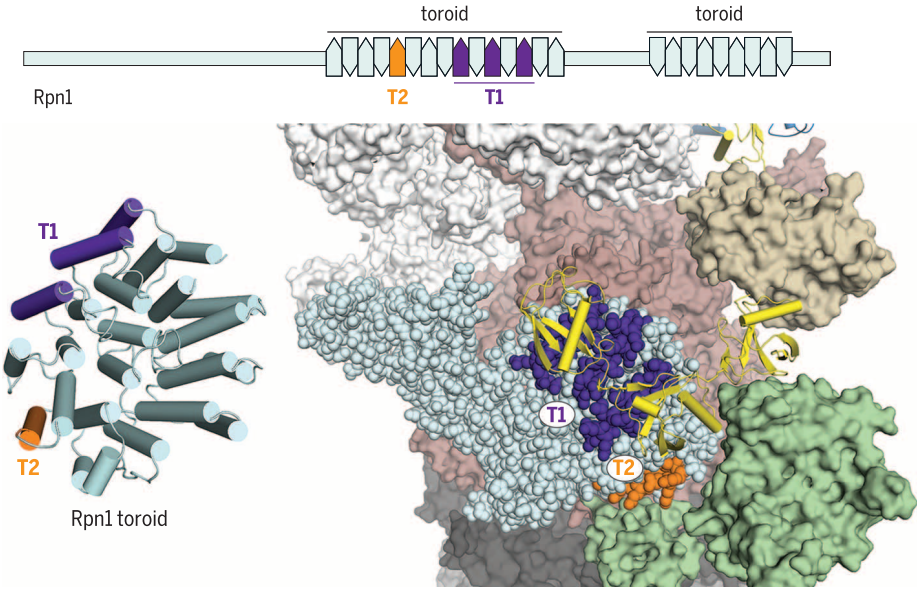
RATIONALE: We found that the five known proteasomal ubiquitin receptors of yeast are collectively nonessential for ubiquitin recognition by the proteasome. We therefore screened for additional ubiquitin receptors in the proteasome and identified subunit Rpn1 as a candidate. We used nuclear magnetic resonance (NMR) spectroscopy to characterize the structure of the binding site within Rpn1, which we term the T1 site. Mutational analysis of this site showed its functional importance within the context of intact proteasomes. T1 binds both ubiquitin and ubiquitin-like (UBL) proteins, in particular the substrate-delivering shuttle factor Rad23. A second site within the Rpn1 toroid, T2, recognizes the UBL domain of deubiquitinating enzyme Ubp6, as determined by hydrogen-deuterium exchange mass spectrometry analysis and validated by amino acid substitution and functional assays. The Rpn1 toroid thus serves a critical scaffolding role within the proteasome, helping to assemble multiple proteasome cofactors, as well as substrates.

RESULTS: Our results indicate that proteasome subunit Rpn1 can recognize both ubiquitin and UBL domains of substrate shuttling factors that themselves bind ubiquitin and function as reversibly associated proteasomal ubiquitin receptors. Recognition is mediated by the T1 site within the Rpn1 toroid, which supports proteasome function in vivo. We found that the capacity of T1 to recognize both ubiquitin and UBL shuttling proteins was shared with Rpn10 and Rpn13. The surprising multiplicity of ubiquitin-recognition domains within the proteasome may promote enhanced, multipoint binding of ubiquitin chains. The structures of the T1 site in its free state and in complex with monoubiquitin or lysine 48 (K48)–linked diubiquitin were solved, which revealed that three neighboring outer helices from the T1 toroid engage two ubiquitins. This ubiquitin-binding domain is structurally distinct from those of Rpn10 and Rpn13, despite their common ligands. Moreover, the Rpn1-binding mode leads to a preference for certain ubiquitin chain types, especially K6- and K48-linked chains, in a distinct configuration that can position substrates close to the entry port of the proteasome. The fate of proteasome-docked ubiquitin conjugates is determined by a competition between substrate degradation and deubiquitination; the latter leads to premature release of substrates. Proximal to the T1 site within the Rpn1 toroid is a second UBL-binding site, T2, that does not assist in ubiquitin chain recognition but, rather, in chain disassembly, by binding to the UBL domain of deubiquitinating enzyme Ubp6. Note that the UBL interactors at T1 and T2 are distinct and assign substrate localization to T1 and substrate deubiquitination to T2.

ON OUR WEB SITE

Read the full article at http://dx.doi.org/10.1126/science.aad9421

CONCLUSION: A ligand-binding hotspot was identified in the Rpn1 toroid, consisting of two adjacent receptor sites, referred to as T1 and T2. The Rpn1 toroid represents a distinct class of binding domains for ubiquitin and UBL proteins. The T1 site functions to recruit substrates directly by binding to ubiquitin itself and indirectly by binding to UBL shuttling factors, a feature shared by Rpn10 and Rpn13 despite a lack of structural similarity among these receptors. The T2 site also binds to a UBL domain protein, in this case deubiquitinating enzyme Ubp6. This study thus defines a two-site recognition domain intrinsic to the proteasome that uses distinct ubiquitin-fold ligands to assemble substrates, substrate shuttling factors, and a deubiquitinating enzyme in close proximity. ■



A ligand-binding hotspot in the proteasome for assembling substrates and cofactors. Schematic (**top**) and model structure (**bottom**, **left**) mapping the UBL-binding Rpn1 T1 (indigo) and T2 (orange) sites. (**Bottom**, **right**) Enlarged region of the proteasome designed to illustrate Rpn1 T1 and T2 sites bound to a ubiquitinated (yellow) substrate (beige) and deubiquitinating enzyme Ubp6 (green), respectively. Aided by PDB 4CR2, 1WGG, 1VJV, and 2B9R.

The list of author affiliations is available in the full article online.
*These authors contributed equally to this research.
†Corresponding author. E-mail: j.engen@neu.edu (J.R.E.); kylie.walters@nih.gov (K.J.W.); daniel_finley@hms.harvard.edu (D.F.)
Cite this article as Y. Shi *et al.*, *Science* 351, aad9421 (2016). DOI: 10.1126/science.aad9421

Downloaded from on February 18, 2016

RESEARCH ARTICLE

PROTEASOME

Rpn1 provides adjacent receptor sites for substrate binding and deubiquitination by the proteasome

Yuan Shi,[1]* Xiang Chen,[2]* Suzanne Elsasser,[1]* Bradley B. Stocks,[3]* Geng Tian,[1] Byung-Hoon Lee,[1] Yanhong Shi,[2,4] Naixia Zhang,[4] Stefanie A. H. de Poot,[1] Fabian Tuebing,[1] Shuangwu Sun,[1] Jacob Vannoy,[2,5] Sergey G. Tarasov,[6] John R. Engen,[3]† Daniel Finley,[1]† Kylie J. Walters[2]†

Hundreds of pathways for degradation converge at ubiquitin recognition by a proteasome. Here, we found that the five known proteasomal ubiquitin receptors in yeast are collectively nonessential for ubiquitin recognition and identified a sixth receptor, Rpn1. A site (T1) in the Rpn1 toroid recognized ubiquitin and ubiquitin-like (UBL) domains of substrate shuttling factors. T1 structures with monoubiquitin or lysine 48 diubiquitin show three neighboring outer helices engaging two ubiquitins. T1 contributes a distinct substrate-binding pathway with preference for lysine 48–linked chains. Proximal to T1 within the Rpn1 toroid is a second UBL-binding site (T2) that assists in ubiquitin chain disassembly, by binding the UBL of deubiquitinating enzyme Ubp6. Thus, a two-site recognition domain intrinsic to the proteasome uses distinct ubiquitin-fold ligands to assemble substrates, shuttling factors, and a deubiquitinating enzyme.

Protein fates are regulated on a global scale by the covalent conjugation of ubiquitin, which can direct target proteins to the proteasome for degradation. Misregulation of the ubiquitin-proteasome system is associated with a broad range of human diseases, such as cancer, developmental disorders, neurodegenerative diseases, immune disorders, and microbial infections. In the vast network of the ubiquitin-proteasome system, the recognition of ubiquitin by the proteasome constitutes a central node. Defects in proteasomal ubiquitin receptors have been implicated in both amyotrophic lateral sclerosis and Alzheimer's disease (*1*, *2*). Although the mechanisms by which the proteasome achieves its substrate specificity are largely unresolved, it is clear that myriad substrates are first committed to degradation through an initial receptor-mediated recognition step.

There are two distinct modes of ubiquitin recognition by a proteasome. The intrinsic recognition pathway uses specific proteasome subunits (Rpn10 and Rpn13) for ubiquitin binding (*3*–*7*), whereas the extrinsic recognition pathway uses shuttling factors (Rad23, Dsk2, and Ddi1 in yeast) to escort ubiquitinated substrates to the proteasome (*8*, *9*). The shuttling factors are known as UBL-UBA proteins, because each binds the proteasome by means of a ubiquitin-like (UBL) domain while binding ubiquitin chains with a ubiquitin-associated domain (UBA). The intrinsic and extrinsic pathways are functionally redundant, at least in part, and cooperate in mediating substrate degradation by the proteasome (*6*, *8*, *9*). These receptors exhibit some substrate specificity but with a mechanistic basis that is poorly understood (*9*–*13*).

Existence of an additional ubiquitin receptor in the proteasome

To investigate ubiquitin binding by the proteasome, we first obtained an *RPN13* allele that abrogates ubiquitin binding while having no discernible effect on proteasome assembly. [Existing alleles of *Rpn13* decrease affinity for ubiquitin to one-eighth that of wild-type (*6*)]. Guided by nuclear magnetic resonance (NMR) data, we introduced two substitutions into the loop segments of the PRU domain, which, when combined with three previously characterized substitutions, completely abolished Rpn13 binding to ubiquitin, as judged by the absence of spectral changes in NMR titration experiments performed at high concentrations of ubiquitin and Rpn13 (fig. S1). The resulting *rpn13 E41K E42K L43A F45A S93D* mutant is referred to as *rpn13-pru* below.

To test whether the five known proteasomal ubiquitin receptors are together required for ubiquitin recognition by the proteasome, we introduced the *rpn13-pru* allele into a strain carrying mutations in the other four receptors, all of which appear to be nulls for ubiquitin recognition. Unexpectedly, this strain, hereafter known as the quintuple mutant, proved to be viable and only moderately defective in growth under standard conditions (Fig. 1A). This strain did display a range of physiological defects, including heat sensitivity, canavanine sensitivity, and high salt sensitivity (Fig. 1A); evidently, its ubiquitin-proteasome system is strongly attenuated. In summary, the viability of the quintuple mutant led us to hypothesize the existence of still unidentified ubiquitin receptors on the proteasome.

Proteasome subunit Dss1/Sem1 was recently proposed to be a novel ubiquitin receptor for this complex (*14*). In this study, recombinant Sem1 was shown to bind ubiquitin, but whether proteasomes lacking Sem1 are defective in ubiquitin recognition was not examined. To evaluate Sem1, we tested the ubiquitin-binding activity of *sem1*Δ proteasomes. We could not resolve any defect, even in genetic backgrounds in which other ubiquitin receptors had been eliminated (fig. S2), and thus, further studies may be required to validate Sem1 as a proteasomal ubiquitin receptor. Because the ubiquitin-binding surface of Sem1 overlaps with its proteasome-binding surface (*14*), simultaneous binding of the proteasome and ubiquitin by Sem1 might not be possible. Although mutations in the ubiquitin-binding region of Sem1 lead to hypomorphic proteasome phenotypes, these mutations are also associated with proteasome assembly defects.

To test further for additional proteasomal ubiquitin receptors, we characterized proteasomes in which all five known ubiquitin receptors were either functionally inactivated by making amino acid substitutions in their ubiquitin-binding sites or removed during purification by salt wash. When such proteasomes were electrophoresed on a native gel in the presence of ubiquitin conjugates, their migration—visualized by an in-gel activity assay—was retarded, which indicated productive binding (Fig. 1B). This binding activity was further localized to the nine-subunit base subcomplex by using native gel-shift assays (fig. S3). With the number of candidate receptors narrowed down in this way, we tested proteins individually for ubiquitin binding. Rpn1, in particular, proved to form a stable complex (Fig. 1C) with a model proteasome substrate, ubiquitinated PY-Sic1 (*15*). Rpn1 binding to this substrate was specific to the ubiquitin moiety, because nonubiquitinated Sic1, an internal control, failed to bind (Fig. 1C). Rpn1, the largest subunit of the base, has been previously suggested to serve in the recognition of UBL proteins, such as Rad23, by the proteasome (*16*–*18*).

Rpn1 is paralogous to Rpn2, the structure of which has been solved by x-ray crystallography (*19*). Both proteins have a centrally located domain composed of 11 repeats of 30 to 40 residues each

[1]Department of Cell Biology, Harvard Medical School, 240 Longwood Avenue, Boston, MA 02115, USA. [2]Protein Processing Section, Structural Biophysics Laboratory, Center for Cancer Research, National Cancer Institute, Frederick, MD 21702, USA. [3]Department of Chemistry and Chemical Biology, Northeastern University, Boston, MA 02115, USA. [4]Department of Analytical Chemistry, Shanghai Institute of Materia Medica, Chinese Academy of Sciences, Shanghai 201203, P. R. China. [5]Linganore High School, Frederick, MD 21701, USA. [6]Biophysics Resource, Structural Biophysics Laboratory, Center for Cancer Research, National Cancer Institute, Frederick, MD 21702, USA.
*These authors contributed equally to this research.
†Corresponding authors. E-mail: j.engen@neu.edu (J.R.E.); kylie.walters@nih.gov (K.J.W.); daniel_finley@hms.harvard.edu (D.F.)

that form helix-turn-helix hairpins, known as PC repeats (*20*). Collectively, these repeats form a closed toroid (*19*). On the basis of these data, we generated a series of deletions in Rpn1. Using ubiquitinated PY-Sic1 as a ligand, the binding activity of Rpn1 was mapped to residues serine 376 (S376) to alanine 635 (A635) (fig. S4). This fragment was trimmed further to obtain a recombinant fragment suitable for NMR, residues glycine 412 (G412) to threonine 625 (T625) (fig. S5A). NMR titration experiments in which unlabeled ubiquitin was added to ^{15}N-labeled Rpn1 (412–625) showed clear binding (Fig. 1D). The signals in the NMR spectrum were assigned to Rpn1 amino acids (fig. S5, A and B), as described below and in the supplementary materials (SM). In an Rpn1 model structure, those residues that contact ubiquitin according to the titration experiment (fig. S6) map to three outer helices of the toroid (Fig. 1E). We thus name this ubiquitin-binding region T1 (toroid 1). Plots of the spectral changes observed for each amino acid with ubiquitin addition revealed two distinct binding affinities, with amino acids from helix 26 (H26) presenting dissociation constant (K_d) values of 350 ± 70 μM and those from H28 and H30 with values of 120 ± 10 μM (fig. S7). Thus, two weak binding sites for monoubiquitin are suggested on T1.

When unlabeled Rpn1 (412–625) was added to ^{15}N- or ^{13}C-labeled ubiquitin, significant shifting was observed for amino acids located in the ubiquitin β-strand surface (Fig. 1F and fig. S8), which is recognized as well by Rpn10 and Rpn13 (*7*, *21*). Included in this surface are specific residues of leucine, arginine, isoleucine, histidine, and valine L8, R42, I44, H68, V70, and R74, which shift significantly when Rpn1 is added.

The Rpn1 T1 site binds two ubiquitins with three outer toroid helices

Because only a model structure was available for Rpn1, we used NMR to solve the structure of the T1 site. The N- and C-terminal portions of Rpn1 (412–625) were poorly behaved, with Y608 to T625 absent from the recorded spectra and G412 to K484 disordered (fig. S5, B and C). In addition, we observed a concentration-dependent dimerization, as determined by dynamic light scattering (fig. S9A), which NMR data suggested to be mediated by the inner helices (H27, H29, and H31) of the toroid (Fig. 1E and fig. S9, B and C). These effects are no doubt the result of truncation artifacts, although larger deletions only destabilized the protein fold further (fig. S10). Nonetheless, by using standard NMR techniques, as well as stereoselective methyl labeling and four-dimensional (4D) nuclear Overhauser effect spectroscopy (NOESY) experiments to record interactions between methyl groups (fig. S11), we were able to solve the structure of the Rpn1 T1 site. This region folds into 3.5 PC repeats (Materials and Methods and table S1), with H25 forming an incomplete hairpin structure (Fig. 2A). H26 to H31, which forms three complete hairpins, converge to a backbone root mean square deviation (RMSD) of 0.8 Å. The 4D NOESY spectrum (fig. S11) and an evaluation based on chemical shift values (fig. S5C) revealed H25 to be helical, but loss of its hairpin partner (presumed to range from A470 to T479) apparently destabilized it and resulted in this helix adopting a dynamic orientation relative to H26 to H31.

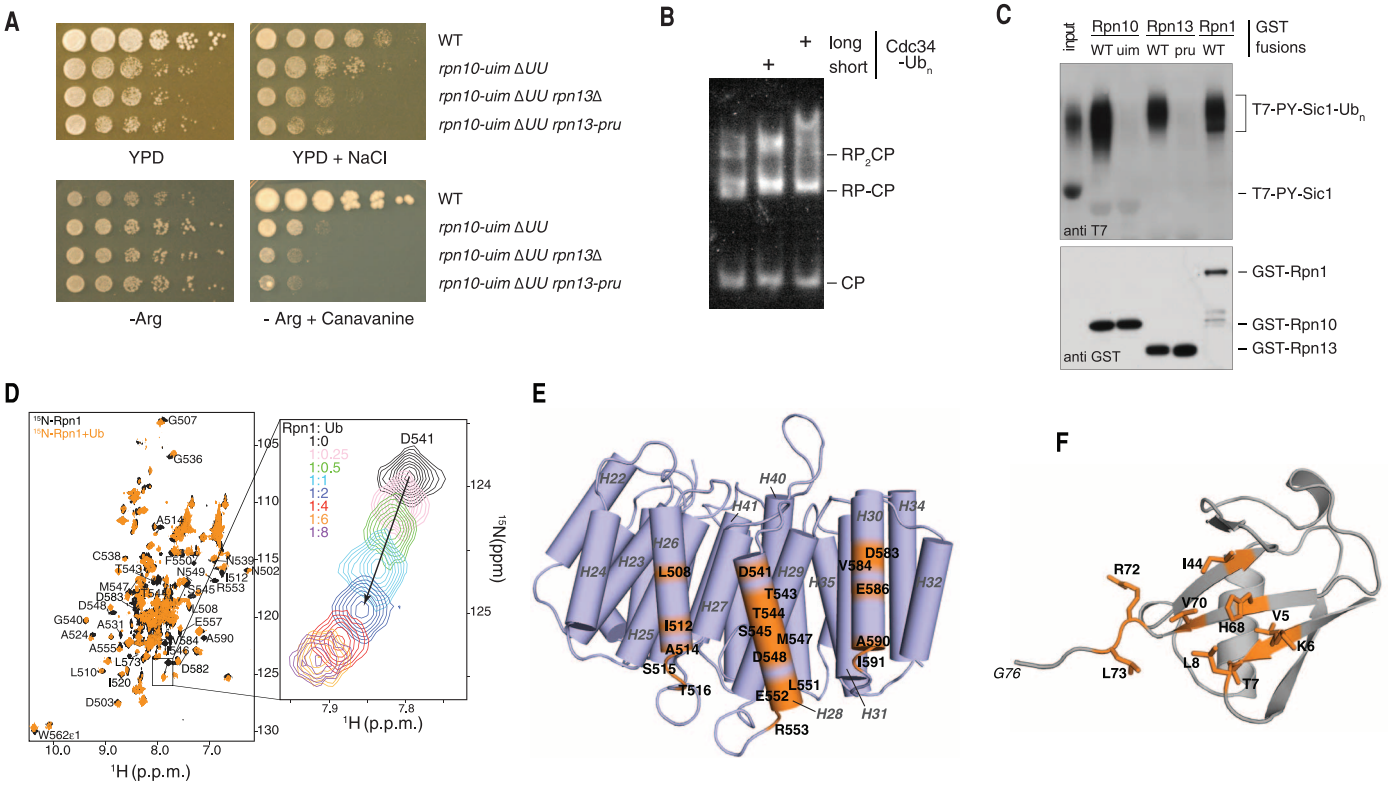


Fig. 1. Evidence for an additional ubiquitin receptor in yeast. (**A**) Yeast strains with the indicated genotypes were serially diluted, transferred to agar plates, and incubated at 30°C. Media were yeast extract peptone dextrose (YPD), YPD with 1 M NaCl (top row), synthetic medium lacking arginine (Arg$^-$), or Arg$^-$ with 6 μm/ml canavanine (bottom row). Δ*UU* designates the *rad23*Δ *dsk2*Δ *ddi1*Δ background. WT, wild type. (**B**) Proteasome association with ubiquitin conjugates evaluated by a mobility-shift assay. RP complexes were purified from an *rpn10-uim rpn13-pru* strain and incubated with core particle. Reconstituted proteasomes were incubated with autoubiquitinated Cdc34, resolved via native PAGE, and visualized with a fluorogenic activity stain. (**C**) Known and candidate ubiquitin receptor proteins were expressed in bacteria as GST fusion proteins and immobilized on glutathione resin. Ubiquitinated T7-PY-Sic1 conjugates were used as ligand. Resin-bound proteins were resolved by SDS-PAGE, blotted, and probed with antibodies as indicated. Direct loading of ubiquitinated T7-PY-Sic1 is also included (input). (**D**) ^{1}H, ^{15}N heteronuclear single-quantum coherence (HSQC) spectra of ^{15}N Rpn1$_{412\text{-}625}$ (black) and with equimolar ubiquitin (orange). A titration series is displayed to the right for D541 with increasing ubiquitin, as indicated. (**E**) Model ribbon diagram of the Rpn1 toroidal domain [PDB 4CR2 (*47*)] showing residues that shift after ubiquitin addition (D) in orange. (**F**) Ubiquitin amino acids with amide signals that shift by 1 SD above average after Rpn1 T1 addition, as shown in fig S8, B and D, are labeled and highlighted in orange on a ribbon diagram [PDB 2K39 (*48*)].

We next solved the structure of the Rpn1 T1 site in complex with ubiquitin, as described in Materials and Methods and (22). Spectra collected on this protein complex showed higher signal-to-noise ratio (fig. S12) compared with those recorded on free Rpn1 and indicated that the structure of the Rpn1 T1 site does not change upon binding to ubiquitin (fig. S13, A, B, and D). Moreover, spectra from NOESY recorded on the complex were used to generate new intramolecular constraints for Rpn1 to be used in the calculation of the Rpn1 T1:ubiquitin complex (table S2). Half-filtered NOESY experiments, specialized to record interactions between Rpn1 and ubiquitin, revealed many contacts involving ubiquitin L8, T9, I44, V70, L71, and L73 (fig. S14, A and B), as expected from the titration experiment (Fig. 1F). Intermolecular contacts involving these amino acids validated the presence of two binding sites. For example, L8 contacted both L508 and T544 (fig. S14A), which are separated by a 16-Å distance across the toroid (fig. S14C). Ultimately, 106 unambiguous intermolecular distance constraints were identified between Rpn1 and two ubiquitin molecules (table S2). Twenty-four intermolecular paramagnetic relaxation enhancement (PRE)–derived constraints were also collected with a spin label substituted for ubiquitin G75 (fig. S15A). The resulting structures converged to a backbone RMSD of 0.93 Å (fig. S16) with one ubiquitin at a surface formed by H28 and H30 (H28/H30) (Fig. 2B, orange) and the other at H26 (Fig. 2B, yellow). Individually, the H28/H30: ubiquitin region converged better than the H26: ubiquitin region, with backbone RMSD values of 0.58 and 0.74, respectively (table S2), owing to fewer detected interactions for the lower-affinity H26 site (figs. S14, A and B, and S7). Both sites use hydrophobic amino acids to engage ubiquitin L8-I44-V70 (Fig. 2C).

One of seven lysines or the N-terminal methionine in ubiquitin is used to generate ubiquitin chains, which differ in their signaling properties (23). To evaluate Rpn1 ubiquitin chain preference experimentally, resin-bound His-scRpn1 was incubated separately with diubiquitin of each linkage type, washed, and complex formation assayed by immunoblotting with ubiquitin-specific antibody. In this experiment, Rpn1 T1 demonstrated the greatest affinity for K6 and K48 diubiquitin (Fig. 2D), the latter of which is an established linkage type for signaling substrate proteolysis by the proteasome (23). Consistent with this result, G76 from ubiquitin at H28/H30 is spatially close to K48 and K6 of the ubiquitin at H26 (Fig. 2B and fig. S14D). An NMR titration experiment revealed Rpn1 to prefer K48-linked ubiquitin chains to monoubiquitin with 11- and 2.7-fold increased affinity at H28/H30 and H26, respectively (Fig. 2E), as supported by isothermal titration calorimetry (ITC, Fig. 2F). The 11 μM affinity of Rpn1 for K48 diubiquitin is similar to the 13 μM affinity reported for scRpn10 binding to K48 diubiquitin (24).

Human Rpn1 (404–617) is 43.8% identical to scRpn1 (412–625) (fig. S17). Glutathione *S*-transferase (GST) fused with hRpn1(GST-hRpn1 (404–617) or GST (as a negative control) was bound to glutathione *S*-Sepharose resin and incubated with diubiquitin of each linkage type. After removal of unbound proteins by washing, binding between hRpn1 T1 and ubiquitin was assessed by immunoblotting. This experiment confirmed that human Rpn1 also harbors the ubiquitin-binding T1 site, which prefers K6 and K48 linkages (Fig. 2G).

The T1 plays a dual role in binding ubiquitin chains and shuttle factor Rad23

Rpn1 H28 contacts both ubiquitins forming electrostatic interactions with D541, D548, and E552 (Fig. 2C). We replaced these residues in the Rpn1 T1 site to generate a *D541A D548R E552R* triple mutant. The structural integrity of this ARR mutant was maintained, as indicated by two-dimensional (2D) NMR analysis (fig. S18). These substitutions eliminated ubiquitin interaction at fivefold molar excess (Fig. 3A), as well as Rpn1 T1 binding to K6 and K48 diubiquitin in GST pull down (Fig. 3B) and ITC (fig. S19) experiments. Using the *D541A D548R E552R* mutant (hereafter *rpn1-ARR*), we tested in vitro ubiquitin binding activity in the context of full-length Rpn1. The Rpn1-ARR protein showed substantially decreased binding activity to ubiquitinated PY-Sic1 (Fig. 3C).

We also tested the binding of Rad23 to the Rpn1-ARR protein. Rpn1-ARR proved to be almost completely defective in Rad23 binding as well (Fig. 3D). This binding was mediated by the UBL domain of Rad23, in agreement with previous studies of the Rad23-Rpn1 interaction (16, 18). Thus, the Rpn1-ARR mutation appears to define a binding site for both ubiquitin and UBL-UBA proteins. To test this model further, we added unlabeled Rad23 UBL domain to ^{15}N-labeled Rpn1 T1 and used 2D NMR to visualize the affected amino acids. This experiment validated the positioning of H28 at the UBL contact surface (Fig. 3E and fig. S20). ITC demonstrated that Rpn1 (412–625) binds Rad23 UBL with an affinity of 64 ± 25 nM (Fig. 3F), and binding was not detectable with the triple mutant (fig. S21). Thus, H28 is a hotspot within the Rpn1 T1 site for directly and indirectly receiving ubiquitinated substrates.

Phenotypic effects of the *rpn1-ARR* mutation

To assess the ubiquitin-binding activity of Rpn1 in vivo, we integrated the *ARR* mutation into the genomic *RPN1* locus. Rpn1-ARR proteasomes were found to resemble those of wild type in their assembly and stability, based on several assays: Proteasomes were purified from *rpn1-ARR* cells without apparent difference in composition or yield (fig. S22A); the amount of Rpn1-ARR protein was comparable to that of wild type (fig. S22); the relative amounts among different subcomplexes of the proteasome were unaffected by the *rpn1-ARR* mutation (fig. S22C); the SDS–polyacrylamide gel electrophoresis (SDS-PAGE) and native gel profiles of wild-type and Rpn1-ARR proteasomes were indistinguishable (fig. S22, A to C); no mutant-specific fragmentation of the protein was observed for total yeast cell extracts probed with an Rpn1-specific antibody (fig. S22D).

To assess the affinity of the proteasome for ubiquitin conjugates and UBL proteins in a defined biochemical system, we used proteasomes reconstituted from their two major subassemblies, the 19-subunit regulatory particle (RP), which contains Rpn1, and the 28-subunit proteolytic core particle (CP). The RP was purified from strains bearing *RPN1-WT* or *rpn1-ARR* alleles in the *rpn13-pru rpn10-uim* background (fig. S23A) and was reconstituted into holoenzyme by adding back purified wild-type CP. Reconstituted proteasomes have a strong ubiquitin-binding activity that is lost in the *rpn1-ARR* mutant (Fig. 4A). This activity cannot be attributed to contaminating UBL-UBA proteins, because the molar ratio of Rad23 to RP is very low in these preparations (between 1:340 to 1:680) (fig. S23, B and C). Moreover, the dependence of ubiquitin binding on Rpn1 was also seen using RPs purified from the *ubl-uba*Δ background (fig. S23D). These results show that the Rpn1 T1 site can function as a ubiquitin receptor on the proteasome and that this ubiquitin-binding surface in whole proteasomes is the same as that characterized by NMR.

To test whether conjugate binding to the T1 site could support protein degradation, we used an established in vitro degradation assay based on ubiquitinated cyclin B1 (25–27); all proteasomes tested were from the *rpn13-pru rpn10-uim ubl-uba*Δ background. The *rpn1-ARR* mutation led to stabilization of cyclin B1 in this assay (Fig. 4B). Stabilization was incomplete, however, which pointed to the possible existence of a fourth intrinsic ubiquitin receptor in the proteasome. Similar results were obtained using ubiquitinated PY-Sic1 (fig. S24).

We next examined the *rpn1-ARR* phenotype for signs of proteasome dysfunction in vivo. Proteasome function in yeast is typically assayed in the presence of the arginine analog canavanine, whose presence in proteins induces misfolding and consequent proteasome-mediated degradation. *rpn1-ARR* exhibited a canavanine-sensitive phenotype when in the presence of the *rpn10-uim* allele (Fig. 4C). Its synthetic interaction with *rpn10-uim* was similar to that of *rpn13-pru*. In these strains, all genes encoding UBL-UBA proteins had been deleted, so that proteasome output should be driven only by direct ubiquitin recognition by intrinsic ubiquitin receptors. Thus, the canavanine-sensitive phenotype of the *rpn1-ARR* allele suggests that Rpn1 can support ubiquitin-dependent substrate recognition in cells. Its ability to do so is at some level redundant with other proteasomal ubiquitin receptors, a common characteristic of these proteins.

As discussed above, the isolated toroid domain of Rpn1 can bind both ubiquitin and the UBL protein Rad23. To assess which of the intrinsic proteasomal ubiquitin receptors can also bind UBL proteins within the context of intact proteasomes, we purified proteasomes from yeast strains that express mutant forms of two of the

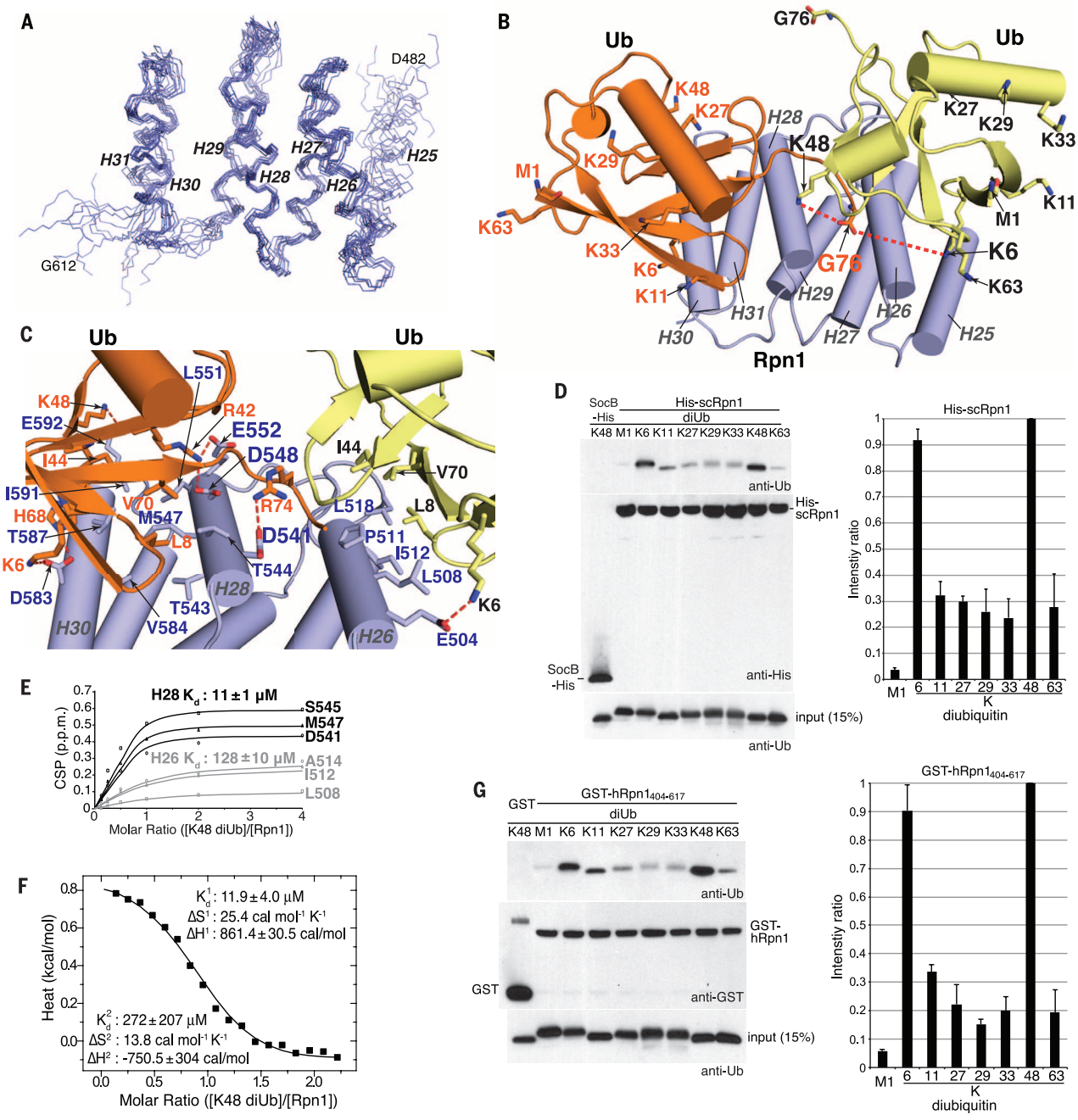


Fig. 2. The Rpn1 T1 site engages two ubiquitin molecules in a mode suited for K48-linked chains. (**A**) Backbone heavy atoms for the 10 lowest energy structures of the Rpn1 T1 site with H26 to H31 superimposed. The N- and C-terminal residues and the individual helices are labeled. (**B**) Ribbon diagram of the lowest energy structure of the Rpn1 T1 site (blue) bound to two monoubiquitin molecules (orange and yellow). Heavy atoms for G76, the M1 backbone, and lysine side chains are displayed with their oxygen and nitrogen atoms in red and blue respectively. Displayed side chains for the ubiquitin at H28/H30 are labeled in orange, whereas those from the ubiquitin centered at H26 are labeled in black. Dashed red lines are drawn between G76 from the ubiquitin at H28/H30 and the closest lysine side chains (K6 and K48) from the ubiquitin at H26; the distance between these two pairs of amino acids is <10 Å and the flexibility of the lysine side chain and C-terminal tail of monoubiquitin allows this distance to be readily shortened. (**C**) Zoomed-in view of (B) highlighting the Rpn1:ubiquitin contact surface with key amino acids displayed and labeled. Electrostatic interactions are indicated with red dashed lines. (**D**) Pull-down assay with His-scRpn1 full length protein and M1-, K6-, K11-, K27-, K29-, K33-, K48-, and K63-diubiquitin, as indicated (top and middle panels, left). Immunoblotting was done with antibody against ubiquitin (anti-ubiquitin) (top, left) or antibody against polyhistidine (anti-His) (middle, left). Intrinsically disordered protein SocB-His (*49*) was used as a negative control with K48 diubiquitin, as indicated. Direct loading for 15% of the diubiquitin input for each chain type with immunoblotting by ubiquitin-specific antibody is included (bottom, left). The pull-down assay was repeated four times, and the diubiquitin signal intensities were separately normalized to the strongest signal by using ImageJ. The average value and standard deviation are plotted (right). (**E**) Shifting for indicated Rpn1 T1 site residues plotted with increasing K48 diubiquitin and fitting to the listed K_d values. CSP, chemical shift perturbation. (**F**) ITC analysis of $Rpn1_{412\text{-}625}$ binding to K48 diubiquitin. K48 diubiquitin (1.91 mM) was injected into a calorimeter cell containing 0.18 mM $Rpn1_{412\text{-}625}$, and the data were fit to a two-site sequential binding mode to yield the indicated thermodynamic values. (**G**) As in (D) but with GST-$hRpn1_{404\text{-}617}$ or GST (as a control). In this case, quantification on the right was done with two independent pull-down assays.

three intrinsic receptors, which left only a single receptor functional. As a control, one strain carried mutant forms of all three receptors. Using a gel-shift assay, we found that all three receptors could bind Rad23 (Fig. 4D). Therefore, the dual ubiquitin-UBL–binding mode seen for Rpn1 is a general feature of proteasomal ubiquitin receptors. These data were confirmed by using endogenous material; copurification of Rad23 with *rpn10-uim rpn13-pru* proteasomes was reduced by the *rpn1-ARR* mutation (Fig. 4E). This effect is not due to a reduced level of Rad23 in the mutant strain (fig. S25). We also found, using recombinant material, that the T1 site was a Dsk2-binding site (fig. S26).

Notably, control proteasomes lacking ubiquitin- and/or UBL-binding sites in all three receptors showed no detectable interaction with Rad23 (Fig. 4D), which suggested that all major proteasomal receptors for this UBL-UBA protein have now been identified. The contribution of Rpn10 to Rad23 binding was unexpected, because several previous studies had found that Rpn10 did not appear to contribute to UBL protein recognition by intact proteasomes (*16*, *28*, *29*). The difficulty in resolving this binding interaction in the past was likely the result of high background binding due to Rpn1 and Rpn13. One possible caveat to these data is that some fraction of copurified Rad23 may be indirectly pulled down by ubiquitin conjugates by the ubiquitin-binding UBA domains that are present in Rad23. This is addressed, however, by the reconstitution experiments of Fig. 4D. In summary, our results reveal a deep interconnectivity between the intrinsic and extrinsic ubiquitin receptors of the proteasome, where each intrinsic receptor can dock ubiquitin conjugates either by direct ubiquitin recognition or indirectly by an extrinsic receptor.

In phenotypic studies, we found that the T1 site of Rpn1 may promote protein degradation, as well as DNA repair, through UBL binding. In particular, the proteasome substrate Gic2, in its tandem affinity purification (TAP)–tagged form (*30*), is strongly stabilized by the T1 site mutation, and this effect depends on the expression of UBL-UBA proteins (Fig. 4F). Similar effects were observed for Gcn4 (fig. S27). Mutation of the T1 site also leads to a phenotype of sensitivity to 4-nitroquinoline 1-oxide (4-NQO), which suggests a defect in DNA repair (Fig. 4G). No difference was seen between mutant and wild-type forms of T1 in the UBL-UBA null genetic background, consistent with mediation of the 4-NQO–sensitive phenotype by an interaction between the proteasome and Rad23, a known DNA repair factor (*31*). In summary, phenotypic data suggest that the T1 site functions by the docking of ubiquitin conjugates at the proteasome but can do so both directly and through docking of ubiquitin receptors.

Structure of Rpn1 T1:K48 diubiquitin reveals a pathway at the proteasome for ubiquitin chains

Because of the importance of K48 ubiquitin chains in targeting substrates for proteolysis, we characterized Rpn1 binding to this chain type more extensively. As observed with monoubiquitin (fig. S13, A and B), binding to K48 diubiquitin did not change the Rpn1 T1 fold, as demonstrated by contacts between methyl groups (fig. S13, A and C). NMR experiments designed to record intermolecular contacts between Rpn1 and each ubiquitin of the K48 dimer revealed the presence of two binding modes. In particular, each ubiquitin moiety can bind to either the H28/H30 or the H26 binding surface (fig. S28). We thus calculated two sets of Rpn1 T1:K48 diubiquitin structures (Materials and Methods and table S2). In addition to nuclear Overhauser effect (NOE)–derived distance constraints, we obtained intermolecular distances between the Rpn1 T1 site and each ubiquitin of the K48 dimer

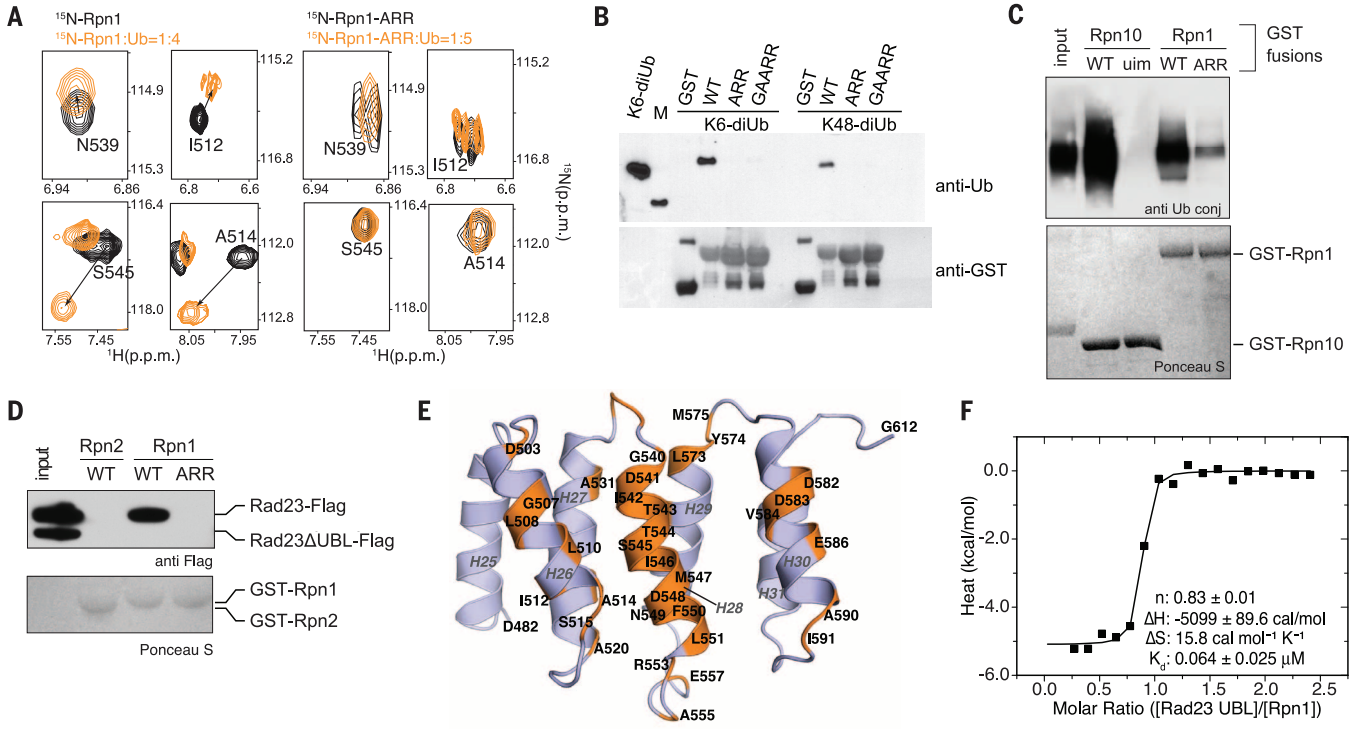


Fig. 3. H28 of the Rpn1 T1 site plays a dual role in binding ubiquitin chains and shuttle factor Rad23. (**A**) Selected regions from ^{1}H, ^{15}N HSQC spectra of ^{15}N wild-type Rpn1$_{412\text{-}625}$ (left) and ^{15}N Rpn1$_{412\text{-}625}$–ARR (D541A/D548R/E552R, right) alone (black) and with ubiquitin (orange) at four- and fivefold molar excess, respectively. (**B**) GST pull-down assay with GST, GST–Rpn1$_{412\text{-}625}$, GST–Rpn1$_{412\text{-}625}$–ARR, or GST–Rpn1$_{412\text{-}625}$ A514G-D517A-D541A-D548R-E552R (GAARR) and the indicated ubiquitin species. Immunoblotting was done with anti-ubiquitin (top) or anti-GST (bottom) antibodies. (**C**) Defective ubiquitin binding by the Rpn1-ARR mutant protein. Full-length GST-Rpn1 fusion protein was expressed, purified, and tested for binding to ubiquitinated T7–PY-Sic1. GST-Rpn10 and GST-Rpn10-uim were included as positive and negative controls, respectively. (**D**) Rad23 variants were tested for binding to Rpn1-WT and Rpn1-ARR. A mixture of recombinant Rad23-Flag and Rad23ΔUBL-Flag (serving as an internal negative control) were used as ligands. UBA domains were absent from both constructs. (**E**) Rpn1 amino acids at the Rad23 UBL domain contact surface, as determined by the data in fig. S20 are highlighted in orange on the ribbon diagram of the Rpn1 T1 site. (**F**) ITC analysis of the Rpn1 T1 site binding to Rad23 UBL. Rad23 UBL (0.407 mM) was injected into a calorimeter cell containing 0.036 mM Rpn1$_{412\text{-}625}$, and the data were fit to a one-site binding mode with the indicated thermodynamic parameters.

by using PRE data obtained by placing a spin label in the loop connecting H26 and H27 at L518 (fig. S15B). In one set of calculations, 104 NOE- and 19 PRE-derived intermolecular distance constraints placed distal ubiquitin at Rpn1 H28/H30 and proximal ubiquitin was centered at Rpn1 H26 (Fig. 5A and fig. S29A); proximal ubiquitin is so-designated for its free G76, which can, in principle, be conjugated to a substrate. We refer to this binding mode as "extended," because addition of ubiquitin moieties at either end of the chain yields an opened configuration across the Rpn1 T1 site, as illustrated in a model structure of $Rpn1_{482-612}$ bound to K48 tetraubiquitin (Fig. 5B, left).

The second set of structural calculations uses 100 NOE- and eight PRE-derived intermolecular distance constraints that place proximal ubiquitin at H28/30 and distal ubiquitin at H26 (Fig. 5C and fig. S29B). In this binding mode, G76 from ubiquitin at H28/H30 is spatially close to ubiquitin at H26 (Fig. 5C, expanded region), a configuration caused by a H-bond between proximal ubiquitin R74 and Rpn1 D541 and by van der Waals interactions between proximal ubiquitin L73 and Rpn1 L510 and A514 (Fig. 5C, expanded region). This binding orientation results in a "contracted" ubiquitin chain, best illustrated in a model structure with K48-linked tetraubiquitin (Fig. 5B, right).

Many electrostatic and hydrophobic interactions used to bind monoubiquitin are preserved when the Rpn1 T1 site binds K48 diubiquitin

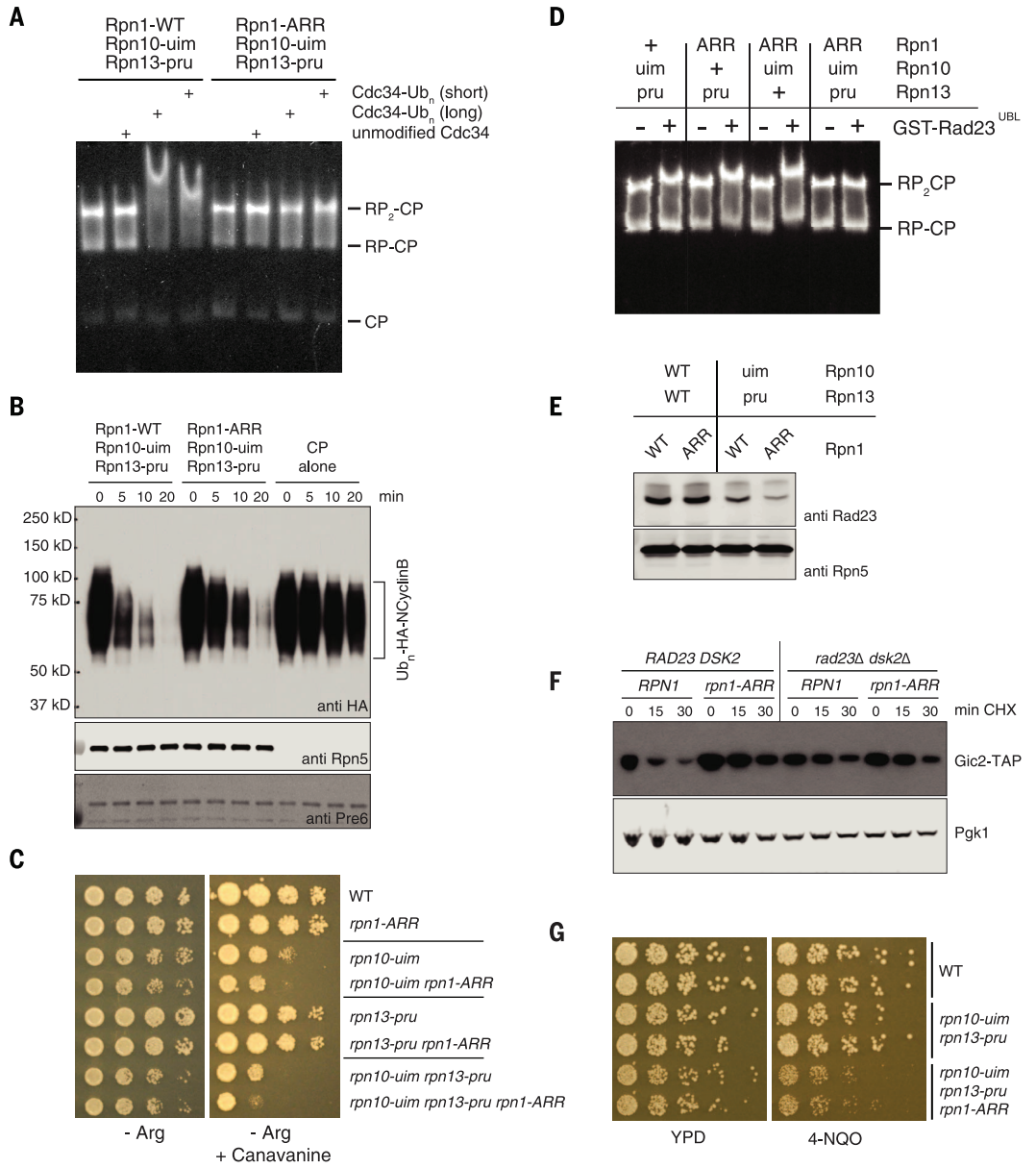


Fig. 4. Rpn1, Rpn10, and Rpn13 play dual roles in recruiting ubiquitin conjugates and shuttling receptors to the proteasome. (**A**) Proteasome association with ubiquitin conjugates evaluated by mobility-shift assay. RP complexes were purified from the indicated yeast strains, incubated with purified CP complex to form holoenzyme, and tested for association with ubiquitin conjugates as described for Fig. 1B. (**B**) Proteasomes were prepared, as described for (A), and assayed for degradation of a ubiquitinated fragment of cyclin B1 (Ub_n-HA-NCyclinB). Rpn5 was probed as a loading control. (**C**) Synthetic canavanine sensitivity of *rpn1-ARR* with other intrinsic ubiquitin receptor mutants. All strains were prepared in the *rad23Δ dsk2Δ ddi1Δ* background and carry additional mutations as indicated. Yeast cultures were serially diluted and transferred to synthetic media agar plates lacking arginine (Arg^-) or Arg^- with 2 μg/ml canavanine, followed by incubation at 30°C. (**D**) Proteasome association with Rad23 evaluated by mobility-shift assay. Proteasomes were purified from *rad23Δ dsk2Δ ddi1Δ* yeast strains bearing the indicated intrinsic ubiquitin receptor mutations and incubated with ligand at 100-fold molar excess. Binding mixtures were resolved by native PAGE and proteasome complexes assayed as described. (**E**) Proteasomes were purified, in the absence of salt, from yeast strains bearing mutations in intrinsic ubiquitin receptors, as indicated. Proteasomes and their associated proteins were resolved by SDS-PAGE, blotted, and probed with antibodies to proteasome-associated UBL protein Rad23 and to proteasome subunit Rpn5, as a loading control. (**F**) In vivo degradation of proteasome substrate Gic2. Yeast strains *rpn10-uim rpn13-pru* bearing TAP-tagged Gic2 integrated at the native genomic locus, and other alleles as indicated, were treated with cycloheximide for the indicated times. Lysates were prepared and resolved by SDS-PAGE. Proteins were blotted and probed for Gic2-TAP, with Pgk1 as a loading control. (**G**) The *rpn1-ARR* allele confers sensitivity to 4-NQO. Cultures of strains carrying the indicated mutations were serially diluted, transferred to YPD plates either lacking or containing 0.1 μg/ml 4-NQO, and incubated at 30°C for 2 days.

(Figs. 2C and 5D). The backbone RMSD between the contracted and extended binding mode is 0.49 and 0.36 Å for ubiquitin binding at Rpn1 H26 and H28/H30, respectively. This similarity reflects that contacts between ubiquitin L8, T9, I44, V70, L71, and L73 and Rpn1 H26, H28, and H30 are retained in all cases, as supported by the experimental data (figs. S14 and S28).

We computationally generated a model substrate (cyclin B1) with an attached K48 triubiquitin chain and docked it in the extended binding mode into the Rpn1 T1 site of a proteasome cryo–electron microscopy (cryo-EM)–based model structure (PDB 4CR2). The resulting model illustrated the substrate to be directed toward the adenosine triphosphatase (ATPase) ring and its substrate entry channel (fig. S30). We next adapted this model to include our Rpn13 Pru:ubiquitin (*7*) and hRpn10:K48 diubiquitin (*32*) structures (Fig. 5E). The full model represents an additional pathway for ubiquitin chain binding contributed by the Rpn1 T1 site that exists on the same proteasome face as the ubiquitin-binding pathway generated by hRpn13 and hRpn10. Additional experiments will be needed to test this model further.

A second UBL-recognizing site on the Rpn1 toroid binds a deubiquitinating enzyme

In transit from Rpn1 and the other proteasome ubiquitin receptors to the catalytic center, substrates are deubiquitinated before passing through a narrow gating mechanism, as reviewed in (*33*). We have previously suggested that the principal binding site for Ubp6 on the proteasome may be in Rpn1 (*18*, *34*), and more recently Rpt1 has also been implicated as an interaction site (*35*, *36*). Using purified Rpn1 and purified Ubp6, we were unable to map the putative Ubp6 binding site of Rpn1 by deletion analysis. We turned to hydrogen exchange mass spectrometry (HX MS), which has proven useful for structural characterization of protein systems intractable by other techniques. HX MS reports on backbone amide hydrogens of proteins, which undergo isotopic exchange in deuterated solvent (*37*–*39*). Exchange rates can vary by many orders of magnitude (*40*) and are influenced by both hydrogen bonding of the backbone and solvent accessibility.

During HX MS analysis of free Rpn1, it became apparent that extensive regions of Rpn1 underwent localized cooperative unfolding, visualized as multiple populations that incorporate deuterium at different, nonsynchronized rates. Such exchange kinetics, termed EX1 (*41*–*43*), are a hallmark of a heterogeneous protein population, often reporting on long-lived conformational fluctuations (*44*) that result from changes in the conformational ensemble during the deuterium labeling. We hypothesized that Rpn1 incorporated into the base complex might be stabilized by intermolecular interactions within this complex, and therefore attempted to map the Rpn1-Ubp6 interaction in the context of the base.

A base-Ubp6 complex was subjected to deuterium labeling, followed by proteolytic digestion,

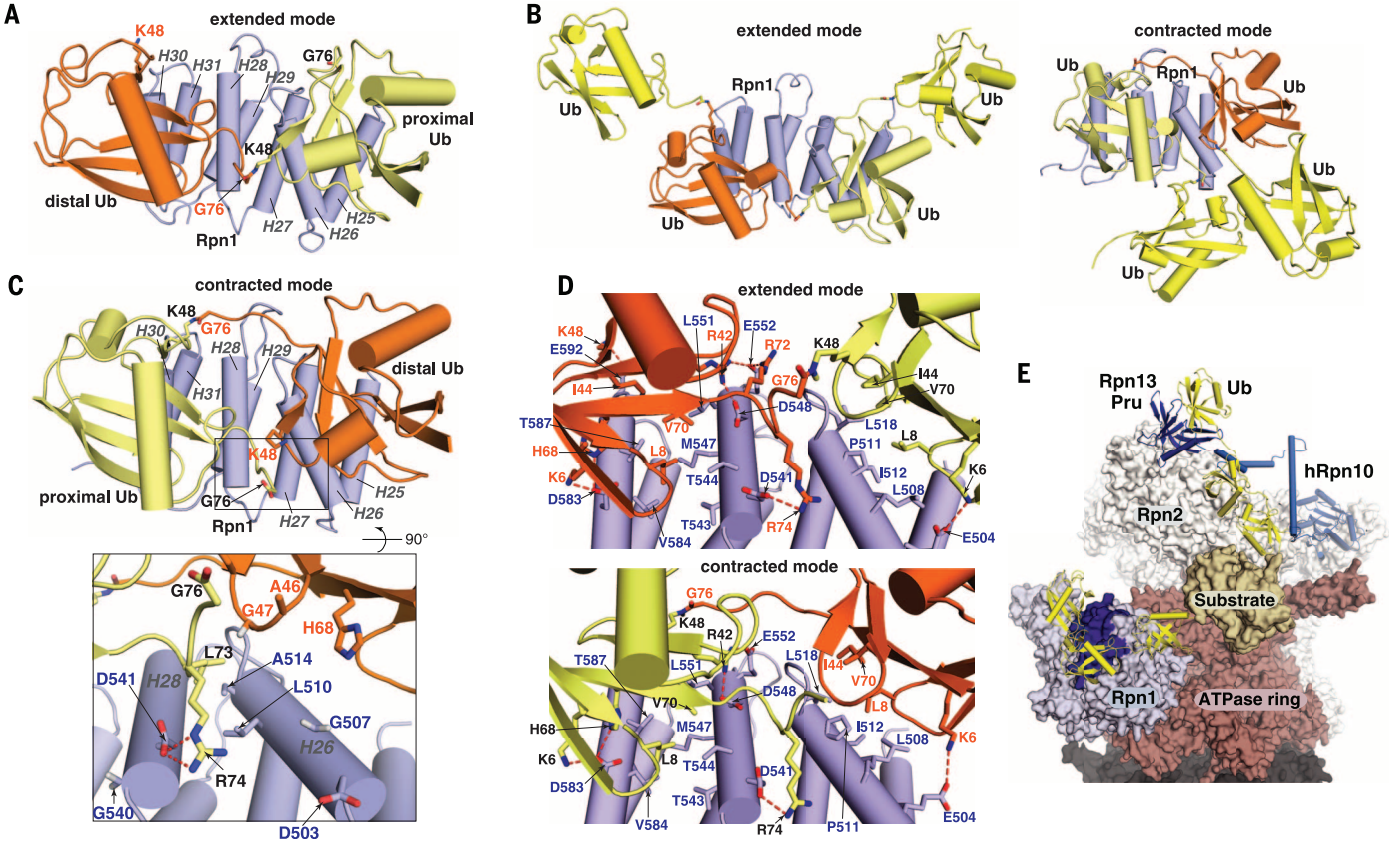


Fig. 5. Structures of the Rpn1 T1:K48 diubiquitin complex suggest a pathway for ubiquitin chain recognition at the proteasome. (**A** and **C**) Lowest-energy structures of $Rpn1_{482-612}$:K48 diubiquitin in the extended (A) or contracted (C) binding mode. These structures were solved experimentally by using a suite of NMR experiments, as described in Materials and Methods by using the data listed in table S2. An enlarged view is included in (C) to illustrate restricted accessibility of proximal ubiquitin G76. Displayed amino acid side chains from distal ubiquitin (orange) are labeled in orange, whereas those from proximal ubiquitin (yellow) are labeled in black. Blue coloring is used for Rpn1, with helices labeled in gray. (**B**) Model of Rpn1 T1:K48 tetraubiquitin by adding a ubiquitin (yellow) to each end of the K48 diubiquitin chain for the extended (left) and contracted (right) experimentally determined Rpn1 T1:K48 diubiquitin structure. The Rpn1 T1:K48 tetraubiquitin structures were energy-minimized by using Schrödinger (www.schrodinger.com). (**D**) Expanded view of the extended (top) or contracted (bottom) binding mode for Rpn1 T1:K48 diubiquitin to illustrate hydrophobic and electrostatic interactions at the contact surface. (**E**) Model of proteasome engaging a ubiquitinated substrate, generated with Rpn1 T1:K48 diubiquitin in the extended binding mode, Rpn13 Pru:ubiquitin (PDB 2Z59), hRpn10:K48 diubiquitin (PDB 2KDF), and human cyclin B1 (PDB 2B9R) placed into a proteasome cryo-EM–based model (PDB 4CR2). Rpn1, blue and indigo; ubiquitin, yellow; Rpn13 Pru, navy; Rpn10, light blue; substrate, beige; ATPase ring, burgundy; CP, gray; remaining RP, white.

and the resulting peptide mixture was analyzed by UPLC, ion mobility spectrometry, and mass spectrometry (fig. S31). We identified and measured the temporal deuterium uptake for 40 Rpn1 peptides covering ~60% of the sequence (Fig. 6A and figs. S32 and S33). As hypothesized, when incorporated into the base complex, Rpn1 was dramatically stabilized in conformation relative to when it was free in solution (Fig. 6A). In particular, the EX1 uptake kinetics indicative of conformational heterogeneity was no longer observable. The addition of Ubp6 to the base provided further protection from exchange exclusively for a highly localized region, suggestive of a well-defined binding site rather than further stabilization of the Rpn1 conformation (Fig. 6B). HX was suppressed most strongly for peptic peptide 419–436, corresponding to inner helix 21 and outer helix 22 of the toroid (Fig. 6B and figs. S4 and S33). These experiments represent to our knowledge the largest unique-sequence multiprotein complex studied to date by HX MS.

Having apparently localized the Ubp6 binding site to residues 419 to 436 of Rpn1, we introduced three sets of mutations into this region of the toroid and in all cases Ubp6 failed to copurify with proteasomes upon affinity purification (Fig. 6C). We refer to this site, a second and distinct UBL binding site within the Rpn1 toroid, as T2. We purified RP complexes from the T2 mutant *rpn1-L430A D431K Q434A Q435A* (hereafter *rpn1-AKAA)*, and found, using the fluorogenic substrate ubiquitin-7-amino-4-methylcoumarin (ubiquitin-AMC) (*34*), that these mutations result in a dramatic loss of affinity for recombinant Ubp6 (Fig. 6D).

We next tested whether the T1 and T2 sites can be loaded independently and whether their specificities are truly distinct. Native gel binding assays carried out with T1 site and T2 site mutants showed that the two sites have nonoverlapping specificities (Fig. 7A). In particular *Rpn1-AKAA* demonstrated a specific defect in Ubp6 and not Rad23 binding, whereas *Rpn1-ARR* bound to Ubp6 but was defective for Rad23 binding (Fig. 7A). This experiment also mapped the T2 site interacting element of Ubp6 to its UBL domain (Fig. 7A), consistent with cryo-EM analysis of the proteasome (*35*, *36*). The lack of effect of T1 site mutations on Ubp6 binding was confirmed with endogenous material (fig. S34). We tested whether the T1 site influences the activity of Ubp6 by using the ubiquitin-AMC assay. Neither the T1 site, nor the ubiquitin-binding sites of Rpn13 and Rpn10, influenced Ubp6-mediated deubiquitinating activity (Fig. 7B), thus demonstrating high specificity among these sites despite their common usage of UBL class domains as ligands. In summary, the Rpn1 toroid contains two proximal binding sites for ubiquitin or UBL domains, as shown in Fig. 7C, and thus Rpn1 serves as a key receptor and spatial organizer of both substrates and cofactors of the proteasome.

We used a molecular modeling program (HADDOCK 2.1) to dock the Ubp6 UBL domain against Rpn1 amino acids L430, D431, Q434, and Q435. Although the orientation of the UBL is not defined experimentally, the resulting model demonstrates the relative positioning of the T1 and T2 sites and was integrated within the overall architecture of the proteasome as determined by cryo-EM (Fig. 7D).

Discussion

We report here a hotspot in the proteasome for assembling and localizing substrates and cofactors. This region is contributed by the toroid domain of Rpn1 and spans at least four of its eleven hairpin repeats. Interestingly, we were able to identify three distinct binding positions for ubiquitin-fold ligands, two of which combine to form a bifurcated binding site for a diubiquitin element, especially when linked by K48 or K6. This additional ubiquitin-binding motif in the Rpn1 toroid also binds to the UBL domain of substrate shuttling factor Rad23 and we name this substrate receptor site T1. The third UBL-binding site, which is adjacent to the T1 site, provides a tether point for deubiquitinating enzyme Ubp6. The location of the T1 and T2 sites within the proteasome places substrate ubiquitin chains and Ubp6 in the neighborhood of the ATPase hexamer, where the Ubp6 catalytic domain is known to form contacts with Rpt1

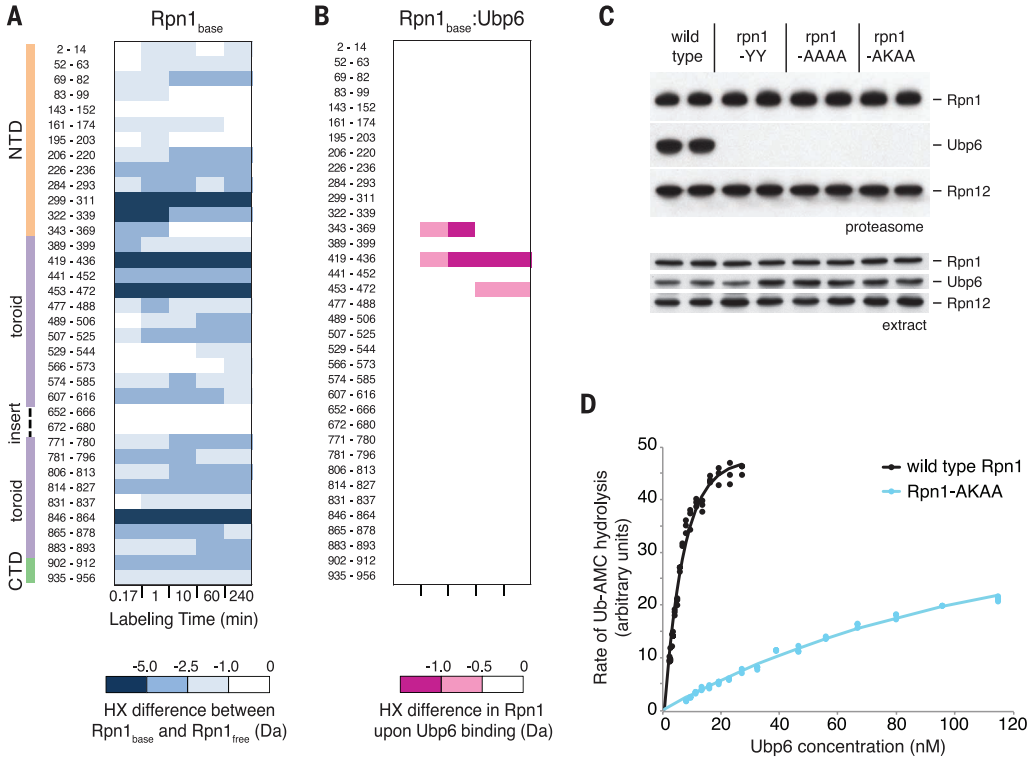


Fig. 6. Evidence for a second UBL-specific receptor site on the Rpn1 toroid, which recognizes Ubp6. (**A**) Deuteration of recombinant Rpn1 ($Rpn1_{free}$) compared with deuteration of Rpn1 in the context of the base ($Rpn1_{base}$). Peptide residue numbers are shown at left, as well as the Rpn1 domain organization as described in the SM. Differences at each time point were calculated using Eq. 6 (see SM) and color-coded according to the scale at the bottom. (**B**) Deuteration differences between $Rpn1_{base}$ when bound to Ubp6 minus $Rpn1_{base}$ without Ubp6. Peptide residue numbers are identical to those in (A), and deuteration differences are indicated by the scale at the bottom. (**C**) Proteasomes were purified from strains bearing wild-type or mutant Rpn1 alleles, as indicated, by using mild washes. The YY mutant is *D431Y Q434Y*; AAAA is *L430A D431A Q434A Q435A;* and AKAA is *L430A D431K Q434A Q435A*. Aliquots of extracts and purified proteasomes were resolved by 10% SDS-PAGE, blotted, and probed with antibodies against Rpn1, Ubp6, and Rpn12. (**D**) Activation of Ubp6 by wild-type and mutant RP. Ubp6 was incubated with RP purified from wild-type and *rpn1-AKAA* strains and assayed for Ub-AMC hydrolysis activity. Concentration of RP was constant at 1 nM, and the concentration of Ubp6 was graded. Curve-fitting, as shown, yields a K_d value of 4.7 nM for wild type. For the AKAA mutant, a concentration of Ubp6 29 times that of the wild type would be required to achieve a hydrolytic rate corresponding to half-maximal for wild type.

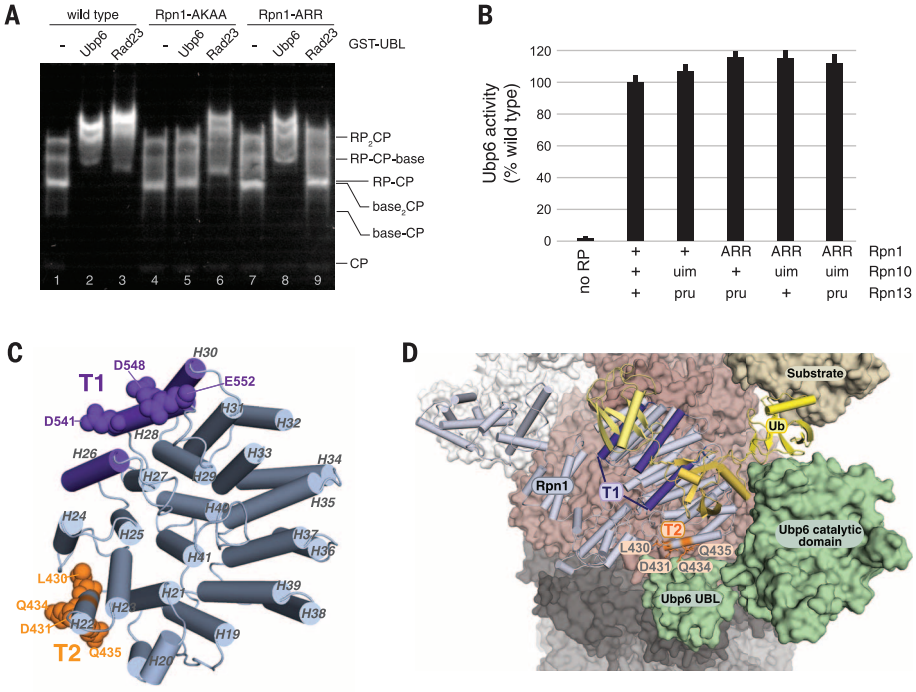


Fig. 7. The Rpn1 toroid spatially registers ubiquitin chains and Ubp6. (**A**) Reconstituted proteasomes, prepared with RPs isolated from wild-type, *rpn1-AKAA*, or *rpn1-ARR* strains, were incubated with GST-Ubp6^{UBL} or GST-Rad23^{UBL} in molar excess, resolved by native PAGE, and assayed as described. (**B**) Ubp6 in RP complexes as indicated was evaluated for activation by the proteasome. Proteins were incubated with 1 μM Ub-AMC, and hydrolytic activity was monitored by the fluorescence of released AMC. (**C**) Toroidal domain of Rpn1 highlighting the T1 and T2 sites. Residues required for interaction with ubiquitin chains and Rad23 are shown in purple, and exposed residues implicated in Ubp6 binding are highlighted in orange. This image is generated by using PDB 4CR2. (**D**) Rpn1 T1 and T2 sites in the context of the proteasome, with sites colored as indicated in (C). This image was generated by docking the Ubp6 structure (PDB 1VJV and 1WGG) onto PDB 4CR2, on the basis of the experimental data of Fig. 6, B and C. The coloring scheme follows that of Fig. 5E and with Ubp6 in green. T2 amino acids L430, D431, Q434, and Q435 are highlighted in orange.

(*35*, *36*). It is furthermore anticipated that the positioning of these sites on the same proteasome face as the ubiquitin-binding pathway generated by hRpn10 and hRpn13 allows for avidity effects that could increase proteasome affinity for ubiquitinated substrates, especially those that carry multiple ubiquitin chains. A recent single molecule study indeed demonstrates greater degradation efficiency for model substrates in which ubiquitin groups are dispersed into multiple chains (*45*). Like Rpn1, Rpn13 functions not only as a ubiquitin receptor but also as a receptor for Uch37, a second proteasomal deubiquitinating enzyme. Thus, both Ubp6 and Uch37 are positioned in apposition to ubiquitin receptors, and it will be interesting to explore the functional implications of this localization in future work.

The ability of the T1 site of Rpn1 to bind both ubiquitin and UBL proteins that shuttle ubiquitinated substrates to the proteasome applies to all intrinsic substrate receptor sites of the proteasome. The multiplicity of intrinsic substrate receptors on the proteasome, taken together with the combinatorial array of states associated with loading of multiple extrinsic receptors on any intrinsic receptor, should allow for tens and possibly hundreds of distinct receptor states for binding of ubiquitin conjugates. The use of multiple sites for substrate recognition, not all showing high affinity, is consistent with a multipoint, avid mode of ubiquitin chain recognition, which may be associated with highly dynamic interactions between ubiquitin receptors and the proteasome-bound substrate (*45*). Substrate binding is thought to be productive for proteolysis only if it results in the presentation of an unstructured initiation site into the substrate translocation channel of the ATPase ring (*46*). A dynamic mode of ubiquitin chain binding may allow for the body of the substrate to present alternative orientations to the proteasome so as to achieve productive positioning of the initiation site. In summary, this work defines a pathway in the proteasome that engages substrates by using avid low affinity binding sites, and places them in the neighborhood of deubiquitinating enzyme Ubp6 and the ATPase ring.

Methods summary

Detailed information for yeast strain construction, plate assays, protein turnover assays, expression and purification of recombinant and native proteins, ubiquitin conjugate preparation, native gel electrophoresis and mobility-shift assays, protein degradation and deubiquitination assays, hydrogen deuterium exchange, mass spectrometry, and NMR spectroscopy is provided in the SM.

REFERENCES AND NOTES

1. T. Zhang, Y. Jia, Meta-analysis of Ubiquilin1 gene polymorphism and Alzheimer's disease risk. *Med. Sci. Monit.* **20**, 2250–2255 (2014). doi: 10.12659/MSM.891030; pmid: 25387430
2. H.-X. Deng *et al.*, Mutations in UBQLN2 cause dominant X-linked juvenile and adult-onset ALS and ALS/dementia. *Nature* **477**, 211–215 (2011). doi: 10.1038/nature10353; pmid: 21857683
3. Q. Deveraux, V. Ustrell, C. Pickart, M. Rechsteiner, A 26 S protease subunit that binds ubiquitin conjugates. *J. Biol. Chem.* **269**, 7059–7061 (1994). pmid: 8125911
4. S. van Nocker *et al.*, The multiubiquitin-chain-binding protein Mcb1 is a component of the 26S proteasome in *Saccharomyces cerevisiae* and plays a nonessential, substrate-specific role in protein turnover. *Mol. Cell. Biol.* **16**, 6020–6028 (1996). doi: 10.1128/MCB.16.11.6020; pmid: 8887631
5. H. Fu *et al.*, Multiubiquitin chain binding and protein degradation are mediated by distinct domains within the 26 S proteasome subunit Mcb1. *J. Biol. Chem.* **273**, 1970–1981 (1998). doi: 10.1074/jbc.273.4.1970; pmid: 9442033
6. K. Husnjak *et al.*, Proteasome subunit Rpn13 is a novel ubiquitin receptor. *Nature* **453**, 481–488 (2008). doi: 10.1038/nature06926; pmid: 18497817
7. P. Schreiner *et al.*, Ubiquitin docking at the proteasome through a novel pleckstrin-homology domain interaction. *Nature* **453**, 548–552 (2008). doi: 10.1038/nature06924; pmid: 18497827
8. S. Elsasser, D. Chandler-Militello, B. Müller, J. Hanna, D. Finley, Rad23 and Rpn10 serve as alternative ubiquitin receptors for the proteasome. *J. Biol. Chem.* **279**, 26817–26822 (2004). doi: 10.1074/jbc.M404020200; pmid: 15117949
9. R. Verma, R. Oania, J. Graumann, R. J. Deshaies, Multiubiquitin chain receptors define a layer of substrate selectivity in the ubiquitin-proteasome system. *Cell* **118**, 99–110 (2004). doi: 10.1016/j.cell.2004.06.014; pmid: 15242647
10. M. Funakoshi, T. Sasaki, T. Nishimoto, H. Kobayashi, Budding yeast Dsk2p is a polyubiquitin-binding protein that can interact with the proteasome. *Proc. Natl. Acad. Sci. U.S.A.* **99**, 745–750 (2002). doi: 10.1073/pnas.012585199; pmid: 11805328
11. L. Kaplun *et al.*, The DNA damage-inducible UbL-UbA protein Ddi1 participates in Mec1-mediated degradation of Ho endonuclease. *Mol. Cell. Biol.* **25**, 5355–5362 (2005). doi: 10.1128/MCB.25.13.5355-5362.2005; pmid: 15964793
12. O. Voloshin, A. Bakhrat, S. Herrmann, D. Raveh, Transfer of Ho endonuclease and Ufo1 to the proteasome by the UbL-UbA shuttle protein, Ddi1, analysed by complex formation in vitro. *PLOS ONE* **7**, e39210 (2012). doi: 10.1371/journal.pone.0039210; pmid: 22815701
13. H. Richly *et al.*, A series of ubiquitin binding factors connects CDC48/p97 to substrate multiubiquitylation and proteasomal targeting. *Cell* **120**, 73–84 (2005). doi: 10.1016/j.cell.2004.11.013; pmid: 15652483
14. K. Paraskevopoulos *et al.*, Dss1 is a 26S proteasome ubiquitin receptor. *Mol. Cell* **56**, 453–461 (2014). doi: 10.1016/j.molcel.2014.09.008; pmid: 25306921
15. Y. Saeki, E. Isono, A. Toh-E, Preparation of ubiquitinated substrates by the PY motif-insertion method for monitoring 26S proteasome activity. *Methods Enzymol.* **399**, 215–227 (2005). doi: 10.1016/S0076-6879(05)99014-9; pmid: 16338358
16. S. Elsasser *et al.*, Proteasome subunit Rpn1 binds ubiquitin-like protein domains. *Nat. Cell Biol.* **4**, 725–730 (2002). doi: 10.1038/ncb845; pmid: 12198498
17. T. A. Gomez, N. Kolawa, M. Gee, M. J. Sweredoski, R. J. Deshaies, Identification of a functional docking site in the Rpn1 LRR domain for the UBA-UBL domain protein Ddi1. *BMC Biol.* **9**, 33 (2011). doi: 10.1186/1741-7007-9-33; pmid: 21627799

18. R. Rosenzweig, V. Bronner, D. Zhang, D. Fushman, M. H. Glickman, Rpn1 and Rpn2 coordinate ubiquitin processing factors at proteasome. *J. Biol. Chem.* **287**, 14659–14671 (2012). doi: 10.1074/jbc.M111.316323; pmid: 22318722
19. J. He *et al*., The structure of the 26S proteasome subunit Rpn2 reveals its PC repeat domain as a closed toroid of two concentric α-helical rings. *Structure* **20**, 513–521 (2012). doi: 10.1016/j.str.2011.12.015; pmid: 22405010
20. A. V. Kajava, What curves alpha-solenoids? Evidence for an alpha-helical toroid structure of Rpn1 and Rpn2 proteins of the 26 S proteasome. *J. Biol. Chem.* **277**, 49791–49798 (2002). doi: 10.1074/jbc.M204982200; pmid: 12270919
21. Q. Wang, P. Young, K. J. Walters, Structure of S5a bound to monoubiquitin provides a model for polyubiquitin recognition. *J. Mol. Biol.* **348**, 727–739 (2005). doi: 10.1016/j.jmb.2005.03.007; pmid: 15826667
22. X. Chen, K. J. Walters, Identifying and studying ubiquitin receptors by NMR. *Methods Mol. Biol.* **832**, 279–303 (2012). doi: 10.1007/978-1-61779-474-2_20; pmid: 22350893
23. F. Liu, K. J. Walters, Multitasking with ubiquitin through multivalent interactions. *Trends Biochem. Sci.* **35**, 352–360 (2010). pmid: 20181483
24. D. Zhang *et al*., Together, Rpn10 and Dsk2 can serve as a polyubiquitin chain-length sensor. *Mol. Cell* **36**, 1018–1033 (2009). pmid: 20064467
25. D. S. Kirkpatrick *et al*., Quantitative analysis of in vitro ubiquitinated cyclin B1 reveals complex chain topology. *Nat. Cell Biol.* **8**, 700–710 (2006). doi: 10.1038/ncb1436; pmid: 16799550
26. J. Hanna *et al*., Deubiquitinating enzyme Ubp6 functions noncatalytically to delay proteasomal degradation. *Cell* **127**, 99–111 (2006). doi: 10.1016/j.cell.2006.07.038; pmid: 17018280
27. N. V. Dimova *et al*., APC/C-mediated multiple monoubiquitylation provides an alternative degradation signal for cyclin B1. *Nat. Cell Biol.* **14**, 168–176 (2012). doi: 10.1038/ncb2425; pmid: 22286100
28. D. Lambertson, L. Chen, K. Madura, Pleiotropic defects caused by loss of the proteasome-interacting factors Rad23 and Rpn10 of *Saccharomyces cerevisiae*. *Genetics* **153**, 69–79 (1999). pmid: 10471701
29. Y. Matiuhin *et al*., Extraproteasomal Rpn10 restricts access of the polyubiquitin-binding protein Dsk2 to proteasome. *Mol. Cell* **32**, 415–425 (2008). doi: 10.1016/j.molcel.2008.10.011; pmid: 18995839
30. S. Ghaemmaghami *et al*., Global analysis of protein expression in yeast. *Nature* **425**, 737–741 (2003). doi: 10.1038/nature02046; pmid: 14562106
31. T. G. Gillette *et al*., The 19S complex of the proteasome regulates nucleotide excision repair in yeast. *Genes Dev.* **15**, 1528–1539 (2001). doi: 10.1101/gad.869601; pmid: 11410533
32. N. Zhang *et al*., Structure of the S5a:K48-linked diubiquitin complex and its interactions with Rpn13. *Mol. Cell* **35**, 280–290 (2009). doi: 10.1016/j.molcel.2009.06.010; pmid: 19683493
33. D. Finley, X. Chen, K. J. Walters, Gates, channels, and switches: Elements of the proteasome machine. *Trends Biochem. Sci.* **41**, 77–93 (2016). doi: 10.1016/j.tibs.2015.10.009; pmid: 26643069
34. D. S. Leggett *et al*., Multiple associated proteins regulate proteasome structure and function. *Mol. Cell* **10**, 495–507 (2002). doi: 10.1016/S1097-2765(02)00638-X; pmid: 12408819
35. A. Aufderheide *et al*., Structural characterization of the interaction of Ubp6 with the 26S proteasome. *Proc. Natl. Acad. Sci. U.S.A.* **112**, 8626–8631 (2015). doi: 10.1073/pnas.1510449112; pmid: 26130806
36. C. Bashore *et al*., Ubp6 deubiquitinase controls conformational dynamics and substrate degradation of the 26S proteasome. *Nat. Struct. Mol. Biol.* **22**, 712–719 (2015). doi: 10.1038/nsmb.3075; pmid: 26301997
37. L. Konermann, J. Pan, Y.-H. Liu, Hydrogen exchange mass spectrometry for studying protein structure and dynamics. *Chem. Soc. Rev.* **40**, 1224–1234 (2011). doi: 10.1039/C0CS00113A; pmid: 21173980
38. A. J. Percy, M. Rey, K. M. Burns, D. C. Schriemer, Probing protein interactions with hydrogen/deuterium exchange and mass spectrometry—a review. *Anal. Chim. Acta* **721**, 7–21 (2012). doi: 10.1016/j.aca.2012.01.037; pmid: 22405295
39. T. E. Wales, J. R. Engen, Hydrogen exchange mass spectrometry for the analysis of protein dynamics. *Mass Spectrom. Rev.* **25**, 158–170 (2006). doi: 10.1002/mas.20064; pmid: 16208684
40. J. J. Skinner, W. K. Lim, S. Bédard, B. E. Black, S. W. Englander, Protein hydrogen exchange: Testing current models. *Protein Sci.* **21**, 987–995 (2012). doi: 10.1002/pro.2082; pmid: 22544567
41. L. Konermann, X. Tong, Y. Pan, Protein structure and dynamics studied by mass spectrometry: H/D exchange, hydroxyl radical labeling, and related approaches. *J. Mass Spectrom.* **43**, 1021–1036 (2008). doi: 10.1002/jms.1435; pmid: 18523973
42. D. D. Weis, T. E. Wales, J. R. Engen, M. Hotchko, L. F. Ten Eyck, Identification and characterization of EX1 kinetics in H/D exchange mass spectrometry by peak width analysis. *J. Am. Soc. Mass Spectrom.* **17**, 1498–1509 (2006). doi: 10.1016/j.jasms.2006.05.014; pmid: 16875839
43. H. Xiao *et al*., Mapping protein energy landscapes with amide hydrogen exchange and mass spectrometry: I. A generalized model for a two-state protein and comparison with experiment. *Protein Sci.* **14**, 543–557 (2005). doi: 10.1110/ps.041001705; pmid: 15659380
44. T. E. Wales, J. R. Engen, Partial unfolding of diverse SH3 domains on a wide timescale. *J. Mol. Biol.* **357**, 1592–1604 (2006). doi: 10.1016/j.jmb.2006.01.075; pmid: 16487539
45. Y. Lu, B. H. Lee, R. W. King, D. Finley, M. W. Kirschner, Substrate degradation by the proteasome: A single-molecule kinetic analysis. *Science* **348**, 1250834 (2015). doi: 10.1126/science.1250834; pmid: 25859050
46. S. Prakash, L. Tian, K. S. Ratliff, R. E. Lehotzky, A. Matouschek, An unstructured initiation site is required for efficient proteasome-mediated degradation. *Nat. Struct. Mol. Biol.* **11**, 830–837 (2004). doi: 10.1038/nsmb814; pmid: 15311270
47. P. Unverdorben *et al*., Deep classification of a large cryo-EM dataset defines the conformational landscape of the 26S proteasome. *Proc. Natl. Acad. Sci. U.S.A.* **111**, 5544–5549 (2014). doi: 10.1073/pnas.1403409111; pmid: 24706844
48. O. F. Lange *et al*., Recognition dynamics up to microseconds revealed from an RDC-derived ubiquitin ensemble in solution. *Science* **320**, 1471–1475 (2008). doi: 10.1126/science.1157092; pmid: 18556554
49. U. Nowicka *et al*., *Mycobacterium tuberculosis* copper-regulated protein SocB is an intrinsically disordered protein that folds upon interaction with a synthetic phospholipid bilayer. *Proteins* **84**, 193–200 (2016). doi: 10.1002/prot.24970; pmid: 26650755

ACKNOWLEDGMENTS

For advice, assistance, or comments on the manuscript, we thank D. Chandler-Militello, M. Gill, J. Hanna, A. Kajava, R. King, Y. Lu, Y. Li, M. Pahre, and J. Roelofs. For gifts of reagents we thank D. Clarke, M. Glickman, F. He, Y. Ye, D. Komander, C. Larsen, J. Li, U. Nowicka, S. Sadis, and W. Tansey. This research was funded by grants from the National Institutes of Health (R37-GM043601 to D.F., CA136472 to K.J.W., and R01-GM101135 to J.R.E.), by the Intramural Research Program of the NIH, National Cancer Institute, Center for Cancer Research to K.J.W., and by a research collaboration with the Waters Corporation (J.R.E). Atomic coordinates for the Rpn1 T1 site, Rpn1 T1:ubiquitin, and Rpn1 T1:K48 diubiquitin are available through the Protein Data Bank with accession codes 2n3t, 2n3u, and 2n3v/2n3w, respectively.

SUPPLEMENTARY MATERIALS

www.sciencemag.org/content/351/6275/aad9421/suppl/DC1
Materials and Methods
Figs. S1 to S34
Tables S1 to S5
References (*50*–*73*)

25 November 2015; accepted 5 January 2016
10.1126/science.aad9421

REPORTS

ORGANIC CHEMISTRY

Catalytic reversible alkene-nitrile interconversion through controllable transfer hydrocyanation

Xianjie Fang, Peng Yu, Bill Morandi*

Nitriles and alkenes are important synthetic intermediates with complementary reactivity that play a central role in the preparation of materials, pharmaceuticals, cosmetics, and agrochemicals. Here, we report a nickel-catalyzed transfer hydrocyanation reaction between a wide range (60 examples) of alkyl nitriles and alkenes. This strategy not only overcomes the toxicity challenge posed by the use of HCN in traditional approaches, but also encompasses distinct chemical advances, including retro-hydrocyanation and anti-Markovnikov regioselectivity. In a broader context, this work highlights an approach to the reversible hydrofunctionalization of alkenes through thermodynamically controlled transfer reactions to circumvent the use of volatile and hazardous reagents in the laboratory.

The nitrile group is among the most versatile polar functionalities and is widely encountered in the preparation of materials, pharmaceuticals, cosmetics, and agrochemicals, both on industrial and laboratory scale (*1*). Nitriles can serve as precursors for aldehydes, acids, esters, ketones, amides, amines, and heterocycles. Additionally, the electron-withdrawing nature of nitrile groups alters the reactivity profile of the surrounding molecule (*2*) and enables functionalization of neighboring positions (α and β position depending on nitrile structure). Alkenes are nonpolar functional groups with a distinct and complementary reactivity profile compared to nitriles (*3*). Alkenes tolerate a wide range of reaction conditions commonly used to transform polar functional groups (*2*). Additionally, they can engage in a number of bond-forming reactions [e.g., alkene metathesis reaction (*4*)] not accessible from polar functional groups (*2*). In light of the central role played by the nitrile and alkene functionalities in chemical synthesis and their complementary reactivity profiles, a protocol for their reversible interconversion would likely have a broad impact across the molecular sciences.

The catalytic addition of hydrogen cyanide (HCN) to alkenes to produce nitriles has been underexploited in routine chemical synthesis (*5*–*17*), even though the DuPont adiponitrile process produces around 1 million tons/year (*8*) of adiponitrile (a precursor to the polymer Nylon 6,6) through the atom-economical hydrocyanation of butadiene (Fig. 1A). The extreme toxicity of the corrosive and explosive (*18*, *19*) hydrogen cyanide gas (boiling point 27°C) poses a substantial safety challenge to research laboratories, whether it is used directly or, in certain cases (*20*–*22*), generated in situ from similarly toxic (*23*, *24*) but less volatile precursors [acetone cyanohydrin, $(Me)_3SiCN$]. The propensity of HCN to poison the nickel hydrocyanation catalysts through formation of catalytically inactive species (*7*, *8*, *25*, *26*) requires careful control of HCN concentration over the course of the reaction. Moreover, the thermodynamic instability of HCN renders synthetically valuable retro-hydrocyanation processes to produce alkenes from nitriles extremely challenging (*27*, *28*). Owing to the serious hazards and limitations associated with the use of HCN, an HCN-free mechanistic manifold that could reversibly interconvert organonitriles and alkenes would be poised to find broad application in synthetic chemistry.

Despite the potential of group transfer reactions to provide complementary, gas-free alternatives

Max-Planck-Institut für Kohlenforschung, Mülheim an der Ruhr, Nordrhein-Westfalen 45470, Germany.
*Corresponding author. E-mail: morandi@kofo.mpg.de

Downloaded from on February 18, 2016

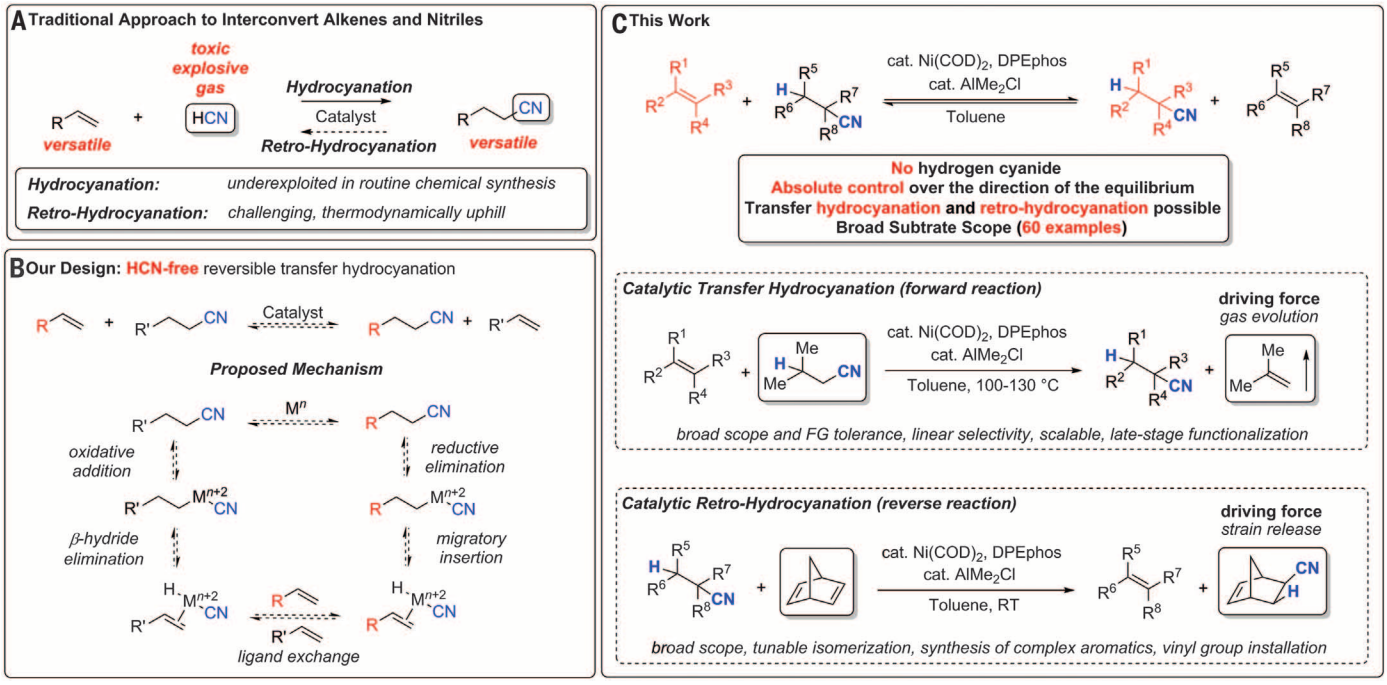


Fig. 1. Development of a transfer hydrocyanation/retro-hydrocyanation protocol. (**A**) Traditional approach to hydrocyanation. (**B**) Our transfer strategy. (**C**) This work. COD, cyclooctadiene; DPEphos, 2,2'-bis(diphenylphosphino)diphenyl ether; RT, room temperature; FG, functional group.

to traditional alkene hydrofunctionalization reactions that employ hazardous reagents, there is currently no catalytic and reversible group transfer reaction that permits both the construction and deconstruction of a polar and versatile functional group from alkenes with absolute control over the direction of the equilibrium (*29*–*32*). Inspired by the transformative power of H_2-free transfer hydrogenation reactions (*33*–*35*), we reasoned that a mechanistically related transfer hydrocyanation between simple alkyl nitriles and alkenes could interconvert these two synthetically versatile functional groups without relying upon HCN as a reagent. We reasoned that if a metal catalyst (M) could mediate a challenging sequence of C-CN oxidative addition, β-hydride elimination, ligand exchange, migratory H-insertion, and reductive elimination of C-CN bonds, a reversible transfer of H and CN would occur between alkyl nitriles and alkenes to reach a thermodynamic equilibrium (Fig. 1B). Such a transformation would be particularly powerful because (i) no toxic HCN would be needed nor produced; (ii) both the forward reaction, hydrocyanation, and the reverse reaction, retro-hydrocyanation, would become accessible; and (iii) either reaction pathway could possibly be favored on demand by shifting the equilibrium of the reaction using simple driving forces. Here, we report a broadly applicable (60 examples) strategy for the HCN-free Ni-catalyzed reversible transfer hydrocyanation between alkyl nitriles and alkenes with tunable control over product selectivity (Fig. 1C).

Nickel was initially chosen as the metal catalyst because Ni(0) complexes are very active species in the oxidative addition of polar bonds, including aliphatic C-CN bonds (*36*, *37*). Moreover, Ni(0) complexes have shown high activity in traditional hydrocyanation protocols using hydrogen cyanide (*8*). However, initial experiments using simple nickel catalysts alone failed to afford any product formation. Because Lewis acids can both accelerate the nickel-mediated C-CN oxidative addition (*36*, *37*) and facilitate C-CN reductive elimination (*8*), we reasoned that the addition of a Lewis acid co-catalyst would likely facilitate the proposed reversible transfer hydrocyanation mechanism. An efficient protocol was developed using a nickel catalyst [generated in situ from $Ni(COD)_2$ and DPEphos] and an Al co-catalyst ($AlMe_2Cl$) (see tables S1 and S2 for details). Although $AlMe_2Cl$ is a highly flammable reagent, safety hazards can be reduced through the manipulation of dilute solutions under an inert atmosphere, particularly for small-scale operations. However, with this concern in mind, we demonstrated in preliminary experiments that the nonflammable $AlCl_3$ can be used as a safe alternative co-catalyst in good yield (80%) using slightly higher catalyst loading (Fig. 3A, product **9**). Next, we were faced with the challenge of efficiently manipulating the reaction equilibrium. In particular, our goal was to identify suitable alkene and alkyl nitrile reagents that would allow us to selectively drive the forward reaction from **1**→**2** and the reverse reaction from **2**→**1** under appropriate conditions (Fig. 2). Inspired by other metal-catalyzed reversible reactions, notably the alkene metathesis reaction (*4*), we reasoned that the use of simple driving forces, such as the extrusion of a gaseous side product or the release of ring strain, would efficiently shift the thermodynamic equilibrium to afford the desired product.

In the case of the forward reaction (Fig. 2B), hydrocyanation, we initially evaluated a range of simple aliphatic nitriles (**3**–**6**) as potential hydrocyanating reagents. Two notable trends emerged from these initial experiments: the degree of substitution of the alkene by-product correlated with the efficiency of the reaction in the order isobutylene > propene > ethylene, a result consistent with the relative thermodynamic stability of the alkene by-products; and the formation of gaseous alkenes further improved the system, particularly when conducted in an open apparatus. Thus, isovaleronitrile (**5**), which releases isobutylene as a gaseous by-product, was identified as the best reagent for the hydrocyanation reaction of **1** and gave 86% yield of product **2** in toluene at 100°C in the presence of catalytic Ni and Al complexes.

Alternatively, alkyl nitrile product **2**, formed in the forward reaction, can be used as a test substrate to evaluate the efficiency of diverse alkene traps to drive the retro-hydrocyanation reaction to completion (Fig. 2C). A control reaction using no acceptor alkene did not lead to any appreciable formation of product **1**. This result clearly shows that the formation of HCN and an alkene from an alkyl nitrile is thermodynamically disfavored, emphasizing the need to use an acceptor alkene to drive the process. Both norbornene (NBE, **7**) and norbornadiene (NBD, **8**) were then evaluated because they possess substantial ring strain that should help to drive the retro-hydrocyanation reaction. Gratifyingly, NBD proved efficient as a trapping reagent, affording good yields of the desired alkene product **1** at room temperature (*38*).

We next studied the scope of the hydrocyanation process (Fig. 3A). The transfer hydrocyanation of styrene derivatives gave the products in high yields and good linear-to-branched ratios (up to 88% for monosubstituted styrenes and full linear selectivity in the case of disubstituted styrenes **2**, **14**, and **15**), an anti-Markovnikov selectivity complementary to previous protocols giving mostly the chiral, branched isomer (*8*, *9*, *11*, *20*, *22*). This reversal of regioselectivity likely stems from the reversible nature of the hydrocyanation under our reaction conditions, producing the thermodynamically more stable linear isomer as the major product. Excitingly, a range of medicinally relevant heterocycles (thiazole, indole, pyrazine, and pyridine **17**–**20**) were tolerated and gave usually good yields and linear selectivities. Nonactivated, terminal aliphatic alkenes were also very active substrates in the transformation and gave the linear isomers as the major products [up to 100% linear selectivity in the case of sterically congested substrates (**27**, **28**, **29**)]. In particular, allylic alcohol derivatives were excellent substrates in the transformation (**27**, **28**). Further aliphatic substrates, such as cycloalkenes (**24**, **25**, and **26**) and strained norbornenes (**33** and **34**) were well tolerated and afforded the cyanated products in high yields. The method is useful for the preparation of medicinally relevant scaffolds, as exemplified by product **38** (a precursor of nabumetone) and **39** (precursor of pheniramine). Our catalytic reaction could also be extended to the efficient hydrocyanation of both

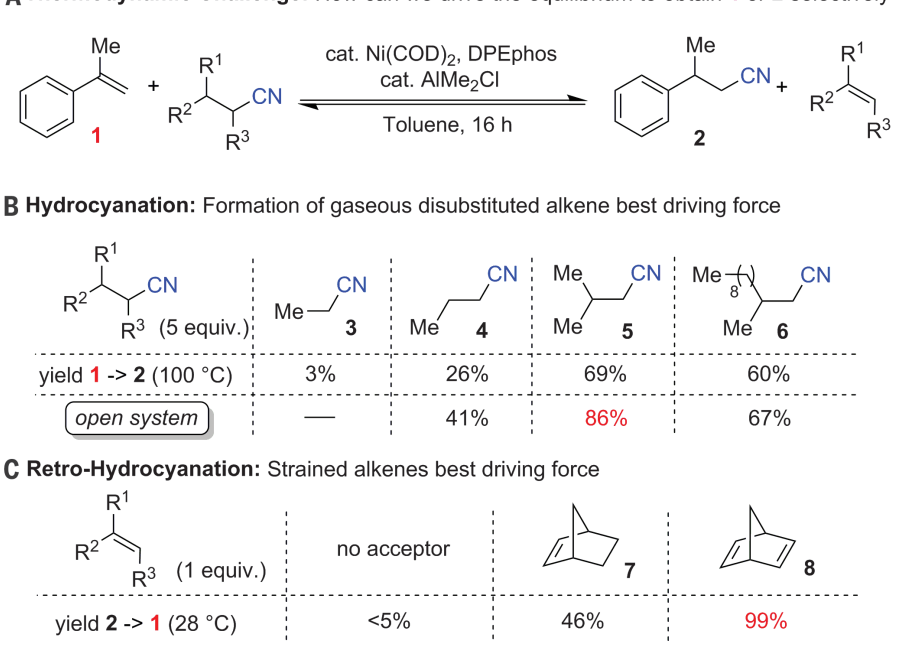


Fig. 2. Selective manipulation of the alkene/nitrile equilibrium. (**A**) Model reaction. (**B**) Reagent optimization for hydrocyanation **1**→**2**. (**C**) Reagent optimization for retro-hydrocyanation **2**→**1**.

conjugated (**36**, **37**) and aliphatic alkynes (**35**) in good yield and regioselectivity. Beyond the tolerance to the above-mentioned heterocyclic sytems, the transformation is also compatible with a wide range of functional groups [F, Cl, ether, ester, ketone, silyl, OBn (benzyloxy), OTBS (dimethyltertbutylsilyloxy), NTs (tosylamino), aniline, imide, trisubstituted double bond] commonly encountered in target-oriented synthesis. Unprotected alcohols and dienes proved unreactive under the reaction conditions and illustrate the current limitations of the reaction. The efficient use of the method in the late-stage transfer hydrocyanation of a cedrene (**42**), sclareol (**43**), tyrosine (**44**), and estrone (**45**) derivative further demonstrates its potential on more complex molecular scaffolds (Fig. 3B). Finally, the reaction of styrene, acetoxystyrene, and cedrene could be performed on a preparative, multigram scale using inexpensive butyronitrile (**4**) as a reagent and solvent and 2 mol% of Ni catalyst to give the products in excellent yields after distillation (Fig. 3C). Overall, the excellent scope and broad functional group tolerance demonstrate the potential of the transfer hydrocyanation reaction to be applied in routine chemical synthesis.

The scope of the retro-hydrocyanation reaction was then studied (Fig. 4A). A range of styrene derivatives could be efficiently prepared by retro-hydrocyanation of primary, secondary, and even tertiary nitriles. Simple aliphatic substrates afforded the desired alkenes with no or little isomerization at room temperature using NBD as an acceptor. This result is noteworthy because of the known propensity of Ni-H intermediates to catalyze the rapid isomerization of alkenes, usually leading to a mixture of products (*7*). Two terpene derivatives (**66** and **68**) were easily transformed into the corresponding aliphatic diene products. When the less strained NBE (**7**) was used as an alkene trap instead of NBD (**8**), the thermodynamically more stable alkene isomer (**75**) was obtained from a tandem retro-hydrocyanation/isomerization process (Fig. 4B). The two protocols are thus complementary, a synthetically attractive result likely due to a fine reactivity balance between the rate of Ni-H insertion into the acceptor alkene and Ni-H catalyzed isomerization. The divergent selectivity observed when using NBE instead of NBD suggests that the hydrocyanation of these reagents is irreversible under the reaction conditions. To clearly illustrate the synthetic power of the reaction, the retro-hydrocyanation was applied to alkene synthesis using CN as a removable activating group in C-C bond coupling reactions (Fig. 4, C and D). First, the synthesis of complex aromatic products from dienes could be realized through a Diels-Alder addition with fumaronitrile

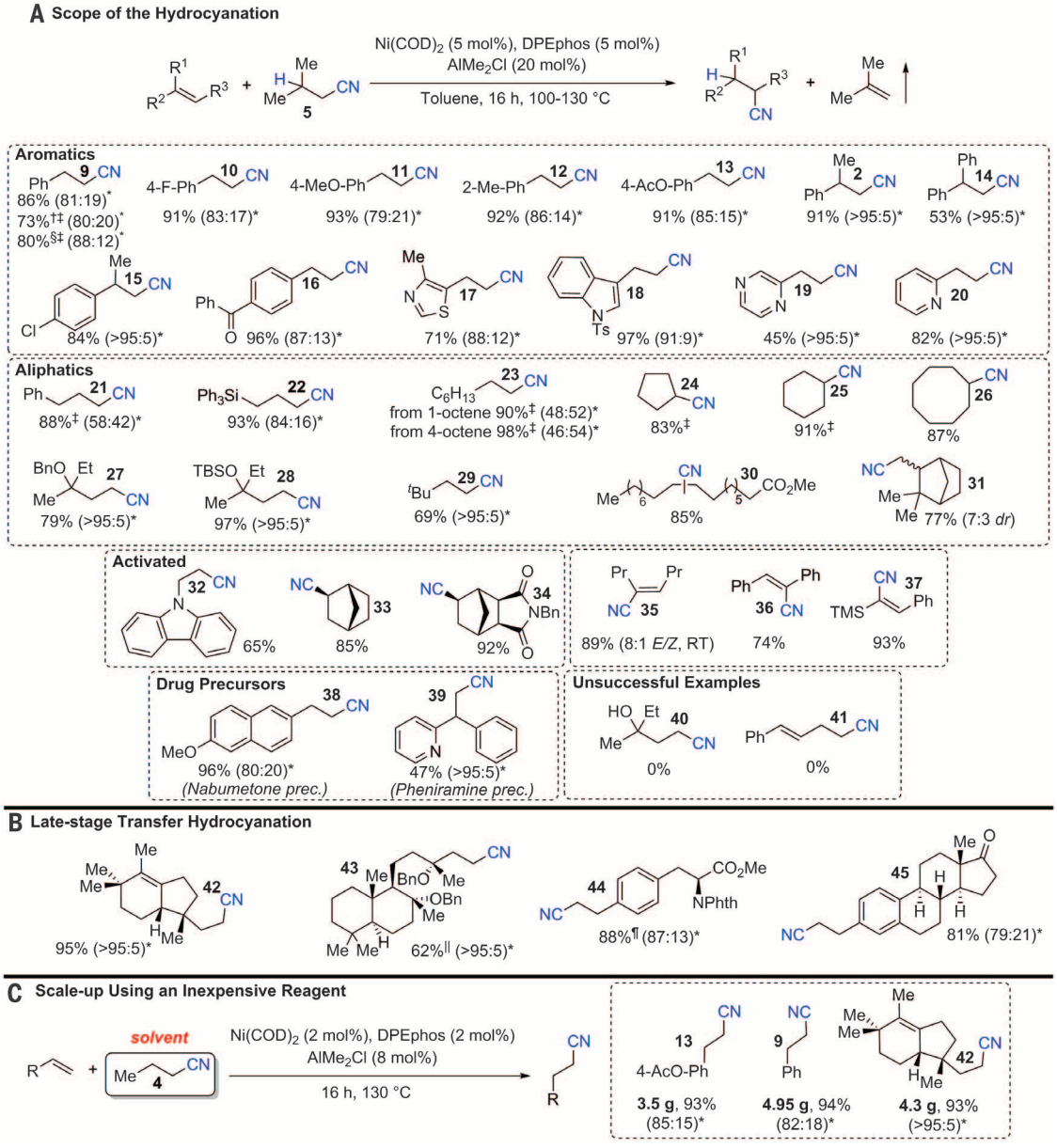


Fig. 3. Exploration of hydrocyanation substrate scope. (**A**) Scope with simple substrates using 5 equiv. of **5**. (**B**) Late-stage transfer hydrocyanation. (**C**) Scale-up experiment. All yields, unless otherwise noted, are isolated yields. *Ratio of linear to branched products. †1.5 equiv. of **5**. ‡GC yield. §10 mol % Ni catalyst, 10 mol % DPEphos, 40 mol % $AlCl_3$. ||10 mol % Ni catalyst. ¶15 equiv. of **5** used as reagent, 15 mol % Ni catalyst. Chiral products in (A) were obtained as racemic mixtures. *dr*: diastereomeric ratio. *E*/*Z*: ratio between *E*-alkene isomer and *Z*-alkene isomer. GC: gas chromatography.

followed by facile retro-hydrocyanation reaction giving the new products **76**, **77,** and **78** in excellent yields. Additionnally, when combined with a literature procedure (*39*), the retro-hydrocyanation reaction could be applied to the challenging, stereoselective late-stage incorporation of a chiral quaternary vinyl group (*40*) into an estrone derivative (**81**). These results show promise for the immediate application of the retro-hydrocyanation reaction to the laboratory-scale synthesis of complex unsaturated small molecules.

Finally, we performed preliminary mechanistic experiments in support of the proposed transfer mechanism (fig. S1). First, a deuterium-labeled nitrile substrate (***d*-2**) was subjected to the reaction conditions with norbornadiene as an acceptor alkene (fig. S1A). The corresponding deuterated adduct **82** was isolated in 80% yield with 80% D-atom incorporation at the position cis to the nitrile group, unambiguously confirming the transfer of the D and CN moiety between the two substrates. Additionally, the stereochemistry of the product indicates an overall syn-addition mechanism, consistent with previously reported labeling experiments (*14*). We also performed an experiment to evaluate the time scale to reach thermodynamic equilibrium under the reaction conditions (fig. S1B). For that purpose, we designed two transfer experiments using compounds $\mathbf{A_{CN}}$, $\mathbf{B_{OL}}$, $\mathbf{A_{OL}}$, and $\mathbf{B_{CN}}$. $\mathbf{A_{CN}}$ and $\mathbf{B_{OL}}$ were used as starting materials in one experiment, while in a second experiment, $\mathbf{A_{OL}}$ and $\mathbf{B_{CN}}$ were employed. If the reaction mixture were to

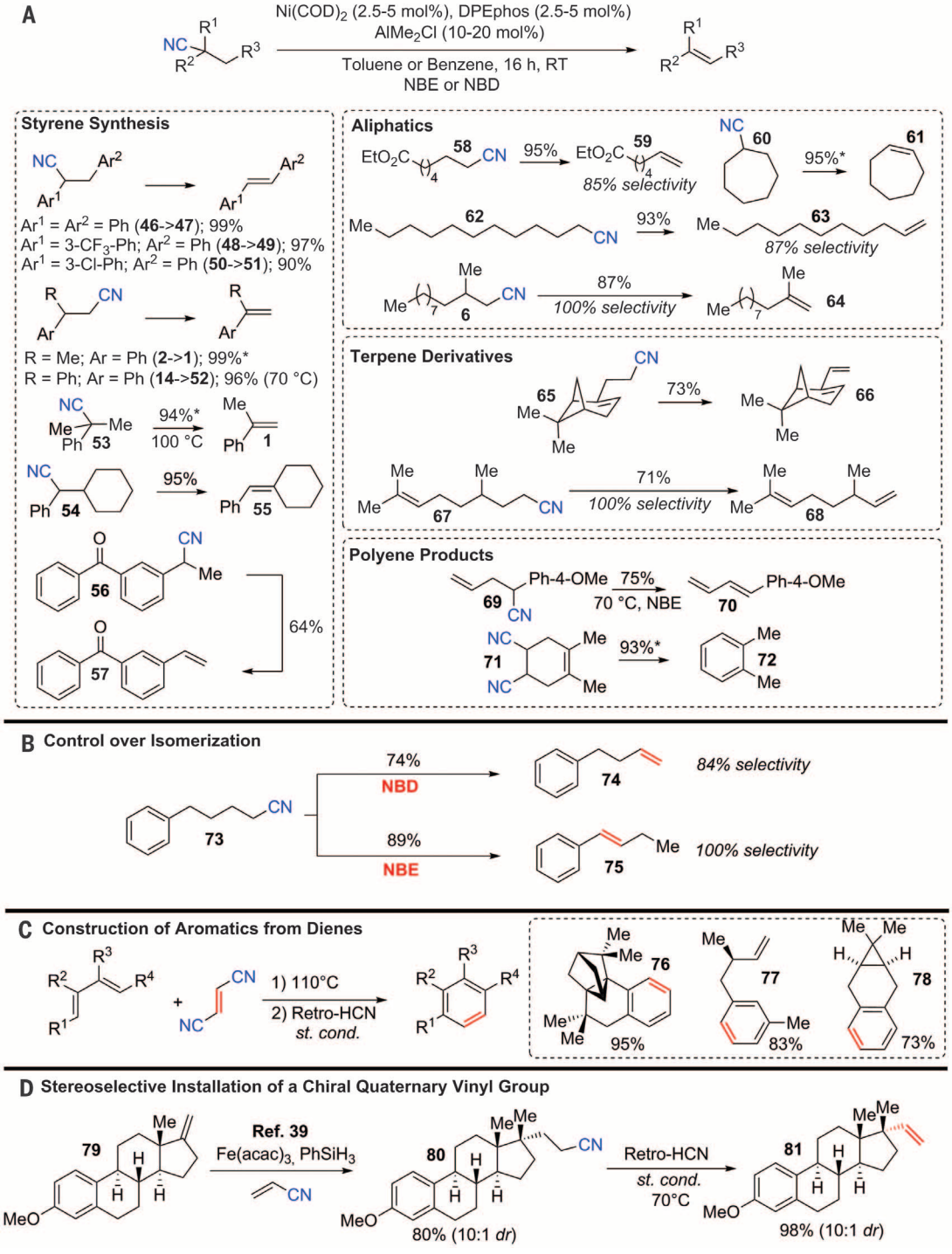


Fig. 4. Exploration of retro-hydrocyanation substrate scope. (**A**) Scope with simple substrates. (**B**) Divergent product selectivity via control of isomerization. (**C**) Synthesis of complex aromatic products. (**D**) Installation of vinyl groups. All yields, unless otherwise noted, are isolated yields. *GC yield.

reach the thermodynamic equilibrium under our reaction conditions, the final concentrations of all the four compounds should be the same in both experiments. The experimental results matched the prediction very well, and nearly identical final concentrations of all the four reaction components were obtained in both experiments. Thus, we can conclude that the reaction of these substrates is reversible and that thermodynamic equilibrium can be reached under our normal reaction conditions. Collectively, these preliminary mechanistic experiments strongly support the proposed transfer mechanism shown in Fig. 1B.

In a broader context, the functional group metathesis strategy delineated in this work will likely stimulate the development of reversible hydrofunctionalization reactions of alkenes that elude the use of hazardous gases in the laboratory.

REFERENCES AND NOTES

1. P. Pollak, G. Romeder, F. Hagedorn, H. Gelbke, "Nitriles," in *Ullman's Encyclopedia of Industrial Chemistry* (Wiley-VCH, Weinheim, Germany, ed. 5, 1985), vol. A17, p. 363.
2. M. B. Smith, J. March, *March's Advanced Organic Chemistry: Reactions, Mechanisms, and Structure* (Wiley-Interscience, Hoboken, NJ, ed. 6, 2007).
3. S. Patai, J. Zabicky, Eds., "The Alkenes: Volumes 1 and 2," in *PATAI's Chemistry of Functional Groups* (Wiley, 1964/1970).
4. R. H. Grubbs, *Handbook of Metathesis* (Wiley-VCH, Weinheim, Germany, 2003).
5. W. C. Drinkard Jr., US 3496218A, **1970**.
6. P. W. N. M. van Leeuwen, *Homogeneous Catalysis: Understanding the Art* (Springer, Netherlands, 2004), chap. 5.
7. J. F. Hartwig, *Organotransition Metal Catalysis* (Palgrave Macmillan, 2009), pp. 668–676.
8. L. Bini, C. Müller, D. Vogt, *ChemCatChem* **2**, 590–608 (2010).
9. A. L. Casalnuovo, T. V. Rajanbabu, "Transition-metal-catalyzed alkene and alkyne hydrocyanations," in *Transition Metals for Organic Synthesis: Building Blocks and Fine Chemicals*, M. Beller, C. Bolm, Eds. (Wiley-VCH, 2008), chapter 2.5.
10. M. Beller, J. Seayad, A. Tillack, H. Jiao, *Angew. Chem. Int. Ed.* **43**, 3368–3398 (2004).
11. T. V. Rajanbabu, *Org. React.* **75**, 1–74 (2011).
12. C. A. Tolman, R. J. Mckinney, W. C. Seidel, J. D. Druliner, W. R. Stevens, *Adv. Catal.* **33**, 1–46 (1985).
13. C. A. Tolman, W. C. Seidel, J. D. Druliner, P. J. Domaille, *Organometallics* **3**, 33–38 (1984).
14. J. E. Bäckvall, O. S. Andell, *Organometallics* **5**, 2350–2355 (1986).
15. N. M. Brunkan, D. M. Brestensky, W. D. Jones, *J. Am. Chem. Soc.* **126**, 3627–3641 (2004).
16. B. Gaspar, E. M. Carreira, *Angew. Chem. Int. Ed.* **46**, 4519–4522 (2007).
17. S. L. Buchwald, S. J. LaMaire, *Tetrahedron Lett.* **28**, 295–298 (1987).
18. G. Romeder, Hydrogen Cyanide. *e-EROS Encyclopedia of Reagents for Organic Synthesis* (2001).
19. HCN LD_{50} (intravenous): 1.1 mg/Kg. *Medical Management of Chemical Casualties Handbook*. United States Army Medical Research Institute of Chemical Defense (USAMRICD).
20. M. de Greef, B. Breit, *Angew. Chem. Int. Ed.* **48**, 551–554 (2009).
21. M. J. Baker, P. G. Pringle, *J. Chem. Soc. Chem. Commun.* **18**, 1292–1293 (1991).
22. A. Falk, A.-L. Göderz, H.-G. Schmalz, *Angew. Chem. Int. Ed.* **52**, 1576–1580 (2013).
23. S. A. Haroutounian, Acetone cyanohydrin. *e-EROS Encyclopedia of Reagents for Organic Synthesis* (2001).
24. W. C. Groutas, Cyanotrimethylsilane. *e-EROS Encyclopedia of Reagents for Organic Synthesis* (2001).
25. A. L. Casalnuovo, T. V. Rajanbabu, T. A. Ayers, T. H. Warren, *J. Am. Chem. Soc.* **116**, 9869–9882 (1994).
26. W. Goertz *et al.*, *J. Chem. Soc., Dalton Trans.* **18**, 2981–2988 (1998).
27. D. R. Lide, Ed., *CRC Handbook of Chemistry and Physics, Internet Version 2005* (CRC Press, Boca Raton, FL, 2005).
28. Heat of formation (*27*) of ethene (52.4 KJ/mol), HCN (135.1 KJ/mol), and propanenitrile (51.7 KJ/mol) indicate that hydrocyanation is exothermic whereas retro-hydrocyanation is endothermic.
29. C. R. Landis, *Science* **347**, 29–30 (2015).
30. Y. J. Park, J.-W. Park, C.-H. Jun, *Acc. Chem. Res.* **41**, 222–234 (2008).
31. S. K. Murphy, J.-W. Park, F. A. Cruz, V. M. Dong, *Science* **347**, 56–60 (2015).
32. S. Kusumoto, T. Tatsuki, K. Nozaki, *Angew. Chem. Int. Ed.* **54**, 8458–8461 (2015).
33. A. S. Goldman *et al.*, *Science* **312**, 257–261 (2006).
34. G. E. Dobereiner, R. H. Crabtree, *Chem. Rev.* **110**, 681–703 (2010).
35. J. R. Zbieg, E. Yamaguchi, E. L. McInturff, M. J. Krische, *Science* **336**, 324–327 (2012).
36. Y. Nakao, A. Yada, S. Ebata, T. Hiyama, *J. Am. Chem. Soc.* **129**, 2428–2429 (2007).
37. A. Yada, T. Yukawa, H. Idei, Y. Nakao, T. Hiyama, *Bull. Chem. Soc. Jpn.* **83**, 619–634 (2010).
38. P. R. Khoury, J. D. Goddard, W. Tam, *Tetrahedron* **60**, 8103–8112 (2004).
39. J. C. Lo, Y. Yabe, P. S. Baran, *J. Am. Chem. Soc.* **136**, 1304–1307 (2014).
40. Y. Liu, S. C. Virgil, R. H. Grubbs, B. M. Stoltz, *Angew. Chem. Int. Ed.* **54**, 11800–11803 (2015).

ACKNOWLEDGMENTS

We thank Z. K. Wickens (Harvard University) and R. H. Grubbs (California Institute of Technology) for critical proofreading of this manuscript. Generous funding from the Max-Planck-Society and the Max-Planck-Institut für Kohlenforschung is acknowledged. We thank B. List for sharing analytical equipment, and our nuclear magnetic resonance, gas chromatography, and mass spectrometry departments for technical assistance. P.Y. thanks the China Scholarship Council for a scholarship. A provisional patent application has been filed on this reaction.

SUPPLEMENTARY MATERIALS

www.sciencemag.org/content/351/6275/832/suppl/DC1
Materials and Methods
Fig. S1
Tables S1 and S2
References (*41*–*66*)

14 December 2015; accepted 19 January 2016
10.1126/science.aae0427

APPLIED PHYSICS

Nuclear magnetic resonance detection and spectroscopy of single proteins using quantum logic

I. Lovchinsky,[1] A. O. Sushkov,[1,2]* E. Urbach,[1] N. P. de Leon,[1,2]† S. Choi,[1] K. De Greve,[1] R. Evans,[1] R. Gertner,[2] E. Bersin,[1] C. Müller,[3] L. McGuinness,[3] F. Jelezko,[3] R. L. Walsworth,[1,4,5] H. Park,[1,2,5,6]‡ M. D. Lukin[1]‡

Nuclear magnetic resonance spectroscopy is a powerful tool for the structural analysis of organic compounds and biomolecules but typically requires macroscopic sample quantities. We use a sensor, which consists of two quantum bits corresponding to an electronic spin and an ancillary nuclear spin, to demonstrate room temperature magnetic resonance detection and spectroscopy of multiple nuclear species within individual ubiquitin proteins attached to the diamond surface. Using quantum logic to improve readout fidelity and a surface-treatment technique to extend the spin coherence time of shallow nitrogen-vacancy centers, we demonstrate magnetic field sensitivity sufficient to detect individual proton spins within 1 second of integration. This gain in sensitivity enables high-confidence detection of individual proteins and allows us to observe spectral features that reveal information about their chemical composition.

Conventional nuclear magnetic resonance (NMR) spectroscopy relies on detecting the weak magnetization of a thermally polarized ensemble of nuclear spins and therefore typically requires high magnetic fields and macroscopic sample quantities (*1*). Recently, it has been shown that single nitrogen-vacancy (NV) color centers in diamond can serve as atomic-sized magnetometers that are capable of label-free detection of the statistical nuclear polarization of nanoscale ensembles (*2*, *3*), and even single nuclear spins (*4*), under ambient conditions (*5*, *6*). Our method is based on the coherent control of an individual NV center, which is a localized defect in the diamond lattice consisting of a substitutional nitrogen atom and an adjacent vacancy in the carbon lattice. The spin state of the negatively charged NV center has an exceptionally long coherence time, even at room temperature, and its electronic level structure allows efficient, all-optical spin polarization

[1]Department of Physics, Harvard University, Cambridge, MA 02138, USA. [2]Department of Chemistry and Chemical Biology, Harvard University, Cambridge, MA 02138, USA. [3]Institute for Quantum Optics and Center for Integrated Quantum Science and Technology (IQST), Ulm University, D-89081, Ulm, Germany. [4]Harvard-Smithsonian Center for Astrophysics, Cambridge, MA 02138, USA. [5]Center for Brain Science, Harvard University, Cambridge, MA 02138, USA. [6]Broad Institute of MIT and Harvard, 7 Cambridge Center, Cambridge, MA 02142, USA. *Present address: Department of Physics, Boston University, 590 Commonwealth Avenue, Boston, MA 02215, USA. †Present address: Department of Electrical Engineering, Princeton University, Olden Street, Princeton, NJ 08544, USA. **‡Corresponding author. E-mail: lukin@physics.harvard.edu (M.D.L.); hongkun_park@harvard.edu (H.P.)**

reach the thermodynamic equilibrium under our reaction conditions, the final concentrations of all the four compounds should be the same in both experiments. The experimental results matched the prediction very well, and nearly identical final concentrations of all the four reaction components were obtained in both experiments. Thus, we can conclude that the reaction of these substrates is reversible and that thermodynamic equilibrium can be reached under our normal reaction conditions. Collectively, these preliminary mechanistic experiments strongly support the proposed transfer mechanism shown in Fig. 1B.

In a broader context, the functional group metathesis strategy delineated in this work will likely stimulate the development of reversible hydrofunctionalization reactions of alkenes that elude the use of hazardous gases in the laboratory.

REFERENCES AND NOTES

1. P. Pollak, G. Romeder, F. Hagedorn, H. Gelbke, "Nitriles," in *Ullman's Encyclopedia of Industrial Chemistry* (Wiley-VCH, Weinheim, Germany, ed. 5, 1985), vol. A17, p. 363.
2. M. B. Smith, J. March, *March's Advanced Organic Chemistry: Reactions, Mechanisms, and Structure* (Wiley-Interscience, Hoboken, NJ, ed. 6, 2007).
3. S. Patai, J. Zabicky, Eds., "The Alkenes: Volumes 1 and 2," in *PATAI's Chemistry of Functional Groups* (Wiley, 1964/1970).
4. R. H. Grubbs, *Handbook of Metathesis* (Wiley-VCH, Weinheim, Germany, 2003).
5. W. C. Drinkard Jr., US 3496218A, **1970**.
6. P. W. N. M. van Leeuwen, *Homogeneous Catalysis: Understanding the Art* (Springer, Netherlands, 2004), chap. 5.
7. J. F. Hartwig, *Organotransition Metal Catalysis* (Palgrave Macmillan, 2009), pp. 668–676.
8. L. Bini, C. Müller, D. Vogt, *ChemCatChem* **2**, 590–608 (2010).
9. A. L. Casalnuovo, T. V. Rajanbabu, "Transition-metal-catalyzed alkene and alkyne hydrocyanations," in *Transition Metals for Organic Synthesis: Building Blocks and Fine Chemicals*, M. Beller, C. Bolm, Eds. (Wiley-VCH, 2008), chapter 2.5.
10. M. Beller, J. Seayad, A. Tillack, H. Jiao, *Angew. Chem. Int. Ed.* **43**, 3368–3398 (2004).
11. T. V. Rajanbabu, *Org. React.* **75**, 1–74 (2011).
12. C. A. Tolman, R. J. Mckinney, W. C. Seidel, J. D. Druliner, W. R. Stevens, *Adv. Catal.* **33**, 1–46 (1985).
13. C. A. Tolman, W. C. Seidel, J. D. Druliner, P. J. Domaille, *Organometallics* **3**, 33–38 (1984).
14. J. E. Bäckvall, O. S. Andell, *Organometallics* **5**, 2350–2355 (1986).
15. N. M. Brunkan, D. M. Brestensky, W. D. Jones, *J. Am. Chem. Soc.* **126**, 3627–3641 (2004).
16. B. Gaspar, E. M. Carreira, *Angew. Chem. Int. Ed.* **46**, 4519–4522 (2007).
17. S. L. Buchwald, S. J. LaMaire, *Tetrahedron Lett.* **28**, 295–298 (1987).
18. G. Romeder, Hydrogen Cyanide. *e-EROS Encyclopedia of Reagents for Organic Synthesis* (2001).
19. HCN LD_{50} (intravenous): 1.1 mg/Kg. *Medical Management of Chemical Casualties Handbook*. United States Army Medical Research Institute of Chemical Defense (USAMRICD).
20. M. de Greef, B. Breit, *Angew. Chem. Int. Ed.* **48**, 551–554 (2009).
21. M. J. Baker, P. G. Pringle, *J. Chem. Soc. Chem. Commun.* **18**, 1292–1293 (1991).
22. A. Falk, A.-L. Göderz, H.-G. Schmalz, *Angew. Chem. Int. Ed.* **52**, 1576–1580 (2013).
23. S. A. Haroutounian, Acetone cyanohydrin. *e-EROS Encyclopedia of Reagents for Organic Synthesis* (2001).
24. W. C. Groutas, Cyanotrimethylsilane. *e-EROS Encyclopedia of Reagents for Organic Synthesis* (2001).
25. A. L. Casalnuovo, T. V. Rajanbabu, T. A. Ayers, T. H. Warren, *J. Am. Chem. Soc.* **116**, 9869–9882 (1994).
26. W. Goertz *et al.*, *J. Chem. Soc., Dalton Trans.* **18**, 2981–2988 (1998).
27. D. R. Lide, Ed., *CRC Handbook of Chemistry and Physics, Internet Version 2005* (CRC Press, Boca Raton, FL, 2005).
28. Heat of formation (*27*) of ethene (52.4 KJ/mol), HCN (135.1 KJ/mol), and propanenitrile (51.7 KJ/mol) indicate that hydrocyanation is exothermic whereas retro-hydrocyanation is endothermic.
29. C. R. Landis, *Science* **347**, 29–30 (2015).
30. Y. J. Park, J.-W. Park, C.-H. Jun, *Acc. Chem. Res.* **41**, 222–234 (2008).
31. S. K. Murphy, J.-W. Park, F. A. Cruz, V. M. Dong, *Science* **347**, 56–60 (2015).
32. S. Kusumoto, T. Tatsuki, K. Nozaki, *Angew. Chem. Int. Ed.* **54**, 8458–8461 (2015).
33. A. S. Goldman *et al.*, *Science* **312**, 257–261 (2006).
34. G. E. Dobereiner, R. H. Crabtree, *Chem. Rev.* **110**, 681–703 (2010).
35. J. R. Zbieg, E. Yamaguchi, E. L. McInturff, M. J. Krische, *Science* **336**, 324–327 (2012).
36. Y. Nakao, A. Yada, S. Ebata, T. Hiyama, *J. Am. Chem. Soc.* **129**, 2428–2429 (2007).
37. A. Yada, T. Yukawa, H. Idei, Y. Nakao, T. Hiyama, *Bull. Chem. Soc. Jpn.* **83**, 619–634 (2010).
38. P. R. Khoury, J. D. Goddard, W. Tam, *Tetrahedron* **60**, 8103–8112 (2004).
39. J. C. Lo, Y. Yabe, P. S. Baran, *J. Am. Chem. Soc.* **136**, 1304–1307 (2014).
40. Y. Liu, S. C. Virgil, R. H. Grubbs, B. M. Stoltz, *Angew. Chem. Int. Ed.* **54**, 11800–11803 (2015).

ACKNOWLEDGMENTS

We thank Z. K. Wickens (Harvard University) and R. H. Grubbs (California Institute of Technology) for critical proofreading of this manuscript. Generous funding from the Max-Planck-Society and the Max-Planck-Institut für Kohlenforschung is acknowledged. We thank B. List for sharing analytical equipment, and our nuclear magnetic resonance, gas chromatography, and mass spectrometry departments for technical assistance. P.Y. thanks the China Scholarship Council for a scholarship. A provisional patent application has been filed on this reaction.

SUPPLEMENTARY MATERIALS

www.sciencemag.org/content/351/6275/832/suppl/DC1
Materials and Methods
Fig. S1
Tables S1 and S2
References (*41*–*66*)

14 December 2015; accepted 19 January 2016
10.1126/science.aae0427

APPLIED PHYSICS

Nuclear magnetic resonance detection and spectroscopy of single proteins using quantum logic

I. Lovchinsky,[1] A. O. Sushkov,[1,2]* E. Urbach,[1] N. P. de Leon,[1,2]† S. Choi,[1] K. De Greve,[1] R. Evans,[1] R. Gertner,[2] E. Bersin,[1] C. Müller,[3] L. McGuinness,[3] F. Jelezko,[3] R. L. Walsworth,[1,4,5] H. Park,[1,2,5,6]‡ M. D. Lukin[1]‡

Nuclear magnetic resonance spectroscopy is a powerful tool for the structural analysis of organic compounds and biomolecules but typically requires macroscopic sample quantities. We use a sensor, which consists of two quantum bits corresponding to an electronic spin and an ancillary nuclear spin, to demonstrate room temperature magnetic resonance detection and spectroscopy of multiple nuclear species within individual ubiquitin proteins attached to the diamond surface. Using quantum logic to improve readout fidelity and a surface-treatment technique to extend the spin coherence time of shallow nitrogen-vacancy centers, we demonstrate magnetic field sensitivity sufficient to detect individual proton spins within 1 second of integration. This gain in sensitivity enables high-confidence detection of individual proteins and allows us to observe spectral features that reveal information about their chemical composition.

Conventional nuclear magnetic resonance (NMR) spectroscopy relies on detecting the weak magnetization of a thermally polarized ensemble of nuclear spins and therefore typically requires high magnetic fields and macroscopic sample quantities (*1*). Recently, it has been shown that single nitrogen-vacancy (NV) color centers in diamond can serve as atomic-sized magnetometers that are capable of label-free detection of the statistical nuclear polarization of nanoscale ensembles (*2*, *3*), and even single nuclear spins (*4*), under ambient conditions (*5*, *6*). Our method is based on the coherent control of an individual NV center, which is a localized defect in the diamond lattice consisting of a substitutional nitrogen atom and an adjacent vacancy in the carbon lattice. The spin state of the negatively charged NV center has an exceptionally long coherence time, even at room temperature, and its electronic level structure allows efficient, all-optical spin polarization

[1]Department of Physics, Harvard University, Cambridge, MA 02138, USA. [2]Department of Chemistry and Chemical Biology, Harvard University, Cambridge, MA 02138, USA. [3]Institute for Quantum Optics and Center for Integrated Quantum Science and Technology (IQST), Ulm University, D-89081, Ulm, Germany. [4]Harvard-Smithsonian Center for Astrophysics, Cambridge, MA 02138, USA. [5]Center for Brain Science, Harvard University, Cambridge, MA 02138, USA. [6]Broad Institute of MIT and Harvard, 7 Cambridge Center, Cambridge, MA 02142, USA. *Present address: Department of Physics, Boston University, 590 Commonwealth Avenue, Boston, MA 02215, USA. †Present address: Department of Electrical Engineering, Princeton University, Olden Street, Princeton, NJ 08544, USA. **‡Corresponding author. E-mail: lukin@physics.harvard.edu (M.D.L.); hongkun_park@harvard.edu (H.P.)**

Downloaded from on February 18, 2016

and readout. In our approach (Fig. 1), we measure individual Fourier components of the time-varying magnetic field created by a statistically polarized subset of proximal nuclear spins contained within a protein. The transverse magnetization of the spin ensemble undergoes precession at the nuclear Larmor frequency with a phase and amplitude that vary stochastically with every repetition of the sequence. Averaging over many iterations yields a zero mean magnetization but a nonzero variance, which results in a measurable magnetic resonance signal. To use the NV center as a sensor, its spin state is manipulated with a series of periodic microwave pulses separated by free-evolution intervals of length τ (Fig. 1B). This periodic modulation of the NV center spin creates a narrow band-pass frequency filter, allowing phase accumulation when the modulation frequency, defined as $1/\tau$, is close to twice the nuclear Larmor frequency (*5*, *7*, *8*). Varying the spacing between the π pulses yields a frequency spectrum that encodes information about the nuclear spins within the protein. Assuming that the spins are situated on the diamond surface at distance d directly above the NV center, the optimal sensitivity of this technique (defined by the minimum number N of nuclear spins detectable after 1 s of integration) is achieved when the pulse-sequence duration is approximately equal to the coherence time T_2 of the NV electronic spin (*5*) [see (*8*) for derivation]

$$N \approx \frac{16\pi^4 d^6}{(\mu_0 \hbar \gamma_e \gamma_n)^2 \mathcal{F}} \frac{\sqrt{T_2 + T_R}}{T_2^2}$$

Here, $\gamma_e = 1.76 \times 10^{11}$ s^{-1} T^{-1} and γ_n are the electron and nuclear gyromagnetic ratios (for proton spins $\gamma_n = 2.68 \times 10^8$ s^{-1} T^{-1}), d is the NV center depth, μ_0 is the vacuum permeability, $\hbar$ is Planck's constant h divided by 2π, and T_R is the readout time. The readout fidelity $\mathcal{F} = [1 + 2(\alpha_0 + \alpha_1)/(\alpha_0 - \alpha_1)^2]^{-\frac{1}{2}}$ is determined by the mean number of photons α_0, α_1 detected per shot from the $m_s = 0$ and 1 spin sublevels of the NV center, respectively. The readout fidelity encapsulates the effect of photon shot noise and approaches unity for an ideal, projection noise-limited measurement.

One limitation to the sensitivity is due to the imperfect readout of the NV center. For typical fluorescence collection efficiencies, $\mathcal{F} \approx 0.03$ (*8*). Thus, ~10^3 repetitions of the experiment are required to distinguish the fluorescence of the $m_s = 0$ and ± 1 sublevels. To circumvent this imperfection, we use a two-qubit quantum system consisting of an NV center electronic spin and its associated ^{15}N nuclear spin, such that after the sensing sequence, the resulting NV spin can be repeatedly probed without resetting its state via optical pumping (*9*, *10*). We use quantum logic (Fig. 1B) to manipulate the two coupled qubits and to improve readout fidelity [see (*8*) for details]. The experimentally measured gain in the readout fidelity as a function of readout cycles (Fig. 1C, red points) demonstrates an almost 10-fold improvement for several hundred repetitions, as compared with conventional readout (dashed blue line). Although repetitive readout of the electronic spin state leads to an increase in the readout time T_R (*8*), the sensitivity is only weakly dependent on this variable. Therefore, in the regime where T_R is on the order of T_2, we achieve a significant gain in sensitivity.

Another key limitation to the sensitivity is attributable to the decoherence of near-surface NV centers (i.e., those with small d) (*11*). To quantify the effect of the surface on the NV spin coherence, we measure the decoherence rates ($1/T_2$) and depths (*8*) for a large number of NV centers created by implantation of 2-keV ^{15}N ions. As shown in table S1, the depths and decoherence rates of shallow NV centers are inversely correlated. To improve the coherence properties, we use wet oxidative chemistry combined with annealing at 465°C (*12*, *13*) in a dry oxygen environment (*8*). This procedure etches away the diamond surface while improving the coherence times by more than an order of magnitude. When combined with the 10-fold improvement in readout fidelity resulting from quantum logic–based readout, this increase in T_2 yields shallow (3 to 6 nm) NV centers with an overall sensitivity gain greater than a factor of 500 (Fig. 2A), exceeding sensitivities reported in previous experiments (fig. S2). The resulting sensitivity is sufficient to detect a single proton spin or ~10 statistically polarized ^{13}C or ^{2}H spins after 1 s of integration (Fig. 2A) (*8*).

We use our enhanced sensitivity to probe ubiquitin, a small regulatory protein consisting of 76 residues that is found in almost all eukaryotic cells (*14*). The size of this protein (*15*) is on the

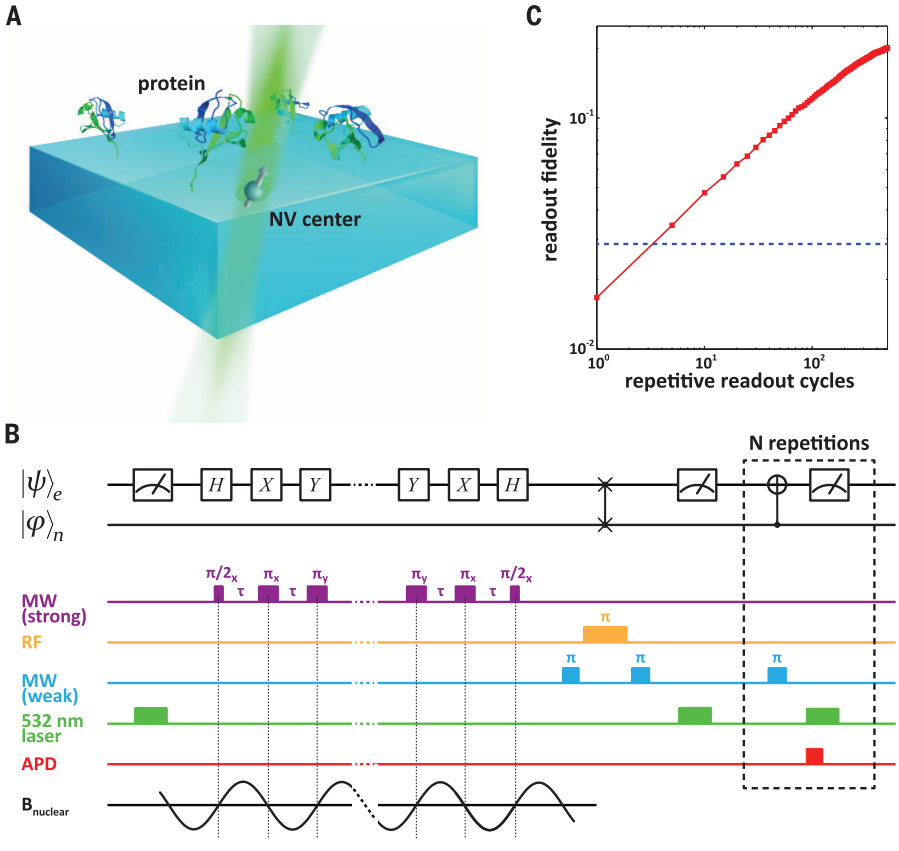


Fig. 1. Experimental setup and magnetometry with repetitive readout. (**A**) Schematic of the experimental setup. Ubiquitin proteins attached to the diamond surface are probed using a proximal quantum sensor consisting of a NV center electronic spin and its associated ^{15}N nuclear spin. The image of ubiquitin was taken from the Protein Data Bank (PDB ID: 1UBQ) (*15*). (**B**) Quantum circuit diagram and experimental magnetometry pulse sequence. Here the NMR signal is measured using a modified XY8-k dynamical decoupling sequence (*8*) and detected using repetitive readout of the electronic spin state. $|\psi\rangle_e$ and $|\varphi\rangle_n$ correspond to the electric and nuclear spin states, respectively. MW and RF correspond to microwave and radio frequency drive fields, respectively. APD denotes the photodetector used for optical measurement. $B_{nuclear}$ corresponds to the magnetic field created by the target nuclear spins. (**C**) Measured gain in the readout fidelity $\mathcal{F}$ as a function of repetitive readout cycles (red curve). The dashed blue line indicates the measured fidelity using conventional readout. The readout fidelity is measured by detecting the average number of photons scattered from the NV center after preparing it in the $m_s = 0$ or 1 sublevel and applying eq. S9 (*8*).

order of the NV detection area/volume (*8*), determined by the NV center depth for $d \sim 3$ to 5 nm. Thus, any observed NMR signals can be attributed to individual or small aggregates of proteins. We immobilize the proteins on the diamond surface by means of carbodiimide cross-linker chemistry (*16*, *17*) [see also Fig. 2B and (*8*)]. We then use atomic force microscopy (AFM) to characterize the topography of the diamond surface after protein attachment (*8*). The AFM images (Fig. 2C) exhibit circular features with heights and radii (Fig. 2D) that are consistent with the known size of the protein. We observe almost no features with height larger than 5 nm, suggesting that our attachment protocol does not lead to aggregation. The resolution in the lateral dimensions is consistent with the limit imposed by the radius of the AFM probe (9 ± 2 nm). We confirm that individual spots in Fig. 2C mostly correspond to individual proteins by conjugating the proteins to Cy3 fluorophores and comparing the resulting mean fluorescence rate with that of optically resolved Cy3+ubiquitin complexes and individual Cy3 dye molecules (*8*). We find that the mean protein spacing, as extracted from optical measurements (20.9 ± 1.4 nm), is in excellent agreement with that based on AFM measurements (21.6 ± 0.4 nm). Importantly, these measurements show that the mean spacing of the proteins is much greater than the typical NV center depth ($d \approx 4$ nm) and the protein size. Due to the strong $\sim 1/r^6$ dependence of the NMR contrast on the NV-protein separation r (*8*), the NMR signal is negligible for proteins located far outside the NV detection area. Therefore, with our protein density, we expect ~10% of NV centers to contain a single protein within their detection areas. The statistical probability of detecting two or more proteins using a single NV center is ~1% (*8*).

To spectrally differentiate the magnetic fields produced by protein nuclear spins from background sources—such as ^{1}H spins on the diamond surface (*18*) and ^{13}C spins in the diamond lattice—we use diamond samples enriched in ^{12}C (99.999% abundance) and proteins enriched in the rare isotopes ^{2}H and ^{13}C (both at >98% abundance). We first carried out NMR measurements on 20 shallow NV centers, with isotopically enriched ubiquitin proteins attached to the diamond surface. Three of the NV probes exhibited NMR signals at both the ^{2}H and ^{13}C Larmor frequencies (*8*). No instances occurred in which only one of these nuclear species was detected. Representative spectra (Fig. 3, A and B) were obtained by varying the spacing of the periodic π pulses. Here, the data were normalized to subtract the effect of NV decoherence (*8*). The ^{2}H and ^{13}C spectra were acquired using XY8-507 and XY8-1011 pulse sequences (*8*), respectively, and measured via 500 repetitive readout cycles. The identities of the nuclear species were verified by observing the linear scalings of the nuclear Larmor frequencies with the applied magnetic field (Fig. 3C, blue and red points).

The spectral resolution Δν of the present method is Fourier-limited by the total duration of the coherent evolution of the quantum spin sensor (Fig. 3D). Note that the 10-fold increase in the coherence time T_2 demonstrated in Fig. 2A directly yields a corresponding 10-fold improvement in spectral resolution (*8*), allowing us to resolve features in the protein spectra and revealing information about its chemical composition.

Figure 3E shows the ^{2}H and ^{13}C NMR spectra (top two panels), corresponding to ubiquitin proteins enriched with ^{2}H and ^{13}C, performed on another NV center. Consistent with the results of Fig. 3, A and B, for the first NV center, we find that the deuterium spectrum exhibits an extremely broad line shape, whereas the ^{13}C spectral width is considerably narrower and is consistent with the Fourier limit. The bottom panel in Fig. 3E shows the ^{13}C NMR spectrum after attaching ubiquitin proteins enriched only in ^{13}C.

We observe a ^{13}C line shape that is significantly broader (~20 kHz) than that of the deuterated proteins. The spectral resolution, determined by the external magnetic field and the number of applied π pulses, is indicated by the shaded green regions in Fig. 3. Figure 3F shows the average deconvolved spectral widths of ^{2}H and ^{13}C, as observed in independent measurements of three NV centers with deuterated proteins and three NV centers with nondeuterated proteins.

Previous studies (*19*) have shown that solid-state ^{2}H NMR spectra typically exhibit line broadening due to the inhomogeneous distribution of quadrupole shifts within the protein

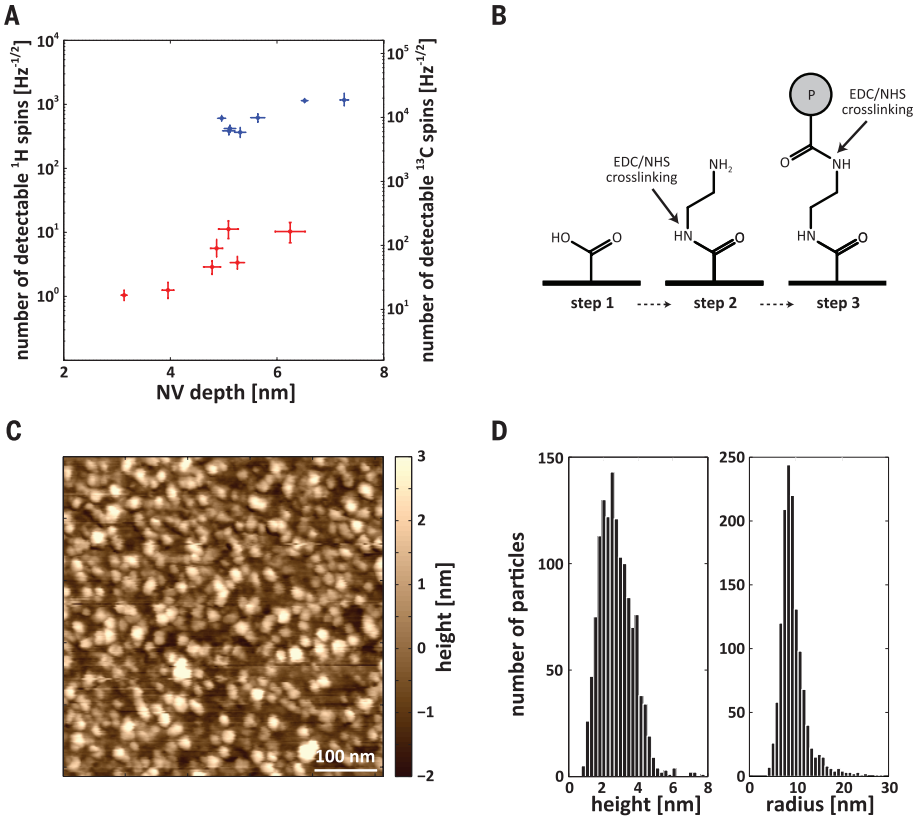


Fig. 2. Surface preparation of diamond samples and single-protein attachment. (**A**) Measured depths and sensitivities (^{1}H and ^{13}C spins) for a representative sample of NV centers before (blue) and after (red) oxygen surface treatment and quantum logic–based readout. See table S1 for numerical values of measured depths and decoherence rates. (**B**) Attachment protocol using carbodiimide cross-linker chemistry (*8*). EDC, 1-ethyl-3-(3-dimethylaminopropyl) carbodiimide; NHS, *N*-hydroxysuccinimide. (**C**) AFM height image of diamond surface after protein attachment. The color bar indicates height values. (**D**) Histograms of heights and radii of circular features in a 1 μm–by–1 μm AFM image (*8*).

(*20*) (see also Fig. 4A). The broadening of our ^{2}H spectra is consistent with this effect. Our ^{2}H NMR signals are probably dominated by the deuterons in methyl groups, which rotate rapidly at room temperature about the methyl group symmetry axis. The remaining (nonaveraged) quadrupolar shifts are on the order of 30 kHz (*19*) (the deuterons in other chemical groups, such as methylene or aromatic groups, give rise to much broader spectral features and, hence, smaller signals). The ^{13}C linewidths are consistent with the expected broadening created by dipolar interactions with proximal ^{2}H (in deuterated proteins) and ^{1}H (in nondeuterated proteins) spins (*19*), with ^{1}H giving rise to broader linewidths due to its larger gyromagnetic ratio.

Our method can be extended in a number of ways. The sensitivity can be further improved by using spin-to-charge readout (*21*) or more advanced pulse sequences that could extend the coherence time to the limit imposed by the population relaxation time T_1 (see, for example, fig. S2B, which shows coherent spin locking for up to 1 ms). Nuclear hyperpolarization (*8*), such as Hartmann-Hahn double resonance (*22*), can also be used to improve sensitivity via direct detection of nuclear magnetic moments rather than their variances. Alternatively, reporter spin–based sensing can be used to reach single-spin sensitivity by resolving individual nuclear spins in a field gradient created by an electronic reporter spin (*4*). Similarly, if background protons can be removed from the diamond surface [protons in liquid water diffuse quickly and do not contribute to the NMR signal (*23*)] by deuteration (*3*), ^{1}H spins, with their large gyromagnetic ratio, can be used for indirect detection of nuclei with low magnetic moments (*24*). In addition, the coupling to a long-lived quantum memory associated with an ancillary nuclear spin qubit and the use of new pulse sequences (*4*, *25*) should allow further improvement in spectral resolution to the limit determined by the lifetime of the nuclear spin ancilla, which could be >10 mHz (*6*). Independently of the NV and nuclear spin manipulation, the detection sensitivity and utility of the method can be greatly enhanced by deterministically positioning the molecules in close proximity to

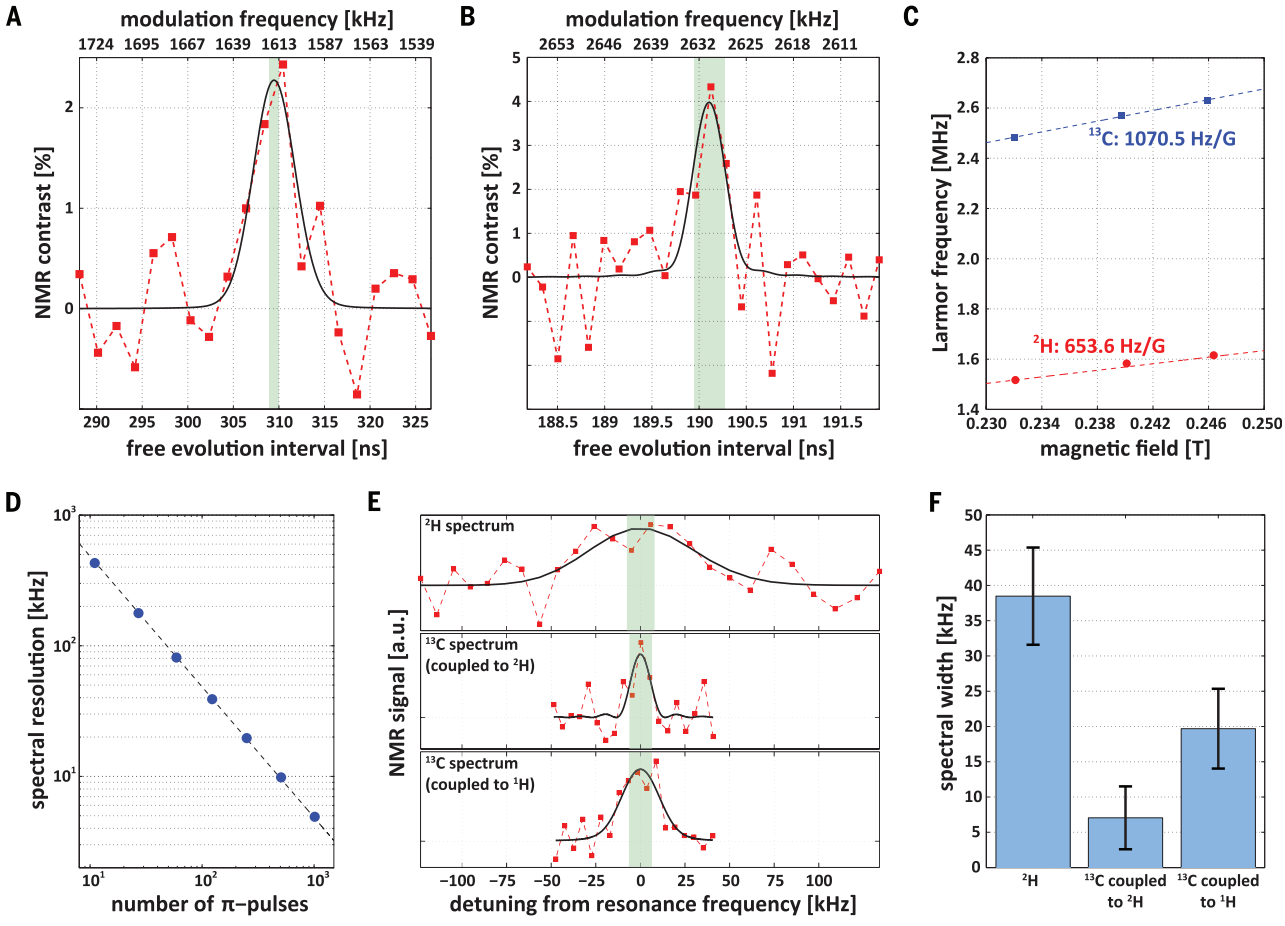


Fig. 3. NMR detection and spectroscopy of individual ubiquitin proteins. (**A**) ^{2}H NMR spectrum at magnetic field B = 2473 G, using the XY8-507 sequence with 500 repetitive readout cycles (red points) and Gaussian fit (black solid line). The spectrum consists of the NV optical signal, normalized by the Rabi contrast and corrected for the reduced contrast caused by decoherence (*8*). (**B**) Analogous ^{13}C NMR spectrum at B = 2457 G, using the XY8-1011 sequence with 500 repetitive readout cycles (red points) and Gaussian fit (black solid line). (**C**) Scalings of resonance frequencies with applied magnetic field. Red and blue points indicate the ^{2}H and ^{13}C resonances, respectively (*8*). The expected scalings based on the known gyromagnetic ratios are indicated with dashed lines. Error bars are approximately on the scale of the marker sizes. (**D**) Measured spectral resolution (blue points) as a function of the number of π pulses. The dashed black line indicates the theoretical limit imposed by the detector filter function (*8*). A 2.63-MHz radio frequency waveform, corresponding to τ = 190 ns and applied using an external coil, was used as the calibration signal. The resulting NMR signal was measured using an XY8 sequence. (**E**) ^{2}H and ^{13}C NMR linewidths (red points) measured on deuterated (top and middle panels) and nondeuterated (bottom panel) ubiquitin proteins. B = 2422 G (top), 2402 G (middle), and 2455 G (bottom). a.u., arbitrary units. In (A), (B), and (E), fitted curves are Gaussian functions, convolved with the detector filter function. Green shaded regions correspond to the spectral resolution (*8*). (**F**) Average spectral widths from several independent measurements of ^{2}H and ^{13}C NMR spectra (*8*). Here, the observed spectra have been deconvolved from the detector filter function to yield the true linewidths [as extracted from fits presented in (*8*)]. Error bars correspond to SEM of the spectral widths, for each of the three categories of spectra. For all ^{13}C spectra of nondeuterated proteins, we verified that the ^{13}C signal disappears when the proteins are removed from the diamond (*8*).

an NV center—for instance, by activating local chemical sites using superresolution microscopy (*26*) or by placing them with a magnetized AFM tip (*27*, *28*). Though at present the inability to position the protein over a desired NV center results in long required integration times (*8*), deterministic placement, combined with a factor of ~3 improvement in coherence time, would enable detection of an individual deuteron after several seconds of integration [see (*8*), section 9].

The demonstrated technique, along with these potential improvements, may enable applications for probing the structure and dynamics of biological systems at the single-molecule level. For example, the single-molecule NMR method using quadrupolar nuclei with nuclear spin $I > 1/2$ can be used to study conformations and electrostatic environments within individual molecules. One can use the dependence of the nuclear spin level structure on the orientation of its quadrupolar axes with respect to the applied magnetic field to determine the spin's electrostatic environment (quadrupole coupling constant $\overline{Q}$ and asymmetry parameter), as well as the orientation of its molecular axes (Fig. 4A) (*19*). In our experiments (Fig. 3E), these quadrupolar shifts result in broadening of the observed spectral lines. However, if the number of nuclear spins in the molecule N_m is such that $\overline{Q}/(N_m\Delta\nu) > 1$, which ensures that the spectral range ~ $\overline{Q}$ is not overcrowded with resonances, the spectral lines associated with individual nuclei can be resolved and analyzed. As an example, Fig. 4B shows the simulated ^{2}H and ^{14}N quadrupolar spectra of a single phenylalanine molecule for two orthogonal orientations (top and upper middle panels) and two distinct conformations (two middle panels). These orientation-dependent shifts wash out in bulk NMR measurements (bottom panel). Yet unlike in bulk NMR with crystallized samples, the weights of the various single-molecule NMR resonances in a finite magnetic field (Fig. 4C) encode information about the positions of the spins within the molecule, thus allowing structural information to be deduced (*8*) regardless of the location of the target molecule.

Our approach provides a set of tools, complementary to conventional NMR, that can be

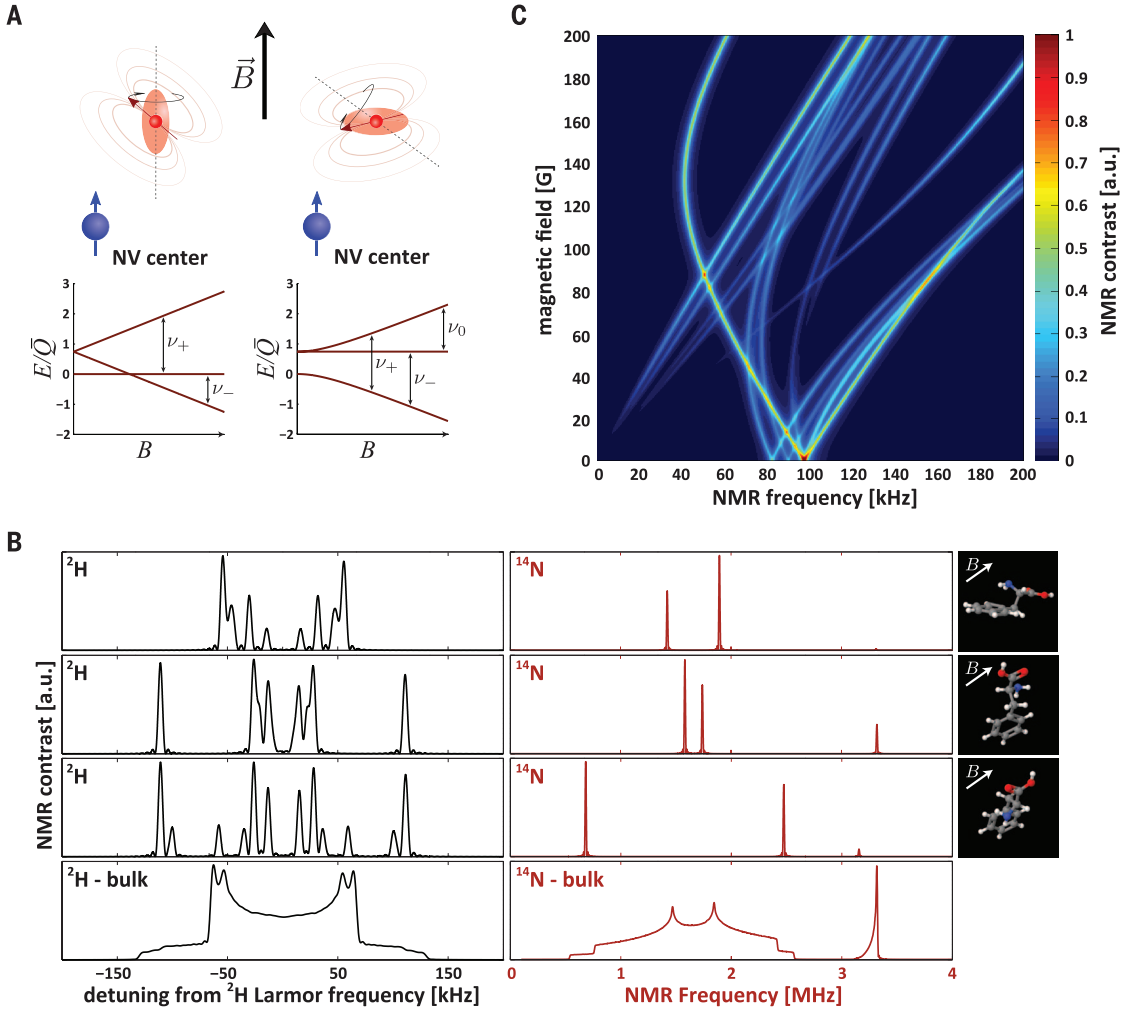


Fig. 4. Proposed analysis of individual molecules. (**A**) Orientation-dependent level structure of quadrupolar nuclear spins in an external magnetic field. The two spin-1 nuclei shown are interacting with a proximal NV center through magnetic dipole-dipole interactions. The major axes of the ellipses denote the orientation of the molecular axis. The quantization axis in each case is indicated by the dashed line. The effect of a nonzero asymmetry parameter is neglected. Allowed transitions ($\nu_\pm$ and ν_0) are indicated by arrows (*8*). *E*, energy. (**B**) Simulated quadrupolar ^{2}H and ^{14}N spectra of deuterated phenylalanine in two orthogonal orientations relative to the diamond surface (top and upper middle panels), two distinct conformations (two middle panels), and the simulated bulk spectra (bottom panels), where all possible orientations contribute equally to the spectrum. Images of phenylalanine (at right) were taken from the Protein Data Bank (PDB ID: PHE) and visualized using Jmol (www.jmol.org/). For the case of ^{2}H, only the spectral lines corresponding to $\nu_\pm$ (*8*) are shown. We assume that a magnetic field of 0.5 T is applied along the NV symmetry axis. (**C**) Magnetic field dependence of the ^{2}H spectrum corresponding to the lower middle panel at left in (B), at low magnetic field. The color bar represents NMR contrast.

used to probe the structure and dynamics of biological and chemical systems at the single-molecule level and reveal properties normally obscured in ensemble measurements. With additional improvements in sensitivity, these tools (*8*) can potentially be applicable to NMR-based label-free detection and analysis of single molecules; characterization of structural and conformational changes in systems that are not easily accessible by conventional techniques; and studies of dynamic phenomena, such as protein folding (*29*) and enzyme-substrate interactions at the single-molecule level (*30*).

REFERENCES AND NOTES

1. P. Glover, S. P. Mansfield, *Rep. Prog. Phys.* **65**, 1489–1511 (2002).
2. H. J. Mamin *et al.*, *Science* **339**, 557–560 (2013).
3. T. Staudacher *et al.*, *Science* **339**, 561–563 (2013).
4. A. O. Sushkov *et al.*, *Phys. Rev. Lett.* **113**, 197601 (2014).
5. J. M. Taylor *et al.*, *Nat. Phys.* **4**, 810–816 (2008).
6. L. Childress, R. L. Walsworth, M. D. Lukin, *Phys. Today* **67**, 38–43 (2014).
7. S. Kolkowitz, Q. P. Unterreithmeier, S. D. Bennett, M. D. Lukin, *Phys. Rev. Lett.* **109**, 137601 (2012).
8. Materials, methods, and supplementary text are available as supplementary materials on *Science* Online.
9. L. Jiang *et al.*, *Science* **326**, 267–272 (2009).
10. P. Neumann *et al.*, *Science* **329**, 542–544 (2010).
11. Y. Romach *et al.*, *Phys. Rev. Lett.* **114**, 017601 (2015).
12. Y. Chu *et al.*, *Nano Lett.* **14**, 1982–1986 (2014).
13. M. Kim *et al.*, *Appl. Phys. Lett.* **105**, 042406 (2014).
14. G. Goldstein *et al.*, *Proc. Natl. Acad. Sci. U.S.A.* **72**, 11–15 (1975).
15. S. Vijay-Kumar, C. E. Bugg, W. J. Cook, *J. Mol. Biol.* **194**, 531–544 (1987).
16. J. C. Sheehan, P. A. Cruickshank, G. L. Boshart, *J. Org. Chem.* **26**, 2525–2528 (1961).
17. A. O. Sushkov *et al.*, *Nano Lett.* **14**, 6443–6448 (2014).
18. M. Loretz, S. Pezzagna, J. Meijer, C. L. Degen, *Appl. Phys. Lett.* **104**, 033102 (2014).
19. D. B. Zax, A. Bielecki, K. W. Zilm, A. Pines, D. P. Weitekamp, *J. Chem. Phys.* **83**, 4877–4905 (1985).
20. T. P. Das, E. L. Hahn, *Nuclear Quadrupole Resonance Spectroscopy* (Academic Press, 1958).
21. B. J. Shields, Q. P. Unterreithmeier, N. P. de Leon, H. Park, M. D. Lukin, *Phys. Rev. Lett.* **114**, 136402 (2015).
22. P. London *et al.*, *Phys. Rev. Lett.* **111**, 067601 (2013).
23. T. Staudacher *et al.*, *Nat. Commun.* **6**, 8527 (2015).
24. S. Cavadini, *Prog. Nucl. Magn. Reson. Spectrosc.* **56**, 46–77 (2010).
25. A. Ajoy, U. Bissbort, M. D. Lukin, R. L. Walsworth, P. Cappellaro, *Phys. Rev. X* **5**, 011001 (2015).
26. T. A. Klar, R. Wollhofen, J. Jacak, *Phys. Scr.* **2014**, 014049 (2014).
27. D. Rugar, R. Budakian, H. J. Mamin, B. W. Chui, *Nature* **430**, 329–332 (2004).
28. C. L. Degen, M. Poggio, H. J. Mamin, C. T. Rettner, D. Rugar, *Proc. Natl. Acad. Sci. U.S.A.* **106**, 1313–1317 (2009).
29. H. S. Chung, K. McHale, J. M. Louis, W. A. Eaton, *Science* **335**, 981–984 (2012).
30. I. A. Yudushkin *et al.*, *Science* **315**, 115–119 (2007).

ACKNOWLEDGMENTS

We thank M. L. Pham, N. Chisholm, G. Kucsko, B. Harada, A. Ajoy, and P. Cappellaro for helpful discussions and experimental help. This work was supported by the Defense Advanced Research Projects Agency (QuASAR program), NSF, the Center for Ultracold Atoms, the Army Research Office Multidisciplinary University Research Initiative, the National Security Science and Engineering Faculty Fellowship program, and the Gordon and Betty Moore Foundation. I.L. was supported by the Air Force Office of Scientific Research National Defense Science and Engineering Graduate Fellowship (32 CFR 168a). Work at Ulm University was supported by the European Research Council. L.M. acknowledges support by a German Academic Exchange Service (DAAD) P.R.I.M.E. Fellowship. E.B. was supported by the Herchel Smith–Harvard Undergraduate Summer Research Program.

SUPPLEMENTARY MATERIALS

www.sciencemag.org/content/351/6275/836/suppl/DC1
Materials and Methods
Supplementary Text
Figs. S1 to S10
Table S1
References (*31*–*38*)

3 November 2015; accepted 21 January 2016
Published online 4 February 2016
10.1126/science.aad8022

NANOMATERIALS

DNA-controlled dynamic colloidal nanoparticle systems for mediating cellular interaction

Seiichi Ohta,[1,2] Dylan Glancy,[1,3] Warren C. W. Chan[1,3,4,5]*

Precise control of biosystems requires development of materials that can dynamically change physicochemical properties. Inspired by the ability of proteins to alter their conformation to mediate function, we explored the use of DNA as molecular keys to assemble and transform colloidal nanoparticle systems. The systems consist of a core nanoparticle surrounded by small satellites, the conformation of which can be transformed in response to DNA via a toe-hold displacement mechanism. The conformational changes can alter the optical properties and biological interactions of the assembled nanosystem. Photoluminescent signal is altered by changes in fluorophore-modified particle distance, whereas cellular targeting efficiency is increased 2.5 times by changing the surface display of targeting ligands. These concepts provide strategies for engineering dynamic nanotechnology systems for navigating complex biological environments.

Fundamental studies on the interactions of nanoparticle designs with biomolecules, cells, tissues, and organs are providing guiding principles with which to build nanosystems for imaging, diagnosis, and the treatment of disease. An optimal nanoparticle physicochemical property (for example, size, shape, and surface chemistry) for biological use varies with time and place within the living body, and current nanoparticle designs do not have the engineering range to meet these design requirements (*1*–*3*). For example, rod-shaped particles are reported to be preferable for tumor penetration (*4*), whereas spherical nanoparticles are better for subsequent cellular uptake by cancer cells (*5*); nanoparticles coated with polymer polyethylene glycol (PEG) can increase blood circulation time by reducing serum protein adsorption and macrophage uptake (*6*) but can impede surface-coated antibodies from cell targeting (*7*). These variations have inspired the development of interactive nanoparticle systems that can alter their properties in response to biological stimuli (*8*–*10*). However, dynamic control over the physicochemical properties of nanoparticles, especially particle shape, remains a challenge. DNA provides exquisite control and flexibility in engineering the physicochemical, morphological, optical, and electrical properties of three-dimensional (3D) nanosystems (*11*–*14*). But these DNA-assembled structures have not been fully exploited for cellular and biological application. We explored the use of DNA to assemble shape-shifting nanostructures with controlled biological function.

We used single-stranded DNA–functionalized gold nanoparticles (AuNPs) of different sizes (denoted as large, medium, and small) as building blocks to assemble shape-changing nanostructures (Fig. 1A and fig. S1). Each AuNP was functionalized with two DNA sequences: one for nanostructure assembly and the other for shape-changing (*15*). Valencies of these nanoparticles were 114, 25, and 6 DNA strands on 13-, 6-, and 3-nm AuNPs, respectively (fig. S2). The nanoparticle building blocks were assembled into "core-satellite" structures (*16*, *17*) by a linker DNA strand (L1 and L2) whose ends were complementary to two different nanoparticle types. The assembled nanostructure consists of a large core with surrounding satellites of medium and small size (Fig. 1, assembly morphology 1). An important design feature here is that the linkage between the core and the small satellites contains a single-stranded

[1]Institute of Biomaterials and Biomedical Engineering, Donnelly Center for Cellular and Biomolecular Research, University of Toronto, 164 College Street, Toronto, ON M5S 3G9, Canada. [2]Center for Disease Biology and Integrative Medicine, University of Tokyo, 7-3-1 Hongo, Bunkyo-ku, Tokyo, 113-0033, Japan. [3]Department of Chemistry, University of Toronto, 80 St. George Street, Toronto, ON M5S 3H6, Canada. [4]Department of Chemical Engineering, University of Toronto, 200 College Street, Toronto, ON M5S 3E5, Canada. [5]Department of Material Science and Engineering, University of Toronto, 160 College Street, Room 450, University of Toronto, Toronto, ON M5S 3E1, Canada.
***Corresponding author. E-mail: warren.chan@utoronto.ca**

used to probe the structure and dynamics of biological and chemical systems at the single-molecule level and reveal properties normally obscured in ensemble measurements. With additional improvements in sensitivity, these tools (*8*) can potentially be applicable to NMR-based label-free detection and analysis of single molecules; characterization of structural and conformational changes in systems that are not easily accessible by conventional techniques; and studies of dynamic phenomena, such as protein folding (*29*) and enzyme-substrate interactions at the single-molecule level (*30*).

REFERENCES AND NOTES

1. P. Glover, S. P. Mansfield, *Rep. Prog. Phys.* **65**, 1489–1511 (2002).
2. H. J. Mamin *et al.*, *Science* **339**, 557–560 (2013).
3. T. Staudacher *et al.*, *Science* **339**, 561–563 (2013).
4. A. O. Sushkov *et al.*, *Phys. Rev. Lett.* **113**, 197601 (2014).
5. J. M. Taylor *et al.*, *Nat. Phys.* **4**, 810–816 (2008).
6. L. Childress, R. L. Walsworth, M. D. Lukin, *Phys. Today* **67**, 38–43 (2014).
7. S. Kolkowitz, Q. P. Unterreithmeier, S. D. Bennett, M. D. Lukin, *Phys. Rev. Lett.* **109**, 137601 (2012).
8. Materials, methods, and supplementary text are available as supplementary materials on *Science* Online.
9. L. Jiang *et al.*, *Science* **326**, 267–272 (2009).
10. P. Neumann *et al.*, *Science* **329**, 542–544 (2010).
11. Y. Romach *et al.*, *Phys. Rev. Lett.* **114**, 017601 (2015).
12. Y. Chu *et al.*, *Nano Lett.* **14**, 1982–1986 (2014).
13. M. Kim *et al.*, *Appl. Phys. Lett.* **105**, 042406 (2014).
14. G. Goldstein *et al.*, *Proc. Natl. Acad. Sci. U.S.A.* **72**, 11–15 (1975).
15. S. Vijay-Kumar, C. E. Bugg, W. J. Cook, *J. Mol. Biol.* **194**, 531–544 (1987).
16. J. C. Sheehan, P. A. Cruickshank, G. L. Boshart, *J. Org. Chem.* **26**, 2525–2528 (1961).
17. A. O. Sushkov *et al.*, *Nano Lett.* **14**, 6443–6448 (2014).
18. M. Loretz, S. Pezzagna, J. Meijer, C. L. Degen, *Appl. Phys. Lett.* **104**, 033102 (2014).
19. D. B. Zax, A. Bielecki, K. W. Zilm, A. Pines, D. P. Weitekamp, *J. Chem. Phys.* **83**, 4877–4905 (1985).
20. T. P. Das, E. L. Hahn, *Nuclear Quadrupole Resonance Spectroscopy* (Academic Press, 1958).
21. B. J. Shields, Q. P. Unterreithmeier, N. P. de Leon, H. Park, M. D. Lukin, *Phys. Rev. Lett.* **114**, 136402 (2015).
22. P. London *et al.*, *Phys. Rev. Lett.* **111**, 067601 (2013).
23. T. Staudacher *et al.*, *Nat. Commun.* **6**, 8527 (2015).
24. S. Cavadini, *Prog. Nucl. Magn. Reson. Spectrosc.* **56**, 46–77 (2010).
25. A. Ajoy, U. Bissbort, M. D. Lukin, R. L. Walsworth, P. Cappellaro, *Phys. Rev. X* **5**, 011001 (2015).
26. T. A. Klar, R. Wollhofen, J. Jacak, *Phys. Scr.* **2014**, 014049 (2014).
27. D. Rugar, R. Budakian, H. J. Mamin, B. W. Chui, *Nature* **430**, 329–332 (2004).
28. C. L. Degen, M. Poggio, H. J. Mamin, C. T. Rettner, D. Rugar, *Proc. Natl. Acad. Sci. U.S.A.* **106**, 1313–1317 (2009).
29. H. S. Chung, K. McHale, J. M. Louis, W. A. Eaton, *Science* **335**, 981–984 (2012).
30. I. A. Yudushkin *et al.*, *Science* **315**, 115–119 (2007).

ACKNOWLEDGMENTS

We thank M. L. Pham, N. Chisholm, G. Kucsko, B. Harada, A. Ajoy, and P. Cappellaro for helpful discussions and experimental help. This work was supported by the Defense Advanced Research Projects Agency (QuASAR program), NSF, the Center for Ultracold Atoms, the Army Research Office Multidisciplinary University Research Initiative, the National Security Science and Engineering Faculty Fellowship program, and the Gordon and Betty Moore Foundation. I.L. was supported by the Air Force Office of Scientific Research National Defense Science and Engineering Graduate Fellowship (32 CFR 168a). Work at Ulm University was supported by the European Research Council. L.M. acknowledges support by a German Academic Exchange Service (DAAD) P.R.I.M.E. Fellowship. E.B. was supported by the Herchel Smith–Harvard Undergraduate Summer Research Program.

SUPPLEMENTARY MATERIALS

www.sciencemag.org/content/351/6275/836/suppl/DC1
Materials and Methods
Supplementary Text
Figs. S1 to S10
Table S1
References (*31*–*38*)

3 November 2015; accepted 21 January 2016
Published online 4 February 2016
10.1126/science.aad8022

NANOMATERIALS

DNA-controlled dynamic colloidal nanoparticle systems for mediating cellular interaction

Seiichi Ohta,[1,2] Dylan Glancy,[1,3] Warren C. W. Chan[1,3,4,5]*

Precise control of biosystems requires development of materials that can dynamically change physicochemical properties. Inspired by the ability of proteins to alter their conformation to mediate function, we explored the use of DNA as molecular keys to assemble and transform colloidal nanoparticle systems. The systems consist of a core nanoparticle surrounded by small satellites, the conformation of which can be transformed in response to DNA via a toe-hold displacement mechanism. The conformational changes can alter the optical properties and biological interactions of the assembled nanosystem. Photoluminescent signal is altered by changes in fluorophore-modified particle distance, whereas cellular targeting efficiency is increased 2.5 times by changing the surface display of targeting ligands. These concepts provide strategies for engineering dynamic nanotechnology systems for navigating complex biological environments.

Fundamental studies on the interactions of nanoparticle designs with biomolecules, cells, tissues, and organs are providing guiding principles with which to build nanosystems for imaging, diagnosis, and the treatment of disease. An optimal nanoparticle physicochemical property (for example, size, shape, and surface chemistry) for biological use varies with time and place within the living body, and current nanoparticle designs do not have the engineering range to meet these design requirements (*1*–*3*). For example, rod-shaped particles are reported to be preferable for tumor penetration (*4*), whereas spherical nanoparticles are better for subsequent cellular uptake by cancer cells (*5*); nanoparticles coated with polymer polyethylene glycol (PEG) can increase blood circulation time by reducing serum protein adsorption and macrophage uptake (*6*) but can impede surface-coated antibodies from cell targeting (*7*). These variations have inspired the development of interactive nanoparticle systems that can alter their properties in response to biological stimuli (*8*–*10*). However, dynamic control over the physicochemical properties of nanoparticles, especially particle shape, remains a challenge. DNA provides exquisite control and flexibility in engineering the physicochemical, morphological, optical, and electrical properties of three-dimensional (3D) nanosystems (*11*–*14*). But these DNA-assembled structures have not been fully exploited for cellular and biological application. We explored the use of DNA to assemble shape-shifting nanostructures with controlled biological function.

We used single-stranded DNA–functionalized gold nanoparticles (AuNPs) of different sizes (denoted as large, medium, and small) as building blocks to assemble shape-changing nanostructures (Fig. 1A and fig. S1). Each AuNP was functionalized with two DNA sequences: one for nanostructure assembly and the other for shape-changing (*15*). Valencies of these nanoparticles were 114, 25, and 6 DNA strands on 13-, 6-, and 3-nm AuNPs, respectively (fig. S2). The nanoparticle building blocks were assembled into "core-satellite" structures (*16*, *17*) by a linker DNA strand (L1 and L2) whose ends were complementary to two different nanoparticle types. The assembled nanostructure consists of a large core with surrounding satellites of medium and small size (Fig. 1, assembly morphology 1). An important design feature here is that the linkage between the core and the small satellites contains a single-stranded

[1]Institute of Biomaterials and Biomedical Engineering, Donnelly Center for Cellular and Biomolecular Research, University of Toronto, 164 College Street, Toronto, ON M5S 3G9, Canada. [2]Center for Disease Biology and Integrative Medicine, University of Tokyo, 7-3-1 Hongo, Bunkyo-ku, Tokyo, 113-0033, Japan. [3]Department of Chemistry, University of Toronto, 80 St. George Street, Toronto, ON M5S 3H6, Canada. [4]Department of Chemical Engineering, University of Toronto, 200 College Street, Toronto, ON M5S 3E5, Canada. [5]Department of Material Science and Engineering, University of Toronto, 160 College Street, Room 450, University of Toronto, Toronto, ON M5S 3E1, Canada.
***Corresponding author. E-mail: warren.chan@utoronto.ca**

spacer sequence [17 bases (Fig. 1A, black)], which if precisely designed can allow nanoparticles to change into different shapes via a "toe-hold strand displacement" mechanism (*18*–*20*) to reconfigure the DNA assembly (Fig. 1A). An attaching strand, A1, was first added in order to anchor small satellites to the medium-sized nanoparticles under hybridization and purification conditions. No substantial change in shape was observed with transmission electron microscopy (TEM) at this step (denoted as "intermediate" structure hereafter). Then, $L1_{comp}$, a fully complementary detaching strand to the linker strand between the core and small satellites (L1), was added. Because the duplex formation with $L1_{comp}$ is energetically favorable, L1 was displaced from the superstructure, resulting in the detachment of small satellites from the core. Through these two steps, small satellites were relocated from the core to the medium satellite, transforming the nanoassemblies into a new shape in which medium particles became the new core, surrounded by small satellites (assembly morphology 2). The successful shape change of nanoassemblies mediated by DNA are shown in representative images in Fig. 1B.

The reversibility of the transforming nanoassemblies is shown in Fig. 2A TEM images. The nanoassemblies first changed their assembled shape from morphology 1 to morphology 2 by the addition of A1 and $L1_{comp}$ strands. Similarly, addition of L1 and $A1_{comp}$ allowed the nanoassemblies to revert back to their original shape. The low-magnification TEM images (fig. S3) and ultraviolet-visible absorbance spectra (fig. S4) showed that the nanoassemblies are monodisperse, and dynamic light scattering measurements showed hydrodynamic sizes of 94 and 74 nm for morphologies 1 and 2, respectively (fig. S5). These characterizations indicate that the shape-changing nanoassemblies are colloidally stable in phosphate-buffered saline. We analyzed a larger population of nanoassemblies with TEM to determine the efficiency of the shape shift (Fig. 2A). We defined assembly morphologies 1 and 2 by particle distance, as illustrated in fig. S6. We measured the proximity of 3-nm (small) particles to either 6-nm (medium) or 13-nm (large) particles for each nanoassembly in order to determine its conformation. Structures in which satellites were concentrated near 3-nm particles were categorized as assembly morphology 1, whereas assemblies with 3-nm particles more closely associated with 6-nm cores were classified as morphology 2. Nanoassemblies that met neither of the above criteria were categorized as "other." The analysis showed that conversion of morphology 1 to morphology 2 occurred at an efficiency of 89% and was capable of reverting back to morphology 1 at an efficiency of 88%. During these shape changes, some of the satellites detach from the assembly because of imperfect anchoring; the average number of 6-nm particles on a nanoassembly of morphology 1, morphology 2, and the reversed morphology 1 was 1.8, 1.6, and 1.5, respectively, whereas that of 3-nm particles was 9.7, 6.6, and 5.6, respectively (fig. S7). The shape change was further evaluated by means of 2D radial distribution function (RDF) analysis (*21*). RDF of satellites from a core particle was calculated from the TEM images (Fig. 2B). In morphology 1, a single peak around 16 nm was observed, indicating the isotropic position of 3- and 6-nm satellites with respect to the 13-nm core. On the other hand, broadened multiple peaks were observed in morphology 2, which reflected the new position of 3-nm satellites. This RDF reverted back to the single peak after adding L1 and $A1_{comp}$ strands. These differences confirmed the reversible shape change of nanoassemblies. The shape change was not induced by the addition of DNA that has a noncomplementary sequence (fig. S8), suggesting specificity of this system. This shape-shifting property was not limited to a single design. By changing the linker stoichiometry, we successfully generated core-satellite structures with various numbers of 6-nm secondary cores (two to four) (fig. S9). Using the same procedures, each of the base structures could successfully change their shape (Fig. 2C).

We next determined whether the optical properties of the nanoassemblies could be controlled through morphological changes. The optical properties of a nanoparticle, such as fluorescence and surface plasmon resonance, are sensitive to the location of neighboring particles. For example, changes in the distance of neighboring fluorescent nanoparticles can alter their Förster resonance energy transfer (FRET) signals (*22*, *23*). The overall principle of our experiment is described in Fig. 3A. DNA strands on 13-, 6-, and 3-nm building block particles were end-labeled with fluorescein amidite (FAM), Cy5, or Cy3, respectively, then coated onto the nanoparticle

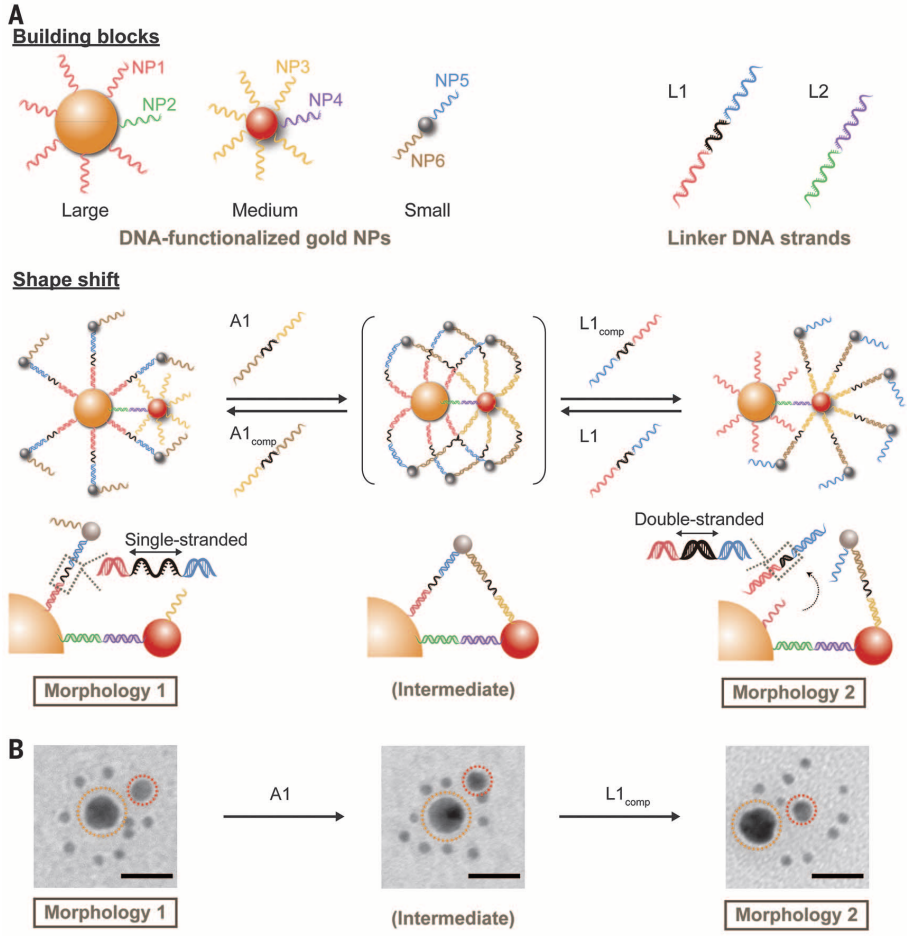


Fig. 1. Schematic illustration and corresponding TEM images of the shape change of nanoparticle assemblies mediated by DNA. (**A**) Individual nanoparticles (large, medium, and small) were functionalized with strands of two distinct single-stranded DNA sequences (NP1 to NP6). By using linker DNA strands containing complementary sequence regions (L1 and L2), they were then assembled into the core-satellite structure (assembly morphology 1). To change the shape of the nanoassembly, attaching strands (A1) were added to anchor small satellites to the medium particle (intermediate). After that, the detaching strand ($L1_{comp}$) was added to dislocate L1, resulting in the relocation of small satellites from the large core to the medium satellites (assembly morphology 2). This shape change can be reversed by adding extra attaching and detaching strands, L1 and $A1_{comp}$. For clarity, the schematics represent a cross-section of the 3D nanoassemblies that are composed of core particles surrounded by satellite particles. (**B**) Representative TEM images of the nanoassemblies of morphology 1, intermediate, and morphology 2. They consist of 13-, 6-, and 3-nm gold nanoparticles. The orange and red circles indicate a 13- and 6-nm particle, respectively. Scale bar, 20 nm.

and assembled. Given that the 3-nm particles are anchored to the 13-nm core in morphology 1, FAM and Cy3 are close enough to induce FRET. When we excite FAM, florescence from Cy3 can be observed. However, no FRET is observed by the excitation of Cy3 because the 3- and 6-nm particles are farther from one another. After shifting to the intermediate structure, FRET can be observed with the excitation of either FAM or Cy3 as 3-nm particles are anchored to both 13- and 6-nm particles. When the shape is finally shifted to morphology 2, FRET can be detected only through Cy3 excitation because 3-nm particles are now detached from the 13-nm core. Experimentally, DNA strands were fluorescently labeled according to supplier, coated onto the AuNPs, and purified, and the photoluminescent spectra were measured in order to verify successful coating (fig. S10). Because strands NP1 to NP6 were composed of 25 bases, which roughly corresponds to 5 to 10 kDa of linear polymer chain, they are remote enough to prevent fluorescent quenching by AuNPs (*24*). Photoluminescent spectra of the assembled nanostructures are shown in Fig. 3, B and C, at each step of the shape-changing process. After excitation of FAM, a prominent signal from Cy3 was observed at 561 nm for assembly morphology 1 and the intermediate structure (Fig. 3B). This signal was decreased after shifting to morphology 2. After Cy3 excitation, the shift from morphology 1 to the intermediate shape was accompanied by the emergence of the signal from Cy5 at 665 nm, but the subsequent shift to morphology 2 did not affect the signal (Fig. 3C). These changes in FRET signals are consistent with the expected position of fluorophores (Fig. 3A), validating our proposed mechanism. Real-time monitoring of the shape shift was also carried out with FRET measurement (Fig. 3D). A1 and $L1_{comp}$ strands were sequentially added to the nanoassemblies in a hybridization buffer, during which the changes in fluorescent signals from Cy3 and Cy5—obtained through the excitation of FAM and Cy3, respectively—were measured in real time at room temperature. The signals from Cy3 and Cy5 respond specifically to the addition of the attaching and detaching strands, illustrating the fidelity of the shape change. We found that each step of the transformation is predominantly complete within 10 min. Assuming first-order reaction kinetics, the reaction rate constant for the first and the second step of the shape change was estimated to be 1.9×10^{-3} and 1.7×10^{-3} s^{-1}, respectively (fig. S11). These results not only confirm successful shape-shifting of the nanoassemblies but also suggest possible applications as imaging probes that are responsive to specific DNA sequences.

Last, we determined whether we could alter the cellular interaction of our nanoassemblies by changing their shape and thus, indirectly, changing the presentation of the surface chemistry. This is an important feature because the optimal physicochemical properties to mediate transport in cells, tissues, and whole animals necessitate particles of different sizes, shapes, and surface chemistries (*4*–*7*). It is unlikely that current single-particle design systems will be able to fulfill these engineering requirements. We controlled the presentation of targeting ligands on the surface of the nanoassembly system by changing its shape via DNA. We functionalized the core particle with folic acid

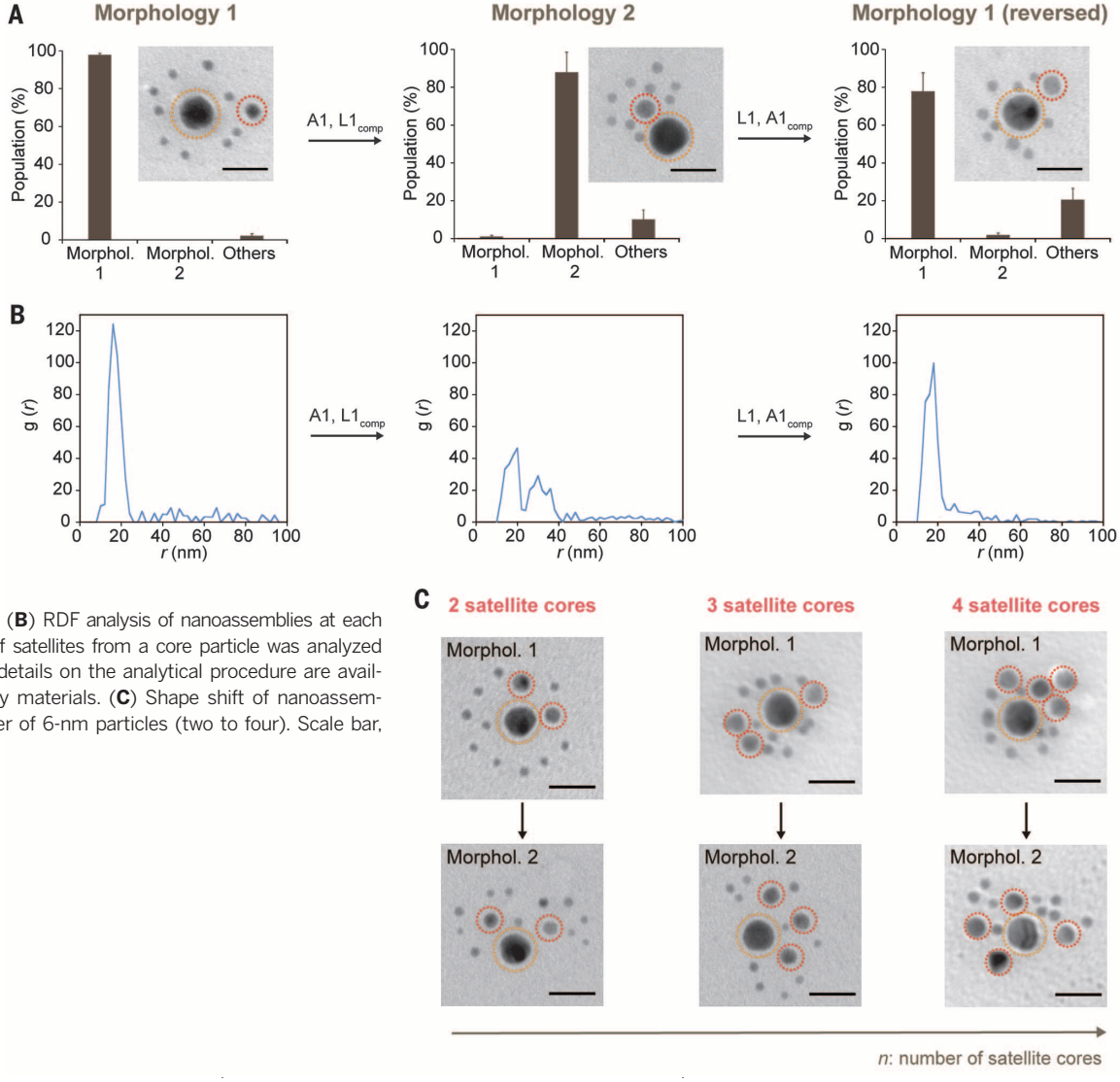


Fig. 2. Reversibility and design versatility of the nanoassembly shape change. (**A**) TEM images and histograms of the nanoparticle assemblies at each shape-shifting step. Scale bar, 20 nm. The shape of the nanoassembly was categorized as assembly morphology 1, 2, and others by particle distance (the definition is provided in fig. S6), and then the proportion of each shape was analyzed from TEM images. More than 100 assemblies were analyzed for each condition. (**B**) RDF analysis of nanoassemblies at each shape-shifting step. RDF of satellites from a core particle was analyzed from TEM images. More details on the analytical procedure are available in the supplementary materials. (**C**) Shape shift of nanoassemblies with different number of 6-nm particles (two to four). Scale bar, 20 nm.

(FA) as a targeting ligand for overexpressed folate receptor in many types of cancer cells (Fig. 4A) (*25*). In assembly morphology 1, FAs are surrounded by 3- and 6-nm satellites, which sterically hinder their targeting ability (OFF state). After transformation to morphology 2, "hidden" FAs are exposed to the outer environment via the relocation of 3-nm satellites, activating the targeting property of the nanoassemblies (ON state).

The FA functionalization was achieved by concurrently conjugating FA-functionalized PEG [molecular weight (M_w) = 5 kDa] terminated with thiol and DNA strands to 13-nm particles. The resulting grafting density was 40.0 ± 5.2 FA molecules per particle. The cellular uptake of the FA-functionalized nanoassemblies was examined by using folate receptor–expressing U87-MG human glioblastoma-astrocytoma cells (*25*, *26*). The cells were incubated with the nanoassemblies of morphology 1 or 2 in serum-free media, as described in the supplementary materials, materials and methods. Serum was not added to the media so as to avoid the interaction of nonspecifically adsorbed serum proteins with nanoparticles and influencing cellular interaction (*27*). TEM images of the nanoassemblies internalized by U87-MG cells are shown in Fig. 4, B and C. Nanoparticles were found within vesicles inside the cells, suggesting that they were internalized via endocytosis. Moreover, as we reported (*28*), the nanostructures were disassembled into their respective building blocks in the vesicles, whereas fully assembled nanostructures were still found in the culture media.

We quantified the amount of cellular uptake by means of inductively coupled plasma mass spectrometry (ICP-MS). Nanoassemblies conjugated with the same amount of PEG but without FA functionalization were used as a control. ICP-MS revealed that the cellular uptake of FA-conjugated nanoassemblies of morphology 2 was 2.5 times higher than that of morphology 1, indicating the ON/OFF switching of the targeting property. It was also found that the ON/OFF switching was moderately effective even without FA functionalization; the cellular uptake of morphology 2 was 1.5 times higher than that of morphology 1 (Fig. 4D). We deduced that both shape and surface chemistry (type of DNA sequences exposed on the outer surface) of the nontargeted nanoassembly is responsible for this difference (figs. S14 and S15). This effect is amplified by the FA conjugation. A competition experiment was conducted in order to confirm the contribution of FA functionalization in cellular uptake. Free FA was added to the culture media with the nanoassemblies (Fig. 4E). The ON/OFF ratio of the control nanoassemblies exhibited little change in the presence of free FA. Conversely, for FA-functionalized assemblies, the ON/OFF ratio substantially decreased with increasing free FA concentration toward control level, suggesting that the cellular uptake was indeed mediated by FA-folate receptor interaction. These results demonstrate that DNA-mediated shape change of the nanoassembly can alter the surface display of targeting ligands and thus control its cellular uptake property.

Some natural biomolecules, such as proteins, switch their function by changing their 3D conformation in response to biological signals. This quality allows them to display varying conformations to activate functions or stay dormant until needed. Like these biomolecules, the nanoassemblies presented here alter their fluorescent and cellular uptake properties by transforming their structure in response to specific DNA sequences. A next step is to design the linker sequences to respond to circulating DNA or intracellular RNA sequences and to determine the impact of payload on shape-shifting property. Although further development is needed for their practical use, the concept presented here can be expanded to develop more complex systems that can mimic the diverse functions of a protein to selectively control the biological functions of the engineered nanosystem. Our proposed design strategy provides a new opportunity and general method with which to develop future dynamic nanomaterials that can travel through the blood stream and into diseased sites, transforming into the required shapes to overcome diverse biological barriers and activating their function to diagnose or treat targeted sites.

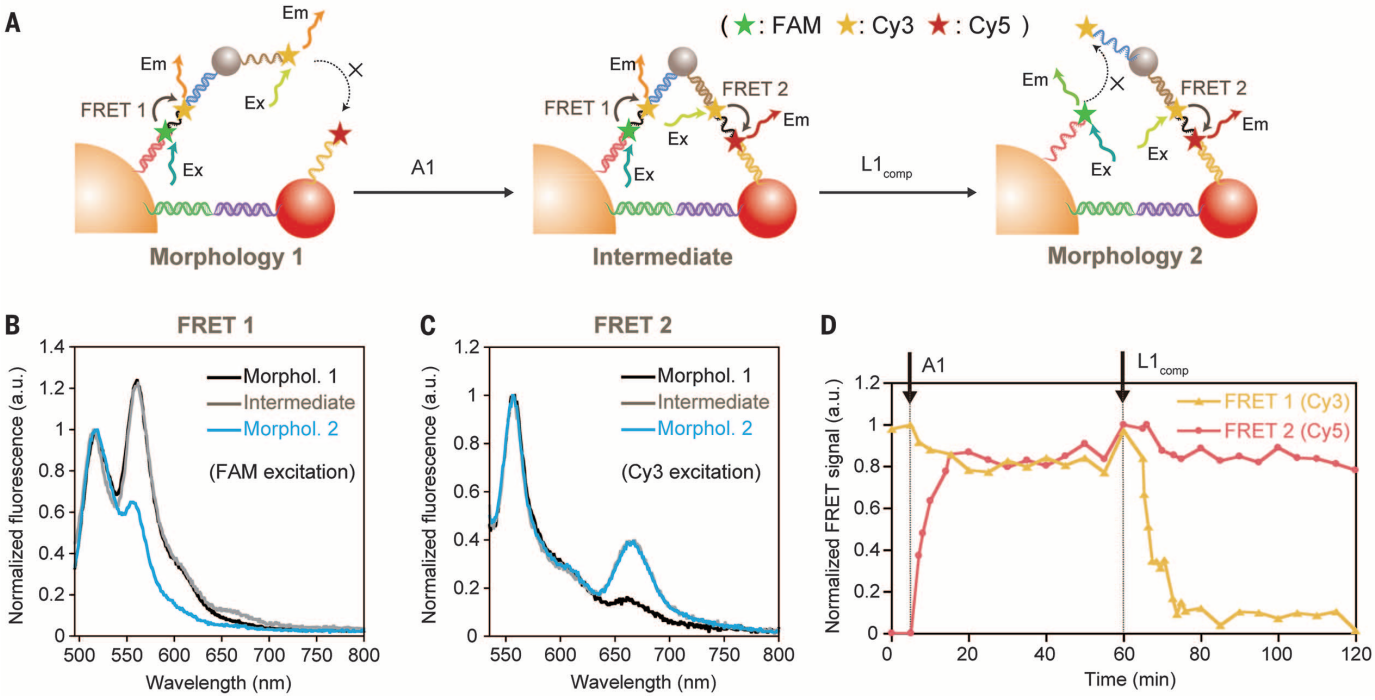


Fig. 3. Changes in FRET signals from the nanoparticle assemblies induced by shape change. (**A**) Schematic illustration of the FRET occurring in the nanoassemblies. In assembly morphology 1, FRET between FAM and Cy3 (FRET 1) can be observed through excitation of FAM, whereas FRET between Cy3 and Cy5 (FRET 2) does not occur through excitation of Cy3. After the shift to intermediate structure, FRET is observed between FAM and Cy3 and between Cy3 and Cy5. Then, in morphology 2, FRET can be detected only between Cy3 and Cy5. (**B** and **C**) Photoluminescent spectra from nanoassemblies (morphology 1, intermediate, and morphology 2). They are excited at (B) 480 nm for FAM or (C) 520 nm for Cy3. Each spectrum is normalized to the peak from (B) FAM at 519 nm or that from (C) Cy3 at 561 nm, respectively. (**D**) Real-time monitoring of FRET signals during the shape change. A1 and $L1_{comp}$ DNA strands were added at 5 and 60 min, respectively, to the nanostructure solution, whereas FRET signals from Cy3 (FRET 1, excitation at 480 nm) and Cy5 (FRET 2, excitation at 520 nm) were monitored in real time.

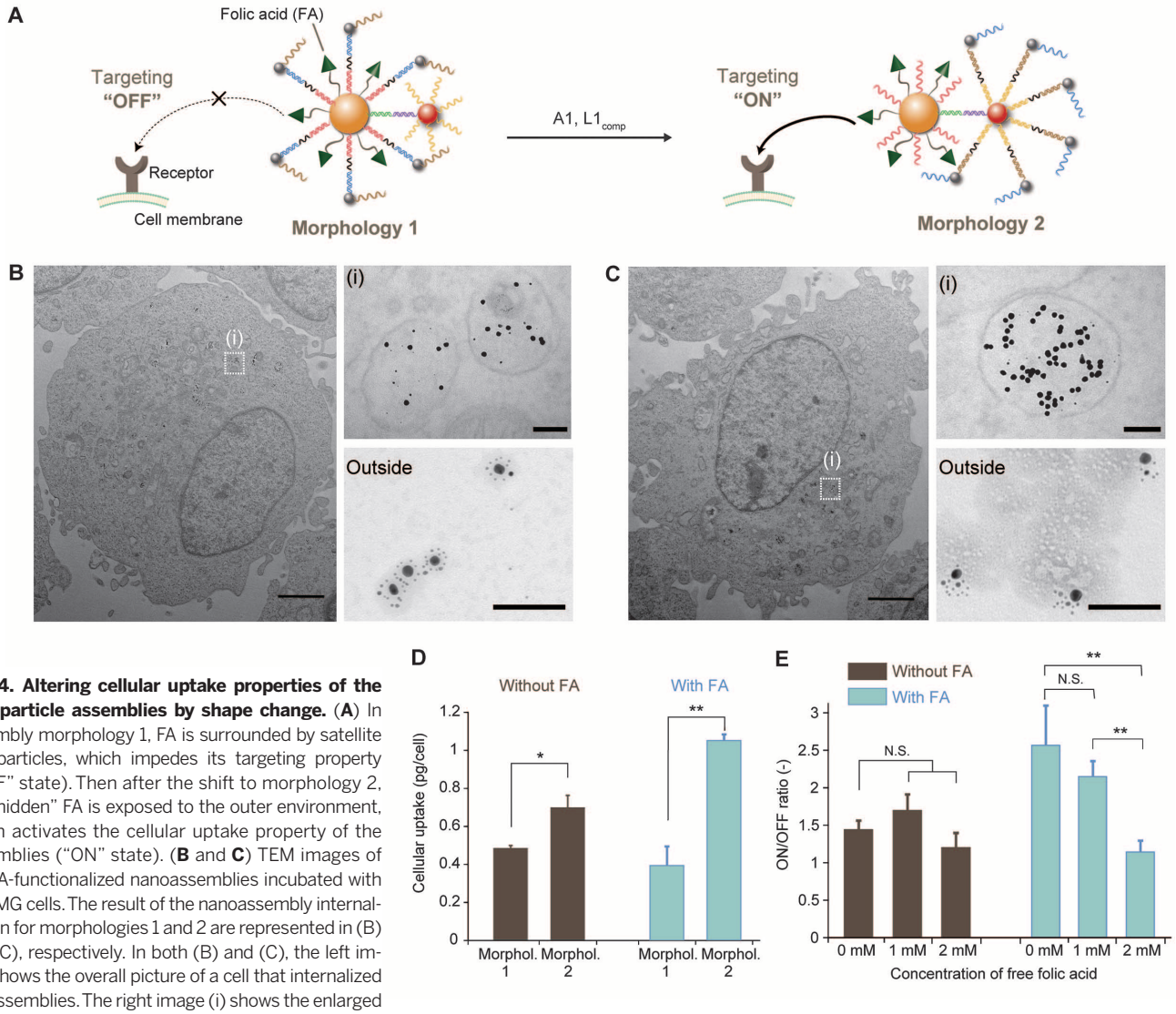


Fig. 4. Altering cellular uptake properties of the nanoparticle assemblies by shape change. (**A**) In assembly morphology 1, FA is surrounded by satellite nanoparticles, which impedes its targeting property ("OFF" state). Then after the shift to morphology 2, the "hidden" FA is exposed to the outer environment, which activates the cellular uptake property of the assemblies ("ON" state). (**B** and **C**) TEM images of the FA-functionalized nanoassemblies incubated with U87-MG cells. The result of the nanoassembly internalization for morphologies 1 and 2 are represented in (B) and (C), respectively. In both (B) and (C), the left image shows the overall picture of a cell that internalized the assemblies. The right image (i) shows the enlarged image of its corresponding part of the overall picture. The nanoassemblies found in the culture media after the incubation are also shown. Scale bars, 2.0 μm (low-magnification images) and 100 nm (enlarged images). More enlarged images inside cells are provided in fig. S12. Nanoassemblies without FA functionalization are provided in fig. S13. (**D**) Comparison of the amount of cellular uptake of the FA-functionalized nanoassemblies between morphology 1 and morphology 2 measured with ICP-MS. Nanoassemblies without FA functionalization were also used as controls. Data are averages ± SD ($n > 3$ experimental replicates). (**E**) Effect of free FA on the ON/OFF switching ratio of the cellular uptake. The ON/OFF ratio was defined as the ratio of the amount of cellular uptake of the assemblies between morphology 2 and morphology 1 (raw data are shown in fig. S16). Data are averages ± SD ($n > 3$ experimental replicates). $^{**}P < 0.01$, $^{*}P < 0.05$. N.S., not significant.

REFERENCES AND NOTES

1. W. Jiang, B. Y. Kim, J. T. Rutka, W. C. Chan, *Nat. Nanotechnol.* **3**, 145–150 (2008).
2. R. A. Petros, J. M. DeSimone, *Nat. Rev. Drug Discov.* **9**, 615–627 (2010).
3. H. Cabral *et al.*, *Nat. Nanotechnol.* **6**, 815–823 (2011).
4. V. P. Chauhan *et al.*, *Angew. Chem. Int. Ed. Engl.* **50**, 11417–11420 (2011).
5. B. D. Chithrani, A. A. Ghazani, W. C. Chan, *Nano Lett.* **6**, 662–668 (2006).
6. K. Knop, R. Hoogenboom, D. Fischer, U. S. Schubert, *Angew. Chem. Int. Ed. Engl.* **49**, 6288–6308 (2010).
7. Q. Dai, C. Walkey, W. C. Chan, *Angew. Chem. Int. Ed. Engl.* **53**, 5093–5096 (2014).
8. C. Wong *et al.*, *Proc. Natl. Acad. Sci. U.S.A.* **108**, 2426–2431 (2011).
9. G. von Maltzahn *et al.*, *Nat. Mater.* **10**, 545–552 (2011).
10. J. W. Yoo, S. Mitragotri, *Proc. Natl. Acad. Sci. U.S.A.* **107**, 11205–11210 (2010).
11. M. R. Jones, N. C. Seeman, C. A. Mirkin, *Science* **347**, 1260901 (2015).
12. A. Kuzyk *et al.*, *Nature* **483**, 311–314 (2012).
13. Y. Zhang *et al.*, *Nat. Mater.* **14**, 840–847 (2015).
14. S. M. Douglas, I. Bachelet, G. M. Church, *Science* **335**, 831–834 (2012).
15. X. Zhang, M. R. Servos, J. Liu, *J. Am. Chem. Soc.* **134**, 7266–7269 (2012).
16. X. Xu, N. L. Rosi, Y. Wang, F. Huo, C. A. Mirkin, *J. Am. Chem. Soc.* **128**, 9286–9287 (2006).
17. J. H. Yoon, J. Lim, S. Yoon, *ACS Nano* **6**, 7199–7208 (2012).
18. D. Y. Zhang, G. Seelig, *Nat. Chem.* **3**, 103–113 (2011).
19. B. Yurke, A. J. Turberfield, A. P. Mills Jr., F. C. Simmel, J. L. Neumann, *Nature* **406**, 605–608 (2000).
20. Y. Tian, C. Mao, *J. Am. Chem. Soc.* **126**, 11410–11411 (2004).
21. X. Yu *et al.*, *Nano Today* **8**, 480–493 (2013).
22. C. S. Yun *et al.*, *J. Am. Chem. Soc.* **127**, 3115–3119 (2005).
23. P. D. Howes, R. Chandrawati, M. M. Stevens, *Science* **346**, 1247390 (2014).
24. L. Y. Chou, W. C. Chan, *Adv. Healthc. Mater.* **1**, 714–721 (2012).
25. Z. Xu *et al.*, *Int. J. Pharm.* **426**, 182–192 (2012).
26. J. Zhu *et al.*, *Biomaterials* **35**, 7635–7646 (2014).
27. C. D. Walkey *et al.*, *ACS Nano* **8**, 2439–2455 (2014).
28. L. Y. Chou, K. Zagorovsky, W. C. Chan, *Nat. Nanotechnol.* **9**, 148–155 (2014).

ACKNOWLEDGMENTS

W.C.W.C. acknowledges the Natural Sciences and Engineering Research Council (NSERC) for support (2014-06397), Canadian Institute of Health Research (MOP-130143), and Prostate Cancer Canada (D2014-12). S.O. acknowledges the Japan Society for the Promotion of Science (JSPS) for a Research Fellowship (PD, no. 5621) and the Ministry of Education, Culture, Sports, Science and Technology (MEXT) of Japan for a Grant-in-Aid for Young Scientists (B, no. 26820356). D.G. acknowledges NSERC for a graduate fellowship. The authors thank the Advanced Bioimaging Centre at Mount Sinai Hospital for the use of the TEM and Toronto Nanofabrication Center at University of Toronto for the use of ICP-MS. The authors also thank L. Chou for interesting discussions.

SUPPLEMENTARY MATERIALS

www.sciencemag.org/content/351/6275/841/suppl/DC1
Materials and Methods
Figs. S1 to S16
References (*29*–*31*)

19 September 2015; accepted 15 January 2016
10.1126/science.aad4925

DNA REPAIR

Ubiquitinated Fancd2 recruits Fan1 to stalled replication forks to prevent genome instability

Christophe Lachaud,[1] Alberto Moreno,[2] Francesco Marchesi,[3] Rachel Toth,[1] J. Julian Blow,[2] John Rouse[1]*

Mono-ubiquitination of Fancd2 is essential for repairing DNA interstrand cross-links (ICLs), but the underlying mechanisms are unclear. The Fan1 nuclease, also required for ICL repair, is recruited to ICLs by ubiquitinated (Ub) Fancd2. This could in principle explain how Ub-Fancd2 promotes ICL repair, but we show that recruitment of Fan1 by Ub-Fancd2 is dispensable for ICL repair. Instead, Fan1 recruitment—and activity—restrains DNA replication fork progression and prevents chromosome abnormalities from occurring when DNA replication forks stall, even in the absence of ICLs. Accordingly, Fan1 nuclease-defective knockin mice are cancer-prone. Moreover, we show that a Fan1 variant in high-risk pancreatic cancers abolishes recruitment by Ub-Fancd2 and causes genetic instability without affecting ICL repair. Therefore, Fan1 recruitment enables processing of stalled forks that is essential for genome stability and health.

Interstrand cross-links (ICLs) block DNA replication. Defects in repairing ICLs are implicated in Fanconi anemia (FA), a rare autosomal recessive disease typified by hypersensitivity to ICL-inducing agents such as mitomycin-C (MMC) or diepoxybutane (DEB), exaggerated G2 arrest, and increased chromosome abnormalities after exposure to these agents (*1*). FA is caused by mutations in any of the 19 Fanc proteins comprising the FA network (*2*). The mono-ubiquitination of Fancd2 at Lysine-561 is essential for ICL repair, but the underlying mechanisms are unclear (*2*, *3*). The Fan1 nuclease is recruited to ICLs in S-phase via the interaction between its ubiquitin-binding (UBZ) domain and ubiquitinated (Ub) Fancd2 (*4*–*7*). However, mutations in Fan1 do not cause FA, as might be expected, but rather lead to karyomegalic interstitial nephritis (KIN) (*8*), suggesting that Fan1 and Fancd2 play distinct roles in ICL repair. Therefore, the functional importance of the Fan1/Ub-Fancd2 interaction is unclear, and we took several approaches to address this problem.

First, we tested the ability of UBZ-mutated Fan1 (UBZ*) to rescue the MMC sensitivity of human U2OS Fan1$^{-/-}$ cells (*9*). Mutating two conserved residues (C44A+C47A) in the Fan1 UBZ domain that abolishes foci (*4*) fully rescued the MMC hypersensitivity of Fan1$^{-/-}$ cells (Fig. 1A and fig. S1A). Embryonic fibroblasts (MEFs) from Fan1 nuclease-defective (nd) mice harboring a deletion of the last 41 amino acids of Fan1, including key catalytic residues (figs. S2 and S3) (mice described in the supplementary materials), were hypersensitive to MMC (Fig. 1B). The murine Fan1 UBZ* mutant fused to green fluorescent protein (GFP), expressed at roughly four times the level of endogenous Fan1, failed to form foci (fig. S1, B to D). However, this mutant rescued the MMC hypersensitivity of Fan1$^{nd/nd}$ MEFs (Fig. 1B). These data suggest that the recruitment of Fan1 by Ub-Fancd2 is dispensable for ICL repair. Furthermore, we found that the UBZ-mutated Fan1 fully rescued the exaggerated G2 arrest seen in Fan1$^{nd/nd}$ MEFs (Fig. 1C) but failed to rescue the increase in chromosome abnormalities (radial structures and chromatid breaks) induced by MMC (Fig. 1D).

Fan1$^{nd/nd}$ MEFs also showed a high level of chromosome abnormalities in response to fork-stalling agents such as methylmethanesulfonate (MMS) (fig. S4) and hydroxyurea (HU) (Fig. 2A), which cause base alkylation and nucleotide depletion, respectively. The increase in chromosome abnormalities in Fan1$^{nd/nd}$ MEFs induced by HU was not reversed by the Fan1 UBZ* mutant (Fig. 2A). These data indicate that Fan1 nuclease activity and interaction with Ub-Fancd2 prevent chromosome abnormalities at stalled forks independent of ICL repair. This is consistent with Fancd2 null cells showing high levels of chromosome abnormalities after exposure to HU (*10*), but the requirement of ubiquitination was not investigated. We found that the non-ubiquitinatable mouse Fancd2 K559R mutant was unable to rescue the high levels of chromosome abnormalities induced by MMC or HU in Fancd2$^{-/-}$ MEFs (Fig. 2B and fig. S5A), consistent with the idea that interaction of Fan1 with Ub-Fancd2 is required for this response. However, Ub-Fancd2 and Fan1

[1]Medical Research Council Protein Phosphorylation and Ubiquitylation Unit, College of Life Sciences, Sir James Black Centre, University of Dundee, Dundee DD1 5EH, Scotland, UK. [2]Centre for Gene Regulation and Expression, College of Life Sciences, Sir James Black Centre, University of Dundee, Dundee DD1 5EH, Scotland, UK. [3]School of Veterinary Medicine, College of Medical, Veterinary and Life Sciences, University of Glasgow, Bearsden Road, Glasgow G61 1QH, UK.
*Corresponding author. E-mail: j.rouse@dundee.ac.uk

Downloaded from on February 18, 2016

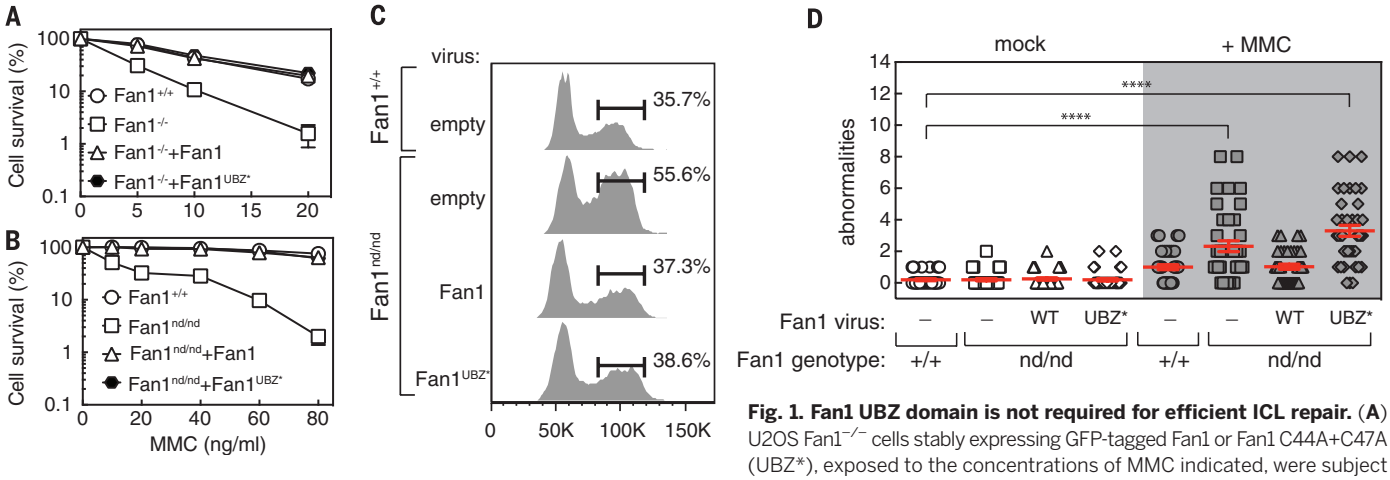


Fig. 1. Fan1 UBZ domain is not required for efficient ICL repair. (**A**) U2OS Fan1$^{-/-}$ cells stably expressing GFP-tagged Fan1 or Fan1 C44A+C47A (UBZ*), exposed to the concentrations of MMC indicated, were subject to clonogenic survival assays. For each cell population, viability of untreated cells is defined as 100%. (**B**) Clonogenic survival analysis of Fan1$^{nd/nd}$ MEFs stably expressing GFP-tagged murine Fan1 or Fan1 UBZ* mutant. Wild-type MEFs were used as control. (**C**) FACS analysis of DNA content in Fan1$^{nd/nd}$ MEFs stably expressing GFP- Fan1 or GFP-Fan1 UBZ* mutant after exposure to MMC for 24 hours. Wild-type MEFs (Fan1$^{+/+}$) with empty vector were used as control. (**D**) The number of chromosome abnormalities per metaphase in spreads of MEFs exposed to MMC. Data in (A) and (B) are represented as mean ± SD. In (D), significance was calculated using one-way analysis of variance (ANOVA) (****P < 0.0001) followed by Bonferroni's Multiple Comparison Test.

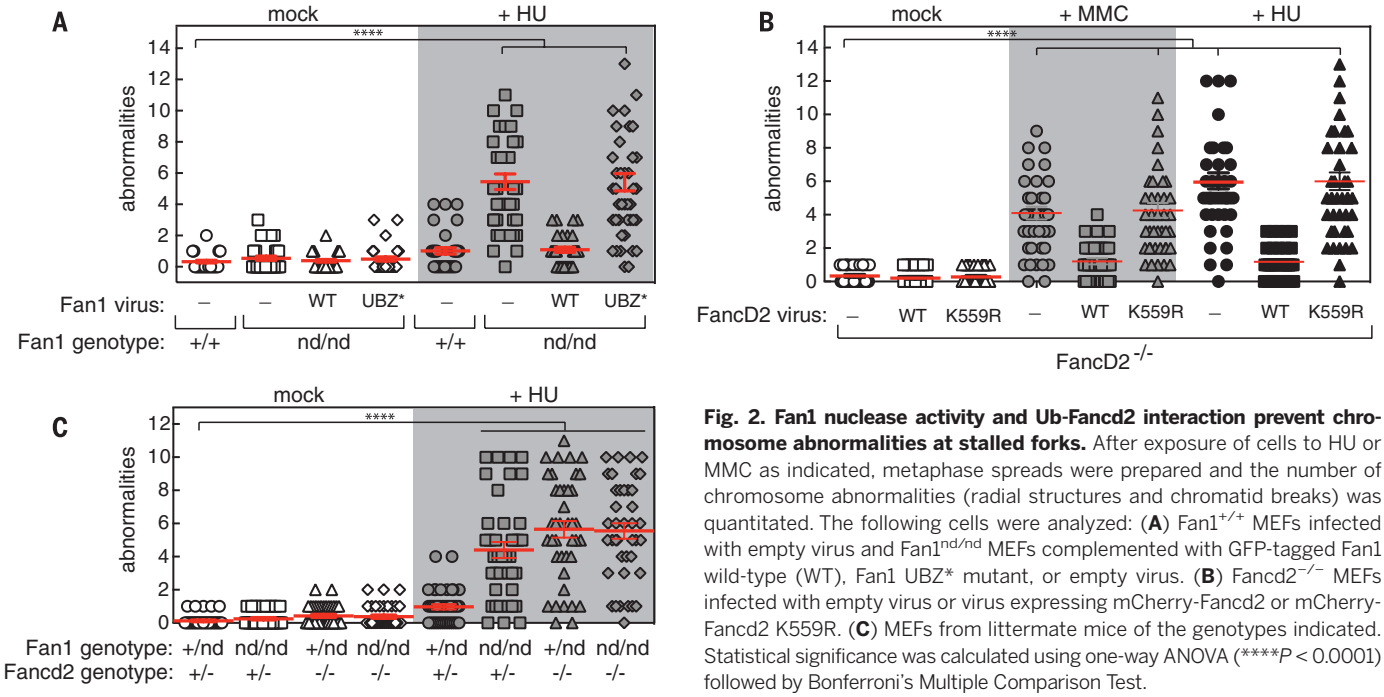


Fig. 2. Fan1 nuclease activity and Ub-Fancd2 interaction prevent chromosome abnormalities at stalled forks. After exposure of cells to HU or MMC as indicated, metaphase spreads were prepared and the number of chromosome abnormalities (radial structures and chromatid breaks) was quantitated. The following cells were analyzed: (**A**) Fan1$^{+/+}$ MEFs infected with empty virus and Fan1$^{nd/nd}$ MEFs complemented with GFP-tagged Fan1 wild-type (WT), Fan1 UBZ* mutant, or empty virus. (**B**) Fancd2$^{-/-}$ MEFs infected with empty virus or virus expressing mCherry-Fancd2 or mCherry-Fancd2 K559R. (**C**) MEFs from littermate mice of the genotypes indicated. Statistical significance was calculated using one-way ANOVA (****$P < 0.0001$) followed by Bonferroni's Multiple Comparison Test.

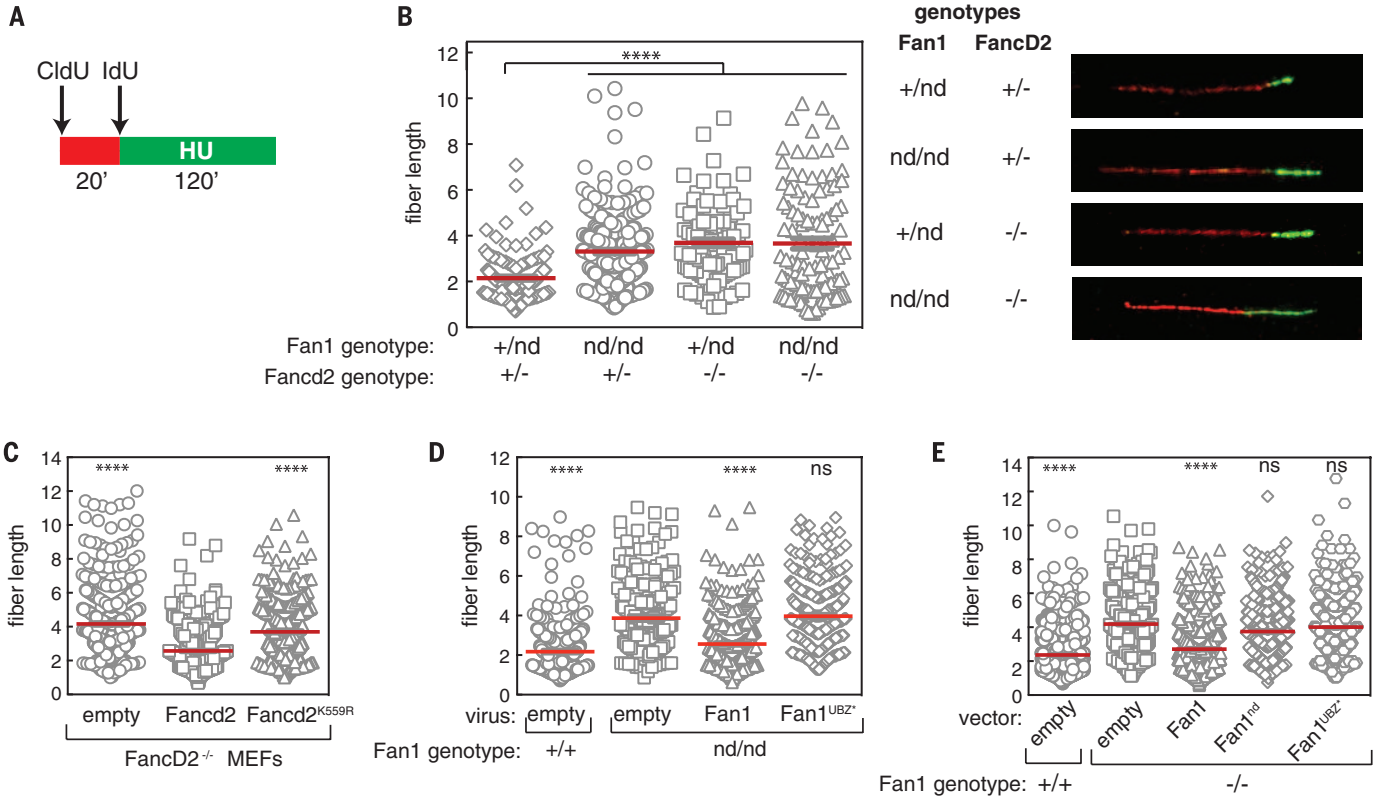


Fig. 3. Fan1 nuclease activity and Ub-Fancd2 interaction control progression of stalled forks. (**A**) Fiber labeling protocol. Primary MEFs were pulsed with CldU followed by IdU with HU, and IdU track length was measured. (**B** to **D**) Dot plots of IdU replication tracks in MEFs of the genotypes indicated. In (B), representative CldU and IdU replication tracks are shown (right panels). Cells were infected with viruses expressing the Fancd2 (C) or Fan1 (D) proteins indicated. (**E**) Dot plot of IdU replication tracks in U2OS cells, and U2OS Fan1$^{-/-}$ cells stably transfected with the vectors indicated. nd, nuclease-defective. Red lines represent mean track length. Statistical significance was calculated using one-way ANOVA (****$P < 0.0001$) followed by Bonferroni's Multiple Comparison Test.

may prevent chromosome abnormalities at stalled forks by different mechanisms. To address this point, we crossed Fan1$^{nd/nd}$ mice with Fancd2$^{-/-}$ mice to generate double mutants. As shown in Fig. 2C, the level of HU-induced chromosome abnormalities in MEFs from Fan1$^{nd/nd}$ Fancd2$^{-/-}$ double-mutant mice was not higher than in the respective single mutants, suggesting that Fan1 and Fancd2 are epistatic in this respect. Therefore the Fan1/Ub-Fancd2 interaction, and Fan1 nuclease activity, is required for preventing chromosome abnormalities when forks stall, and this role appears to be independent of ICL repair.

As well as preventing chromosome abnormalities, Fancd2 has been implicated in restraining progression of forks that stall after exposure to HU (*11*). We set out to investigate whether Fan1 plays a similar role using DNA fiber analysis. Primary MEFs were pulsed with chlorodeoxyuridine (CldU) followed by 5′-iododeoxyuridine (IdU) with or without HU, and IdU track length was measured (Fig. 3A). Fancd2$^{-/-}$ MEFs had substantially longer IdU tracks in HU than wild-type MEFs (*11*), and a similar effect was seen in Fan1$^{nd/nd}$ MEFs (Fig. 3B). Tracks from Fan1$^{nd/nd}$ Fancd2$^{-/-}$ double-mutant MEFs were not longer than in the respective single-mutant cells, implying epistasis (Fig. 3B). No differences in track length were observed in the absence of HU (fig. S5B). Consistent with the fiber data, we observed more DNA synthesis in Fan1$^{nd/nd}$ MEFs exposed to HU than in Fan1$^{+/nd}$ MEFs, judged by fluorescence-activated cell sorting (FACS) analysis of 5-ethynyl-2′-deoxyuridine (EdU) incorporation (fig. S6). Thus, Fancd2 and Fan1 restrain the progression of stalled forks, and we next tested whether their interaction is required. Fancd2$^{-/-}$ MEFs expressing the murine Fancd2 K559R mutant had substantially longer IdU tracks in HU than cells expressing Fancd2 (Fig. 3C). Furthermore, we found that the Fan1 UBZ* mutant failed to restore normal track length in HU-treated Fan1$^{nd/nd}$ MEFs, in contrast with wild-type Fan1 (Fig. 3D). Accordingly, U2OS Fan1$^{-/-}$ cells had longer replication tracks in HU than parental cells, and neither the Fan1 UBZ* mutant nor the nuclease-dead mutant rescued this defect (Fig. 3E). Together these data show that the Fan1/Ub-Fancd2 interaction restrains the progression of stalled forks, a function that also requires Fan1 nuclease activity.

Biallelic mutations in Fancd2, or genes that promote Fancd2 ubiquitination, cause FA, typified by cancer predisposition (*1*, *2*). We speculated, therefore, that Fan1 defects might also cause cancers. No tumors were observed in Fan1$^{nd/nd}$ mice at 6 months (data not shown), but by 20 months, around 85% of Fan1$^{nd/nd}$ mice developed cancers; no malignancies were evident in age-matched Fan1$^{+/+}$ mice (Fig. 4A). Pulmonary carcinomas, epithelial-type cancers similar to those reported in FA patients and Fancd2$^{-/-}$ mice (*12*), were observed in 28% of the mice, and 57% developed lymphoma (Fig. 4, A and B). These data suggest that Fan1 nuclease activity is a tumor suppressor, at least in mice.

Because suppression of chromosome abnormalities by Fan1 requires interaction with Ub-Fancd2 as well as Fan1 nuclease activity, we postulated that mutations in the human Fan1 UBZ domain might cause cancers. Whole-exome sequencing recently identified a recurrent germline Fan1 variant, M50R, occurring at a relatively

A

Genotype		Nb.	% of mice	Total (%)
Fan1 $^{+/+}$	carcinoma	0	0	0
	lymphoma	0	0	
Fan1 $^{nd/nd}$	carcinoma	3	28.5	85.7
	lymphoma	4	57.1	

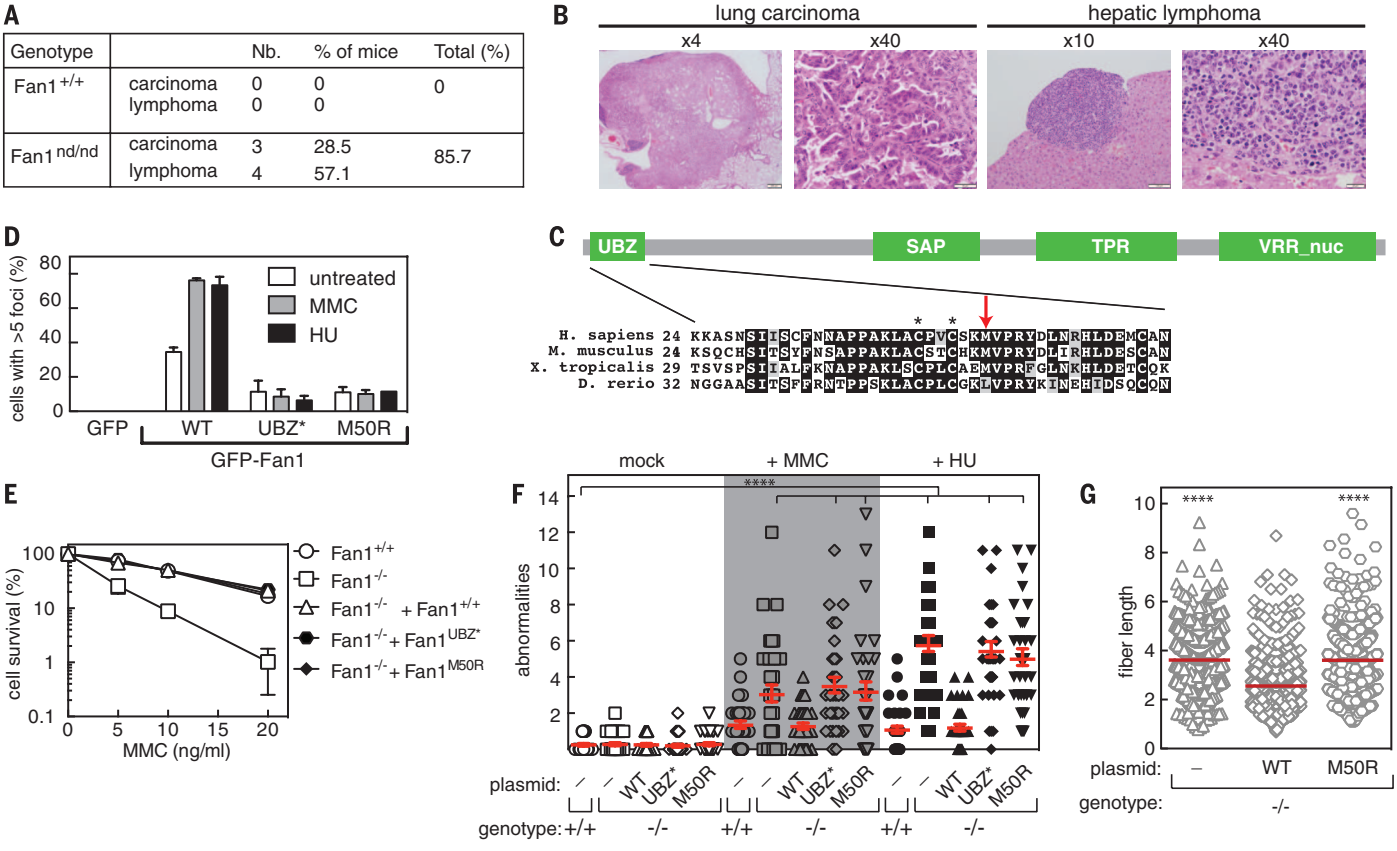


Fig. 4. Fan1 nuclease activity and interaction with Ub-Fancd2 prevent cancers. (**A**) Incidence of carcinoma and lymphoma in Fan1$^{+/+}$ and Fan1$^{nd/nd}$ mice at ~20 months of age revealed by genotype-blind whole-body pathological analyses. (**B**) Representative images of pulmonary carcinoma and hepatic lymphoma from Fan1$^{nd/nd}$ mice. (**C**) Alignment of the UBZ domain of FAN1. Identical residues, black; similar residues, gray. Asterisks denote C44 and C47 residues. Red arrow denotes M50. (**D**) U2OS Fan1$^{-/-}$ cells stably expressing the proteins indicated were treated, or not, with MMC or HU, and the proportion of cells with >5 GFP-FAN1 foci were counted. (**E**) Clonogenic survival analysis of U2OS Fan1$^{-/-}$ stably expressing the GFP-tagged Fan1 proteins indicated, after exposure to the indicated concentrations of MMC for 18 hours. (**F**) Chromosome abnormalities in U2OS Fan1$^{-/-}$ cells, stably expressing the proteins indicated, after treatment with MMC or HU. (**G**) Dot plots of IdU replication tracks in U2OS Fan1$^{-/-}$ cells, stably expressing the GFP-Fan1 proteins indicated, after exposure to HU. In (D) and (E), data are represented as mean ± SD. In (F) and (G), significance was calculated using one-way ANOVA (****P < 0.0001) followed by Bonferroni's Multiple Comparison Test.

high frequency in high-risk pancreatic cancers (*13*). The M50R Fan1 variant, which cosegregates with pancreatic cancer in two separate families, is a strong candidate pancreatic cancer predisposition gene. M50 lies in the UBZ domain of Fan1 (Fig. 4C). Similar to the UBZ* mutation (C44A+C47A), the Fan1 M50R mutation abolished Fan1 foci but rescued the MMC sensitivity of U2OS Fan1$^{-/-}$ cells (Fig. 4, D and E). The M50R mutant failed, however, to prevent chromosome abnormalities induced by HU or MMC in Fan1$^{-/-}$ cells (Fig. 4F). Moreover, expression of wild-type Fan1 in Fan1$^{-/-}$ cells restored normal track length in HU, but the Fan1 M50R mutant failed to do so (Fig. 4G). Therefore, the Fan1 M50R variant associated with high-risk pancreatic cancers causes unrestrained replication fork progression and chromosomal instability known to drive carcinogenesis.

In this study, we made the unexpected finding that although Ub-Fancd2 recruits Fan1 to ICL-blocked replication forks, this is not required for ICL repair judged by MMC sensitivity and G_2 arrest. Instead, Fan1 recruitment is vital for protective responses when forks stall, even in the absence of DNA cross-links. Cells defective in Fan1 recruitment, or activity, show a high frequency of chromosome abnormalities and increased fork rate when forks are forced to stall. The mechanisms underlying these defects are not yet clear, but cells depleted of the HLTF translocase or RAD51 recombinase, which both drive fork reversal, show longer replication tracks in HU, similar to Fan1-defective cells (*14*, *15*). Therefore, Fan1 recruitment and activity might promote fork reversal, but this remains to be tested. It is not yet clear whether the chromosome abnormalities seen after fork stalling in Fan1-defective cells are related to the increased fork speed or whether they arise independently. It seems counter-intuitive, perhaps, that a nuclease activity is required to prevent chromosome breaks at stalled forks. One potential explanation is that Fan1 cleaves stalled forks in a way that enables replication to resume after fork stalling, consistent with a recent report that Fan1 promotes replication fork recovery (*16*). Failure of Fan1-mediated fork processing may result in the persistence of structures that are cleaved inappropriately by other nucleases, leading to forks breaking in a way that is refractory to repair.

Our observations that Fan1 nuclease activity and interaction with Ub-Fancd2 prevent cancers prompt future investigations as to whether cancer predisposition associated with FA might be caused by defective fork processing, as opposed to defective ICL repair. Identifying a separation-of-function Fan1 mutant affecting ICL repair but not stalled fork processing would be valuable for these efforts. Besides pancreatic cancer, germline mutations in Fan1 have been identified in colon cancer (*17*). Loss of heterozygosity (LOH) has not been observed in tumors from the M50R carriers or in Fan1-mutated colon cancers (*13*, *17*). Epigenetic inactivation of Fan1, haplo-insufficiency, or dominant-negative effects may provide explanations, but these ideas remain to be investigated. KIN caused by biallelic Fan1 mutations is a very rare disease, but early-onset cancers were reported in two affected families (*17*). These reports, together with the present study, are consistent with Fan1 acting as a tumor suppressor with multiple roles in genome maintenance vital for preventing human diseases.

REFERENCES AND NOTES

1. A. D. Auerbach, *Mutat. Res.* **668**, 4–10 (2009).
2. H. Kim, A. D. D'Andrea, *Genes Dev.* **26**, 1393–1408 (2012).
3. I. Garcia-Higuera *et al.*, *Mol. Cell* **7**, 249–262 (2001).
4. C. MacKay *et al.*, *Cell* **142**, 65–76 (2010).
5. K. Kratz *et al.*, *Cell* **142**, 77–88 (2010).
6. T. Liu, G. Ghosal, J. Yuan, J. Chen, J. Huang, *Science* **329**, 693–696 (2010).
7. A. Smogorzewska *et al.*, *Mol. Cell* **39**, 36–47 (2010).
8. W. Zhou *et al.*, *Nat. Genet.* **44**, 910–915 (2012).
9. I. M. Munoz, P. Szyniarowski, R. Toth, J. Rouse, C. Lachaud, *PLOS ONE* **9**, e109752 (2014).
10. K. Schlacher, H. Wu, M. Jasin, *Cancer Cell* **22**, 106–116 (2012).
11. G. Lossaint *et al.*, *Mol. Cell* **51**, 678–690 (2013).
12. S. Houghtaling *et al.*, *Genes Dev.* **17**, 2021–2035 (2003).
13. A. L. Smith *et al.*, *Cancer Lett.* **370**, 302–312 (2016).
14. R. Zellweger *et al.*, *J. Cell Biol.* **208**, 563–579 (2015).
15. A. C. Kile *et al.*, *Mol. Cell* **58**, 1090–1100 (2015).
16. I. Chaudhury, D. R. Stroik, A. Sobeck, *Mol. Cell. Biol.* **34**, 3939–3954 (2014).
17. N. Seguí *et al.*, *Gastroenterology* **149**, 563–566 (2015).

ACKNOWLEDGMENTS

We are grateful to J. Hastie, H. MacLauchlan, and the Antibody Production Team at Division of Signal Transduction Therapy (DSTT) and the DNA Sequencing Service at the School of Life Sciences, University of Dundee. We thank Centre for Interdisciplinary Research Resource Unit (CIRRU) staff, especially L. Malone and C. Clacher, for help with animal husbandry and G. Gilmour and E. Forsyth for help with genotyping. We thank L. Oxford and L. Stevenson (Veterinary Diagnostic Services, University of Glasgow) for support with tissue processing. We thank A. d'Andrea for Fancd2$^{-/-}$ mice. We are grateful to L. Feeney for critical reading of this manuscript. We thank A. Connor, A. Smith, S. Gallinger, and G. Zogopoulos for communicating data prior to publication. C.L. is the recipient of a Marie Curie Intra-European fellowship. A.M. was supported by Wellcome Trust Investigator Award WT096598MA to J.J.B. This study was supported by the Medical Research Council (MRC) and the pharmaceutical companies supporting the DSTT (AstraZeneca, Boehringer-Ingelheim, GlaxoSmithKline, Merck KgaA, Janssen Pharmaceutica, and Pfizer) associated with the MRC Protein Phosphorylation and Ubiquitylation Unit. Fan1 nuclease–defective mice are available from J.R. under a material transfer agreement with the University of Dundee.

SUPPLEMENTARY MATERIALS

www.sciencemag.org/content/351/6275/846/suppl/DC1
Materials and Methods
Figs. S1 to S6
References

1 October 2015; accepted 11 January 2016
Published online 21 January 2016
10.1126/science.aad5634

NEUROSCIENCE

Neurons diversify astrocytes in the adult brain through sonic hedgehog signaling

W. Todd Farmer,[1] Therése Abrahamsson,[1] Sabrina Chierzi,[1] Christopher Lui,[1] Cristian Zaelzer,[1] Emma V. Jones,[1] Blandine Ponroy Bally,[1] Gary G. Chen,[2,3] Jean-Francois Théroux,[2,3] Jimmy Peng,[4,5] Charles W. Bourque,[1] Frédéric Charron,[4,5] Carl Ernst,[2,3,6,7] P. Jesper Sjöström,[1] Keith K. Murai[1]*

Astrocytes are specialized and heterogeneous cells that contribute to central nervous system function and homeostasis. However, the mechanisms that create and maintain differences among astrocytes and allow them to fulfill particular physiological roles remain poorly defined. We reveal that neurons actively determine the features of astrocytes in the healthy adult brain and define a role for neuron-derived sonic hedgehog (Shh) in regulating the molecular and functional profile of astrocytes. Thus, the molecular and physiological program of astrocytes is not hardwired during development but, rather, depends on cues from neurons that drive and sustain their specialized properties.

Astrocytes have fundamental roles in nearly all aspects of brain function, including extracellular ion and neurotransmitter homeostasis, neurometabolism, and cerebrovasculature control (*1*–*3*). Prime examples are pH-sensing brainstem astrocytes that mediate respiratory control (*4*) and AMPA (α-amino-3-hydroxy-5-methyl-4 isoxazolepropionic acid)–type glutamate receptor–expressing glia that function in cerebellar motor learning (*5*). Distinct patterns of transcription (*6*, *7*) implicate select genetic programs and possibly distinct signaling mechanisms that establish astrocyte subtypes (*2*, *8*). These processes participate in early developmental patterning events to promote astrocyte heterogeneity in vivo (*9*–*12*).

We explored how molecular features of astrocytes are created and sustained in the mature mouse brain. Because of the complexity of astrocyte heterogeneity in brain areas such as the cerebral cortex, we focused on the cerebellar cortex, which contains two specialized astrocyte

high frequency in high-risk pancreatic cancers (*13*). The M50R Fan1 variant, which cosegregates with pancreatic cancer in two separate families, is a strong candidate pancreatic cancer predisposition gene. M50 lies in the UBZ domain of Fan1 (Fig. 4C). Similar to the UBZ* mutation (C44A+C47A), the Fan1 M50R mutation abolished Fan1 foci but rescued the MMC sensitivity of U2OS Fan1$^{-/-}$ cells (Fig. 4, D and E). The M50R mutant failed, however, to prevent chromosome abnormalities induced by HU or MMC in Fan1$^{-/-}$ cells (Fig. 4F). Moreover, expression of wild-type Fan1 in Fan1$^{-/-}$ cells restored normal track length in HU, but the Fan1 M50R mutant failed to do so (Fig. 4G). Therefore, the Fan1 M50R variant associated with high-risk pancreatic cancers causes unrestrained replication fork progression and chromosomal instability known to drive carcinogenesis.

In this study, we made the unexpected finding that although Ub-Fancd2 recruits Fan1 to ICL-blocked replication forks, this is not required for ICL repair judged by MMC sensitivity and G_2 arrest. Instead, Fan1 recruitment is vital for protective responses when forks stall, even in the absence of DNA cross-links. Cells defective in Fan1 recruitment, or activity, show a high frequency of chromosome abnormalities and increased fork rate when forks are forced to stall. The mechanisms underlying these defects are not yet clear, but cells depleted of the HLTF translocase or RAD51 recombinase, which both drive fork reversal, show longer replication tracks in HU, similar to Fan1-defective cells (*14*, *15*). Therefore, Fan1 recruitment and activity might promote fork reversal, but this remains to be tested. It is not yet clear whether the chromosome abnormalities seen after fork stalling in Fan1-defective cells are related to the increased fork speed or whether they arise independently. It seems counter-intuitive, perhaps, that a nuclease activity is required to prevent chromosome breaks at stalled forks. One potential explanation is that Fan1 cleaves stalled forks in a way that enables replication to resume after fork stalling, consistent with a recent report that Fan1 promotes replication fork recovery (*16*). Failure of Fan1-mediated fork processing may result in the persistence of structures that are cleaved inappropriately by other nucleases, leading to forks breaking in a way that is refractory to repair.

Our observations that Fan1 nuclease activity and interaction with Ub-Fancd2 prevent cancers prompt future investigations as to whether cancer predisposition associated with FA might be caused by defective fork processing, as opposed to defective ICL repair. Identifying a separation-of-function Fan1 mutant affecting ICL repair but not stalled fork processing would be valuable for these efforts. Besides pancreatic cancer, germline mutations in Fan1 have been identified in colon cancer (*17*). Loss of heterozygosity (LOH) has not been observed in tumors from the M50R carriers or in Fan1-mutated colon cancers (*13*, *17*). Epigenetic inactivation of Fan1, haplo-insufficiency, or dominant-negative effects may provide explanations, but these ideas remain to be investigated. KIN caused by biallelic Fan1 mutations is a very rare disease, but early-onset cancers were reported in two affected families (*17*). These reports, together with the present study, are consistent with Fan1 acting as a tumor suppressor with multiple roles in genome maintenance vital for preventing human diseases.

REFERENCES AND NOTES

1. A. D. Auerbach, *Mutat. Res.* **668**, 4–10 (2009).
2. H. Kim, A. D. D'Andrea, *Genes Dev.* **26**, 1393–1408 (2012).
3. I. Garcia-Higuera *et al.*, *Mol. Cell* **7**, 249–262 (2001).
4. C. MacKay *et al.*, *Cell* **142**, 65–76 (2010).
5. K. Kratz *et al.*, *Cell* **142**, 77–88 (2010).
6. T. Liu, G. Ghosal, J. Yuan, J. Chen, J. Huang, *Science* **329**, 693–696 (2010).
7. A. Smogorzewska *et al.*, *Mol. Cell* **39**, 36–47 (2010).
8. W. Zhou *et al.*, *Nat. Genet.* **44**, 910–915 (2012).
9. I. M. Munoz, P. Szyniarowski, R. Toth, J. Rouse, C. Lachaud, *PLOS ONE* **9**, e109752 (2014).
10. K. Schlacher, H. Wu, M. Jasin, *Cancer Cell* **22**, 106–116 (2012).
11. G. Lossaint *et al.*, *Mol. Cell* **51**, 678–690 (2013).
12. S. Houghtaling *et al.*, *Genes Dev.* **17**, 2021–2035 (2003).
13. A. L. Smith *et al.*, *Cancer Lett.* **370**, 302–312 (2016).
14. R. Zellweger *et al.*, *J. Cell Biol.* **208**, 563–579 (2015).
15. A. C. Kile *et al.*, *Mol. Cell* **58**, 1090–1100 (2015).
16. I. Chaudhury, D. R. Stroik, A. Sobeck, *Mol. Cell. Biol.* **34**, 3939–3954 (2014).
17. N. Seguí *et al.*, *Gastroenterology* **149**, 563–566 (2015).

ACKNOWLEDGMENTS

We are grateful to J. Hastie, H. MacLauchlan, and the Antibody Production Team at Division of Signal Transduction Therapy (DSTT) and the DNA Sequencing Service at the School of Life Sciences, University of Dundee. We thank Centre for Interdisciplinary Research Resource Unit (CIRRU) staff, especially L. Malone and C. Clacher, for help with animal husbandry and G. Gilmour and E. Forsyth for help with genotyping. We thank L. Oxford and L. Stevenson (Veterinary Diagnostic Services, University of Glasgow) for support with tissue processing. We thank A. d'Andrea for Fancd2$^{-/-}$ mice. We are grateful to L. Feeney for critical reading of this manuscript. We thank A. Connor, A. Smith, S. Gallinger, and G. Zogopoulos for communicating data prior to publication. C.L. is the recipient of a Marie Curie Intra-European fellowship. A.M. was supported by Wellcome Trust Investigator Award WT096598MA to J.J.B. This study was supported by the Medical Research Council (MRC) and the pharmaceutical companies supporting the DSTT (AstraZeneca, Boehringer-Ingelheim, GlaxoSmithKline, Merck KgaA, Janssen Pharmaceutica, and Pfizer) associated with the MRC Protein Phosphorylation and Ubiquitylation Unit. Fan1 nuclease–defective mice are available from J.R. under a material transfer agreement with the University of Dundee.

SUPPLEMENTARY MATERIALS

www.sciencemag.org/content/351/6275/846/suppl/DC1
Materials and Methods
Figs. S1 to S6
References

1 October 2015; accepted 11 January 2016
Published online 21 January 2016
10.1126/science.aad5634

Downloaded from on February 18, 2016

NEUROSCIENCE

Neurons diversify astrocytes in the adult brain through sonic hedgehog signaling

W. Todd Farmer,[1] Therése Abrahamsson,[1] Sabrina Chierzi,[1] Christopher Lui,[1] Cristian Zaelzer,[1] Emma V. Jones,[1] Blandine Ponroy Bally,[1] Gary G. Chen,[2,3] Jean-Francois Théroux,[2,3] Jimmy Peng,[4,5] Charles W. Bourque,[1] Frédéric Charron,[4,5] Carl Ernst,[2,3,6,7] P. Jesper Sjöström,[1] Keith K. Murai[1]*

Astrocytes are specialized and heterogeneous cells that contribute to central nervous system function and homeostasis. However, the mechanisms that create and maintain differences among astrocytes and allow them to fulfill particular physiological roles remain poorly defined. We reveal that neurons actively determine the features of astrocytes in the healthy adult brain and define a role for neuron-derived sonic hedgehog (Shh) in regulating the molecular and functional profile of astrocytes. Thus, the molecular and physiological program of astrocytes is not hardwired during development but, rather, depends on cues from neurons that drive and sustain their specialized properties.

Astrocytes have fundamental roles in nearly all aspects of brain function, including extracellular ion and neurotransmitter homeostasis, neurometabolism, and cerebrovasculature control (*1*–*3*). Prime examples are pH-sensing brainstem astrocytes that mediate respiratory control (*4*) and AMPA (α-amino-3-hydroxy-5-methyl-4 isoxazolepropionic acid)–type glutamate receptor–expressing glia that function in cerebellar motor learning (*5*). Distinct patterns of transcription (*6*, *7*) implicate select genetic programs and possibly distinct signaling mechanisms that establish astrocyte subtypes (*2*, *8*). These processes participate in early developmental patterning events to promote astrocyte heterogeneity in vivo (*9*–*12*).

We explored how molecular features of astrocytes are created and sustained in the mature mouse brain. Because of the complexity of astrocyte heterogeneity in brain areas such as the cerebral cortex, we focused on the cerebellar cortex, which contains two specialized astrocyte

types, Bergmann glial cells (BGs) and velate astrocytes (VAs), that have distinct cell positioning, morphology, and molecular composition (*13*, *14*). BGs localized within the Purkinje cell (PC) layer extend processes that enwrap PC dendrites and synapses (Fig. 1A). In contrast, VAs in the granule cell layer (GCL) surround granule cells (GCs) and mossy fiber glomeruli (Fig. 1A) (*15*). BGs and VAs display distinct, but overlapping, molecular profiles. Although BGs and VAs show comparable expression of genes, including *GFAP* (glial fibrillary acidic protein), *Sox9* [*SRY*-related high mobility group (HMG)–box gene 9], and *GLT1* (glutamate transporter 1), BGs are enriched in AMPA receptors GluA1 and GluA4, and GLAST (glial high-affinity glutamate transporter) (Fig. 1B) (*5*). VAs, in contrast, have low amounts of GluA1, GluA4, and GLAST and large amounts of the water channel aquaporin 4 (AQP4) (Fig. 1B) (*16*). Note that components of the sonic hedgehog (Shh) signaling pathway, a developmental morphogen pathway (*17*, *18*), including the *Gli1* transcription factor and Shh receptors Patched (patched domain–containing protein) 1 and 2 (Ptch1/2), are also enriched in mature BGs but not VAs (www.brain-map.org; www.gensat.org) (Fig. 1B). Ptch2 and Smoothened (Smo) are also expressed by cultured cerebellar astrocytes expressing GLAST (fig. S1).

[1]Centre for Research in Neuroscience, Department of Neurology and Neurosurgery, Brain Repair and Integrative Neuroscience Program, The Research Institute of the McGill University Health Centre, Montreal General Hospital, Montreal, Quebec, Canada. [2]Department of Psychiatry, McGill University, Montreal, Quebec, Canada. [3]McGill Group for Suicide Studies, Douglas Hospital, Montreal, Quebec, Canada. [4]Molecular Biology of Neural Development, Institut de Recherches Cliniques de Montréal, Department of Medicine, University of Montreal, Montreal, Quebec, Canada. [5]Department of Biology, McGill University, Montreal, Quebec, Canada. [6]Department of Human Genetics, McGill University, Montreal, Quebec, Canada. [7]Douglas Hospital Research Institute, Verdun, Quebec, Canada.
***Corresponding author. E-mail: keith.murai@mcgill.ca**

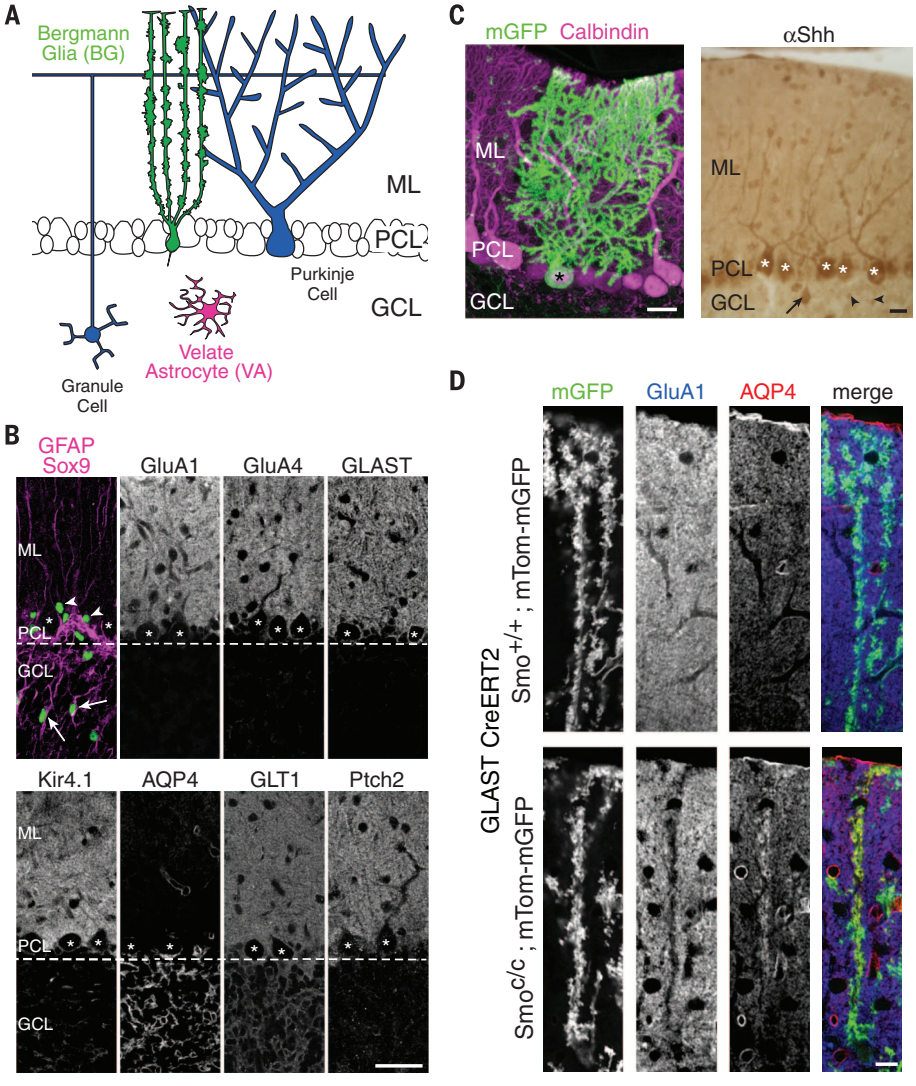


Fig. 1. Astrocytes in cerebellar cortex, expression of Shh, and Smo deletion. (**A**) BG (green) with soma in the Purkinje cell layer (PCL) and processes in the molecular layer (ML), and VAs (magenta) in GCL. (**B**) Immunofluorescence microscopy for proteins in BGs and VAs. (**C**) Expression of Shh in PCs expressing calbindin (magenta, asterisks), GCs (right, arrowheads), and interneurons (right, arrow) in Shh reporter mice and after Shh immunolabeling. (**D**) Removal of Smo through Cre recombination at 5 weeks and analysis 4 weeks later (n = 6 pairs). Scale bars: (B) 30 μm. (C) 15 μm, (D) 10 μm.

In the developing central nervous system (CNS), various cells produce Shh to regulate cell specification, axon guidance, and cell proliferation (*17*, *18*). To identify which cells produce Shh in the mature brain, we used a mouse line that produces tamoxifen-sensitive Cre recombinase from the Shh gene locus (fig. S2A). Cre activation with tamoxifen in >5-week-old mice revealed that PCs, GCs, and interneurons expressed Shh (Fig. 1C and fig. S2, B to E). Immunolabeling for Shh showed localization in neurons, including PCs, and an overall enrichment in the molecular layer (Fig. 1C and fig. S2, F and G). To determine whether Shh signaling regulates mature BGs in vivo, we removed the Shh signal transducer Smo from BGs using controlled activation of Cre with tamoxifen in astrocytes expressing GLAST (GLAST CreERT2) (fig. S3A) (*19*, *20*). Quantitative reverse transcriptase polymerase chain reaction (qRT-PCR) showed a 24% loss of *Smo* mRNA after Cre activation (fig. S3B), an amount that did not disrupt cerebellar organization or motor performance (fig. S3C). BGs lacking Smo extended processes that enwrapped PC dendrites, detected by staining of calbindin, and spines, seen by staining of metabotropic glutamate receptor 1 (mGluR1) (fig. S4).

Although Smo was not essential for the structure of BGs, Smo regulated expression of molecules that confer BG specialized properties (*5*). Shh signaling sustained GluA1 expression and prevented expression of AQP4 (Fig. 1D and fig. S3D). Virally expressed Cre in patches of BGs (Fig. 2A) revealed that Smo was needed for expression of GluA1, GluA4, GLAST, the inward rectifying potassium channel Kir4.1 (*21*), and Ptch2 (Fig. 2, B and C, and fig. S5) (*22*). This loss was accompanied by an increase in the amount of AQP4 (Fig. 2, B and C). No changes were observed for GLT1 or overall anatomy (figs. S5 and S6). To assess physiological changes to BGs, we used AMPA uncaging to elicit AMPA-receptor responses in BGs (Fig. 2D). This showed reduced AMPA receptor–mediated currents after Smo loss (Fig. 2E). To determine whether Shh expressed by PCs maintains BG gene expression, we removed Shh from PCs using Cre (fig. S7A). BGs next to PCs lacking Shh had decreased amounts of GluA1, Kir4.1, and GLAST and increased amounts of AQP4 (Fig. 2F and fig. S7B), with no disruption to the presence or position of cells containing SOX9 or the expression of GLT1 (fig. S8).

Cerebellar VAs are exposed to lower amounts of Shh than BGs, as indicated by Shh immunolabeling (Fig. 1C) and the low amounts of Shh receptor Ptch2, which is positively regulated by Shh signaling (Fig. 1B). To test whether the Shh pathway could control VAs, constitutively active Smo (SmoM2) was expressed in VAs under the control of Cre (fig. S9A) (*23*). Virally and genetically induced expression of SmoM2 in VAs

reduced amounts of AQP4 and increased GluA1, GLAST, and Kir4.1 (Fig. 3, A to C, and fig. S9, B to D) without affecting cell proliferation (fig. S10). To determine whether increasing the Shh pathway allowed VAs to obtain an mRNA profile resembling that of BGs, we performed RNA sequencing (RNA-seq) on small groups of VAs and BGs individually isolated from fresh brain slices (Fig. 3D and fig. S11). This identified 415 mRNAs that significantly distinguish control VAs from BGs. Hierarchical clustering analysis based on these mRNAs showed that SmoM2-expressing VAs (SmoM2 VAs) showed greater similarity to BGs than control VAs. Genes strongly expressed in control VAs like *Edn1* (*endothelin 1*) and *Tlr2* (*Toll-like receptor 2*) are substantially reduced in SmoM2 VAs, whereas genes expressed in BGs like *Anxa7* (*annexin A7*) are up-regulated in SmoM2 VAs (Fig. 3, E and F). Thus, Shh signaling drives specific changes in VAs, which causes them to acquire a molecular profile that is intermediate between a BG and a VA.

We also tested if Shh signaling regulates BGs during development by altering Shh signaling at postnatal day 2 (P2) and analyzing mice at P15 (fig. S12). *Smo* deletion decreased amounts of GluA1 and increased amounts of AQP4 in developing BGs (fig. S13, A and B), whereas *SmoM2* expression increased abundance of GluA1, GluA4, and Kir4.1 in VAs (fig. S13, C and D). *SmoM2* expression led to a small, significant increase in proliferating glia that contained Ki67, which suggested that Shh signaling promotes cell division during early stages (fig. S14). Thus, cerebellar astrocytes use the Shh pathway at developing and adult stages to establish and sustain their molecular features.

Shh is expressed by neurons in several adult brain regions (*24*–*26*). To determine whether astrocytes in these areas respond to the Shh pathway, we expressed SmoM2 in mature astrocytes (fig. S15) and examined the expression of proteins, including Kir4.1, which shows heterogeneous expression (Fig. 4 and fig. S15). In the hippocampus, SmoM2 expression increased Kir4.1 protein in CA1 and dentate gyrus astrocytes and overall *Kir4.1* mRNA (Fig. 4, A to C, and figs. S15 and S16). *Kir4.1* mRNA was also decreased in Shh haploinsufficient mice, which showed reduced *Shh* and *Gli1* mRNA (Fig. 4D). Kir4.1 upregulation also increased barium-sensitive Kir4.1 currents, as revealed by changes in the rectification index (Fig. 4, E to H, and fig. S17) (*21*). Similarly, Kir4.1 mRNA levels were reduced in cultured hippocampal astrocytes exposed to Shh pathway inhibitors (fig. S18) (*27*, *28*). GLAST, GluA1, and GluA4 expression were unaffected (figs. S19 to S21). In cortical astrocytes, removal of Smo reduced Kir4.1 protein (fig. S22, A and B), whereas expression of SmoM2 increased astrocyte Kir4.1 protein (fig. S22, C and D, and fig. S23). This was consistent with decreased and increased Kir4.1 mRNA in the cortex of Shh haploinsufficient and SmoM2 mice, respectively (fig. S22, E and F). GLAST and AQP4 mRNAs remained unchanged in SmoM2 and Shh haploinsufficient mice (figs. S22, S24, and S25).

We found that astrocytes depend on cues from mature neurons to control their complex molecular profile in vivo. This challenges the concept that astrocytes contain hardwired molecular and physiological programs that are fully determined during development and indicates that neurons

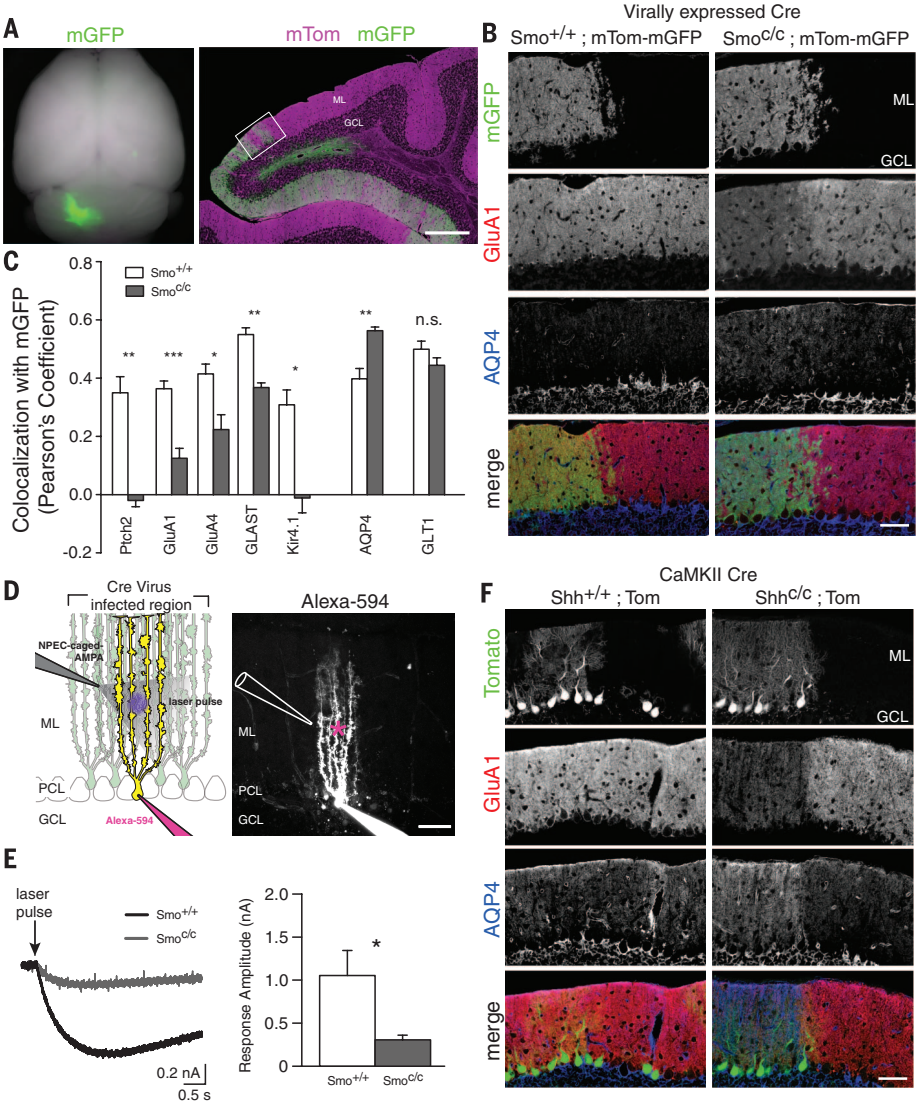


Fig. 2. Purkinje cells diversify BGs in the mature cerebellum. (**A**) (Left) Fluorescence microscopy of membrane-targeted green fluorescent protein (GFP) (mGFP, green) in the cerebellum after viral expression of Cre. (Right) BGs that express mGFP or not (mTom; magenta). (**B** and **C**) Smo loss in BGs (green; virus delivered at >5 weeks, analyzed 4 weeks later) [Ptch2 (n = 3 pairs), GluA1 (n = 5), GluA4 (n = 3), GLAST (n = 3), Kir4.1 (n = 3), and AQP4 (n = 5)]. Protein expression determined by colocalization with mGFP reference protein. (**D**) (Left) Setup to elicit AMPA receptor currents in BGs. (Right) Patched BGs showing the location of the compound (*N*)-1-(2-nitrophenyl)ethylcarboxy-(*S*)-α-1-(2-nitrophenyl)ethylcarboxyamino-3-hydroxy-5-methyl-4-isoxazolepropionic acid (NPEC-AMPA) puff pipette and laser pulse (asterisk). (**E**) AMPA receptor currents in BGs. (Left) Representative trace and quantification of uncaging-evoked AMPA receptor currents in cells with Smo (n = 7; $Smo^{+/+}$) or not (n = 8; $Smo^{c/c}$). (**F**) Immunofluorescence detection of GluA1 and AQP4 in BG after loss of Shh from PCs (n = 4 pairs). Error bars represent SEM. Student's t test. $^{*}P \le 0.05$, $^{**}P \le 0.01$, $^{***}P \le 0.001$. Scale bars: (A) 300 μm, (B), (D), and (F) 40 μm.

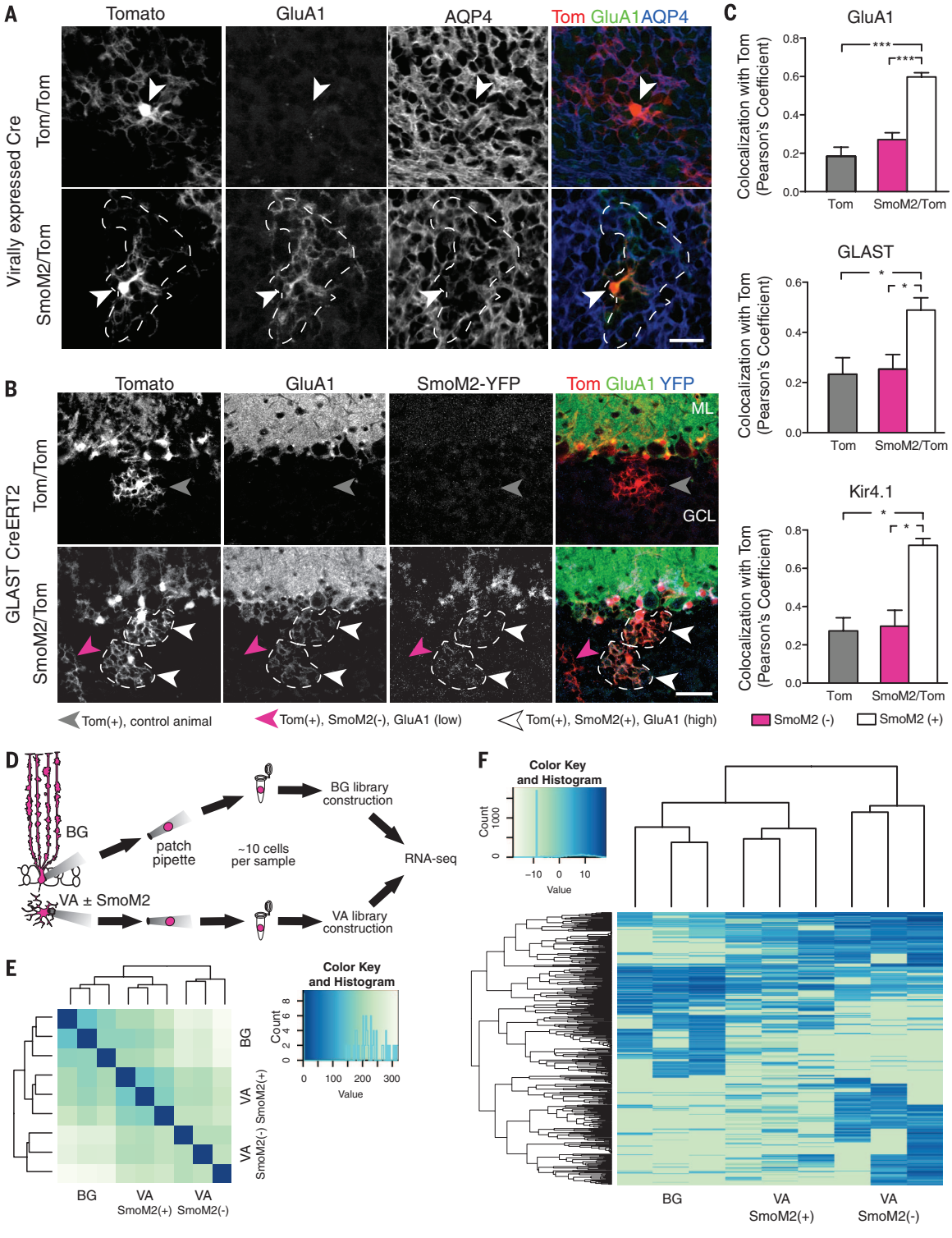


Fig. 3. VAs acquire BG-like profiles upon Shh signaling. (**A**) Immunofluorescence detection of GluA1 and AQP4 in VAs upon SmoM2 and Tomato expression after viral Cre expression (>5-week-old mice) (n = 4 pairs). (**B**) Detection of GluA1 in VAs expressing SmoM2 (white arrowheads) or not (gray and magenta arrowheads). (**C**) Quantification of GluA1, GLAST, and Kir4.1 in VAs through fluorescence colocalization with Tomato reference protein (n = 4). One-way analysis of variance (ANOVA) with Tukey's. (**D**) Experimental steps for single-cell RNA-seq. (**E**) Dendrogram representing a hierarchical clustering of gene expression distances between samples used in the single-cell RNA-seq experiment. Histogram shows a pseudo-color representation of the Euclidean distance matrix (from dark blue for zero distance to white for large distance). (**F**) Gene expression heat map from 415 differentially expressed genes identified in BGs compared with VAs. Colors reflect relative differences of each gene (y axis) for each sample (x axis). Unsupervised clustering trees are shown, and histogram shows relative expression level (white for lower expression and blue for higher expression). Error bars represent SEM. *$P \leq 0.05$, ***$P \leq 0.001$. Scale bars: (A) 20 μm, (B) 30 μm.

communicate with astrocytes to actively regulate their local environment in the brain. Neurons use Shh to control the properties of astrocytes and thus extend its role beyond cell proliferation, specification, and axon guidance during CNS development (*17*, *18*). Surprisingly, astrocytes across brain regions use Shh signaling differently. Cerebellar BGs use Shh signaling to promote glutamate detection (GluA1 and 4) and recovery (GLAST), as well as potassium homeostasis (Kir4.1) (*21*). This is presumably related to the dense glutamatergic inputs onto PCs in the molecular layer. Note that cerebellar VAs acquire features of the BG transcriptome upon Shh signaling. Cortical and hippocampal astrocytes, in contrast, use Shh signaling for more selective regulation of Kir4.1. It is possible that neurons release an array of factors, including Shh, to create astrocyte complexity

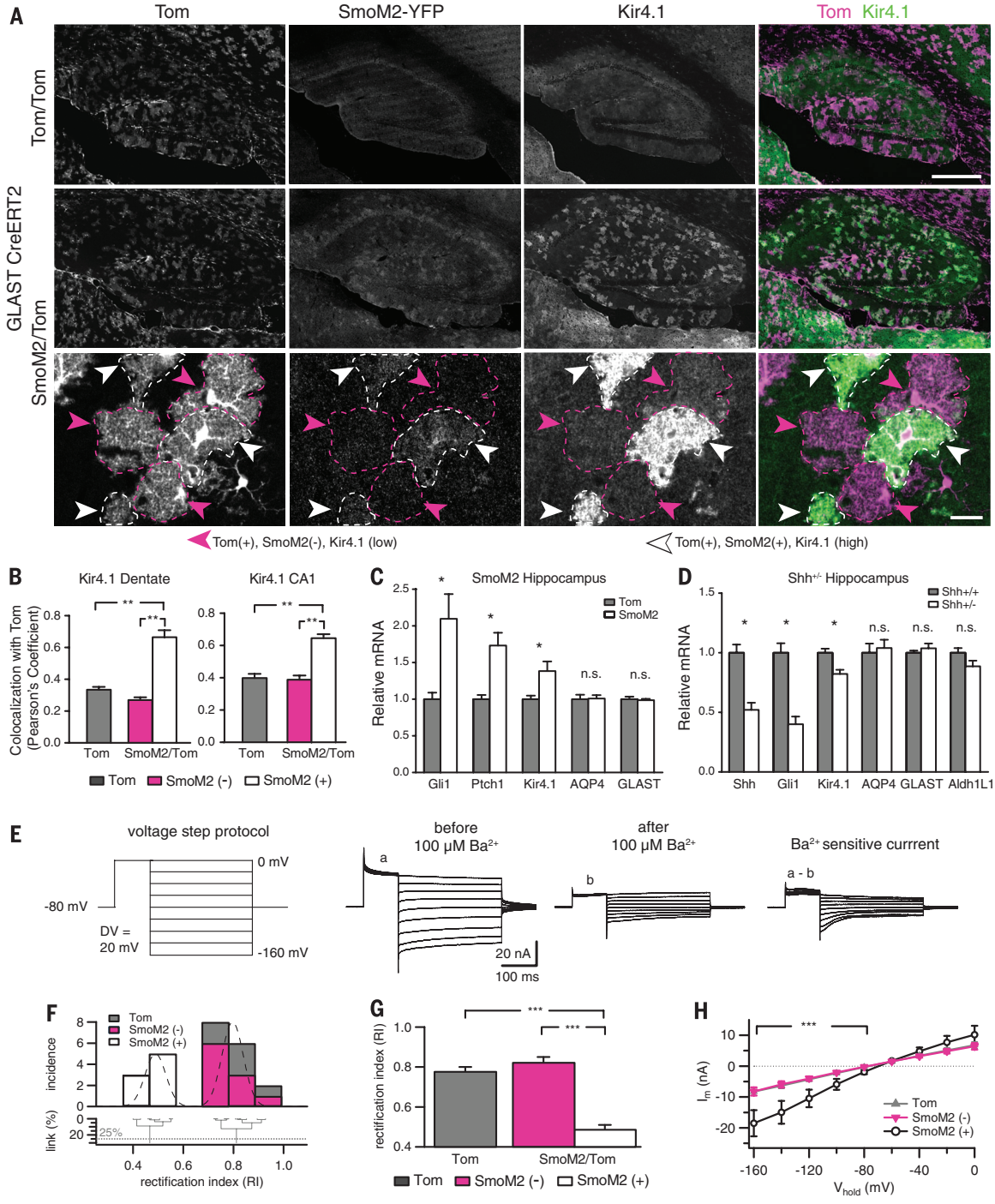


Fig. 4. Shh signaling controls hippocampal astrocytes. (**A**) Astrocytes containing SmoM2 (white arrowheads) or not (magenta arrowheads). Cre was activated at 5 weeks with mice analyzed 4 weeks later. (**B**) Quantification of Kir4.1 expression in CA1 and dentate gyrus through fluorescence colocalization with Tomato reference protein (n = 4 pairs). One-way ANOVA with Tukey's. (**C**) mRNA levels in hippocampus (>5 weeks; 2 weeks after Cre induction; n = 7 control and 8 SmoM2 mice). Student's t test. (**D**) mRNA levels in Shh haploinsufficient mice (>5 weeks; n = 6 pairs). Student's t test. (**E** to **H**) Ba^{2+}-sensitive Kir4.1 currents in astrocytes 2 weeks after SmoM2 expression. (E) (Left) Voltages were stepped from –160 to 0 mV, with initial step to inactivate non-Kir K^+ currents. (Middle, right) Representative currents before (a) and after (b) Ba^{2+}, with Kir4.1 current determined by subtraction (a – b). (F and G) Hierarchical clustering analysis-grouped SmoM2(–) (n = 6 cells) with controls (Tom, n = 10) but segregated SmoM2(+) (n = 8). (H) SmoM2(+) Ba^{2+}-sensitive current-voltage curve differed below the reversal potential. Wilcoxon-Mann-Whitney test. Error bars represent SEM. $*P \le 0.05$, $**P \le 0.01$, $***P \le 0.001$. (A) Scale bars, 500 μm and 20 μm.

in the mature brain (*6*, *7*). These factors likely cooperate with developmental patterning events to generate astrocyte heterogeneity (*10*, *11*, *29*) and ultimately ensure that astrocytes are properly specialized for the needs of local neural circuits (*30*).

REFERENCES AND NOTES

1. V. Matyash, H. Kettenmann, *Brain Res. Brain Res. Rev.* **63**, 2–10 (2010).
2. Y. Zhang, B. A. Barres, *Curr. Opin. Neurobiol.* **20**, 588–594 (2010).
3. N. A. Oberheim, S. A. Goldman, M. Nedergaard, *Methods Mol. Biol.* **814**, 23–45 (2012).
4. A. V. Gourine *et al.*, *Science* **329**, 571–575 (2010).
5. A. S. Saab *et al.*, *Science* **337**, 749–753 (2012).
6. J. D. Cahoy *et al.*, *J. Neurosci.* **28**, 264–278 (2008).
7. Y. Zhang *et al.*, *J. Neurosci.* **34**, 11929–11947 (2014).
8. M. R. Freeman, *Science* **330**, 774–778 (2010).
9. Y. Muroyama, Y. Fujiwara, S. H. Orkin, D. H. Rowitch, *Nature* **438**, 360–363 (2005).
10. C. Hochstim, B. Deneen, A. Lukaszewicz, Q. Zhou, D. J. Anderson, *Cell* **133**, 510–522 (2008).
11. H. H. Tsai *et al.*, *Science* **337**, 358–362 (2012).
12. M. R. Freeman, D. H. Rowitch, *Neuron* **80**, 613–623 (2013).
13. K. Yamada, M. Watanabe, *Anat. Sci. Int.* **77**, 94–108 (2002).
14. Y. Kita, K. Kawakami, Y. Takahashi, F. Murakami, *PLOS ONE* **8**, e70091 (2013).
15. T. M. Hoogland, B. Kuhn, *Cerebellum* **9**, 264–271 (2010).
16. M. C. Papadopoulos, A. S. Verkman, *Nat. Rev. Neurosci.* **14**, 265–277 (2013).

17. M. Fuccillo, A. L. Joyner, G. Fishell, *Nat. Rev. Neurosci.* **7**, 772–783 (2006).
18. J. Briscoe, *EMBO J.* **28**, 457–465 (2009).
19. T. Mori *et al.*, *Glia* **54**, 21–34 (2006).
20. F. Long, X. M. Zhang, S. Karp, Y. Yang, A. P. McMahon, *Development* **128**, 5099–5108 (2001).
21. B. Djukic, K. B. Casper, B. D. Philpot, L.-S. Chin, K. D. McCarthy, *J. Neurosci.* **27**, 11354–11365 (2007).
22. R. V. Pearse 2nd, K. J. Vogan, C. J. Tabin, *Dev. Biol.* **239**, 15–29 (2001).
23. J. Jeong, J. Mao, T. Tenzen, A. H. Kottmann, A. P. McMahon, *Genes Dev.* **18**, 937–951 (2004).
24. A. D. R. Garcia, R. Petrova, L. Eng, A. L. Joyner, *J. Neurosci.* **30**, 13597–13608 (2010).
25. C. C. Harwell *et al.*, *Neuron* **73**, 1116–1126 (2012).
26. L. E. Gonzalez-Reyes *et al.*, *Neuron* **75**, 306–319 (2012).
27. M. K. Cooper, J. A. Porter, K. E. Young, P. A. Beachy, *Science* **280**, 1603–1607 (1998).
28. A. Rohner *et al.*, *Mol. Cancer Ther.* **11**, 57–65 (2012).
29. A. V. Molofsky *et al.*, *Nature* **509**, 189–194 (2014).
30. X. Tong *et al.*, *Nat. Neurosci.* **17**, 694–703 (2014).

ACKNOWLEDGMENTS

Glast-CreERT2 mice are available from M. Götz under a material transfer agreement with Helmholtz Zentrum München–Deutsches Forschungszentrum für Gesundheit und Umwelt. This work was supported by the Canadian Institutes of Health Research (FDN 143337 to C.W.B., MOP 126137/NIA 288936 to P.J.S., and MOP 111152/MOP 123390 to K.K.M.); Natural Sciences and Engineering Research Council of Canada (DG 418546-2 to P.J.S. and 408044-2011 to K.K.M.); Canada Research Chairs Program (F.C., C.E., and K.K.M.); Brain Canada/W. Garfield Weston Foundation (F.C. and K.K.M.); James McGill Chair Program (C.W.B.); and Canadian Foundation for Innovation (LOF 28331 to P.J.S.). W.T.F was supported by a postdoctoral fellowship from the Research Institute of the McGill University Health Centre. J.P. was supported by a Vanier fellowship. We thank M. Götz for GLAST CreERT2 mice; G. Quesseveur for help with tissue processing; L. Li for mouse technical assistance; S. Scales (Genentech) for Shh antibody; T. Alves-Ferreira for ImageJ support; A. Montpetit, A. Staffa, and staff at Genome Quebec and the Research Institute of McGill University Hospital Centre Molecular Imaging Platform for support and use of instrumentation; and E. Ruthazer and D. van Meyel for helpful feedback on the manuscript. The authors declare no conflicts of interest.

SUPPLEMENTARY MATERIALS

www.sciencemag.org/content/351/6275/849/suppl/DC1
Materials and Methods
Figs. S1 to S25
Tables S1 to S5
References (*31*–*40*)

21 April 2015; accepted 7 January 2016
10.1126/science.aab3103

MICROBIOME

Lactobacillus plantarum strain maintains growth of infant mice during chronic undernutrition

Martin Schwarzer,[1,2]* Kassem Makki,[1,3] Gilles Storelli,[1] Irma Machuca-Gayet,[1]† Dagmar Srutkova,[2] Petra Hermanova,[2] Maria Elena Martino,[1] Severine Balmand,[4] Tomas Hudcovic,[2] Abdelaziz Heddi,[4] Jennifer Rieusset,[3] Hana Kozakova,[2] Hubert Vidal,[3] François Leulier[1]*

In most animal species, juvenile growth is marked by an exponential gain in body weight and size. Here we show that the microbiota of infant mice sustains both weight gain and longitudinal growth when mice are fed a standard laboratory mouse diet or a nutritionally depleted diet. We found that the intestinal microbiota interacts with the somatotropic hormone axis to drive systemic growth. Using monocolonized mouse models, we showed that selected lactobacilli promoted juvenile growth in a strain-dependent manner that recapitulated the microbiota's effect on growth and the somatotropic axis. These findings show that the host's microbiota supports juvenile growth. Moreover, we discovered that lactobacilli strains buffered the adverse effects of chronic undernutrition on the postnatal growth of germ-free mice.

During the juvenile growth period, the gain in animal body size varies widely as a result of the interactions between nutritional input and the organism's hormonal cues. In mammals, postnatal growth is controlled by the activity of the somatotropic axis (fig. S1), in which growth hormone (GH) instructs the liver and peripheral tissues to produce insulin-like growth factor–1 (IGF-1), to promote organ and systemic growth (*1*–*3*). Chronic undernutrition triggers a state of GH resistance (*4*, *5*) that leads to stunting, and juveniles become small and thin (*6*). Acute malnutrition, in contrast, causes wasting, defined as severe weight loss and mediated in part through the disruption of the gut microbiota (*7*). However, the contribution of the gut microbiota to normal postnatal growth and its influence on the activity of the somatotropic axis during chronic undernutrition remain unknown.

To address this question, we first compared the growth parameters of wild-type (WT) and germ-free (GF) infant male mice fed a standard breeding diet (25% proteins, 9% fats; table S1) until young adulthood (8 weeks old, Fig. 1 and fig. S2). After weaning, the GF and WT animals ingested similar amounts of food relative to body weight (fig. S3), yet at 8 weeks of age, GF mice weighed 14.5% less and were 4% shorter than WT mice (Fig. 1, A and C; fig. S2, A and B; and table S2). These growth differences were most pronounced after weaning (Fig. 1, A to D, and fig. S2, C and D). Thus, with a standard breeding diet, the gut microbiota ensures optimal weight gain and longitudinal growth, especially around weaning. Remarkably, the 17% weight gain seen in WT animals (fig. S2A and table S2) was not a consequence of increased adiposity. The epididymal fat pads and adipocyte size of WT and GF males remained similar (fig. S4, A to D). Likewise, levels of leptin, a circulating marker of fat stores (*8*), were similar in the sera of WT and GF animals (fig. S4E). However, the weight gain of the organs of WT animals was greater than that of GF mice (fig. S2E and table S2), confirming that a WT microbiota is associated with optimal systemic somatic growth. This contrasts with the increased adiposity that results from subtherapeutic antibiotic treatments in infant mice that is apparently caused by disrupting the gut microbiota community (*9*, *10*). WT animals were 4% longer (fig. S2B and table S2), indicating that the microbiota also influences skeletal growth. Bone growth parameters, including femur length, cortical thickness, cortical bone fraction, and the trabecular fraction of the femur (Fig. 1, E and F; fig. S2, F to I; and table S2) were all reduced in GF animals, although cortical bone mineral density (BMD) was unaffected (fig. S2J). Previously, Sjögren *et al.* showed that trabecular BMD was increased in GF animals relative to their WT siblings (*11*). However, that study was conducted on females of a different genetic background than ours. Nevertheless, taken together, our results show that the gut microbiota sustains postnatal somatic tissue growth, leading to increased mass gain and enhanced longitudinal growth.

Postnatal systemic growth is mainly driven by the activity of the somatotropic axis (*1*–*3*), where the pituitary gland produces GH, which induces the production of IGF-1. The liver is the major source of circulating IGF-1 and together with IGF-1 binding protein-3 (IGFBP-3) serves as an endocrine determinant of somatic growth (*3*, *12*, *13*) (fig. S1). In addition, IGF-1 is produced by peripheral tissues, including muscles, and acts to promote tissue growth in an autocrine/paracrine manner

[1]Institut de Génomique Fonctionnelle de Lyon, Université de Lyon, Ecole Normale Supérieure de Lyon, Centre National de la Recherche Scientifique, Université Claude Bernard Lyon 1, Unité Mixte de Recherche 5242, 46 Allée d'Italie, 69364 Lyon Cedex 07, France. [2]Laboratory of Gnotobiology, Institute of Microbiology of the Czech Academy of Sciences, v. v. i., Novy Hradek, Czech Republic. [3]Laboratoire CarMeN, Université Lyon 1, Unité Mixte de Recherche INSERM U-1060 et INRA U-1397, Faculté de Médecine Lyon-Sud, Chemin du Grand Revoyet, 69600 Oullins, France. [4]UMR203 BF2I, Biologie Fonctionnelle Insectes et Interactions, Université de Lyon, INRA, INSA-Lyon, F-69621 Villeurbanne, France.
***Corresponding author. E-mail: francois.leulier@ens-lyon.fr (F.L.); martin.schwarzer@ens-lyon.fr (M.S.)** †Present address: Institut National de la Santé et de la Recherche Médicale, Université Claude Bernard Lyon 1, Unité Mixte de Recherche 1033, Faculté de Médecine Lyon-Est, Rue Guillaume Paradin, 69372 Lyon Cedex 08, France.

Downloaded from on February 18, 2016

(*14*) (fig. S1). We therefore measured circulating levels of GH and IGF-1, the major components of this axis (*3*, *15*, *16*), in the sera of WT and GF animals. GH levels peaked around birth and gradually declined during postnatal growth in both WT and GF animals (Fig. 2A). IGF-1 titers were significantly reduced in GF animals (Fig. 2B), as were the circulating levels of IGFBP-3 in sera (*17*) (Fig. 2C). In addition, *Igf1* expression was reduced in muscles of GF animals at both 28 and 56 days (fig. S5, A and B). In the liver, both *Igf1* and *Igfbp3* expression were reduced in GF mice at 28 days (Fig. 2, D and E), at the same time that IGF-1 circulating titers peaked in WT animals (Fig. 2B). Likewise, the phosphorylation of Akt at Ser 473 (phospho-S473-Akt), a marker of IGF-1 receptor (IGF-1R) signaling activity (*18*) (fig. S1), was reduced in the liver of GF animals as compared to WT animals both at 28 (Fig. 2F) and 56 days (fig. S5C).

To assess the importance of IGF-1 levels in mediating postnatal growth dynamics, we repeatedly injected GF and WT animals with recombinant IGF-1 (rIGF-1) for 10 days after weaning and analyzed their growth parameters. GF animals significantly increased their weight, as well as body and femur length, over the treatment period (fig. S5, D to G). Injections of rIGF-1 into WT animals did not promote growth (fig. S5, D to F), even though they modulated two established markers of IGF-1 activity: reduced glycemia and increased phospho-S473-Akt signals in the liver (fig. S5, H and I). In GF mice, IGF-1 levels in sera were reduced compared to those in WT mice despite normal circulating GH levels, and an exogenous supply of rIGF-1 was sufficient to enhance growth to levels seen in WT animals (fig. S5, D, E, and G). We thus concluded that the microbiota promoted growth by facilitating IGF-1 production and activity. To further test this hypothesis, we treated WT animals with the cyclolignan compound picropodophyllin (PPP), a specific noncompetitive inhibitor of IGF-1R (*19*, *20*), for 10 days. The PPP treatment significantly retarded the growth gains expected of WT animals (Fig. 4, D to F) and decreased the rIGF-1–mediated impact on phospho-S473-Akt signals in the liver and glycemia dynamics (fig. S8, J and K). These results established that IGF-1 activity is necessary for growth in WT animals. Together, our data show that the gut microbiota influences the production and activity of IGF-1 required for postnatal growth.

We then tested the effects of chronic undernutrition on, and the contribution of the gut microbiota to, postnatal growth. To this end, we weaned GF and WT juveniles onto a nutritionally depleted diet low in proteins (8.6%), fats (2.4%), and vitamins (table S1) and monitored their growth until 8 weeks of age (Fig. 3). During the week of adaptation to solid food, both GF and

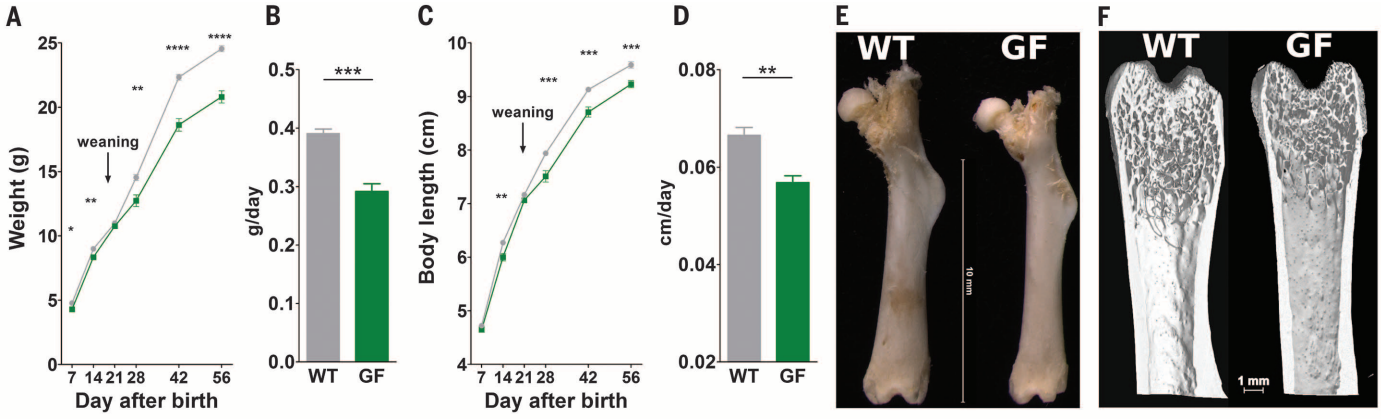


Fig. 1. The microbiota maintains mouse juvenile growth. (**A** to **D**) Weight (A) and body length (C) growth curves during the juvenile period (day 7 to day 56 after birth) and daily weight (B) and body size (D) gains after weaning (day 21 to day 56) of WT (gray) (n = 16) and GF (green) (n = 12) infant male mice bred with their mothers from birth until day 21, weaned, and then fed a breeding diet from 21 to 56 days old. (**E**) Photograph of representative femur bones at day 56. (**F**) Three-dimensional reconstructions of representative distal parts of femur bones at day 56. Error bars indicate SEM. *P < 0.05, **P < 0.01, ***P < 0.001, ****P < 0.0001.

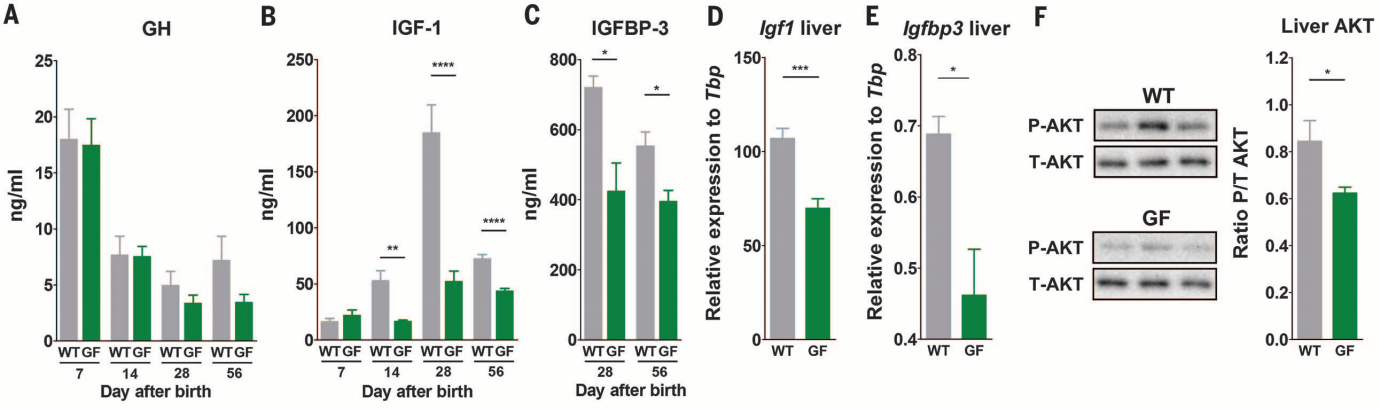


Fig. 2. The microbiota maintains systemic somatotropic axis activity. (**A** to **C**) Levels of GH (A), IGF-1 (B), and IGFBP-3 (C) in sera of WT (gray) and GF (green) mice at given time points after birth, $n \geq 5$ mice per group. (**D** to **F**) Expression levels of *Igf1* (D) and *Igfbp3* in liver (E) at day 28 after birth (n = 5 or 6 mice per group). (F) Western blots and quantification of phospho-S473-Akt in liver of WT and GF mice (n = 5 or 6 mice per group) at day 28 after birth . Representative blots of three mice per group are shown. Data are presented as means ± SEM. *P < 0.05, ***P < 0.001, ****P < 0.0001.

WT animals lost weight, yet weight loss was more extensive in GF animals (fig. S6C). After adaptation to solid food, the growth of GF animals was arrested, whereas WT animals resumed growth and recovered weight and longitudinal growth (Fig. 3, A to C, and fig. S6, A to E), albeit to a lesser extent than those on the breeding diet. The stunted phenotype of GF animals was not the result of an alteration of the GF animals' food intake relative to their body weight (fig. S7, A to D) nor of an altered capacity to absorb energy from the diet (fig. S7E). We conclude therefore that the gut microbiota contributes to maintaining mouse juvenile growth during chronic undernutrition.

We then analyzed how the gut microbiota influences the somatotropic axis during undernutrition (Fig. 4). We quantified GH, IGF-1, and IGFBP-3 levels in GF and WT animals after weaning onto the depleted diet. At 28 days, GH levels were elevated in GF animals as compared with WT animals, whereas at 56 days, GF animals displayed reduced circulating levels of GH, similar to WT animals (Fig. 4A). In contrast to WT animals, both IGF-1 and IGFBP-3 circulating levels failed to peak at 56 days in GF animals (Fig. 4, B and C). In muscle at 28 days (7 days after weaning onto the depleted diet), the expression of both *GH-receptor* (*Ghr*) and *Igf1* in WT animals was elevated compared to that in GF animals (fig. S8, A and B). Further, *Socs3,* a transcriptional target of GHR signaling (*21*) (fig. S1), was also increased in WT muscles (fig. S8C). In the liver at 28 days, *Ghr* expression was increased in WT animals as compared with GF counterparts (fig. S8D). At 56 days, circulating titers of IGF-1 (Fig. 4B), along with *Igf1* expression in the muscles and liver (fig. S8, E and F), increased; *Igfbp3* and *Socs3* expression (fig. S8, G and H) and the phospho-S473-Akt signal were also increased in the liver of WT animals (fig. S8I). Collectively, these results indicate a reduced activity of the somatotropic axis in GF animals. Next, we repeatedly injected 28-day-old WT animals weaned on the depleted diet with the PPP compound for 10 days and monitored their growth. We observed that PPP-treated animals had reduced weight, body length, and femur length gains over the treatment period as compared with untreated mice (Fig. 4, D to G). Taken together, these results indicate that during undernutrition, the gut microbiota helps to maintain systemic somatotropic axis activity and that this activity does result in some postnatal growth.

We have previously showed that gut microbiota promote *Drosophila* juvenile growth during undernutrition (*22*). Furthermore, monoassociation of GF *Drosophila* with selected lactobacilli strains recapitulates the growth promotion seen when a more complex microbiota is present (*22*). Lactobacilli strains are commensal in a variety of animals, including *Drosophila* and mammals (*23*, *24*). These taxa also share evolutionarily conserved nutrient-sensing endocrine pathways that regulate juvenile growth (i.e, *Drosophila* insulin/IGF-like peptides and mammalian IGFs) (*25*). We thus tested the functional potential of specific lactobacilli strains on murine juvenile growth and

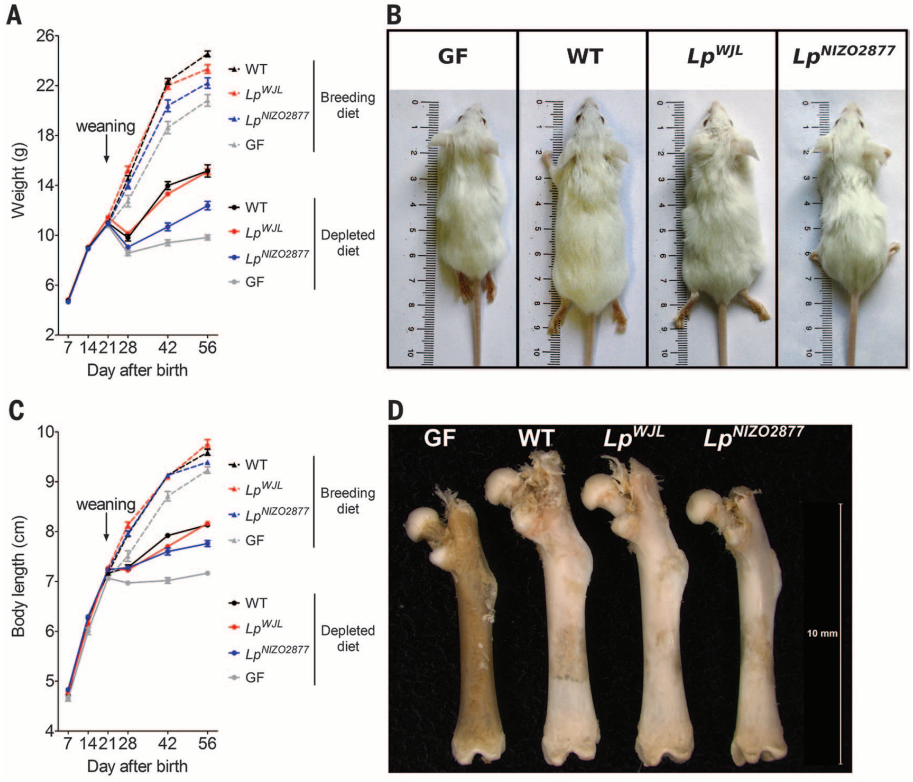


Fig. 3. The microbiota and a *L. plantarum* strain maintain mouse juvenile growth upon undernutrition. (**A** to **C**) Weight (A) and body length (C) growth curves of WT (n = 12 and 15, black lines), GF (n = 12 and 20, gray lines), Lp^{WJL} (n = 8 and 28, red line), and $Lp^{NIZO2877}$ (n = 12 and 15, blue line) monocolonized male mice on breeding (triangles and dashed lines) or nutritionally depleted (circles and solid lines) diets. (B) Representative photographs of mice on depleted diet at day 56 after birth. (**D**). Photographs of representative femur bones at day 56 after birth of GF, WT, Lp^{WJL}-, and $Lp^{NIZO2877}$-associated mice raised on the depleted diet.

the somatotropic axis during undernutrition. Two *Lactobacillus plantarum* strains that display different growth-promoting capacities in *Drosophila* monocolonized models were selected for monoassociation experiments in GF mice. Using monocolonized *Drosophila*, we identified *L. plantarum*^{WJL} (Lp^{WJL}) as a potent growth promoter, whereas *L. plantarum*^{NIZO2877} ($Lp^{NIZO2877}$) showed a statistically less pronounced effect on *Drosophila* growth (fig. S9). We then monitored postnatal growth of monocolonized infant male mice with Lp^{WJL} and $Lp^{NIZO2877}$ strains. These mice were obtained after monocolonizing GF adult mice of both sexes with the Lp^{WJL} or $Lp^{NIZO2877}$ strains; monocolonized adults were mated 20 days after colonization, and groups of six offspring were nursed by their monocolonized dam and naturally colonized by the respective *Lactobacillus* strain acquired from the dam. Lactating mice and their pups were maintained on the breeding diet. Twenty-one days after birth, the juveniles were weaned on either the breeding or the depleted diet (fig. S10). On the depleted diet, although both Lp^{WJL} and $Lp^{NIZO2877}$ juveniles gained more weight (+52% and +27% respectively; Fig. 3, A and B; fig. S6, A to D; and table S2) and body length (+14% and +8% respectively; Fig. 3, B and C; fig. S6E; and table S2) as compared with GF animals, the Lp^{WJL}-associated animals grew better (+25% weight and +6% length) than $Lp^{NIZO2877}$-associated animals (Fig. 3, A to C, and fig. S6, A to E). The quantitative difference between the two strains was not a result of differences in food intake relative to body weight (fig. S7, A to D), differential capacity to absorb energy from the diet (fig. S7E), or a marked difference in the efficiency of bacterial colonization of the intestinal tract (fig. S7, F to H). Lp^{WJL}-colonized animals showed a 14% body length gain when compared to GF animals, whereas $Lp^{NIZO2877}$-associated animals gained only 8% (fig. S6E and table S2). Similarly, bone growth such as femur length was differentially affected (Fig. 3D, fig. S6F, and table S2), indicating that the growth benefit depends on the strain of *L. plantarum*. In terms of weight gain, on the depleted diet, WT animals were 53% heavier than GF animals (fig. S6D and table S2). Lp^{WJL}-colonized animals showed a 52% weight gain, whereas $Lp^{NIZO2877}$-associated animals only showed 27% weight gain (fig. S6D and table S2). A similar effect was observed in all organs tested (fig. S6, G to J, and table S2). Collectively, the data show that during postnatal growth, selected lactobacilli strains can recapitulate the effect of a WT microbiota on mouse juvenile growth that would otherwise be stunted

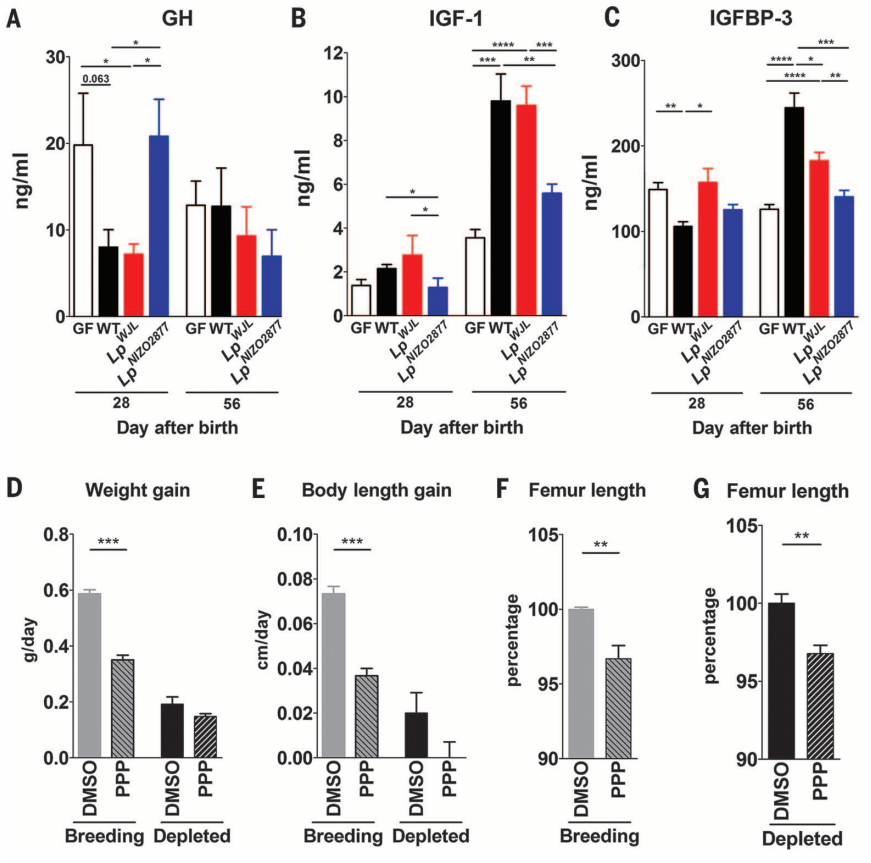


Fig. 4. The microbiota and a *L. plantarum* strain maintain somatotropic axis activity upon undernutrition. (**A** to **C**) Levels of GH (A), IGF-1 (B), and IGFBP-3 (C) in sera of GF (white), WT (black), Lp^{WJL}- (red), and $Lp^{NIZO2877}$-(blue) colonized mice at day 28 (n = 5 or 6 mice per group) and day 56 ($n \geq 15$ mice per group) after birth. (**D** to **G**) Weight gain (D), body length gain (E), and femur length [(F) and (G)] of WT mice weaned at day 21 on the breeding (gray bars) or depleted (black bars) diets and treated with DMSO or the IGF-1R inhibitor PPP (cross-hatched bars) for 10 days (n = 3 or 4 mice per group). Data are presented as means ± SEM. $^{**}P < 0.01$, $^{***}P < 0.001$.

by undernutrition. Strain-dependent promotion of juvenile growth and IGF-1 titers were not restricted to undernourished mice but were also observed with those fed the breeding diet (Fig. 3, A to C, and fig. S6, A to F, and K).

We observed that Lp^{WJL}- and $Lp^{NIZO2877}$-colonized animals differed in their ability to sustain somatotropic axis activity. Lp^{WJL}-colonized mice largely recapitulated the growth features of WT animals, but $Lp^{NIZO2877}$-colonized animals had either an intermediate or similar response to that of the GF animals (Fig. 4, A to C). By 56 days, the GH titers of WT animals fed on the depleted diet were comparable to those observed in WT animals raised on the breeding diet. However, the IGF-1 titers of these mice had dwindled by more than sevenfold (compare Fig. 2, A and B, and Fig. 4, A and B), confirming that chronic undernutrition affects the activity of the GH/IGF-1 axis (*4*). Furthermore, although GH titers of GF and $Lp^{NIZO2877}$-associated animals at 28 days were elevated, they failed to elicit adequate tissue responses, implying that the activity of the somatotropic axis is impaired in GF juveniles and that their tissues are in a state of GH resistance. We hypothesized that reduced GH sensitivity is less severe in WT and Lp^{WJL}-associated animals but remains in $Lp^{NIZO2877}$-associated animals. To directly test this hypothesis, we injected 28–day-old GF, WT, Lp^{WJL}-, and $Lp^{NIZO2877}$-associated animals weaned on the depleted diet with recombinant GH (rGH) and assayed the activation of the GHR signaling pathway in their liver. We examined the phosphorylation of Tyr^{694} of STAT5a and Tyr^{699} of STAT5b, which are direct signatures of GHR signaling activity (*26*, *27*) (fig. S11). GF and $Lp^{NIZO2877}$-colonized animals were less sensitive to rGH injection than WT and Lp^{WJL}-colonized animals (fig. S11). Our data showed that the microbiota is necessary and that a selected lactobacillus strain is sufficient to partly abrogate the GH resistance of peripheral tissues caused by chronic undernutrition.

Our study shows that GF infant mice enter a GH-resistant state upon chronic undernutrition, and a WT microbiota is necessary and sufficient to boost postnatal growth by enhancing GH sensitivity and thereby increasing IGF-1 activity in peripheral tissues. In addition, this study establishes that a selected strain of *L. plantarum* can recapitulate the beneficial effects of the microbiota on the somatotropic axis and on mouse juvenile growth, a functionality that may be shared with other commensal bacteria in the microbiota. We envision that, together with nutritional therapy, microbial interventions using selected bacterial strains may represent a novel and complementary strategy to buffer the adverse effects of chronic undernutrition on human postnatal growth, which still affects more than 160 million of children below 5 years of age in low- and middle-income countries (*28*).

REFERENCES AND NOTES

1. A. A. Butler, D. Le Roith, *Annu. Rev. Physiol.* **63**, 141–164 (2001).
2. A. Efstratiadis, *Int. J. Dev. Biol.* **42**, 955–976 (1998).
3. S. A. Kaplan, P. Cohen, *J. Clin. Endocrinol. Metab.* **92**, 4529–4535 (2007).
4. J. P. Thissen, J. M. Ketelslegers, L. E. Underwood, *Endocr. Rev.* **15**, 80–101 (1994).
5. P. K. Fazeli, A. Klibanski, *J. Endocrinol.* **220**, R57–R65 (2014).
6. S. Hizli, A. Abaci, B. Büyükgebiz, A. Büyükgebiz, *Pediatr. Endocrinol. Rev.* **4**, 186–195 (2007).
7. M. I. Smith *et al.*, *Science* **339**, 548–554 (2013).
8. R. C. Frederich *et al.*, *Nat. Med.* **1**, 1311–1314 (1995).
9. L. M. Cox *et al.*, *Cell* **158**, 705–721 (2014).
10. I. Cho *et al.*, *Nature* **488**, 621–626 (2012).
11. K. Sjogren *et al.*, *J. Bone Mineral Res.* **27**, 1357–1367 (2012).
12. E. Stratikopoulos, M. Szabolcs, I. Dragatsis, A. Klinakis, A. Efstratiadis, *Proc. Natl. Acad. Sci. U.S.A.* **105**, 19378–19383 (2008).
13. C. Ohlsson *et al.*, *Endocr. Rev.* **30**, 494–535 (2009).
14. P. Klover, L. Hennighausen, *Endocrinology* **148**, 1489–1497 (2007).
15. R. Renaville, M. Hammadi, D. Portetelle, *Domest. Anim. Endocrinol.* **23**, 351–360 (2002).
16. B. H. Breier, *Domest. Anim. Endocrinol.* **17**, 209–218 (1999).
17. D. R. Clemmons, *Cytokine Growth Factor Rev.* **8**, 45–62 (1997).
18. M. Laplante, D. M. Sabatini, *Cell* **149**, 274–293 (2012).
19. A. Girnita *et al.*, *Cancer Res.* **64**, 236–242 (2004).
20. S. C. Yin, W. Guo, Z. Z. Tao, *Biochem. Biophys. Res. Commun.* **439**, 1–5 (2013).
21. T. E. Adams *et al.*, *J. Biol. Chem.* **273**, 1285–1287 (1998).
22. G. Storelli *et al.*, *Cell Metab.* **14**, 403–414 (2011).
23. F. Turroni *et al.*, *Cell. Mol. Life Sci.* **71**, 183–203 (2014).
24. R. C. Matos, F. Leulier, *Microb. Cell Fact.* **13**, S6 (2014).
25. S. Hyun, *Cell. Mol. Life Sci.* **70**, 2351–2365 (2013).
26. G. B. Udy *et al.*, *Proc. Natl. Acad. Sci. U.S.A.* **94**, 7239–7244 (1997).
27. M. J. Waters, H. N. Hoang, D. P. Fairlie, R. A. Pelekanos, R. J. Brown, *J. Mol. Endocrinol.* **36**, 1–7 (2006).
28. R. E. Black *et al.*, *Lancet* **382**, 427–451 (2013).

ACKNOWLEDGMENTS

The authors thank B. Prud'homme and colleagues at the Institut de Génomique Fonctionnelle de Lyon for critical reading of the manuscript and the Arthro-Tools and ANIRA-ImmOs platforms of Structure Fédérative de Recherche Biosciences (UMS3444/US8) for providing *Drosophila* and bone microtomography facilities. This work was funded by a European Research Council starting grant (FP7/2007-2013-N°309704) (to F.L.), CNRS grant Echange chercheur CNRS/AVCR 13-14 (to F.L. and H.K.), grant P303-12-0535 of the Czech Science Foundation (to T.H.), a 2014 grant from the Fondation Innovations en Infectiologie (FINOVI, to H.V.), and the Institutional Research Concept grant RVO 61388971 (to H.K.). F.L.'s lab is supported by the ATIP/Avenir program, FINOVI foundation, the Fondation Schlumberger pour l'Education et la Recherche, and the European Molecular Biology Organization's Young Investigator Program. The authors declare no conflicts of interest. A pending patent (WO 2015/173386 A1) applies to methods and data presented in this manuscript. F.L. directed the study, which was designed with M.S.; M.S., K.M., I.M.-G., A.H., J.R., H.K., H.V., and F.L. analyzed and interpreted the data; M.S., D.S., P.H., and T.H. performed the mouse work and animal macroscopic analysis; K.M. and M.S. performed the molecular phenotyping; G.S. and M.E.M. performed the *Drosophila* work; I.M.-G. performed the study of bone parameters; S.B. performed FISH analyses; and M.S. and F.L. wrote the paper.

SUPPLEMENTARY MATERIALS

www.sciencemag.org/content/351/6275/854/suppl/DC1
Materials and Methods
Figs. S1 to S12
Tables S1 and S2
References (*29*–*32*)

12 November 2015; accepted 13 January 2016
10.1126/science.aad8588

MUCOSAL IMMUNOLOGY

Dietary antigens limit mucosal immunity by inducing regulatory T cells in the small intestine

Kwang Soon Kim,[1,2] Sung-Wook Hong,[1,2] Daehee Han,[1,2] Jaeu Yi,[1,2] Jisun Jung,[1,2] Bo-Gie Yang,[1,2] Jun Young Lee,[1,2] Minji Lee,[1,2] Charles D. Surh[1,2,3]*

Dietary antigens are normally rendered nonimmunogenic through a poorly understood "oral tolerance" mechanism that involves immunosuppressive regulatory T (T_{reg}) cells, especially T_{reg} cells induced from conventional T cells in the periphery (pT_{reg} cells). Although orally introducing nominal protein antigens is known to induce such pT_{reg} cells, whether a typical diet induces a population of pT_{reg} cells under normal conditions thus far has been unknown. By using germ-free mice raised and bred on an elemental diet devoid of dietary antigens, we demonstrated that under normal conditions, the vast majority of the small intestinal pT_{reg} cells are induced by dietary antigens from solid foods. Moreover, these pT_{reg} cells have a limited life span, are distinguishable from microbiota-induced pT_{reg} cells, and repress underlying strong immunity to ingested protein antigens.

The ingestion of certain foods can trigger an immune reaction, ranging from mild allergy to anaphylaxis, in a fraction of the population. How dietary antigens (Ags) are normally rendered nonimmunogenic through oral tolerance is poorly understood, but it is known to require the participation of regulatory T (T_{reg}) cells expressing the transcription factor Foxp3 (*1*, *2*). Two types of Foxp3$^+$ CD4$^+$ T_{reg} cells exist: the thymic T_{reg} (tT_{reg}) cells that develop from hematopoietic progenitors in the thymus, and the peripheral T_{reg} (pT_{reg}) cells that develop extrathymically from conventional T cells (*3*–*6*).

pT_{reg} cells are abundant in the intestine but not in the secondary lymphoid tissues (*7*), implying that pT_{reg} cells develop in response to enteric Ags derived from the commensal microbiota and/or food. In the colon, the intestinal microbes induce the development of pT_{reg} cells, and these cells are depleted in germ-free (GF) mice (*7*–*9*). However, GF mice possess normal numbers of pT_{reg} cells in the small intestine (*7*), the origin of which has yet to be documented. Oral administration of a nominal protein Ag under experimental conditions can induce a fraction of Ag-specific CD4$^+$ T cells to differentiate into pT_{reg} cells (*10*), but whether pT_{reg} cells are generated in response to a typical diet thus far has been unknown. To address this, we studied the effect of depleting dietary Ags by raising mice on a chemically defined elemental diet devoid of macromolecules. We derived such Ag-free (AF) mice by producing offspring from GF mice that were weaned onto and subsequently raised on the elemental Ag-free diet (table S1) (*11*).

Young adult AF C57BL/6 (B6) mice appeared healthy, were similar in size and weight, and possessed comparable serum biochemical and metabolic markers, except for moderately low levels of vitamin A and D, albeit within the acceptable ±100% range relative to those of specific pathogen-free (SPF) and GF B6 mice (fig. S1). As previously reported (*12*, *13*), AF mice had lower serum immunoglobulins, normal-sized spleens, and lower lymphocyte counts in the small intestinal lamina propria (siLP), but not in the colonic lamina propria (cLP), relative to SPF mice (fig. S2). The hypocellularity in the siLP was particularly pronounced for CD4$^+$ T cells because of the depletion of memory-phenotype (CD44^{hi} CD62L^{lo}) cells, including Tbet$^+$ cells (Fig. 1, A and B, and fig. S4); CD4$^+$ T cell counts in the cLP were normal, but memory-phenotype CD4$^+$ T cells were significantly decreased, as in GF mice (figs. S3 and S4). These phenotypes suggest that local activation of CD4$^+$ T cells in the small intestine is driven mainly by dietary Ags, whereas in the colon it is induced by the microbiota.

Foxp3$^+$ CD4$^+$ T_{reg} cell counts in adult AF B6 mice were also normal in the periphery but much reduced in the intestine compared with those of SPF mice. In the cLP, AF mice resembled GF mice and possessed about half the percentages and total numbers of T_{reg} cells relative to SPF mice (Fig. 1C and fig. S5B). In the siLP of AF mice, despite higher percentages, total numbers of T_{reg} cells were about one-fifth those of GF and SPF mice (Fig. 1, C and D). To distinguish between tT_{reg} and pT_{reg} cell subsets, the expression of neuropilin-1 (Nrp-1) was analyzed. As reported previously (*7*), pT_{reg} cells expressing little Nrp-1 (Nrp-1^{lo}) were largely absent in the spleen and lymph nodes but made up 50 to 70% of T_{reg} cells in the siLP and cLP in SPF mice; in GF mice, pT_{reg} cells were rare in the cLP but prominent in the siLP (Fig. 1E). In contrast, in AF mice, Nrp-1^{lo} pT_{reg} cells were depleted in both the siLP and cLP (Fig. 1E). Intestinal Nrp-1^{lo} pT_{reg} cells in SPF mice, but not the few remaining in AF mice, also expressed higher levels of CTLA-4 and the cytokine interleukin (IL)–10 than Nrp-1^{hi} tT_{reg} cells did (figs. S6 and S7). IL-10$^+$ Foxp3$^-$ CD4$^+$ cells, which were presumably type 1 regulatory T (T_r1) cells, were present in low numbers in the gut of SPF but not of GF and AF mice, and T_r1 cells expressed lower levels of IL-10 than did Foxp3$^+$ T_{reg} cells (fig. S7, A and B). Together, these results indicate that dietary Ags induce the development of most of pT_{reg} cells in the siLP under normal conditions, and pT_{reg} cells appear more essential than T_r1 or tT_{reg} cells in regulating immune responses to dietary Ags.

To assess the relative contributions of milk versus solid-food Ags in inducing the development of intestinal pT_{reg} cells, neonatal and adult mice were examined. pT_{reg} cells in the siLP were sparse before weaning in AF, GF, and SPF B6 mice but became prominent shortly after weaning these mice onto a normal chow diet (Fig. 2A and fig. S8). Furthermore, the deprivation of dietary Ags, accomplished by weaning neonatal GF mice onto the Ag-free diet or onto an "amino acid" diet that was devoid of proteins, prevented efficient development of pT_{reg} cells in the siLP (Fig. 2, B and C); in addition, unlike regular AF mice, these mice had normal levels of serum vitamin A, which promotes the generation of pT_{reg} cells through its metabolite retinoic acid (fig. S9, A and B) (*14*, *15*). Moreover, the administration of retinoic acid to adult AF mice did not result in the emergence of siLP pT_{reg} cells (fig. S9C). Hence, the majority of pT_{reg} cells in the siLP develop in response to Ags derived from proteins in a solid-food diet. As expected, siLP pT_{reg} cells underwent rapid turnover and had a short life span when deprived of food Ags. Thus, when adult (8-week-old) GF mice were placed on the Ag-free diet, the fraction of siLP pT_{reg} cells decreased considerably (by ~40%) after ~4 weeks (Fig. 2D). These results indicate that pT_{reg} cells in the siLP are continuously generated and replaced in response to dietary Ags, with a half-life of 4 to 6 weeks.

In addition to dietary Ags, commensal microbial Ags presumably contribute to the generation of pT_{reg} cells in the siLP. To determine whether such pT_{reg} cells can be selectively identified, we examined the expression of RAR (retinoic acid receptor)–related orphan receptor gamma t (RORγt), which is expressed by lymphocytes that interact with microbes (*16*). As previously reported (*17*), in SPF B6 mice, RORγt$^+$ T_{reg} cells were present in the siLP and cLP, mostly as Nrp-1^{lo} pT_{reg} cells (Fig. 3, A and B). In contrast, RORγt$^+$ T_{reg} cells were almost undetectable in GF and AF B6 mice (Fig. 3, A and B); RORγt$^+$ CD4$^+$ conventional T cells were similarly absent (fig. S10, A and B). The gut RORγt$^+$ T_{reg} cells rapidly appeared in GF mice after conventionalization (fig. S10, C and D). Moreover, treatment of SPF mice with a cocktail of antibiotics for 4

[1]Academy of Immunology and Microbiology, Institute for Basic Science, Pohang, Republic of Korea. [2]Department of Integrative Biosciences and Biotechnology, Pohang University of Science and Technology, Pohang, Republic of Korea. [3]Division of Developmental Immunology, La Jolla Institute for Allergy and Immunology, La Jolla, CA 92037, USA.
*Corresponding author. E-mail: csurh@ibs.re.kr

Downloaded from on February 18, 2016

weeks from the time of weaning led to a depletion of RORγt$^+$ pT$_{reg}$ cells in the siLP and cLP, without affecting the generation of RORγt$^-$ pT$_{reg}$ cells (Fig. 3C). In addition, weaning SPF mice onto the Ag-free diet or an amino acid diet caused a severe reduction of Nrp-1^{lo} pT$_{reg}$ cells in the siLP, mostly due to a depletion of RORγt$^-$ pT$_{reg}$ cells (Fig. 3D and fig. S11). The bacterial load, but not the composition, in the feces of SPF mice that were weaned onto the Ag-free diet was relatively normal (fig. S12). Collectively, these findings add to recent reports (*18*, *19*) by showing that whereas RORγt$^+$ pT$_{reg}$ cells are induced by commensal microbiota, RORγt$^-$ pT$_{reg}$ cells are driven by dietary Ags.

We next examined the dendritic cell (DC) subsets in the intestines of AF mice. Unexpectedly, the siLP of AF mice contained a ~40% lower representation of the CD103$^+$ CD11b$^+$ subset that promotes pT$_{reg}$ cell development (*14*, *20*) and about three times the proportion of the CD103$^+$ CD11b$^-$ subset, relative to SPF and GF mice, resembling conventional splenic DCs (fig. S13, A to C) (*21*). However, such a skewed DC composition only partially explains the paucity of pT$_{reg}$ cells in the intestines of AF mice. This is because a normal DC subset composition was found in the mesenteric lymph nodes of AF mice, which are the induction sites of pT$_{reg}$ cell development; moreover, purified CD103$^+$ CD11b$^+$ DCs from the siLP of AF mice were able to efficiently stimulate T cells (fig. S14, A and B) and induce upregulation of Foxp3 in OT-II cells under in vitro conditions (fig. S14, C and D). Furthermore, weaning neonatal AF or GF mice, which also possess the skewed DC subsets (fig. S13D), onto a chow diet led to the normalization of DC subsets within 1 week (fig. S13, D and E) and efficient development of pT$_{reg}$ cells within 2 weeks in the siLP (Fig. 2A). Lastly, siLP pT$_{reg}$ cells from neonatal AF mice weaned onto a chow diet exhibited ~50% demethylation at the CNS2 regions of the *Foxp3* locus (fig. S15), indicative of stable Foxp3 expression, as previously reported (*7*, *22*).

Despite the deficiency in siLP pT$_{reg}$ cells, B6 SPF or GF neonatal mice do not develop food allergies when they are weaned onto a chow diet. This could be due to various anti-inflammatory proteins in milk (*23*), such as immunoglobulins, transforming growth factor (TGF)–β, osteopontin, and lactadherin, which could ameliorate

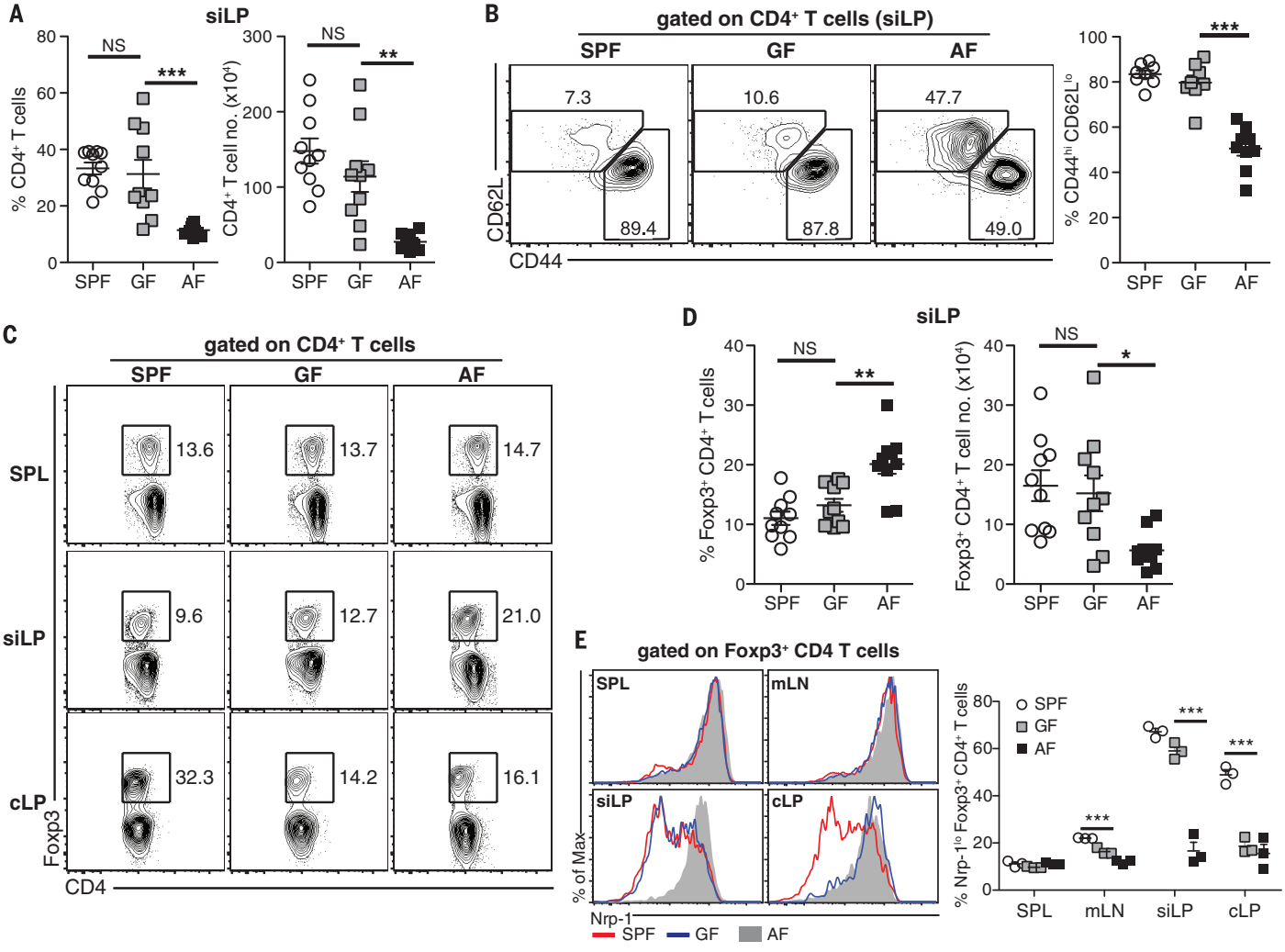


Fig. 1. Depletion of macromolecules from the diet precludes the development of pT$_{reg}$ cells in the small intestine. Shown are comparisons of T cell populations from the siLP and cLP harvested from aged-matched young adult (6- to 10-week-old) SPF, GF, and AF B6 mice. (**A**) CD4$^+$ T cells from the siLP, expressed as percentages of lymphocytes (left) and total numbers (right). (**B**) Representative fluorescence-activated cell sorting (FACS) plots of CD44 versus CD62L (numbers in the boxes indicate percentages of cells in the gate), with a graph of the percentages of CD44^{hi} CD62L^{lo} cells among the siLP CD4$^+$ T cells. (**C**) Representative FACS plots of CD4 versus Foxp3 on gated CD4$^+$ T cells from the spleen (SPL), siLP, and cLP. (**D**) Foxp3$^+$ CD4$^+$ T cells from the siLP are expressed as percentages of lymphocytes (left) and total numbers (right). (**E**) Representative histograms of Nrp-1 expression, with a graph of the percentages of Nrp-1^{lo} cells among gated Foxp3$^+$ CD4$^+$ T cells from the SPL, mesenteric lymph node (mLN), siLP, and cLP. At least four independent experiments had similar results. Graphs in (A), (B), and (D) show pooled data points from four independent experiments. *P* values were determined by one-way analysis of variance (ANOVA) with the Bonferroni post-test. Error bars show SEM. *$P < 0.05$; **$P < 0.01$; ***$P < 0.001$; NS, not significant.

the allergic response. We therefore examined the effect of feeding adult B6 AF mice a sterile chow diet; this failed to induce any gross sign of intestinal pathology. However, the initial local immune response to dietary Ags could be vigorous because of the absence of pT_{reg} cells and the increased numbers of siLP $CD103^+$ $CD11b^-$ DCs. Hence, we adoptively transferred ovalbumin (OVA)–specific naïve OT-II $CD4^+$ T cells into adult AF mice and then gave them OVA orally. Examination on day 7 revealed that OT-II cells in the siLP of AF mice expanded ~50 and 7 times as much as in control SPF and GF mice, respectively (Fig. 4A). Moreover, whereas the majority (~60%) of expanded OT-II cells upregulated Foxp3 in SPF and GF mice, only ~30% of OT-II cells up-regulated Foxp3 in AF mice (Fig. 4B).

The expanded OT-II cells in AF mice, some of which could be due to homeostatic proliferation, readily differentiated into $Tbet^+$ T helper 1 (T_h1) cells, leading to the generation of ~400 or ~14 times as many T_h1 cells as in SPF or GF mice, respectively; a similar trend, at smaller magnitudes, applied to interferon-γ^+ OT-II cells (Fig. 4C and fig. S16A). Moreover, the relative ratio of T_{reg} to T_h1 OT-II cell generation in AF mice was one-twentieth that in SPF mice (fig. S16B). Unlike the T_h1 response, T_h2 and T_h17 responses in AF hosts were comparable to that in control SPF hosts. Hence, whereas GF hosts had increased T_h2 responses to OVA, AF hosts possessed only background levels of OVA-specific and total serum immunoglobulin E (IgE), a minimal number of $GATA3^+$ OT-II cells, and a similarly moderate percentage of $ROR\gamma t^+$ OT-II cells as that observed in control SPF hosts (Fig. 4D and fig. S16, C to F). As expected, $Foxp3^+$ OT-II cells in AF hosts were mostly $Nrp\text{-}1^{lo}$ pT_{reg} cells and expressed higher levels of CTLA-4 and IL-10 than host T_{reg} cells, which were mostly tT_{reg} cells (fig. S17, A to C). Unexpectedly, the majority of $Foxp3^+$ OT-II cells were $ROR\gamma t^+$ (fig. S16, E and F), indicating that dietary proteins can induce the development of $ROR\gamma t^+$ pT_{reg} cells from a fraction of the T cell repertoire in the absence of the commensal microbiota. Nonetheless, the major characteristics of the OT-II response observed in the siLP of AF

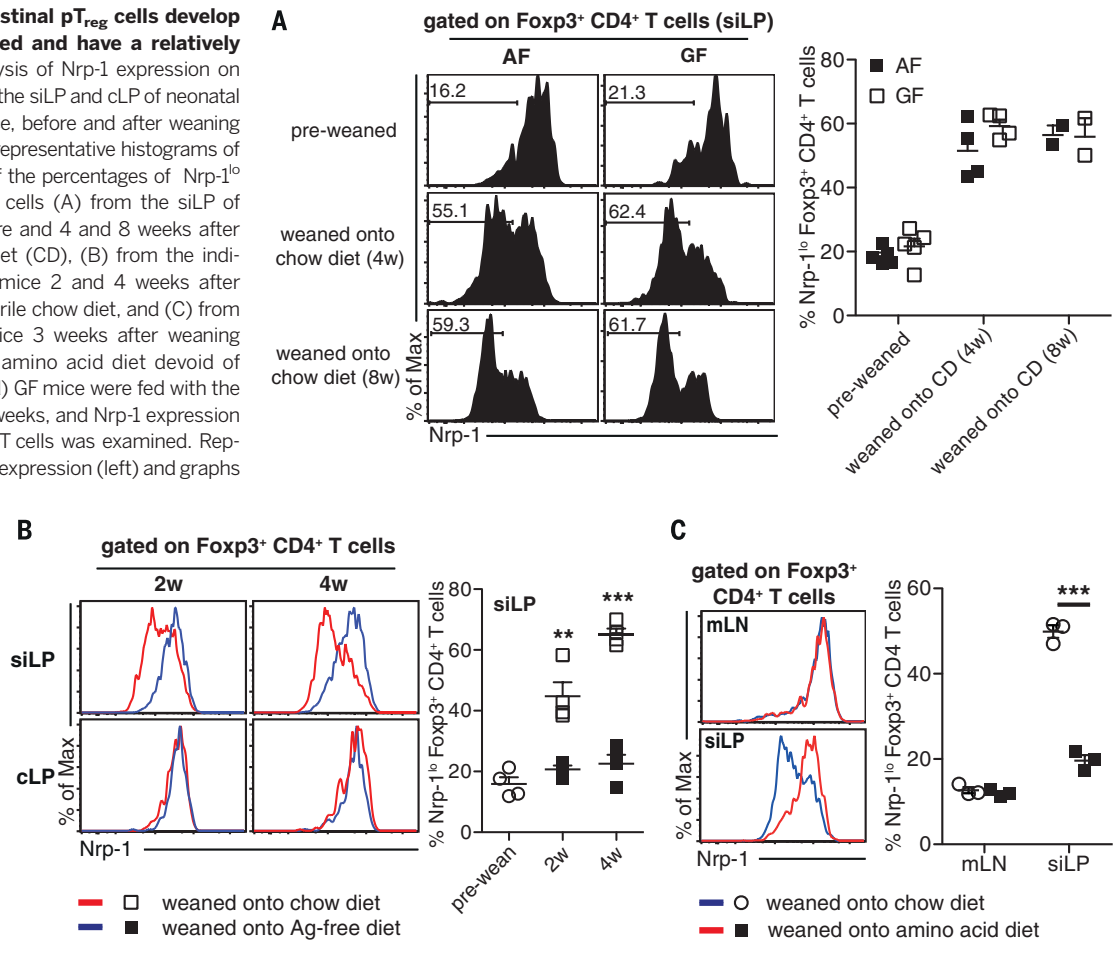


Fig. 2. The bulk of small intestinal pT_{reg} cells develop when solid food is introduced and have a relatively short life span. (**A** to **C**) Analysis of Nrp-1 expression on gated $Foxp3^+$ $CD4^+$ T cells from the siLP and cLP of neonatal (3-week-old) GF and AF B6 mice, before and after weaning onto a specific diet. Shown are representative histograms of Nrp-1 expression, with graphs of the percentages of $Nrp\text{-}1^{lo}$ cells on gated $Foxp3^+$ $CD4^+$ T cells (A) from the siLP of neonatal GF and AF mice before and 4 and 8 weeks after weaning onto a sterile chow diet (CD), (B) from the indicated tissues of neonatal GF mice 2 and 4 weeks after weaning onto the Ag-free or sterile chow diet, and (C) from the indicated tissues of GF mice 3 weeks after weaning onto a sterile chow diet or an amino acid diet devoid of proteins. (**D**) Adult (8-week-old) GF mice were fed with the Ag-free diet (AFD) for 2 and 4 weeks, and Nrp-1 expression on siLP and cLP $Foxp3^+$ $CD4^+$ T cells was examined. Representative histograms of Nrp-1 expression (left) and graphs of percentages and numbers (right) of $Nrp\text{-}1^{lo}$ $Foxp3^+$ $CD4^+$ T cells are shown. Graphs in (A), (B), and (D) show combined data points from two independent experiments. The graph in (C) is representative of two independent experiments. *P* values were determined by two-tailed unpaired Student's *t* tests [(B) and (C)] and one-way ANOVA with the Bonferroni post-test (D). Error bars show SEM. $*P < 0.05$; $**P < 0.01$; $***P < 0.001$.

hosts were also evident in the mesenteric lymph nodes, but not in the spleen, indicating that the pronounced OVA-driven OT-II cell response in AF mice is restricted to the gut-associated lymphoid tissues. The massive OT-II response in AF hosts also was not due to more efficient Ag presentation of OVA related to a lack of competition from other proteins or low vitamin A levels, because similar T cell expansion occurred in a group of AF mice that were fed with a sterilized chow diet just before introducing OVA or injected with retinoic acid during OVA feeding (fig. S18). Overall, these findings indicate that siLP pT_{reg} but not tT_{reg} cells are essential to suppressing a default strong immune response to newly introduced dietary Ags.

Lastly, based on the OT-II response observed above, we tested whether food allergies can be induced in an experimental model. Hence, neonatal SPF BALB/c mice were weaned onto an amino acid diet (because B6 mice are generally resistant to food allergies) and immunized with OVA. Two weeks later, repeated gavage with OVA led to a higher incidence and severity of diarrhea, with a trend toward higher OVA-specific serum IgE, in the amino acid diet–fed mice than in control mice (Fig. 4E and fig. S19). Hence, the lack of pT_{reg} cells led to an increased susceptibility to OVA-induced intestinal allergy.

Our work demonstrates that under normal physiological conditions, macromolecules from the diet induce the bulk of pT_{reg} cell development in the siLP, but not in the cLP. Most siLP pT_{reg} cells develop after weaning onto solid food, presumably reflecting the limited antigenic complexity of milk, an immature state of the immune system in neonatal mice, and/or the presence of components exclusively found in solid food that boost pT_{reg} cell development. The expansion of

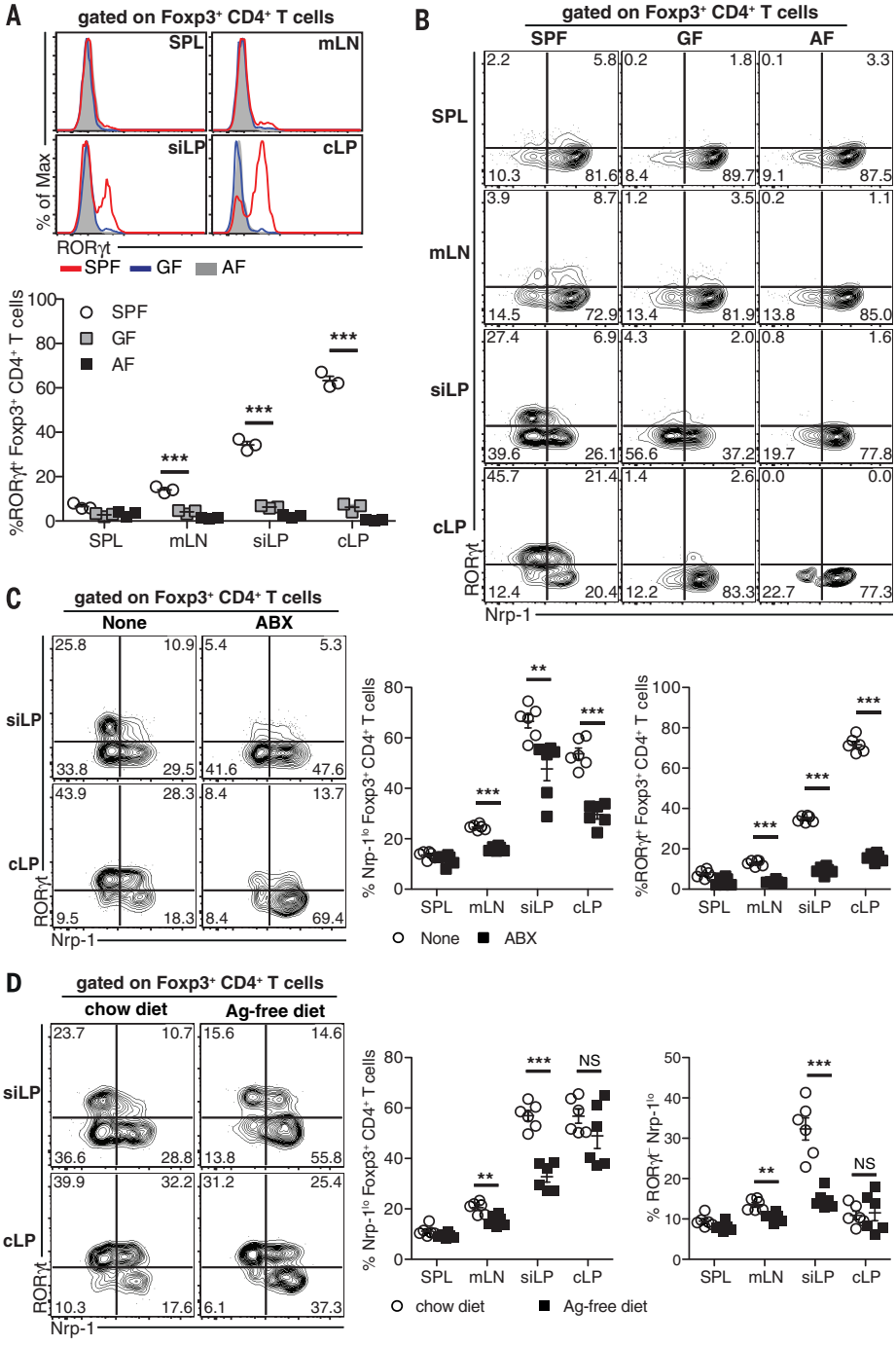


Fig. 3. Under normal conditions, a subset of small intestinal pT_{reg} cells is induced to develop by the commensal microbiota and expresses RORγt. Shown are analyses of RORγt expression on gated Foxp3$^+$ CD4$^+$ T cells from the siLP and cLP of young adult SPF, GF, and AF B6 mice [(A) and (B)] or on SPF mice after treatment with antibiotics or after weaning onto an Ag-free diet [(C) and (D)]. (**A**) Representative histograms of RORγt expression, with a graph of the percentages of RORγt$^+$ cells among gated Foxp3$^+$ CD4$^+$ T cells from the SPL, mLN, siLP, and cLP of SFP, GF, and AF mice. (**B**) Representative FACS plot of Nrp-1 versus RORγt on gated Foxp3$^+$ CD4$^+$ T cells from the indicated tissues and mice. (**C** and **D**) Representative FACS plots of Nrp-1 versus RORγt, with graphs of the percentages of Nrp-1^{lo} (left) and RORγt$^+$ cells (right) among Foxp3$^+$ CD4$^+$ T cells in the siLP and cLP of recently weaned SFP mice; the mice were given water with or without broad-spectrum antibiotics (ABX) (C) or a chow diet or Ag-free diet (D) for 4 weeks. The graph in (A) is representative of at least two independent experiments, and graphs in (C) and (D) show combined data points from two independent experiments. *P* values were determined by one-way ANOVA with the Bonferroni post-test in (A) and by two-tailed unpaired Student's *t* tests or *t* tests with Welch's correction in case of unequal variance in (C) and (D). Error bars show SEM. $*P < 0.05$; $**P < 0.01$; $***P < 0.001$.

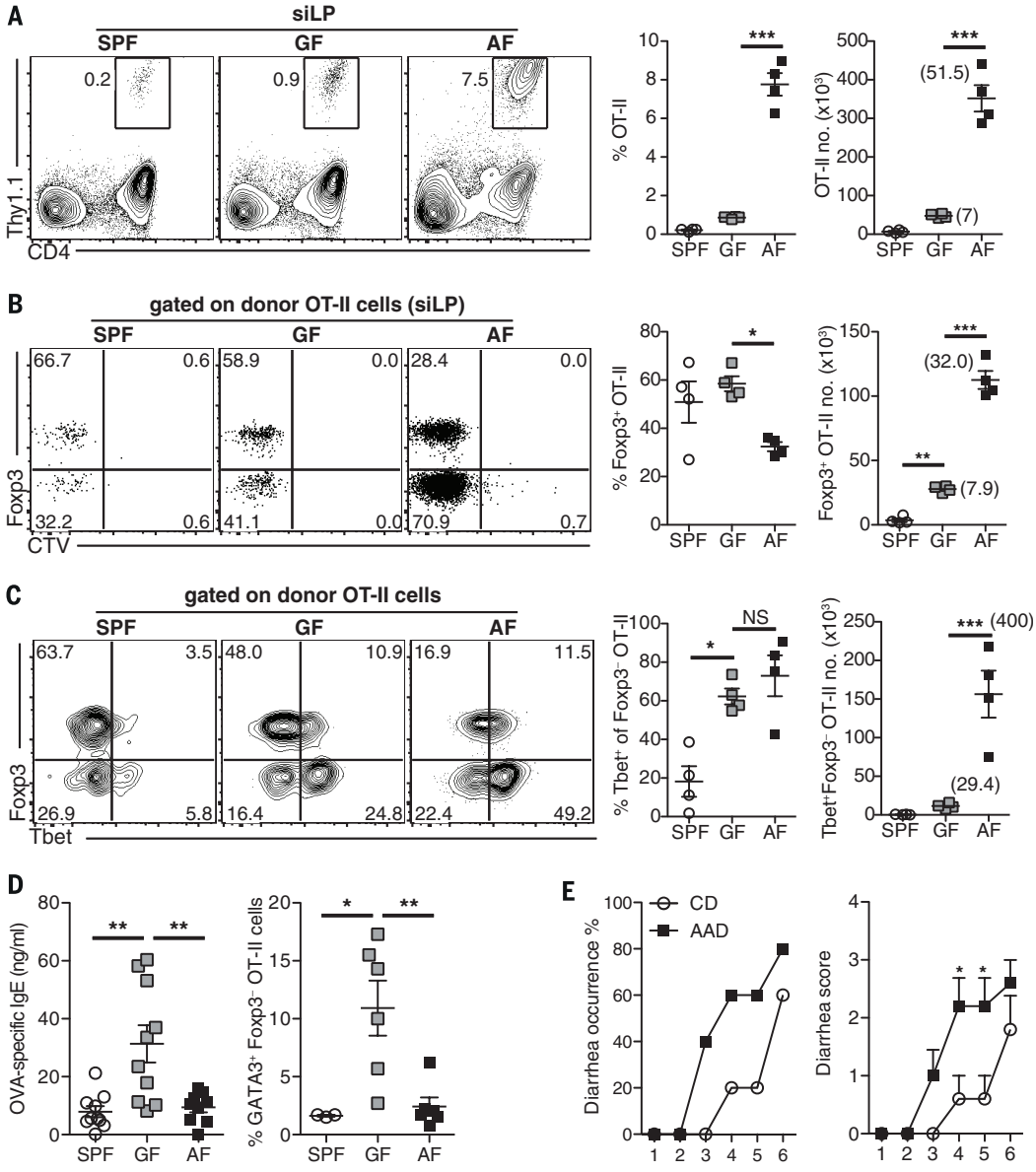


Fig. 4. Conditions in which pT_{reg} cells are depleted allow strong immune responses to dietary antigens and an increased susceptibility to intestinal allergy. In (A) to (D), adult SPF, GF, and AF B6 mice (N = 4 per group) were adoptively transferred with Cell Trace Violet–labeled naïve Thy1$^+$ OT-II cells and fed with OVA for 7 days; donor OT-II cells from the siLP were then analyzed along with serum IgE specific to OVA. (**A**) OT-II cells in representative FACS plots of all lymphocytes, with graphs of percentages (left) and total numbers (right) of OT-II cells. (**B**) Foxp3 up-regulation in OT-II cells in representative FACS plots of gated OT-II cells, with graphs of percentages (left) and total numbers (right) of Foxp3$^+$ OT-II cells. (**C**) Tbet up-regulation in OT-II cells in representative FACS plots of gated OT-II cells, with graphs of percentages (left) and total numbers (right) of Tbet$^+$ Foxp3$^-$ OT-II cells. (**D**) Graphs of serum OVA-specific IgE (left) and percentages of GATA3$^+$ Foxp3$^-$ OT-II cells (right). (**E**) Neonatal SPF BALB/c mice were weaned onto a normal chow diet or an amino acid diet (AAD), immunized with OVA plus alum, rested for 2 weeks, gavaged with OVA on an every-other-day basis, and observed for diarrhea. Graphs of percentages of mice with diarrhea (left) and diarrhea scores (right) (N = 5 per group). In the graphs in (A) to (C), the numbers in parentheses denote the fold of cell expansion above that found in SPF hosts. Graphs in (A), (B), and (E) are representative of at least two independent experiments, and graphs in (D) show pooled data points from at least two independent experiments. P values were determined by one-way [(A) to (D)] or two-way (E) ANOVA with the Bonferroni post-test. Error bars show SEM. *P < 0.05; **P < 0.01; ***P < 0.001.

siLP pT_{reg} cells after weaning appears to be essential to suppressing a default strong immune response to dietary Ags, supporting the view that pT_{reg} cells are important for controlling mucosal inflammatory and allergic responses (*6*, *10*, *24*). The data could also explain why children suffer from a higher incidence of food allergies than adults do and why childhood allergies spontaneously dissipate with time (*25*). Nevertheless, despite their lack of siLP pT_{reg} cells, most neonates do not exhibit food allergies. Such tolerance might reflect multiple mechanisms, including efficient pT_{reg} cell induction by the high levels of TGF-β in milk (*23*), compensatory suppression by tT_{reg} cells, and/or rapid generation of pT_{reg} cells induced by commensal microbial Ags. For the last of these, it is known that germ-free mice spontaneously produce large amounts of IgE and that this can be prevented by colonization with a complex commensal microbiota (*26*, *27*). Hence, the presence of both diet- and microbe-induced populations of pT_{reg} cells may be required for complete tolerance to food Ags.

REFERENCES AND NOTES

1. H. L. Weiner, A. P. da Cunha, F. Quintana, H. Wu, *Immunol. Rev.* **241**, 241–259 (2011).
2. O. Pabst, A. M. Mowat, *Mucosal Immunol.* **5**, 232–239 (2012).
3. A. M. Bilate, J. J. Lafaille, *Annu. Rev. Immunol.* **30**, 733–758 (2012).
4. K. Kretschmer *et al.*, *Nat. Immunol.* **6**, 1219–1227 (2005).
5. D. Mucida *et al.*, *J. Clin. Invest.* **115**, 1923–1933 (2005).
6. D. Haribhai *et al.*, *Immunity* **35**, 109–122 (2011).
7. J. M. Weiss *et al.*, *J. Exp. Med.* **209**, 1723–1742 (2012).
8. Y. Furusawa *et al.*, *Nature* **504**, 446–450 (2013).
9. N. Arpaia *et al.*, *Nature* **504**, 451–455 (2013).
10. U. Hadis *et al.*, *Immunity* **34**, 237–246 (2011).
11. J. R. Pleasants, M. H. Johnson, B. S. Wostmann, *J. Nutr.* **116**, 1949–1964 (1986).
12. P. Pereira *et al.*, *Eur. J. Immunol.* **16**, 685–688 (1986).
13. B. S. Wostmann, J. R. Pleasants, *Proc. Soc. Exp. Biol. Med.* **198**, 539–546 (1991).
14. J. L. Coombes *et al.*, *J. Exp. Med.* **204**, 1757–1764 (2007).
15. D. Mucida *et al.*, *Science* **317**, 256–260 (2007).
16. G. Eberl, *Immunol. Rev.* **245**, 177–188 (2012).
17. M. Lochner *et al.*, *J. Exp. Med.* **205**, 1381–1393 (2008).
18. C. Ohnmacht *et al.*, *Science* **349**, 989–993 (2015).
19. E. Sefik *et al.*, *Science* **349**, 993–997 (2015).
20. C. M. Sun *et al.*, *J. Exp. Med.* **204**, 1775–1785 (2007).
21. K. Fujimoto *et al.*, *J. Immunol.* **186**, 6287–6295 (2011).

22. J. K. Polansky *et al.*, *Eur. J. Immunol.* **38**, 1654–1663 (2008).
23. D. E. Chatterton, D. N. Nguyen, S. B. Bering, P. T. Sangild, *Int. J. Biochem. Cell Biol.* **45**, 1730–1747 (2013).
24. S. Z. Josefowicz *et al.*, *Nature* **482**, 395–399 (2012).
25. G. Longo, I. Berti, A. W. Burks, B. Krauss, E. Barbi, *Lancet* **382**, 1656–1664 (2013).
26. J. Cahenzli, Y. Köller, M. Wyss, M. B. Geuking, K. D. McCoy, *Cell Host Microbe* **14**, 559–570 (2013).
27. K. D. McCoy *et al.*, *Immunity* **24**, 329–339 (2006).

ACKNOWLEDGMENTS

We thank A. Macpherson, K. McCoy, and D. Artis for generously providing various strains of germ-free mice to start our colony; T. K. Kim, J. W. Seo, M. O. Lee, H. J. Woo, H. J. Jung, H.J. Ko, J. Kirundi, S. Sakaguchi, and N. Ohkura for technical support; and J. Sprent, S. H. Im, M. H. Jang, D. Rudra, and J. H. Cho for discussions. The data from this study are tabulated in the main paper and in the supplementary materials. This work was supported by project IBS-R005-D1 of the Institute for Basic Science, Korean Ministry of Science, Information/Communication Technology and Future Planning.

SUPPLEMENTARY MATERIALS

www.sciencemag.org/content/351/6275/858/suppl/DC1
Materials and Methods
Figs. S1 to S19
Table S1
References (*28*–*32*)

14 May 2015; accepted 5 January 2016
Published online 28 January 2016
10.1126/science.aac5560

ION CHANNELS

Sequential ionic and conformational signaling by calcium channels drives neuronal gene expression

Boxing Li,[1]* Michael R. Tadross,[2,3]*† Richard W. Tsien[1,2]

Voltage-gated $Ca_V1.2$ channels (L-type calcium channel α1C subunits) are critical mediators of transcription-dependent neural plasticity. Whether these channels signal via the influx of calcium ion (Ca^{2+}), voltage-dependent conformational change (VΔC), or a combination of the two has thus far been equivocal. We fused $Ca_V1.2$ to a ligand-gated Ca^{2+}-permeable channel, enabling independent control of localized Ca^{2+} and VΔC signals. This revealed an unexpected dual requirement: Ca^{2+} must first mobilize actin-bound Ca^{2+}/calmodulin-dependent protein kinase II, freeing it for subsequent VΔC-mediated accumulation. Neither signal alone sufficed to activate transcription. Signal order was crucial: Efficiency peaked when Ca^{2+} preceded VΔC by 10 to 20 seconds. $Ca_V1.2$ VΔC synergistically augmented signaling by *N*-methyl-D-aspartate receptors. Furthermore, VΔC mistuning correlated with autistic symptoms in Timothy syndrome. Thus, nonionic VΔC signaling is vital to the function of $Ca_V1.2$ in synaptic and neuropsychiatric processes.

Voltage-gated $Ca_V1.2$ channels (L-type calcium channel α1C subunits) play an important role in transcription-dependent forms of synaptic and homeostatic plasticity (*1*–*6*), and $Ca_V1.2$ alterations have been linked to severe neuropathologies (*7*, *8*). The influx of Ca^{2+} is required in $Ca_V1.2$-mediated transcription (*4*), but it remains unclear whether voltage-dependent conformational change (VΔC) provides a necessary additional signal. There is precedence for VΔC signaling: $Ca_V1.1$ uses only VΔC to initiate skeletal-muscle contraction (*9*, *10*). However, a signaling role for VΔC has been difficult to establish in excitation-transcription coupling, because eliminating voltage-dependent opening of the channel also prevents Ca^{2+} influx through the Ca_V [but see (*11*)].

We fused $Ca_V1.2$ to an adenosine triphosphate (ATP)–gated, Ca^{2+}-permeable, tandem-trimeric P2X2 channel (ttP2X) (Fig. 1A). The ttP2X was used to provide Ca^{2+} influx independently of whether $Ca_V1.2$ was open or closed; the tethering between the channels (Fig. 1A) localized ttP2X influx to the $Ca_V1.2$ nanodomain (*12*, *13*).

We confirmed the integrity of the chimeric protein and the functionality of its components (fig. S1). In human embryonic kidney (HEK) 293 cells, the Ca^{2+} current appeared only at depolarized potentials in the absence of ATP (Fig. 1B, black u-shaped trace), as expected for a voltage-gated $Ca_V1.2$. On addition of ATP, the ttP2X portion of the chimera also supported Ca^{2+} influx, evident as an additional inward current at negative potentials (Fig. 1B, gray trace). Cd^{2+}, which blocks the $Ca_V1.2$ pore (*14*) but not the opening of ttP2X, did not prevent the ttP2X-mediated entry of Ca^{2+} (Fig. 1B, blue trace). We further validated the function of the chimeric components in cultured neurons, rendering the $Ca_V1.2$ portion dihydropyridine-insensitive (DHPi) to enable its distinction from endogenous channels (*6*) and confirming that ATP had no effect on untransfected neurons (fig. S1). Whereas ttP2X on its own distributed uniformly over the somatodendritic surface, ttP2X fused to $Ca_V1.2$ formed puncta and signaled more potently (fig. S1), consistent with localization to signaling hotspots.

These control experiments framed critical tests of the roles of Ca^{2+} and VΔC in signaling to nuclear CREB (cyclic adenosine monophosphate response–element binding protein), a transcription factor that is critical in many forms of learning and memory (Fig. 1, D and E) (*1*, *2*, *15*). Providing Ca^{2+} and VΔC in combination via the depolarization of neurons (3 min of exposure to 40 mM K^+ ($40K^+$)] (Fig. 1C, black traces) increased the phosphorylation of nuclear CREB (pCREB) at Ser^{133} threefold (Fig. 1D, second row) (*3*–*5*). The pCREB response was abolished by Cd^{2+} (Fig. 1D, third row), which prevents $Ca_V1.2$ from conducting Ca^{2+} without affecting depolarization (Fig. 1C, gray traces) or voltage-dependent gating (*14*); this confirms the known requirement for Ca^{2+} influx in signaling to pCREB (*4*, *6*, *13*). Next, we rerouted Ca^{2+} through the neighboring ttP2X by blocking the $Ca_V1.2$ pore with Cd^{2+} and opening the ttP2X portion of the chimera with ATP. This generated depolarizations and increases in bulk Ca^{2+} that were nearly identical to those achieved with $40K^+$ (Fig. 1C, compare blue with black traces, and fig. S2, A and B) and increased pCREB to the same degree as $40K^+$ (compare Fig. 1E, top row, with Fig. 1D, second row), confirming the utility of the chimeric channel approach.

We thus could use the chimera to determine whether localized Ca^{2+} influx can drive CREB activation in the absence of VΔC. In a first test, we provided the localized influx of Ca^{2+} by means of ATP activation of the chimeric ttP2X, but we attenuated VΔC signals through hyperpolarization, which was achieved by coexpressing and activating an ivermectin-gated chloride channel (GlyIVR) (*16*). This manipulation prevented neuronal depolarization (fig. S2C) and thus increased Ca^{2+} flux through the chimeric ttP2X (Fig. 1B, blue). Nonetheless, this manipulation inhibited signaling to CREB (Fig. 1E, second row). The attenuation of CREB signaling required a combination of GlyIVR expression and ivermectin (fig. S2D) and could not be attributed to increased Ca^{2+} influx (fig. S2E).

In a second test, we inhibited $Ca_V1.2$ conformational opening with nimodipine. This Ca_V1-selective agent (*17*, *18*) blocked ATP-mediated CREB signaling (Fig. 1E, third row) without affecting depolarization or Ca^{2+} influx (Fig. 1C, compare orange with blue). Nimodipine did not block the pCREB response when the chimeric $Ca_V1.2$ was rendered nimodipine-insensitive (Fig. 1E, bottom row), excluding potential off-target effects of the drug. Similar results were obtained with CREB-dependent expression of the immediate early gene *c-fos* (fig. S3). Thus, $Ca_V1.2$ signaling to pCREB and gene expression requires two distinct messages: The Ca^{2+} signal works in conjunction with an equally indispensable VΔC signal arising from $Ca_V1.2$.

[1]Department of Neuroscience and Physiology and New York University Neuroscience Institute, New York, NY 10016, USA. [2]Department of Molecular and Cellular Physiology, Beckman Center, School of Medicine, Stanford University, Stanford, CA 94305, USA. [3]Janelia Research Campus, Howard Hughes Medical Institute, Ashburn, VA 20147, USA.
*These authors contributed equally to this work. †Corresponding author. E-mail: tadrossm@janelia.hhmi.org

Downloaded from on February 18, 2016

Previous work has implicated Ca^{2+}/calmodulin-dependent protein kinase II (CaMKII) in mediating the signaling from $Ca_V1.2$ to nuclear CREB (*3*–*5*, *19*). CaMKIIs are activated and recruited into puncta near $Ca_V1.2$ upon depolarization (*4*, *5*), where they play a critical role in dispatching a signal to the nucleus (*19*). We confirmed the critical role of α- and βCaMKII by means of pharmacology (Fig. 2A and fig. S4A) and selective knockdowns of either isoform with small hairpin RNA (shRNA) (Fig. 2, B and C, and fig. S4, B and C). In contrast, signaling remained intact when protein kinase C, protein kinase A, or mitogen-activated protein kinase pathways (*3*, *6*, *20*) were blocked (fig. S4A). We further established that αCaMKII forms an activity-dependent complex with $Ca_V1.2$: Immunoprecipitation with a $Ca_V1.2$ antibody pulled down αCaMKII, and the degree of the coimmunoprecipitation was increased by stimulation with $40K^+$ (Fig. 2D).

We next assessed the contributions of Ca^{2+} and VΔC signals in mediating the spatial recruitment of CaMKII to the $Ca_V1.2$ channel. Staining with a phospho-specific CaMKII antibody revealed the formation of intense phospho-CaMKII (pCaMKII) puncta near surface ttP2X-$Ca_V1.2$ channels after dual Ca^{2+} and VΔC stimulation (Fig. 2, E and F), but not after stimulation by Ca^{2+} or VΔC alone (Fig. 2F). A similar pattern was observed for isoform-specific antibodies against αCaMKII (Fig. 2, G and H, and fig. S4, D and E) or βCaMKII (Fig. 2, I and J, and fig. S4E), which is consistent with CaMKII isomers relocating as heteromultimers (*21*, *22*). Thus, $Ca_V1.2$ communication to multiple isoforms of CaMKII follows the signaling logic observed in $Ca_V1.2$-mediated CREB signaling; all demand a conjunction of Ca^{2+} and VΔC signals.

We looked for dynamic changes of CaMKII produced by Ca^{2+} or VΔC signals in isolation. Whereas VΔC-only stimuli had no effect, Ca^{2+}-only stimuli (10 s) mobilized βCaMKII [Fig. 3, A (green trace) and B (top two images)], which is consistent with its known dissociation from F-actin upon Ca^{2+} stimulation (*21*, *22*). The mobilization of βCaMKII (Fig. 3A, green trace) outlasted bulk Ca^{2+} elevation (Fig. 3A, blue trace) but returned to the initial distribution within 60 s, which is consistent with the kinetics of calmodulin trapping (*23*). Evidently, mobilized βCaMKII reverted to its cytoskeleton-bound state in the absence of VΔC signaling (Fig. 3B). To find out when VΔC signaling was most effective, we varied the timing of brief (10-s) pulses of Ca^{2+} and VΔC inputs (Fig. 3C), quantifying efficacy by downstream CREB activation (Fig. 3D). Synchronous stimuli (difference in time, $\Delta t = 0$) were suboptimal. Instead, VΔC potency peaked at $\Delta t = 10$ to 20 s after Ca^{2+} influx and persisted at $\Delta t = 40$ s (Fig. 3D, black bars). Reversing the order of stimuli (VΔC first) resulted in little signaling to CREB (Fig. 3D; $\Delta t = -10$ s), a pronounced temporal asymmetry. The dynamics of VΔC potency (Fig. 3D, black bars) and of βCaMKII mobilization (Fig. 3D, green trace from Fig. 3A) were similar. This suggests that Ca^{2+} mobilization of βCaMKII [or α/βCaMKII heteromultimers (*21*)] is a prerequisite for their subsequent VΔC-mediated accumulation at $Ca_V1.2$ channels and for downstream signaling to pCREB (fig. S5) (*19*).

To test whether VΔC signals interact with other Ca^{2+} sources, such as *N*-methyl-D-aspartate receptors (NMDARs) (*21*, *22*), we examined CaMKII puncta formation in response to NMDAR activity in isolation (Fig. 4A, right; nimodipine present) or in combination with $Ca_V1.2$ VΔC (Fig. 4A, left; nimodipine absent and $Ca_V1.2$ pore blocked with Cd^{2+}). VΔC inclusion enhanced the amplitude of the NMDAR-induced signal (CaMKII puncta formation) (Fig. 4, B and C). Thus, VΔC signals not only interact with Ca^{2+} entry from the home $Ca_V1.2$ (Fig. 3) but also synergistically modulate the signaling potency of other Ca^{2+} sources (Fig. 4).

With regard to disease, Timothy syndrome (TS) (*7*) arises from either of two point mutations in helix IS6 of $Ca_V1.2$ (fig. S6A). Both the G406R and G402S TS variants cause a prolonged Ca^{2+} current (arising from the slowing of $Ca_V1.2$ inactivation), and both variants produce a long-QT cardiac arrhythmia (fig. S6B) (*7*, *8*). Whereas G406R produces autism spectrum disorder with >60% penetrance, G402S patients are neurologically intact, suggesting that Ca^{2+} influx is not what determines the neurological phenotype (fig. S6B, black symbols) (*8*, *24*, *25*). To test the role of VΔC in TS, we made TS variants in the $Ca_V1.2$ portion of the chimera while holding the Ca^{2+} flux fixed via the fused ttP2X (Fig. 4D). Mutant-specific

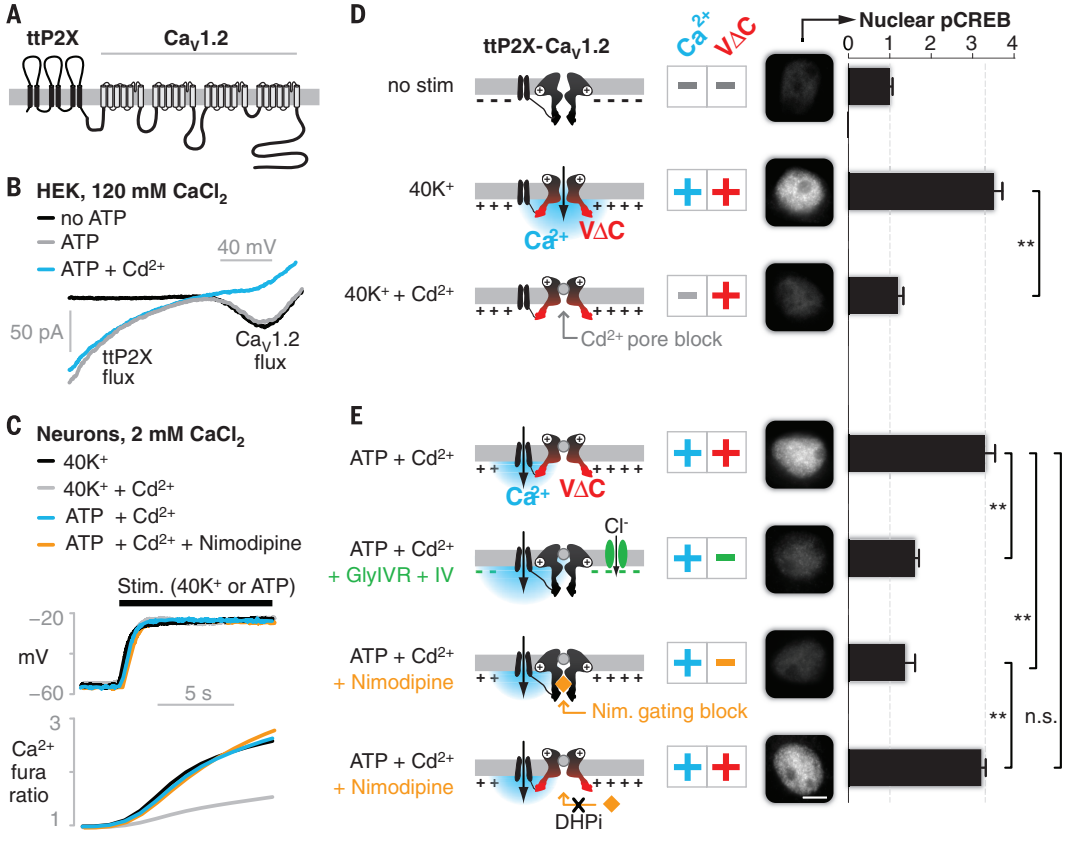


Fig. 1. Decoupling $Ca_V1.2$ Ca^{2+} and VΔC signals reveals dual requirement for CREB activation. (**A**) The engineered chimeric construct, showing transmembrane domains and intra- and extracellular loops. (**B**) Ca^{2+} currents mediated by the chimeric channel in HEK cells. (**C**) Changes in voltage (top, current clamp recording) and Ca^{2+} influx (bottom, fura-2 imaging) under key stimulation conditions ($N = 6$ cells; fig. S2, A and B, shows SEM). (**D** and **E**) Nuclear pCREB in cultured cortical neurons assayed after 3 min of stimulation (conditions are indicated on the left; the cartoons represent the ttP2X-$Ca_V1.2$ chimera, with plus and minus signs indicating the presence and absence of the signals, respectively). pCREB was elevated only with dual Ca^{2+} and VΔC stimuli [second row in (D) and first and fourth rows in (E)]. Elimination of either Ca^{2+} [third row in (D)] or VΔC [second and third rows in (E)] abrogated signaling. Black bars show means ± SEM (normalized to no stimulation) of 50 cells from three independent cultures. Scale bar, 5 μm. $^{**}P <$ 0.01, determined by one-way analysis of variance (ANOVA) followed by Fisher's least significant difference test.

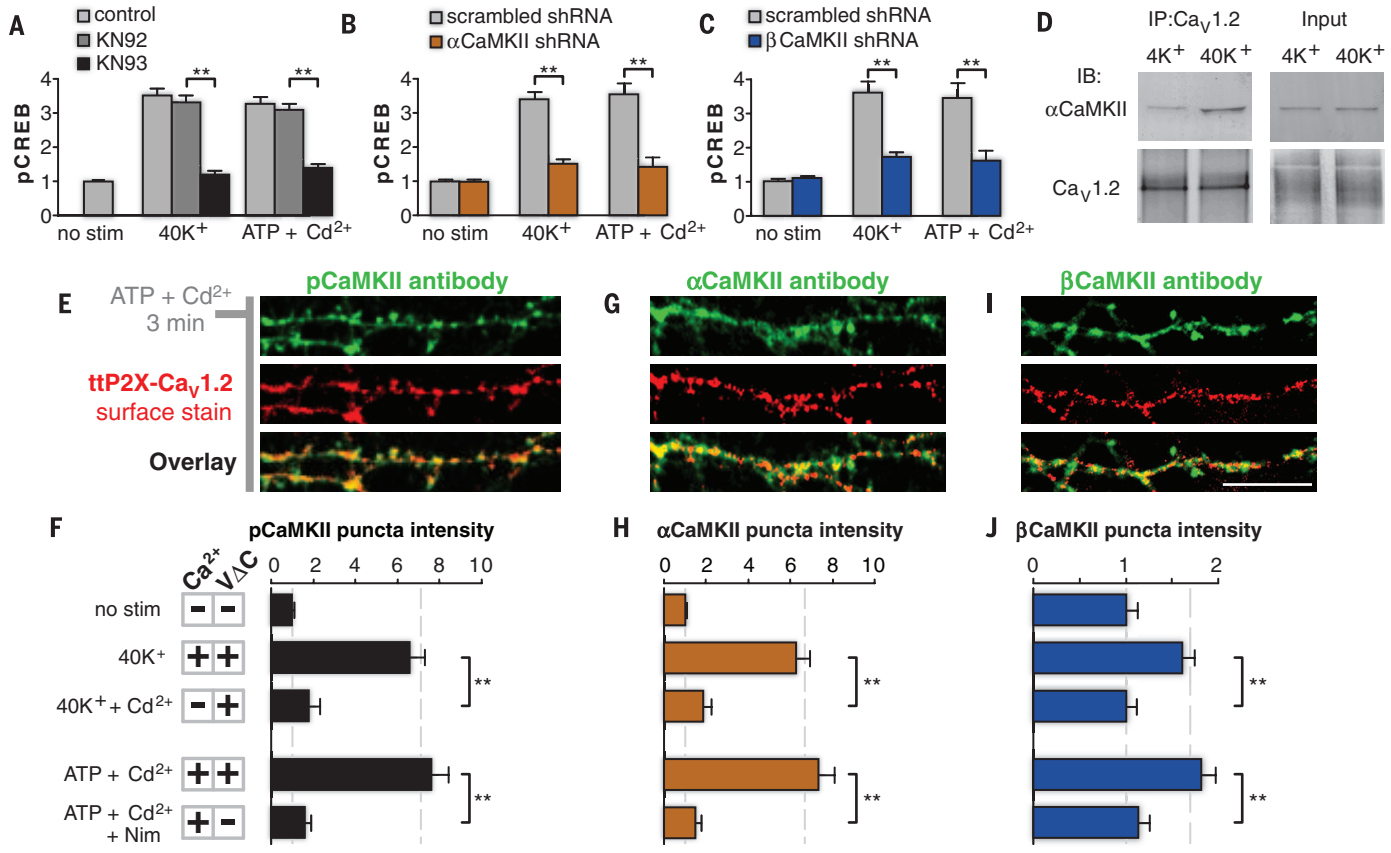


Fig. 2. Redistribution of CaMKII to $Ca_V1.2$ puncta requires dual Ca^{2+} and VΔC signals. (**A** to **C**) pCREB signaling (3 min of $40K^+$ or ATP-plus-Cd^{2+} stimulation) was blocked by the CaMKII inhibitor KN93 (KN92 is an inactive analog) (A), or by shRNA against either αCaMKII (B) or βCaMKII (C). (**D**) Co-immunoprecipitation with antibodies against $Ca_V1.2$ indicated that the association between $Ca_V1.2$ and αCaMKII increased after stimulation (IB, immunoblotting; IP, immunoprecipitation). (**E**, **G**, and **I**) pCaMKII (E), αCaMKII (G), and βCaMKII (I) in dendrites of cultured cortical neurons after stimulation (ATP plus Cd^{2+} for 3 min). Their staining is punctate (green) and colocalizes with surface ttP2X-$Ca_V1.2$ channels (red). Scale bar, 10 μm. (**F**, **H**, and **J**) Quantification of puncta intensity for pCaMKII (F), αCaMKII (H), and βCaMKII (J) (Nim, nimodipine). Puncta intensity increases with dual Ca^{2+} and VΔC signals (second and fourth rows) but not with Ca^{2+} or VΔC signals in isolation (third and fifth rows). The bars show means ± SEM (normalized to no stimulation) of 50 cells from three independent cultures. $^{**}P < 0.01$, determind by one-way ANOVA followed by Fisher's least significant difference test.

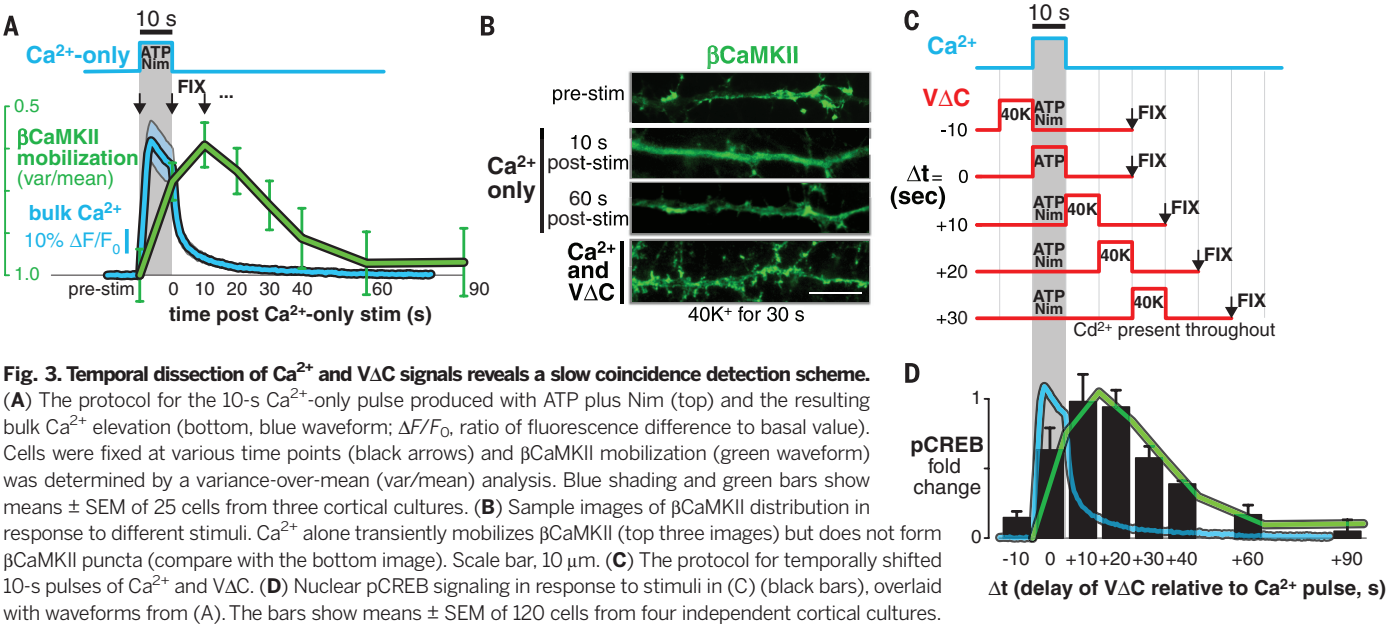


Fig. 3. Temporal dissection of Ca^{2+} and VΔC signals reveals a slow coincidence detection scheme. (**A**) The protocol for the 10-s Ca^{2+}-only pulse produced with ATP plus Nim (top) and the resulting bulk Ca^{2+} elevation (bottom, blue waveform; $\Delta F/F_0$, ratio of fluorescence difference to basal value). Cells were fixed at various time points (black arrows) and βCaMKII mobilization (green waveform) was determined by a variance-over-mean (var/mean) analysis. Blue shading and green bars show means ± SEM of 25 cells from three cortical cultures. (**B**) Sample images of βCaMKII distribution in response to different stimuli. Ca^{2+} alone transiently mobilizes βCaMKII (top three images) but does not form βCaMKII puncta (compare with the bottom image). Scale bar, 10 μm. (**C**) The protocol for temporally shifted 10-s pulses of Ca^{2+} and VΔC. (**D**) Nuclear pCREB signaling in response to stimuli in (C) (black bars), overlaid with waveforms from (A). The bars show means ± SEM of 120 cells from four independent cortical cultures.

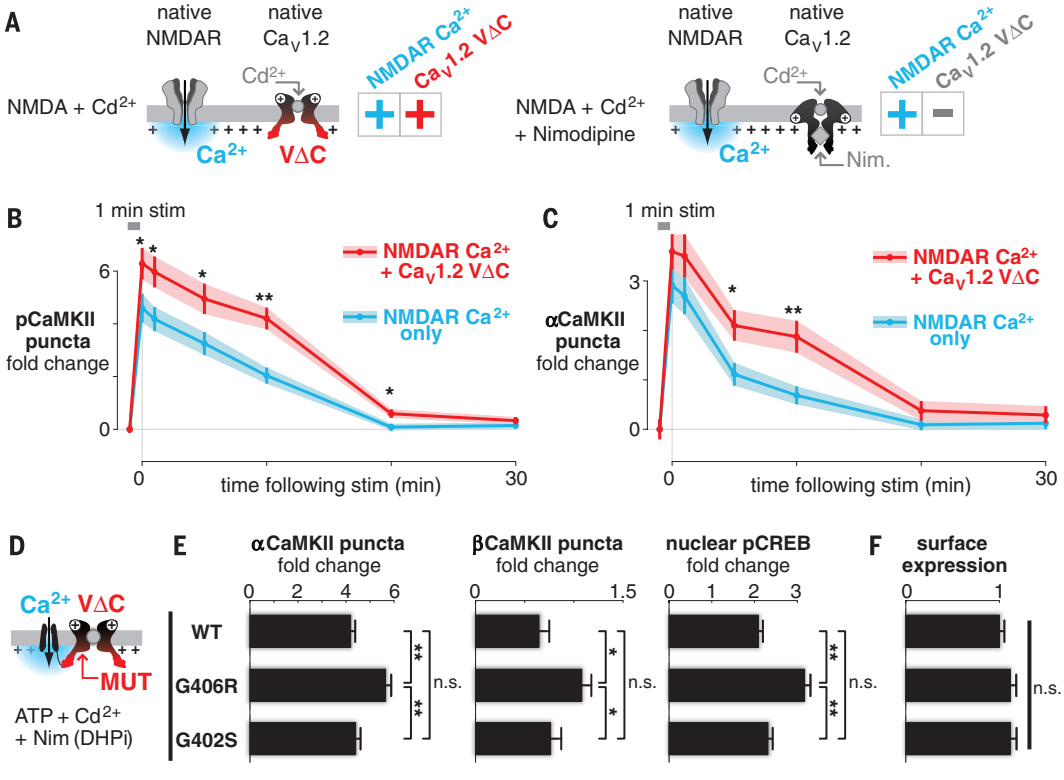


Fig. 4. $Ca_V1.2$ VΔC synergistically augments NMDAR signaling and is mistuned in TS mutations. (**A**) Scheme for examining the functional crosstalk of NMDAR and $Ca_V1.2$ VΔC. (**B** and **C**) pCaMKII (B) and αCaMKII (C) puncta intensity analysis in neurons after 1 min of stimulation. Shown are means (points) ± SEM (bars) of 50 cells for each condition. *P < 0.05 and **P < 0.01, determined by a two-tailed independent Student's t test. (**D**) Approach to examining the VΔC potency of $Ca_V1.2$ variants by means of chimeras (MUT, mutation). (**E**) Signaling to both CaMKII and CREB is substantially elevated (~30 to 70%) in G406R relative to either WT or G402S $Ca_V1.2$. Bars show means ± SEM of 50 cells from three cultures. *P < 0.05 and **P < 0.01, determined by one-way ANOVA followed by Fisher's least significant difference test. (**F**) Surface expression of TS mutants is indistinguishable from WT $Ca_V1.2$ (live-cell surface stain).

effects on $Ca_V1.2$ Ca^{2+} flux (*7*, *8*, *24*–*27*) were suppressed with Cd^{2+}, and nimodipine eliminated endogenous Ca_V1 VΔC contributions, whereas chimeric channels were nimodipine-insensitive (Fig. 4D). We found that G406R $Ca_V1.2$ exhibited gain-of-function VΔC signaling: α/βCaMKII and CREB signaling were substantially elevated (~30 to 70%). However, chimera surface expression was no different than in wild-type (WT) $Ca_V1.2$ (Fig. 4, E and F). In contrast, G402S $Ca_V1.2$ did not differ at all from WT $Ca_V1.2$ (Fig. 4E). Thus, mistuning of VΔC is associated with the G406R (*28*) but not with the G402S variant of TS (fig. S6B, colored symbols), in correlation with the autistic symptoms in TS.

Since the classic discovery of flux-independent $Ca_V1.1$ signaling (*9*, *10*), other nonionic modes of channel signaling have been reported to operate independently from ionic signaling (*11*, *28*–*30*). In this study, we found that conformational and ionic signals from the same channel can work in concert to regulate transcription. Such dual-mode signaling offers enhanced specificity: Maximal $Ca_V1.2$-mediated CREB activity requires a sequence of Ca^{2+} influx followed ~10 to 20 s later by VΔC signaling, a form of coincidence detection that is reminiscent of spike timing–dependent plasticity (*31*) but more than a thousand times slower (fig. S5). A second benefit is an increase in the voltage dependence of signaling. Voltage-dependent contributions from Ca^{2+} and VΔC signals render $Ca_V1.2$-mediated transcription more sensitive to small changes in depolarization (*4*). Taken together, these two advantages—heightened temporal specificity and voltage sensitivity—would make suboptimal patterns of activity less effective, while allowing temporally optimal stimuli of even small magnitudes to signal strongly. This may explain why synaptic plasticity that is dependent on Ca_V1-mediated transcription typically requires prolonged bouts of activity or multiple bursts spread over tens of seconds (*2*, *32*).

Yet another advantage of dual-mode signaling is the possibility of interaction between VΔC signals and recent Ca^{2+} entry from other sources. We found that $Ca_V1.2$ VΔC synergizes with NMDAR signaling (Fig. 4), raising the possibility of interactions with Ca^{2+} signals derived from other sources, such as internal Ca^{2+} stores or Ca^{2+}-permeable AMPA (α-amino-3-hydroxy-5-methyl-4-isoxazolepropionic acid) receptors. Looking beyond $Ca_V1.2$, our chimeric-channel approach may provide a generalizable strategy to investigate nonconducting roles of NMDARs (*29*) and of other Ca^{2+}-permeant channels such as $Ca_V1.3$. $Ca_V1.3$ variants that produce autism (*33*) consistently display negative shifts in voltage dependence that would be expected to enhance VΔC signaling, much as we found for $Ca_V1.2$ G406R (Fig. 4E).

REFERENCES AND NOTES

1. E. R. Kandel, *Science* **294**, 1030–1038 (2001).
2. C. R. Raymond, *Trends Neurosci.* **30**, 167–175 (2007).
3. G. Y. Wu, K. Deisseroth, R. W. Tsien, *Proc. Natl. Acad. Sci. U.S.A.* **98**, 2808–2813 (2001).
4. D. G. Wheeler, C. F. Barrett, R. D. Groth, P. Safa, R. W. Tsien, *J. Cell Biol.* **183**, 849–863 (2008).
5. D. G. Wheeler *et al.*, *Cell* **149**, 1112–1124 (2012).
6. R. E. Dolmetsch, U. Pajvani, K. Fife, J. M. Spotts, M. E. Greenberg, *Science* **294**, 333–339 (2001).
7. I. Splawski *et al.*, *Cell* **119**, 19–31 (2004).
8. I. Splawski *et al.*, *Proc. Natl. Acad. Sci. U.S.A.* **102**, 8089–8096 (2005).
9. C. M. Armstrong, F. M. Bezanilla, P. Horowicz, *Biochim. Biophys. Acta* **267**, 605–608 (1972).
10. B. A. Adams, T. Tanabe, A. Mikami, S. Numa, K. G. Beam, *Nature* **346**, 569–572 (1990).
11. E. Kobrinsky, E. Schwartz, D. R. Abernethy, N. M. Soldatov, *J. Biol. Chem.* **278**, 5021–5028 (2003).
12. M. R. Tadross, R. W. Tsien, D. T. Yue, *Proc. Natl. Acad. Sci. U.S.A.* **110**, 15794–15799 (2013).
13. K. Deisseroth, H. Bito, R. W. Tsien, *Neuron* **16**, 89–101 (1996).
14. J. B. Lansman, P. Hess, R. W. Tsien, *J. Gen. Physiol.* **88**, 321–347 (1986).
15. R. Bourtchuladze *et al.*, *Cell* **79**, 59–68 (1994).
16. T. Lynagh, J. W. Lynch, *J. Biol. Chem.* **285**, 14890–14897 (2010).
17. R. W. Hadley, W. J. Lederer, *Am. J. Physiol.* **269**, H1784–H1790 (1995).
18. M. R. Tadross, M. B. Johny, D. T. Yue, *J. Gen. Physiol.* **135**, 197–215 (2010).
19. H. Ma *et al.*, *Cell* **159**, 281–294 (2014).
20. L. B. Rosen, D. D. Ginty, M. J. Weber, M. E. Greenberg, *Neuron* **12**, 1207–1221 (1994).
21. K. Shen, T. Meyer, *Science* **284**, 162–167 (1999).
22. K. Shen, M. N. Teruel, K. Subramanian, T. Meyer, *Neuron* **21**, 593–606 (1998).
23. T. Meyer, P. I. Hanson, L. Stryer, H. Schulman, *Science* **256**, 1199–1202 (1992).
24. S. Fröhler *et al.*, *BMC Med. Genet.* **15**, 48 (2014).
25. J. Tallila, A. Hiippala, S. Myllykangas, T. P. Alastalo, J. W. Koskenvuo, *Heart Lung Circ.* **23**, e4–e5 (2014).
26. R. P. Xiao, H. Cheng, W. J. Lederer, T. Suzuki, E. G. Lakatta, *Proc. Natl. Acad. Sci. U.S.A.* **91**, 9659–9663 (1994).
27. C. Erxleben *et al.*, *Proc. Natl. Acad. Sci. U.S.A.* **103**, 3932–3937 (2006).
28. J. F. Krey *et al.*, *Nat. Neurosci.* **16**, 201–209 (2013).
29. S. Nabavi *et al.*, *Proc. Natl. Acad. Sci. U.S.A.* **110**, 4027–4032 (2013).
30. D. Atlas, *Annu. Rev. Biochem.* **82**, 607–635 (2013).
31. G. Q. Bi, M. M. Poo, *J. Neurosci.* **18**, 10464–10472 (1998).
32. L. M. Grover, T. J. Teyler, *Nature* **347**, 477–479 (1990).
33. A. Pinggera *et al.*, *Biol. Psychiatry* **77**, 816–822 (2015).

ACKNOWLEDGMENTS

We thank B. Mensh, A. Lee, N. Spruston, and H. Bito for critical feedback on the manuscript; R. Groth, S. Sanchez, S. Cohen,

J. Emery, and B. Shields for assistance with primary neuronal cultures; and H. Ma and other Tsien laboratory members for discussions throughout the execution of this project. The chimera construct is available from M.R.T. upon request. This work was supported by research grants to R.W.T. from the National Institute of General Medical Sciences; the National Institute of Mental Health; the National Institute of Neurological Disorders and Stroke; and the Simons, Mathers, and Burnett Family Foundations. M.R.T. was supported by the Howard Hughes Medical Institute, the Jane Coffin Childs Fellowship, and the Stanford Dean's Fellowship. The authors declare no conflicts. Author contributions were as follows: R.W.T. framed the question and provided overall guidance. M.R.T. conceived of the approach, engineered the chimera, discovered the coincidence of Ca^{2+} and VΔC in activating CREB in WT and TS $Ca_V1.2$, and designed the Δt and NMDAR experiments. B.L. showed that coincidence detection was mediated by CaMKII signaling, implemented the Δt and NMDAR experiments, and performed biochemistry analyses. M.R.T. led the writing, B.L. shortened the manuscript to its published form, and R.W.T. provided editorial oversight. The data are included in the main manuscript and the supplementary materials.

SUPPLEMENTARY MATERIALS

www.sciencemag.org/content/351/6275/863/suppl/DC1
Materials and Methods
Figs. S1 to S6
References (*34*–*52*)
DNA Construct Sequence

3 September 2015; accepted 11 January 2016
10.1126/science.aad3647

STRUCTURAL BIOLOGY

Structures of a CRISPR-Cas9 R-loop complex primed for DNA cleavage

Fuguo Jiang,[1]* David W. Taylor,[1,2]* Janice S. Chen,[1] Jack E. Kornfeld,[3] Kaihong Zhou,[3] Aubri J. Thompson,[4] Eva Nogales,[1,2,3,5]† Jennifer A. Doudna[1,2,3,4,5,6]†

Bacterial adaptive immunity and genome engineering involving the CRISPR (clustered regularly interspaced short palindromic repeats)–associated (Cas) protein Cas9 begin with RNA-guided DNA unwinding to form an RNA-DNA hybrid and a displaced DNA strand inside the protein. The role of this R-loop structure in positioning each DNA strand for cleavage by the two Cas9 nuclease domains is unknown. We determine molecular structures of the catalytically active *Streptococcus pyogenes* Cas9 R-loop that show the displaced DNA strand located near the RuvC nuclease domain active site. These protein-DNA interactions, in turn, position the HNH nuclease domain adjacent to the target DNA strand cleavage site in a conformation essential for concerted DNA cutting. Cas9 bends the DNA helix by 30°, providing the structural distortion needed for R-loop formation.

Bacteria and archaea defend themselves against infection using adaptive immune systems comprising CRISPR (clustered regularly interspaced short palindromic repeats) loci and their associated *cas* genes (*1*–*4*). CRISPR-Cas systems use Cas proteins in complex with small CRISPR RNAs (crRNAs) to identify and cleave complementary target sequences in foreign DNA (*5*, *6*). A defining feature of type I and type II CRISPR-Cas systems is R-loop formation in which the guide RNA segment of crRNAs invades double-helical DNA to form an RNA-DNA hybrid helix with the target DNA strand while displacing the opposing nontarget strand (*7*–*10*). In type II CRISPR-Cas systems, the Cas9 endonuclease together with crRNA and a trans-activating crRNA (tracrRNA) or an engineered single-guide RNA (sgRNA), which is widely used in Cas9-based genome engineering, is sufficient to form this R-loop (*8*, *11*). The R-loop interaction occurs at target DNA sequences bearing guide RNA segment complementarity and a short protospacer adjacent motif (PAM) leading to double-stranded DNA (dsDNA) cleavage 3 base pairs (bp) upstream of the PAM via the HNH and RuvC nuclease domains (*11*, *12*). Comparison of crystal structures of Cas9 alone (*13*), bound to guide RNA (*14*), or to a single target strand of DNA (*15*–*17*) revealed substantial conformational rearrangement of Cas9 to form a DNA recognition-competent structure. However, in all available structures, the HNH domain active site is more than 30 Å away from the target-strand DNA cleavage site, and the active DNA-bound state of the RuvC domain has not been observed due to the lack of an intact nontarget strand in these complexes.

To determine the structural basis for R-loop formation and concerted DNA cleavage by the two Cas9 endonuclease domains, we solved the 3.4-Å resolution crystal structure of wild-type *Streptococcus pyogenes* Cas9 bound to sgRNA and a 30-bp target dsDNA containing a canonical 5′-TGG-3′ PAM (*11*, *18*) (Fig. 1, A and B, and table S1). Metal ion chelation prevented DNA cleavage during complex assembly and crystallization. The Cas9-sgRNA-dsDNA ternary complex, representing the cleavage-competent state of the enzyme, has a bi-lobed architecture in which the bound target DNA resides within the central channel between the alpha-helical recognition (REC) and the nuclease (NUC) lobes (Fig. 1, C and D). The dsDNA substrate is trapped in an unwound but precleaved state, with the target DNA strand engaged in a pseudo-A-form RNA-DNA hybrid spanning the length of the central protein channel.

The displaced nontarget single-stranded DNA (ssDNA) runs parallel to the RNA-DNA heteroduplex but threads into a tight side tunnel located within the NUC lobe (Fig. 1D and fig. S1). Unambiguous electron density is observed for 9 nucleotides (nt) of nontarget DNA upstream of the PAM (Fig. 2A). Analysis of crystals containing dsDNA with 5-iododeoxyuridine (5-IdU) in place of three thymidines in the nontarget strand shows two strong peaks of iodine anomalous difference density at the expected positions (fig. S2). Lack of density for the third 5-IdU-substituted nucleotide, located at the 5′ end of the nontarget strand, indicates high mobility of the PAM-distal end of this strand. These crystallographic results are consistent with footprinting data showing that only 9 nt of the PAM-proximal displaced DNA strand are protected from P1 nuclease cleavage (*13*).

The ordered nontarget DNA exhibits an extended, distorted helical conformation in which the first nucleotide upstream of the PAM (referred to as position −1) stacks onto the PAM-proximal DNA duplex (Fig. 2A). Whereas the target DNA strand kinks at the +1 phosphodiester linkage, as observed previously (*16*, *17*), the nontarget DNA strand undergoes a sharp kink at the −1 phosphate position. In contrast to the +1 phosphate on the target strand, there are no direct protein contacts to the −1 phosphate on the nontarget strand. Instead, Cas9 makes extensive interactions with the flipped nucleotides at the −2 and −3 positions to stabilize the kinked DNA configuration of the nontarget strand (Fig. 2B). The nontarget strand kinks again, with the base orientation at −4 twisted by ~90° with respect to −3 and stabilized by stacking with two conserved Cas9 residues, Phe^{916} and Leu^{921}. After position −5, the nontarget DNA strand extrudes laterally through the narrow side tunnel formed by the NUC lobe without many direct protein-DNA interactions.

The observed orientation of the nontarget DNA strand reveals its position in the RuvC catalytic center. The four catalytically essential residues (Asp^{10}, Glu^{762}, His^{983}, and Asp^{986}) of this nuclease domain are positioned near the scissile phosphate between positions −3 and −4 (Fig. 2C). RuvC, which employs a carboxylate-chelated two-metal-ion cleavage mechanism (*13*, *15*), adopts the same structure and position as observed in the Mn^{2+}-bound apo-Cas9 structure (*13*). Notably, the distances between the superimposed metal ions and the nonbridging oxygen of the scissile phosphate (~5.5 Å) are slightly longer than the typical Mg-O coordination distance (2.1 Å). We speculate that binding of divalent cations in the active site may facilitate movement of the scissile

[1]Department of Molecular and Cell Biology, University of California, Berkeley, CA 94720, USA. [2]California Institute for Quantitative Biosciences, University of California, Berkeley, CA 94720, USA. [3]Howard Hughes Medical Institute, University of California, Berkeley, CA 94720, USA. [4]Department of Chemistry, University of California, Berkeley, CA 94720, USA. [5]Life Sciences Division, Lawrence Berkeley National Laboratory, Berkeley, CA 94720, USA. [6]Physical Biosciences Division, Lawrence Berkeley National Laboratory, Berkeley, CA 94720, USA.
*These authors contributed equally to this work. **†Corresponding author. E-mail: doudna@berkeley.edu (J.A.D.); enogales@lbl.gov (E.N.)**

Downloaded from on February 18, 2016

phosphate in the nontarget strand toward the bound metal ions for catalysis.

The presence of the nontarget strand induces a more compact (closed) conformation of Cas9, relative to previous ssDNA- or PAM-containing partial duplex-bound structures, in which both the REC and NUC lobes move toward the central nucleic acid–binding channel (fig. S3). This repositioning drives helical domain 2 of the REC lobe, which does not contact the RNA-DNA heteroduplex in previously reported structures (*15*, *16*), to interact directly with the phosphate backbone in the target DNA strand through residues Ser^{267} and Asp^{269} (Fig. 2B and fig. S4). Thermal shift assays show that Cas9 exhibits greater stability upon dsDNA substrate binding relative to association with a single target DNA strand or a PAM-containing partial duplex (fig. S5 and table S2). Together, these observations show how binding to both strands of a dsDNA target coordinates Cas9 conformational changes required for efficient catalysis.

The most prominent Cas9 conformational rearrangement upon dsDNA binding occurs in the position of the HNH nuclease domain, which rotates by ~180° and translates by ~20 Å toward the RNA-DNA heteroduplex as a rigid body from its location in the PAM-containing partial duplex-bound complex (Fig. 3A). In contrast to previous structures, in which the HNH active site was neither pointed toward nor located near the target DNA strand cleavage site (fig. S6), this rotated HNH position locates the active-site residue His^{840} adjacent to the scissile phosphate (Fig. 3B). The observed structural states of the HNH domain agree with intramolecular Förster resonance energy transfer (FRET) experiments showing that the HNH domain exists in conformational equilibrium between inactive and active states, favoring the active state observed here only upon on-target dsDNA binding (*19*). In our present dsDNA-bound structure, the distance between the catalytic residue His^{840} and the scissile phosphate is slightly farther apart (~10 Å) than required for catalysis, probably owing to omission of diavalent metal ions during crystallization. Given the high mobility exhibited by the HNH domain, it is reasonable to speculate that introduction of metal ions would drive the HNH active site to the target DNA strand for cleavage (*13*, *15*).

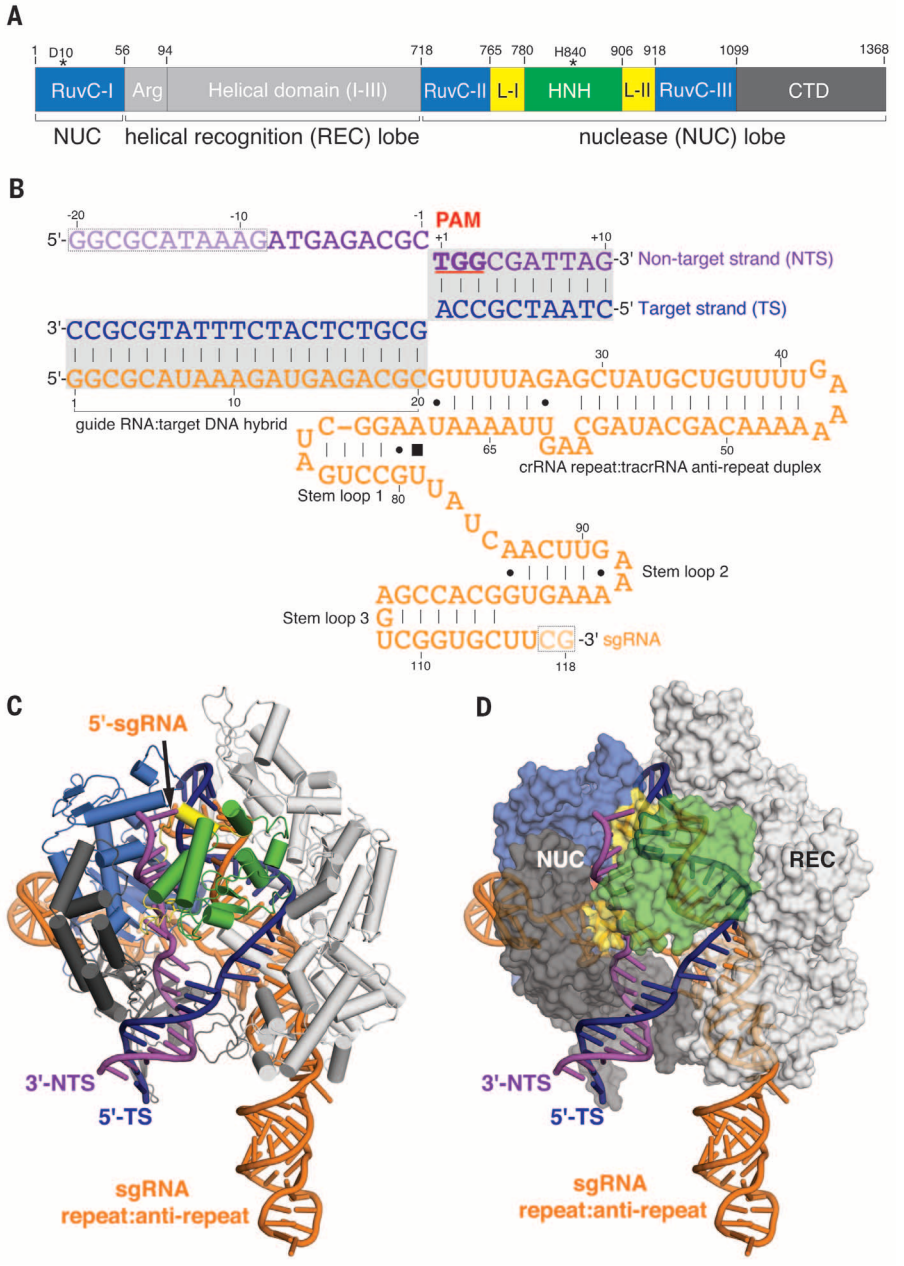


Fig. 1. Crystal structure of Cas9-sgRNA-dsDNA ternary complex. (**A**) Domain organization of *S. pyogenes* Cas9. (**B**) Schematic diagram of the sgRNA–target DNA complex. The target DNA strand and displaced nontarget strand are colored dark blue and purple, respectively. The PAM sequence is underlined, and the sgRNA sequence is highlighted in orange. Dashes and dots represent canonical and noncanonical Watson-Crick base pairs, respectively. Filled square denotes the base stacking interaction. Dashed boxes outline the portions of sgRNA and DNA that are not visible in the electron density map. (**C** and **D**) Ribbon (C) and surface (D) representations of the Cas9-sgRNA-dsDNA structure, color-coded as defined in (A) and (B).

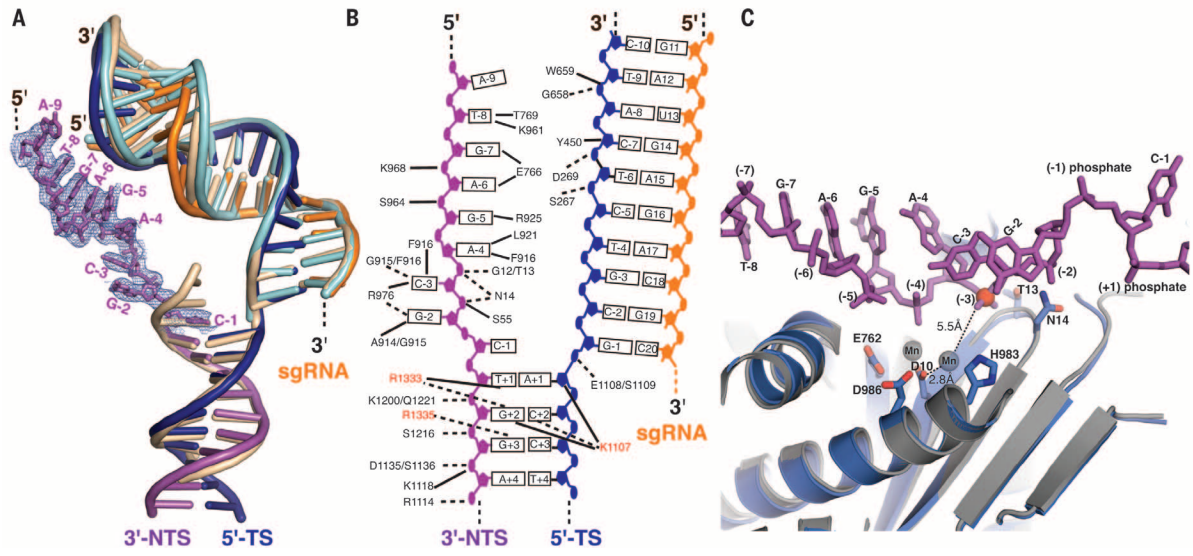


Fig. 2. Protein contacts that open and kink the nontarget DNA strand. (**A**) Structural comparison of sgRNA-DNA complexes in existing DNA-bound Cas9 structures (with sgRNA scaffold omitted for clarity). The ordered nontarget DNA strand in the dsDNA-bound structure is shown with a simulated-annealing omit F_o-F_c electron density map contoured at 1.5 σ. The sgRNA-DNA complexes in the ssDNA-bound (PDB ID 4OO8) and PAM-containing partial duplex-bound (PDB ID 4UN3) structures are colored in cyan and beige, respectively. (**B**) Schematic showing key Cas9-dsDNA interactions. For clarity, only the unwound nontarget strand and the seed RNA–target DNA heteroduplex are shown. Residues specifically interacting with the PAM motif are highlighted in red. Hydrogen bonds or electrostatic interactions are indicated by dashed lines; hydrophobic contacts and van der Waals interactions are shown as solid lines. (**C**) Position of nontarget strand in RuvC active site. The red sphere depicts the scissile phosphate. Notably, the RuvC domain in the dsDNA-bound structure (marine) superimposes well with that in the Mn^{2+}-bound apo-Cas9 form (gray), with two Mn^{2+} ions fit snugly in the active center.

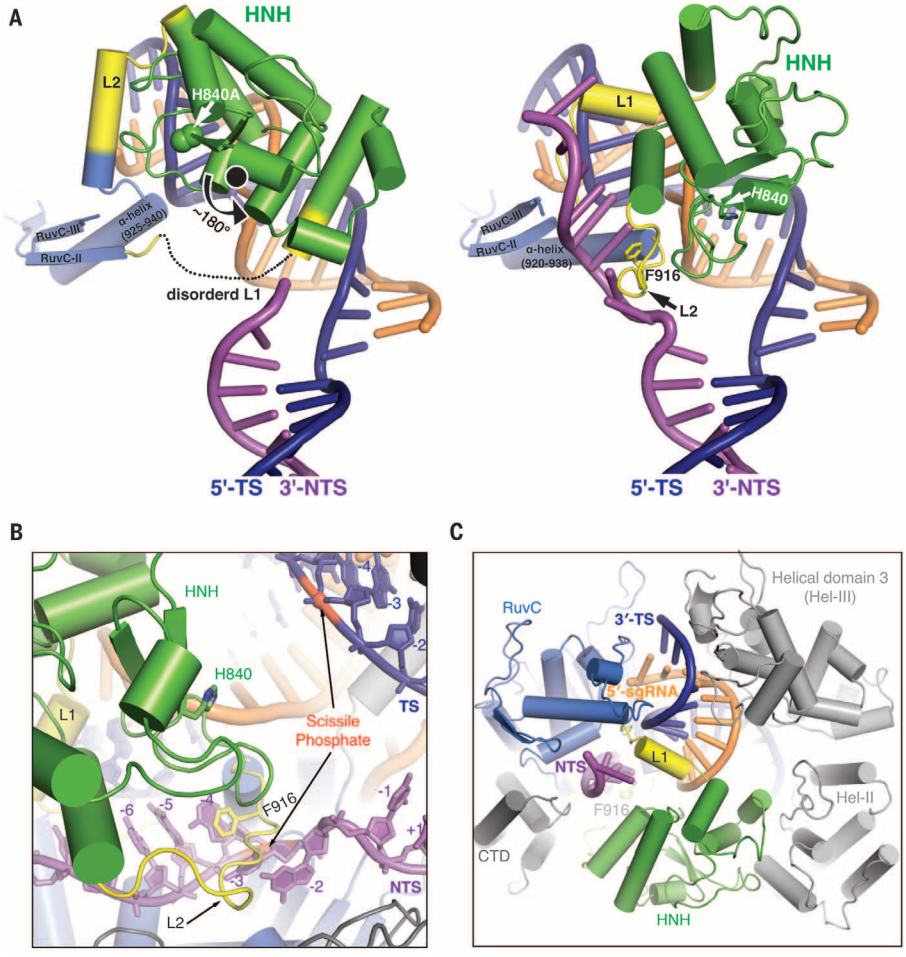


Fig. 3. dsDNA unwinding induces drastic conformational changes in Cas9's HNH domain and the linker regions connecting it to RuvC domain. (**A**) Comparison of HNH nuclease domain with that observed in a PAM-containing partial duplex-bound structure. The complexes are aligned through the less-flexible RuvC, helical domain 1, and PAM-interacting C-terminal domain (CTD) and presented in the same direction, but side by side. There is a ~180° rotation (marked by an arrow) of the L1-HNH-L2 region in the dsDNA-bound structure (right) along an axis perpendicular to the central channel relative to that of the partial duplex-bound state (left). (**B**) Close-up view of the HNH active site and L2 linker. The aromatic ring of Phe^{916} intercalated between positions −3 and −4 is shown as a stick. (**C**) Close-up view of the L1 linker.

Double-stranded DNA binding induces additional changes in the Cas9 structure that explain both HNH domain repositioning and R-loop stabilization. The two hinge regions connecting the HNH domain with the RuvC domain—L1 (residues 765 to 780) and L2 (residues 906 to 918)—are switched in the dsDNA-bound structure relative to their positions in the PAM-containing partial duplex-bound state (Fig. 3A). This rearrangement involves local changes in protein secondary structure. L1, which is completely disordered in prior structures, refolds into a well-ordered loop and a short α helix and lies between the target DNA strand and the displaced nontarget DNA strand (Fig. 3C). The refolding of L1 appears to be critical for stabilizing the R-loop structure, owing to multiple contacts made with the RNA-DNA hybrid minor groove and the distal region of the nontarget DNA strand (Fig. 2B). In contrast, L2 unfolds from its previously observed α helical structure into an extended loop in which many residues, including Phe^{916} and Leu^{921}, contact the nontarget DNA strand, thereby directing the scissile phosphate toward the RuvC active center (Fig. 2, B and C, and Fig. 3B). This dsDNA-induced unfolding of L2 is reminiscent of conformational changes observed in other protein–DNA complexes, such as the restriction enzyme BamHI-DNA complex (*20*) and the T7 RNA polymerase elongation complex (*21*). The structural rearrangements displayed by L1 and L2 upon dsDNA binding, in concert with the reorientation of the HNH domain, provide direct structural evidence for allostery between the HNH and RuvC nuclease domains through these hinge regions.

To visualize how Cas9 holds both ends of unwound dsDNA within a longer helix, we used cryo-electron microscopy (cryo-EM) to determine the structure of a wild-type *S. pyogenes* Cas9-sgRNA complex bound to a 40-bp dsDNA (table S2). We obtained structures of Cas9-sgRNA (Fig. 4, A and B) and Cas9-sgRNA-dsDNA (Fig. 4C) at 4.5 Å and 6.0 Å resolution, respectively (figs. S7 to S11). The 4.5-Å structure of Cas9-sgRNA perfectly accommodates the crystal structure of the preorganized Cas9–guide RNA complex (*14*). In contrast to the crystal structure, in which the 5′ end of the guide RNA (nucleotides 1 to 10) were disordered, density was visible for the entire 20-nt 5′ end of the guide RNA segment. The 5′ end of the guide lies inside the cavity formed between the HNH and RuvC nuclease domains (Fig. 4B). In the dsDNA-bound EM structure, the HNH domain and helical domain 2 are observed at lower resolution than the overall structure (~8 to 10 Å), indicating conformational plasticity of these two domains (Fig. 4C). This is consistent with a recent report showing that the HNH domain populates both active and inactive states (*19*). Density for dsDNA is observed on either side of the Cas9 protein complex, revealing a bend angle of ~30° in the DNA double helix as it traverses the protein (Fig. 4, C to E). The PAM-distal end duplex protrudes from the protein between the RNA-DNA heteroduplex and the RuvC nuclease domain. This end of the DNA is held rigidly on opposite sides through contacts with the RuvC and REC-lobe helical domain 3, stabilizing the distortion of the target DNA from a linear helical axis (Fig. 4F).

The structures of the Cas9-sgRNA-dsDNA complex presented here show how Cas9 holds unwound dsDNA to enable RNA-DNA hybrid formation without requiring an adenosine triphosphate–dependent helicase activity. DNA binding at a sequence complementary to the 20-nt guide RNA segment in the Cas9-RNA complex induces protein structural rearrangements that accommodate both the RNA-DNA helix and the displaced nontarget DNA strand. Those protein–nucleic acid interactions in turn direct the nontarget DNA strand into the RuvC domain active site, favoring local conformational changes that position the HNH domain active site near the scissile phosphate of the target DNA strand. Cas9 interacts with both ends of the open DNA helix, conferring a 30° helical bend angle that provides the structural distortion required for R-loop stabilization. Collectively, these findings explain how Cas9, an individual nonpolymerase enzyme able to catalyze R-loop formation, achieves this structural change leading to accurate, precise, and programmable DNA cleavage.

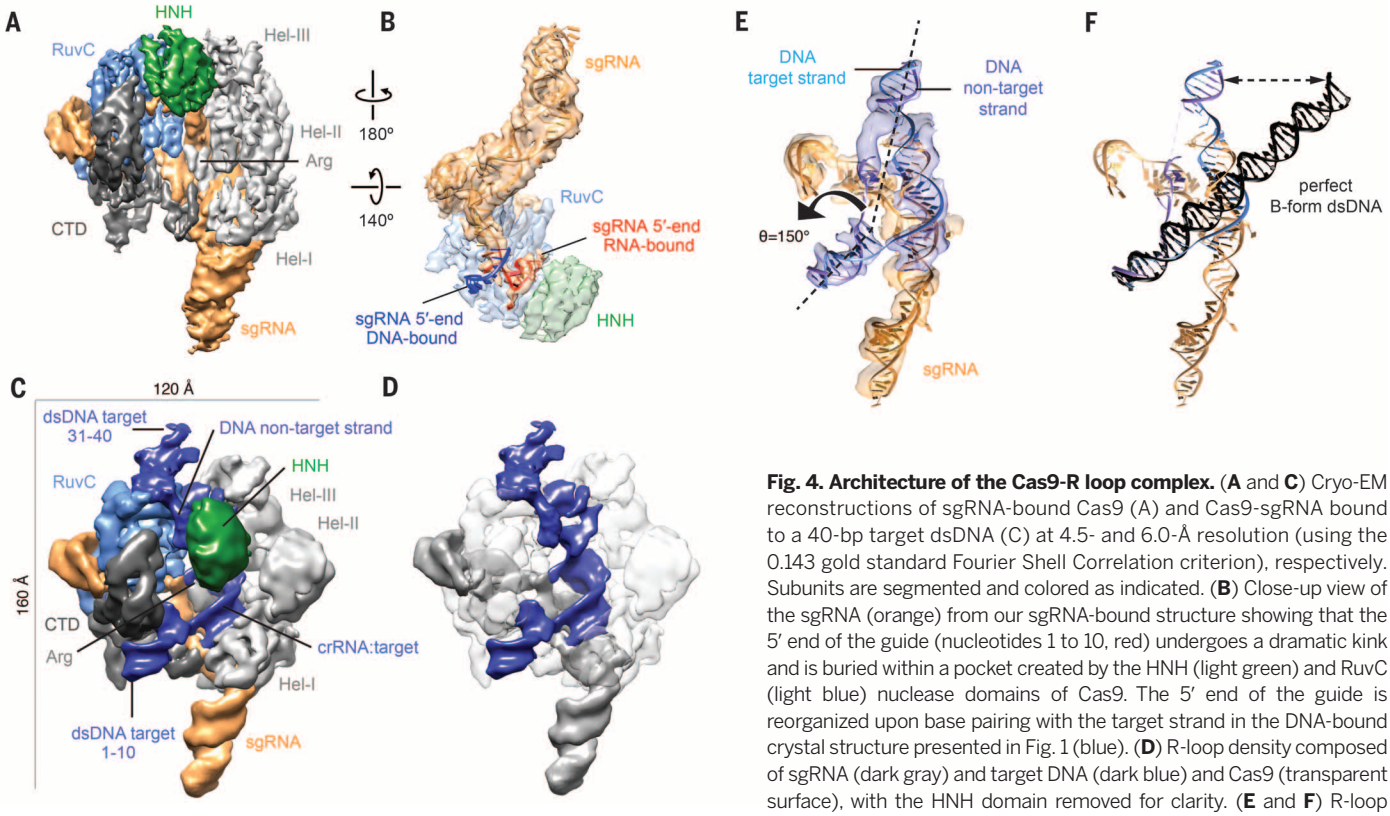


Fig. 4. Architecture of the Cas9-R loop complex. (**A** and **C**) Cryo-EM reconstructions of sgRNA-bound Cas9 (A) and Cas9-sgRNA bound to a 40-bp target dsDNA (C) at 4.5- and 6.0-Å resolution (using the 0.143 gold standard Fourier Shell Correlation criterion), respectively. Subunits are segmented and colored as indicated. (**B**) Close-up view of the sgRNA (orange) from our sgRNA-bound structure showing that the 5′ end of the guide (nucleotides 1 to 10, red) undergoes a dramatic kink and is buried within a pocket created by the HNH (light green) and RuvC (light blue) nuclease domains of Cas9. The 5′ end of the guide is reorganized upon base pairing with the target strand in the DNA-bound crystal structure presented in Fig. 1 (blue). (**D**) R-loop density composed of sgRNA (dark gray) and target DNA (dark blue) and Cas9 (transparent surface), with the HNH domain removed for clarity. (**E** and **F**) R-loop density composed of sgRNA (orange) and target DNA (dark blue) with the pseudo-atomic model reveals local bending of the dsDNA by ~30°, creating an angle of 150° between ends (arrow) (E) and large distortions as compared to a linear helical duplex extending from the PAM-proximal end (F).

REFERENCES AND NOTES

1. B. Wiedenheft, S. H. Sternberg, J. A. Doudna, *Nature* **482**, 331–338 (2012).
2. R. Sorek, C. M. Lawrence, B. Wiedenheft, *Annu. Rev. Biochem.* **82**, 237–266 (2013).
3. R. Barrangou, L. A. Marraffini, *Mol. Cell* **54**, 234–244 (2014).
4. L. A. Marraffini, *Nature* **526**, 55–61 (2015).
5. J. van der Oost, E. R. Westra, R. N. Jackson, B. Wiedenheft, *Nat. Rev. Microbiol.* **12**, 479–492 (2014).
6. F. Jiang, J. A. Doudna, *Curr. Opin. Struct. Biol.* **30**, 100–111 (2015).
7. M. M. Jore *et al*., *Nat. Struct. Mol. Biol.* **18**, 529–536 (2011).
8. M. D. Szczelkun *et al*., *Proc. Natl. Acad. Sci. U.S.A.* **111**, 9798–9803 (2014).
9. M. Rutkauskas *et al*., *Cell Reports* **10**, 1534–1543 (2015).
10. T. R. Blosser *et al*., *Mol. Cell* **58**, 60–70 (2015).
11. M. Jinek *et al*., *Science* **337**, 816–821 (2012).
12. G. Gasiunas, R. Barrangou, P. Horvath, V. Siksnys, *Proc. Natl. Acad. Sci. U.S.A.* **109**, E2579–E2586 (2012).
13. M. Jinek *et al*., *Science* **343**, 1247997 (2014).
14. F. Jiang, K. Zhou, L. Ma, S. Gressel, J. A. Doudna, *Science* **348**, 1477–1481 (2015).
15. H. Nishimasu *et al*., *Cell* **156**, 935–949 (2014).
16. C. Anders, O. Niewoehner, A. Duerst, M. Jinek, *Nature* **513**, 569–573 (2014).
17. H. Nishimasu *et al*., *Cell* **162**, 1113–1126 (2015).
18. F. J. M. Mojica, C. Díez-Villaseñor, J. García-Martínez, C. Almendros, *Microbiology* **155**, 733–740 (2009).
19. S. H. Sternberg, B. LaFrance, M. Kaplan, J. A. Doudna, *Nature* **527**, 110–113 (2015).
20. M. Newman, T. Strzelecka, L. F. Dorner, I. Schildkraut, A. K. Aggarwal, *Science* **269**, 656–663 (1995).
21. Y. W. Yin, T. A. Steitz, *Science* **298**, 1387–1395 (2002).

ACKNOWLEDGMENTS

The atomic coordinate of Cas9-sgRNA-dsDNA structure has been deposited in the Protein Data Bank with accession code 5F9R. The cryo-EM structures of guide RNA-bound Cas9 and target DNA-bound Cas9 have been deposited into the EMDataBank with accession codes EMD-3276 and EMD-3277, respectively. We thank G. Meigs, J. Holton (beamline 8.3.1 of the Advanced Light Source, Lawrence Berkeley National Laboratory) for assistance with data collection; Y. Cheng, R. Louder, S. Howes, E. Kellogg, R. Zhang, T. Houweling, Z. Yu, and M. J. de la Cruz for expert electron microscopy assistance; and members of the Doudna and Nogales laboratories for critical reading of the manuscript. F.J. is a Merck Fellow of the Damon Runyon Cancer Research Foundation (DRG-2201-14). D.W.T is a Damon Runyon Fellow of the Damon Runyon Cancer Research Foundation (DRG-2218-15). J.A.D and E.N. are Howard Hughes Medical Institute Investigators.

SUPPLEMENTARY MATERIALS

www.sciencemag.org/content/351/6275/867/suppl/DC1
Materials and Methods
Figs. S1 to S11
Tables S1 and S2
Movies S1 to S3
References (*22*–*44*)

7 November 2015; accepted 29 December 2015
Published online 14 January 2016
10.1126/science.aad8282

STRUCTURAL BIOLOGY

2.3 Å resolution cryo-EM structure of human p97 and mechanism of allosteric inhibition

Soojay Banerjee,[1]* Alberto Bartesaghi,[1]* Alan Merk,[1] Prashant Rao,[1] Stacie L. Bulfer,[2] Yongzhao Yan,[3] Neal Green,[4] Barbara Mroczkowski,[5] R. Jeffrey Neitz,[2] Peter Wipf,[3] Veronica Falconieri,[1] Raymond J. Deshaies,[6] Jacqueline L. S. Milne,[1] Donna Huryn,[3] Michelle Arkin,[2] Sriram Subramaniam[1]†

p97 is a hexameric AAA+ adenosine triphosphatase (ATPase) that is an attractive target for cancer drug development. We report cryo–electron microscopy (cryo-EM) structures for adenosine diphosphate (ADP)–bound, full-length, hexameric wild-type p97 in the presence and absence of an allosteric inhibitor at resolutions of 2.3 and 2.4 angstroms, respectively. We also report cryo-EM structures (at resolutions of ~3.3, 3.2, and 3.3 angstroms, respectively) for three distinct, coexisting functional states of p97 with occupancies of zero, one, or two molecules of adenosine 5′-*O*-(3-thiotriphosphate) (ATPγS) per protomer. A large corkscrew-like change in molecular architecture, coupled with upward displacement of the N-terminal domain, is observed only when ATPγS is bound to both the D1 and D2 domains of the protomer. These cryo-EM structures establish the sequence of nucleotide-driven structural changes in p97 at atomic resolution. They also enable elucidation of the binding mode of an allosteric small-molecule inhibitor to p97 and illustrate how inhibitor binding at the interface between the D1 and D2 domains prevents propagation of the conformational changes necessary for p97 function.

The superfamily of AAA+ proteins (ATPases associated with diverse cellular activities) consists of molecular chaperones that serve major roles in cellular protein quality control; DNA replication, transcription, recombination, and repair; membrane fusion; movement of intracellular cargo; and cell cycle regulation (*1*, *2*). These oligomeric ring-like enzymes, which typically form hexamers, contain common functional features including one or more conserved AAA+ ATPase cassettes in each protomer. These cassettes bind and hydrolyze ATP at the interface between adjacent subunits. The acquired energy from binding and catalysis of nucleotides induces a series of conformational changes to enable these enzymes to modulate their substrates. p97, a well-characterized member of this protein family, binds multiple proteins including deubiquitylating enzymes as well as ubiquitin-binding adaptors and ligases (*3*–*7*). The central role that p97 plays in protein quality control makes it an attractive target for cancer chemotherapy, as disruption of both of these processes hinders cancer cell survival (*8*). Up-regulation of p97 expression in cancer cells supports this premise (*9*), as do reports of numerous structurally diverse inhibitor types (*10*–*14*), including a potent inhibitor that entered a phase I clinical trial in 2015 (*15*).

Structurally, each p97 protomer has a predicted molecular weight of ~90 kDa and comprises an N-terminal domain (henceforth N domain), two tandem ATPase domains (designated D1 and D2) that pack as hexameric rings, and a short C-terminal domain. Structural studies of full-length p97 by x-ray crystallography have so far been limited to medium resolution (3.5 Å to 4.7 Å) (*16*), although higher-resolution structures of subcomplexes that contain D1 and the N domain or the D2 domain have revealed further architectural insights in these regions of the protein (*16*–*20*). Determination of the atomic-resolution structure of native, full-length p97 in different conformational states and in complex with inhibitors is therefore of considerable biological and clinical interest.

Using cryo-EM, we first performed structural analysis of p97 without addition of exogenous nucleotides. This structure, determined at an overall resolution of 2.4 Å, shows the expected architecture of the hexameric complex (fig. S1, A and B). ADP occupies both the D1 and D2 domain nucleotide-binding pockets (fig. S1, C and D). Analysis of the conformational variants that emerge during three-dimensional classification suggests that subtle conformational heterogeneity in the ADP-bound D2 hexamer (fig. S2) is a likely reason for the lower resolutions achieved in x-ray crystallographic analyses of full-length p97. Overall, the cryo-EM–derived structure of the D2 domain in the full-length hexamer is comparable to that determined for full-length p97 at 3.5 Å by x-ray crystallography, except for some differences in the relative disposition of the N domain (*16*) and better definition of the C-terminal α-helical subdomain that spans amino acid residues 645 to 763.

[1]Laboratory of Cell Biology, National Cancer Institute, Bethesda, MD 20892, USA. [2]Small Molecule Discovery Center, Pharmaceutical Chemistry, School of Pharmacy, University of California, San Francisco, CA 94143, USA. [3]University of Pittsburgh Chemical Diversity Center, University of Pittsburgh, Pittsburgh, PA 15260, USA. [4]Leidos Biomedical Research Inc., Frederick, MD 21702, USA. [5]Division of Cancer Treatment and Diagnosis, National Cancer Institute, Bethesda, MD 20892, USA. [6]Division of Biology and Biological Engineering and Howard Hughes Medical Institute, California Institute of Technology, Pasadena, CA 91107, USA.
*These authors contributed equally to this work. †**Corresponding author. E-mail: ss1@nih.gov**

Downloaded from on February 18, 2016

Several classes of inhibitors, including those that act in an allosteric or competitive manner, have been identified that impair p97 ATPase activity (*10*–*14*, *21*–*27*). Determination of the cryo-EM structure at 2.3 Å resolution of p97 in complex with UPCDC30245, a phenyl indole derivative (fig. S3) that is structurally related to a recently described series of allosteric inhibitors (*14*), shows that this compound (half-maximal inhibitory concentration ~27 nM) binds at the junction between the D1 and D2 domains (Fig. 1, A and B). A detailed view of the structure of a single p97 protomer shows the location of the inhibitor and bound ADP (Fig. 1, C to E), including features such as the interaction of the ADP β-phosphate with a water molecule in the D1 domain (Fig. 1D) and hydrogen bonding of a water molecule to the α-phosphate moiety and to the hydroxyl group on the ribose ring proximal to the α-phosphate group (Fig. 1E). Furthermore, the distal hydroxyl group of the ribose ring interacts with a water molecule hydrogen-bonded to the side-chain oxygen atom of Asn^{660} and the main-chain carbonyl atom of residue Asp^{478}. Local map resolution measured by ResMap (*28*) indicates that the density is weakest in the N domain, consistent with plots of B-factor profiles of the refined structure, which show that the average B-factor is highest in the N domain and in the D1-D2 connector region and lowest in the core of the D1 and D2 domains (Fig. 1, F and G, and fig. S4). The most ordered regions are at the p97 core, with a clear gradient toward higher B-factors at the periphery (movie S1).

Selected examples of the quality of the cryo-EM map in the D2 domain (residues 481 to 763) are presented in Fig. 2, A to C. It is conceivable that the two discrete conformations of the Arg^{599} side chain (Fig. 2B) are relevant to the ability of p97 to locally adapt to structural variations in bound substrates because this residue has been implicated in substrate interactions in the pore region surrounded by the D2 hexamer. UPCDC30245 binding did not result in significant changes in conformation of the polypeptide backbone, including at the nucleotide-binding sites (fig. S5). Visualization of density for the bound inhibitor in the map enabled determination of its conformation in the bound state and the local interactions involved in its binding at the D1-D2 interface. The inhibitor conformation is most ordered in the half that includes the indole ring that nestles into a binding pocket (fig. S6A). This inhibitor-binding site is sandwiched by the C-terminal regions of two α-helical segments that range from residues 483 to 498 and 523 to 534 (Fig. 2D). The binding tunnel is capped at the end where the fluorinated indole ring is docked between two loop elements (amino acid residues 506 to 512

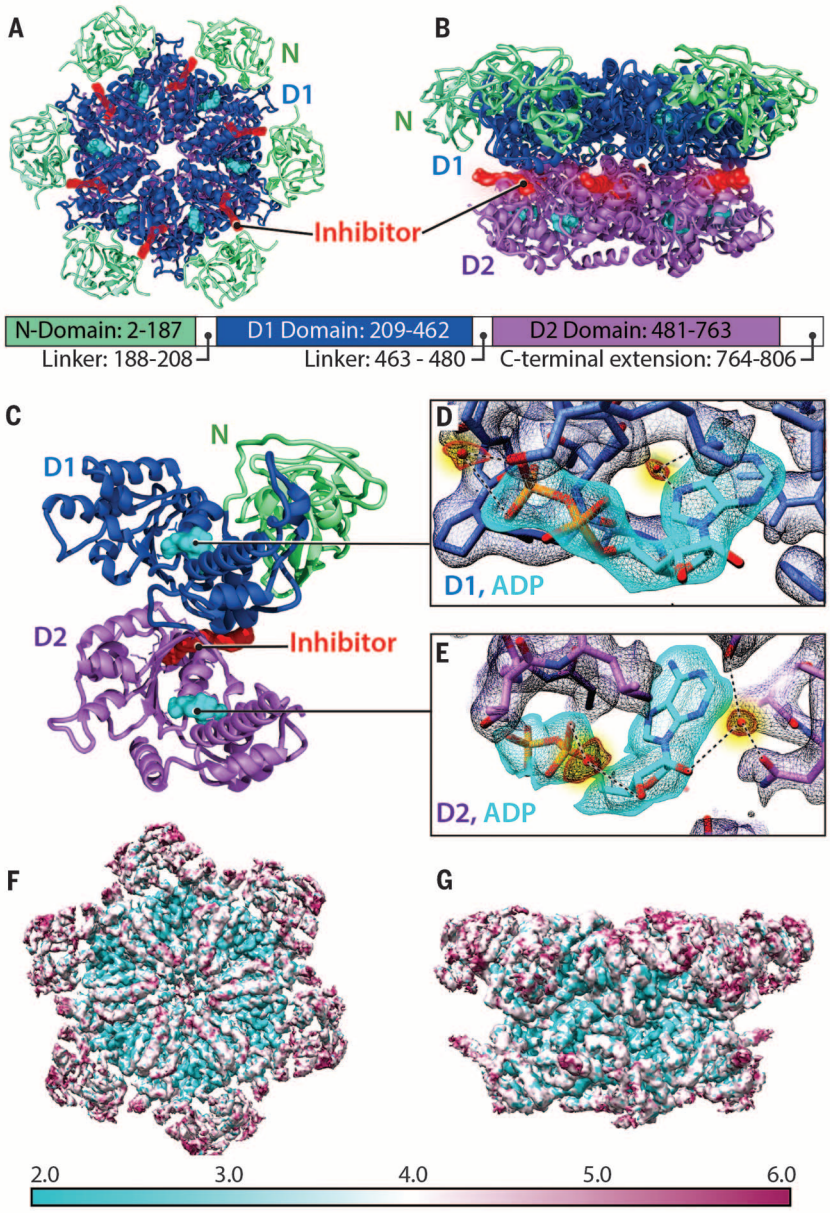


Fig. 1. Atomic-resolution model derived from cryo-EM structure of p97 in the presence of bound inhibitor. (**A** and **B**) Top and side views, respectively, of the cryo-EM structure of the p97 hexamer presented as a ribbon diagram, showing the N (green), D1 (blue), and D2 (purple) domains. The ADP molecule is colored cyan. The inhibitor (red) is bound at the junction between the D1 and D2 domains. The relative position of each domain in the primary sequence is indicated. (**C**) Ribbon diagram of a p97 protomer highlighting the location of the bound inhibitor (red) relative to the two bound nucleotides (cyan) in D1 and D2 domains. (**D** and **E**) Density maps for bound nucleotides, establishing that ADP is bound to both D1 and D2 domains, and visualization of densities for tightly bound water molecules (colored red, highlighted in yellow) at the nucleotide-binding sites. (**F** and **G**) Top and side views, respectively, of the structure (uncorrected density map), color-coded to represent variation in resolution across the protein as determined using ResMap (*28*).

and 610 to 618) that lead into two parallel β strands. The other end of the binding cleft is open and solvent-exposed (Fig. 2, E and F), with the piperazine ring of the inhibitor protruding outward into the bulk solvent. Residues that interact with ADP in the D1 and D2 sites are summarized in fig. S6, B and C, respectively.

The key interactions that anchor the inhibitor arise from the main-chain carbonyl oxygen of Val^{493} hydrogen-bonded to the N-H of the indole ring (2.9 Å), weak interaction of the fluorine atom present on the indole ring with the main-chain carbonyl oxygen atom of Ser^{511}, hydrogen bonding of the thiol group of Cys^{535} to the nitrogen atom in the piperidine ring (3.4 Å), and the side chain of Glu^{498} hydrogen-bonded to the nitrogen atom in the linker between the piperidine and piperazine groups (3.2 Å). The rest of the binding environment is largely hydrophobic in nature, stemming from interactions with residues Phe^{618}, Pro^{496}, Pro^{510}, Pro^{571}, Ala^{537}, and Val^{497} (Fig. 2D). Interactions at the indole ring end are central to the binding of UPCDC30245 to p97, with a potential edge-to-face, weak π-π interaction between Phe^{618} and the indole ring. Consistent with these findings, recent functional studies show that substitutions at the 5-position of the indole ring (where the fluorine atom is attached) have profound effects on activity, with both steric and electronic factors being important (*14*). The interactions at the piperazine ring end are minimal, suggesting high conformational flexibility in this region, although the highly negatively charged outer surface of the binding tunnel (fig. S6A) may enable better anchoring to the surface of p97. Mutagenesis studies have shown that the D1-D2 interface is important for p97 function (*11*, *12*) and provide support for the structural studies we report here.

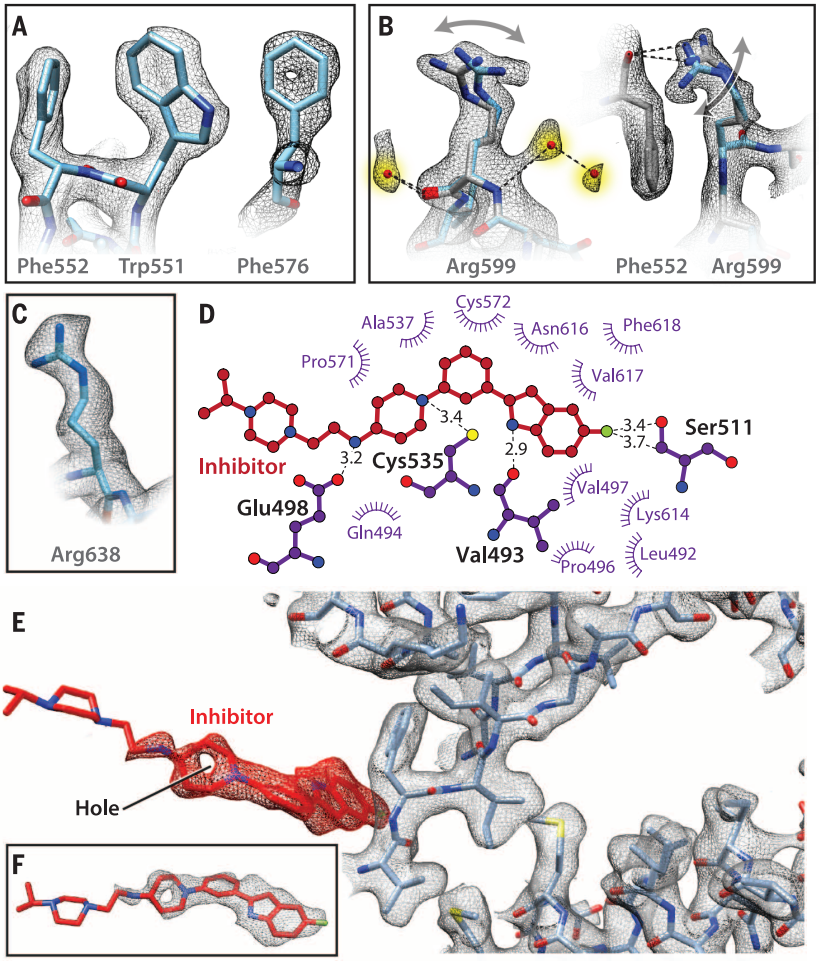


Fig. 2. Depiction of cryo-EM map quality and inhibitor interactions. (**A**) Illustration of hydrophobic packing between the aromatic side chains of Trp^{551} and Phe^{552}, and the presence of a hole in the aromatic ring of Phe^{576}. (**B**) Density for water molecules hydrogen-bonded to the Arg^{599} backbone and evidence for alternate conformations of the terminal guanidinium group, shown in orthogonal orientations. The main-chain oxygen atom of Phe^{552} shown in (A) is hydrogen-bonded to the Arg^{599} guanidinium moiety. (**C**) Density for Arg^{638}, part of the "arginine finger" motif at the outer surface of the D2 domain. (**D**) LIGPLOT representation showing residues in p97 that are in close proximity to the inhibitor, highlighting key H-bond interactions between the nitrogen on the indole ring and the backbone carbonyl oxygen atom of Val^{493} and side chain of Glu^{498} with the nitrogen atom in the linker of the inhibitor. The interaction between the fluorine atom present on the indole ring of the inhibitor and the main-chain carbonyl atom of Ser^{511} is also indicated. (**E** and **F**) Close-up view of the conformation of UPCDC30245 bound to p97 shown along with selected residues in its vicinity. There is strong density for the bound inhibitor for the segment encompassing the indole group to the piperidine ring and virtually no density at the other extremity, where the molecule is expected to be highly flexible because of minimal interactions with the protein.

To unravel the intra- and interprotomer conformational changes that occur with ATP binding, we performed structural analysis of p97 in the presence of ATPγS at physiologically relevant concentrations. Earlier crystallographic studies of p97 with ATP analogs revealed only modest structural changes (*16*), raising the concern that crystal packing constraints may have prevented capturing functionally relevant protein conformational changes. Cryo-EM methods have been applied previously to study p97 conformational changes; however, the resulting structures were at very low resolutions [~20 to 30 Å (*29*–*31*)] and did not result in definitive identification of the structural changes relative to the ADP-bound conformation. Here, we report separation of three well-defined, coexisting conformational states at near-atomic resolution (~3.2 to 3.3 Å) that are simultaneously populated when ATPγS is added to p97 (Fig. 3 and figs. S7 and S8). In conformation I, ADP is bound in both D1 and D2 nucleotide-binding domains; in conformation II, ADP is bound in the D1 domain while ATPγS is bound in the D2 domain; and in conformation III, ATPγS is bound in the nucleotide-binding regions of both D1 and D2.

The differences in structure among the three states reveal an unambiguous and stepwise evolution of the conformational change with binding of ATPγS (Fig. 3, A to C). Conformation II differs from I only at the D2 domain, while the N and D1 domains remain essentially unchanged (Fig. 3, D to F). The changes in the D2 domain occur largely proximal to the nucleotide-binding region and result from the exchange of the bound ADP with ATPγS, as verified by direct visualization of density for the additional phosphate moiety in the binding site (fig. S8). Within each protomer, there is a ~10° to 15° rotational twist of the D2 domain with respect to the D1 domain, with the D1-D2 linker region serving as a hinge. This relative rotational displacement of the D2 ring with respect to the D1 ring is consistent with atomic force microscopy studies that have reported ATP-dependent rotation in p97 (*32*).

The difference between conformation II and III is primarily in the N and D1 domains, with minimal changes in the D2 domain (Fig. 3, G to I). Here again, the change in conformation is directly associated with the exchange of ADP for ATPγS, with the density map demonstrating density for the additional phosphate moiety present in the D1 nucleotide-binding site (fig. S8). The most striking feature of this transition is the large-scale motion of the N domain away from the plane of the D1 hexamer. The structure of the N and D1 domains in conformation III is

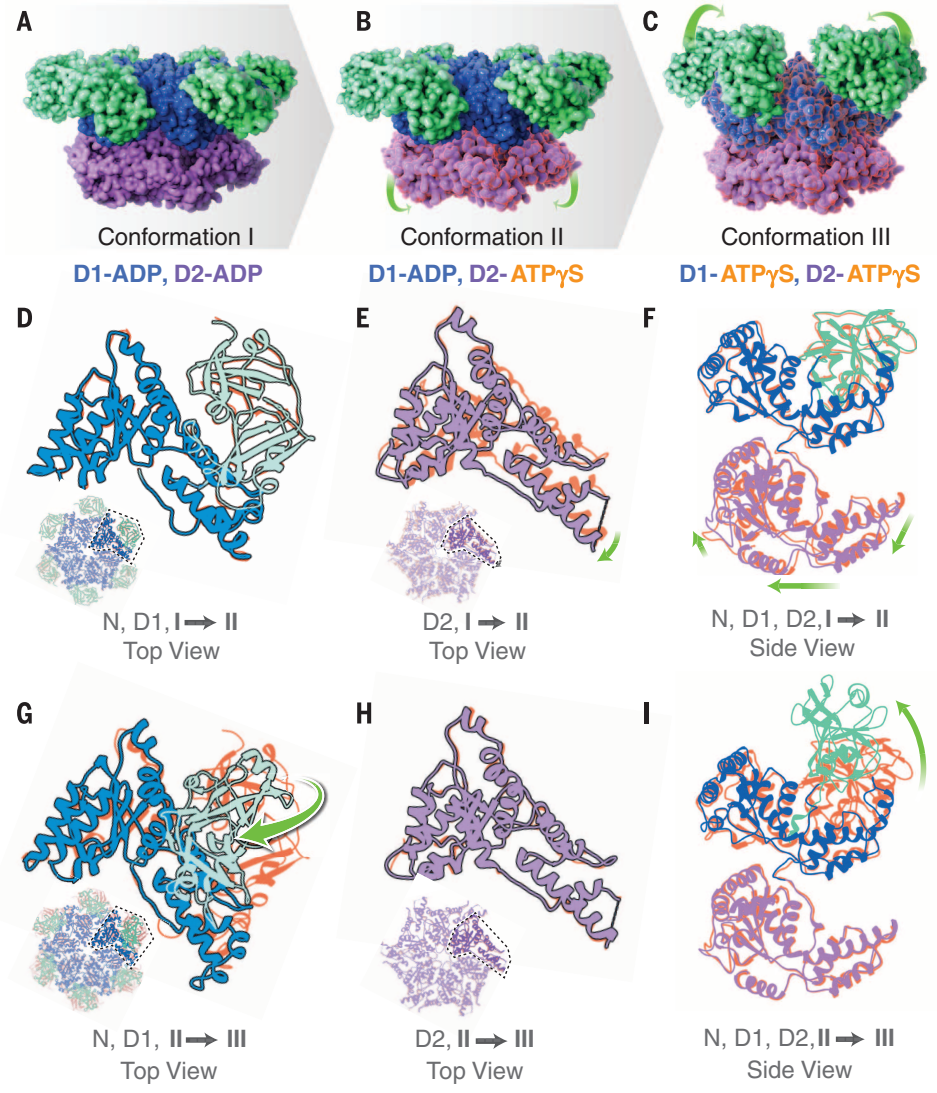


Fig. 3. Cryo-EM structures at ~3.3 Å, ~3.2 Å, and ~3.3 Å resolution, respectively, of three distinct p97 conformational states populated upon addition of ATPγS. (**A** to **C**) Side views of molecular surface models of the three states, color-coded to show the N, D1, and D2 domains in green, blue, and purple, respectively. The green arrows indicate the motion of the D2 domain in the transition from conformation I to II (B) and the motion of the N domain in the transition from conformation II to III (C). (**D** to **F**) Superposition of the polypeptide backbones of conformations I and II in ribbon representation to illustrate that the N and D1 domains display similar conformations but that there are substantial differences in the D2 domain, as indicated by the green arrows. The color scheme for conformation II is as in (A) to (C), with conformation I shown in orange. (**G** to **I**) Superposition of the polypeptide backbones of conformations II and III in ribbon representation to illustrate that the D2 domain is similar but that there are substantial differences in conformation of the N and D1 domains, as indicated by the green arrows. The color scheme for conformation III is as in (A) to (C), with conformation II now shown in orange. The insets in (D) and (G) show top views of the D1 domain; the insets in (E) and (H) show top views of the D2 domain, providing context for the superpositions shown in the main panels.

essentially the same as that reported from x-ray crystallographic analysis of an isolated N-D1 fragment derived from a mutant p97 (*33*). The changes include rearrangements at the peripheral helix in D1 and its interface with the D2 domain, and movement of the N domain from its original isoplanar or "down" position to an "up" position, where it is rotated by ~75° and displaced by ~14 Å. This out-of-plane conformation of the N-D1 domain and the double occupancy of both nucleotide-binding regions with ATPγS have not been reported in any of the full-length p97 structures solved by x-ray crystallography (*16*). Additionally, the presence of ATPγS in conformations II and III results in the stabilization of the C-terminal helix of the D2 domain and extension of the traceable density from residue 763 to residue 768 (fig. S8, G to I).

Our structural analyses thus show that the effect of ATPγS binding is a two-step, sequential conformational change in the D2 and D1 hexameric layers, respectively (Fig. 4A). Analysis of the images without imposition of six-fold symmetry shows that the majority of the molecules are in one of the three conformations obtained with the use of symmetry, indicating that the structural differences among conformations I, II, and III are cooperative in nature (fig. S9). The location of the inhibitor-binding site at the interface of domains D1 and D2 suggests that inhibitor binding prevents the nucleotide-driven conformational changes at the interface that are pivotal for p97 activity. To explore this further, we superimposed the structure of the p97-UPCDC30245 complex onto that of the ATPγS-bound p97 conformation II. The superposed models (Fig. 4B and fig. S8J) suggest that there would be steric clashes between the indole ring of the inhibitor and residues in the D2 loop (amino acid residues 611 to 616). Even if there is some flexibility in the D2 domain that enables some level of binding, key interactions that enable the binding of UPCDC30245 in the p97-ADP complex, such as that between the terminal fluorine atom and the backbone carbonyl Ser^{511} (Fig. 2D), cannot be achieved in the ATPγS-bound state. These observations indicate that UPCDC30245 is a conformation-selective inhibitor that preferentially binds the ADP state to act as a "wrench in the works."

The pivot-like movement of the D2 hexamer with ATPγS binding also affects pore dimensions (Fig. 4C). Thus, with ATPγS binding, the diameter of the cytoplasmic face of the pore in the center of the D2 hexamer (measured by the α carbon of residue 755 in the 750-760 helix) contracts from ~61 Å to ~54 Å (movie S2), whereas the average outer (~28 Å) and inner (~6 Å) diameters of D1 are similar in the three conformations. Many of the residues that line the central pore are negatively charged and could be important in the context of binding of ubiquitylated substrates. The cavity at the center is large enough to accommodate substrates destined for degradation, but given that the changes in size with nucleotide binding are relatively small, our results are consistent with the suggestion (*16*) that substrates degraded by p97 may not be threaded through the central axis across the length of the barrel.

The ability to determine atomic-resolution structures for multiple conformational states that are present simultaneously in a dynamic molecular machine such as p97 is likely to be an increasingly common signature of the application of cryo-EM methods in structural biology. p97 mediates its function in the cell by interacting with a large array of effector proteins, most of

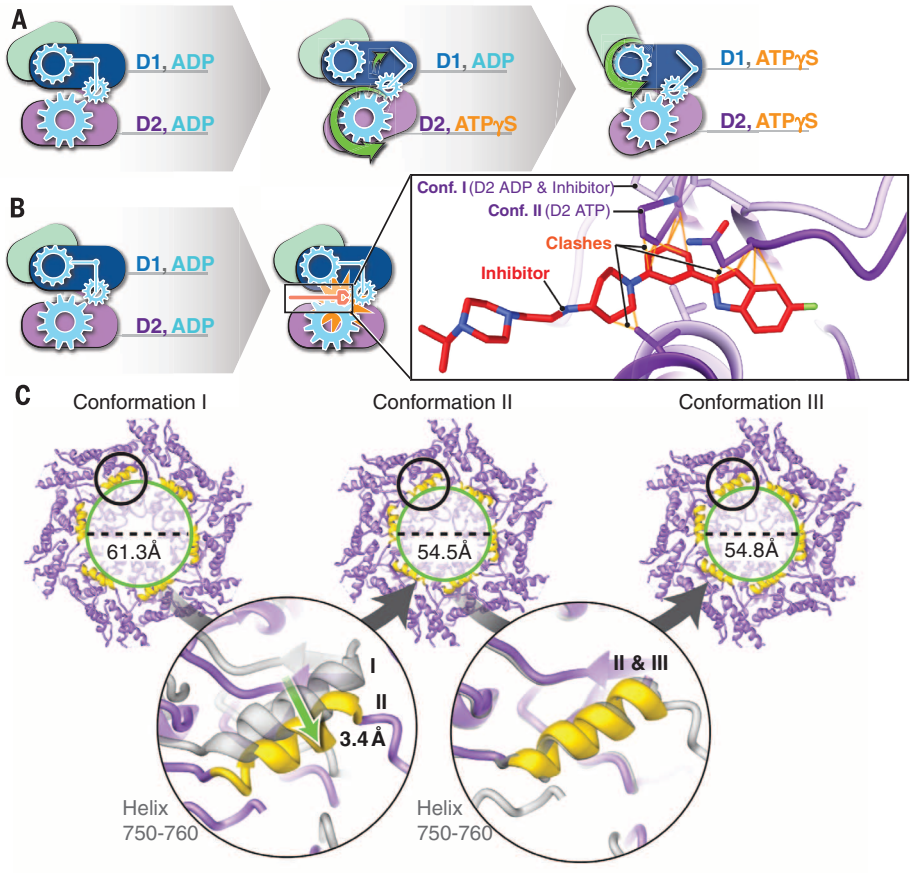


Fig. 4. Mechanism of ATP-driven conformational change. (**A**) Schematic of the two-step sequence involved in p97 activation resulting from the sequential binding of ATPγS first to D2 and then to D1, resulting in a large-scale movement of the N domain. (**B**) Close-up view of the location of the bound inhibitor when ADP is present in both D1 and D2 domains, indicating that there is a steric clash with the structure adopted by the D2 polypeptide upon ATPγS binding and that binding of the inhibitor blocks the conformational changes. The steric clashes between conformation II and the bound inhibitor are marked. (**C**) View of the D2 domain in the three conformational states, illustrating narrowing of the pore diameter (green circles) upon transition from conformation I to II, with minimal further changes upon transition to conformation III. The regions marked by the black circles are highlighted in magnified form in the lower part of the figure. They show views of the protein in the vicinity of residues 750 to 760 in one protomer and illustrate the extent of the helix movement in narrowing of the pore.

which bind at the N domain, which undergoes a large movement with ATP binding, as our present work and previous structural studies demonstrate (*5*, *18*, *34*–*36*). Cryo-EM studies could therefore be useful for a more detailed understanding of the structural basis of these interactions in normal cells and in diseases such as cancer. Further, the delineation of the inhibitor-bound p97 structure provides another example [besides β-galactosidase (*37*)] of a regulatory metabolic enzyme where cryo-EM at ~2 Å resolution enables visualization of structural detail such as hydrogen-bonded water molecules, with features comparable to those seen in model-based $2F_{obs} - F_{calc}$ maps at similar reported resolutions obtained using x-ray crystallography (fig. S10). The discovery of the specific mode of binding of a compound that blocks p97 activity provides new insights into the interactions and residues that are critical for function, and may enable the design of clinically useful inhibitors.

REFERENCES AND NOTES

1. P. I. Hanson, S. W. Whiteheart, *Nat. Rev. Mol. Cell Biol.* **6**, 519–529 (2005).
2. T. Ogura, A. J. Wilkinson, *Genes Cells* **6**, 575–597 (2001).
3. D. Barthelme, R. T. Sauer, *J. Mol. Biol.* 10.1016/j.jmb.2015.11.015 (2015).
4. M. Otter-Nilsson, R. Hendriks, E. I. Pecheur-Huet, D. Hoekstra, T. Nilsson, *EMBO J.* **18**, 2074–2083 (1999).
5. H. Meyer, C. C. Weihl, *J. Cell Sci.* **127**, 3877–3883 (2014).
6. D. Avci, M. K. Lemberg, *Trends Cell Biol.* **25**, 611–622 (2015).
7. L. Fang *et al.*, *Front. Cell. Neurosci.* **9**, 16 (2015).
8. R. J. Deshaies, *BMC Biol.* **12**, 94 (2014).
9. C. W. Valle *et al.*, *PLOS ONE* **6**, e29073 (2011).
10. T. F. Chou *et al.*, *Proc. Natl. Acad. Sci. U.S.A.* **108**, 4834–4839 (2011).
11. T. F. Chou, K. Li, K. J. Frankowski, F. J. Schoenen, R. J. Deshaies, *ChemMedChem* **8**, 297–312 (2013).
12. P. Magnaghi *et al.*, *Nat. Chem. Biol.* **9**, 548–556 (2013).
13. P. Polucci *et al.*, *J. Med. Chem.* **56**, 437–450 (2013).
14. C. Alverez *et al.*, *ACS Med. Chem. Lett.* **6**, 1225–1230 (2015).
15. D. J. Anderson *et al.*, "Inhibition of the AAA-ATPase p97 with the first in class inhibitor CB-5083 as a novel approach to treat cancer." Paper presented at the American Association for Cancer Research annual meeting, Philadelphia, 18 to 22 April 2015.
16. J. M. Davies, A. T. Brünger, W. I. Weis, *Structure* **16**, 715–726 (2008).
17. S. J. Kim *et al.*, *J. Biol. Chem.* **289**, 12264–12274 (2014).
18. P. Hänzelmann, A. Buchberger, H. Schindelin, *Structure* **19**, 833–843 (2011).
19. I. Dreveny *et al.*, *EMBO J.* **23**, 1030–1039 (2004).
20. W. K. Tang, D. Xia, *J. Biol. Chem.* **288**, 36624–36635 (2013).
21. E. Chapman, N. Maksim, F. de la Cruz, J. J. La Clair, *Molecules* **20**, 3027–3049 (2015).
22. C. J. Fang *et al.*, *ChemMedChem* **10**, 52–56 (2015).
23. T. F. Chou, R. J. Deshaies, *Autophagy* **7**, 1091–1092 (2011).
24. S. Tao *et al.*, *ACS Chem. Biol.* **10**, 1916–1924 (2015).
25. P. Yi *et al.*, *Mol. Cancer Ther.* **11**, 2610–2620 (2012).
26. S. J. Brown *et al.*, in *Probe Reports from the NIH Molecular Libraries Program* (National Center for Biotechnology Information, Bethesda, MD, 2010).
27. M. S. Chimenti *et al.*, *J. Biomol. Screen.* **20**, 788–800 (2015).
28. A. Kucukelbir, F. J. Sigworth, H. D. Tagare, *Nat. Methods* **11**, 63–65 (2014).
29. X. Zhang *et al.*, *Mol. Cell* **6**, 1473–1484 (2000).
30. H. Niwa *et al.*, *J. Biol. Chem.* **287**, 8561–8570 (2012).
31. H. O. Yeung *et al.*, *Open Biol* **4**, 130142 (2014).
32. K. Noi *et al.*, *Structure* **21**, 1992–2002 (2013).
33. W. K. Tang *et al.*, *EMBO J.* **29**, 2217–2229 (2010).
34. W. S. Chia, D. X. Chia, F. Rao, S. Bar Nun, S. Geifman Shochat, *PLOS ONE* **7**, e50490 (2012).
35. F. Beuron *et al.*, *EMBO J.* **25**, 1967–1976 (2006).
36. B. Almeida *et al.*, *Biochim. Biophys. Acta* **1852**, 1950–1959 (2015).
37. A. Bartesaghi *et al.*, *Science* **348**, 1147–1151 (2015).

ACKNOWLEDGMENTS

This research was supported by funds from the Center for Cancer Research, National Cancer Institute, and with federal funds from the National Cancer Institute under Chemical Biology Consortium Contract No. HHSN261200800001E Agreement No. 29XS127TO15. R.J.D. is an investigator of the Howard Hughes Medical Institute. This work used the computational resources of the NIH High-Performance Computing Biowulf cluster (http://hpc.nih.gov). We thank K. Moynihan, R. Mueller, and J. Cometa for technical assistance with electron microscopy; F. Ulmer, P. Mooney, and C. Booth for advice and assistance with optimizing K2 detector performance; and M. G. Laporte for contributions to the medicinal chemistry program. The University of Pittsburgh has filed a provisional patent application that covers the inhibitor compound described in this manuscript. R.J.D. is on the Scientific Advisory Board of Cleave Biosciences. The density maps and refined atomic models have been deposited in the Electron Microscopy Data Bank with accession numbers EMD-3295, 3296, 3297, 3298, and 3299, and in the Protein Data Bank with matching accession numbers of PDB-5FTJ, 5FTK, 5FTL, 5FTM, and 5FTN, respectively, for native p97 in the presence and absence of bound inhibitor, and for p97 conformational states I, II, and III observed in the presence of ATPγS.

SUPPLEMENTARY MATERIALS

www.sciencemag.org/content/351/6275/871/suppl/DC1
Materials and Methods
Figs. S1 to S10
Movies S1 and S2

3 November 2015; accepted 14 January 2016
Published online 28 January 2016
10.1126/science.aad7974

STRUCTURAL BIOLOGY

Structural basis of lipoprotein signal peptidase II action and inhibition by the antibiotic globomycin

Lutz Vogeley,[1]* Toufic El Arnaout,[1]* Jonathan Bailey,[1]* Phillip J. Stansfeld,[2] Coilin Boland,[1] Martin Caffrey[1]†

With functions that range from cell envelope structure to signal transduction and transport, lipoproteins constitute 2 to 3% of bacterial genomes and play critical roles in bacterial physiology, pathogenicity, and antibiotic resistance. Lipoproteins are synthesized with a signal peptide securing them to the cytoplasmic membrane with the lipoprotein domain in the periplasm or outside the cell. Posttranslational processing requires a signal peptidase II (LspA) that removes the signal peptide. Here, we report the crystal structure of LspA from *Pseudomonas aeruginosa* complexed with the antimicrobial globomycin at 2.8 angstrom resolution. Mutagenesis studies identify LspA as an aspartyl peptidase. In an example of molecular mimicry, globomycin appears to inhibit by acting as a noncleavable peptide that sterically blocks the active site. This structure should inform rational antibiotic drug discovery.

The threat of antibiotic resistance is recognized as a serious public health issue. Governments have introduced incentives to encourage work on anti-infectives by major drug makers in the face of a global rise in antimicrobial-resistant infections.

The enzymes involved in bacterial lipoprotein posttranslational processing (Fig. 1) are essential in many pathogenic bacteria and have no equivalents in humans, making them potential drug targets (*1*–*3*). LspA, as a key enzyme involved in the posttranslational processing of lipoproteins in *Pseudomonas aeruginosa*, an opportunistic human pathogen, is a target for antibiotic development (*1*, *4*). LspA does not have sequence homology to proteins of known structure. Globomycin, an antibiotic produced by select strains of *Streptomyces*, inhibits LspA (*1*). This cyclic depsipeptide (fig. S1) is an antimicrobial effective against Gram-negative bacteria. Synthetic analogs also inhibit the growth of Gram-positive bacteria, including methicillin-resistant *Staphylococcus aureus* (MRSA) (*5*).

P. aeruginosa has 175 lipoproteins, and presumably all are processed by LspA. The prolipoprotein substrates of LspA are cleaved at a four-residue consensus sequence (LAGC, $L^{-3}A^{-2}G^{-1}C^{+1}$) known as the lipobox that always ends with a cysteine, and the consensus allows for limited variability of the first three residues. In the prolipoprotein form, the cysteine is in thioether linkage to diacylglycerol (DAG). We refer to the dagylated cysteine as Cys*. The prolipoproteins consist of an N-terminal signal peptide that includes the first three residues of the lipobox and a C-terminal lipoprotein starting with the lipobox cysteine.

We sought to obtain a crystal structure of LspA so as to gain insights into its substrate binding and catalytic mechanisms. We conducted crystallization trials using recombinant LspA from *P. aeruginosa* (strain PAO1) expressed in *Escherichia coli*. Affinity and size-exclusion chromatography provided material of high purity (fig. S2) (*6*). LspA was crystallized by means of the in meso (lipid cubic phase) method (*7*) in the presence of globomycin (fig. S2). A structure of the complex was obtained at a resolution of 2.8 Å by using seleno-methionine, single-wavelength anomalous diffraction phasing (Fig. 2). The seleno-methionine derivative was produced through in vivo and cell-free expression.

LspA is a small protein consisting of 169 amino acids (*4*). It is a monomer in the crystal. Structurally, the protein can be broken down into two domains, each assembled from secondary structure elements from discontinuous stretches of the protein chain (Fig. 2). The first consists of four transmembrane helices (MH1-4), with the N- and C-termini in the cytoplasm. The second is the periplasmic domain, which has two subdomains. The bigger of the two is a four-stranded, amphiphilic β-sheet that rests on the membrane. The sheet has the appearance of a cupped hand or cradle (β-cradle) that extends away from the helical core of the protein. Its hydrophobic surface is in contact with the membrane, whereas its polar surface faces the periplasm. The second

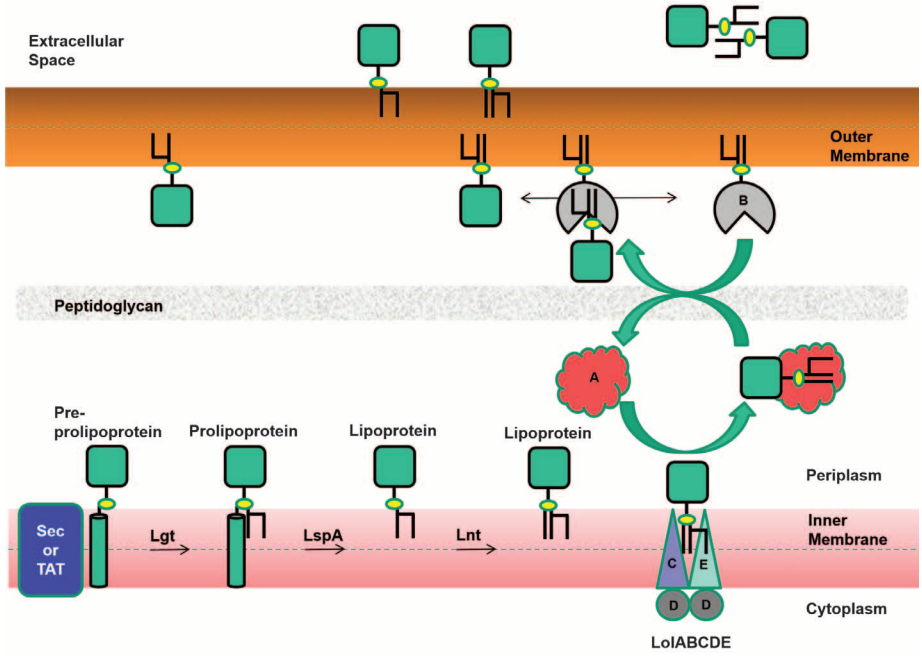


Fig. 1. Posttranslational processing leading to lipoprotein maturation in Gram-negative bacteria. Lipoproteins are synthesized as preprolipoprotein precursors via the Sec or TAT pathways, with an N-terminal signal peptide (green cylinder) securing them to the cytoplasmic membrane and the lipoprotein domain (green square) in the periplasm. Posttranslational processing requires, at a minimum, the sequential action of lipoprotein diacylglycerol transferase (Lgt) to lipid modify with a diacylglycerol and signal peptidase II (LspA) to remove the signal peptide. For some lipoproteins, the lipoprotein N-acyl transferase (Lnt) is required to N-acylate the N-terminal cysteine of the lipoprotein. LspA cuts in the lipobox, a consensus sequence of form LAGC* in which C* (yellow oval) has been dagylated by Lgt, to the amino side of the C*. Trafficking to the outer membrane uses the lipoprotein outer-membrane localization (Lol) pathway that involves the ABC transporter (LolCDE), a carrier chaperone (LolA), and a receptor (LolB), itself a lipoprotein. Lipoproteins reside mostly on the outer leaflet of the inner membrane and on the inner leaflet of the outer membrane facing into the periplasm. Some are located facing and in the extracellular space.

[1]School of Medicine and School of Biochemistry and Immunology, Trinity College Dublin, Dublin, Ireland. [2]Department of Biochemistry, University of Oxford, South Parks Road, Oxford, UK.
*These authors contributed equally to this work. †Corresponding author. E-mail: martin.caffrey@tcd.ie

Downloaded from on February 18, 2016

subdomain consists of a long loop with a single helical turn, the periplasmic helix (PH). The PH also sits on the membrane, with the long axis of the periplasmic PH loop orthogonal to that of the β-cradle.

Globomycin was modeled into a distinctive, donut-shaped region of electron density between MH2, MH3, and MH4 on the periplasmic side of the membrane (Fig. 2D). The ligand density allowed unambiguous placement and orientation of the entire globomycin molecule, a 19-member cyclic depsipeptide that includes an α-methyl–β–hydroxy fatty acid, *N*-methyl-L-Leu (g·Leu), L-*allo*-Ile (g·Ile), L-Ser (g·Ser), L-*allo*-Thr (g·Thr), and Gly (g·Gly) (fig. S1A) (*5*). Globomycin is amphiphilic, with g·Ser and g·Thr comprising the polar half while the hydroxy fatty acid, g·Leu, and g·Ile make up the apolar half. As expected, the apolar half of globomycin extends into the membrane, and its polar end faces the interface. In the unbound state, molecular dynamics simulations (MDS) show globomycin partitions into the membrane oriented essentially as it is in the complex (fig. S3). The PH loop sits over and blocks direct access from the periplasm to the active site, suggesting that globomycin first partitions into the membrane and then diffuses laterally into the active site to inhibit the enzyme. Conserved residues decorate the globomycin-binding pocket (Fig. 3A), a region that has been implicated in peptidase activity.

Globomycin is firmly anchored to LspA by hydrogen bonds and hydrophobic interactions (Fig. 3A and fig. S4). The most notable hydrogen bond is that between the β-hydroxy of g·Ser and the carboxyl of Asp^{143}, tentatively identified as one of the catalytic dyad aspartates (*8*). In MDS, this interaction persists throughout the 500 ns simulation. The backbone carbonyls of g·Leu, g·Ile, and g·Ser, to one side of the globomycin ring, face the protein and hydrogen bond with the side chains of strictly conserved Asn^{112} and Arg^{116}. The side chain of g·Leu, as well as the acyl chain of the hydroxy fatty acid, have extensive hydrophobic interactions with apolar residues in the protein (Fig. 2D). These are particularly well developed in the case of the fatty acid, which is in close contact with the membrane-exposed surface of the PH and with residues on MH2. MDS confirms these interactions (fig. S4).

We investigated LspA by means of MDS in the complex and apo forms. In both, the enzyme was stable in a palmitoyloleoylphosphatidylethanolamine (POPE): palmitoyloleoylphosphatidylglycerol (POPG) membrane through the 500 ns simulation (movies S1 and S2). In the apo form, simulations showed a minor rearrangement of the active site, with a network of hydrogen bonds emerging that involve Asn^{54}, Asp^{124}, Asn^{140}, Asp^{143}, and Asn^{112}, all of which are strictly conserved residues. In addition, there was enhanced flexibility of the PH loop, which moved laterally at the interface while remaining anchored to the membrane by highly conserved Phe^{59} and Phe^{61}.

If globomycin in the complex indicates the active site in LspA, an examination of this part of the protein immediately suggests how the prolipoprotein substrate orients itself for binding and Michaelis complex formation. The signal peptide helix of the prolipoprotein is the right size and shape to slot into the space between MH2 and MH4 of LspA (Fig. 3B). Upon signal peptide helix binding, the lipobox of the substrate would sit in the active site similar to the g·Leu–g·Ile–g·Ser tripeptide of globomycin (Fig. 3C) in the complex structure. The Cys* of the lipobox would now reside further up in the active site, positioning the lipoprotein in the periplasm (Fig. 3B). With this alignment, the scissile Gly-Cys* bond is extended and positioned between the carboxyls of the proposed catalytic residues, Asp^{124} and Asp^{143}. The DAG modification on Cys*, with its long hydrophobic chains, must remain anchored in the membrane. An indication as to where its glycerol head group and one of the acyl chains might reside comes from a lobe of electron density modeled in the complex structure as a monoacylglycerol (MAG, the host lipid used for crystallization), which sits to one side of the active site in a groove between MH4 and the β-cradle (fig. S5). Although host lipid density, at 2.8 Å resolution, is often poorly and incompletely defined, density for the active-site lipid is clearly present in all four molecules of the asymmetric unit extending to C7 or C8 of the MAG acyl chain in omit maps. We suggest that one of the DAG acyl chains of the prolipoprotein substrate occupies a similar position on LspA, helping position and orient the scissile bond in the active site. The above model for how the prolipoprotein substrate interacts with LspA is supported by MDS (Fig. 3B and movie S3).

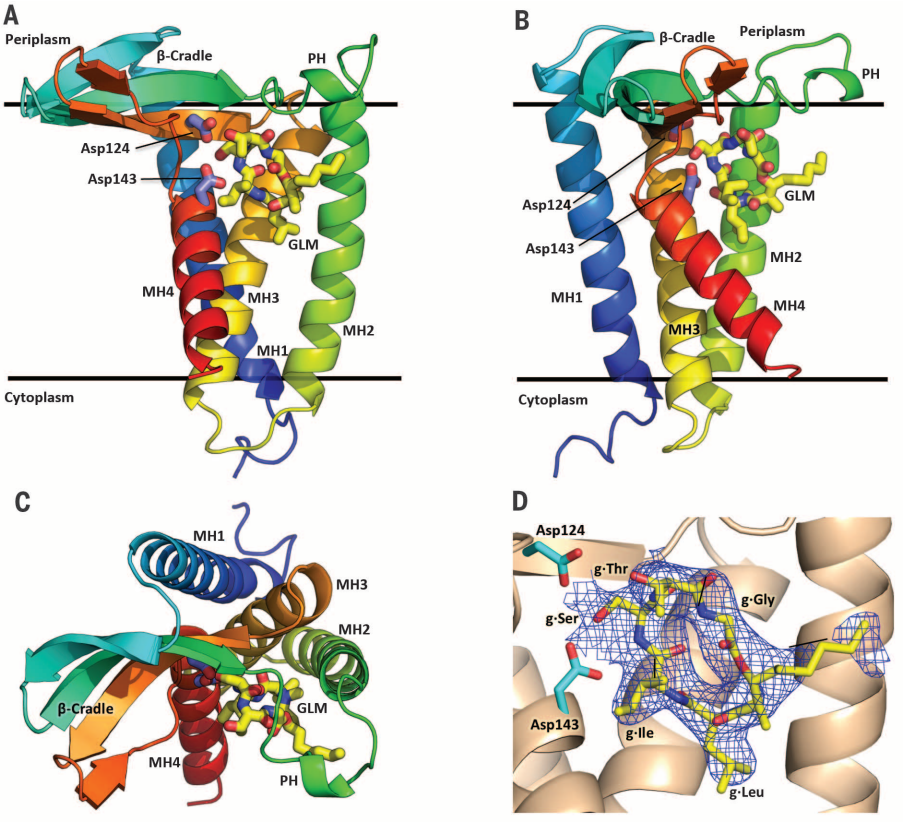


Fig. 2. LspA-globomycin complex structure. (**A**) Illustration of LspA viewed from within the membrane, with the membrane interface shown as horizontal lines and globomycin as a stick figure (yellow carbons). Transmembrane helices are labeled MH1 to MH4. The β-stranded cradle (labeled) at the membrane interface is poised to accommodate the soluble domain of the prolipoprotein substrate and lipoprotein product. The C-terminal "strand" of the β-cradle leading into the proposed active site is interrupted by conserved Pro^{137} and does not conform to standard β-sheet hydrogen-bonding patterns. (**B**) As in (A), rotated by ~60°. (**C**) As in (A), viewed from the periplasm. (**D**) 2Fo-Fc simulated-annealing composite OMIT map contoured at 1σ and carved at 2.3 Å around globomycin. Proposed catalytic aspartates, Asp^{124} and Asp^{143}, are shown on either side of the β-hydroxyl of globomycin serine (g·Ser). Globomycin and catalytic aspartates are shown in stick representation with yellow and dark blue [(A) to (C)] or light blue (D) carbons, respectively.

Residues 56 to 62, which include the PH, are highly conserved. This stretch of protein sits on the surface of the membrane directly over the active site (Fig. 2) and constrains extension of the substrate from the active site to the periplasm to a deep cleft between the β-cradle and PH loop subdomains. In this model, the Cys* of the substrate is clamped between the β-cradle and the PH loop, with the dipole of the PH aligned with the carbonyl oxygen of Cys* (Fig. 3B).

Despite lacking the consensus Asp-Thr-Gly sequence of aspartyl proteases (*9*), LspA has been tentatively identified as an aspartyl endopeptidase (*8*). In the absence of evidence to the contrary, we assume here that the catalytic mechanism is as described for other aspartyl proteases (*9*). Accordingly, we envision Michaelis complex formation involving a conjunction in the active site of two aspartates, a catalytic water and the scissile bond. Using globomycin to demark the active site, two aspartate residues, Asp^{124} and Asp^{143}, with suitably poised side chain carboxyls are apparent in the structure that, in all likelihood, represents the catalytic dyad (Figs. 2 and 3). We propose therefore that these aspartates play a general acid-base role, with the one closest to the proposed water [not seen in the complex but apparent in MDS (movie S4)] being charged and abstracting a proton from it, creating a nucleophile (fig. S1C). The nucleophile attacks the carbonyl carbon of the scissile bond, forming a tetrahedral intermediate. Protonation of the amide nitrogen in the scissile bond and rearrangement causes the tetrahedral intermediate to collapse and hydrolysis products to form. Separation of the substrate's binding moieties by means of proteolysis would logically result in a sharply lower binding affinity of the two reaction products as compared with substrate. The lipoprotein product is anchored in the membrane only by the DAG chains of its C-terminal Cys* and should readily diffuse out of the active site, resetting LspA for another round of catalysis. When it occurs, further processing of the signal peptide and lipoprotein products of the LspA reaction involves signal peptide peptidases and N-acylation by lipoprotein N-acyl transferase (Lnt), respectively (Fig. 1).

Many aspartyl proteases are important drug targets. The hypertension regulator renin (*10*, *11*) and HIV protease (*9*, *12*) are examples. Of the thousands of inhibitors designed to target aspartyl proteases, most contain a noncleavable core structure of the hydroxyethylene or hydroxyethylamine type designed to recapitulate the tetrahedral intermediate in the proteolytic reaction (fig. S2B) (*9*). For those that have been crystallized bound to target proteases, the hydroxyl group sits between and is within hydrogen bonding distance of the two catalytic aspartates. Strikingly, the hydroxyethylamide of g·Ser in globomycin incorporates elements of a noncleavable transition-state isostere (fig. S1). In the complex, the hydroxyl group of g·Ser nestles between and hydrogen bonds with the two catalytic aspartates, Asp^{124} and Asp^{143} (Fig. 3C). This suggests that part of the globomycin molecule likewise mimics a noncleavable transition state analog (fig. S1) and that the antibiotic is a competitive inhibitor of LspA. Further mimicking other features of the prolipoprotein substrate, globomycin contains the peptide backbone and side chains corresponding to the P^{-3}, P^{-2}, and P^{-1} sites relative to the scissile bond in the lipobox. As noted, this feature of globomycin has been used to model a convincing lipobox and prolipoprotein into the substrate binding and active sites of LspA (Fig. 3, B and C). The prolipoprotein model has been exploited successfully in MDS (Fig. 3B and movie S3).

An analysis of deduced amino acid sequences of LspAs from 485 organisms having between 35 and 95% sequence identity with the signal peptidase II of PAO1 identified 14 strictly conserved residues (D23, K27, N54, G56, G108, A109, N112, R116, V122, D124, F139, N140, A142, D143). (Single-letter abbreviations for the amino acid residues are as follows: A, Ala; C, Cys; D, Asp; E, Glu; F, Phe; G, Gly; H, His; I, Ile; K, Lys; L, Leu; M, Met; N, Asn; P, Pro; Q, Gln; R, Arg; S, Ser; T, Thr; V, Val; W, Trp; and Y, Tyr.) The bulk of these map onto the proposed binding and active sites in the LspA

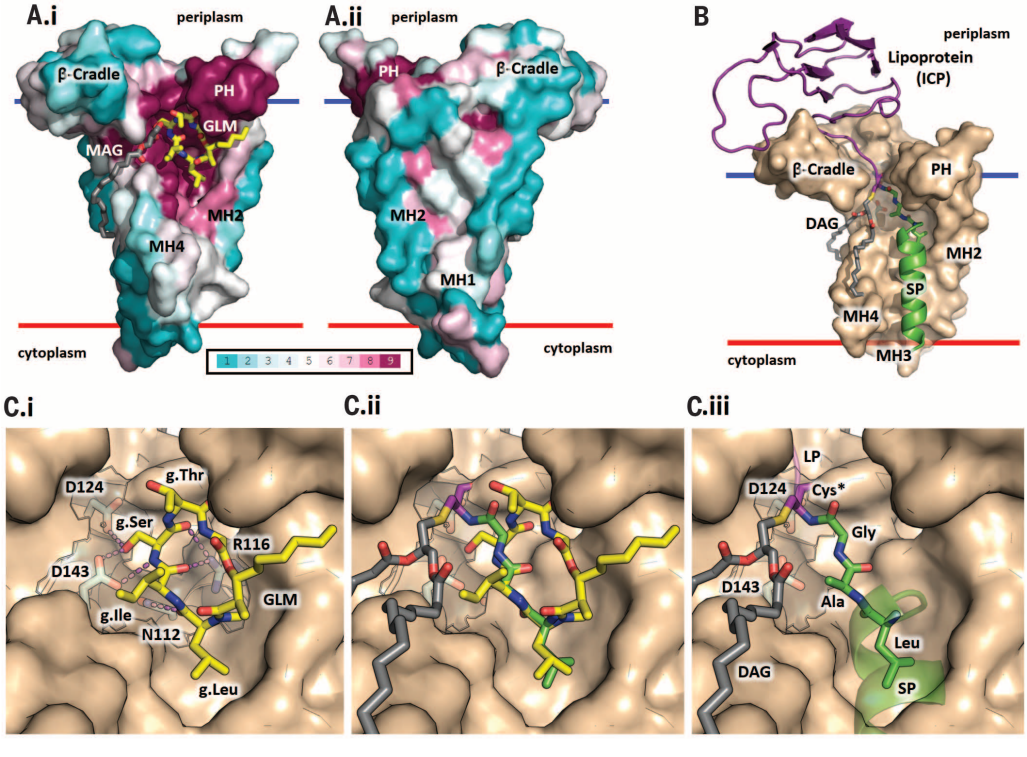


Fig. 3. Conserved residues in and globomycin and prolipoprotein binding to LspA. (**A**) Conserved residue surface representation of LspA based on an analysis of 485 orthologs with 35 to 95% sequence identity with *P. aeruginosa* (PAO1) LspA by using the ConSurf server (*15*). (i) View into the globomycin binding site. (ii) As in (i), rotated by 180°. LspA in surface representation is colored by conservation value; light blue, white, and purple correspond to low, average, and high conservation, respectively (*15*). Residue conservation values are reported in the supplementary materials (database S1). Globomycin and MAG are indicated as sticks with yellow and gray carbons, respectively. (**B**) Model of the prolipoprotein proICP from *P. aeruginosa* docked into LspA. The signal peptide helix (SP, green) docks into the pocket created by MH2, MH3, and MH4. The lipobox cysteine, Cys* (sulfur; yellow), is dagylated (gray sticks), and the lipoprotein (purple) extends across the β-cradle into the periplasm. The complex, as shown, is stable in MDS, especially in the region of the signal peptide helix and the lipobox. Full details of docking and simulations are available in the suppplementary materials, materials and methods. Catalytic dyad Asp^{143} is shown as transparent sticks, with light blue carbons. (**C**) The g·Leu–g·Ile–g·Ser tripeptide of globomycin mimics the first three residues in the substrate's conserved Leu-Ala-Gly-Cys lipobox tetrapeptide. (i) Globomycin (yellow carbons) alone in the binding pocket of LspA with its g·Leu–g·Ile–g·Ser tripeptide clearly visible. (ii) As in (i), with the dagylated lipobox tetrapeptide from proICP (green carbons) aligned with and superposed on the globomycin tripeptide backbone. (iii) As in (ii), with globomycin omitted and the signal peptide (SP; green) and lipoprotein (LP; purple) extensions to the lipobox tetrapeptide in place. In the interests of clarity, (ii) has been left unlabeled.

complex (Fig. 3A). This lends credence to the location of both sites in the protein as identified in the complex structure. All strictly conserved polar residues are involved in a hydrogen-bonded network extending into the membrane between the two periplasmic subdomains (fig. S6), which serves multiple purposes. It provides structural integrity and definition to the active and binding sites. At the same time, it positions and orients active-site residues optimally for K_a modulation (where K_a is the acid dissociation constant) and catalysis. Such a hydrogen-bonded network of polar residues facilitates access to the active site for catalytic water molecules from the periplasm, which was confirmed with MDS (movie S4).

Mutagenesis studies performed on LspA from *Bacillus subtilis* identified six amino acids—corresponding to Asp^{23}, Asn^{112}, Asp^{115}, Asn^{140}, Ala^{142}, and Asp^{143} in *P. aeruginosa*—as being important for activity (*8*). Only Asp^{23} was required for stability, suggesting that the other five residues were needed for catalysis, active-site geometry, or the recognition of prolipoproteins (*8*). Four of the five residues map onto the proposed active site in the LspA-globomycin complex in ways that make sense. However, Asp^{115} is a highly conserved residue on the periplasmic end of MH3 (fig. S6). It coordinates with conserved Lys^{27}, which interacts indirectly with catalytic Asp^{143} via conserved Asn^{112}. Mutating Asp^{115} to Ala inhibited peptidase activity in the Tjalsma *et al.* study (*8*), and Asp^{115} and Asp^{143} were therefore proposed to form the catalytic dyad. In light of the current structure, this is unlikely. We conclude that the catalytic dyad is Asp^{124} and Asp^{143}. Both are strictly conserved and suitably disposed for proteolysis.

To test this hypothesis, we analyzed peptidase activity of LspA by means of SDS–polyacrylamide gel electrophoresis (SDS-PAGE), with the dagylated form of the preprolipoprotein inhibitor of cysteine peptidase (ICP) (*13*) as substrate (Fig. 4). Dagylation was effected through the action of Lgt on ICP with dioleoylphosphatidylglycerol (DOPG) as lipid substrate. The undagylated preprolipoprotein was not an LspA substrate (fig. S7C). Under standard assay conditions, wild-type LspA activity was evident by the appearance of bands corresponding to the dagylated lipoprotein (13 kDa) and the signal peptide (4 kDa). Asp^{124}Asn and Asp^{143}Asn mutants were devoid of activity, which is consistent with the hypothesis that Asp^{124} and Asp^{143} are the catalytic dyad residues (Fig. 4, G and H). In contrast, the Asp^{115}Ala and Asp^{115}Asn mutants had small and significant activities, respectively, suggesting that this residue is functionally important but not catalytic. MDS revealed transient interactions involving Asp^{115} not seen in the crystal structure and provide a plausible explanation for how these two mutations

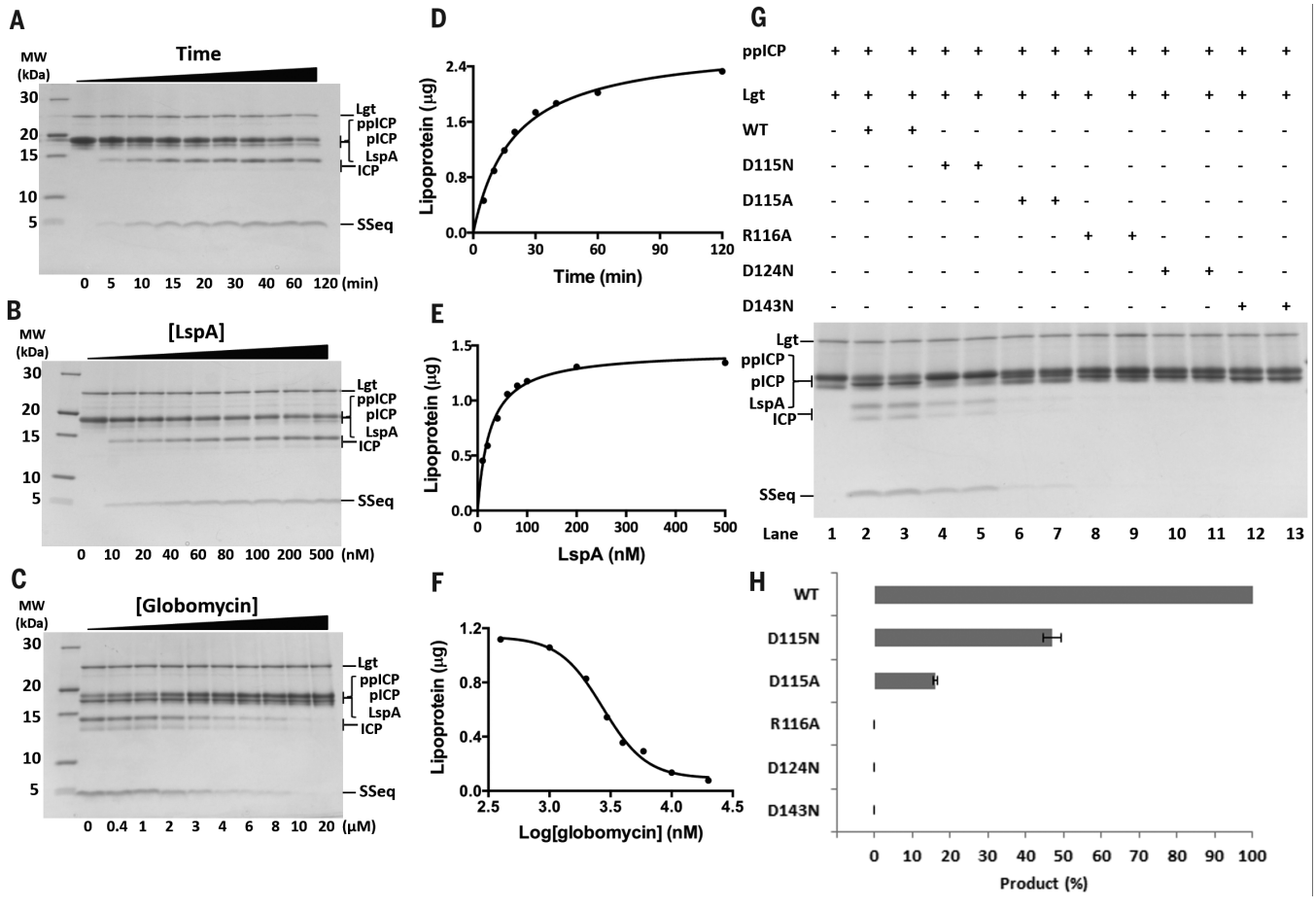


Fig. 4. Endopeptidase activity of LspA with the substrate prolipoprotein, generated in situ, based on the preprolipoprotein ICP. (**A**) Reaction time course. (**B**) Dependence on LspA concentration. (**C**) Inhibition by globomycin. (**D** to **F**) Quantitative representation of the data in (A), (B), and (C), respectively, based on SDS-PAGE gel image analysis. Lines are drawn to guide the eye. (**G**) Effect of single-site mutations in LspA. A schematic to aid in the interpretation of the SDS-PAGE data is presented in fig. S7A. (**H**) Quantitative representation of the data in (G) based on gel image analysis. Assays were performed by using proICP (pICP) generated in situ by the DOPG-dependent dagylation of pre-proICP (ppICP) catalyzed by Lgt (suppplementary materials, materials and methods). The Lgt substrate pre-proICP appears as two closely spaced bands (ppICP and ppICP') (fig. S7A), with the higher-molecular-weight band the stronger of the two [best seen in (G)]. The relative intensities of the two bands vary from prep to prep, which is apparent in (A) to (C) and (G). The LspA product ICP also runs as a pair of bands (ICP and ICP') (fig. S7A). It is the integrated intensity of the well-resolved ICP band that is quantified on the gel by using ImageJ and reported in (D) to (F) and (H). The mobility of LspA is very similar to that of ppICP'. The mobility of the LspA mutants differs slightly from that of the wild-type enzyme, which (G) makes them visible on the gel to varying degrees, depending on the mutant (fig. S7B).

compromise catalysis to different degrees (movie S5). The Arg^{116}Ala mutant was inactive, as expected given Arg^{116}'s interaction with globomycin and its proposed role in orienting the lipobox backbone of the peptide substrate in the active site. Globomycin inhibited the enzyme (Fig. 4C).

Synthetic analogs of globomycin have been tested for efficacy against a number of bacterial species as part of a structure-activity relationship study (*7*). The most effective congeners, which were 10 times more potent than globomycin, were modifications in which the fatty acyl chain was lengthened. This finding makes sense in light of the complex structure in which a longer chain would provide for more extensive interactions with the apolar surface of MH2 (Fig. 2). The hydroxyl group in g.Ser was shown to be essential for globomycin inhibitory activity, which agrees with this residue's proposed role in sterically blocking the active site.

P. aeruginosa has 175 different lipoproteins (*4*). Their signal peptide and lipoprotein parts differ greatly in size, sequence, and structure, and of the four residues in the lipobox consensus sequence, only the cysteine is strictly conserved. A feature common to all prolipoproteins is the dagylated lipobox cysteine in which the lipoprotein, the signal peptide, and the DAG modification converge (Fig. 3B). The LspA structure reported here has grooves and clefts radiating about the active site with remarkable shape complementarity to this trigonal feature of the prolipoprotein substrate (fig. S8). Upon docking, the scissile bond of the substrate sits in the active site of the enzyme poised for cleavage. Thus, although LspA is highly specific in terms of the proteolytic reaction it catalyzes, its impressive array of diverse substrates can be explained by a shape complementarity around the scissile bond likely shared by all prolipoproteins.

The complex structure reported here can be used to inform the design of globomycin analogs with improved binding, efficacy, selectivity, and pharmacokinetic properties. As an alternative, because LspA is an aspartyl endopeptidase, it is a suitable target with which to explore the thousands of inhibitors developed for other medically relevant aspartyl proteases (*9*, *12*). Although the sequence identity of LspA from *P. aeruginosa* and MRSA is only 32%, the majority of active-site residues are conserved. MDS of both the apo and globomycin-bound homology models of MRSA LspA show remarkable stability and fidelity to the observed dynamics of the crystal structure of *P. aeruginosa* LspA (fig. S9). Together with the crystal structure presented here, these homology models should also prove useful for the design and discovery of antibiotics targeting Gram-positive as well as Gram-negative bacteria.

Conserved residues in LspA surround the proposed active site where globomycin binds. They are networked to such a degree (fig. S6) that mutations interfering with antibiotic binding there would likely also impair how the enzyme binds and cleaves substrate. Because antibiotics that do not elicit resistance are invaluable medically (*14*), lessons in effective drug design might be learned from the Actinomycetes, microbes that may well have achieved this in globomycin.

REFERENCES AND NOTES

1. H. Remaut, R. Fronzes, Eds., in *Bacterial Membranes: Structural and Molecular Biology* (Caister Academic Press, 2014), pp. 55–179.
2. W. R. Zückert, *Biochim. Biophys. Acta* **1843**, 1509–1516 (2014).
3. N. Buddelmeijer, *FEMS Microbiol. Rev.* **39**, 246–261 (2015).
4. K. Remans, K. Vercammen, J. Bodilis, P. Cornelis, *Microbiology* **156**, 2597–2607 (2010).
5. T. Kiho *et al*., *Bioorg. Med. Chem.* **12**, 337–361 (2004).
6. T. El Arnaout, thesis, Trinity College Dublin (2013).
7. M. Caffrey, V. Cherezov, *Nat. Protoc.* **4**, 706–731 (2009).
8. H. Tjalsma, G. Zanen, G. Venema, S. Bron, J. M. van Dijl, *J. Biol. Chem.* **274**, 28191–28197 (1999).
9. A. Brik, C. H. Wong, *Org. Biomol. Chem.* **1**, 5–14 (2003).
10. W. J. Greenlee, P. K. S. Siegl, *Annu. Rep. Med. Chem.* **27**, 59–68 (1992).
11. S. S. Abdel-Meguid, *Med. Res. Rev.* **13**, 731–778 (1993).
12. A. Das *et al*., *J. Am. Chem. Soc.* **132**, 6366–6373 (2010).
13. Y. Fu, thesis, University of Glasgow (2009).
14. K. Lewis, *Nat. Rev. Drug Discov.* **12**, 371–387 (2013).
15. M. Landau *et al*., *Nucleic Acids Res.* **33**, W299–W302 (2005).

ACKNOWLEDGMENTS

We thank past and present members (D. Aragão, D. Doyle, A. Haffner, N. Howe, C-Y. Huang, J. Lyons, P. Ma, V. Pye, D. Weichert, and M. Wiktor) of the Membrane Structural and Functional Biology group for their assorted contributions to this study. The assistance and support of beamline scientists at the Swiss Light Source (PXII), Diamond Light Source (I24), and the Advanced Photon Source (23-ID) are acknowledged. The work was funded by Science Foundation Ireland grant 12/IA/1255. P.J.S. is supported by Biotechnology and Biological Sciences Research Council grant BB/I019855/1. All MDS were performed by using the Irish Centre for High-End Computing (ICHEC) facilities. Atomic coordinates and structure factors for the LspA-globomycin complex are deposited in the Protein Data Bank under accession code 5DIR. Correspondence and requests for materials should be addressed to M.C.

SUPPLEMENTARY MATERIALS

www.sciencemag.org/content/351/6275/876/suppl/DC1
Materials and Methods
Supplementary Text
Figs. S1 to S9
References (*16*–*34*)
Movies S1 to S5
Database S1

22 September 2015; accepted 12 January 2016
10.1126/science.aad3747



What if you could...

- use up to **44% less plastic** for your nucleic acid purification*
- **recycle ALL** of your packaging and plastics
- AND, still recover the same **highly pure DNA**?

Now, you can.

NEW ENGLAND BioLabs® Inc.

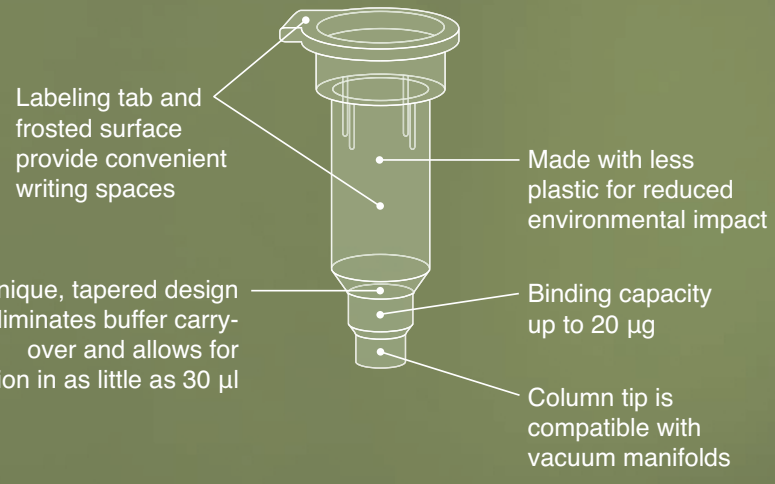
It's time for change.

Introducing Monarch™ Nucleic Acid Purification Kits

It's time to transform your DNA purification experience. NEB's Monarch Nucleic Acid Purification Kits are optimized for maximum performance and minimal environmental impact. With an innovative column design, buffer retention is prevented, eliminating risk of carryover contamination and enabling elution in smaller volumes. The result – highly pure DNA for your downstream applications.

Make the change and migrate to Monarch today.

Optimized design of Monarch Miniprep Columns



Request your free sample at **NEBMonarch.com**

NEW ENGLAND BIOLABS® and NEB® are registered trademarks of New England Biolabs, Inc.
MONARCH™ is a trademark of New England Biolabs, Inc.
*Visit NEBMonarchPackaging.com for details.

Science
AAAS



DATA STORIES

Wow us with the stunning discoveries and probing insights you can bring to life with data visualization.

Submit your short-form video entries to **sciencemag.org/datastories**

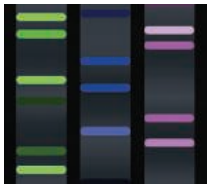
ACCEPTING SUBMISSIONS

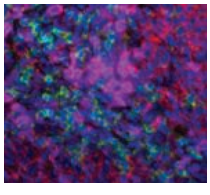
March 7 – April 15, 2016

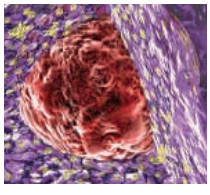
want new technologies?

antibodies
apoptosis
biomarkers
cancer
cytometry
data
diseases
DNA
epigenetics
genomics
immunotherapies
medicine
microbiomics
microfluidics
microscopy
neuroscience
proteomics
sequencing
toxicology
transcriptomics









watch our webinars

Learn about the latest breakthroughs, new technologies, and ground-breaking research in a variety of fields. Our expert speakers explain their quality research to you and answer questions submitted by live viewers.

VIEW NOW!
webinar.sciencemag.org

Science
AAAS

Brought to you by the *Science*/AAAS Custom Publishing Office

@SciMagWebinars

AAAS *Travels*



MONGOLIA
June 30–July 13, 2016

Explore Mongolia, "**Land of the Blue Sky**" with Chris Carpenter! See vast landscapes from the Gobi Desert to the granite mountains of Khogno Khan Nat'l. Park. Enjoy the renowned Nadaam Festival in Karakorum, once the capital of the Mongolia Empire, and visit Okhon Valley World Heritage Site. Look for wild horses at Hustai Nat'l. Park. $3,995 + air.

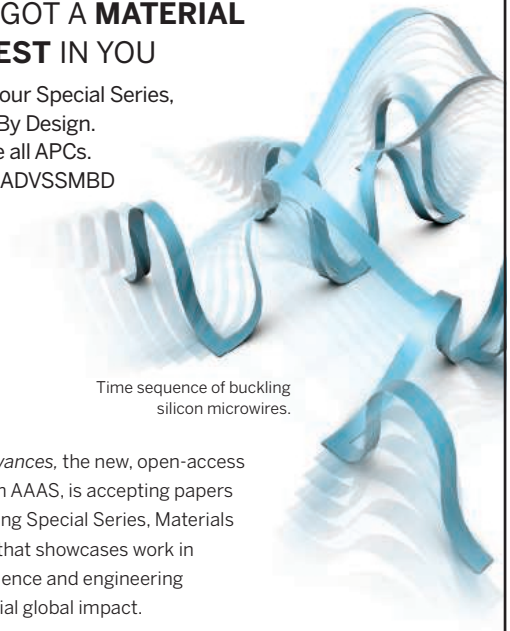
For a detailed brochure, call (800) 252-4910
All prices are per person twin share + air

BETCHART EXPEDITIONS Inc.
17050 Montebello Rd, Cupertino, CA 95014
Email: AAASInfo@betchartexpeditions.com
www.betchartexpeditions.com

CALL FOR PAPERS! MANUSCRIPTS DUE MAY 1, 2016.

WE'VE GOT A **MATERIAL INTEREST** IN YOU

Publish in our Special Series, Materials By Design.
We'll waive all APCs.
Use code: ADVSSMBD



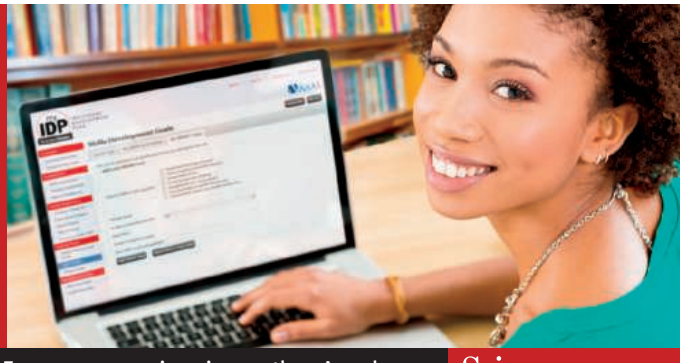
Time sequence of buckling silicon microwires.

Science Advances, the new, open-access journal from AAAS, is accepting papers for an exciting Special Series, Materials By Design, that showcases work in material science and engineering with potential global impact.

Submit your research at ScienceAdvances.org

Science Advances | AAAS
SIGNIFICANT RESEARCH, GLOBAL IMPACT

myIDP:
A career plan customized for you, by you.



For your career in science, there's only one Science

my IDP
Science Careers

Recommended by leading professional societies and the NIH

Features in myIDP include:

- Exercises to help you examine your skills, interests, and values
- A list of 20 scientific career paths with a prediction of which ones best fit your skills and interests
- A tool for setting strategic goals for the coming year, with optional reminders to keep you on track
- Articles and resources to guide you through the process
- Options to save materials online and print them for further review and discussion
- Ability to select which portion of your IDP you wish to share with advisors, mentors, or others
- A certificate of completion for users that finish myIDP.

Visit the website and start planning today!
myIDP.sciencecareers.org

Science Careers In partnership with:

FASEB · UCSF University of California San Francisco · Medical College of Wisconsin · Burroughs Wellcome Fund

Gel Documentation System

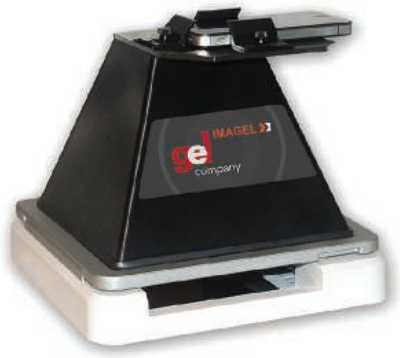
The HeroDoc Plus is a compact system for imaging gels and blots. The compact darkroom/hood assembly will sit comfortably on any laboratory bench within its small footprint. A unique lift-up hood and a built-in ultraviolet (UV) protection shield enable the user to do preparative work easily and safely. Should the user wish to raise the shield, an automatic cutoff switch will provide protection from any harmful effects of UV light. A high-sensitivity charge-coupled device (CCD) camera combined with a distortion free, software-controlled lens, ensures quality image capture from 10 ms up to 60 minutes. This is more than adequate for most fluorescent gel and blot image capture. Illumination comes from a massive 28 cm × 22 cm filter midrange transilluminator, while built-in white and blue light-emitting diodes (LEDs) provide epi-illumination as standard. Multilanguage, Herostore image capture and control software effortlessly enables the user to acquire images of their gels and blots.

Herolab
For info: +49-(0)-6222-5802-0
www.herolab.com

Noise-Free Microscope Camera

With the new Olympus UC90 microscope camera, it is now possible to maximize the information captured from life and materials science samples with ease and simplicity. The UC90 excels in capturing and documenting real-life details, while a 4K ultrahigh definition (UHD) mode supports scientists in overcoming the limitations of the oculars with the many benefits of complete on-screen operation. In-depth sample analysis is achieved without compromise, with the UC90's 9-megapixel, 1-inch charge-coupled device (CCD) color sensor. This not only provides a large field of view covering nearly all the sample area normally observed through the oculars, but the high resolution in combination with perfect color reproduction also retains the sample's every detail. Without the need to switch objectives to capture large sample structures, monitor operation is fast and efficient, allowing quick creation of detailed images that are ideal for documentation and accurate retrospective analysis.

Olympus
For info: +49-(0)-40-23773-5913
www.olympus-lifescience.com



Gel Imager

The Imagel Gel Doc system for iPhone or Android is the smart way to quickly grab your gel images. Just hook up your smartphone to the compact hood and start to collect images of all your gels quickly and easily. The Imagel can be used with three different light sources. Use the blue light-emitting diode (LED) transilluminator for DNA applications that use Green DNA, GelGren, SYBR Green, SYBR Safe, SYBR Gold, and for protein applications using LavaPurple. An ultraviolet transilluminator will let you work with AmberDNA, ethidium bromide, SYBR, Oriole, fluorescent gel stain, GelRed, SYPRO Ruby, Coomassie, Fluor Orange, and Krypton. Also, using a white light source you can capture images of proteins using Coomassie Blue, copper, silver, or zinc stains. The Imagel is very simple to use. Just snap a photo and save on your phone or upload to the cloud for hosting, sharing, and image analysis and annotation features.

Eikonix
For info: +44-(0)-1223-515440
www.eikonix.com

Plant Nucleic Acid Extraction Kit

The GF-1 Plant DNA extraction kit is designed for rapid and efficient purification of genomic DNA from a wide range of plant tissues. The purification is based on the usage of denaturing agents to provide lysis of tissue cells, denaturation of proteins, and the subsequent release of genomic DNA. Special buffers provided in the kit are optimized to enhance binding of DNA onto a specially treated glass filter membrane for efficient recovery of highly pure genomic DNA. The GF-1 will give yields of up to 20 μg of DNA. The genomic DNA is ready to use for routine molecular biology applications such as restriction enzyme digestion, polymerase chain reaction (PCR), Southern blotting, and DNA fingerprinting. Each kit contains buffer, wash buffer, elution buffer, and proteinase K.

Vivantis
For info: +44-(0)-1223-515440
www.vivantechnologies.com

Large-Scale Transient Transfection Medium

BalanCD Transfectory CHO is a cell culture medium for rapid, scalable production of recombinant proteins through transient transfection in Chinese hamster ovary (CHO) cells. The new medium is chemically defined, animal component free, and specifically designed to support sustained high growth with increased transfection efficiency that can yield gram-scale protein expression. Transient gene expression (TGE) has evolved into a cost-effective, rapid alternative to stable cell-line engineering for the production of recombinant proteins and antibodies needed for early-stage biopharmaceutical development activities. CHO cells are the most prevalent platform used for commercial production of biopharmaceuticals and are therefore viewed as preferential hosts for TGE. The challenge has been in obtaining protein yield of sufficient quantity and quality, leading many scientists to focus on human embryonic kidney (HEK) 293 cell transfection. The ability to obtain gram-scale yields by transient transfection in CHO cells is a real step forward toward cutting costs and development time for biotherapeutic research.

Irvine Scientific
For info: 800-577-6097
www.irvinesci.com

Electronically submit your new product description or product literature information! Go to www.sciencemag.org/about/new-products-section for more information.

Newly offered instrumentation, apparatus, and laboratory materials of interest to researchers in all disciplines in academic, industrial, and governmental organizations are featured in this space. Emphasis is given to purpose, chief characteristics, and availability of products and materials. Endorsement by *Science* or AAAS of any products or materials mentioned is not implied. Additional information may be obtained from the manufacturer or supplier.

AAAS 2016 ANNUAL MEETING | WASHINGTON, DC FEBRUARY 11–15

Global Science Engagement

AAAS, publisher of *Science*, thanks the sponsors and supporters of the 2016 Annual Meeting

European Commission

SUBARU

THE GEORGE WASHINGTON UNIVERSITY WASHINGTON, DC

RESEARCH COUNCILS UK

HELMHOLTZ ASSOCIATION

THE KAVLI FOUNDATION

for its generous support of the Science Journalism Awards

NANYANG TECHNOLOGICAL UNIVERSITY

Bristol-Myers Squibb

Johnson & Johnson INNOVATION

Institute for Basic Science

NATIONAL ACADEMY OF SCIENCES

SIMONS FOUNDATION

As of February 9, 2016

CELL SIGNALING TECHNOLOGY

EPIGENETICS:
DISCOVERY THROUGH VALIDATION

692 CST antibodies for epigenetic-related targets, including histone modifications, epigenetic regulators, and general transcription factors.

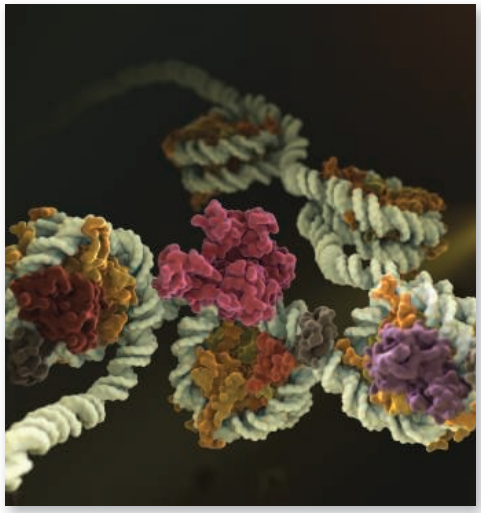
226 CST antibodies validated for ChIP according to ENCODE* Consortium guidelines.

Validated Tools for Discovery:

» SimpleChIP® Kits to facilitate Chromatin IP from cells and tissue.

» PTMScan® Kits and Services to enable MS-based discovery of methylated and acetylated proteins.

» Most ChIP-validated antibodies approved for additional applications like IHC, Flow, IF and WB.



Molecular model of chromatin.

Learn more at: www.cellsignal.com/epigeneticdiscovery

*Landt S.G. et al. (2012) *Genome Res.* 22, 1813–1831.

© 2015 Cell Signaling Technology, Inc. Cell Signaling Technology, CST, PTMScan, and SimpeChIP are trademarks of Cell Signaling Technology, Inc.

15PADEPIGNONE0079ENG_00

Cell Signaling TECHNOLOGY®

ScienceCareers online @sciencecareers.org



Science Careers Advertising

For full advertising details, go to ScienceCareers.org and click For Employers, or call one of our representatives.

Tracy Holmes
Worldwide Associate Director, *Science* Careers
Phone: +44 (0) 1223 326525

THE AMERICAS

E-mail: advertise@sciencecareers.org
Fax: +1 (202) 289 6742

Tina Burks
Phone: +1 (202) 326 6577

Nancy Toema
Phone: +1 (202) 326 6578

Online Job Posting Questions
Phone: +1 (202) 312 6375

EUROPE/INDIA/AUSTRALIA/NEW ZEALAND/REST OF WORLD

E-mail: ads@science-int.co.uk
Fax: +44 (0) 1223 326532

Sarah Lelarge
Phone: +44 (0) 1223 326527

Kelly Grace
Phone: +44 (0) 1223 326528

Online Job Posting Questions
Phone: +44 (0) 1223 326528

JAPAN

Katsuyoshi Fukamizu (Tokyo)
E-mail: kfukamizu@aaas.org
Phone: +81 3 3219 5777

Hiroyuki Mashiki (Kyoto)
E-mail: hmashiki@aaas.org
Phone: +81 75 823 1109

CHINA/KOREA/SINGAPORE/TAIWAN/THAILAND

Ruolei Wu:
Phone: +86 186 0082 9345
E-mail: rwu@aaas.org

All ads submitted for publication must comply with applicable U.S. and non-U.S. laws. *Science* reserves the right to refuse any advertisement at its sole discretion for any reason, including without limitation for offensive language or inappropriate content, and all advertising is subject to publisher approval. *Science* encourages our readers to alert us to any ads that they feel may be discriminatory or offensive.

ScienceCareers
FROM THE JOURNAL SCIENCE AAAS

ScienceCareers.org

UNIVERSITY OF LIVERPOOL

Faculty of Science and Engineering
Materials Innovation Factory (MIF)

Chair, Reader/Senior Lecturer, Lecturer in Materials Research

(Full-Time or Part-Time)

Post 1: Chair - Salary Negotiable

Post 2: Reader/Senior Lecturer Grade 9
£50,702 - £62,323 pa (or pro rata)

Post 3: Lecturer Grade 7/8
£32,600 - £49,230 pa (or pro rata)

The University is seeking to recruit to up to 10 academic positions in the Faculty of Science and Engineering in the broad area of materials research, distributed across the School of Physical Sciences (Chemistry, Physics & Mathematics), School of Engineering, the School of Electrical, Electronic Engineering and Computer Science, and the School of Environmental Sciences across the areas of Chemistry, Physics, Materials Science, Engineering, Computer Science. You should have an outstanding research track record, as demonstrated by publications and other relevant outputs. Applications will be considered from any area of materials research, but would be particularly welcomed in the areas of computational materials chemistry, polymer physics, rheology, robotics and/or automated metrology, biomaterials, materials processing and related areas. The posts will be aligned with the Materials Innovation Factory (MIF), a major new £68m research institute that is being established at the University. For the Chair or Readership positions you will be expected to demonstrate a significant track record of funding and a capacity for leadership in your field.

The University is an Athena SWAN Bronze Award holder and is committed to encouraging, developing and supporting women in their research and academic careers. We are working to create an inclusive environment which values a diverse workforce and we recognise that many individuals value flexibility in their work/life balance, therefore these posts may be taken up on a part-time (a minimum of 0.5fte) or full-time basis (including a job share).

Job Ref: A-590406/S **Closing date: 11 April 2016**

For full details, or to request an application pack, visit www.liv.ac.uk/working/job_vacancies/ or e-mail jobs@liv.ac.uk

Please quote job ref in all enquiries.

COMMITTED TO DIVERSITY AND EQUALITY OF OPPORTUNITY

Stonewall DIVERSITY CHAMPION
POSITIVE ABOUT DISABLED PEOPLE
LIFE CHANGING World Shaping









OAK RIDGE National Laboratory

Oak Ridge National Laboratory seeks Associate Laboratory Director for Energy & Environmental Sciences

The successful candidate will hold a PhD and have a proven scientific and organizational leadership record within field of expertise. The candidate should be able to demonstrate national or international recognition in science and should possess a reputation for development of scientific and organizational leaders. The Associate Laboratory Director (ALD) leads an organization of approximately 600 staff and $400M in annual funding for the energy and environmental science research in support of Department of Energy (DOE) missions. The ALD is a member of the senior management team, reporting to the ORNL Director. The ALD will provide leadership to expand scientific knowledge and develop innovative strategies to strengthen ORNL's leadership for delivering world class scientific solutions to environmental, engineering, and manufacturing dimensions of energy and climate. The ALD will provide scientific leadership of complex research programs spanning basic to applied disciplines with a focus on successful implementation and execution of scientific strategy. The ALD will work across directorates to provide leadership support and engagement for interdisciplinary institutes established to integrate diverse staff and world class resources across the Laboratory. Broad experience in helping to develop and implement strategies at the national and DOE program levels is highly desirable.

http://bit.ly/EESD_ALD



FEATURED EMPLOYER
ScienceCareers online @sciencecareers.org

Vienna University of Technology

Vienna Doctoral Programme on Water Resource Systems

The Centre for Water Resource Systems at the Vienna University of Technology announces competition for the third intake of doctoral candidates for the Doctoral Programme on Water Resource Systems. The programme is anticipated to host a total of 70 doctoral students over a period of 12 years. This is a dedicated programme of the Austrian Science Fund (FWF) that promotes doctoral research and education at the highest standards and provides excellent opportunities for cross-disciplinary research. International networking is facilitated by a mobility programme with a spectrum of attractive international partner institutions and a comprehensive guest scientist programme.

Seven PhD student positions are available in the following research themes related to Water Resource Systems:

- Flood-hydrology
- Aquatic microbiology
- Micro-meteorology
- Socio-hydrology
- Environmental economics
- Environmental engineering
- Soil moisture remote sensing
- Mechanics of structures

Applicants must have a Master's degree (or equivalent), preferably in a subject related to water resource systems. The working language of the programme is English. Students are expected to work across disciplines and in cooperation with others. A capacity and willingness to integrate and collaborate is essential.

The Programme provides a salary according to the FWF scheme (approx. EUR 20000/year net), together with health and social security benefits. There is also significant allowance for travel and research support. TU Wien is an Equal Opportunities Employer. The preferred starting date is Oct. 1, 2016.

Candidates should send a letter of application, a statement of research interests, a Curriculum Vitae, and copies of education certificates including transcripts of grades as a single .pdf file to: **office@waterresources.at**.

Application deadline is April 30, 2016. Short listed candidates will be invited to a selection seminar. Financial support towards travel expenses is available on request.

Information about the Doctoral Programme on Water Resource Systems may be viewed at **http://waterresources.at**

MAX-PLANCK-INSTITUT FÜR BIOPHYSIKALISCHE CHEMIE

KARL-FRIEDRICH-BONHOEFFER-INSTITUT
GÖTTINGEN

The **Department for Molecular Biology** (Director: Prof. Dr. Patrick Cramer) at the Max Planck Institute for Biophysical Chemistry invites applications for a

Scientist Position (m/f) "biological electron microscopy"

(Code Number 05-16)

The Max Planck Institute for Biophysical Chemistry is upgrading and expanding its facilities for high-end biological cryo-electron microscopy. A new FEI Titan Krios microscope equipped with K2 and Falcon-III direct detectors will be installed soon and used by several groups at the institute. The candidate will operate the new microscope and perform advanced single-particle cryo-electron microscopy. He/she will be involved in cutting-edge structural biology research projects and will train PhD students and postdoctoral researchers in sample grid preparation and data collection. The scientist should also advise on data processing and manage collaborations. He/she will have opportunities to develop and apply emerging EM-based structural biology techniques, and to extend our efforts towards cryo-electron tomography. The scientist will closely interact with the newly established Department of Structural Dynamics (Director: Holger Stark) that hosts electron microscopes at the institute.

We look for a team-oriented person with a PhD in the natural sciences and relevant experience. We offer a stimulating environment and a long-term perspective. The working language is English.

The Scientist Position is limited to two years, but intended to become permanent. The payment and benefits are based on the German TVöD guidelines.

The Max Planck Society is committed to increasing the number of individuals with disabilities in its workforce and therefore encourages applications from such qualified individuals.

Furthermore, the Max Planck Society seeks to increase the number of women in those areas where they are underrepresented and therefore explicitly encourages women to apply.

Please send your application including cover letter (explaining background and motivation), CV, list of publications, and contact information for two referees preferably via e-mail as single PDF file in relation to the code number 05-16 until March 15th, 2016 to: **ausschreibung05-16@mpibpc.mpg.de**

Max Planck Institute for Biophysical Chemistry
Department of Molecular Biology
Ms. Janine Koschmieder
Am Fassberg 11, D-37077 Göttingen

Phone +49 551 201-2800
Web http://www.mpibpc.mpg.de/cramer

Zertifikat seit 2006 audit familiengerechte hochschule

NC STATE UNIVERSITY

Analytical Chemistry Faculty Positions
Department of Chemistry

The Department of Chemistry at **NORTH CAROLINA STATE UNIVERSITY** is seeking to fill TWO tenure track faculty positions in the area of **Analytical Chemistry**. Of particular interest are those individuals developing innovative and sophisticated programs in measurement science to quantitatively characterize complex chemical and biological systems. These are open rank searches; however, preference will be given to candidates at the junior level whose research interests will complement existing programs in the Department, College of Sciences, and University.

Successful candidates are expected to establish a nationally and internationally recognized research program and to demonstrate strong interests and abilities in teaching at both the undergraduate and graduate levels. Candidates must possess a PhD and postdoctoral experience in Chemistry or a related scientific field to be considered for this position. Candidates should submit electronic copies of their curriculum vitae, research proposals, and a cover letter at: **http://jobs.ncsu.edu** under position number **00105377**. The candidates should also arrange to have three letters of recommendation sent on their behalf to Professor David C. Muddiman, Chair of the Search Committee. Review of applicant materials will begin on **March 15, 2016** and will continue until the positions are filled.

We welcome the opportunity to work with candidates to identify suitable employment opportunities for spouses or partners. AA/EOE. All qualified applicants will receive consideration for employment without regard to race, color, national origin, religion, sex, gender identity, age, sexual orientation, genetic information, status as an individual with a disability, or status as a protected veteran. Individuals with disabilities requiring disability-related accommodations in the application and interview process, please call 919-515-3148.

Bioengineering Faculty Position: Caltech Pasadena, CA, United States

The California Institute of Technology invites applications for a tenure-track professorial position in the Division of Biology and Biological Engineering. Bioengineering research at Caltech focuses on the application of engineering principles to the design, analysis, construction, observation and manipulation of biological systems, and on the discovery and application of new engineering principles inspired by the properties of biological systems.

Applications are invited in any area of bioengineering research. Candidates with strong commitments to research and teaching excellence are encouraged to apply. Initial appointments will be made at the assistant professor level for four years and are contingent upon completion of the Ph.D. degree.

The Bioengineering Option (http://www.be.caltech.edu) includes faculty from the Divisions of Biology and Biological Engineering (http://www.bbe.caltech.edu), Chemistry and Chemical Engineering (http://www.cce.caltech.edu), Engineering and Applied Science (http://www.eas.caltech.edu), and Physics, Mathematics, and Astronomy (http://www.pma.caltech.edu).

Please submit online application at **http://bbe.caltech.edu/Positions** and include a brief cover letter; curriculum vitae; relevant publications, a description of proposed research; and a statement of teaching interests. Instructions will be given for submission of letters of reference when you apply on-line.

Position will remain open until filled, however, **applications completed by March 31, 2016** will be assured of receiving full consideration.

EOE of Minorities/Females/Protected Vets/Disability.

ScienceCareers online @sciencecareers.org

EMBL

EMBL is a European-scale centre of excellence in life science research, services and training and one of the highest ranked scientific research organisations in the world. EMBL is international, innovative and interdisciplinary – its 1,600 employees, from over 80 nations, operate across six sites in Germany, France, Italy, Spain and the UK: the main laboratory in Heidelberg, and outstations in Hamburg; Grenoble; Monterotondo, near Rome; Barcelona; and Hinxton, near Cambridge (the European Bioinformatics Institute). Founded in 1974, EMBL is an inter-governmental organisation with a current annual budget of roughly 200 million Euro funded by public research monies from its member states. The cornerstones of EMBL's mission are: to perform basic research in molecular biology; to train scientists (internal and external) at all career levels; to offer vital services to scientists in the member states; to develop new instruments and methods in the life sciences and actively engage in technology transfer activities; to promote integration in European life science research; and to offer a platform for dialogue with the general public through science communication activities.

Director General

European Molecular Biology Laboratory (EMBL)

EMBL seeks an experienced, inspirational and dynamic leader to serve as its next Director General. The EMBL Director General (DG) reports to EMBL Council, the member state body that governs EMBL, and is responsible for the development of the overall policy and strategy across the organisation and for establishing consensus around EMBL's five-year programmes and corresponding funding frameworks. At a time of unprecedented opportunities in the life sciences, the future DG will work with EMBL Council to chart a strategic course for EMBL, to ensure it sustains and evolves its missions according to the needs of the scientific community in the member states, and to consolidate and strengthen its position as Europe's centre of excellence in life science research, services and training. The DG is responsible for the implementation and execution of Council decisions, and to provide accurate information on EMBL's activities and high-level scientific expertise to internal and external advisory bodies.

As the chief executive officer and legal representative of EMBL the DG guides and oversees the evolution of EMBL's role, missions and programmes according to the needs of the scientific community and broader European society with respect to the molecular life sciences. The DG conducts EMBL activities with the aim of achieving the full potential of the Laboratory and supporting the life sciences in Europe for the benefit of all stakeholders. The DG is responsible for overall leadership, strategic direction and management. He/she provides intellectual leadership for the multidisciplinary and international community of EMBL staff and fellows. The DG, assisted by the EMBL Directorate and Senior Management, has overall responsibility for the Laboratory's day-to-day operations and the performance of all parts of the organisation. The DG is the spokesperson for EMBL and serves as an advocate and communicator with all stakeholders and interested parties including the scientific community, policy makers, industry groups, funding organisations, the media and the general public.

Candidates for this position will have:

- an outstanding record in research and service provision in any area of molecular life science;
- a broad interest in and understanding of the molecular life sciences;
- an excellent overview of the European life science research and policy landscape;
- a proven record of senior management experience with significant experience, preferably international, in research and academic administration;
- a leadership style that is both inclusive (participatory) and directive;
- a demonstrated record of successful fundraising, programme development, faculty recruitment and mentoring, and organisational management;
- effective communication skills and the ability to interact and negotiate productively with many categories of people at different levels, both inside and outside EMBL;
- fluent written and spoken English, other member state languages, in particular German and French, are an advantage.

APPLICATION INSTRUCTIONS

Applications should be submitted as a single pdf-file containing a letter of motivation, short CV, evidence of the required leadership skills, and a list of 20 key research publications, to: **applications.embl@mpibpc.mpg.de** before April 30, 2016.

www.embl.org

By **Roc Ordman**

Room for a new generation

Back in the 1980s, when I began my research on human aging, I believed that within the next few decades we would find a way to live 300 years with healthy minds and bodies. I optimistically planned to hold a professor position for about 30 years, retire for 5 years, go back to school for a fresh education for 4 years, and start a new career for 20 more—repeating this cycle many times. But a year ago, when I was 66 years old, the liberal arts college where I had spent most of my career offered me a generous retirement package. By then, no longer certain of reaching 300, I was happy with my relatively long career. Nonetheless, being presented with the option to retire took me by surprise, and I was dismayed to be asked to leave.

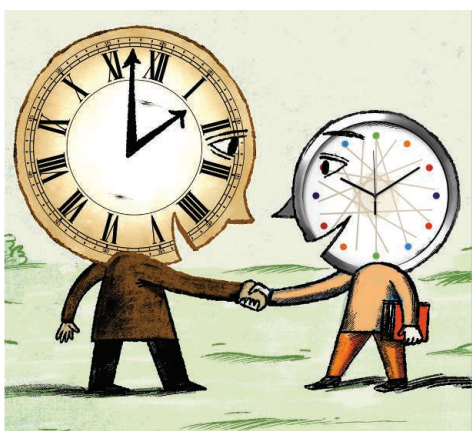
My first struggle was whether to accept the offer. "Should I abandon a well-paid, tenured teaching position that I dearly love?" I asked myself. I would miss meeting and teaching interesting new students each year. But during the past few years, I had read so much about the scarcity of professor positions that I knew that some of those students I loved teaching, and many others, were now talented young scientists who wanted my job. I also knew they would cost my institution, which I greatly value, far less than I did.

The offer, which was presented to me as "the opportunity to do the many other things you have wanted to do," had its appeal. I would be able to devote myself to research on the human health span without the obligations of teaching and the administrative duties connected with being a faculty member. And I still felt energetic and ready to tackle new career challenges.

The conditions also seemed right. My personal financial situation was robust enough that I could make ends meet if I retired. As for research, I mostly wanted to pursue clinical trials, which would not require lab space. I negotiated access to the institutional review board for clinical trial approval, and the college also agreed to continue managing my research funds. I signed the retirement agreement.

What surprises lay ahead of me!

I missed being in a classroom full of enthusiastic students even more than I had expected. To fill the void, I became a substitute science and math teacher in local public schools. Another challenge was finding ways to stay physically and mentally engaged now that I wasn't going to college every day. I started taking yoga, karate, and singing lessons and spending more time reading science, nutrition, and consciousness journals.



"My current approach is to team up with a younger professor."

But finding grants for the research I want to do has proved to be the greatest struggle. The college has a grants officer, but she is busy assisting current faculty members, so I am on my own. And although there are many grant sources designated for young scientists, there are few for older ones, especially retirees, who are taking new directions. Seeking just $200,000 to run a clinical trial on a cancer treatment has been an ongoing struggle.

My current approach is to team up with a younger professor who agreed to be my co-principal investigator on a grant proposal. We are still waiting to find out whether we will receive funding, but even though the odds are long, I feel that partnering has made the proposal all the stronger.

Finding where I fit in the scientific community and how I can best continue to contribute has been difficult—and I am not alone. With so many senior faculty members nearing retirement age but not yet ready to abandon science, it would be wonderful if institutions, granting bodies, and scientific societies would recognize what we have to offer and give us more support. They could, for example, set up grant centers, job opportunity and consulting services, and social networks for people like us. Ultimately, if senior scientists partner with the younger generation while also leaving them room to develop their own careers, it could benefit us all. ■

Roc Ordman is a professor emeritus of chemistry and biochemistry at Beloit College in Wisconsin. For more on life and careers, visit sciencecareers.org. Send your story to SciCareerEditor@aaas.org.

ILLUSTRATION: ROBERT NEUBECKER

Downloaded from on February 18, 2016

Published by AAAS